Durham University

Durham E-Theses

Chemical and Photophysical Behaviour of -Extended Tropyliums

PROMEET SAHA

How to cite:

SAHA, PROMEET (2023) Chemical and Photophysical Behaviour of -Extended Tropyliums. Doctoral thesis, Durham University.

Use policy

The full-text may be used and/or reproduced, and given to third parties in any format or medium, without prior permission or charge, for personal research or study, educational, or not-for-profit purposes provided that:

- a full bibliographic reference is made to the original source
- a https://etheses.durham.ac.uk/id/eprint/15347/ is made to the metadata record in Durham E-Theses
- the full-text is not changed in any way

The full-text must not be sold in any format or medium without the formal permission of the copyright holders.

Please consult the full Durham E-Theses policy for further details.

Academic Support Office, The Palatine Centre, Durham University, Stockton Road, Durham, DH1 3LE
e-mail: e-theses.admin@durham.ac.uk Tel: +44 0191 334 6107
https://etheses.durham.ac.uk

Durham University

Department of Chemistry

Chemical and Photophysical Behaviour of π-Extended Tropyliums

Promeet K. Saha

A Thesis Submitted for the Degree of Doctor of Philosophy

September 2023

Dedicated to my loving parents

Mousumi Kar Saha

Bratin Saha

Table of Contents

Abstract

Non-benzenoid annulenes have long fascinated organic chemists, due to their chemical properties, aromaticity, and photophysical behaviour. When incorporated into a polycyclic aromatic framework, such non-hexagonal rings can give rise to nonplanar structures with modified optical properties and improved solubility compared to planar, defect-free graphene.

Among non-benzenoid annulenes, the tropylium cation has been of special interest, due to its unique blend of reactivity (owing to its positive charge) and stability (a result of its aromaticity). Indeed, this cation has found wide utility as a versatile ligand[1], stimulus-responsive dye[2], and an organocatalyst.[3] Yet, reports of polycyclic aromatics featuring this heptagonal annulene are sparse.

This Thesis employs tropylium and its neutral, nonaromatic homologue, cycloheptatriene (Figure 1) as key structural motifs within an extended π-framework to gain fundamental insights into the electronic and optical properties of non-benzenoid and charged polycyclic aromatics. We find that judicious engineering of strain into the framework of sterically overcrowded tropyliums can cause its aromaticity to rupture, forming an "aromatic-to-nonaromatic" equilibrium at room temperature.[4] Moreover, modifying the conjugation length in a series of cycloheptatriene-rotors was found to vastly alter their photoluminescence properties, allowing for new modes of chemical reactivity.[5] We also report our synthetic forays toward a highly warped redox-active warped nanographene, as well as preliminary findings on the excited-state proton transfer dynamics in a series of hydroxybenzotropyliums.

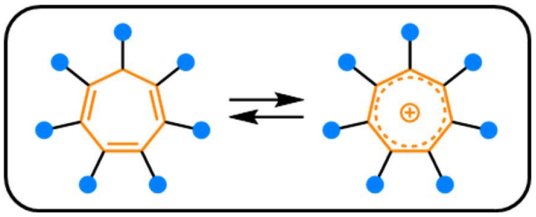

Figure 1. Substituted cycloheptatrienes and tropyliums.

[1]. T. Murahashi, M. Fujimoto, M. A. Oka, Y. Hashimoto, T. Uemura, Y. Tatsumi, Y. Nakao, A. Ikeda, S. Sakaki and H. Kurosawa, *Science*, 2006, **313**, 1104–1107

[2]. U. P. N. Tran, G. Oss, D. P. Pace, J. Ho and T. V. Nguyen, *Chem. Sci.*, 2018, **9**, 5145–5151.

[3] D. J. M. Lyons, R. D. Crocker and T. V. Nguyen, *Chem.—Eur. J.*, 2018, **24**, 10959–10965.

[4] P. K. Saha, A. Mallick, A. T. Turley, A. N. Bismillah, A. Danos, A. P. Monkman, A. J. Avestro, D. S. Yufit and P. R. McGonigal, *Nature Chem.*, 2023 **15**, 516–525.

[5] A. T. Turley, P. K. Saha, A. Danos, Aisha N. Bismillah, A. P. Monkman, D. S. Yufit, B. F. E. Curchod, M. K. Etherington, and Paul R. McGonigal, *Angew. Chem. Int. Ed.*, 2022, **61**, e202202193.

Declaration

The scientific work described in this Thesis was carried out in the Chemistry Department in Durham University between January 2020–December 2022 and at the Chemistry Department in the University of York between January 2023–September 2023. Unless otherwise stated, it is the work of the author and has not been submitted in whole or in support of an application for another degree or qualification at Durham University or any other University or institute of learning.

Signed:

Date: 15th September 2023.

Conferences Attended and Presentations Given

14. Chem@York Conference. York, UK, 2023 | **Oral Presentation.**

13. The 5th International Symposium on the Synthesis and Application of Curved Organic π-Molecules and Materials (CURO- π^5). Prague, Czechia, 2023 | **Poster Presentation.**

12. International Symposium on Macrocyclic and Supramolecular Chemistry (ISMSC). Reykjavik, Iceland, 2023 | **Poster Presentation.**

11. RSC Organic Division North East Regional Meeting. Newcastle, UK, 2023 | **Poster Presentation.**

10. Macrocyclic and Supramolecular Chemistry (MASC). Nottingham, UK, 2022 | **Poster Presentation.**

9. RSC Organic Division Annual Poster Symposium. London, UK, 2022 | **Invited Poster Presentation.**

8. Early Career MASC Meeting, Loughborough. UK, 2022 | **Poster Presentation.**

7. International Conference on Synthetic Metals (ICSM). Glasgow, UK, 2022 | **Attended.**

6. International Symposium on Novel Aromatics (ISNA). Warsaw, Poland, 2022 | **Poster Presentation.**

5. Durham Chemistry Annual Postgraduate Symposium. Durham, UK, 2022 | **Oral Presentation.**

4. Maximising the rISC. Online, 2021 | **Attended**.

3. ChiralMat. Online, 2021 | **Attended**.

2. RSC Macrocyclic and Supramolecular Chemistry Meeting. Online, 2020 | **Attended**.

1. Chiral Functional Materials Symposium. London, UK, 2019 | **Attended**.

Acknowledgements

"*Il fault imaginer Sisyphe heureux.*"

"*One must imagine Sisyphus happy.*"

Albert Camus, *The Myth of Sisyphus*

First and foremost, I would like to thank Dr. Paul McGonigal for being the best mentor and teacher I could ask for. You granted me the independence to explore a rich and fascinating area of chemistry and provided me with all the resources I ever needed. Thank you for believing in me and giving me the opportunity to be a part of the McGonigal group—it has truly been a privilege to learn from you and traverse the world of academia under your guidance. I always aspire to honor the exceptionally high standards you set, and I will carry your invaluable lessons with me for life.

During my time in the McGonigal group, I have worked with some exceptionally talented scientists, whose contributions have been instrumental to the work described in this Thesis. I outline their contributions at the beginning of each chapter, but I would like to echo my gratitude to Dr. Marc Etherington, Dr. Andrew Danos, and Dr. Basile Curchod for helping a team of organic chemists understand complex photophysical measurements and computational results. I would also like to thank the technical staff at the Universities of Durham and York for their continual support, especially Dr. Juan Aguilar Malavia for running an exceptional NMR service and Dr. Dmitry Yufit for being the greatest crystallographer of all time.

I knew I had big shoes to fill when I started my PhD, because I was taking over Dr. Andrew "Big T" Turley's projects. I was extremely fortunate to have shared a fume hood with you because it gave me the opportunity to witness the incredible pace and dexterity with which you work. I have especially fond memories of our legendary lockdown feasts and summer walks. Dr. Phil Hope also graced my time in Durham with his helpful advice and countless laughs shared over countless cups of Musgrave room coffee. On the occasions where coffee did not suffice, I could always rely on Dr. Matt Kitching to unwind over a pint and rediscover my passion for the weird and wonderful world of chemistry. My wider chemistry education would be incomplete without my daily conversations with our exceptional team of postdocs. A special

thanks go to Dr. Senthil Kumar Kabali and Dr. Abhijit Mallick, and Dr. Rabia Ayub, whose vast breadth of knowledge and technical skills continue to amaze and inspire me.

I would be remiss not to thank the wonderful friends I have made along the way, whose support has been indispensable. Will Maturi, thank you for being a persistent source of joy and laughter these past few years, and for reminding me to look after myself. Your encyclopedic knowledge of music and talent for games ensured that there was not a day was spent in the lab, in the office, or at the pub that wasn't filled with enjoyment and camaraderie. For that, your seemingly endless kindness, and for the countless extraordinary memories, I thank you. Dr. Aisha Bismillah, I would like to thank you not only for your scientific contributions to this Thesis, but also for proofreading and offering advice on my applications. Your dedication and thoughtfulness have fostered a truly wholesome group culture that I have always cherished. I would also like to thank Juliet/Julia Barclay for reminding me to be kinder not only to others but also to myself. Your friendship has kept me sane these fast few months, and our daily lunchtime crosswords have provided some very welcome escapism. All members (both past and present) of the McGonigal, Avestro, and Walton groups; my CG233 and E214 families have also been tremendous friends and coworkers. Thank you for the amazing times! My PhD has been an incredible journey that I could not have completed without the support of my dearest friends, Alex, Bella Bearcroft, Bella Brown, Char, Emma, Imi, Mat, Oscar, Owen, Theo, Tom, and Will. Thank you for the adventures we had, I look forward to many more.

An honorable mention goes to Simon & Garfunkel, the Kinks, Hendrix, Vaughan, the Beatles, the Stones, Bowie, the White Stripes, Fleetwood Mac, Dylan, Mitchell, King, Joel, the Honeydrops, Próxima Parada, and the countless other artists who kept me singing and dancing through the many long hours spent at my fume hood or in front of my computer screen.

Ultimately, I owe all I have ever accomplished to my parents. Thank you for your enduring love and support; for celebrating my victories and consoling me during my losses. I am forever grateful for the sacrifices you have made to give me all the opportunities I have had. I love you both, and I dedicate this Thesis to you.

List of Abbreviations

Ac	Acetyl
ACID	Anisotropy of the induced current density
ACQ	Aggregation-caused quenching
AIE	Aggregation-induced emission
APCI	Atmospheric pressure chemical ionisation
ASAP	Atmospheric solids analysis probe
ASE	Aromatic stabilisation energy
BLA	Bond length alternation
BTZ	Benzothiazole
Cbz	9*H*-Carbazole
CHT	Cycloheptatriene
cod	Cyclooctadiene
Cp	Cyclopentadienyl
CPL	Circularly polarised luminescence
CSA	Covalent self-sorting assembly
Cy	Cyclohexyl
d	Doublet
dba	Dibenzylideneacetone
DBU	1,8-Diazabicycloundecene
DCB	Dichlorobenzene
DCC	Dicyclohexylcarbodiimide
DCE	1,2-Dichloroethane
DDQ	2,3-Dichloro-5,6-dicyano-1,4-benzoquinone
DFT	Density functional Theory
DMAP	*N*,*N*-Dimethylaminopyridine
DMF	Dimethylformamide
DMSO	Dimethylsulfoxide
DPE	Diphenylethylene
DSC	Differential scanning calorimetry
DT	Dewar tropylium
EDDB	Electron density of delocalised bonds
ESAA	Excited-state antiaromaticity
ESI	Electrospray ionisation
ESIPT	Excited-state intramolecular proton transfer
Et	Ethyl
EXSY	Exchange spectroscopy
GIMIC	Gauge including magnetically induced current
GNR	Graphene nanoribbon
GS	Ground state
HAB	Hexaarylbenzene

HBC	Hexabenzocoronene
HBP	Hexabenzoperylene
HBT	Hydroxybenzotropylium
HF	Hartree–Fock
HMBC	Heteronuclear multiple bond correlation
HOMA	Harmonic oscillator model of aromaticity
HOMO	Highest occupied molecular orbital
HPB	Hexaphenylbenzene
HR	High resolution
HSQC	Heteronuclear Single Quantum Coherence
HT	Hydroxytropylium
ICT	Intramolecular charge transfer
IEFPCM	Integral equation formalism variant polarisable continuum model
IOCD	Intramolecular oxidative cyclodehydrogenation
^{i}Pr	Isopropyl
IR	Infrared
IRC	Internal reaction coordinate
IRF	Instrument response function
ISE	Isomerisation stabilisation energy
LC	Liquid crystal
LR	Linear response
LUMO	Lowest occupied molecular orbital
m	Multiplet
MCH	Methylcyclohexane
M.P.	Melting point
*m*CPBA	*meta*-cloroperoxybenzoic acid
Me	Methyl
Me_2CO	Acetone
MeCN	Acetonitrile
MO	Molecular orbital
Ms	Methanesulfonyl
MS	Mass spectrometry
MT	Möbius tropylium
Naph	Naphthyl
^{n}Bu	*n*-Butyl
NCD	Norcaradiene
NEA	Nuclear ensemble approach
$Ni(dppp)_2Cl_2$	1,3-bis(diphenylphosphino)propanenickel (II) chloride
NICS	Nucleus independent chemical shift
NMR	Nuclear magnetic resonance
NOESY	Nuclear Overhauser effect spectroscopy
OFET	Organic field-effect transistor

OLED	Organic light-emitting diode
PAH	Polycyclic aromatic hydrocarbon
PDI	Perylenetetracarboxydiimide
PES	Potential energy surface
Ph	Phenyl
PIFA	Phenyliodine bis(trifluoroacetate)
PIQ	Photocyclisation-induced quenching
PLQY	Photoluminescence quantum yield
PO	Propylene oxide
POM	Polarised optical microscopy
q	Quartet
RACI	Restricted access to a conical intersection
RIM	Restricted intramolecular motion
s	Singlet
SM	Starting material
t	Triplet
TADF	Thermally activated delayed fluorescence
^{t}Bu	*tert*-Butyl
TCSPC	Time-correlated single photon counting
TDDFT	Time-dependent density functional theory
TEM	Transmission electron microscopy
Tf	Trifluoromethanesulfonyl
TFA	Trifluoroacetic acid
TfOH	Triflic acid
THF	Tetrahydrofuran
THS	Tetrahexylsilyl
TLC	Thin-layer chromatography
TP	Tropylium
TPE	Tetraphenylethylene
TosMIC	Toluenesulfonylmethylisocyanide
TS	Transition state
Ts	*para*-Toluenesulfonyl
UV	Ultraviolet
VT	Variable temperature
XPhos	Dicyclohexyl[2′,4′,6′-tris(propan-2-yl)[1,1′-biphenyl]-2-yl]phosphane
XRD	X-ray diffraction
μW	Microwave

Note: conventional abbreviations for units, physical quantities and stereochemical terms are not included here.

General Experimental Methods

Materials: All reagents were purchased from commercial suppliers (Sigma-Aldrich, Acros Organics, Fluorochem or Alfa Aesar) and used without further purification.

Instrumentation and Analytical Techniques: Analytical thin-layer chromatography (TLC) was performed on neutral aluminium sheet silica gel plates (Fluka, 60778-25EA) and visualised under UV irradiation (254 nm). Nuclear magnetic resonance (NMR) spectra were recorded using a Bruker Advance (III)-400 (^{1}H 400.130 MHz and ^{13}C 100.613 MHz), Varian Inova-500 (^{1}H 500.130 MHz and ^{13}C 125.758 MHz), Varian VNMRS-600 (^{1}H 600.130 MHz and ^{13}C 150.903 MHz) a Varian VNMRS-700 (^{1}H 700.130 MHz and ^{13}C 176.048 MHz), or a Joel ECS-400 spectrometer (^{1}H 400 MHz and ^{13}C 101 MHz), at a constant temperature of 298 K unless otherwise stated. For variable-temperature (VT) measurements, operating temperatures were calibrated using an internal calibration solution of MeOH and glycerol. Chemical shifts (δ) are reported in parts per million (ppm) relative to the signals corresponding to residual non-deuterated solvents $CDCl_3$: δ / ppm = 7.26 or 77.16, CD_2Cl_2: δ = 5.32 or 54.00, CD_3CN: δ = 1.94, 1.32 or 118.26, $(CD_3)_2CO$: δ = 2.50 or 39.5. Coupling constants (J) are reported in Hertz (Hz). ^{13}C NMR Experiments were proton-decoupled, whereas ^{19}F NMR experiments are coupled and referenced to an internal standard, hexafluorobenzene (HFB, δ = 164.99 ppm), unless otherwise stated. Assignments of ^{1}H and ^{13}C NMR signals were accomplished by two-dimensional NMR spectroscopy (COSY, NOESY, HSQC, HMBC). NMR spectra were processed using MestReNova version 14. Data are reported as follows: chemical shift; multiplicity; coupling constants; integral and assignment. Low-resolution atmospheric solids analysis probe (ASAP)-MS were performed using a Waters Xevo QTOF equipped with an ASAP. Atmospheric pressure chemical ionisation (APCI)-MS was performed using a Bruker compact time-of-flight mass spectrometer. High-resolution electrospray (HR-ESI) and ASAP (HR-ASAP) mass spectra were measured using a Waters LCT Premier XE high resolution, accurate mass UPLC ES MS (also with ASAP ion source). Atmospheric Melting points (M.P.) were recorded using a Gallenkamp (Sanyo) apparatus and are uncorrected. UV-Vis-NIR absorbance spectra of solution samples were recorded using an Agilent Technologies Cary Series UV-vis-NIR spectrophotometer at room temperature. Dynamic light scattering was performed using a Zetasizer Nano. X-ray single crystal data were collected at 120 K unless

otherwise stated, on an Agilent XCalibur (Sapphire-3 CCD detector, finefocus sealed xv tube, graphite monochromator, λMoKα radiation, λ=0.71073 Å) diffractometer equipped with a Cryostream (Oxford Cryosystems) open-flow nitrogen cryostat. Structures were solved by direct method and refined by full-matrix least squares on F2 for all data using Olex23 and SHELXTL4 software. All non-hydrogen atoms were refined anisotropically and hydrogen atoms were placed in the calculated positions and refined in riding mode. Steady-state photoluminescence of films and solutions were measured using Jobin Yvon Fluoromax and Fluorolog with machine specific calibration curves. The low temperature and temperature-dependent photoluminescence spectra were measured using a Janis Research Co. Inc. nitrogen filled cryostat. Thus, at low temperature, films were in a nitrogen atmosphere and solutions in a sealed long-neck cuvette. Time-correlated single photon counting experiments were conducted using a Ti:Sapphire laser (Mira 900, Coherent) with a narrow pulse width (> 2 ps), which was frequency tripled (using a beta barium borate (BBO) crystal) to 293 nm. The beam was vertically polarised, initially by rotating the horizontal beam and then passing it through two separate Glan-Thompson polarisers, to ensure it was highly polarised. The sample, either a solution in a quartz cuvette at room temperature or a longnecked cuvette in a cryostat for temperature dependent measurements, was illuminated by this beam. Emission collection optics, perpendicular to the excitation beam, allowed the emission to pass through a polariser and a double monochromator (Acton Spectra Pro 2300i) before being collected by a micro-channel plate which covers a total time of with a detection channel width of 3.26 ps. Microwave-assisted reactions were carried out with a Biotage Initiator+ Microwave System with Robot Eight in Biotage microwave vials.

Thesis Layout

Chapter 1 introduces the concept of aromaticity in both benzenoid and non-benzenoid molecules (especially tropyliums). The discussion is then extended to the synthesis of polycyclic aromatic hydrocarbons, as well as their properties. This chapter ends with the latest advances in tropylium-embedded polycyclic aromatics. Chapters 2 and 3 are each presented in the form of articles which have recently been published in peer reviewed journals. No attempts have been made to rewrite this work out of context, however minor aesthetic alterations have been made in the interest of consistency throughout the Thesis, and footnotes have been added to provide further experimental details. The corresponding original papers are reproduced in their original format in the Appendix. Chapter 4 presents our on-going attempts to synthesise a redox-active tropylium-embedded warped nanographene and its partially fused helical derivative. Finally, Chapter 5 describes preliminary findings in the investigation of the excited-state proton transfer dynamics of a series of hydroxybenzotropyliums.

CHAPTER 1 |

BENZENOID AND NON-BENZENOID POLYCYCLIC AROMATIC HYDROCARBONS: SYNTHESIS, PROPERTIES, AND APPLICATIONS

Synopsis

This introductory chapter begins with a discourse on the concept of aromaticity in both benzenoid and non-benzenoid molecules (focusing predominantly on cycloheptatrienes and tropyliums), as well as a discussion on evidence for its existence. Following this, the synthesis of polycyclic aromatic hydrocarbons is discussed: the benefits and drawbacks of both traditional and newer synthetic routes to both planar and nonplanar polycyclic aromatics are assessed. The nuanced approaches taken to deviate molecules from planarity are explored in detail. Finally, recent advances in the synthesis of tropylium-containing polycyclic aromatics—a rare class of molecules, whose electronic, optical, and structural properties remain largely unexplored—are presented. In the interest of brevity and relevance, these discussions are limited to polycyclic aromatic hydrocarbons that are not doped with heteroatoms.

1.1. Aromaticity

Traditionally, aromaticity refers to the extraordinary stabilisation energy originating from the delocalisation of π-electrons over multiple atoms in planar, cyclic systems. The most common aromatic structure is benzene (C_6H_6). Though first isolated by Faraday as early as 1825[1], the famous cyclic structure of benzene was only proposed forty years later by Kekulé (Figure 1.1a).[2] Despite the elucidation of its structure, benzene's chemical behaviour remained enigmatic until the development of electron theory and molecular orbital (MO) calculations.

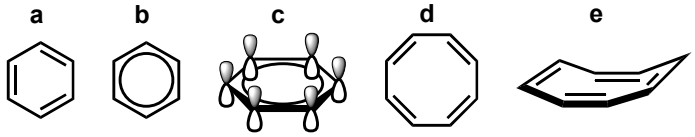

Figure 1.1. a) Kekulé's proposed structure of benzene; **b)** Delocalisation of π-electrons over all carbon atoms in benzene; **c)** Overlap of p-orbitals that allows for this conjugation; **d)** Theoretical, planar structure of the fully conjugated, antiaromatic cyclooctatetraene (COT); **e)** the actual, 'tub-shaped' ground-state conformer of COT.

In 1931, Hückel's seminal work on the topic laid the foundation for a quantum mechanical treatment of aromaticity.[3] His principle of σ–π separability introduced a simple method of measuring π-electron energies in conjugated systems. He discovered that cyclic compounds with $4n+2$ π-electrons (where n is an integer) had lower-energy HOMOs than the corresponding acyclic polyenes, which explained benzene's exceptional stability (Figure 1.1b–c). In contrast, unsaturated rings with $4n$ π-electrons are *anti*aromatic; they assume non-planar geometries that hinder p_z orbital conjugation, as this has a destabilizing effect (Figure 1.1d–e). These findings were succinctly summarised by Doering and others in the form of Hückel's "$4n+2$" rule in 1951.[4] It follows that a structure exhibits aromatic character if: i) it is cyclic; ii) all atoms involved are coplanar; iii) all atoms in the ring participate in electron delocalisation by having by having p-orbitals or a lone pair of electrons, which can be donated into the ring system; and iv) if it has $4n+2$ π-electrons.

While Hückel's rule accurately predicts aromaticity for monocyclic systems, its validity is limited for polycyclic aromatic hydrocarbons (PAHs), such as pyrene and coronene (Figure 1.2a–b), which are aromatic despite disobeying the $4n+2$ rule. The

most successful attempt to extend Hückel's rule to PAHs was made by Clar in 1972.[5] Clar's π-sextet rule states, the resonance structure with the most disjoint aromatic π-sextets is the most representative of the structure's chemical reactivity and aromaticity. Application of this rule to phenanthrene (Figure 1.2c–d) predicts that the outer rings have enhanced local aromaticity relative to the central ring, as confirmed by experimental data and theoretical calculations.[6,7]

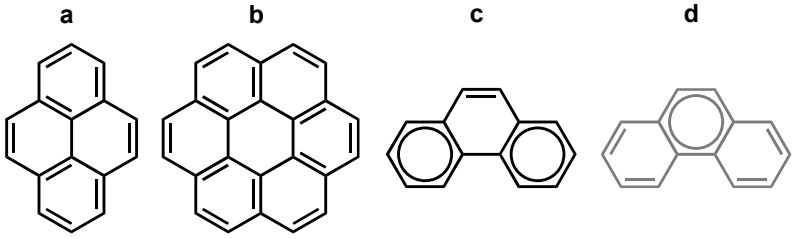

Figure 1.2. (a) Pyrene (16 π-electrons); **(b)** Coronene (24 π-electrons); **(c)** Clar's structure of phenanthrene; **(d)** The less accurate representation of phenanthrene.

1.1.1. Experimental Evidence for Aromaticity

Though (anti)aromaticity is a widely studied concept, it is one that is difficult to observe. Attempts have been made to measure the aromatic stabilisation energy (ASE) of small, monocyclic annulenes such as benzene directly through calorimetric experiments that measure heats of hydrogenation.[8] However, due to variations in experimental design and reference compounds, the experimentally-measured values range from 90–150 kJ mol^{-1}. When working with larger systems with more structural complexity, often the only option available to chemists is to assess the consequences of aromaticity on the chemical structure, reactivity, spectroscopic properties, and electronic properties of a molecule.[9]

In monocyclic systems, X-ray crystallography reveals important structural parameters (such as bond length equalisation and planarisation), which indicate aromaticity in monocyclic systems.[10] However, polycyclic systems often display nonplanarity and significant bond length alternation.[11] In such cases, comparing the chemical inertness and reactivity of different rings offers information about their local aromaticity. Landmark examples include the Diels–Alder reaction of anthracene with dienophiles, as well as the hydrogenation of phenanthrene, both of which proceed regioselectively at the 9,10-positions.[12,13]

One of the most useful diagnostic probes for aromaticity is that aromatic molecules experience a diatropic ring current when placed in a magnetic field, while antiaromatic molecules experience a paratropic ring current.[14] The former generates a magnetic field that *opposes* the external magnetic field inside a ring, while the latter adds to it. As a result, chemical environments immediately outside aromatic rings are deshielded (*i.e.*, they resonate at higher frequencies), while environments inside annulenes are shielded (*i.e.*, they resonate at lower frequencies) compared to non-aromatic molecules. This phenomenon is responsible for the unusually low-frequency ^{1}H NMR resonances of the central –CH_2 protons in [7]paracyclophane[15] (Figure 1.3a), as well as the large difference in chemical shifts between protons located inside and outside the carbon framework of [18]annulene (Figure 1.3b).[16]

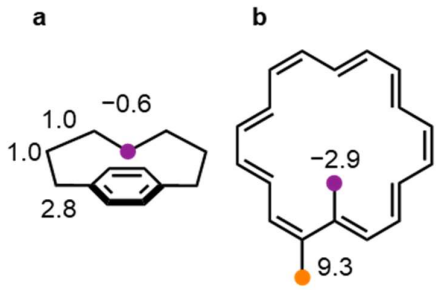

Figure 1.3. Chemical shifts (ppm) of selected protons in **(a)** [7]paracyclophane, and **(b)** [18]annulene.

NMR-based methods have also been used to probe the aromaticity of more complex systems; Anderson has leveraged this magnetic property to confirm the presence of global aromatic and antiaromatic ring currents in a series of giant porphyrin macrocycles.[17] A representative example (***c*-P6[b$_6$]**) is shown below in Figure 1.4. The pyridyl protons of the macrocycle's template (**α** and **β**), as well as the tetrahexylsilyl (THS) groups appended to the porphyrin moieties serve as the indicators for aromaticity in this structure. The 3,5-bis(tetrahexylsilyl)phenyl moieties undergo slow rotation, such that the THS groups are effectively 'locked' pointing inside (THS_{in}) or outside (THS_{out}) the macrocycle (Figure 1.4b). In ***c*-P6[b$_6$]$^{2+}$**, which is globally aromatic (82 π-electrons), the pyridyl and THS_{in} protons experience a strong shielding effect, with chemical shifts (δ) of ~1 and −0.5 ppm respectively.

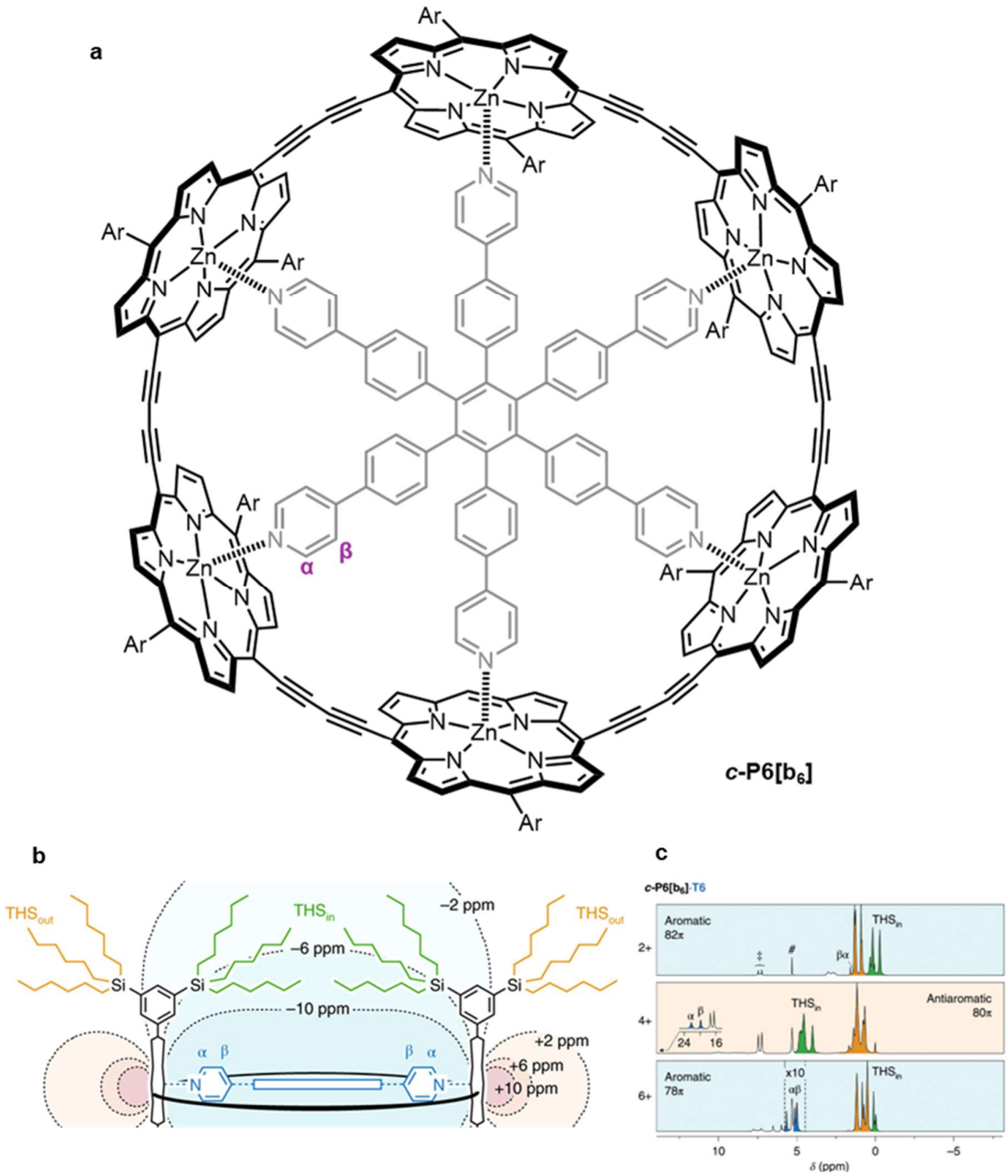

Figure.1.4. Assessing the global aromaticity of a porphyrin macrocycle, using the magnetic properties of aromatic molecules. **a)** the chemical structure of the macrocycle ***c*-P6[b$_6$]**, where **Ar** = 3,5-bis(tetrahexylsilyl)phenyl; **b)** Impact of an external magnetic field on the chemical shifts of the tetrahexylsilane (THS) groups pointing inside and outside the porphyrin ring; **c)** Changes in the chemical shifts (^{1}H NMR / 500 MHz / CD_2Cl_2 / 298 K) of the THS groups and pyridyl protons (**α**, **β**) upon successive two-electron oxidations that toggle between the aromatic and antiaromatic states of the macrocycle. Panels **b** and **c** were reproduced from reference **17**.

Upon a two-electron oxidation of ***c*-P6[b$_6$]$^{2+}$** to ***c*-P6[b$_6$]$^{4+}$**, concomitant with global antiaromaticity (80 π-electrons) of the macrocycle, these protons are deshielded due to the paratropic ring current. The pyridyl protons now resonate with $\delta \sim 20$ ppm, while the THS_{in} environments resonate with $\delta \sim 5$ ppm. Upon further oxidation to ***c*-P6[b$_6$]$^{6+}$**, the macrocycle recovers its aromaticity, and the shielding effect within the aromatic ring shifts the pyridyl and THS_{in} resonances to ~5 and 0 ppm respectively.

The following year, Anderson also experimentally determined the aromatic stabilisation energy in a series of related porphyrin macrocycles, by measuring the energy barrier to rotation of an individual porphyrin unit by exchange NMR spectroscopy (EXSY), finding values in the range of 1–5 $kJ \cdot mol^{-1}$.[18]

1.1.2. Theoretical Evidence for Aromaticity

Anderson's elegant study succeeds in finding extensive evidence of aromaticity in a large, structurally complex system. Yet, its wider application is hampered by the intricacy of its experimental design. In lieu of accessible experimental methods of assessing aromaticity in polycyclic systems, chemists have turned to computational methods that rely on the structural, magnetic, energetic, and electronic properties of aromatic molecules.[19]

The simplest, most common geometric parameter of aromaticity is the harmonic oscillator model of aromaticity (HOMA), which uses the bond length of benzene as a standard for 'ideal' aromaticity (Table 1.1).[20] The greater the deviation from this value, and the larger the bond length alternation in a ring, the lower the HOMA index of a ring. A perfectly aromatic ring (benzene) has a HOMA value of 1, while the hypothetical Kekulé benzene (cyclohexatriene) has a HOMA value of 0.[21] Solà notes that the HOMA index's validity is limited to planar systems only, as it overestimates the loss of aromaticity due to structural deformation.[22]

von Ragué Schleyer espoused the belief that the magnetic behaviour of annulenes was most intimately linked to the cyclic delocalisation of electrons characteristic of aromatic species.[23] Guided by this, he developed nucleus-independent chemical shifts (NICS) as a computationally inexpensive magnetic aromaticity index (Table 1.1). This technique follows a thought experiment that measures the chemical shift of a dummy

proton that is placed above the centre of an annulene lying orthogonal relative to an external magnetic field.[24] If the annulene is aromatic, its diatropic ring current produces a shielding effect on the dummy proton, which corresponds to a NICS value < 0. Conversely, an antiaromatic annulene would generate a paratropic ring current, which would create a shielding effect (NICS > 0). A non-aromatic species generates NICS values close to 0.

Herges expanded the set of magnetic aromatic indices with the addition of anisotropy of the induced current density (ACID) plots (Figure 1.5b).[25,26] This qualitative method visualises the induced ring currents in aromatic molecules when placed in a magnetic field. By convention, a clockwise ring current is diatropic (indicating aromaticity), while an anticlockwise ring current is paratropic (indicating antiaromaticity). Sundholm's gauge including magnetically induced current method (GIMIC) adds a quantitative aspect to magnetic aromaticity indices, by calculating the magnitude of diatropic and paratropic ring currents in molecule, when placed in a magnetic field.[27]

The geometric and magnetic criteria mentioned above only assess the consequences of aromatic delocalisation; ultimately, they are indirect indicators of aromaticity. Electronic indices, such as Solà's aromatic fluctuation index (FLU)[28] and Szczepanik's electron density of delocalised bonds index (EDDB)[29] (Table 1.1) measure the extent of electron sharing and delocalisation between atoms. The FLU index (analogous to the HOMA index) compares structures to an internal reference (benzene), while the EDDB index generates an absolute number of delocalised electrons.

Finally, von Ragué Schleyer developed the most commonly used protocol of computing ASEs: the isomerisation stabilisation (ISE) method (Figure 1.5c).[30] The ISE method involves the design of a thermodynamic cycle (ideally, a hyperhomodesmotic one) that disrupts the π-conjugation of an aromatic ring. Wheeler Houk, and Allen define a hyperhomodesmotic reaction of hydrocarbons as one where i) the number of C–C bond types (CH_3–CH_2, CH_3–CH, CH_2–CH_2, etc.) and ii) the number of C atoms (sp^3, sp^2, or sp hybridised) with zero, one, two, or three hydrogens remains unchanged in the reagents and products.[31] As shown in Figure 1.5c, von Ragué Schleyer's indene–isoindene ISE method (ISE-II) abides by these criteria.

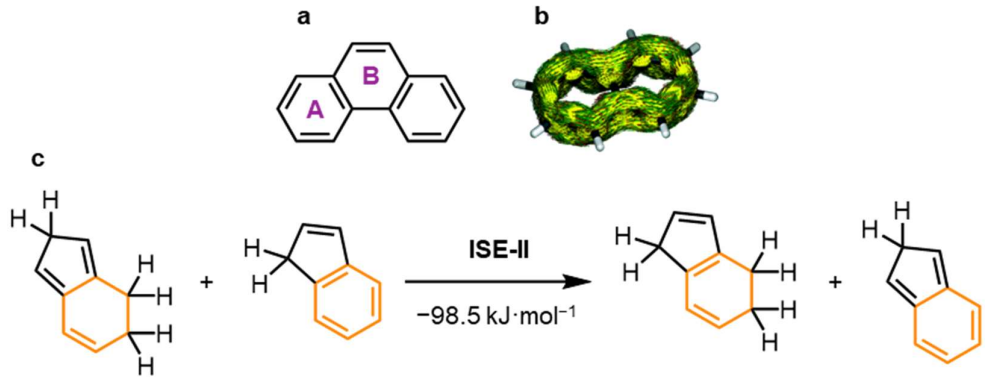

Figure. 1.5. Aromaticity indices. **(a)** The rings of phenanthrene with different aromatic characters (Table 1.1); **(b)** ACID Plot of naphthalene (B3LYP/6-31G*)[26]; **(c)** A hyperhomodesmotic equation to calculate the ASE of benzene using von Ragué Schleyer's ISE-II method [B3LYP(GD3BJ)/6-31G(d) / CH_2Cl_2].[32] Panel **b** was reproduced from reference **26**.

Table 1.1. Theoretical assessment of the local aromaticity of phenanthrene (as shown in Figure. 1.4b)

Phenanthrene ring	NICS(1) [33,†]	HOMA[34]	EDDB[k 29,‡]
A	−10.71	0.907	0.77
B	−8.40	0.568	0.40

† The number in the brackets indicates the dummy proton is 1 Å above the ring (RB3LYP/6-311+G**); ‡ the number of delocalised electrons as a fraction of benzene's aromaticity (B3LYP/6-311++G**)

1.1.3. Aromatic Ions

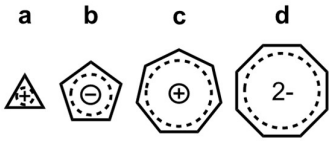

Figure 1.6. (a) Cyclopropenium cation ($C_3H_3^+$) with 2 π-electrons; **(b)** Cyclopentadienide anion ($C_5H_5^-$) with 6 π-**electrons**; **(c)** Tropylium cation ($C_7H_7^+$) with 6 π-electrons; **(d)** Cyclooctatetraenide anion ($C_8H_8^{2-}$) with 10 π-electrons.

While the vast majority of aromatic compounds are neutral, ionic species also show aromatic character.[35] Some of the simplest members of the Hückel-aromatic ion family include cyclopropenium, cyclopentadienide, tropylium, and cyclooctatetraenide (Figure 1.6). Perhaps the most common aromatic ion: cyclopentadienide (**Cp**$^-$),

formed by deprotonation of cyclopentadiene has been widely exploited as an η^5-ligand in organometallic complexes with versatile catalytic properties.[36]

Tropylium (**TP**$^+$) is a seven-membered carbocycle with six π-electrons delocalised *via* an empty p_z orbital, leading to an overall charge of 1+. Its salts were first obtained by Merlin in 1891[37], though tropylium's structure was only hypothesised by Hückel in 1931 and confirmed by Doering and Knox in 1954 using IR and UV-vis spectroscopy.[38] The latter obtained tropylium bromide as a decomposition product of dibromotropilidine. X-ray crystallographic evidence of tropylium's planar structure provided by Wagler *et al.*[39] revealed seven equivalent C-C bonds with bond length 1.39 Å (*c.f.* 1.40 Å for benzene).[40] The high symmetry of tropylium (point group D_{7h}) is reflected by its small number of Raman and IR absorption bands.[41] Extensive study has been dedicated to the investigation of this cation's photophysical properties. Due to its electron-deficient nature, it engages in charge-transfer interactions with halide ions, as well as electron-rich aromatics.[42] Aryl-substituted tropyliums have demonstrated weak fluorescence, though electron-rich moieties turn off emission, by reducing the S_1−T_1 energy gap and promoting fast non-radiative decay.[43] The most common synthetic strategy to access tropyliums involves oxidation of the parent cycloheptatriene.

1.2. Synthesis of Cycloheptatrienes

Cycloheptatriene or CHT (C_7H_8) is a non-aromatic, non-planar, seven-membered carbocycle consisting of a conjugated triene and an sp^3 hybridised methylene bridge, which sits above the plane of the triene (Figure 1.7a). In its ground state, cycloheptatriene adopts a boat conformation that can interconvert to an inverted boat *via* a planar structure with an energy barrier of ~24 kJ mol^{-1} (Figure 1.7b).[44] Butcher measured the out-of-plane angles at the bow and the stern of the boat as $\theta = 50°$ and $\varphi = 30°$ respectively through X-ray crystal analysis (Figure 1.7c).[45] *Ab initio* DFT calculations performed by Donovan and White support these figures.[46]

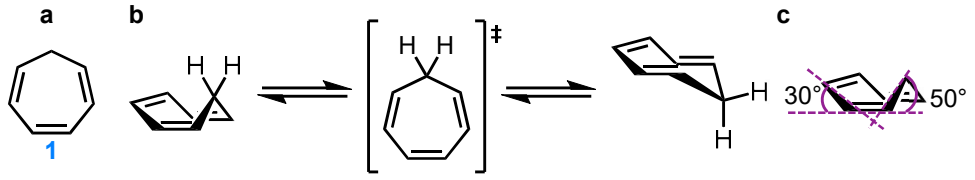

Figure 1.7. (a) Chemical structure of CHT; (**b)** Conformational interconversion of CHT; (**c)** Ground-state geometry of CHT with out-of-plane angles of 30° and 50°.

Cycloheptatriene was first isolated by Ladenburg[47] in 1881 *via* the decomposition of tropine, however its structure was unknown until Willstätter reported its characterisation and synthesis from cycloheptanone two decades later.[48] Over the following century, CHT was widely exploited in the synthesis of taxanes, rotaxanes[49], as an η^6-ligand[50,51], and even as a reference in electrospray mass spectrometry.[52] Though less common than its aromatic homologue benzene, CHT is found in the carbon framework of a diverse range of natural products, such as colchicine; a treatment for gout and Bechet's disease.[53]

1.2.1. Buchner Ring Expansion

Following Curtius's report[54] on diazocarbonyl compounds in 1883, Buchner and Curtius began investigating the addition of carbenes (by thermal decomposition of α-diazocarbonyl compounds *in situ*, leading to the entropically favourable release of $N_{2\,(g)}$) to benzene, in hopes of accessing novel CHTs.[55] The eponymous Buchner ring expansion (Figure 1.8)—regarded as a powerful means of preparing CHTs from functionalised aromatics—produced three isomeric CHT esters, as well as an ethyl 7-noncaradienecarboxylate intermediate. The reaction proceeds *via* a [2+1] cycloaddition between a double bond in benzene and carbene intermediate (**3**) to form norcaradiene (NCD) derivative (**4**), which undergoes thermally allowed disrotatory electrocyclic ring opening to form the more stable CHT tautomer (**5**).[56] Subsequent isomerisation *via* [1,3] sigmatropic shifts affords a mixture of the three isomers of **5**. Transition metal catalysis—most notably by a rhodium (II) trifluoroacetate dimer—has been widely employed to optimise this reaction, dramatically increasing yields to > 90%, by stabilizing the carbene intermediate.[57]

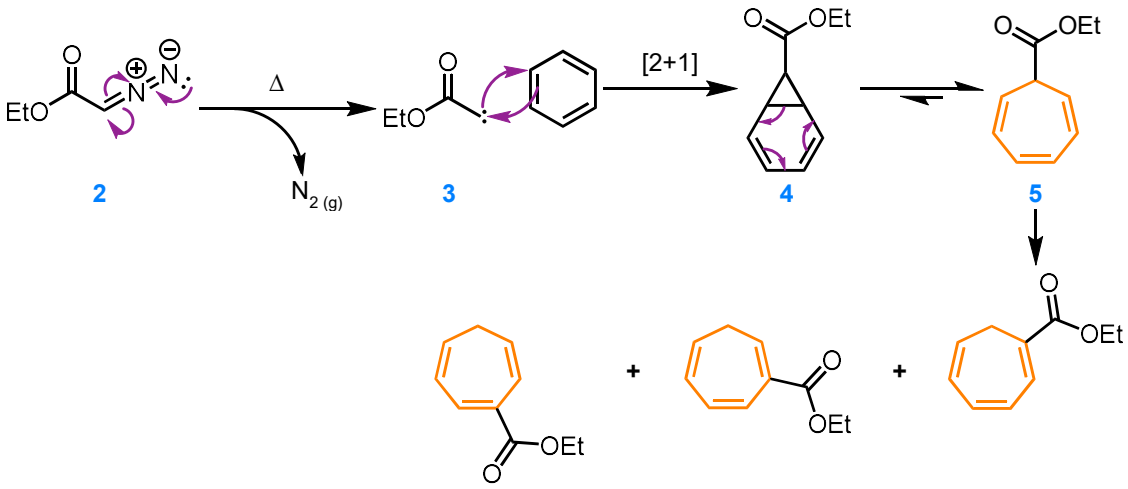

Figure.1.8. Mechanism for the Buchner ring expansion of benzene by ethyl diazoacetate (EDA).

Following Buchner's pioneering work, several groups have studied the NCD–CHT equilibrium in depth (Figure 1.9). Generally, the CHT tautomer is favoured over NCD, due to the presence of the strained cyclopropane ring.[58] While initial variable-temperature (VT) ^{1}H NMR studies[59,60] failed to observe NCD at temperatures as low as −150 °C, in 1975, Günther and Werner successfully observed a 97:3 mixture of CHT:NCD in dynamic equilibrium at −151 °C by VT ^{13}C NMR.[61] Subsequent studies focused extensively on substituent effects on the position of the equilibrium. While simple systems favour the CHT tautomer, Assour and Harrison reported a dicyano compound (**6a**) as a stable norcaradiene.[62] This observation was justified by Hoffmann's postulate that π-acceptors interact with the HOMO of the cyclopropane ring, stabilizing the ring by delocalizing electrons over the π-system.[58] Conversely, π-donors donate electrons into the cyclopropane's LUMO, increasing the anti-bonding character of the ring and destabilizing the ring. von Ragué Schleyer's computational study in 1984 augmented Hoffmann's theory, by claiming σ-donation into the σ-antibonding MO of cyclopropane elongates the C^1–C^7 bond and shortens the C^1–C^6 bond, thus stabilizing the ring, while σ-acceptors have the opposite effect.[63]

While Buchner ring expansion provides a convenient synthetic route towards CHTs, its viability is limited by the necessity for expensive rhodium catalysts. Further, the harsh conditions required to facilitate carbene formation—coupled with the high reactivity of carbenes—often leads to poor chemoselectivity, dimerisation, or

unwanted side-reactions, especially in more complex structures.[64] As a result, alternate routes have been explored to optimise CHT synthesis.

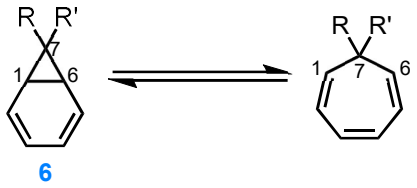

6

Figure 1.9. The NCD-CHT equilibrium.

Table 1.2. Effects of substitution in the C^7 position on the NCD-CHT tautomeric equilibrium.[63,65]

Compound	R	R'	Type	Major Tautomer
1	H	H	–	CHT
6a	CN	CN	π-acceptor	NCD
6b	CF_3	CF_3	σ-acceptor	CHT
6c	OMe	OMe	π-donor	CHT
6d	^{i}Pr	^{i}Pr	σ-donor	NCD

1.2.2. Cycloadditions

Cycloadditions are a class of pericyclic reactions that produce a cyclic product from two or more unsaturated building blocks. Owing to their ability to form multiple bonds in a single reaction, cycloadditions have flourished as a popular synthetic route towards complex cyclic molecules. The allowed route of cycloaddition (thermal or photochemical) is governed by the symmetry of the overlapping orbitals. Hence, the reaction mechanism can be understood in terms of frontier molecular orbital (FMO) theory[66], which only takes into account the HOMO–LUMO interactions between reacting molecules, and the Woodward–Hoffmann rules (summarised in Table 1.3).[67]

Table 1.3. Summary of the Woodward–Hoffman rules for cycloadditions.

Number of π-electron pairs	Photochemically Allowed Overlap	Thermally Allowed Overlap
Even ($4n$)	suprafacial–suprafacial	suprafacial–antarafacial
Odd ($4n$+2)	suprafacial–antarafacial	suprafacial–suprafacial

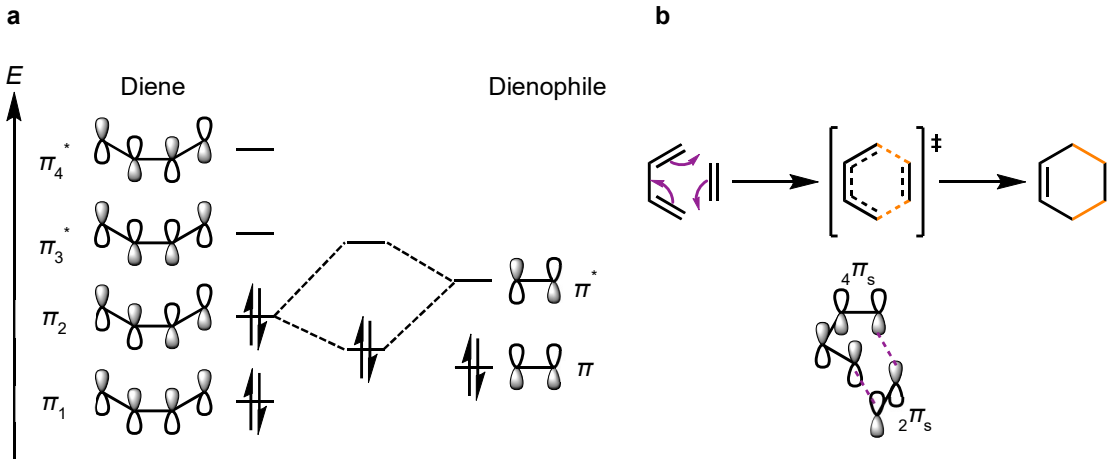

Figure 1.10. (a) Interactions between FMOs in a thermally allowed [4+2] cycloaddition; **(b)** Mechanism of the Diels–Alder cycloaddition showing orbital overlap.

A Diels–Alder reaction (Figure 1.10); one of the most explored pericyclic reactions for the synthesis of CHTs is a thermally allowed [4+2] cycloaddition that forms a six-membered carbocycle through the concerted reaction of a conjugated diene (4 π-electrons) and a dienophile (2 π-electrons). In such reactions, the diene's HOMO interacts with the dienophile's LUMO in a suprafacial manner, simultaneously forming two C–C σ-bonds. In 1935, Dierichs used the Diels–Alder reaction between diphenylacetylene (**7**) and tetraphenylcyclopentadienone (**8**) to synthesise hexaphenylbenzene (**9**).[68] This method was adapted by Battiste and Breslow[69,70] in the 1960s using a triphenylcyclopropene dienophile (**10**) to synthesise heptaphenylcycloheptatriene (**11**), with further optimisation recently by McGonigal (Figure 1.11).[71] In both cases, the initial cycloaddition forms a bicyclic product, which undergoes a chelotropic rearrangement to the desired product, with the entropically driven loss of $CO_{(g)}$.

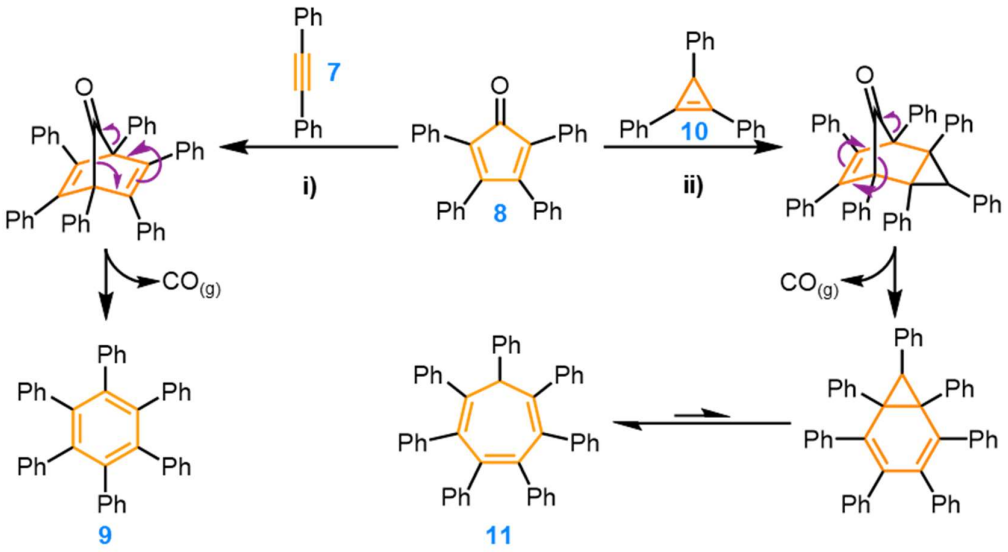

Figure 1.11. Synthesis of hexaphenylbenzene[69] (**9**) and heptaphenylcycloheptatriene[71] (**11**). Reagents and conditions: (i) Ph_2O, reflux, 2 h, 84%; (ii) *p*-xylene, 140 °C μw heating, 24 h, 74%.

In 1973, Tilborg extended the scope of the above strategy to access non-aryl CHTs (Figure 1.12) using modified thiophene dioxide substrates (**12**).[72,73] The subsequent reaction is an inverse electron demand Diels–Alder reaction, wherein the electron-deficient diene's LUMO overlaps with the dienophile's HOMO to form a bicyclic adduct, which undergoes rapid loss of $SO_{2\,(g)}$ to afford the desired CHT in high yields (> 95%).

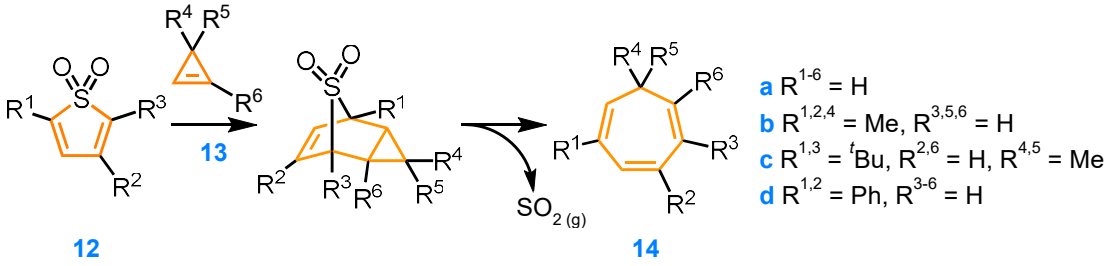

Figure 1.12. Tilborg's synthesis of functionalised CHTs.

More recent strategies to synthesise functionalised seven-membered carbocycles have employed less common cycloadditions aided by transition-metal catalysis.[74–76] Notably, Shu *et al.* have reported a [2+2+2+1] cycloaddition between naphthoquinones and *N*-(acylmethyl)pyridinium iodide mediated by Mn(II) under mild conditions to prepare complex structures with a CHT core (Figure 1.13).[77]

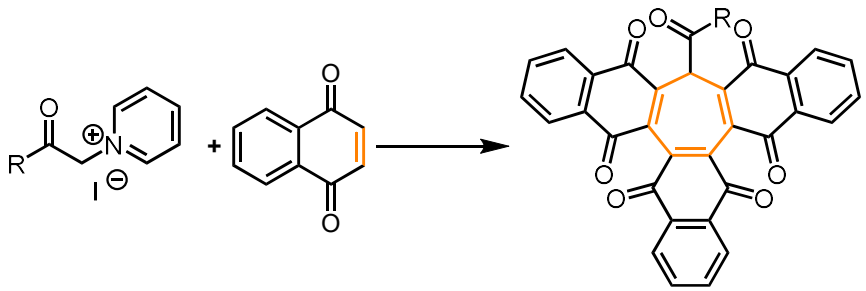

15 16 17

Figure 1.13. Shu's Mn(II) mediated [2+2+2+1] cycloaddition. Reagents and conditions: $Mn(OAc)_2 \cdot 4H_2O$, DMSO, 90 °C.

1.3. Synthesis of the Tropylium Cation

Since its discovery, several conditions and oxidants have been screened to perform the oxidation of CHT with varying degrees of success. In 1954, Doering and Knox reported the first synthesis of tropylium by direct oxidation of unsubstituted CHT, employing bromine as an oxidant (Figure 1.14).[38] In 1959, Geske presented an alternative electrochemical route, wherein oxidation was achieved by applying a voltage of +1.13 V to a solution of tropylium in MeCN (vs. Ag / $AgNO_3$) using a Pt electrode.[78] A more recent approach involves the treatment of 7-cycloheptatrienol[79] or 7-methoxy CHT[80] with a strong acid (most commonly tetrafluoroboric acid) to afford the tetrafluoroborate salt. Subsequent salt exchange reactions allow access to other tropylium salts, most notably halides.[81]

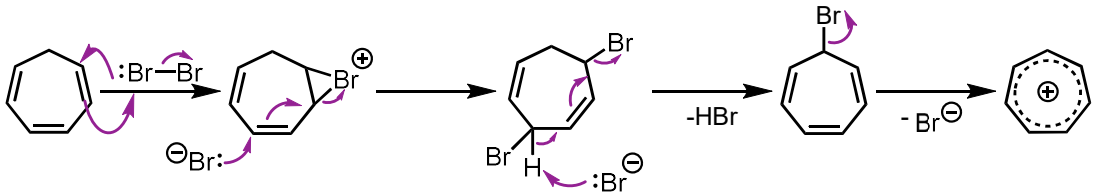

Figure.1.14. Formation of tropylium by treatment of CHT with bromine.

1.3.1. Substituted Tropyliums

While the oxidation of unsubstituted CHT is straightforward, the oxidation of complex CHTs is more nuanced. Conrow discovered that tropylium (**18**) and 7-methyl CHT (**19**) are involved in a hydride exchange equilibrium with CHT (**1**) and 7-methyltropylium (**20**) (Figure 1.15).[82] As the methyltropylium ion is 3.7 kcal mol^{-1}

more stable than unsubstituted tropylium, due to the inductive effect of the methyl group, **20** can be used to oxidise **19** to the corresponding tropylium. Following the initial oxidation, another competing equilibrium emerges, where **20** is able to oxidise the remaining **1** to produce a mixture of methyl CHT isomers.

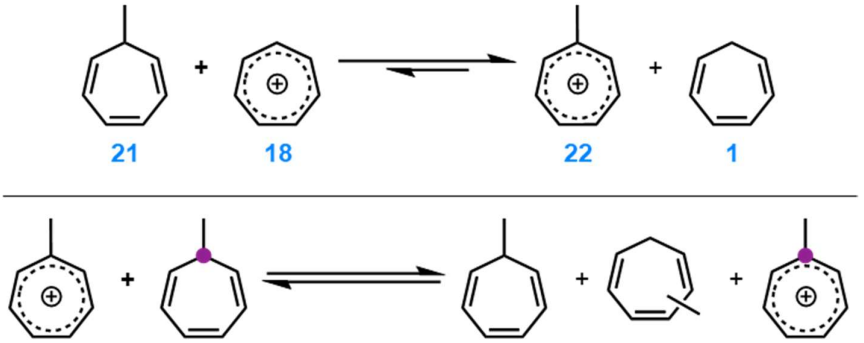

Figure 1.15. The two equilibria in Conrow's oxidation of 7-Me CHT (**19**) to 7-Me TP (**20**) by tropylium tetrafluoroborate (**18**).

A tropylium with higher alkyl substitution is expected to be more thermodynamically stable relative to **18** and should consequently behave as a stronger hydride donor. Phenyl groups on the other hand have a weak electron withdrawing effect on tropylium, as evidenced by the lower pK_a of 7-Ph tropylium (**21a**) (3.87) compared to **18** (4.74).[83] Jutz attributed this to the phenyl ring in **21a** twisting out of the plane of the tropylium by 45–50°, which weakens the conjugation between the phenyl and the tropylium moieties, leading to an inverse inductive effect.[84]

Kharlanov's computational study showed that modification of the electronic properties of the phenyl ring allows control over the torsion angle (α) between the tropylium and aryl moieties (Figure 1.16). Increasing the donor strength of the phenyl ring, by incorporating electron donating *p*-OMe (**21b**) and *p*-NMe_2 (**21c**) groups lowered the activation energy barrier ($\Delta G^{\ddagger}$) to rotation, planarizing the compound.[43] This correlation was further substantiated by Kharlanov's observation that an increase in donor strength accompanied fluorescence emission in this series; a corollary of charge transfer from the aryl group to the tropylium, facilitated by enhanced conjugation upon planarisation.

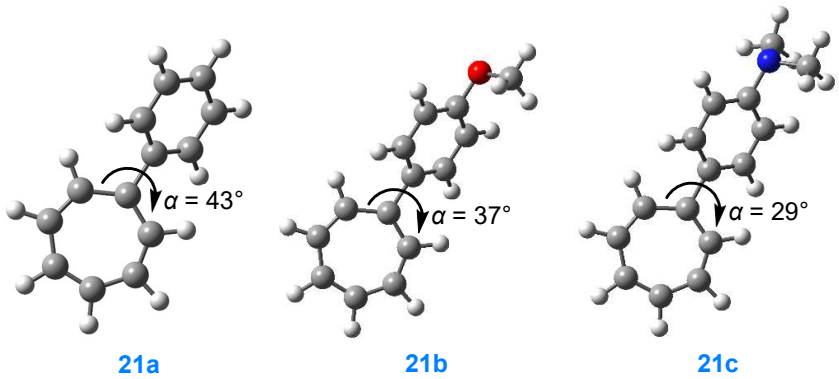

Figure 1.16. HF/6-31G* Optimised ground state geometries of tropyliums **21a**–**c**, showing the dihedral angle between the plane of the tropylium and the aryl moiety (α).[43]

1.3.2. Steric Overcrowding

Treatment of heptaphenylcycloheptatriene (**11**) with Br_2 yields heptaphenyltropylium (**22**) bromide: $Ph_7C_7^+Br^-$.[69] It follows from Jutz's discussion that heptaphenyl substitution destabilises the cation, as the inability of the peripheral phenyl rings to coplanarise with the central tropylium—as a result of steric overcrowding—precludes conjugative stabilisation. Battiste quantified this destabilisation effect through pK_a measurements of $Ph_nC_7H_{7-n}$ homologues, reporting a general decrease in pK_a with increasing phenyl substitution.[85] Interestingly, $Ph_7C_7^+$ exhibited higher stability than $Ph_6C_7H^+$, most likely due to the greater relief of steric crowding in Ph_7C_7H upon ionisation, compared to lower homologues.

The full impact of steric overcrowding in $Ph_7C_7^+$ was not fully understood until its structure was elucidated by McGlinchey through single-crystal X-ray diffraction (shown in Figure 1.17).[86] Heptaphenyl substitution distorts the planar geometry of tropylium into a shallow boat conformation, with out-of-plane angles of $\theta = 12.8°$ and $\varphi = 10.7°$ at the stern and bow respectively.[87] Further, the peripheral Ph rings possess an average dihedral angle of 80° relative to the plane containing their attached central-ring carbon and neighboring atoms, forming a seven-bladed propeller.

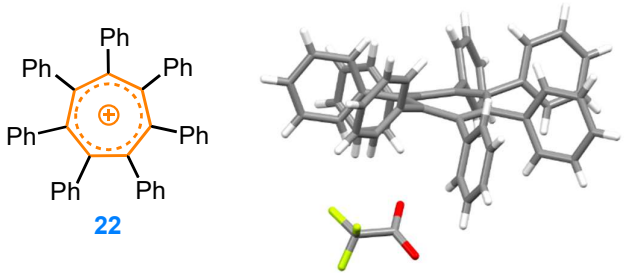

Figure 1.17. Crystal structure of heptaphenyltropylium trifluoroacetate.

Since their discovery, CHTs and tropyliums have emerged as important structural motifs in many areas. Nguyen's work has shown that tropylium is a versatile organocatalyst for a range of transformations, including carbonyl-olefin metathesis[88] and retro-Claisen bond cleavages.[89] The cationic nature of this aromatic molecule has been exploited as an electron-deficient η^6-ligand for a range of complexes, including a trinuclear palladium sandwich complex.[90] Further, tropyliums have garnered interest due to their rich optoelectronic properties. This has led to their use as push-pull, stimuli-responsive dyes[91], a station in a photoswitchable rotaxane[92], and hybrid organic–inorganic materials with promising charge transfer properties.[93] CHTs have been studied as aggregation-induced emitters[94,95] and stable open-shell diradicaloids.[96] Seven-membered rings also feature extensively in polycyclic aromatic hydrocarbons.

1.4. From PAHs to Nanographenes

Polycyclic aromatics are a class of organic compounds, which consist of two or more fused aromatic rings. The resulting π-electron delocalisation in these structures imbues them with desirable optoelectronic properties. The discovery of graphene by Geim and Novoselov in 2004 has sparked a renaissance in interest in PAH chemistry.[97] Indeed, PAHs with nanometer-scale dimensions can be considered molecular nanographenes.[98] While often termed the "wonder material"[99] of the century on account of its exceptional properties, most notably its high electron mobility (~15 000 cm^2 V^{-1} s^{-1} at room temperature[97], with reported values as high as 230 000 cm^2 V^{-1} s^{-1} on a Si / SiO_2 electrode at 5 K[100]), graphene's applications in electronic and optical devices are limited by nature of its zero band gap; a result of its conduction (π^*) and valence (π) bands being indistinguishable at the Fermi level.[101]

Deviation from graphene's infinite two-dimensional hexagonal lattice, by forming finite one-dimensional structures (graphene nanoribbons—GNRs) or smaller graphene fragments (nanographenes) gives rise to a non-zero band gap. As such, molecular nanographenes have been the focal point of research in organic materials chemistry in recent years. Unlike graphene preparation, nanographene syntheses typically involve a bottom-up approach from simple PAH precursors to produce monodisperse species, with well-defined structures.[102] As the field expands, more complex and extended structures are reported, with the inclusion of heteroatoms[103], as well as edge-functionalisation.[104] Studies on heteroatom-containing nanographenes are not discussed here in detail, as they are beyond the scope of this work.

1.4.1. The Scholl Oxidation

Over the past century, Scholl and Clar's seminal work has laid the foundation for the synthesis of PAHs. Indeed, the most efficient route to access these compounds is an intramolecular oxidative cyclodehydrogenation, commonly known as a Scholl oxidation, which involves the coupling of two aryl rings in the presence of an acid and a one-electron oxidant.[105] As this coupling does not require any aryl group pre-functionalisation, it can be considered a C–H activation. This reaction has proven to be especially versatile, as it uses conditions that are tolerant to a wide range of substrates to form multiple C–C bonds in one step, even if this is accompanied by the introduction of significant strain.

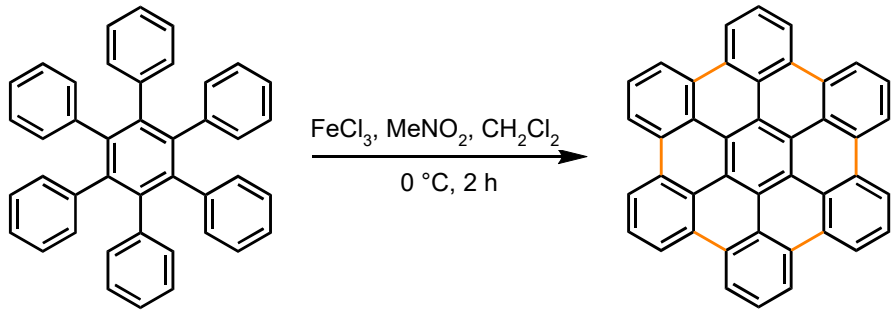

Figure 1.18. Typical conditions for the formation of *p*-HBC *via* a Scholl oxidation.

A wide range of oxidants, such as DDQ/TfOH,[106] $AlCl_3$,[107] $MoCl_5$,[108], PIFA/$BF_3{\cdot}Et_2O$, $Et_3O^+SbCl_6^-$,[109] and $FeCl_3$[110] has been used for this transformation. In 1958, Clar used the Scholl reaction to synthesise hexa-*peri*-hexabenzocoronene (*p*-HBC) (**23**) from

HPB (**9**), as shown above in Figure 1.18.[105] With subsequent optimisation, near quantitative yields have been attained.[111] Unlike its unfused analogue HPB, which is a six-bladed propeller, *p*-HBC exhibits planar topology and is sparingly soluble in nearly all organic solvents, as a result of molecular aggregation driven by strong intermolecular π–π interactions. In addition to serving as a model compound for graphene, *p*-HBC can be exploited as a versatile building block to synthesise extended graphenoid structures.[112]

While the aromatic cores of PAHs are the origin of their electronic and photophysical properties, edge-functionalisation of the peripheral rings can tune them and often dictate the nature of their application. As such, driven largely by the efforts of Klaus Müllen and co-workers, a diverse library of functionalised *p*-HBCs with interesting properties has been developed over the past decades. In 1996, Spiess and Müllen synthesised highly soluble hexaalkyl-derivatives of HBC, which exhibit both high symmetry and structural anisotropy, enabling self-assembly into a columnar mesophase.[113] The high charge mobility of *p*-HBC, coupled with the discotic liquid crystal (LC) behaviour of these compounds gives rise to numerous applications in optoelectronic devices. The synthesis, outlined in Figure 1.19 involves early-stage alkylation to boost solubility, followed by a Sonogashira coupling to form diarylacetylene **24**, which undergoes Co(0)-mediated [2+2+2] cyclotrimerisation to form the corresponding hexaarylbenzene (HAB) **25**. An IOCD affords the target HBC **26** in high yields (> 80%). Choi investigated the LC phase behaviour of *p*-HBC **26a** in *p*-xylene through differential scanning calorimetry (DSC), polarised optical microscopy, small angle neutron scattering, and wide-angle X-ray scattering, to conclude that **26a** self-assembles into cylindrical structures comprising ~11–13 monomer units in the isotropic phase.[114]

More importantly perhaps, the introduction of chemically reactive moieties, such as halogens allows for further structural functionalisation. An early-stage functionalisation approach may present synthetic challenges and disrupt IOCD in later synthetic stages, by introducing unwanted steric hindrance or vastly modifying the electronic properties of the precursor. Instead, Müllen reports an alternate strategy involving late-stage halogenation of HPB, as shown in Figure 1.19, followed by IOCD to form an edge-halogenated nanographene **28**, which acts as a substrate for transition-metal catalysed cross-couplings.[115] The resulting arylamine, HBC **29** stacks in a

columnar manner owing to strong π–π interactions, allowing them to act as efficient hole-transport materials. More recently, Müllen and Narita mounted six benzothiadiazole (BTZ) π-electron withdrawing moieties around an electron rich *p*-HBC to form a donor-acceptor molecule **30**, *via* Sonogashira cross-couplings.[116] The presence of acetylene spacers greatly reduces the dihedral angles between the HBC core and the peripheral BTZ groups, leading to a planar conformation. The resulting molecules self-assemble into LC columns, which remain assembled over a broad temperature range. Such face-to-face π–π interactions had also previously been observed by Müllen in hexa-perylenetetracarboxydiimide (PDI) substituted HBCs, as confirmed by scanning tunneling microscopy, as well as powder X-ray diffraction.[117]

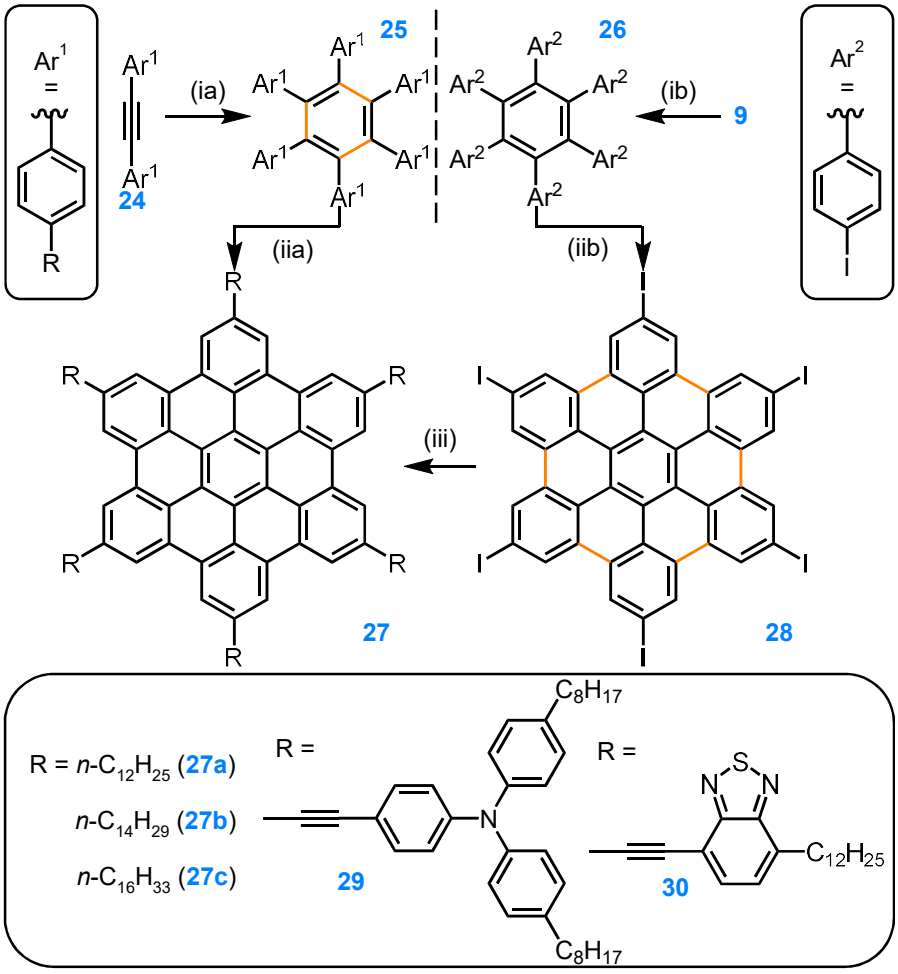

Figure 1.19. Spiess and Müllen's synthesis of discotic LCs with a *p*-HBC core (**27**). Reagents and conditions: (ia) $Co_2(CO)_8$, dioxane, 92%; (iia) $AlCl_3$, $Cu(OTf)_2$, CS_2, > 80%. Müllen's synthesis of hexa-arylamine- (**29**) and hexa-BTZ-substituted (**30**) *p*-HBCs. Reagents and conditions: (ib) I_2, PIFA, CH_2Cl_2, rt, 73%; (iib) $FeCl_3$, $MeNO_2$, CH_2Cl_2, quant.; (iii) $Pd(PPh_3)_4$, CuI, piperidine, THF, 50 °C, 61–80%.

1.4.2. Regioselectivity in the Scholl Oxidation

Despite its broad utility, the outcome of a Scholl oxidation can be challenging to predict, as the reaction is highly sensitive to individual substrates and the conditions used. This is underpinned by Wu's observation (Figure 1.20) that treating **31** with $FeCl_3$ leads to the formation of 6 C–C bonds (as in **32**), whereas treatment with DDQ/TfOH forms 2 eight-membered rings instead (as in **33**).[118] These divergent outcomes can be attributed to the two competing pathways for the Scholl oxidation: the arenium and the radical cation and the mechanisms. Gryko postulates that the radical cation mechanism dominates at room temperature in the presence of a mild Lewis acid, whereas the arenium mechanism is preferred at high temperatures in the presence of strong Lewis acid.[119]

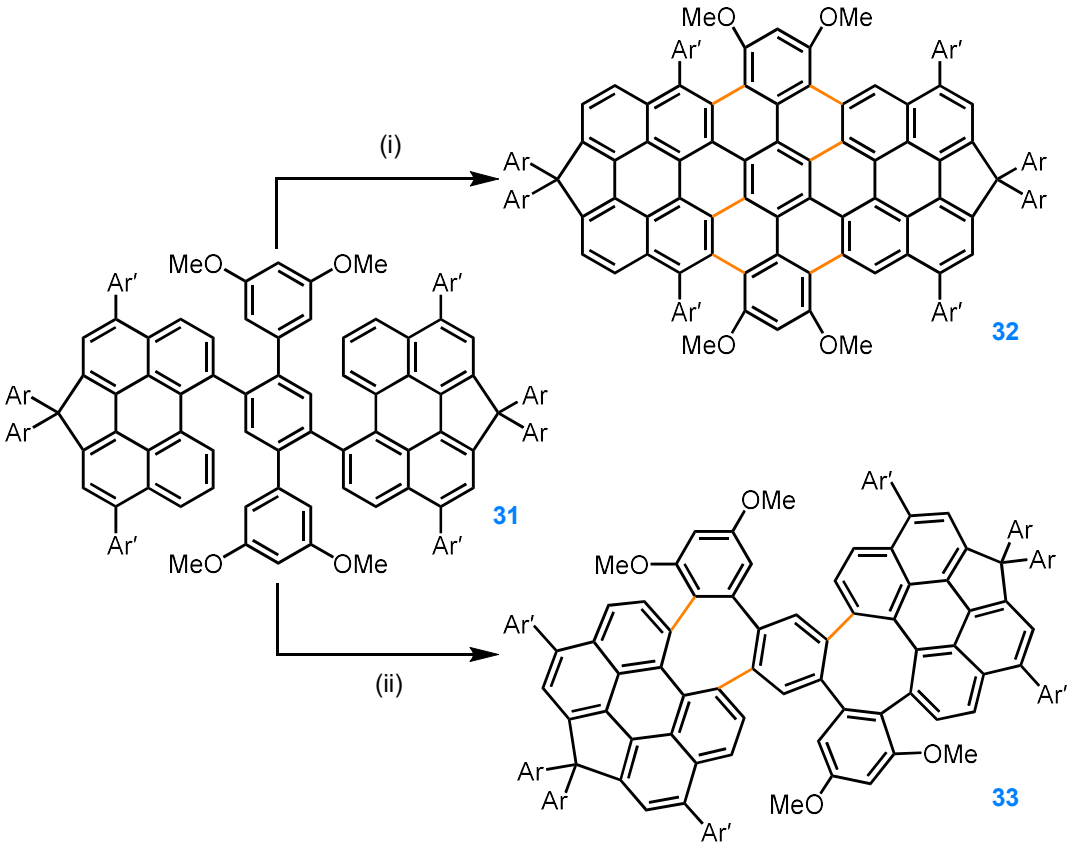

Figure 1.20. Differing Scholl reaction outcomes under different conditions: (i) $FeCl_3$, $MeNO_2$, CH_2Cl_2, 0 °C → rt, 1 h, 32%; (ii) DDQ, MsOH, CH_2Cl_2, rt, 30 min, quant.

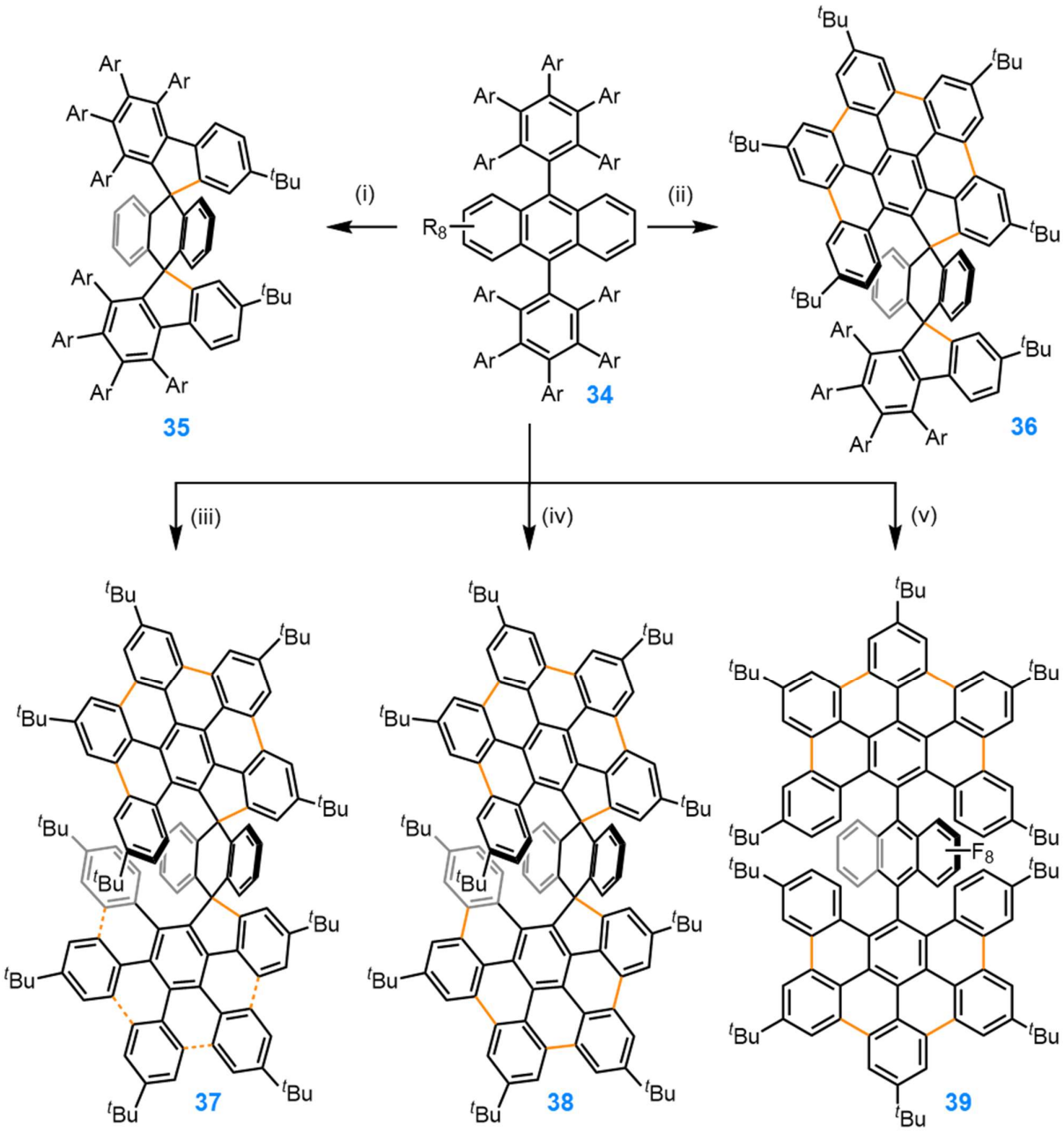

Figure 1.21. Effect of electronic character and oxidant strength on the outcome of the Scholl oxidation. Reagents and conditions: (i) $FeCl_3$, $AgPF_6$, DCE, $MeNO_2$, 85 °C, 4 h, 61%); (ii) $FeCl_3$, CH_2Cl_2, $MeNO_2$, −30 °C, 30 min, 40%; (iii) DDQ, TfOH, CH_2Cl_2, −60 °C, 40 min, 27%; (iv) DDQ, TfOH, CH_2Cl_2, 40 °C, 2 h, 25%; (v) DDQ, TfOH, CH_2Cl_2, 0 °C, 40 min, 63%.

A recent report by Fernandez and Martín echoes this observation. By varying the reaction temperature, time, and the oxidant used, the authors attained increasing degrees of graphitisation in anthracene-centred polyphenylene **34** (Figure 1.21).[120] DFT calculations indicate this reaction proceeds *via* an arenium mechanism, however,

the positive charge resides not on the peripheral phenyl rings, but rather on the electron-rich anthracene moiety. The barrier to forming this arenium is lowered further by the aromaticity gained by the anthracene. Intermediate **34** undergoes an unusual rearrangement to form a spirocentre (**35**). Harsher conditions are required to affect the expected Scholl oxidation (**36**–**38**). The authors demonstrated control over the competing spiranation and oxidative dehydrogenation by tuning the electronic character of the anthracene core. Replacing this electron-rich moiety with an electron-deficient perfluoroanthracene (as in **39**) precludes the possibility of spiranation, and only the Scholl oxidation is observed, giving rise to helical nanographenes.

1.4.3. Benzannulation

Conventional bottom-up nanographene syntheses *via p*-HBC derivatives are often plagued by incomplete ring fusions[121], unwanted chlorination[122], unexpected structural rearrangements during the Scholl reaction[123], as well as steric or electronic factors, which impede the key Diels–Alder step. Overall, these factors limit the range of nanographenes that can be prepared by this method.

Instead, Dichtel reports a non-conventional synthesis of dibenzo-*p*-HBC derivative **44** through sequential benzannulation and cyclodehydrogenation of oligophenylene precursor **42** (Figure 1.22).[124] Benzannulation of the di(arylethynyl)benzene derivatives (**40**) proceeded readily upon treatment with 2-(phenylethynyl)benzaldehyde (**41**), $Cu(OTf)_2$, and TFA, despite the high steric congestion. Interestingly, the $FeCl_3$-mediated IOCD proceeds in a controlled two-step process. While the initial four-fold oxidation occurs rapidly, oxidation of the more hindered positions is significantly slower, and with the introduction of bulky ^{t}Bu groups (**44b**, not observed) unfeasible. In such cases, the final product is the partly fused nanographene **44b**, which is inaccessible through conventional *p*-HBC routes and possesses a non-planar structure. Since Dichtel's method showed no signs of unwanted rearrangements previously reported by King, it offers a more selective route to novel nanographenes.[123]

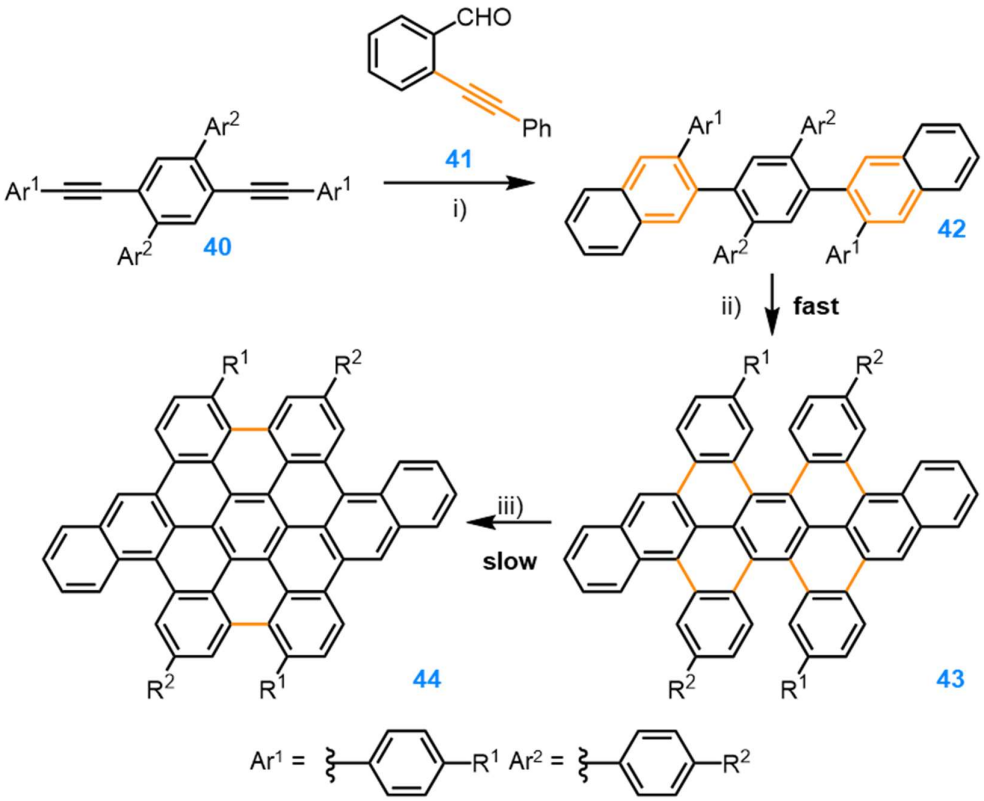

Figure 1.22. Dichtel's synthesis of dibenzo-*p*-HBC (**38**). Reagents and conditions: (i) Cu(OTf), TFA, DCE, 100 °C, 20 min, 65–98%; (ii),(iii) $FeCl_3$, $MeNO_2$, CH_2Cl_2, rt, 32–68%; **a**) R^1 = H, R^2 = ^{n}C$_9$H$_{19}$, **b**) $R^{1,2}$ = ^{t}Bu.

Despite Clar and Stephen's synthesis of unsubstituted hexa-*cata*-HBC (*c*-HBC) over half a century ago, it was not until 2014 that advances reported by Wei[125] allowed for the high yielding synthesis of C_3 symmetrically substituted (*c*-HBC) **49**.[126] As Figure 1.23 demonstrates, the first step of the elegant two-step synthesis is a threefold Suzuki coupling between 1,3,5-tri(bromomethyl)-benzene (**45**) and a di-substituted phenylboronic acid **46** to afford intermediate **47**. The following step, described by the authors as a covalent self-sorting assembly (CSA) entails a one-pot $FeCl_3$-mediated Friedel–Crafts hydroarylation, intramolecular alkylation, dehydrogenative aromatisation, and finally, IOCD to yield *c*-HBC **49**. Similarly, using phenanthrene-9-carbaldehyde **50**, the authors were able to synthesise an even larger nanographene **51**, which can be considered a hexabenzo-*c*-HBC.

Screening a large scope of R groups, Wei discovered that yields in the CSA step are higher for electron-rich aldehydes compared to electron-deficient variants. The

remarkable efficiency of the CSA method has provided a platform for the construction of larger, more complex graphenoids, as well supramolecular structures without the often-tedious preparation of complex oligophenylene precursors.[127–129]

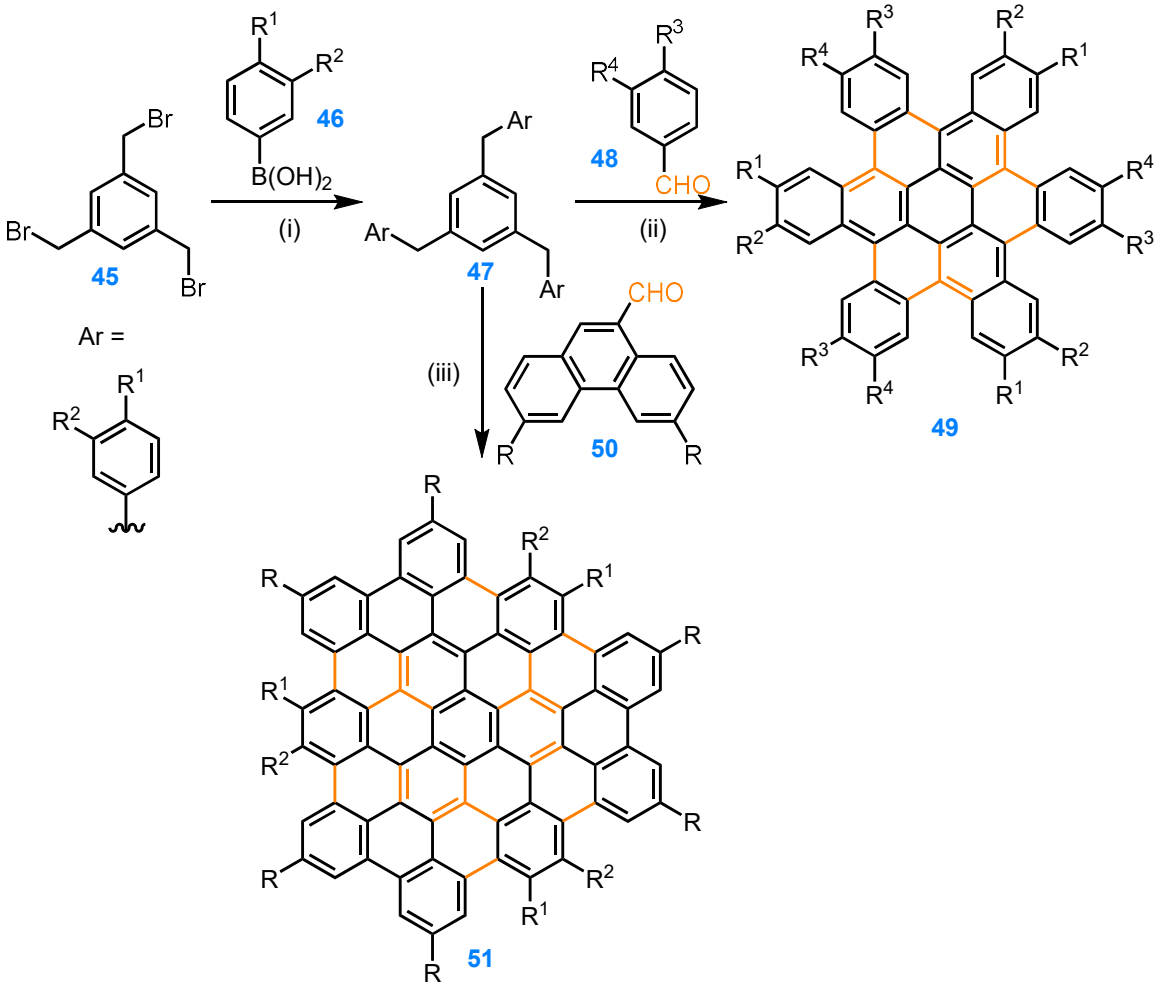

Figure 1.23. Wei's synthesis of *c*-HBC derivative (**49**) and hexabenzo-*c*-HBC (**51**). Reagents and conditions: (i) $PdCl_2$, Na_2CO_3, Me_2CO, H_2O, rt, 12 h, then 38 °C, 72 h, 64–83%; (ii), (iii) $FeCl_3$, Ac_2O, CH_2Cl_2, $MeNO_2$, rt, 39–97% and 36–53% respectively.

1.4.4. Aryne Cycloadditions

In recent decades, aryne chemistry in the form of [4+2] or [2+2+2] cycloadditions has emerged as a useful alternative in PAH synthesis.[130] A representative example is Peña's two-step synthesis of a C_3 symmetric extended triphenylene derivative **55**, outlined in Figure 1.24.[131] Treatment of bisbenzyne precursor **53** with a silyl deprotecting agent generated aryne **56**, which underwent a cycloaddition to form the initial adduct **54**. Curiously, through judicious control over solvent and temperature,

the authors were able to precipitate the intermediate **54**, avoiding the formation of unwanted aryne **57**, which may lead to oligomerisation. Subjecting **54** to similar conditions as **53** in the presence of a Pd-catalyst afforded nanographene **55** through a [2+2+2] cycloaddition.

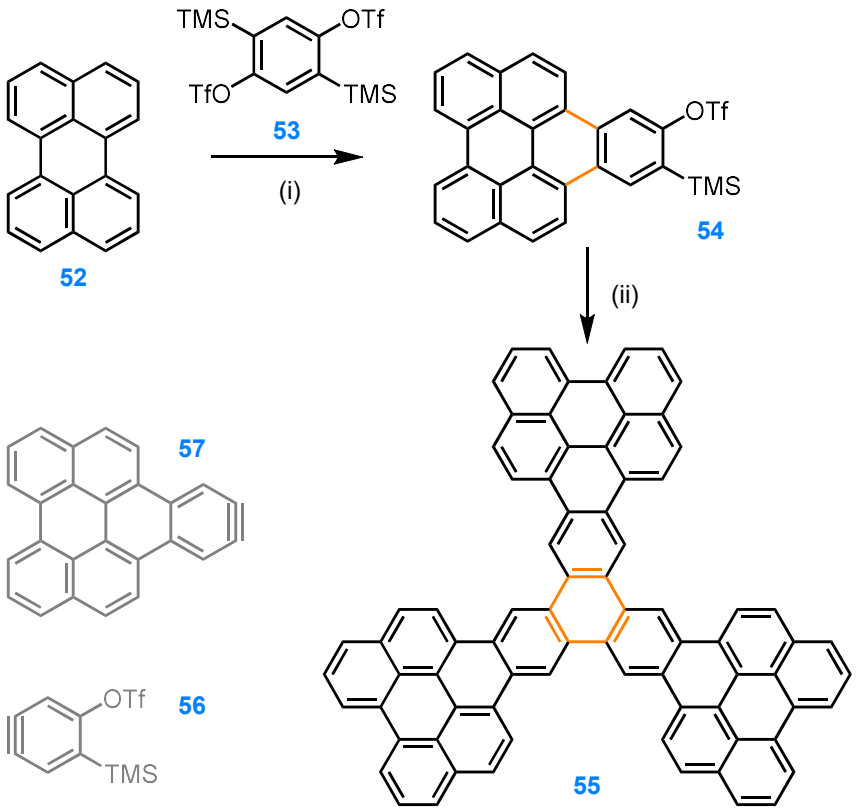

Figure 1.24. Peña's synthesis of a C_3-symmetric warped nanographene. Reagents and conditions: (i), (ii) CsF, THF, MeCN, 60 °C, 16 h, 49%; ii) $Pd_2(dba)_3$, CsF, THF, MeCN, 16 h, 46%.

1.4.5. Photocyclisations

Photochemical methods are a convenient alternative to access fully or partially fused PAHs and nanographenes.[132] The most common synthetic protocol applied is the oxidative photocyclodehydrogenation of diarylethene (stilbene) moieties, commonly known as the Mallory reaction.[133] This reaction proceeds *via* excitation of the *cis*-stilbene moiety to the S_1 state, followed by a Woodward–Hoffmann symmetry-allowed reversible conrotatory cyclisation to form a *trans*-dihydrophenanthrene intermediate, which can be trapped by an oxidant such as oxygen or iodine to form a phenanthrene moiety (Figure 1.25). Katz and co-workers discovered that the

introduction of a HI scavenger (propylene oxide) precludes the unwanted side-reaction of stilbene with the hydrogen iodide generated in this reaction, allowing for the reaction to be carried out under anaerobic conditions.[134,135] The Mallory reaction has proven particularly useful for the synthesis of a series of PAHs known as helicenes, which consist of a series of *ortho*-fused arenes.[136] Due to the strain present in these systems, they adopt a helical geometry that endows them with chirality.

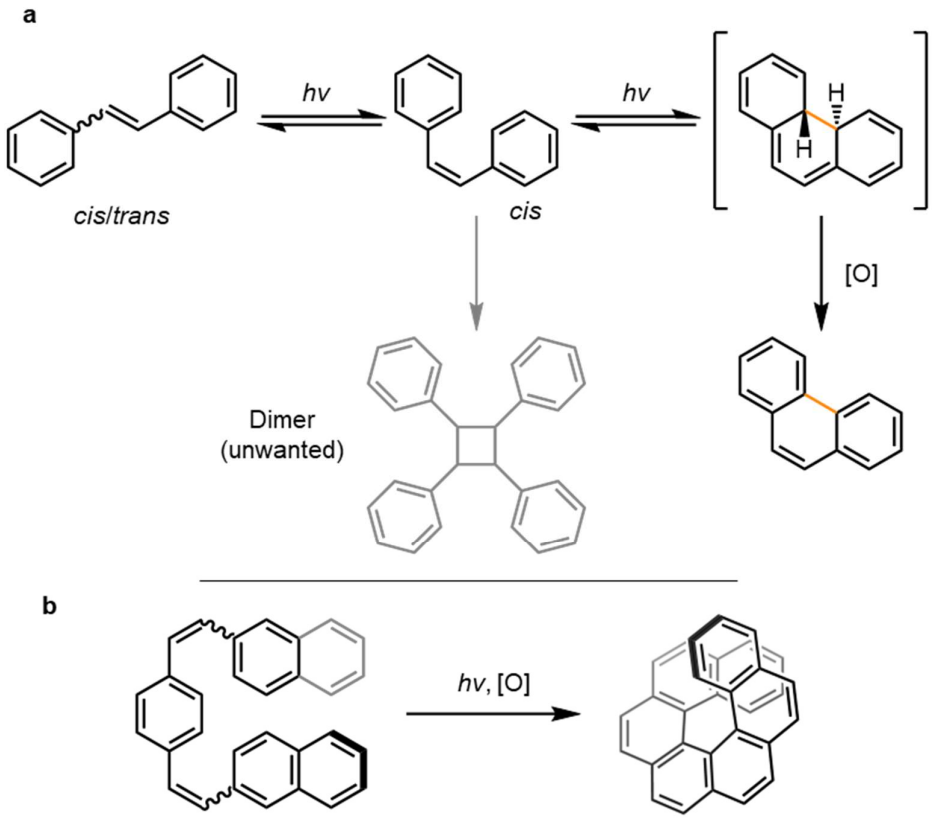

Figure 1.25. (a) Mechanism of the Mallory reaction; **(b)** Application of this reaction to form helicenes.

Morin extended the scope of photocyclisations as a mode of PAH synthesis to include photochemical cyclodehydrochlorination reactions.[137] A representative example is reproduced below (Figure 1.26) Though the exact mechanism of this cyclisation is unknown, its potential use in the synthesis of graphene nanoribbons has been of note.[138]

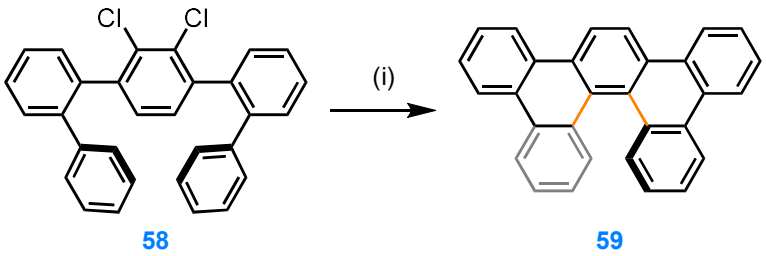

58 59

Figure 1.26. Morin's cyclodehydrochlorination. Reagents and conditions: i) Me_2CO, Na_2CO_3, *hv* (medium-pressure Hg lamp), rt, 2 h, 85%.

1.4.6. Intramolecular C–H Activation

While the traditional routes to PAH synthesis described above are robust, the quest for structurally diverse polyaromatics has compelled chemists to explore more nuanced strategies. Of these, Pd-catalysed C–H activation has emerged as the most promising candidate, and has been employed widely to access otherwise inaccessible targets.[139] Wu showcased the versatility of this method in 2013, when he used it as the key step in the synthesis of Buckminster fullerene fragment **61** (Figure 1.27).[140] Despite the high catalyst loading and low yield for this step, it is superior to many previously-known syntheses of such molecules, which often involved flash-vacuum pyrolysis with yields around ~0.1%.[141]

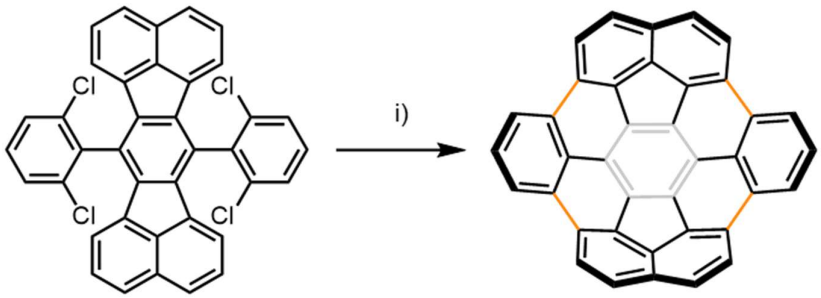

60 61

Figure 1.27. Wu's synthesis of "buckyball" fragment **61**. Reagents and conditions: $PdCl_2(PCy_3)_2$ (40 mol%), DBU, DMF, 160 °C, 36 h, 10%.

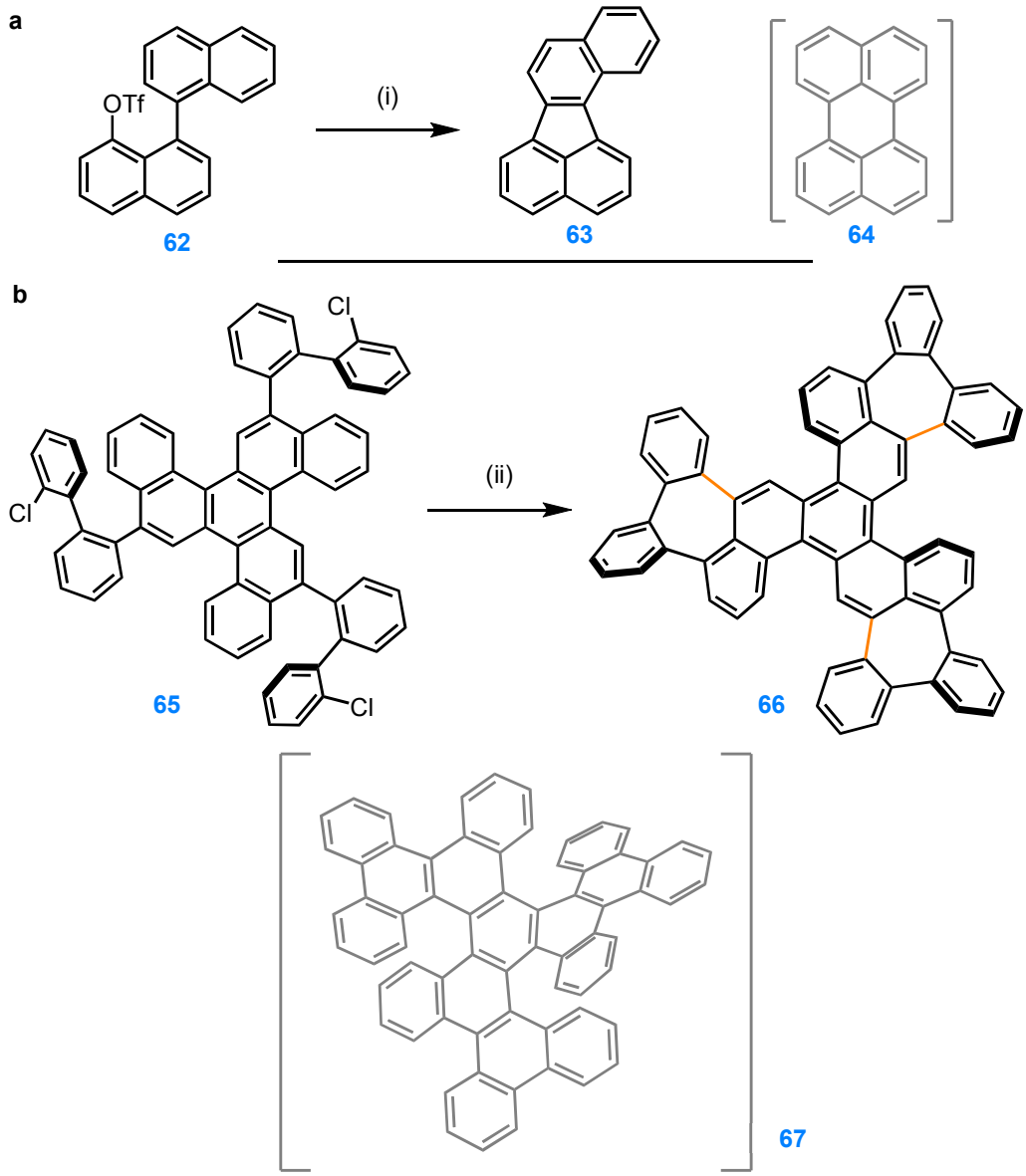

Figure 1.28. Unexpected selectivity in Pd-catalysed C–H activations, as reported by **(a)** Rice, and **(b)** Itami and Scott. Reagents and conditions: (i) $Pd(PPh_3)_2Cl_2$, LiCl, DBU, DMF, 135 °C, 6 h,93%; (ii) $Pd(PCy_3)Cl_2$, $^tBuCO_2H$, Cs_2CO_3, DMAc, 150 °C, 15 h, 26%. The structures shown in brackets were not observed.

Curiously, many groups have observed that in certain substrates, Pd-catalysed C–H activations exhibit regioselectivity for the formation of five-[142] and seven-membered rings[143] over six-membered rings. Figure 1.28 displays two examples by Rice, Itami, and Scott. This has boosted their popularity as a reliable method for the synthesis of non-benzenoid PAHs, which will be discussed in greater detail in Section 1.5.[144] Scott

and Itami attribute this unexpected selectivity for non-hexagonal ring formation to the lower strain present in the intermediates that lead to the formation of pentagonal or heptagonal rings. In addition to Pd-catalysed C–H activations, there have been a few notable examples of PAH synthesis through Ni-catalysed Yamamoto couplings[145] and Suzuki-Miyaura couplings.[146]

1.5. Twisted PAHs

Most of the PAHs and nanographenes discussed thus far are all fully planar (much like graphene). However, deviation from planarity through exo-skeletal approaches, such as steric overcrowding in partially fused systems or endo-skeletal approaches, such as the inclusion of intrinsic defects gives rise to a new class of twisted PAHs and warped nanographenes with unique chemical and photophysical properties.[147]

1.5.1. Steric Crowding

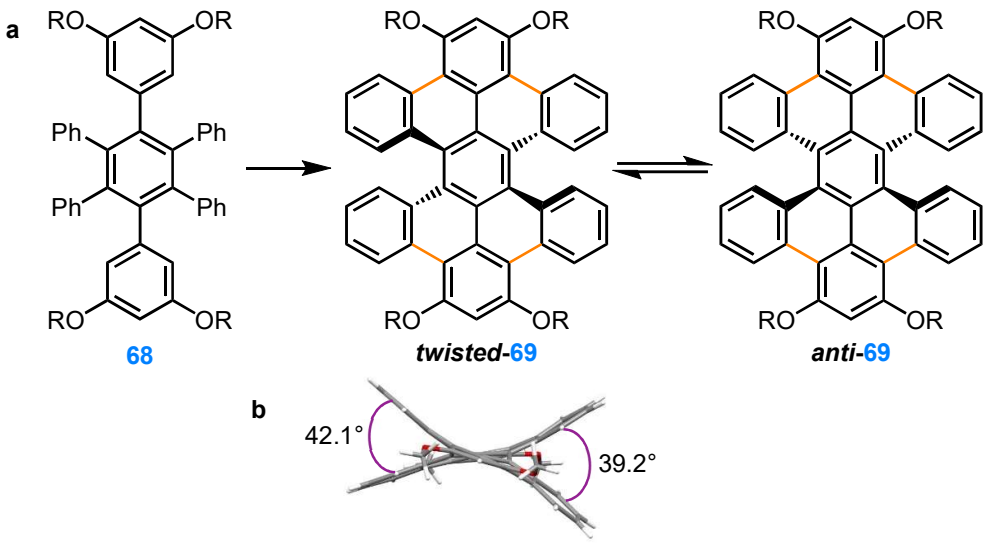

Figure 1.29. (a) Miao's synthesis of hexabenzoperylene derivative **69** (R: **a** = Me, **b** = $^{n}C_6H_{11}$); **(b)** Side-on view of the crystal structure of **52a** showing the torsion angles in the fjord region.

While *peri*-HBCs (e.g. **23**) are typically planar, the isomeric *cata*-HBCs (e.g. **49**) are forced out of planarity by steric congestion in the cove positions.[148] Miao has exploited a similar principle to design hexabenzoperylene (HBP) derivatives **69a** and **59b** (see

Figure 1.29), which exhibit exceptionally high degrees of twist, due to steric congestion in the fjord region.[149] The key step of the synthesis involves a selective, *para*-directed Scholl oxidation of **68**, promoted by electron donating OMe groups. A computational study indicated that in its lowest-energy state, **69** adopts a chiral-twisted conformation. This prediction was corroborated by single-crystal XRD, which revealed torsional angles of ~40° relative to the central plane, though isomerisation to the anti-isomer can occur at elevated temperatures. In the solid state, **69a** exhibits both face-to-face and edge-to-face π–π interactions, the former of which allow it to function as a p-type semiconductor in thin-film transistors.

Miao's HPBs can be described as double [5]helicenes. Analogous reports by Itami (see Figure 1.30)[150] and Kamikawa[151] have added to the structural diversity of such multihelicenes, whose unique chiroptical properties make them attractive candidates for circularly polarised luminogens.

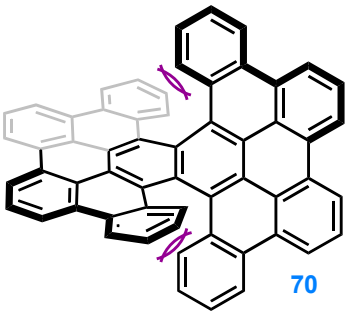

Figure 1.30. Itami's double [6]helicene.

1.5.2. Warped Nanographenes

While graphene owes its unprecedented electronic properties to its pristine, periodic structure, the presence of irregularities or non-hexagonal defects can greatly modify its structure (and hence its properties), by forcing rings out-of-plane in order to minimise C–C bond strain. However, far from considering this a problem, chemists have used these "warped nanographenes" as well-defined models for the detailed study of defective graphene and strived to harness the defects for the design of molecules with various optoelectronic properties.[152] Most commonly, these defects present themselves as one- or two-atom vacancies, which give rise to sets of five- and seven-membered rings (and occasionally eight- and nine-membered rings). Further, the inclusion of odd-membered rings into a PAH forms non-alternant hydrocarbons, where the arrangement of atoms is such that they cannot be divided into two groups, where atoms of the first group are directly bonded to atoms of the second group

only.[153] Such molecules exhibit markedly different electronic and chemical properties compared to benzenoid, alternant PAHs.

Embedding pentagons into PAHs results in geodesic (bowl-shaped) structures with positive Gaussian curvatures, as found in fullerenes or carbon nanotube endcaps (Figure 1.31). Meanwhile, the presence of higher order polygons (heptagons, octagons, etc.) gives rise to saddle-shaped topologies, with negative Gaussian curvatures.[154] The smallest curved PAHs are [n]circulenes, shown above. While [6]circulene, also known as coronene (first reported by Scholl and Meyer)[155] is planar, its homologue [5]circulene, also known as corannulene is bowl-shaped.[156] Conversely, higher homologues, such as [7]circulenes are saddle-shaped.[157] Despite extensive efforts to synthesise and explore the properties of geodesic PAHs in the form of fullerenes and fullerene fragments, little is known about their saddle-shaped counterparts, which are fragments of new carbon allotropes, such as schwarzite or toroidal nanotubes.[154]

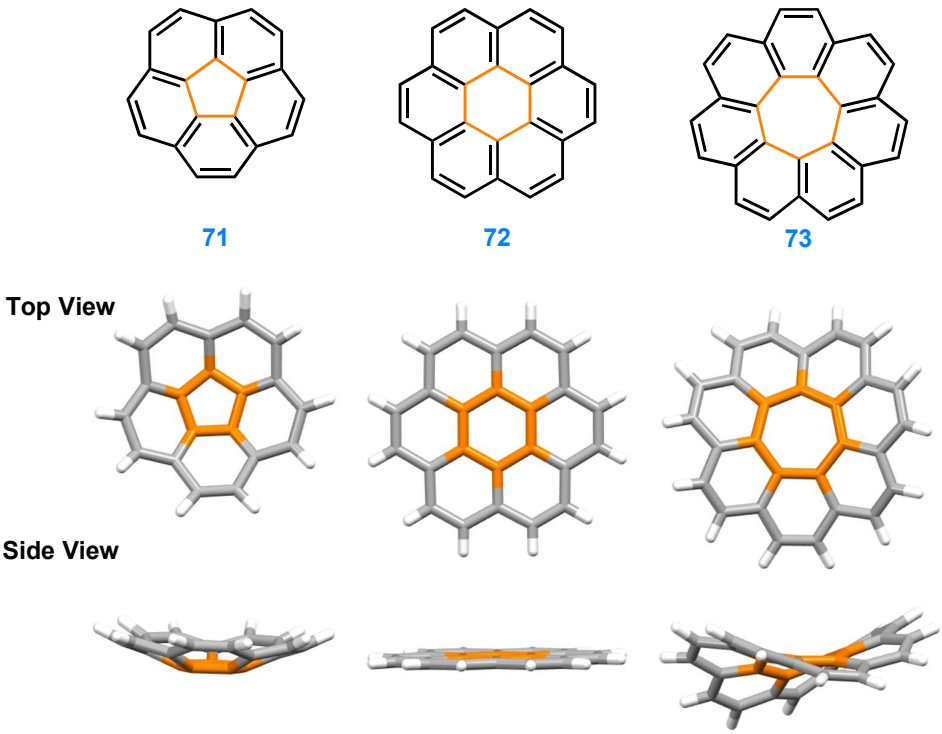

Figure 1.31. Comparison of the crystal structures of corannulene (**71**), coronene (**72**), and [7]circulene (**73**).

Due to the strain imposed by non-hexagonal defects, accessing larger warped nanographenes has required unusual, low-yielding synthetic methods, such as flash

vacuum pyrolysis.[158] However, in 2013, Scott and Itami achieved a major breakthrough, reporting the synthesis of a 'grossly warped nanographene' (see Figure 1.32) with a corannulene core through conventional cyclodehydrogenation.[159] The synthesis begins with the direct Pd-catalysed C–H arylation of corannulene to form unfused derivatives **71** and **72**. A tenfold IOCD catalysed by either $FeCl_3$ or DDQ/TfOH affords nanographenes **77a** and **77b** respectively. While the corannulene core itself has geodesic curvature, the presence of the five peripheral heptagonal rings introduces a saddle-shaped topology, which gives rise to **77**'s unique 'double concave' structure. While the structure may seem rigid in the solid state, bowl-inversions and rotations around the rim bonds rapidly equilibrate the *M* (left-handed) and *P* (right-handed) hexa[7]circulene moieties in solution at room temperature.

As expected, Scott and Itami's warped nanographene has vastly different physical and optoelectronic properties compared to planar nanographene $C_{78}H_{30}$ (synthesised by Müllen)[160] of comparable sise (Figure 1.33). To illustrate, **77a,b** demonstrate high solubility in common organic solvents, owing to weakened intermolecular forces between molecules with non-planar geometries. Since its non-planar shape precludes aggregation-induced fluorescence quenching, **77a** is fluorescent (λ_{max} = 504, 535 nm with φ = 0.26). Moreover, **77** shows a larger band gap compared to $C_{78}H_{30}$ (3.06 eV and 2.90 eV respectively), indicating weaker conjugation due to its non-planar geometry, as well as easier oxidation/reduction compared to corannulene and C_{60}, which are known to be excellent electron acceptors (facile reduction), but poor donors (difficult oxidation).

Grossly warped nanographene **77** represents renewed interest in heptagon-embedded nanographenes since [7]circulene was first synthesised in 1983 by Yamamoto and Nakazaki.[157] In addition to Scott and Itami, Miao has pioneered the synthesis of warped nanographenes containing heptagonal carbocycles over the past decade. In 2012, Miao reported a heptagon-embedded nanographene **82** that is isoelectronic to *p*-HBC.[149] The synthesis, as shown in Figure 1.34 involves a Diels–Alder reaction between aryne precursor **79** and tetraarylcyclopentadienone **80**. A *para*-directed IOCD affords warped nanographene **82** in moderate yields.

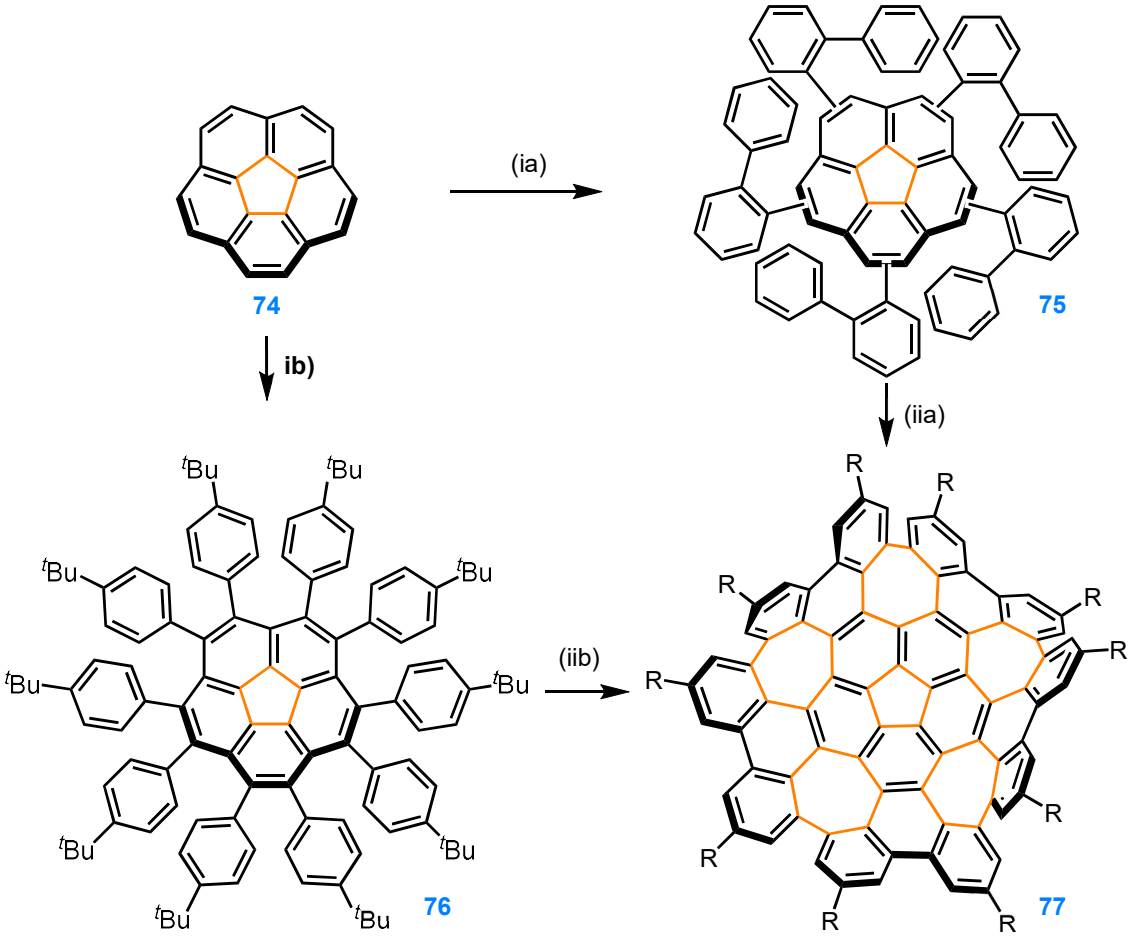

Figure 1.32. Scott and Itami's synthesis of a 'grossly warped nanographene'. Reagents and conditions: (ia) tris(*o*-biphenylyl)boroxine, $Pd(OAc)_2$, *o*-chloranil, DCE, 80 °C, 16 h, 21%; (iia) DDQ, TfOH, CH_2Cl_2, 0 °C, 30 min, 50%; (ib) tris(*p*-(^{t}butyl)phenyl)boroxine, $Pd(OAc)_2$, *o*-chloranil, DCE, 80 °C, 23%; (iib) $FeCl_3$, CH_2Cl_2, $MeNO_2$, 25 °C, 1 h, 62%; **59a**) R = H, **b**) ^{t}Bu.

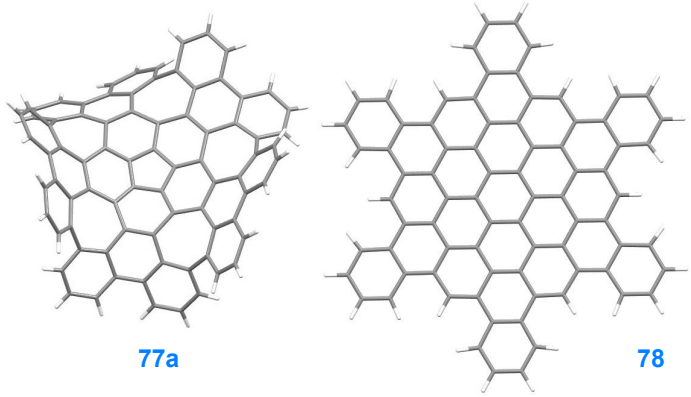

Figure 1.33. Comparison of the X-ray crystal structures of Scott and Itami's nanographene (**77a**) and Müllen's $C_{78}H_{30}$ (**78**).

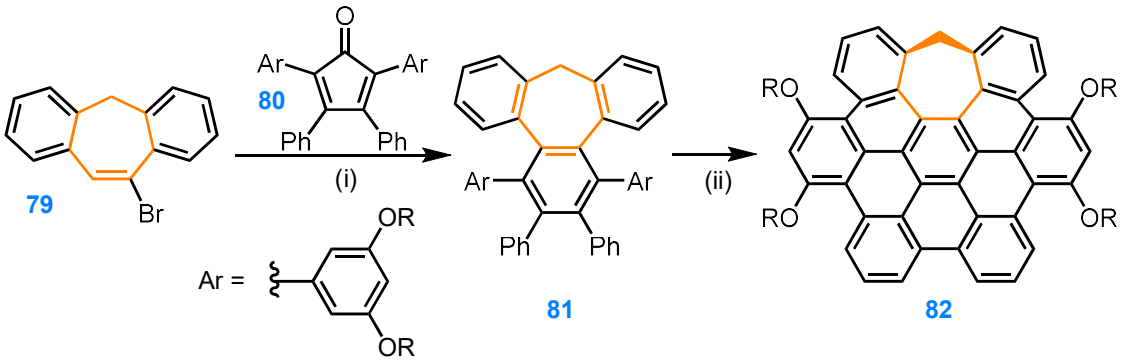

Figure 1.34. Miao's synthesis of warped nanographene **64**. Reagents and conditions: (i) KO^{t}Bu, Et_2O, 32%; (ii) $FeCl_3$, CH_2Cl_2, $MeNO_2$, 62%; R = $^n C_6H_{13}$.

Building on this work, Miao reported a series of extended nanographenes with two embedded heptagons (Figure 1.35).[161] The authors described these as highly distorted, deep saddles with flexible polycyclic backbones. Consequently, **87** and **88** show very weak fluorescence, as conformational changes (e.g. flapping) consume the energy of the excited state, while the more rigid **68** fluoresces green in solution. Promisingly, both **87** and **88** behaved as p-type semiconductors in thin films with hole mobilities of 1.3×10^{-5} and 6×10^{-4} $cm^2\ V^{-1}\ s^{-1}$ respectively. The stark contrast in optoelectronic properties between **82** and **87**/**88** exemplifies the profound and complex impact that the quantity and position of defects can have on nanographenes. A careful approach is required to design optoelectronically active molecules. Miao's work demonstrates that functionalised heptagons are a versatile means of building extended distorted nanographenes

Campaña has developed a novel synthetic route to tropone-embedded warped nanographenes *via* intermolecular Co(0)-mediated cyclotrimerisation, followed by IOCD to yield **92** and **93** (Figure 1.36a).[162] The versatility of this method allows facile introduction of functional groups and enlargement by Ni-catalysed C–OMe cross-coupling and cyclodehydrogenations. As expected, structure **94** is fluorescent, with an exceptionally high fluorescence lifetime of 14.5 ns compared to related perylene bisimides[163] and a low band gap of 2.66 eV. These properties, alongside the presence of π–π interactions between molecules of **94** (as evidenced by an intermolecular distance of 3.8 Å) support these compounds' application as solid-state organic semiconductors and printable OFETs.

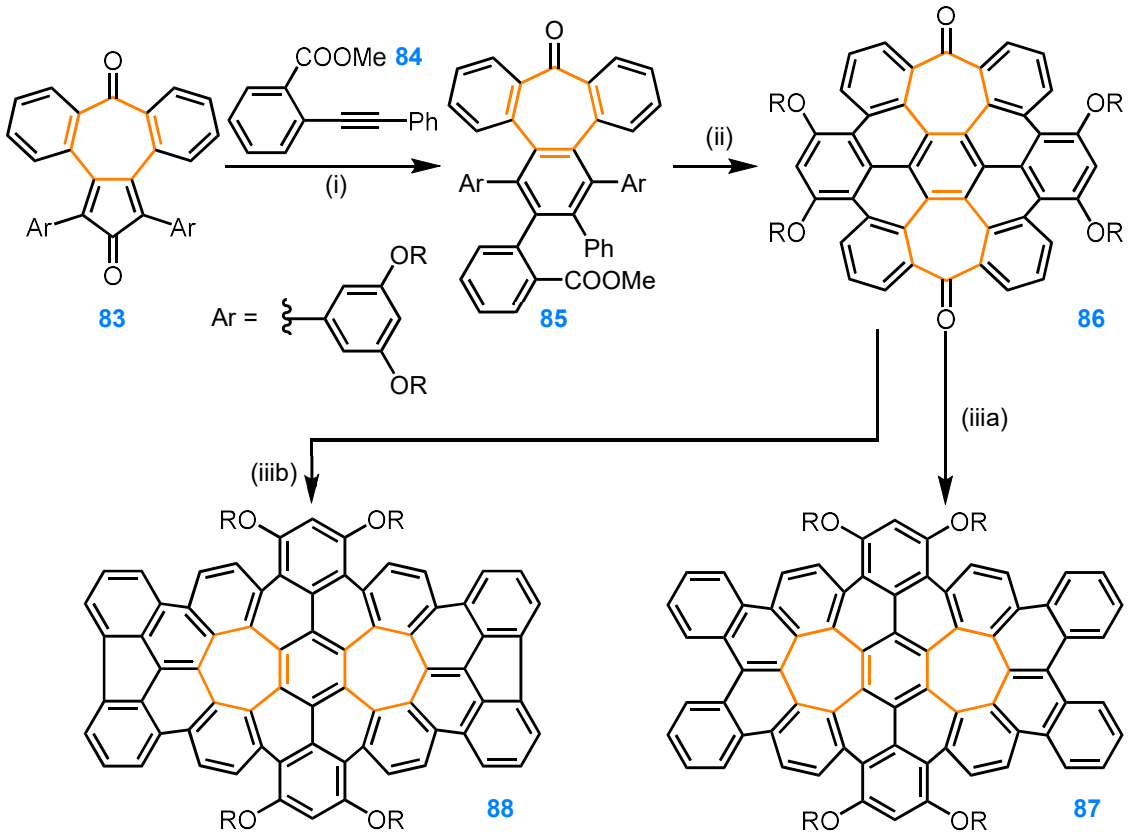

Figure 1.35. Miao's synthesis of two saddle-shaped nanographenes **87** and **88**. Reagents and conditions: (i) Ph_2O, reflux, 61%; (ii) 1. DDQ, TfOH, CH_2Cl_2, 2. $MeSO_3H$, 45%; (iiia) 1. PPh_3, CBr_4, PhMe, 2. $PhB(OH)_2$, $Pd(PPh_3)_4$, K_2CO_3, PhMe, H_2O, EtOH, 3. DDQ, $MeSO_3H$, CH_2Cl_2, 20–52%; (iiib) 1. ^{n}BuLi, fluorene, THF, 2. TsOH, PhMe, 3. DDQ, $MeSO_3H$, CH_2Cl_2, 19–29%; R: **a**) $^n C_8H_{17}$, **b**) $^n C_6H_{13}$.

Following on from her previous work, Campaña expanded the tropone-nanographene fragment **93** to undecabenzo[7]helicene **95**, as well as twisted nanographene ribbon **96** (Figure 1.36b).[164,165] The synthesis of both nanographenes proceeds *via* the introduction of *p*-HBC moieties by a similar method to the one discussed in Figure 1.19. The large π-surfaces of both species underpin their use as graphene quantum dots with high two-photon absorption (TPA) cross-sections (870 GM at 800 nm and 696 GM at 730 nm respectively) compared to similar PAHs. Additionally, the chiral helical nature of **95** gives it chiroptical properties, such as circularly polarised luminescence (CPL).

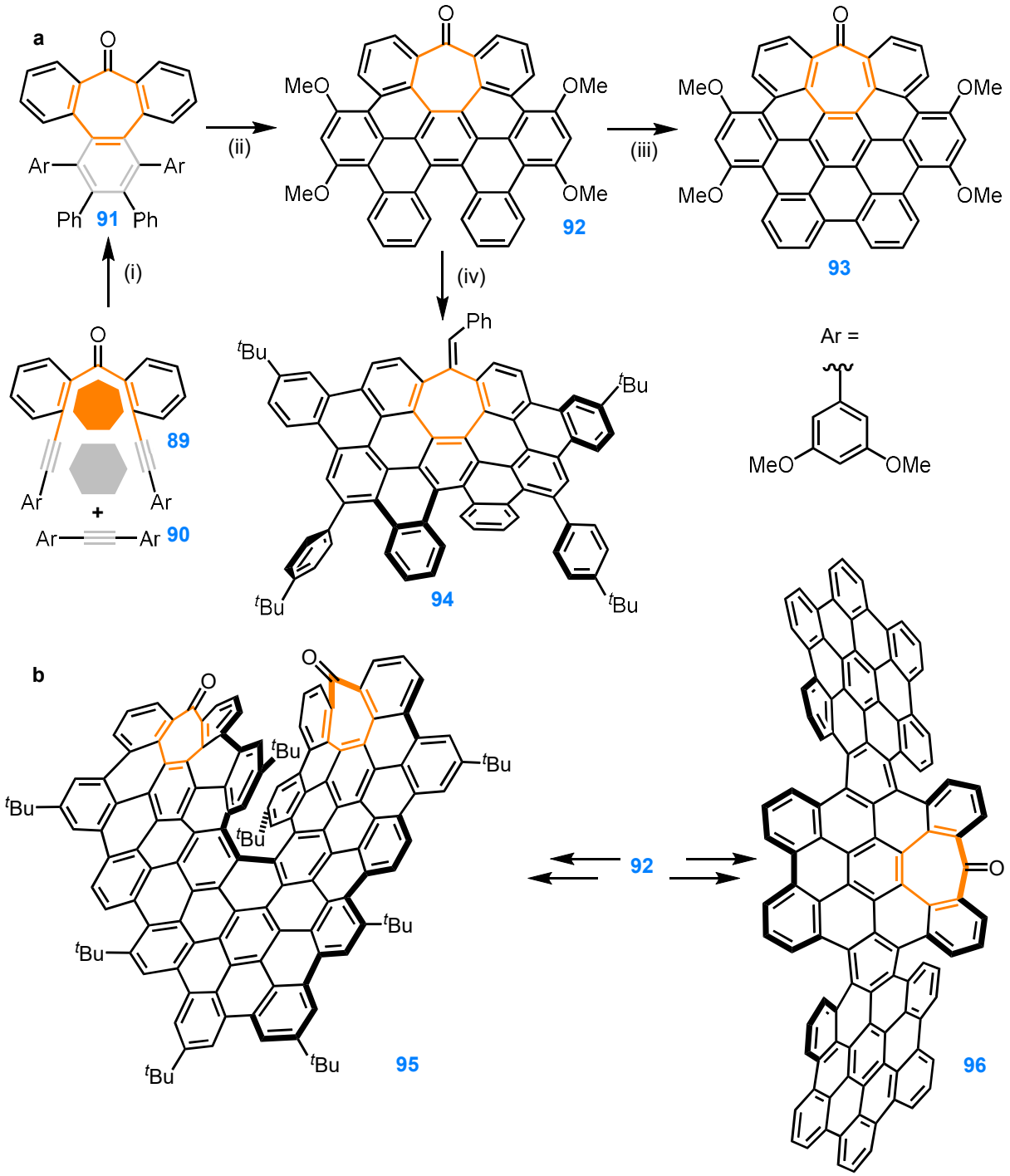

Figure 1.36. (a) Campaña's synthesis of tropone-embedded nanographene **93** and heptagon-embedded nanographene **94**. Reagents and conditions: (i) $Co_2(CO)_8$, 1,4-dioxane, 100 °C, 16 h, 61%; (ii) DDQ, $MeSO_3H$, CH_2Cl_2, 0 °C, 5 min, 48%.; (iii) $FeCl_3$, CH_2Cl_2, $MeNO_2$, 60 °C, 16 h, 60%; (iv) 1. $PhCH_2MgCl$, THF, rt, 2 h, 2. $SOCl_2$, pyridine, rt, 1 h, 3. $Ni(cod)_2$, PCy_3, *p*-^{t}BuPhMgBr, PhMe, 100 °C, 16 h, 4. DDQ, $MeSO_3H$, CH_2Cl_2, rt, 10 min, 20% (over 4 steps); **(b)** An undecabenzo[7]helicene (**95**) and a tropone-embedded nanoribbon (**96**) synthesised from **92**.

1.5.3. Tropylium-Embedded PAHs

A computational analysis of the individual rings in structures **88** based on the harmonic oscillator model of aromaticity (HOMA) index indicated general agreement with Clar's rules and revealed that the heptagonal rings are non-aromatic.[161] This is also likely true for Campaña's tropone-embedded nanographenes, though no such analysis was conducted. In general, while the geometric contribution of nonaromatic seven-membered defects in PAHs have been explored widely, the potential electronic and geometric implications of an aromatic heptagonal annulene (*i.e.*, a tropylium) are scarcely ever reported. These motifs are generally introduced by oxidation of a cycloheptatriene moiety or dehydration of a suitable alcohol.

In 2018, Chi reported a series of non-alternant hydrocarbon featuring two azulene moieties appended onto an *s*-indacene core with differing fusion patterns (Figure 1.37).[166] Both **97** and **99** underwent facile 2-electron oxidations (both chemically and electrochemically) to afford PAHs containing two tropylium moieties. Due to the linear fusion of arenes in these structures (neutral), (resembling the structure of acenes), these molecules possess a small singlet–triplet energy gap (ΔE_{S-T} ~3 kcal·mol^{-1}) and high diradical character. Interestingly, the authors found that **99** had a higher diradical character than **97**, due to the recovery of an additional azulene moiety.

More recently, Zhao synthesised a zwitterionic non-alternant PAH containing an expanded azulene framework with an even narrower ΔE_{S-T} of 0.95 kcal·mol^{-1} (as determined by variable temperature EPR spectroscopy) and high diradical character at room temperature (Figure 1.38).[167] The stability of the open shell **103** is attributed to the gain of two Clar sextets in the resonance structure containing two radicals. **103** was obtained by deprotonation of its conjugate acid **102**, which in turn was prepared by sequential treatment of precursor **101** with a hydride source (Et_3SiH) and a Lewis acid ($BF_3 \cdot Et_2O$). The authors noted that **103** could be reverted to **102** quantitatively by adding an acid in excess. In fact, iterative additions of acid and base allowed for reversible switching between **103** and **102** over multiple cycles. As such, this system is the first example of a pH-responsive switch between a diamagnetic and paramagnetic species.

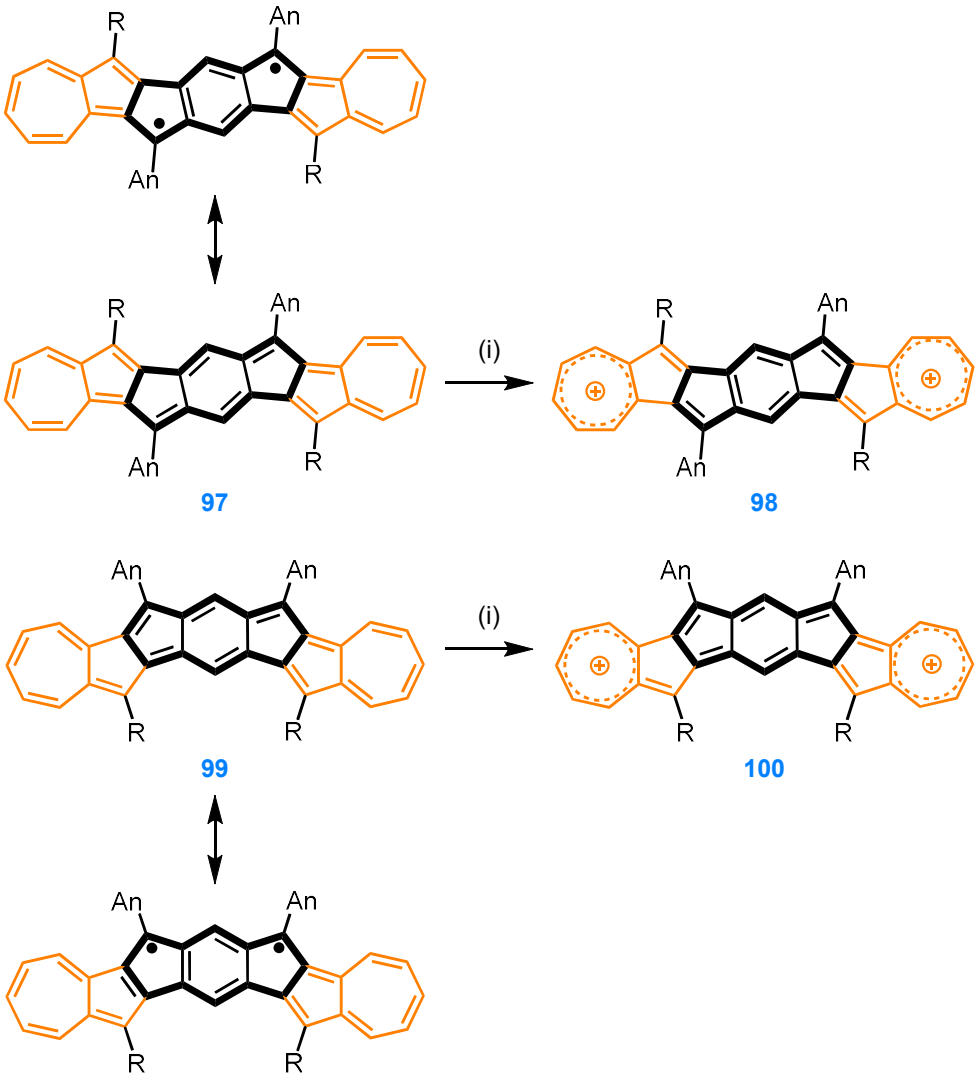

Figure 1.37. Chi's redox-active azulene-*s*-indacene-fused PAH, showing the open-shell (triplet) and closed-shell (singlet) resonance forms of the neutral molecules, as well as their 2-electron oxidation to the dicationic tropylium species. For clarity, the azulene moiety is highlighted in orange, while the *s*-indacene moiety is bold. Reagents and conditions: (i) $NO{\cdot}SbF_6$, CH_2Cl_2, MeCN, rt, 5 min, quant. **An** = 10-(3,5-di-*tert*-butylphenyl)anthracene, **R** = H, CF_3CO.

Chi and Zhao's work provides valuable insight into the redox-behaviour, electronic structure, and photophysical properties of tropyliums embedded into larger azulene-type systems. Some early work by Heilbronner has explored acenes with terminal tropylium moieties, but characterisation of these compounds is limited to optical spectroscopy.[168] Yet, as the structures discussed above are fully planar, they offer limited information on the structural impact of a tropylium in a strained PAH.

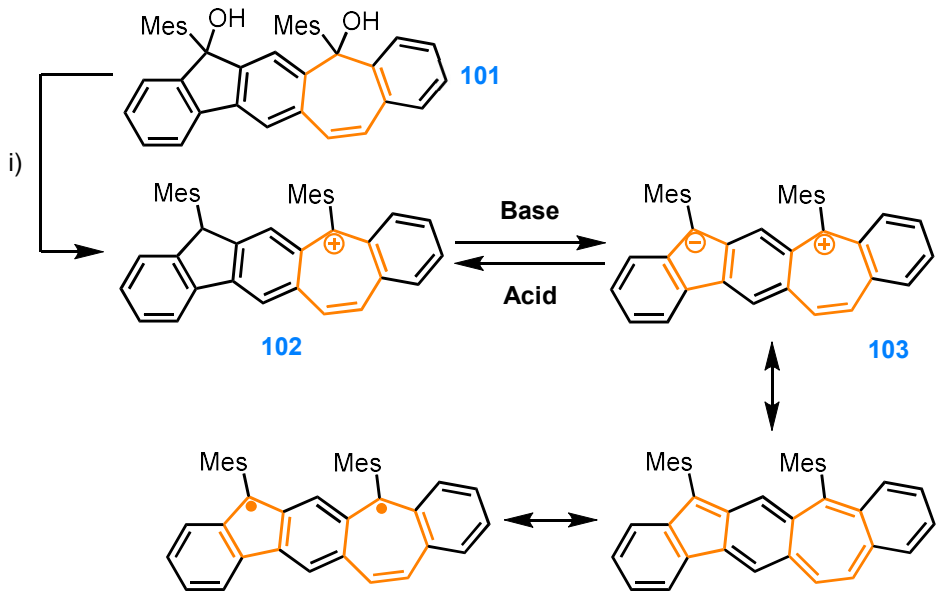

Figure 1.38. Zhao's zwitterionic PAH (**103**) and its various resonance structures, outlining the source of its diradical character. Reagents and conditions: i) $BF_3{\cdot}Et_2O$, Et_3SiH, CH_2Cl_2, 0 °C, 1 h.

Würthner presents an intriguing molecule **104**, which shows highly reversible redox-activity; a 1-electron oxidation (either electrochemically or chemically using $NO{\cdot}SbF_6$) forms the radical species $\mathbf{104}^{\cdot+}$, which can be oxidised further to form the dicationic $\mathbf{104}^{2+}$, which contains two tropylium moieties.[146] As shown in Figure 1.39, this PAH displays large conformational changes as it undergoes each sequential oxidation; X-ray crystallographic analysis of the compounds revealed that **104** adopts a *cisoid* saddle-shaped conformation with a dihedral angle of 86.3° between the two ends of the molecule. Similarly, $\mathbf{104}^{\cdot+}$ adopts two *cisoid* saddle conformations, albeit with larger dihedral angles of 110.5° (shown) and 90.3° (not shown). $\mathbf{104}^{2+}$ on the other hand adopts a significantly flatter *transoid* saddle conformation with a large dihedral angle of 151.6°. These data, along with DFT calculations indicate that the gain in aromaticity of the tropylium moieties induces planarisation and bond length equalisation in $\mathbf{104}^{2+}$ relative to the neutral species. These findings are in accordance with Yasuda's report of bond length equalisation upon aromatisation of the heptalene moiety in a polycyclic framework to form two tropylium moieties.[169]

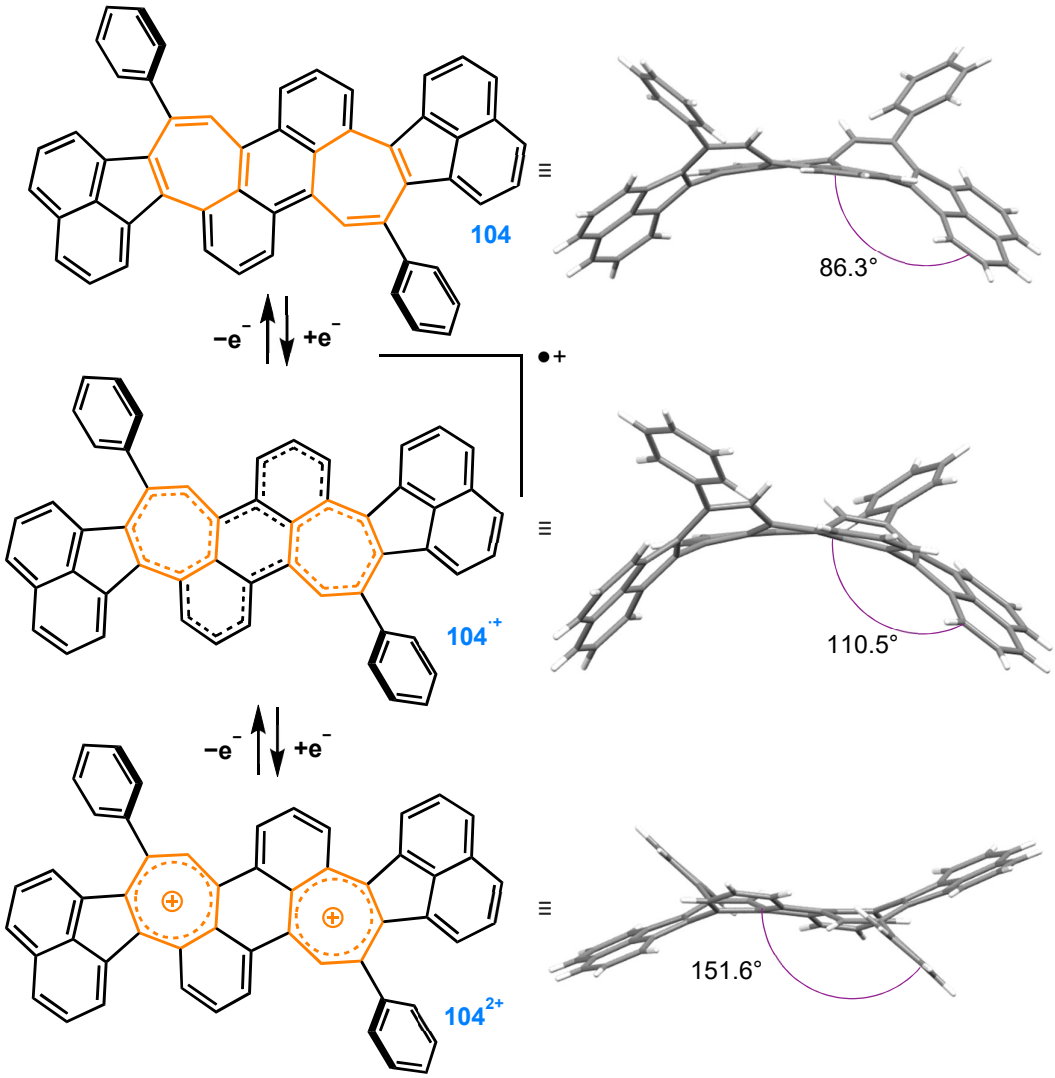

Figure 1.39. Würthner's redox-active, curved PAH **104**, which exhibits large conformational changes (as shown in the single-crystal X-ray structures on the right) concomitant with two reversible one-electron oxidations. Counterions are omitted for clarity.

Further, Yamada and Aratani report a serendipitous discovery of a ring-contraction of a cyclooctatetraene-containing PAH to the spirocentric cycloheptatriene **105**, which undergoes reversible protonation to afford the tropylium **105**$^{+}$.[170] In the solid state, **105**·OTf crystallises as the *meso*-form of a double helicene, where the central tropylium adopts a shallow boat conformation (Figure 1.40).

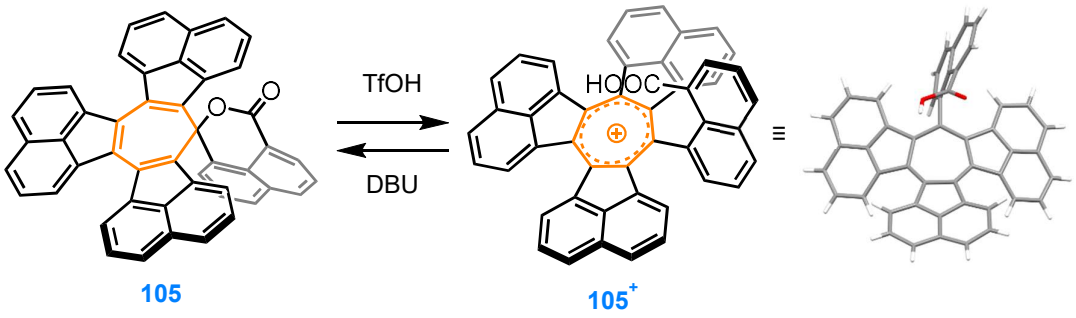

Figure 1.40. Yamada's spirocentric CHT **105**, which forms the tropylium-embedded **105**$^{+}$ (crystal structure shown on the right) upon protonation. The counterion (OTf^{-}) is omitted for clarity.

1.6. Summary and Outlook

The unique blend of reactivity and stability of cycloheptatrienes and tropyliums has fascinated organic chemists for decades. These structural motifs have found use as organocatalysts, dyes, fluorophores, and redox-active materials. Yet, they are often overlooked in a polycyclic aromatic framework. Closer analysis of these motifs not only reinforces our understanding of fundamental concepts that govern the structure and properties of organic molecules, but also enables the preparation of organic materials with enhanced optoelectronic properties. This thesis explores the rich chemistry of the seven-membered ring.

1.7. References

1 M. Faraday, *Philos. Trans. R. Soc. London*, 1825, **115**, 440–466.

2 S. Kikuchi, *J. Chem. Educ.*, 1997, **74**, 194–201.

3 E. Hückel, *Zeitschrift für Phys.*, 1931, **70**, 204–286.

4 T. M. Krygowski, M. K. Cyrañski, Z. Czarnocki, G. Häfelinger and A. R. Katritzky, *Tetrahedron*, 2000, **56**, 1783–1796.

5 M. Solà, *Front. Chem.*, 2013, **1**, 4–11.

6 A. R. Mahjoub, S. Ghammami and M. Z. Kassaee, *Tetrahedron Lett.*, 2003, **44**, 4555–4557.

7 Z. Chen, C. S. Wannere, C. Corminboeuf, R. Puchta and P. von Ragué Schleyer, *Chem. Rev.*, 2005, **105**, 3842–3888.

8 M. K. Cyrański, *Chem. Rev.*, 2005, **105**, 3773–3811.

9 G. Merino, M. Solà, I. Fernández, C. Foroutan-Nejad, P. Lazzeretti, G. Frenking, H. L. Anderson, D. Sundholm, F. P. Cossío, M. A. Petrukhina, J. Wu, J. I. Wu and A. Restrepo, *Chem. Sci.*, 2023, **14**, 5569–5576.

10 K. Lonsdale, *Proc. R. Soc. Lond. A, Math. Phys. Character*, 1929, **123**, 494–515.

11 J. K. F. Awcett and J. Trotter, *Proc. R. Soc. Lond. A Math. Phys. Sci.*, 1966, **289**, 366–376.

12 V. N. Huynh, M. Leitner, A. Bhattacharyya, L. Uhlstein, P. Kreitmeier, P. Sakrausky, J. Rehbein and O. Reiser, *Commun. Chem.*, **3**, 158.

13 J. R. Durland, and H. Adkins, *J. Am. Chem. Soc.*, 1937, **59**, 135–137.

14 M. D. Peeks, T. D. W. Claridge, and H. L. Anderson, *Nature*, 2017, **541**, 200–203.

15 N. L. Allinger, T. J. Walter and M. G. Newton, *J. Am. Chem. Soc.*, 1974, **96**, 4588–4597.

16 Y. Gaoni, A. Melera, F. Sondheimer. and R. Wolovsky, *Proc. Chem. Soc.*, 1964, 397–398.

17 M. Rickhaus, M. Jirasek, L. Tejerina, H. Gotfredsen, M. D. Peeks, R. Haver, H. W. Jiang, T. D. W. Claridge, and H. L. Anderson *Nature Chem.*, 2020, **12**, 236–241.

18 M. Jirásek, M. Rickhaus, L. Tejerina and H. L. Anderson, *J. Am. Chem. Soc.*, 2021, **143**, 2403–2412.

19 P. von Ragué Schleyer and H. Jiao, *Pure Appl. Chem.*, 1996, **68**, 209–218.

20 J. Kruszewski and T. M. Krygowski, *Tetrahedron Lett.*, 1972, **13**, 3839–3842.

21 J. C. Dobrowolski, *ACS Omega*, 2019, **4**, 18699–18710.

22 F. Feixas, E. Matito, J. Poater, and M. Solà, *J. Phys. Chem. A*, 2007, **111**, 4513–4521.

23 P. von Ragué Schleyer, *Chem. Rev.*, 2001, **101**, 1115–1117.

24 P. von Ragué Schleyer, C. Maerker, A. Dransfeld, H. Jiao and N. J. R. van Eikema Hommes, *J. Am. Chem. Soc.*, 1996, **118**, 6317–6318.

25 R. Herges and D. Geuenich, *J. Phys. Chem. A*, 2001, **105**, 3214–3220.

26 D. Geuenich, K. Hess, F. Köhler and R. Herges, *Chem. Rev.*, 2005, **105**, 3758–3772.

27 H. Fliegl, S. Taubert, O. Lehtonen and D. Sundholm, *Phys. Chem. Chem. Phys.*, 2011, **13**, 20500–20518.

28 E. Matito, P. Salvador, M. Duran and M. Solà, *J. Phys. Chem. A*, 2006, **110**, 5108–5113.

29 D. W. Szczepanik, M. Andrzejak, J. Dominikowska, B. Pawełek, T. M. Krygowski, H. Szatylowicz and M. Solà, *Phys. Chem. Chem. Phys.*, 2017, **19**, 28970–28981.

30 P. von Ragué Schleyer and F. Puhlhofer, *Org. Lett.*, 2002, **4**, 2873–2876.

31 S. E. Wheeler, K. N. Houk, P. von Ragué Schleyer and W. D. Allen, *J. Am. Chem. Soc.*, 2009, **131**, 2547–2560.

32 P. K. Saha, A. Mallick, A. T. Turley, A. N. Bismillah, A. Danos, A. P. Monkman, A. J. Avestro, D. S. Yufit and P. R. McGonigal, *Nature Chem.*, 2023 **15**, 516–525.

33 Z. Chen, C. S. Wannere, C. Corminboeuf, R. Puchta and P. von Ragué Schleyer, *Chem. Rev.*, 2005, **105**, 3842–3888.

34 S. Ostrowski and J. C. Dobrowolski, *RSC Adv.*, 2014, **4**, 44158–44161.

35 K. Hafner, *Angew. Chem. Int. Ed. Engl.*, 1964, **3**, 165–173.

36 B. Ye and N. Cramer, *Science*, 2012, **338**, 504–506.

37 G. Merling, *Ber. Dtsch. Chem. Ges.*, 1891, **24**, 3108–3126.

38 W. von E. Doering and L. H. Knox, *J. Am. Chem. Soc.*, 1954, **76**, 3203–3206.

39 F. Hoffmann, G. W. Fester and J. Wagler, *Zeitschrift fur Naturforschung — Sect. B J. Chem. Sci.*, 2010, **65**, 1137–1142.

40 M. J. S. Dewar and E. Haselbach, *J. Am. Chem. Soc.*, 1970, **92**, 590–598.

41 W. G. Fateley and E. R. Lippincott, *J. Am. Chem. Soc.*, 1955, **77**, 249–250.

42 W. Abraham, B. Dreher and D. Kreysig, *J. Prakt. Chem.*, 1987, **329**, 569–578.

43 W. R. V. A. Kharlanov, W. Abraham, *J Photochem. Photobiol. A Chem.*, 2001, **143**, 109–117.

44 F. A. L. Anet, *J. Am. Chem. Soc.*, 1964, **86**, 458–460.

45 S. S. Butcher, *J. Chem. Phys.*, 1965, **42**, 1833–1836.

46 W. H. Donovan and W. E. White, *J. Org. Chem.*, 1996, **61**, 969–977.

47 A. Ladenburg, *Ber. Dtsch. Chem. Ges.*, 1881, **14**, 2126–2131.

48 R. Willstätter, *Justus Liebigs Ann. Chem.*, 1901, **317**, 204–265.

49 W. Abraham, L. Grubert, U. W. Grummt and K. Buck, *Chemistry—A Eur. J.*, 2004, **10**, 3562–3568.

50 N. Toselli, D. Martin, M. Achard, A. Tenaglia, T. Bürgi and G. Buono, *Adv. Synth. Catal.*, 2008, **350**, 280–286.

51 B. W. T. A. Pidcock, *J. Chem. Soc. A*, 1967, **0**, 877–879.

52 P. G. Georg Hvistendahl, Kjell Undheim, *Org. Mass Spectrom.*, 1973, **7**, 903–905.

53 E. E. van Tamelen, T. A. Spencer, D. S. Allen and R. L. Orvis, *J. Am. Chem. Soc.*, 1959, **81**, 6341–6342.

54 T. Curtius, *Ber. Dtsch. Chem. Ges.*, 1883, **16**, 2230–2231.

55 E. B. T. Curtius, *Mittheilung aus d. chem. Labor. d. kgl. Acad. der Wissensch. zu Miinchen*, 1884, 2377–2379.

56 J. F. Liebman and A. Greenberg, *Chem. Rev.*, 1989, **89**, 1225–1246.

57 A. J. Anciaux, A. Demonceau, A. F. Noels, A. J. Hubert, R. Warin and P. Teyssié, *J. Org. Chem.*, 1981, **46**, 873–876.

58 R. Hoffmann, *Tetrahedron Lett.*, 1970, **11**, 2907–2909.

59 F. A. L. Anet, *J. Am. Chem. Soc.*, 1964, **86**, 458–460.

60 F. R. Jensen and L. A. Smith, *J. Am. Chem. Soc.*, 1964, **86**, 956–957.

61 R. Wehner and H. Günther, *J. Am. Chem. Soc.*, 1975, **97**, 923–924.

62 J. M. Assour and S. E. Harrison, *J. Am. Chem. Soc.*, 1965, **87**, 652–653.

63 T. Clark, G. W. Spitznagel, R. Klose and P. von Ragué Schleyer, *J. Am. Chem. Soc.*, 1984, **106**, 4412–4419.

64 H. E. Winberg, *J. Org. Chem.*, 1959, **24**, 264–265.

65 L. M. Bateman, O. A. McNamara, N. R. Buckley, P. O'Leary, F. Harrington, N. Kelly, S. O'Keeffe, A. Stack, S. O'Neill, D. G. McCarthy and A. R. Maguire, *Org. Biomol. Chem.*, 2015, **13**, 11026–11038.

66 K. Fukui, T. Yonezawa and H. Shingu, *J. Chem. Phys.*, 1952, **20**, 722–725.

67 R. B. Woodward and R. Hoffmann, *Angew. Chem. Int. Ed. Engl.*, 1969, **8**, 781–853.

68 H. D. W. Dilthey, W. Schommer, W. Höschen, *Ber. Dtsch. Chem. Ges. (A and B Series)*, 1935, **68**, 1159–1162.

69 M. A, Battiste, *J. Am. Chem. Soc.*, 1961, **83**, 4101–4102.

70 R. Breslow and H. W. Chang, *J. Am. Chem. Soc.*, 1965, **87**, 2200–2203.

71 J. Sturala, M. K. Etherington, A. N. Bismillah, H. F. Higginbotham, W. Trewby, J. A. Aguilar, E. H. C. Bromley, A.-J. Avestro, A. P. Monkman and P. R. Mcgonigal, *J. Am. Chem. Soc.*, 2017, **139**, 17882–17889.

72 D. N. Reinhoudt, P. Smael, W. J. M. van Tilborg, J. P. Visser, *Tetrahedron Lett.*, 1973, **39**, 3755–3758.

73 W. J. M. van Tilborg, P. Smael, J. P. Visser, C. G. Kouwenhoven and D. N. Reinhoudt, *Recl. des Trav. Chim. des Pays-Bas*, 1975, **94**, 85–88.

74 T. A. Engler, K. D. Combrink and F. Takusagawa, *J. Chem. Soc., Chem. Commun.*, 1989, **2**, 1573–1576.

75 W. Treibs, *Angew. Chem. Int. Ed. Engl.*, 1979, **18**, 162–163.

76 M. Harmata, *Chem. Commun.*, 2010, **46**, 8886–8903.

77 W. M. Shu, J. R. Ma, Y. Yang and A. X. Wu, *Org. Lett.*, 2014, **16**, 1286–1289.

78 D. H. Geske, *J. Am. Chem. Soc.*, 1959, **81**, 4145–4147.

79 C. A. Bunton, F. Davoudazedeh and W. E. Watts, *J. Am. Chem. Soc.*, 1981, **103**, 3855–3858.

80 T. Shono, T. Nozoe, H. Maekawa, Y. Yamaguchi, S. Kanetaka, H. Masuda, T. Okada and S. Kashimura, *Tetrahedron*, 1991, **47**, 593–603.

81 A. W. Johnson, A. Langemann and M. Tisler, *J. Chem. Soc.*, 1955, 1622–1626.

82 K. Conrow, *J. Am. Chem. Soc.*, 1961, **83**, 2343–2350.

83 C. Jutz, *Chem. Ber.*, 1964, **97**, 2050–2065.

84 G. D. Kolomnikova and Z. N. Parnes, *Rus. Chem. Rev.*, 1967, **36**, 735–753.

85 M. A. Battiste and T. J. Barton, *Tetrahedron Lett.*, 1968, **25**, 2951–2954.

86 L. C. F. Chao, H. K. Gupta, D. W. Hughes, J. F. Britten, S. S. Rigby, A. D. Bain and M. J. McGlinchey, *Organometallics*, 1995, **14**, 1139–1151.

87 S. Brydges, J. F. Britten, L. C. F. Chao, H. K. Gupta, M. J. McGlinchey and D. L. Pole, *Chem—Eur. J.*, 1998, **4**, 1201–1205.

88 U. P. N. Tran, G. Oss, D. P. Pace, J. Ho and T. V. Nguyen, *Chem. Sci.*, 2018, **9**, 5145–5151.

89 M. A. Hussein, V. T. Huynh, R. Hommelsheim, R. M. Koenigs and T. V Nguyen, *Chem. Commun.*, 2018, **54**, 12970–12973.

90 T. Murahashi, M. Fujimoto, M. A. Oka, Y. Hashimoto, T. Uemura, Y. Tatsumi, Y. Nakao, A. Ikeda, S. Sakaki and H. Kurosawa, *Science*, 2006, **313**, 1104–1107.

91 D. J. M. Lyons, R. D. Crocker and T. V. Nguyen, *Chem.—Eur. J.*, 2018, **24**, 10959–10965.

92 W. Abraham, L. Grubert, U. W. Grummt and K. Buck, *Chem.—Eur. J.*, 2004, **10**, 3562–3568.

93 A. E. Maughan, J. A. Kurzman and J. R. Neilson, *Inorg. Chem.*, 2015, **54**, 370–378.

94 V. G. Jiménez, R. Tapia, M. A. Medel, I. F. A. Mariz, T. Ribeiro, V. Blanco, J. M. Cuerva, E. Maçôas and A. G. Campaña, *Chem. Commun.*, 2018, **54**, 3359–3362.

95 R. D. Crocker, B. Zhang, D. P. Pace, W. W. H. Wong and T. V Nguyen, *Chem. Commun.*, 2019, **55**, 11591–11594.

96 V. G. Jiménez, P. Mayorga-Burrezo, V. Blanco, V. Lloveras, C. J. Gómez-García, T. Šolomek, J. M. Cuerva, J. Veciana and A. G. Campaña, *Chem. Commun.*, 2020, **56**, 12813–12816.

97 K. S. Novoselov, A. K. Giem, S. V. Morozov, D. Jiang, Y. Zhang, S. V. Dubonos, I. V. Grigorieva and A. A. Firsov, *Science*, 2004, **306**, 666–669.

98 X. Yan, B. Li and L. S. Li, *Acc. Chem. Res.*, 2013, **46**, 2254–2262.

99 X. Y. Wang, X. Yao and K. Müllen, *Sci. China Chem.*, 2019, 62, 1099–1144.

100 K. I. Bolotin, K. J. Sikes, Z. Jiang, M. Klima, G. Fudenberg, J. Hone, P. Kim and H. L. Stormer, *Solid State Commun*, 2008, **146**, 351–355.

101 Y. Zhang, T. T. Tang, C. Girit, Z. Hao, M. C. Martin, A. Zettl, M. F. Crommie, Y. R. Shen and F. Wang, *Nature*, 2009, **459**, 820–823.

102 K. M. Xiao-Ye Wang, Akimitsu Narita, *Nature Rev. Chem.*, 2018, **2**, 1–10.

103 X. Wang, G. Sun, P. Routh, D. H. Kim, W. Huang and P. Chen, *Chem. Soc. Rev.*, 2014, **43**, 7067–7098.

104 Z. Xiang, Q. Dai, J. F. Chen and L. Dai, *Adv. Mater.*, 2016, **28**, 6253–6261.

105 M. Grzybowski, K. Skonieczny, H. Butenschön and D. T. Gryko, *Angew. Chem. Int. Ed.*, 2013, **52**, 9900–9930.

106 L. Zhai, R. Shukla and R. Rathore, *Org. Lett.*, 2009, **11**, 3474–3477.

107 F. A. Vingiello, J. Yanez and J. A. Campbell, *J. Org. Chem.*, 1971, **36**, 2053–2056.

108 B. T. King, J. Kroulík, C. R. Robertson, P. Rempala, C. L. Hilton, J. D. Korinek and L. M. Gortari, *J. Org. Chem.*, 2007, **72**, 2279–2288.

109 R. Rathore, A. S. Kumar, S. V. Lindeman and J. K. Kochi, *J. Org. Chem.*, 1998, **63**, 5847–5856.

110 M. S. Little, S. G. Yeates, A. A. Alwattar, K. W. J. Heard, J. Raftery, A. C. Edwards, A. V. S. Parry and P. Quayle, *Eur. J. Org. Chem.*, 2017, **2017**, 1694–1703.

111 P. Rempala, J. Kroulik and B. T. King, *J. Org. Chem.*, 2006, **71**, 5067–5081.

112 J. Cai, P. Ruffieux, R. Jaafar, M. Bieri, T. Braun, S. Blankenburg, M. Muoth, A. P. Seitsonen, M. Saleh, X. Feng, K. Müllen and R. Fasel, *Nature*, 2010, **466**, 470–473.

113 P. Herwig, C. W. Kayser, K. Müllen and H. W. Spiess, *Adv. Mater.*, 1996, **8**, 510–513.

114 H. S. Kim, J. H. Lee, T. H. Kim, S. Okabe, M. Shibayama and S. M. Choi, *J. Phys. Chem. B*, 2011, **115**, 7314–7320.

115 J. Wu, M. Baumgarten, M. G. Debije, J. M. Warman and K. Müllen, *Angew. Chem. Int. Ed.*, 2004, **43**, 5331–5335.

116 Y. Hu, L. F. Dössel, X. Y. Wang, S. Mahesh, W. Pisula, S. De Feyter, X. Feng, K. Müllen and A. Narita, *Chempluschem*, 2017, **82**, 1030–1033.

117 L. F. Dössel, V. Kamm, I. A. Howard, F. Laquai, W. Pisula, X. Feng, C. Li, M. Takase, T. Kudernac, S. De Feyter and K. Müllen, *J. Am. Chem. Soc.*, 2012, **134**, 5876–5886.

118 Y. Zou, Y. Han, S. Wu, X. Hou, C. H. E. Chow and J. Wu, *Angew. Chem. Int. Ed.*, 2021, **60**, 17654–17663.

119 M. Grzybowski, B. Sadowski, H. Butenschön and D. T. Gryko, *Angew. Chem. Int. Ed.*, 2020, **59**, 2998–3027.

120 P. Izquierdo-García, J. M. Fernández-García, J. Perles, I. Fernández and N. Martín, *Angew. Chem. Int. Ed.*, 2023, **62**, e202215655.

121 F. Morgenroth, C. Kübel, M. Müller, U. M. Wiesler, A. J. Berresheim, M. Wagner and K. Müllen, *Carbon*, 1998, **36**, 833–837.

122 C. D. Simpson, J. D. Brand, A. J. Berresheim, L. Przybilla, H. J. Raeder and K. Müllen, *Chem.—Eur. J.*, 2002, **8**, 1424–1429.

123 J. L. Ormsby, T. D. Black, C. L. Hilton, Bharat and B. T. King, *Tetrahedron*, 2008, **64**, 11370–11378.

124 H. Arslan, F. J. Uribe-Romo, B. J. Smith and W. R. Dichtel, *Chem. Sci.*, 2013, **4**, 3973–3978.

125 Q. Zhang, H. Peng, G. Zhang, Q. Lu, J. Chang, Y. Dong, X. Shi and J. Wei, *J. Am. Chem. Soc.*, 2014, **136**, 5057–5064.

126 E. Clar and J. F. Stephen, *The Synthesis of 1:2, 3:4, 5:6, 7:8, 9:10, 11:12-Hexabenzocoronene*, Pergamon Press Ltd, Oxford, vol. 21, 1965.

127 B. Liu, D. Shi, Y. Yang, D. Liu, M. Li, E. Liu, X. Wang, Q. Zhang, M. Yang, J. Li, X. Shi, W. Wang and J. Wei, *Eur. J. Org. Chem.*, 2018, 869–873.

128 N. C. Davy, G. Man, R. A. Kerner, M. A. Fusella, G. E. Purdum, M. Sezen, B. P. Rand, A. Kahn and Y. L. Loo, *Chem. Mater.*, 2016, **28**, 673–681.

129 J. Yu, Y. Chen, Y. H. Zhang, X. Xu and Y. Liu, *Org. Lett.*, 2016, **18**, 4542–4545.

130 D. Pérez, D. Peña and E. Guitián, *Eur. J. Org. Chem.*, 2013, 5981–6013.

131 B. Schuler, S. Collazos, L. Gross, G. Meyer, D. Pérez, E. Guitián and D. Peña, *Angew. Chem. Int. Ed.*, 2014, **53**, 9004–9006.

132 J. Storch, J. Žádný, V. Církva, M. Jakubec, J. Hrbáč and J. Vacek, *Helicenes: The Photochemical Approach to Helicenes*, Wiley, New York, 2022.

133 F. B. Mallory, C. S. Wood and J. T. Gordon, *J. Am. Chem. Soc.*, 1964, **86**, 3094–3102.

134 A. Sudhakar and T. J. Katz, *Tetrahedron Lett.*, 1986, **27**, 2231–2234.

135 L. Liu, B. Yang, T. J. Katz and M. K. Poindexter, *J. Org. Chem.*, 1991, **56**, 3769–3775.

136 P. Ravat, R. Hinkelmann, D. Steinebrunner, A. Prescimone, I. Bodoky and M. Juríček, *Org. Lett.*, 2017, **19**, 3707–3710.

137 M. Daigle, A. Picard-Lafond, E. Soligo and J.-F. Morin, *Angew. Chem.*, 2016, **55**, 2042–2047.

138 A. Jolly, D. Miao, M. Daigle and J. Morin, *Angew. Chem. Int. Ed.*, 2020, **59**, 4624–4633.

139 W. Hagui, H. Doucet and J.-F. F. Soulé, *Chem*, 2019, **5**, 2006–2078.

140 T. C. Wu, M. K. Chen, Y. W. Lee, M. Y. Kuo and Y. T. Wu, *Angew. Chem. Int. Ed.*, 2013, **52**, 1289–1293.

141 L. T. Scott, H. E. Bronstein, D. V Preda, R. B. M. Ansems, M. S. Bratcher and S. Hagen, *Pure Appl. Chem.*, 1999, **71**, 209–219.

142 J. E. Rice and Z. W. Cai, *J. Org. Chem.*, 1993, **58**, 1415–1424.

143 K. Kawai, K. Kato, L. Peng, Y. Segawa, L. T. Scott and K. Itami, *Org. Lett.*, 2018, **20**, 1932–1935.

144 Chaolumen, I. A. Stepek, K. E. Yamada, H. Ito and K. Itami, *Angew. Chem. Int. Ed.*, 2021, **60**, 23508–23532.

145 M. A. Majewski and M. Stępień, *Angew. Chem. Int. Ed.*, 2019, **58**, 86–116.

146 C. Zhu, K. Shoyama and F. Würthner, *Angew. Chem. Int. Ed.*, 2020, **59**, 21505–21509.

147 T. Fujikawa, Y. Segawa and K. Itami, *J. Am. Chem. Soc.*, 2016, **138**, 3587–3595.

148 S. Xiao, M. Myers, Q. Miao, S. Sanaur, K. Pang, M. L. Steigerwald and C. Nuckolls, *Angew. Chem. Int. Ed.*, 2005, **44**, 7390–7394.

149 J. Luo, X. Xu, R. Mao and Q. Miao, *J. Am. Chem. Soc.*, 2012, **134**, 13796–13803.

150 T. Fujikawa, N. Mitoma, A. Wakamiya, A. Saeki, Y. Segawa and K. Itami, *Org. Biomol. Chem.*, 2017, **15**, 4697–4703.

151 H. Kashihara, T. Asada and K. Kamikawa, *Chem.—Eur. J.*, 2015, **21**, 6523–6527.

152 I. R. Márquez, S. Castro-Fernández, A. Millán and A. G. Campaña, *Chem. Commun.*, 2018, **54**, 6705–6718.

153 R. Zahradník, *Angew. Chem. Int. Ed. Engl.*, 1965, **4**, 1039–1050.

154 M. Rickhaus, M. Mayor and M. Juríček, *Chem. Soc. Rev.*, 2017, **46**, 1643–1660.

155 R. Scholl and K. Meyer, *Ber. Dtsch. Chem. Ges. (A and B Series)*, 1932, **65**, 902–915.

156 E. Nestoros and M. C. Stuparu, *Chem. Commun.*, 2018, **54**, 6503–6519.

157 K. Yamamoto, T. Harada, M. Nakazaki, T. Naka, Y. Kai, S. Harada and N. Kasai, *J. Am. Chem. Soc.*, 1983, **105**, 7171–7172.

158 V. M. Tsefrikas and L. T. Scott, *Chem. Rev.*, 2006, 106, 4868–4884.

159 K. Kawasumi, Q. Zhang, Y. Segawa, L. T. Scott and K. Itami, *Nature Chem.*, 2013, **5**, 739–744.

160 F. Dötz, J. D. Brand, S. Ito, L. Gherghel and K. Müllen, *J. Am. Chem. Soc.*, 2000, **122**, 7707–7717.

161 K. Y. Cheung, X. Xu and Q. Miao, *J. Am. Chem. Soc.*, 2015, **137**, 3910–3914.

162 I. R. Márquez, N. Fuentes, C. M. Cruz, V. Puente-Muñoz, L. Sotorrios, M. L. Marcos, D. Choquesillo-Lazarte, B. Biel, L. Crovetto, E. Gómez-Bengoa, M. T. González, R. Martin, J. M. Cuerva and A. G. Campaña, *Chem. Sci.*, 2017, **8**, 1068–1074.

163 F. Würthner, *Chem. Commun.*, 2004, **4**, 1564–1579.

164 S. Castro-Fernández, C. M. Cruz, I. F. A. Mariz, I. R. Márquez, V. G. Jiménez, L. Palomino-Ruiz, J. M. Cuerva, E. Maçôas and A. G. Campaña, *Angew. Chem. Int. Ed.*, 2020, **59**, 7139–7145.

165 C. M. Cruz, S. Castro-Fernández, E. Maçôas, J. M. Cuerva and A. G. Campaña, *Angew. Chem. Int. Ed.*, 2018, **57**, 14782–14786.

166 Q. Jiang, T. Tao, H. Phan, Y. Han, T. Y. Gopalakrishna, T. S. Herng, G. Li, L. Yuan, J. Ding and C. Chi, *Angew. Chem. Int. Ed.*, 2018, **130**, 16979–16983.

167 X. Fu, H. Han, D. Zhang, H. Yu, Q. He and D. Zhao, *Chem. Sci.*, 2020, **11**, 5565–5571.

168 G. Naville, H. Strauss and E. Heilbronner, *Helv. Chim. Acta*, 1960, **43**, 1221–1243.

169 A. Konishi, K. Horii, D. Shiomi, K. Sato, T. Takui and M. Yasuda, *J. Am. Chem. Soc*, 2019, **141**, 10165–10170.

170 A. Tamoto, N. Aratani and H. Yamada, *Chem.—Eur. J.*, 2017, **23**, 16388–16392.

CHAPTER 2 |

RUPTURING AROMATICITY BY PERIPHERY OVERCROWDING

Published as '*Rupturing Aromaticity by Periphery Overcrowding*'. P. K. Saha, A. Mallick, A. T. Turley, A. N. Bismillah, A. Danos, A. P. Monkman, A.-J. Avestro, D. S. Yufit, and P. R. McGonigal*. *Nature Chem.*, 2023, **15**, 516–525.

Abstract

The balance between strain relief and aromatic stabilisation dictates the form and function of non-planar π-aromatics. Overcrowded systems are known to undergo geometric deformations, but the energetically favorable π-electron delocalisation of their aromatic ring(s) is typically preserved. In this study we incremented the strain energy of an aromatic system beyond its aromatic stabilisation energy, causing it to rearrange and its aromaticity to be ruptured. We noted that increasing the steric bulk around the periphery of π-extended tropylium rings leads them to deviate from planarity to form contorted conformations in which aromatic stabilisation and strain are close in energy. Under increasing strain, the aromatic π-electron delocalisation of the system is broken, leading to the formation of a non-aromatic, bicyclic analogue referred to as 'Dewar tropylium'. The aromatic and non-aromatic isomers have been found to exist in rapid equilibrium with one another. This investigation demarcates the extent of steric deformation tolerated by an aromatic carbocycle and thus provides direct experimental insights into the fundamental nature of aromaticity.

Acknowledgements

The following people are gratefully acknowledged for their contribution to this chapter: Dr. A. Mallick and Dr. A. T. Turley assisted with synthesis and compound characterisation. Dr. A. N. Bismillah and Dr. P. R. McGonigal carried out dynamic NMR spectroscopy. D. S. Yufit solved the X-ray crystal structures. Dr. P. R. McGonigal conceived of the overall project idea and jointly drafted the published work, along with the Author.

2.1. Introduction

Aromaticity has been one of the fundamental tenets of chemical structure for over a century.[1–3] One school of thought defines it as the ability of a molecule to maintain a diatropic ring current when placed in a magnetic field.[4–6] The cyclic electron delocalisation in aromatic systems gives rise to extraordinary stability, equal bond lengths, modified chemical reactivity, and unique electronic properties.[4,7] For example, benzene, the archetypal aromatic compound, exhibits exceptionally high stability relative to other $(CH)_6$ isomers, such as prismane, benzvalene, Möbius benzene, and Dewar benzene (Figure 2.1a).[8,9]

The extraordinary electronic stabilisation brought about by aromatic electron delocalisation is also evident in the properties of tropylium—an aromatic homologue of benzene that exists (Figure 2.1a) as a stable C_7-symmetric carbocation. Since Doering and Knox's seminal work[10] on its isolation and structural elucidation, its electronic properties have been exploited in organocatalysis,[11] stimuli-responsive dyes,[12] and redox-active polycyclic aromatic hydrocarbons (PAHs).[13–15] Relative to benzene, its larger ring size, increased conformational flexibility, and the smaller 51.4° angles subtended by its substituents (cf. 60.0° for benzene) allow tropylium to undergo more facile strain-induced deformations.[16,17] Consequently, it has the potential to form highly twisted structures and to serve as a versatile subunit to probe aromaticity in geometrically deformed systems.[18]

In recent years, there has been increasing interest in nonplanar aromatic structures, including helicenes,[19] twistacenes,[20,21] Möbius aromatics,[22,23] nanohoops,[24–26] nanobelts,[27,28] and warped nanographenes.[29,30] Relatively large deviations from planarity induced by strain are accommodated in these structures while maintaining significant π-electron delocalisation. However, it is challenging to experimentally probe the limits of such deformations. At what point is the aromatic stabilisation energy[26] (ASE) of a ring system outweighed by its strain?

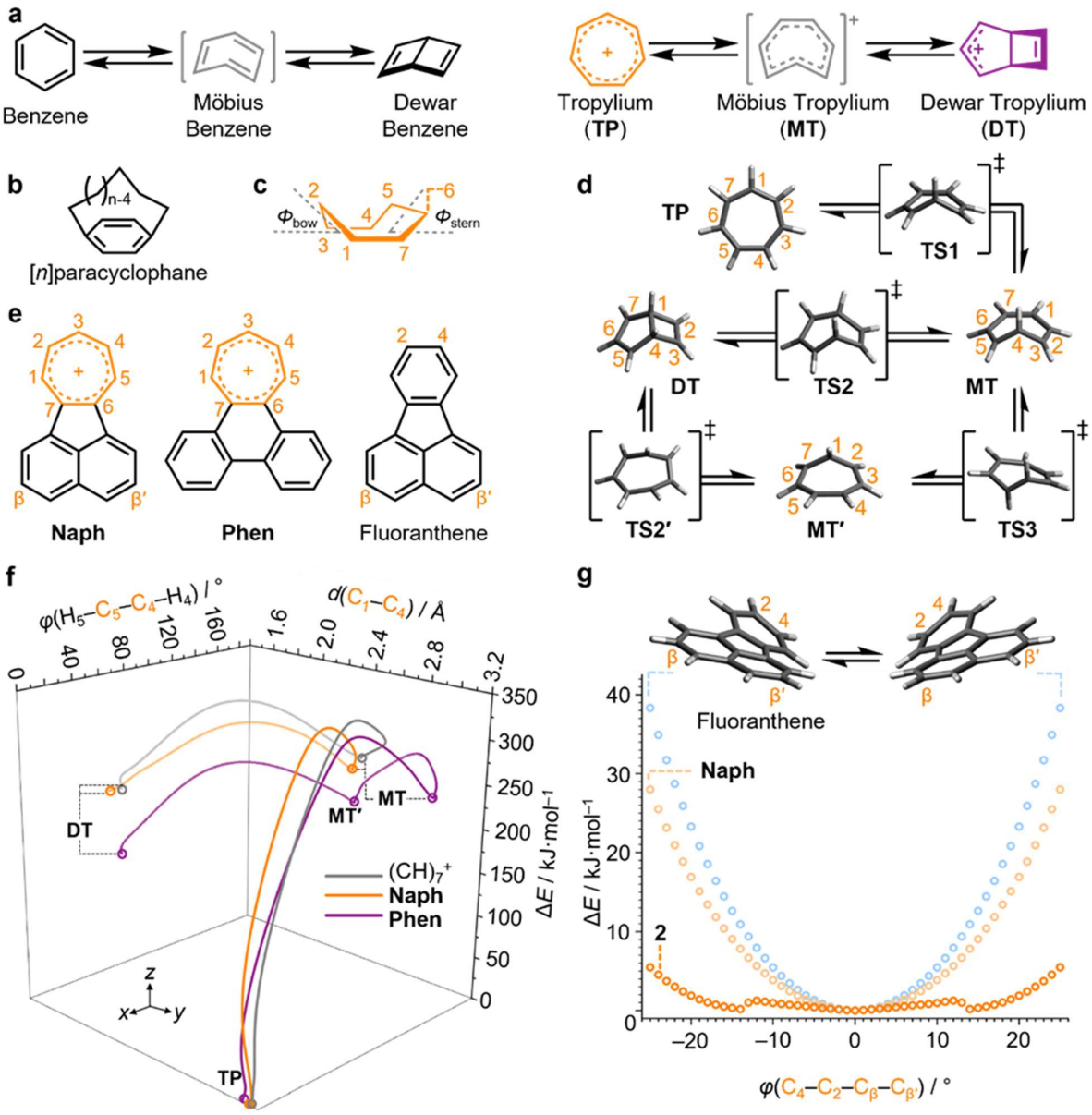

Figure 2.1. Geometric and Valence Isomerism of Aromatic Ring Systems. **a)** Comparison of the planar and bicyclic isomers of $(CH)_6$ and $(CH)_7^+$; **b)** Structural formula of [*n*]paracyclophanes; **c)** A boat conformation of a seven-membered ring; **d)** DFT-optimised energy minima and transition states in the isomerisation pathway between tropylium and Dewar tropylium; **e)** Structural formulas of **Naph**, **Phen**, and fluoranthene; **f)** IRCs for the rearrangements of $(CH)_7^+$, **Naph**, and **Phen**, plotted against the C_1–C_4 internuclear distances, *d,* and the H_5–C_5–C_4–H_4 dihedral angles, φ; **g)** A plot of the energy differences of the twisted aromatic systems relative to their planar geometries (ΔE) obtained by performing a relaxed potential energy scan as the C_4–C_2–C_β–$C_{\beta'}$ torsion angle is varied in 1° increments. See Figure 2.2a for the structural formula of **2**. All DFT calculations were performed using B3LYP (GD3BJ) / 6-31G(d) / CH_2Cl_2.

Certain annulated aromatic rings, such as Siegel's trisbicyclo[2.1.1]hexabenzene,[31] experience large amounts of bond angle strain, which causes them to undergo significant geometric distortion.[32,33] Yet, despite the distorted bond lengths present in these π-systems, effective delocalisation still occurs, and the system remains aromatic.[32] Similarly, bending of a benzene ring into a boat conformation with an out-of-plane angle of 23.2°, enforced by the pentamethylene 'strap' in [5]paracyclophanes (Figure 2.1b), diminishes the magnitude of its π-ring current by only 17%.[34,35] Altering the length of the strap gives some crude control of the strain energy. But an increment of just one methylene group causes a large jump in strain. For example, [4]paracyclophanes are enormously strained structures that have tentatively been assigned[36–38] to undergo thermally irreversible isomerisation to the corresponding Dewar benzenes. However, the inherent instability and reactivity of these short-lived systems have limited their analysis to spectroscopic studies at low temperatures. To date, it has not been possible to finetune the level of strain present in an aromatic system, titrating it to the point at which ASE is overcome. The consequences of precisely offsetting ASE through strain have not been investigated.

2.1.1. Periphery Overcrowding

Here, we report the use of periphery overcrowding,[20,39] i.e., the introduction of sterically demanding substituents around the exterior of a molecule, to tune the geometric deformations experienced by π-extended tropylium ring systems beyond the point at which strain exceeds ASE. On one side of this energetic balance point, we identify structures that exhibit twisted geometries while retaining aromaticity. In the most extreme case, single-crystal X-ray diffraction (XRD) analysis shows (i) an end-to-end twist angle along the π-extended ring system of 45.2° and (ii) that the tropylium is in a distorted boat conformation (Figure 2.1c, Φ_{bow} = 13.0° and Φ_{stern} = 29.0°), while computational modelling of its electronic properties indicates that these large geometric distortions reduce its aromatic character by only ~13%. On the other side of the energetic balance point, the π-extended ring systems sacrifice aromaticity in favor of relieving strain, i.e., by collapse of their tropylium rings into bicyclic Dewar tropylium structures.[40] Dynamic nuclear magnetic resonance (NMR) spectroscopic analysis reveals that an overcrowded Dewar tropylium undergoes reversible exchange between degenerate structures, passing through a twisted tropylium intermediate. This exchange is indicative of a dynamic intramolecular aromatic-to-nonaromatic

equilibrium process that arises by counterbalancing aromaticity against significant ring strain. Understanding these competing energetics in sterically strained systems is integral to designing and exploiting nonplanar PAHs that exist at the limits of aromaticity.[41]

2.2. Results and Discussion

Previous computational studies[42] in conjunction with kinetic measurements[43] have shown that Dewar benzene-to-benzene isomerisation proceeds (Figure 1a) through a conrotatory electrocyclic ring opening. Initially, a highly strained *cis*,*cis*,*trans*-cyclohexatriene (Möbius benzene) intermediate is formed, before a π-bond rotation produces benzene. Relative to benzene, Dewar benzene is destabilised by 326 kJ·mol^{-1}, while the largest activation energy barrier along the isomerisation pathway lies at 443 kJ·mol^{-1}.[44] With this benchmark in mind, we used density functional theory (DFT) to establish the energetic characteristics of deforming and isomerizing $(CH)_7^+$ through its tropylium (**TP**), Möbius-like tropylium (**MT**), and Dewar tropylium (**DT**) isomers (Figure 2.1), as well as isomerizing our subsequent synthetic targets **1**–**4** (Figure 2.2). Note that **MT** is named by analogy to Möbius benzene but lacks the C_2 symmetry of a genuine Möbius topology.

2.2.1. Aromatic-to-Nonaromatic $(CH)_7^+$ Isomerisation

A screen of functionals and basis sets (section 2.5.2 and Table 2.15) indicated that the B3LYP functional[45] with the D3 version of Grimme's dispersion correction and Becke–Johnson damping,[46] the 6-31G(d) basis set,[47] and a CH_2Cl_2 polarizable continuum solvent model (using the integral equation formalism variant)[48] is suitable for modelling the energetics of these systems. Using this level of theory, we identified (Figure 2.1d) a series of possible transition states and Möbius tropylium intermediates that could link tropylium and Dewar tropylium. We also modelled (Figure 2.1e) the same processes for two π-extended tropylium derivatives containing *ortho*-fused 1,2-acenaphthylene (**Naph**) or 9,10-phenanthrene (**Phen**) ring systems—the parent compounds of our subsequent targets **2**, **3** and **4** (Figure 2a).

We visualised isomerisation pathways (Figure 1f) using intrinsic reaction coordinate (IRC) calculations[49] from the optimised transition state geometries. Transition state **TS1** connects the high-energy **MT** intermediate to the aromatic **TP** isomer. During

this transformation, the most significant geometric change occurs in the torsion angle $\varphi(H_5–C_5–C_4–H_4)$ as it varies (Figure 2.1f) from 0° (**TP**) to approximately 180° (**MT**). Starting from transition state **TS2** (the conrotatory ring-opening transition state), the IRC paths for $(CH)_7^+$ and **Naph** provide the aforementioned Möbius intermediates in one direction and the Dewar tropylium isomers in the other, completing the tropylium-to-Dewar tropylium isomerisation pathway. This structural evolution is best visualised by following (Figure 1f) the change in the internuclear distance $d(C_1–C_4)$, which is shortest (~1.6 Å) when C_1 and C_4 share a single bond in a Dewar tropylium structure and longest (~3.1 Å) when they are separated across an aromatic tropylium ring. Our calculations suggest that a slightly modified isomerisation pathway is preferred for **Phen**. The **MT** state evolves first to another Möbius intermediate (**MT′**) in which C_1 rather than C_4 is in the out-of-plane position, before shortening of $d(C_1–C_4)$ leads to the **DT** structure. **TS1** corresponds to the highest energy point along the IRCs of $(CH)_7^+$ and **Phen**, presenting rate-limiting activation energy barriers, $\Delta G^‡$, of 302 and 297 kJ·mol^{-1}, respectively (Tables 2.16–2.21). **TS2** is the highest energy point along the IRC of **Naph**, with $\Delta G^‡$ = 315 kJ·mol^{-1}. Further details, including the full structures associated with all energy minima and transition states, are included in the Supplementary Information (Figures. 2.36–2.38).

Overall, the aromatic-to-nonaromatic isomerisation of tropylium generally mirrors that of benzene (Figure 1). Similar distortions of the aromatic ring geometry occur, albeit with the increased flexibility and reduced ASE[26] of the seven-membered ring contributing to a lower overall activation energy barrier, $\Delta G^‡$ (302 kJ·mol^{-1} for tropylium vs 443 kJ·mol^{-1} for benzene). We quantified the magnitude of this reduced ASE by calculating the energetics of hyperhomodesmotic[50] reactions (Figure 2.41) according to Schleyer's isomerisation stabilisation energy method.[51] Using the same level of theory outlined above, we found that $(CH)_7^+$, **Naph**, and **Phen** experience (Table 2.1) ASE's in the range of approximately −50 kJ·mol^{-1}, which are approximately half the ASE of benzene (−98.5 kJ·mol^{-1}). As the B3LYP functional is known to overestimate aromatic stabilisation in larger aromatic circuits,[52] we also estimated ASEs using the M06-2X functional and found them to be comparable to our B3LYP predictions (Table 2.22–2.23).

2.2.2. Thermodynamic Tuning by Periphery Overcrowding

We postulated that the introduction of sterically bulky groups around the periphery of $(CH)_7^+$ and its π-extended derivatives would decrease the aromatic-to-nonaromatic ΔG by favoring twisted geometries that more closely resemble the nonplanar Möbius and Dewar structures. To test this hypothesis, we performed a series (Figure 2.1g) of geometry optimisations for fluoranthene, **Naph** and **2**. The torsion angle $\varphi(C_4–C_2–C_\beta–C_{\beta'})$ was scanned in increments of 1° in order to determine the energetic cost of twisting deformations. This end-to-end twisting in **Naph** carries a lower energy penalty compared to its six-membered ring counterpart, fluoranthene, as would be expected given the greater degrees of freedom of its seven-membered ring. Additional peripheral overcrowding caused by the phenyl groups of **2** destabilises the fully coplanar tropylium structure, dramatically flattening (Figure 2.1g) the energy well for twisting deformation. Indeed, subsequent unrestrained geometry optimisations identified two local energy minima for structures with $\varphi(C_4–C_2–C_\beta–C_{\beta'})$ of 14.3° and 0.4° (Table 1). These two conformations strike different balances between the optimal π-electron delocalisation of the planar structure and the reduced steric strain of the nonplanar structure. In keeping with this phenomenon, our calculations also show that this peripheral overcrowding makes the Möbius isomers much more energetically accessible. The ΔG between tropylium **2** and its Möbius form, **2-MT**, is calculated to be only 96 kJ·mol^{-1} (compared to a gap of 259 kJ·mol^{-1} for the model compound **Naph**, which lacks Ph groups). Similarly for compound **4**, the two Möbius isomers **4-MT** and **4-MT′** are only 67 and 28 kJ·mol^{-1} higher in energy than the tropylium form **4-TP** (again showing a significant decrease relative to the analogous structures **Phen-MT** and **Phen-MT′** with ΔG = 232 and 209 kJ·mol^{-1}, respectively).

Table 2.1. Torsion angles and tropylium aromaticity.

	$(CH)_7^+$	Naph	Phen	1	2	3	4-TP
$\varphi(C_4\text{-}C_2\text{-}C_\beta\text{-}C_{\beta'})$ calc.* / °	-	0	31.6	-	14.3, 0.4§	45.4	61.7
$\varphi(C_4\text{-}C_2\text{-}C_\beta\text{-}C_{\beta'})$ exp.◊ / °	-	0	-	-	18.4, 0.4§	45.2	-
Φ_{bow} calc.* / °	0	0		16.3	2.8♦	15.0	16.3

Φ_{bow} exp.$^{\Diamond}$ / °	0	-	-	13.6	6.7$^{\blacklozenge}$	13.0	-
Φ_{stern} calc.* / °	0	0		18.4	7.3$^{\blacklozenge}$	28.8	31.8
Φ_{stern} exp.$^{\Diamond}$ / °	0	-	-	12.2	13.7$^{\blacklozenge}$	29.0	-
ASE / kJ mol^{-1}	−50.3	−55.1	−50.7	-	-	-	-
NICS$_{zz}$(1)*,¶	−29.11	−18.38	−19.22	−18.91	−15.59$^{\blacklozenge}$	−14.01	−16.90
NICS$_{zz}$(−1)*,¶	−29.11	−18.38	−19.22	−18.90	−15.57$^{\blacklozenge}$	−14.07	−16.90
EDDB^{k}**	4.94	3.08, 6.00	3.01, 7.05	4.26	3.09, 5.97$^{\blacklozenge}$	2.69, 5.89	2.84, 6.66

*Calculated using DFT optimised geometries (B3LYP (GD3BJ) / 6-31G(d) / CH_2Cl_2). $^{\Diamond}$Measured by single-crystal XRD analysis. §Energy minima with two different torsion angles are predicted to be close in energy by DFT (5.6 kJ·mol^{-1}), which match closely with the conformers of **2** observed in the crystal lattice. $^{\blacklozenge}$Values given for the twisted conformer of **2**. ¶NICS$_{zz}$(±1) values calculated 1 Å above and below the averaged plane of the tropylium rings. **Where two values are given, they correspond to the number of delocalised electrons in the tropylium ring circuit and the number delocalised over the entire annulated framework, respectively.

We further investigated the impacts of steric and electronic factors on the aromatic-to-nonaromatic Gibbs energy gap by modelling an extended series of compounds. Starting from the previously reported heptaphenyltropylium cation **1**,[17] which exhibits a 26 kJ·mol^{-1} preference for the aromatic tropylium isomer, we sought to increase steric bulk in the plane of the tropylium core. Cation **2** provides an ideal scaffold for this purpose.[53] Despite its overcrowding, this species has an increased preference for the tropylium isomer (ΔG = 75 kJ·mol^{-1}) on account of the extensive π-electron delocalisation between the tropylium and the annulated naphthyl rings.[54] By contrast, the phenyl groups of **1** and **2** lie almost orthogonal to the central rings to minimise steric strain, so they have minimal π-overlap with the tropylium rings.

Our calculations suggest (Figure 2.2) that while electron-donating or -withdrawing substituents at the β- and γ-positions of the acenaphthyl ring system tune the energetic balance of isomers by a few kJ·mol^{-1}, increasing the steric bulk at the α- and α′-positions (which abut the phenyl rings) tunes the relative isomer energies over a larger range. For example, α,α′-dimethyl substitution reduces the energy gap to 42 kJ·mol^{-1}. The gap is reduced to 15 kJ·mol^{-1} by the α,α′-diethyl-substitution of compound **3** and further still to 8.4 kJ·mol^{-1} by α,α′-diisopropyl substitution. The low thermodynamic bias in favour of the aromatic isomer for these overcrowded systems

approaches the critical point where ASE and strain energy are evenly balanced. Consequently, the tropylium ring geometries would be expected to be among the most distorted possible. Indeed, increasing the size of appended moiety to a phenanthrene-annulated system pushes the thermodynamic preference towards the Dewar tropylium isomer. The tropylium form of the parent **Phen** is already destabilised[55] (Figure 2b) relative to $(CH)_7^+$ and **Naph** on account of a more sterically congested tropylium-to-PAH bay region. The added strain caused by the five proximal phenyl rings of **4** is sufficient to tune the energetic balance in favour of the Dewar tropylium by 5.3 kJ·mol^{-1}.

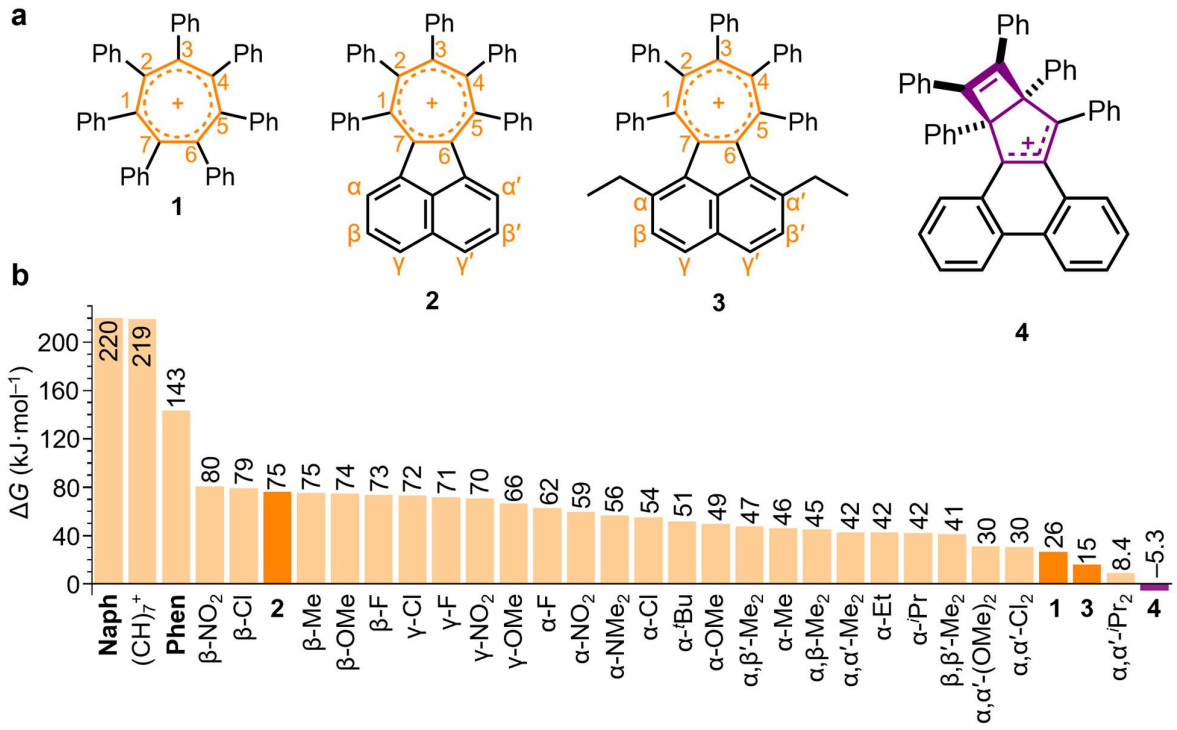

Figure 2.2. Predicted Effects of Periphery Overcrowding. a) Cations **1**–**4** synthesised in this work; **b)** Calculated Gibbs energy differences (ΔG) between tropylium and Dewar tropylium forms of $(CH)_7^+$, **Naph**, **Phen**, **1**–**4** and a series of derivatives of **2** (B3LYP (GD3BJ) / 6-31G(d) / CH_2Cl_2). The substituent positions indicated in panel (b) correspond to the positions of **2** labelled in panel (a). Positive values (orange bars) indicate an energetically favorable tropylium isomer, while negative values (purple bars) denote a bias toward the Dewar tropylium. For asymmetrical substitution patterns that break the C_2 symmetry, the lower energy of the two possible Dewar tropylium isomers has been used to estimate ΔG.

2.2.3. Synthesis of Twisted and Dewar Tropyliums

Cations **1**–**4** were selected as synthetic targets that span a wide range of calculated ΔG values—**1** and **2** favour an aromatic tropylium, **4** is biased towards a Dewar tropylium isomer and **3** is close to the border between the two. Their syntheses are outlined in Figure 3.

Firstly, dienophiles **5** and **6** were both prepared from diphenylacetylene (section 2.4.1). As a precursor to **1**, *sym*-heptaphenylcycloheptatriene, **7**, was formed (Figure 2.3) by the Diels–Alder cycloaddition of **5** with tetraphenylcyclopentadienone (tetracyclone) and subsequent cheletropic elimination of CO.[56] Oxidation of **7** using an excess of ICl then yielded **1** as its iodine dichloride salt (**1**·ICl_2). Analogous phenanthrene- and acenaphthene-annulated cycloheptatrienes, as well as a α,α′-diethyl derivative **8**, were also accessed through the same approach by reacting **5** with an appropriate cyclopentadienone reagent (phencyclone, acecyclone, and diethylacecyclone, respectively). However, attempts to oxidise these compounds with ICl or Br_2 led to unwanted halogenation of the electron-rich annulated ring systems in preference to oxidation of the cycloheptatrienes. Hydride abstraction reactions were also unsuccessful.

Instead, target cations **2** and **4** were prepared successfully (Figure 2.3) by first reacting acecyclone and phencyclone with **6** to afford tropones **9** and **10**, respectively. Subsequent nucleophilic attack by PhMgBr at the carbonyl introduces a final phenyl ring and forms a tertiary alcohol group, which is readily eliminated upon treatment with triethyloxonium hexachloroantimonate to give **2**·$SbCl_6$ and **4**·$SbCl_6$.

We attempted a similar strategy to prepare **3**. However, cycloaddition between **6** and diethylacecyclone did not yield the desired tropone. We observed that the high temperature (190 °C) required for reaction of this sterically crowded diene causes rapid decomposition of **6**. Instead, we employed a stepwise oxidation protocol to convert cycloheptatriene **8** to tropylium **3**. Oxidation of **8** using *m*CPBA in refluxing $CHCl_3$ formed a mixture of products, from which we isolated an epoxide intermediate (**S1**). By treating the epoxide with a stoichiometric amount of BBr_3 under the inert

conditions of a glovebox, we were able to form **3** in trace amounts and isolate single crystals of its tetrabromoborate salt **3**·BBr_4 upon slow evaporation of the reaction mixture. The apparently high reactivity of the contorted cation **3** and associated low yield prevented us from obtaining solution-state spectroscopic data. However, XRD analysis of the crystals confirmed its identity and allowed us to measure its geometric parameters (*vide infra*).

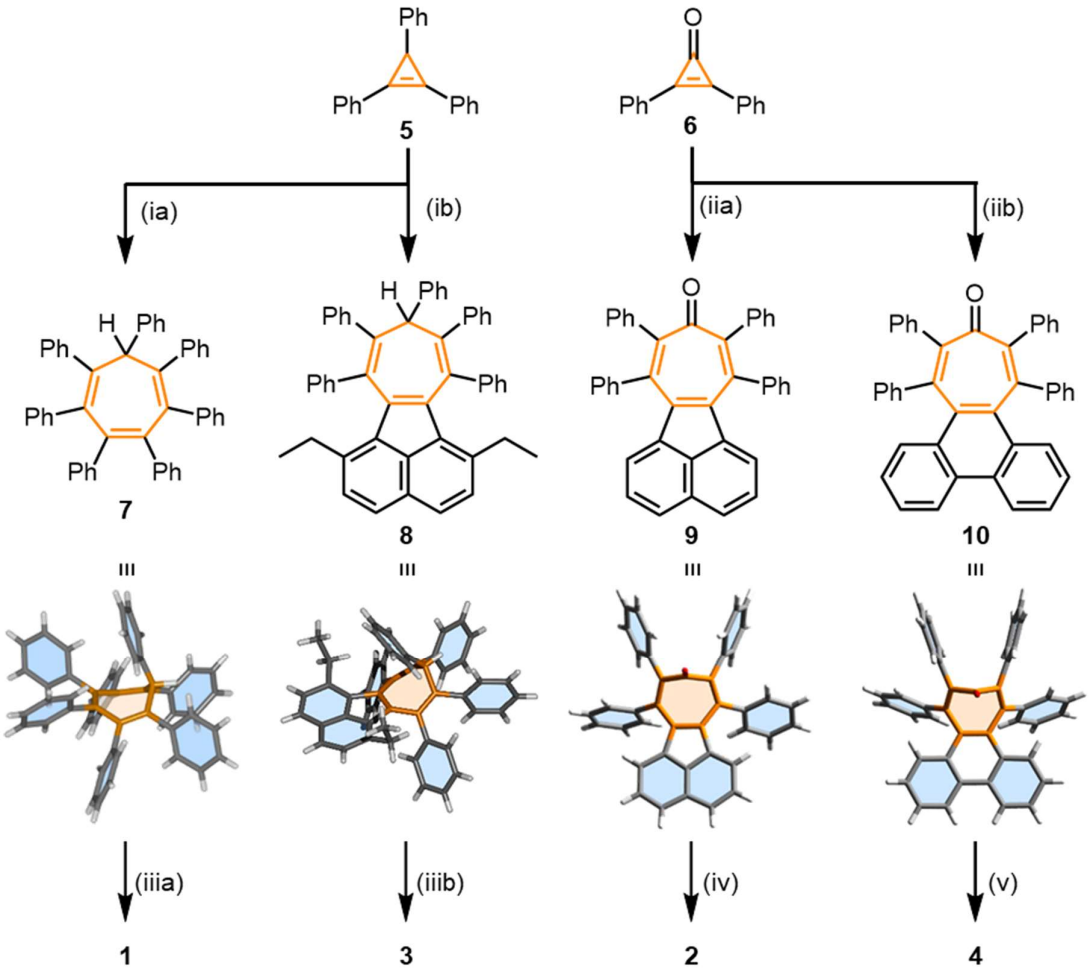

Figure 2.3. **Synthesis of Sterically Overcrowded Tropyliums**. Reagents and conditions: **ai) 5**, tetracyclone, *p*-xylene, 140 °C, 36 h, 82%; **aii)** ICl (1.0 M in CH_2Cl_2), rt, 24 h, 60%; **bi) 5**, diethylacecyclone, *p*-xylene, 190 °C, 84 h, 22%; **bii)** 1. *m*CPBA, $CHCl_3$, sat. $NaHCO_{3\,(aq)}$, reflux, 20 h, 12%; 2. BBr_3, CH_2Cl_2, rt, 10 min; **ci) 6**, acecyclone, PhMe–$CHCl_3$ (5:3), 130 °C, 24 h, 34%; **cii)** 1. PhMgBr, THF, 0 °C → rt, 3h, 68%; 2. $Et_3O{\cdot}SbCl_6$, $CDCl_3$, rt, 10 min, quant.; **di) 6**, phencyclone, PhMe, 130 °C, 24 h, 40%; **dii)** 1. PhMgBr, THF, 0 °C → rt, 3h, 60%; 2. $Et_3O{\cdot}SbCl_6$, $CDCl_3$, rt, 10 min, quant. *m*CPBA = *m*-chloroperbenzoic acid. Solid-state structures determined by XRD analysis are shown for the four key intermediates, **7**–**10.**

2.2.4. Geometric Distortions of Tropylium Rings

We determined the solid-state structures of **1**–**4** (Figure 2.4a) by XRD analysis of single crystals. While the geometries of the cations are influenced by crystal packing effects and the enforced proximity to their anions, we find that the crystal structures of **1**–**4** are in good agreement with our calculated solution-state cation geometries.[57] The geometry of **1** in crystals of **1**·ICl_2 is similar to that found previously for its trifluoroacetate salt.[17] Its tropylium ring adopts a shallow boat conformation to minimise steric interactions between adjacent phenyl rings, giving interplane angles (Table 1) at the bow and the stern (Figure 2.1c) of Φ_{bow} = 13.6° and Φ_{stern} = 12.2°.

Orange crystals of **2**·$SbCl_6$ were grown by slow evaporation of a $CHCl_3$ solution. Pleasingly, the facile twisting of **2** predicted (Figure 1g) by DFT is evident in the solid-state structure determined by XRD analysis (Figure 4a). We found two non-degenerate conformers present in the unit cell—a near-planar structure with $\varphi(C_4–C_2–C_\beta–C_{\beta'})$ = 0.4° and a twisted conformer with $\varphi(C_4–C_2–C_\beta–C_{\beta'})$ = 18.4°, which match the two minima predicted by DFT calculations.

Taking the twisting deformation to its extreme, the solid-state structure of **3**·BBr_4 (Figure 4a) shows that its cation adopts an extremely distorted geometry on account of the severe peripheral overcrowding, while remaining as the aromatic tropylium isomer (rather than a Dewar tropylium). It has a large end-to-end twist of $\varphi(C_4–C_2–C_\beta–C_{\beta'})$ = 45.2°, which matches closely (Table 1) to the predicted twist of $\varphi(C_4–C_2–C_\beta–C_{\beta'})$ = 45.4°. Examination of the crystal packing reveals that the twisted acenaphthyltropylium units all have the same helical screw-sense as one another, i.e., the crystal has formed as a conglomerate.[58] The seven-membered ring of **3** is distorted from planarity to a much greater extent than **1** or **2** (Table 2.1). It has a boat conformation characterised by interplane angles of Φ_{bow} = 13.0° and Φ_{stern} = 29.0°. An informative comparison can also be made to the neutral, benzenoid homologue of this tropylium, 1,6-diethyl-7,8,9,10-tetraphenylfluoranthene (**S5**), which was isolated as a side-product during the synthesis of **3**. The benzene-centred molecule is significantly less distorted than **3** (Figure 2.17). Its torsion angle of $\varphi(C_4–C_2–C_\beta–C_{\beta'})$ = 22.7° and interplane angles of Φ_{bow} = 4.4° and Φ_{stern} = 13.2° are smaller than those measured for

3, reflecting the greater inherent flexibility and increased propensity for peripheral overcrowding of tropylium compared to benzene.

2.2.5. Nonaromatic-to-Aromatic Dynamics of a Dewar Tropylium

^{1}H NMR spectroscopic analysis of **2**·$SbCl_6$ (Figure 2.4b) shows that, as expected for the tropylium structure, the cation retains the C_2-symmetry of its cycloheptatriene precursor. The ^{1}H NMR spectrum of **4**·$SbCl_6$, however, exhibits a larger number of resonances, indicating that **4** lacks C_2-symmetry. Its lower symmetry is consistent with formation of a Dewar tropylium structure in solution. As an illustrative example, the NMR signal arising from the two *peri*-positions of **2** (γ and γ′), which appear as a sharp doublet (i.e., a single resonance), can be contrasted with the resonances arising from the phenanthrene bay region of **4** (hollow and filled star symbols), which appear as two distinct doublets in the ^{1}H NMR spectrum recorded at 179 K (Figure 2.4b). These solution-state data are complemented by XRD analysis of dark purple single crystals grown by slow evaporation of **4**·$SbCl_6$ in CH_2Cl_2, which confirms (Figure 2.4a) the presence of the Dewar tropylium ring system in the solid state. To our knowledge, this is the first nonaromatic valence isomer of a tropylium derivative that has been isolated.

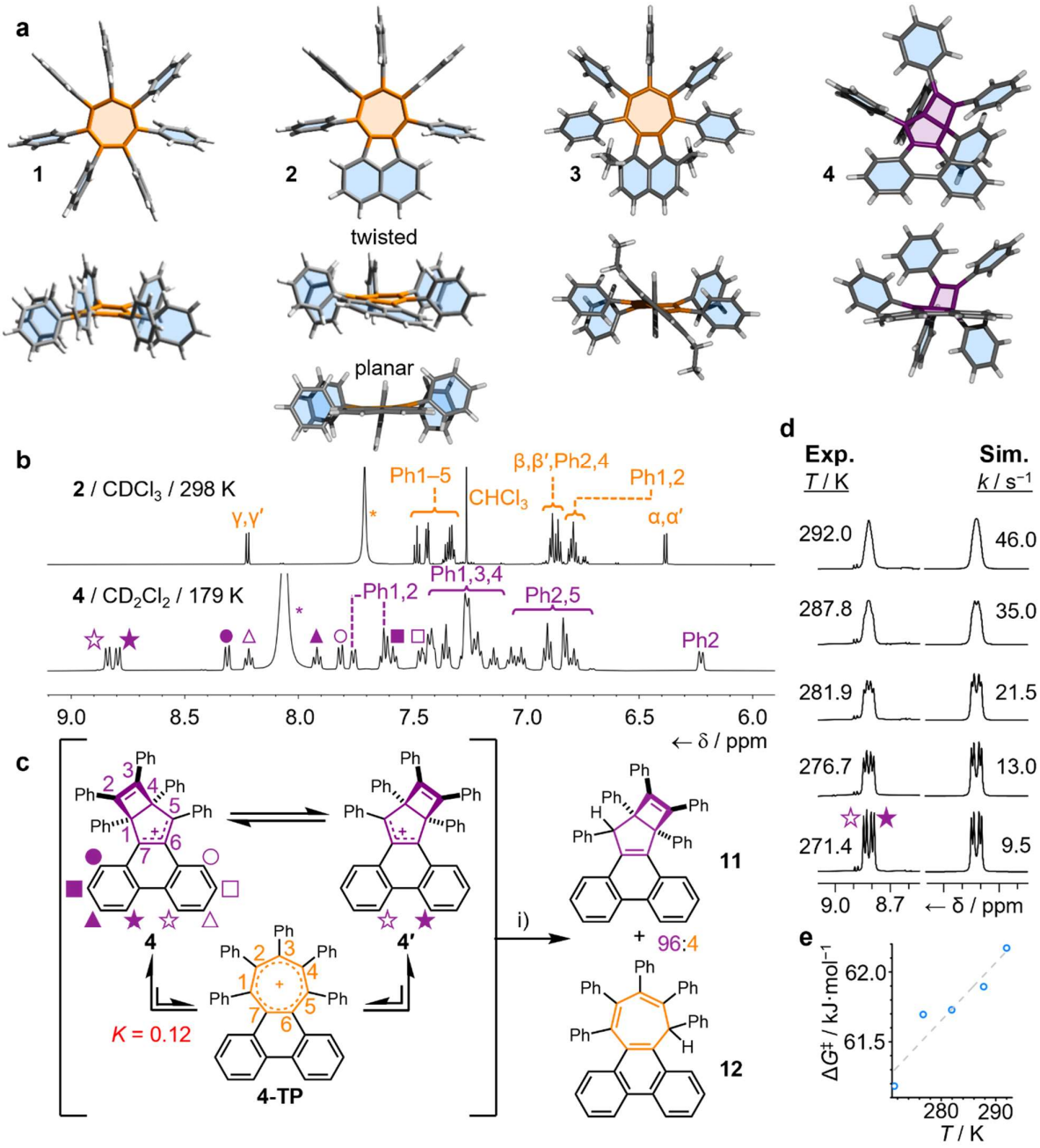

Figure 2.4. **Twisted Tropyliums and a Nonaromatic-to-Aromatic Equilibrium. a)** Plan and side views of single-crystal X-ray structures of cations **1**–**4**. Counterions and solvent molecules are omitted for clarity. Both of the conformers present in the unit cell of **2** are shown in the side view; **b)** ^{1}H NMR spectra of **2**·$SbCl_6$ (top, 700 MHz) and **4**·$SbCl_6$ (bottom, 500 MHz). Peaks of **2** are labelled according to the numbering scheme in Figure 2.2. *Denotes signals corresponding to R_2OH^+ formed as a by-product from reaction of the Et_3O^+ reagent, where R = H or Et; **c)** The dynamic exchange between two degenerate Dewar tropylium isomers of **4** and its tropylium form was intercepted by reduction to give **11** and **12**. Reagents and conditions: (i) $NaBH_4$, THF, rt, 30 min; **d)** This dynamic rearrangement causes broadening of NMR resonance lineshapes as the temperature is raised from 271.4 to 292.0 K. Rate data are obtained by comparing the experimental (Exp.) to simulated (Sim.) lineshapes. Treating this data with the Eyring equation gives (e) an Eyring plot of $\Delta G^{\ddagger}$ against T for the exchange. The linear fit (dashed grey line) indicates $\Delta H^{\ddagger} = 50.0$ kJ·mol^{-1} and $\Delta S^{\ddagger} = -41.5$ J·K^{-1}·mol^{-1}.

Close to room temperature, several of the ^{1}H NMR peaks of **4** broaden and merge (Figure 2.7), which we attribute (Figure 2.4c) to dynamic exchange occurring between its two degenerate valence isomers. Taking the phenanthrene bay protons as an example, these nuclei trade magnetic environments as **4** rearranges to **4′**. A ^{1}H–^{1}H exchange NMR spectroscopy (EXSY) experiment (Figure 2.8) confirms that these proton environments are in exchange. We performed NMR lineshape analysis (Figure 2.4d and section 2.4.2) to derive exchange rates for this process at a series of temperatures close to the signal coalescence point. An Eyring plot based on these data (Figure 2.4e) gives an enthalpy of activation, $\Delta H^{\ddagger}$, of 50.0 kJ·mol^{-1} and entropy of activation, $\Delta S^{\ddagger}$, of −41.5 J·K^{-1}·mol^{-1}, corresponding to a $\Delta G^{\ddagger}$ of 62.4 kJ·mol^{-1} at 298 K.

By analogy to the isomerisation pathways identified (Figure 1f) for $(CH)_7^+$, **Naph**, and **Phen**, the exchange between **4** and **4′** presumably involves cleavage of the C_1–C_4 bond to form (Figure 4c) an aromatic intermediate, **4-TP**. Indeed, DFT modelling of **4-TP** indicates that, despite it having a large end-to-end twist of $\varphi(C_4–C_2–C_\beta–C_{\beta'}) = 61.7°$, it is an energetically viable intermediate. It lies only 5.3 kJ·mol^{-1} higher in energy than **4**. Consequently, it should exist as a minor, but significant, species at equilibrium. With the thermal energy available at 298 K, the Boltzmann distribution of isomers (Table 2.24) for this Gibbs energy gap gives a ~10% probability of any given cation occupying the **4-TP** state, i.e., the dynamic rearrangement of **4** to **4-TP** has an equilibrium constant $K = 0.12$. To test this prediction, we performed a hydride 'trapping' experiment by treating a solution of **4** with $NaBH_4$ (Figure 2.4c). ^{1}H NMR spectroscopic analysis of the crude mixture obtained after aqueous work up shows that two bicyclo[3.2.0]heptadiene diastereoisomers *anti*-**11** and *syn*-**11** are produced along with a cycloheptatriene product[59] **12** in a 38:58:4 ratio (Figure 4c). The structure of *anti*-**11** was confirmed by XRD analysis (Figure 2.34). The observation of **12** is consistent with its tropylium precursor, **4-TP**, being present at equilibrium in solution.

Overall, therefore, the peripheral overcrowding (i) dictates the energy gap from nonaromatic isomer **4** to its aromatic form **4-TP** and (ii) tunes the kinetics of their interconversion. It does so by (iii) selectively destabilizing the aromatic tropylium isomer relative to its Dewar and Möbius tropylium isomers, as well as the transition state structure(s) that bridge(s) them. The **4** and **4-TP** isomers have been brought to within a few kJ·mol^{-1} of one another, establishing a nonaromatic-to-aromatic

equilibrium that is weighted in a ratio of ~90:10 towards the nonaromatic form. The experimentally measured $\Delta G^{\ddagger}$ of 62.4 kJ·mol^{-1} for this rearrangement is significantly lower than the $\Delta G^{\ddagger}$ of the parent compound (**Phen**) lacking the bulky phenyl groups, which is predicted (Figure 1f) to be 297 kJ·mol^{-1}. Consequently, equilibrium is established rapidly with the thermal energy available at room temperature, which is reflected experimentally in the broadening of NMR peaks and formation of a cycloheptatriene product following reaction with $NaBH_4$.

2.2.6. Aromaticity Probes

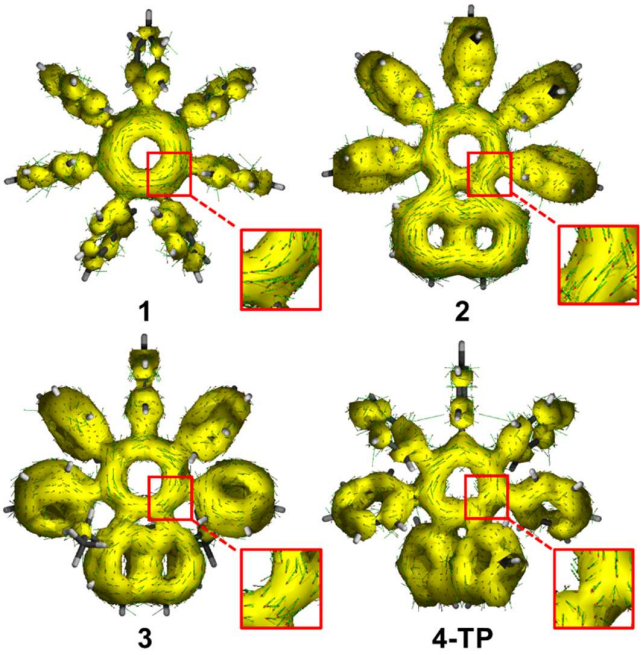

Figure 2.5. **ACID Plots**. The DFT-optimised geometries (B3LYP (GD3BJ) / 6-31G(d) / CH_2Cl_2) of **1**–**3** and **4-TP** overlaid with the ACID isosurfaces (isovalue = 0.01) for their respective π-orbitals (see section 2.5.8 for orbital numbers). Red-headed arrows demonstrate clockwise current density vectors for the seven-membered rings (see magnified areas), which are indicative of aromatic electron delocalisation.

Our experimental results lead us to question: are the large geometric distortions of **3** and the ruptured aromaticity observed for **4** best attributed to them having increased strain relative to the other derivatives (i.e., **1** and **2**), or to them having reduced aromatic character? To investigate the aromaticity of cations **1**–**3** and **4-TP**, we characterised their tropylium units using both magnetic and electronic criteria. Anisotropy of the induced current density (ACID) plots (Figure 5) show the presence

of a clockwise ring current in all four species, which is indicative of aromaticity.[60] The aromatic ring current in **2** extends to the appended naphthalene moiety, corroborating its stabilizing effect through extensive charge delocalisation. The extent of this π-electron delocalisation is reduced in **3** and **4-TP**, as the annulated acenaphthyl and phenanthrenyl groups are twisted further from the plane of the tropylium.

We calculated (Table 1) the *zz*-components of nucleus-independent chemical shifts, $NICS_{zz}(\pm1)$[61,62] to gain insight into the local aromaticity of the tropylium rings. Negative and positive NICS values are characteristic of aromaticity and antiaromaticity respectively, whereas a NICS ~0 suggests nonaromatic character.[63] The $NICS_{zz}(\pm1)$ values of –14.01 to –18.91 calculated (Table 1) for **1**–**3** and **4-TP** are consistent with the aromatic character predicted by their ACID plots.

To complement this magnetic assessment, we also determined (Table 1) electron density of delocalised bond ($EDDB^k$) values for cyclic delocalisation of π-electrons through pathways that can be represented by Kekulean resonance forms. $EDDB^k$ is a quantitative electronic index that estimates the number of electrons delocalised in an aromatic circuit.[64] We assessed electron delocalisation involving (i) the tropylium ring alone (local aromaticity) and, for the π-extended systems **2**, **3**, **4-TP**, **Naph**, and **Phen**, we also assessed electron delocalisation involving (ii) the entire polycyclic framework of the molecule (global aromaticity, shown in Figures 2.42–2.43).[65] A direct comparison is most easily drawn between **Naph**, **2** and **3**, which share the same cyclic framework. The $EDDB^k$ values of **2** are almost identical to that of **Naph**, suggesting perphenylation has little impact on the effectiveness of electron delocalisation along both pathways. Even with the severe deviation from planarity imposed by the additional ethyl groups of **3**, the $EDDB^k$ value for the local aromaticity of the tropylium drops by just 13% compared to **Naph** (from 3.08 to 2.69), suggesting a modest decrease in aromatic character. Similarly, the tropylium moiety in **1** suffers a 13% drop in aromatic character compared to $(CH)_7^+$, while **4-TP** experiences a remarkably small 6% reduction compared to **Phen**.

Together, these analyses demonstrate that cyclic π-electron delocalisation persists despite the steric deformation of these tropyliums. The aromaticity of the tropylium isomer **4-TP** would be comparable to that of **1**–**3**. Therefore, its rearrangement to the Dewar tropylium isomer and associated rupture of aromaticity occur primarily as a

consequence of its greatly increased strain (relative to **Phen**) exceeding the ASE, rather than by the geometric changes causing any significant decrease in the aromatic character of the tropylium.

2.3. Conclusions

Peripheral overcrowding causes considerable structural deformations in a series of π-extended aromatic cations. These deformations manifest as boat-type conformations of their tropylium cores and helical twists along the length of their π-extended polycyclic frameworks, giving experimentally measured torsion angles of up to 45.2° in **3**. The Gibbs energy gap between the aromatic and nonaromatic isomers of **3** is only 15 kJ·mol^{-1}, placing it among the most overcrowded and twisted tropylium structures that can feasibly be synthesised. By imposing even greater peripheral overcrowding, the balance between strain and aromatic stabilisation tips in favour of a bicyclic Dewar tropylium structure, as observed in **4**. Remarkably, spectroscopic and DFT evidence reveals that **4** exists as a dynamic mixture in solution. At room temperature, it passes back and forth rapidly between nonaromatic (**4** and **4′**) and aromatic (**4-TP**) isomers in a ~90:10 ratio, establishing a nonaromatic-to-aromatic equilibrium. Our calculations suggest that even the most deformed aromatic tropylium isomers **3** and **4-TP** retain the electronic and magnetic hallmarks of aromaticity. Yet, when bulky groups are introduced in a manner that raises steric overcrowding for the aromatic isomer preferentially, the ASE can be outweighed, and the equilibrium shifts towards a nonaromatic species.

2.4. Experimental Details

2.4.1. Synthetic Procedures

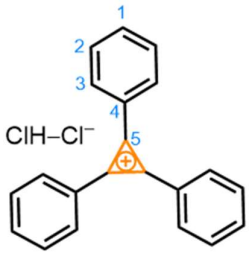

$Ph_3C_3{\cdot}HCl_2$

Triphenylcyclopropenylium hydrogen dichloride (**$Ph_3C_3{\cdot}HCl_2$**): Anhydrous benzene (200 mL) was added to diphenylacetylene (18.5 g, 104 mmol) and KO^{t}Bu (35.0 g, 312 mmol) in an oven-dried two-necked 500 mL round-bottomed flask fitted with a septum under an inert atmosphere. α,α-Dichlorotoluene (25.0 g, 155 mmol) was added uniformly over a period of 30 min using a syringe pump, and the reaction mixture was then heated to reflux for 3 h. After cooling, H_2O (200 mL) was added to dissolve the inorganic salts. The layers were separated and the aqueous layer was extracted with Et_2O (2 × 200 mL). The combined organic extracts were dried over $MgSO_4$, and the solvent was removed under reduced pressure to yield an orange residue. This was dissolved in a mixture of 2:1 Et_2O–CH_2Cl_2 (200 mL) and sparged with gaseous HCl, leading to the formation of a colourless precipitate. Sparging was continued until no more precipitation was observed. The precipitate was collected by filtration, and the solid was washed with Et_2O, then dried under vacuum to yield the title compound as cream powder (18.6 g, 61.4 mmol, 43%). **M.P.** 186–188 °C. **^{1}H NMR** (600 MHz, CD_3CN) δ 8.83–8.39 (m, 6H, H_3), 8.20–8.00 (m, 3H, H_1), 7.97–7.86 (m, 6H, H_2). **^{13}C NMR** (151 MHz, CD_3CN) δ 154.1 (C_5), 139.1 (C_1), 136.6 (C_2), 131.4 (C_3), 121.6 (C_4). **HRESI-MS** *m/z* = 267.1169 $[M]^+$ (calculated for $C_{21}H_{15}^+$ = 267.1168).

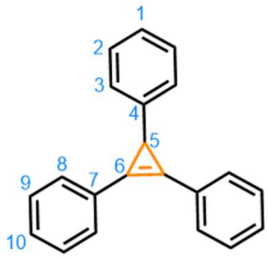

5

***sym*-Triphenylcyclopropene** (**5**): $NaBH_4$ (9.3 g, 246 mmol) was added to a solution of **$Ph_3C_3{\cdot}HCl_2$** (18.6 g, 61.4 mmol) in EtOH (460 mL) at 0°C. The mixture was allowed to stir overnight at rt. The reaction was quenched with H_2O (500 mL) then extracted with Et_2O (3 × 200 mL). The combined organic extracts were washed with H_2O (500 mL), then brine (500 mL), and dried over $MgSO_4$. The solvent was removed under reduced pressure to give **5** as a colourless solid (14.2 g, 53.1 mmol, 97%). **M.P.**

113–115 °C (lit.[66] 114 – 116 °C). **^{1}H NMR** (400 MHz, $CDCl_3$) δ 7.71–7.66 (m, 4H, H_8), 7.47–7.40 (m, 4H, H_9), 7.38–7.32 (m, 2H, H_{10}), 7.24 (br s, 2H, H_2), 7.23–7.22 (m, 2H, H_3), 7.17–7.10 (m, 1H, H_1), 3.27 (s, 1H, H_5). **^{13}C NMR** (101 MHz, $CDCl_3$) δ 144.6 (C_4), 130.0 (C_8), 128.9 (C_9), 128.8 (C_{10}), 128.7 (C_7), 128.3 (C_3), 126.0 (C_2), 125.6 (C_1), 112.7 (C_6), 24.5 (C_5). **HR-ESI MS** *m/z* = 267.1172 $[M-H]^+$ (calculated for $C_{21}H_{15}^+$ = 267.1168).

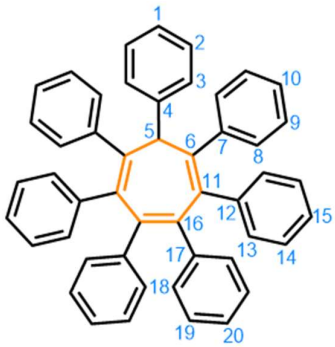

7

sym-**Heptaphenylcycloheptatriene** (**7**): Anhydrous *p*-xylene (13.5 mL) was added to **5** (1.2 g, 4.47 mmol) and tetraphenylcyclopentadienone (1.79 g, 4.47 mmol) in a sealed, oven-dried microwave vial under an inert atmosphere. The mixture was deoxygenated (3 × freeze–pump–thaw cycles under N_2) then stirred for 36 h at 140 °C in a microwave reactor. Upon cooling to rt, a crystalline solid formed, which was isolated by filtration, and washed with Et_2O (3 × 10 mL). The solid was dried under vacuum to yield **7** as a pale pink solid (2.30 g, 3.68 mmol, 82%) in high purity (no observable impurities by ^{1}H NMR spectroscopy). Samples for analytical measurements were further purified by recrystallisation. A saturated solution of **7** in $CHCl_3$–EtOH (1:1) was allowed to evaporate slowly, yielding colourless crystals of analytically pure **7**. **M.P.** 291–292 °C (lit.[68] 285–288 °C). **^{1}H NMR** (700 MHz, $(CD_3)_2CO$) δ 8.17–7.99 (m, 2H, H_3), 7.62–7.48 (m, 2H, H_2), 7.44–7.34 (m, 1H, H_1), 7.26–7.18 (m, 4H, H_8), 7.15 (br s, 4H, H_{13}), 7.05–7.02 (m, 4H, H_{14}), 7.02–6.98 (m, 4H, H_9), 6.98–6.96 (m, 2H, H_{15}), 6.96–6.93 (m, 2H, H_{10}), 6.63–6.59 (m, 2H, H_{20}), 6.60–6.55 (m, 4H, H_{19}), 6.36–6.32 (m, 4H, H_{18}), 5.35 (s, 1H, H_5). **^{13}C NMR** (176 MHz, $(CD_3)_2CO$) δ 144.8 (C_{16}), 144.4 (C_7), 144.1 (C_4), 141.9 (C_{12}), 141.6 (C_{17}), 140.2 (C_6), 138.0 (C_{11}), 132.7 (C_{13}), 132.3 (C_{18}), 130.7 (C_8), 129.4 (C_2), 128.5 (C_9), 128.1 (C_{14}), 127.9 (C_3), 127.7 (C_1), 127.3 (C_{10}), 126.93 (C_{15}), 126.87 (C_{19}), 126.0 (C_{20}), 59.0 (C_5). **HR-ESI MS** *m/z* = 625.2892 $[M+H]^+$ (calculated for $C_{47}H_{37}^+$ = 625.2890).

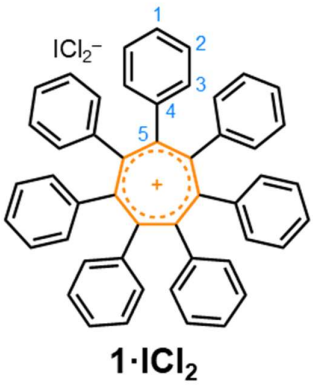

1·ICl₂

Heptaphenyltropylium iodine dichloride (1·ICl₂): ICl (1.0 M in CH_2Cl_2, 1 mL, 1.0 mmol) was added to a solution of **7** (100 mg, 0.16 mmol) in anhydrous CH_2Cl_2 (10 mL), and the mixture was stirred at rt for 24 h. The solvent was removed under reduced pressure to give a crude dark purple solid, which was dissolved in anhydrous MeCN (15 mL) and triturated with anhydrous Et_2O (25 mL). The resulting precipitate was collected by vacuum filtration to yield the title compound as an orange solid (97 mg, 0.096 mmol, 60%) **M.P.** 280–282 °C. **^{1}H NMR** (400 MHz, CD_3CN) δ 6.92–6.88 (m, 14 H, H_3), 6.87–6.78 (m, 21H, H_{1+2}). **^{13}C NMR** (101 MHz, CD_3CN) δ 167.3 (C_5), 141.6 (C_4), 130.5 (C_3), 127.8 (C_2), 127.6 (C_1). **HR-ASAP MS** *m/z*= 623.2712 $[M-ICl_2]^+$ (calculated for $C_{49}H_{35}^+$ = 623.2739).

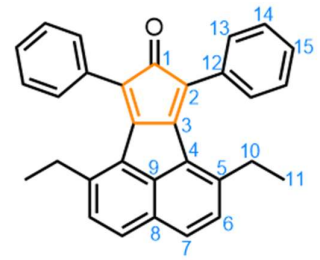

Diethylacecyclone

Diethylacecyclone: A solution of NaOH (0.31 g, 7.7 mmol) in EtOH (20 mL) was added dropwise to a refluxing suspension of 1,3-diphenyl-2-propanone (0.90 g, 4.5 mmol) and 3,8-diethylacenaphthenequinone (0.93 g, 4.1 mmol) in EtOH (20 mL). The reaction mixture was refluxed for 30 min, then immediately placed onto an ice-bath. Once cooled, the resulting precipitate was collected *via* vacuum filtration and washed with cold EtOH (10 mL) to give the title compound as a black solid (0.50 g, 1.2 mmol, 30%). **M.P.** 140–142 °C. **^{1}H NMR** (700 MHz, $CDCl_3$) δ 7.74 (d, *J* = 8.3 Hz, 2H, H_7), 7.45–7.37 (m, 10H, $H_{13,14,15}$), 7.35 (d, *J* = 8.3 Hz, 2H, H_6), 2.40 (q, *J* = 7.5 Hz, 4H, H_{10}), 0.85 (t, *J* = 7.6 Hz, 6H, H_{11}). **^{13}C NMR** (176 MHz, $CDCl_3$) δ 202.9 (C_1), 156.2 (C_3), 146.6 (C_9), 140.5 (C_5), 133.1 (C_{12}), 130.4 (C_4), 129.4 (C_{13}), 128.7 (C_{14}), 128.4 (C_{15}), 128.0 (C_7), 127.6 (C_8), 127.6 (C_6), 121.8 (C_2), 28.2 (C_{10}), 14.9 (C_{11}). **HR-ESI MS** *m/z* = 413.1894 $[M+H]^+$ (calculated for $C_{31}H_{25}O^+$ = 413.1900).

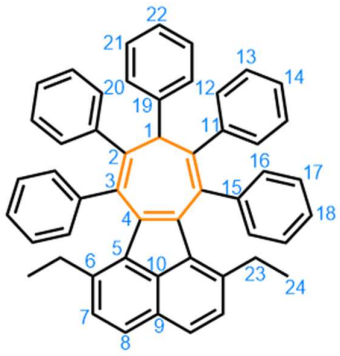

8

8: Anhydrous *p*-xylene (10 mL) was added to **5** (0.13 g, 0.49 mmol) and diethylacecyclone (0.20 g, 0.49 mmol) in a sealed, oven-dried microwave vial under an inert atmosphere. The mixture was deoxygenated (3 × freeze–pump–thaw cycles under N_2), then stirred for 84 h at 190 °C. The solvent was removed under reduced pressure, leaving a brown residue, which was purified by column chromatography (Teledyne Isco CombiFlash Rf+ system, 40 g SiO_2, hexanes−CH_2Cl_2, 0–20% gradient elution), to yield **8** as a yellow solid (0.071 g, 0.11 mmol, 22%). **M.P.** 198–200 °C. **^{1}H NMR** (400 MHz, $CDCl_3$) δ 7.52 (m, 4H, $H_{8,20}$), 7.16–7.10 (m, 4H, $H_{18,21}$), 7.08–7.03 (m, 10H, $H_{12,13,14}$), 7.01–6.84 (m, 8H, $H_{16,17}$), 6.83–6.76 (m, 2H, H_7), 6.66 (t, J = 7.4 Hz, 1H, H_{22}), 5.48 (s, 1H, H_1), 2.27 (m, 4H, H_{23}), 0.68 (t, J = 7.5 Hz, 6H, H_{24}). **^{13}C NMR** (101 MHz, $CDCl_3$) δ 143.4 (C_{19}), 142.9 (C_{15}), 141.5 (C_{11}), 141.1 (C_6), 140.6 (C_9), 137.8 (C_3), 134.7 (C_{10}), 132.4 (C_{16}), 131.9 (C_{20}), 130.6 (C_2), 129.0 (C_5), 128.5 (C_{21}), 127.8 (C_{12}), 127.6 (C_{17}), 127.2 (C_{22}), 126.8 (C_{13}), 126.5 (C_{14}), 126.2 (C_{18}), 125.6 (C_7), 125.5 (C_4), 125.4 (C_8), 60.6 (C_1), 27.1 (C_{23}), 14.2 (C_{24}). **HR-ESI MS** *m/z* = 653.3223 $[M+H]^+$ (calculated for $C_{51}H_{41}^+$ = 653.3208).

In addition to **8**, *trace amounts of the Diels–Alder intermediate* (**S4**) (*identified by single-crystal X-ray crystallography, see section* **2.4.4.4**) *as well as 1,6-diethyl-7,8,9,10-tetraphenylfluoranthene* (**S5**) (0.020 g, 0.071 mmol, 7%) (*section* **2.4.4.5**) *were present in the crude mixture. These were isolated by column chromatography.*

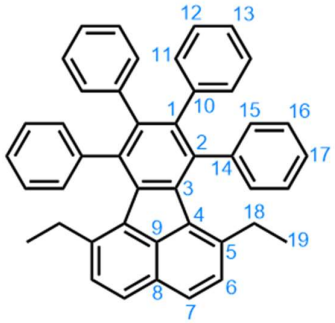

S5

S5: ^{1}H NMR (600 MHz, $CDCl_3$) δ 7.71 (d, J = 8.3 Hz, 2H, H_7), 7.26 (d, J = 8.3 Hz, 2H, H_6), 7.14–7.07 (m, 10 H, $H_{15,16,117}$), 6.90–6.85 (m, 6H, $H_{12,13}$), 6.73–6.69 (m, 4H, H_{11}), 1.75 (q, 4H, J = 7.5 Hz, H_{18}), 0.81 (t, 6H, J = 7.5 Hz, H_{19}). **^{13}C NMR** (151 MHz, $CDCl_3$) δ 142.4 (C_{14}), 141.0 (C_{10}), 140.8 (C_5), 140.2 (C_1), 139.6 (C_3), 136.4 (C_2), 134.4 (C_9), 133.1 (C_4), 131.8 (C_{15}), 131.7 (C_{11}),

129.9 (C_6), 127.7 ($C_{16/17}$), 126.8 (C_7), 126.7 (C_8), 126.6 (C_{12}), 126.5 ($C_{17/16}$), 125.2 (C_{12}), 27.6 (C_{18}), 16.0 (C_{19}).

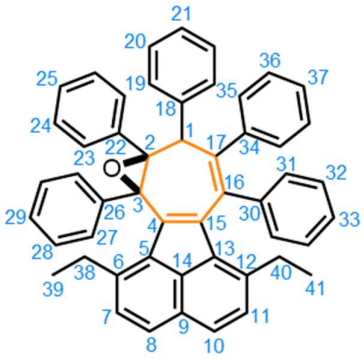

S1

S1: *m*CPBA (38 mg, 150 µmol) was added to a solution of **8** (59 mg, 77 µmol) in $CHCl_3$ (2.5 mL). One drop of a saturated aqueous solution of $NaHCO_3$ was added, and the biphasic mixture was heated to reflux for 20 h. Upon cooling to rt, a saturated aqueous solution of $NaHCO_3$ (10 mL) was added, and the layers were separated. The aqueous layer was extracted with CH_2Cl_2 (2 × 10 mL). The combined organic extracts were dried over $MgSO_4$, and the solvent was removed under reduced pressure, leaving an orange residue, which was purified by column chromatography (Teledyne Isco CombiFlash Rf+ system, 12 g SiO_2, hexanes–CH_2Cl_2, 0–20% gradient elution), to yield **11** as a yellow solid (5.9 mg, 8.3 µmol, 12%). **^{1}H NMR** (600 MHz, $CDCl_3$) δ 7.60 (d, J = 8.3 Hz, 2H, H_{19}), 7.57 (d, J = 8.4 Hz, 1H, H_{10}), 7.53 (d, J = 8.2 Hz, 1H, H_8), 7.25–7.21 (m, 3H, $H_{25/29}$+H_{31}), 7.21–7.17 (m, 2H, H_{36}), 7.16 (d, J = 8.4 Hz, 1H, H_{11}), 7.14–7.10 (m, 4H, $H_{24/28}$+H_{32}), 7.09 (d, J = 8.3 Hz, 1H, H_7), 7.08–6.99 (m, 9H, $H_{23,24/28,27,29/25,35}$), 6.97–6.92 (m, 4H, $H_{20,33,37}$), 6.81 (t, J = 7.3 Hz 1H, H_{21}), 4.90 (s, 1H, H_1), 2.78–2.69 (m, 1H, $H_{38'}$), 2.66–2.57 (m, 2H, $H_{38,40}$), 2.57–2.50 (m, 1H, $H_{40'}$), 0.61 (t, J = 7.4 Hz, 3H, H_{41}), 0.50 (t, J = 7.4 Hz, 3H, H_{39}). **^{13}C NMR** (151 MHz, $CDCl_3$) δ 144.0 (C_{16}), 142.5 (C_6), 142.2 (C_{12}), 141.30 ($C_{15/26}$), 141.29 ($C_{26/15}$), 140.7 ($C_{22/34}$), 140.6 ($C_{34/22}$), 139.1 (C_{17}), 137.5 (C_{30}), 137.0 (C_{18}), 136.8 (C_4), 134.2 (C_{13}), 133.5 (C_5), 131.7 (C_{31}), 129.6 (C_{14}), 129.3 (C_7), 129.0 (C_{19}), 128.7 (C_{27}), 128.4 (C_{11}), 127.9 (C_{36}), 127.58 ($C_{23/24/25/28/29}$), 127.56 (C_{10}), 127.52 (C_{37}), 127.5 (C_8), 127.2 ($C_{20,23/24/25/28/29}$), 127.1 ($C_{35,23/24/25/28/29}$), 126.92 (C_{33}), 126.90 ($C_{32,23/24/25/28/29}$), 126.6 ($C_{23/24/25/28/29}$), 125.5 (C_{21}), 125.2 (C_9), 77.0 (C_2), 64.2 (C_3), 59.0 (C_1), 27.3 (C_{40}), 26.6 (C_{38}), 15.0 (C_{39}), 14.1 (C_{41}). **HR-ASAP MS** *m/z* = 669.3154 $[M+H]^+$ (calculated for $C_{51}H_{41}O^+$ = 669.3157).

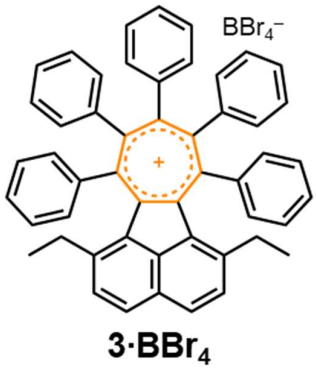

3·BBr4: A solution of BBr_3 (3.3 mg, 13 μmol) in anhydrous CH_2Cl_2 (0.11 mL) was added to a solution of **S1** (5.9 mg, 8.8 μmol) in anhydrous CH_2Cl_2 (0.4 mL) in an oven-dried vial under an inert atmosphere, and the solution was left to stir at rt for 6 h. Anhydrous hexane (0.5 mL) was added, and the vial was placed in the freezer to crystallise. Upon slow evaporation of the solvent, **3·BBr4** was obtained as an orange, crystalline solid. *Due to the small quantity of crystalline material obtained, yields and NMR spectroscopic data were not acquired for this compound. The identity of the compound was confirmed by single-crystal X-ray diffraction and mass spectrometry.* **HR-ESI MS** *m/z* = 651.3055 $[M]^+$ (calculated for $C_{51}H_{39}^+$ = 651.3052).

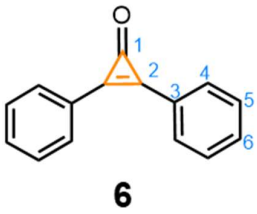

Diphenylcyclopropenone (6): Anhydrous hexane (150 mL) was added to diphenylacetylene (6.02 g, 33.8 mmol) and KO^{t}Bu (10.6 g, 94.5 mmol) under an inert atmosphere, and the mixture was cooled to −20 °C. $CHBr_3$ (2.68 mL, 30.6 mmol) was added slowly over 3 h at this temperature, and the reaction mixture was allowed to warm to rt overnight. The reaction was quenched with H_2O (50 mL) and stirred for 30 min. The layers were separated, and the aqueous layer was extracted with EtOAc (3 × 30 mL). The combined organic extracts were washed with a saturated aqueous solution of $Na_2S_2O_3$ (30 mL) and brine (30 mL), then dried over $MgSO_4$. The solvent was removed under reduced pressure give a dark red viscous oil, which was purified by column chromatography (Teledyne Isco CombiFlash Rf+ system, 80 g SiO_2, hexanes−EtOAc, gradient elution) to yield the title compound as a pale-yellow solid (4.54 g, 21.9 mmol, 65%). **M.P.** 92–94 °C. **^{1}H NMR** (400 MHz, $CDCl_3$) δ 8.08–7.91 (m, 4H, H_4), 7.71–7.52 (m, 6H, $H_{5,6}$). **^{13}C NMR** (101 MHz, $CDCl_3$) δ 156.0 (C_1), 148.5 (C_3), 132.9 (C_4), 131.7 (C_5), 129.5 (C_6), 124.2 (C_2). **HR-ESI MS** *m/z* = 207.0787 $[M+H]^+$ (calculated for $C_{15}H_{11}O^+$ = 207.0810).

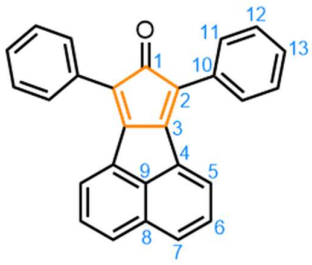

Acecyclone: A solution of NaOH (790 mg, 19.8 mmol) in EtOH (25 mL) was added dropwise to a refluxing suspension of 1,3-diphenyl-2-propanone (2.60 g, 12.4 mmol) and acenaphthenequinone (2.00 g, 11.0 mmol) in EtOH (50 mL). The reaction mixture was refluxed for 15 min, then immediately placed onto an ice-bath. Once cooled, the resulting precipitate was collected *via* vacuum filtration and washed with cold EtOH (10 mL) to give the title compound as a black solid (2.95 g, 8.24 mmol, 75%). **M.P.** 280–282 °C. **^{1}H NMR** (700 MHz, $CDCl_3$) δ 8.07 (dd, J = 7.2, 0.6 Hz, 2H, H_7), 7.90–7.85 (m, 2H, H_5), 7.85–7.80 (m, 4H, H_{11}), 7.59 (dd, J = 8.2, 7.2 Hz, 2H, H_6), 7.54–7.51 (m, 4H, H_{12}), 7.41 (ddt, J = 7.9, 7.0, 1.3 Hz, 2H, H_{13}). **^{13}C NMR** (176 MHz, $CDCl_3$) δ 202.0 (C_1), 154.4 (C_3), 144.9 (C_4), 132.3 (C_2), 131.7 (C_{10}), 131.6 (C_8), 129.2 (C_{11}), 128.7 (C_{12}), 128.6 (C_9), 128.4 (C_6), 127.9 (C_5), 121.8 (C_{13}), 121.1 (C_7). **HR-ESI MS** *m/z* = 357.1256 $[M+H]^+$ (calculated for $C_{27}H_{17}O^+$ = 357.1279).

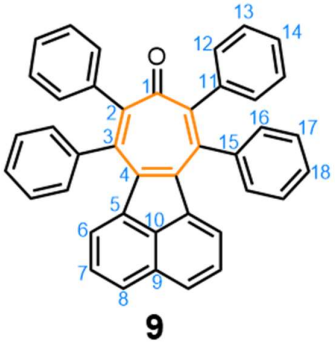

9: Anhydrous PhMe (2.5 mL) and anhydrous $CHCl_3$ (1.5 mL) were added to **6** (0.20 g, 0.97 mmol) and acecyclone (0.23 g, 0.65 mmol) in a sealed, oven-dried microwave vial under an inert atmosphere. The mixture was deoxygenated (3 × freeze-pump-thaw cycles under N_2), then stirred for 24 h at 130 °C in a microwave reactor. Upon cooling to rt, the solvents were removed under reduced pressure, and the crude solid was purified by column chromatography (Teledyne Isco CombiFlash Rf+ system, 12 g SiO_2, hexanes−EtOAc, 0–10% gradient elution). The title compound was isolated as a pale-yellow solid (0.12 g, 0.18 mmol, 34%). **M.P.** 245–247 °C. **^{1}H NMR** (700 MHz, $CDCl_3$) δ 7.65 (d, J = 8.1 Hz, H_8), 7.28–7.33 (m, 8H, $H_{13,17}$), 7.32–7.28 (m, 2H, H_{18}), 7.28–7.23 (m, 4H, H_{16}), 7.17 (dd, J = 8.2, 7.2 Hz, H_7), 7.07–7.01 (m, 4H, H_{12}), 6.36 (d, J = 7.2 Hz, 2H, H_6). **^{13}C NMR** (176 MHz, $CDCl_3$) δ 197.5 (C_1), 140.2 (C_3), 140.0 (C_{15}), 139.0 (C_2), 138.7 (C_{11}), 136.5 (C_4), 134.1 (C_6), 131.9 (C_{13}), 130.6 (C_{12}), 128.6 (C_5), 128.5 (C_{10}), 128.3 (C_{17}), 127.9 (C_{18}), 127.7 (C_9), 127.6 (C_{16}), 127.5 (C_{14}), 127.4

(C_7), 126.1 (C_8). **HR-ESI MS** *m/z* = 535.1953 $[M+H]^+$ (calculated for $C_{41}H_{27}O^+$ = 535.1948).

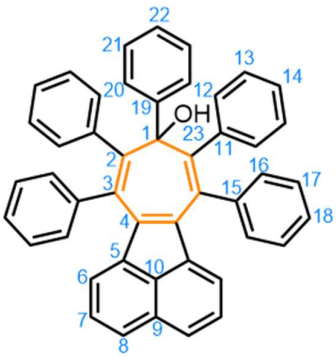

S2

S2: 9 (0.10 g, 0.19 mmol) was placed in a flame-dried two-necked round-bottomed flask under an inert atmosphere. Anhydrous THF (3 mL) was added, and the solution was cooled to 0 °C. PhMgBr (1 M in THF, 0.20 mL, 0.20 mmol) was added slowly, and the mixture was stirred at this temperature for 30 min, then at rt for 3 h. The reaction was quenched with a saturated aqueous solution of NH_4Cl (5 mL) and extracted with Et_2O (2 ×10 mL). The combined organic extracts were dried over $MgSO_4$, and the solvents were removed under reduced pressure. The crude product was purified by column chromatography (Teledyne Isco CombiFlash Rf+ system, 12 g SiO_2, hexanes−EtOAc, 0–10% gradient elution), yielding **12** as a yellow solid (0.080 g, 0.13 mmol, 68%). **M.P.** 205–207 °C. **^{1}H NMR** (700 MHz, $CDCl_3$) δ 7.80–7.75 (m, 2H, H_{20}), 7.44 (d, *J* = 8.2 Hz, 2H, H_8), 7.30–7.27 (m, 4H, H_{16}), 7.30–6.90 (br, 8 H, $H_{12,13}$) 7.16–7.13 (m, 6H, $H_{17,18}$), 7.08 (t, 2H, *J* = 7.4 Hz, H_{14}), 7.04 (dd, 2H, *J* = 8.2, 7.1 Hz, H_7), 6.91–6.87 (m, 2H, H_{21}), 6.70–6.55 (m, 1H, H_{22}), 6.24 (d, 2H, *J* = 7.2 Hz, H_6), 1.84 (s, 1H, H_{23}). **^{13}C NMR** (176 MHz, $CDCl_3$) δ 144.2 (C_{19}), 142.5 (C_4), 141.9 (C_{15}), 140.6 (C_2), 138.8 (C_9), 137.2 ($C_{12/13}$), 133.5 (C_3), 133.2 (C_{14}), 131.9 (C_{16}), 129.8 ($C_{13/12}$) 128.4 (C_{10}), 128.0 (C_5), 127.9 (C_{17}), 127.4 (C_{14}), 127.3, ($C_{7,21,22}$), 126.9 (C_{18}), 126.6 (C_{20}), 126.5 (C_8), 124.4 (C_6), 80.5 (C_1). **HR-ESI MS** *m/z* = 595.2440 $[M–OH]^+$ (calculated for $C_{47}H_{31}^+$ = 595.2426).

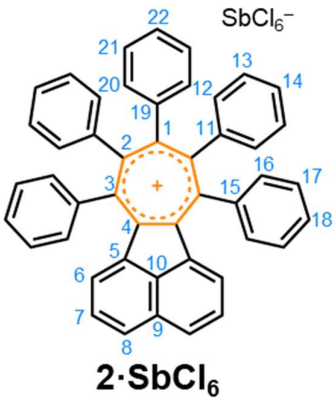

2·SbCl$_6$: $Et_3O{\cdot}SbCl_6$ (5.0 mg, 11 µmol) was added to a solution of **S2** (3.6 mg, 5.9 µmol) in anhydrous $CDCl_3$ (0.6 mL) under an inert atmosphere at rt, causing the initially yellow solution to turn orange immediately. NMR spectroscopic analysis indicated quantitative conversion of the starting material to **2**·$SbCl_6$. **^{1}H NMR** (700 MHz, $CDCl_3$) δ 8.22 (d, J = 8.0 Hz, 2H, H_8), 7.48 (t, J = 7.9 Hz, 2H, H_7), 7.45–7.42 (m, 4H, H_{16}), 7.37–7.30 (m, 6H, $H_{17,18}$), 6.90–6.84 (m, 8H, $H_{13,14,20}$), 6.82–6.76 (m, 6H, $H_{12,21}$), 6.75–6.71 (m, 1H, H_{22}), 6.38 (d, J = 7.8 Hz, 2H, H_6). **^{13}C NMR** (176 MHz, $CDCl_3$) δ 162.2 (C_1), 162.1 (C_2), 159.6 (C_3), 157.2 (C_4), 141.1 ($C_{15/19}$), 141.1 ($C_{19/15}$), 140.4 (C_{11}), 135.4 (C_5), 135.3 (C_8), 135.2 (C_{10}), 134.5 (C_6), 129.9 (C_{20}), 129.8 (C_{21}), 129.8 (C_{16}), 129.6 (C_7), 129.4 (C_9), 129.0 (C_{18}), 128.7 (C_{17}), 127.1 (C_{13}), 126.9 (C_{14}), 126.9 (C_{12}), 126.8 (C_{22}). **HR-ESI MS** *m/z* = 595.2440 $[M]^+$ (calculated for $C_{47}H_{31}^+$= 595.2426).

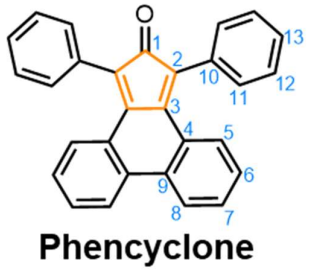

Phencyclone: A solution of NaOH (3.30 g, 81.9 mmol) in EtOH (90 mL) was added dropwise to a refluxing suspension of 1,3-diphenyl-2-propanone (9.91 g, 46.0 mmol) and phenan-threnequinone (9.06 g, 43.5 mmol) in EtOH (300 mL). The reaction mixture was refluxed for 15 min, then immediately placed onto an ice-bath. Once cooled, the resulting precipitate was collected *via* vacuum filtration and washed with cold EtOH (10 mL) to give the title compound as a black solid (14.8 g, 38.7 mmol, 89%). **M.P.** 255–257 °C. **^{1}H NMR** (400 MHz, $CDCl_3$) δ 6.95 (t, J = 7 Hz, 2H), 7.28–7.30 (m, 2H), 7.36–7.45 (m, 10H), 7.55 (dd, J = 8.0, 1.0 Hz, 2H), 7.81 (d, J = 7.5 Hz, 2H). The spectroscopic data were consistent with literature reports.[68]

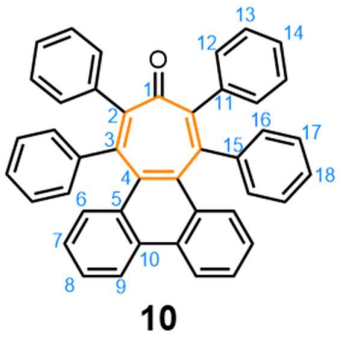

10

10: Anhydrous PhMe (10 mL) was added to phencyclone (0.49 g, 1.2 mmol) and **6** (0.40 g, 1.9 mmol) in a sealed, oven-dried microwave vial under an inert atmosphere. The mixture was deoxygenated (3 × freeze-pump-thaw cycles under N_2), then stirred for 24 h at 130 °C in a microwave reactor. Upon cooling to rt, the solvent was removed under reduced pressure, and the crude solid was purified by column chromatography (Teledyne Isco CombiFlash Rf+ system, 12 g SiO_2, hexanes−CH_2Cl_2, 0–30% gradient elution), to yield **10** as a colourless solid (0.31 g, 0.48 mmol, 40%). **M.P.** 248–250 °C. **^{1}H NMR** (700 MHz, $CDCl_3$) δ 8.59 (dd, *J* = 8.4, 1.3 Hz, 2H, H_9), 7.94 (dd, *J* = 8.5, 1.3 Hz, 2H, H_6), 7.47 (ddd, *J* = 8.3, 6.9, 1.2 Hz, 2H, H_8), 7.20 (ddd, *J* = 8.3, 6.9, 1.2 Hz, 2H, H_7), 7.15–7.13 (m, 4H, H_{17}), 7.13–7.09 (m, 10H, $H_{12,13,14}$), 7.03–6.97 (m, 6H, $H_{18,16}$). **^{13}C NMR** (176 MHz, $CDCl_3$) δ 199.9 (C_1), 146.2 (C_3), 140.6 (C_{15}), 135.8 (C_{11}), 134.9 (C_{10}), 133.6 (C_2), 131.1 (C_4), 130.7 (C_6), 130.4 (C_{13}), 129.8 (C_5), 129.7 (C_{12}), 128.3 (C_{17}), 128.0 (C_{16}), 127.8 (C_{18}), 127.2 (C_{14}), 126.9 (C_8), 125.9 (C_7), 122.4 (C_9). **HR-ESI MS** *m/z* = 561.2222 $[M+H]^+$ (calculated for $C_{43}H_{29}O^+$ = 561.2218).

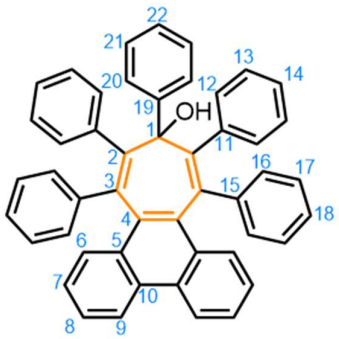

S3

S3: 10 (0.10 g, 0.18 mmol) was placed in an oven-dried two-necked round-bottomed flask under an inert atmosphere. Anhydrous THF (5 mL) was added, and the solution was cooled to 0 °C. PhMgBr (1 M in THF, 0.2 mL, 0.2 mmol) was added slowly, and the mixture was stirred at this temperature for 30 min, then at rt for 3 h. The reaction was quenched with a saturated aqueous solution of NH_4Cl (5 mL) and extracted with Et_2O (2 ×10 mL). The combined organic extracts were dried over $MgSO_4$, and the solvents were removed under reduced pressure. The crude solid was purified by column chromatography (Teledyne Isco CombiFlash Rf+ system, 12 g SiO_2, hexanes−EtOAc, 0–5% gradient elution). The title product was isolated as a colourless solid (0.070 g, 0.11 mmol, 60%). **M.P.** 340–342 °C. **^{1}H NMR** (700 MHz, $CDCl_3$) δ 8.32 (d, *J* = 8.3 Hz, 2H, H_9), 7.85 (d, *J* = 8.3 Hz, 2H, H_6), 7.78 (d, *J* = 7.7 Hz, 2H, H_{16}), 7.62–7.57 (m, 2H, H_{20}), 7.41–7.36 (m, 2H, H_{17}), 7.34–7.28 (m, 2H, H_8), 7.19–7.08 (m, 4H, $H_{7,17'}$),

7.04–6.95 (m, 10H, $H_{12,13,14}$), 6.94–6.87 (m, 2H, H_{18}), 6.84–6.79 (m, 2H, $H_{16'}$), 6.57–6.49 (m, 3H, $H_{21,22}$). **^{13}C NMR** (176 MHz, $CDCl_3$) δ 151.4 (C_{15}), 143.0 (C_3), 142.3 (C_{19}), 137.6 (C_2), 136.7 (C_{11}), 133.9 (C_{10}), 132.6 (C_{16}), 132.2 ($C_{16'}$), 130.9 (C_{12}), 130.1 (C_4), 129.9 (C_6), 128.9 (C_5), 127.6 (C_{18}), 127.3 (C_{13}), 127.2 (C_{17}), 127.2 ($C_{17'}$), 126.7 (C_{21}), 126.4 (C_{22}), 125.8 (C_8), 125.6 (C_{14}), 125.3 (C_{20}), 125.1 (C_7), 121.7 (C_9), 81.1 (C_1). **HR-ESI MS** *m/z* = 621.2560 $[M\text{-}OH]^+$ (calculated for $C_{49}H_{33}^+$ = 621.2582).

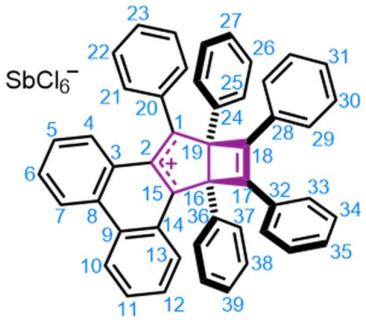

4·SbCl$_6$

4·SbCl$_6$: $Et_3O{\cdot}SbCl_6$ (5.0 mg, 11 µmol) was added to a solution of **S3** (3.5 mg, 5.5 µmol) in anhydrous CD_2Cl_2 (0.6 mL) under an inert atmosphere at rt, causing the initially colourless solution to turn purple. The solution was left to stand for 4 h. NMR spectroscopic analysis indicated quantitative conversion of the starting material to **4**·$SbCl_6$. **^{1}H NMR** (500MHz, CD_2Cl_2, 179 K) δ 8.84 (d, *J* = 8.6 Hz, 1H, H_7), 8.79 (d, *J* = 8.5 Hz, 1H, H_{10}), 8.33 (d, *J* = 8.2 Hz, 1H, H_{13}), 8.25–8.18 (m, 1H, H_6), 7.95–7.87 (m, 1H, H_{11}), 7.81 (d, 1H, *J* = 8.4 Hz, H_4), 7.78–7.72 (m, 1H, H_{29}), 7.67–7.56 (m, 3H, $H_{12,37,39}$), 7.50–7.39 (m, 3H, $H_{5,29',37'}$), 7.38–7.32 (m, 2H, $H_{27,33'}$), 7.31–7.17 (m, 6H, $H_{26,30,38}$), 7.16–7.09 (m, 1H, H_{31}), 7.05 (t, *J* = 7.4 Hz, 1H, H_{23}), 7.00 (t, *J* = 7.6 Hz, 1H, H_{35}), 6.89 (t, *J* = 7.7 Hz, 2H, H_{22}), 6.84–6.79 (m, 2H, H_{21}), 6.76 (t, *J* = 7.7 Hz, 2H, H_{34}), 6.20 (m, 1H, H_{33}). **^{13}C NMR** (126 MHz, CD_2Cl_2, 179 K) δ 185.2 (C_1), 152.6 (C_{15}), 142.7 (C_2), 141.5 (C_6), 141.1 (C_{36}), 139.7 (C_{32}), 139.7 (C_{20}), 139.0 (C_{28}), 138.9 (C_{24}), 138.8 (C_{12}), 136.4 (C_9), 135.7 (C_4), 134.2 (C_8), 134.2 (C_3), 133.6 (C_{39}), 132.9 (C_{14}), 131.7 (C_{21}), 131.0 ($C_{11,33'}$), 129.9 (C_{37}), 129.7 (C_{25}), 129.6 (C_{26}), 129.2 (C_{31}), 129.1 (C_{23}), 128.9 (C_{27}), 128.9 (C_5), 128.8 (C_{30}), 128.8 (C_{38}), 128.6 (C_{19}), 128.4 (C_{22}), 128.4 (C_{33}), 128.0 (C_{35}), 128.0 (C_{34}), 127.6 (C_{16}), 127.5 (C_{29}), 127.35 (C_{18}), 127.0 (C_{13}), 126.75 (C_{17}), 125.0 (C_7), 124.8 (C_{10}). **HR-ESI MS** *m/z* = 621.2560 $[M]^+$ (calculated for $C_{49}H_{33}^+$ = 621.2582).

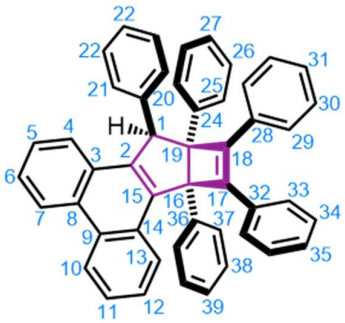

anti-**11**

anti-**11**: A solution of $LiAlH_4$ in THF (0.15 mL, 150 µmol) was added to a solution of **4**·OTf (12 mg, 13 µmol) in anhydrous dioxane (1 mL), and the mixture was stirred at rt for 20 min. The reaction was quenched with water (5 mL) and extracted with EtOAc (3 × 5 mL). The combined organic extracts were washed with brine (10 mL), then dried over $MgSO_4$. The solvents were removed *in vacuo*, leaving a pale-yellow residue, which was purified by preparative TLC (SiO_2, hexanes–CH_2Cl_2, 7:3) to yield the title compound as a colourless solid (5.6 mg, 9.0 µmol, 72%). **^{1}H NMR** (600 MHz, $CDCl_3$) δ 8.75 (d, J = 8.4 Hz, 1H, H_7), 8.72 (d, J = 8.4 Hz, 1H, H_{10}), 7.63 (d, J = 8.2 Hz, 1H, H_4), 7.59–7.56 (m, 1H, H_6), 7.52–7.48 (m, 1H, H_{11}), 7.48–7.42 (m, 4H, $H_{21,29,30'}$), 7.38–7.35 (m, 1H, H_5), 7.35–7.32 (m, 2H, H_{25}), 7.29 (d, J = 8.3 Hz, 1H, H_{13}), 7.27–7.24 (m, 2H, $H_{29',30}$), 7.11–7.07 (m, 3H, $H_{12,22}$), 7.04–6.95 (m, 4H, $H_{26,27,31}$), 6.87–6.81 (m, 2H, $H_{35,39}$), 6.80–6.76 (m, 3H, $H_{23,37}$), 6.74–6.70 (m, 3H, $H_{34,38}$), 6.68–6.85 (m, 1H, $H_{33'}$), 6.52–6.48 (m, 1H, $H_{34'}$), 6.47–6.44 (m, 1H, H_{33}), 5.95 (s, 1H, H_1). **^{13}C NMR** (151 MHz, $CDCl_3$) δ 148.1 (C_{18}), 142.4 (C_{32}), 142.1 (C_{20}), 141.9 (C_{24}), 141.5 (C_2), 140.5 (C_{17}), 139.0 (C_{15}), 136.7 (C_{28}), 133.7 (C_{36}), 131.7 (C_9), 131.7 (C_8), 130.0 ($C_{33'}$), 130.0 (C_{21}), 129.9 (C_3), 129.8 (C_{33}), 129.4 (C_{25}), 129.3 (C_{29}), 129.2 (C_{13}), 128.6 (C_{30}), 128.2 ($C_{34'}$), 128.0 (C_{37}), 127.9 ($C_{22/29'}$), 127.9 $C_{29'/22}$), 127.8 ($C_{30'}$), 127.5 (C_{26}), 127.5 (C_{34}), 127.3 (C_{31}), 126.9 (C_{38}), 126.8 (C_{23}), 126.5 (C_5), 126.4 (C_4), 126.3 ($C_{35/39}$), 126.1 (C_6), 126.1 (C_{27}), 126.1 (C_{11}) 125.9 ($C_{39/35}$), 125.6 (C_{12}), 123.2 (C_7), 122.8 (C_{10}), 76.5 (C_{16}), 71.5 (C_{19}), 57.2 (C_1).

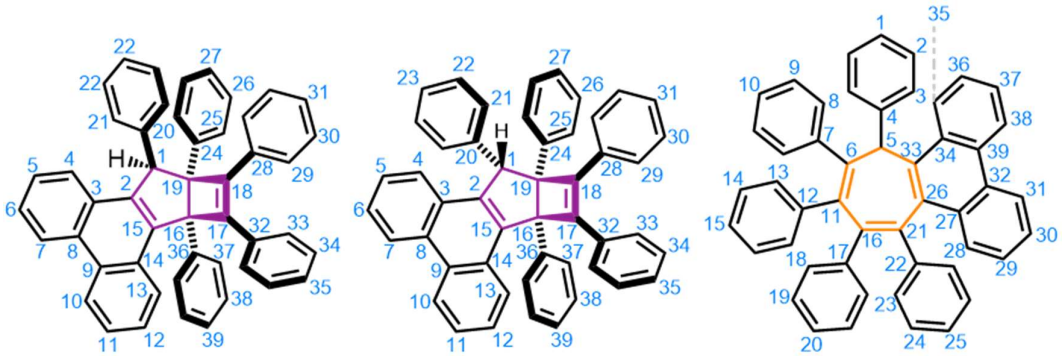

anti-**11** *syn*-**11** **12**

$NaBH_4$ (20 mg, 530 μmol) was added to a solution of **4**·$SbCl_6$ (7.2 mg, 7.8 μmol) in CD_2Cl_2 (0.5 mL), and the solvent was removed *in vacuo*. Anhydrous THF (0.5 mL) was added, and the mixture was stirred for 20 min. Water (10 mL) was added, and the aqueous layer was extracted with EtOAc (3 × 5 mL). The combined organic extracts were washed with brine (10 mL) and dried over $MgSO_4$. The solvents were removed *in vacuo*, leaving a colourless oil, which was passed through a silica plug, eluting in hexanes–CH_2Cl_2 (1:1). Evaporation to dryness afforded a mixture of *anti*-**11**, *syn*-**11**, and **12** as a colourless solid. **^{1}H NMR** spectroscopic analysis showed *anti*-**11**, *syn*-**11**, and **12** were present in a 38:58:4 ratio (96:4 ratio of bicycycloheptadiene:cycloheptatriene isomers). The signals in the mixture corresponding to **12** could be identified unambiguously by comparison with NMR data from a pure sample which we have previously synthesised by an alternative synthetic route, as reported recently.[59] For comparison, the characterisation data for **12** are reproduced below:

^{1}H NMR (700 MHz, $CDCl_3$) δ 8.76 (dd, J = 8.4, 1.2 Hz, 2H, H_{28}), 8.64 (dd, J = 8.4, 1.2 Hz, 1H, H_{38}), 8.16 (d, J = 8.4 Hz, 2H, H_{31}), 7.96–7.92 (m, 1H, H_{35}), 7.66 (ddd, J = 8.2, 6.9, 1.2 Hz, 1H, H_{29}), 7.58 (d, J = 7.6 Hz, 2H, H_{18}), 7.55 (m, 1H, H_{30}), 7.46 (m, 1H, H_{37}), 7.28 (m, 2H, H_{19}), 7.25 (m, 1H, H_{36}), 7.23 (m, 1H, H_{20}), 7.11 (m, 3H, $H_{13,15}$), 7.02–6.95 (m, 5H, $H_{8–10}$), 6.86 (m, 1H, H_1), 6.78 (m, 1H, H_{25}), 6.73 (m, 2H, H_{24}), 6.71 (m, 2H, H_{23}), 6.68 (m, 2H, H_2), 6.36 (s, 1H, H_5), 5.70 (d, J = 7.7 Hz, 2H, H_3). **^{13}C NMR** (176 MHz, $CDCl_3$) δ 143.8 (C_6), 143.5 (C_{26}), 143.4 (C_{16}), 143.1 (C_{11}), 142.7 (C_{21}), 142.5 (C_{33}), 142.1 (C_4), 140.7 (C_{22}), 140.2 (C_{17}), 139.5 (C_{12}), 138.4 (C_7), 138.0 (C_{39}), 132.2 (C_{32}), 131.7 (C_{23}), 131.5 (C_{34}), 131.5 (C_{27}), 131.2 (C_3), 129.5 (C_{35}),

129.43 (C_{14}), 129.0 ($C_{8/9/10}$), 128.7 (C_{36}), 127.7 ($C_{9/8/10}$), 127.67 (C_{15}), 127.6 (C_{30}), 127.1 (C_{18}), 126.9 (C_{29}), 126.79 (C_{24}), 126.7 (C_{13}), 126.5 (C_{20}), 126.5 (C_2), 126.3 ($C_{10/9/8}$), 125.9 (C_{19}), 125.8 (C_{37}), 125.7 (C_{25}), 125.7 (C_1), 124.4 (C_{31}), 123.2 (C_{28}), 122.7 (C_{38}), 50.3 (C_5). **HR-ASAP MS** *m/z* = 622.2662 $[M]^+$ (calculated for $C_{49}H_{34}^+$: 622.2655).

2.4.2. Variable Temperature NMR Spectroscopy

The ^{1}H NMR spectrum of **4**·$SbCl_6$ at room temperature exhibits broad peaks, indicating interconversion between the two isomers of **4** (see Figure 2.7).

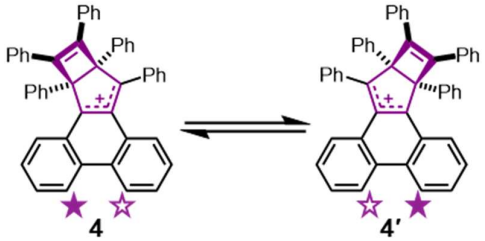

Figure 2.6. Two degenerate isomers of **4**.

Cooling below the coalescence temperature of the broad peaks separates the interconverting environments into the slow-exchange regime, such that the NMR spectrum exhibits sharp peaks. A variable temperature ^{1}H NMR stack of **4**·$SbCl_6$ is shown below in Figure 2.7.

Line shape analysis of the VT ^{1}H NMR spectrum of **4**·$SbCl_6$ was carried out using WinDNMR v. 7.1.[i]

[i] Developed by H. J. Reich (available at: https://www2.chem.wisc.edu/areas/reich/plt/windnmr.htm). Simulated lineshapes were derived from the experimentally determined frequencies of proton resonances and their full width at half maxima in the slow exchange region. Various rates of exchange were inputted to observe the variance of the simulated lineshape compared to experimental data. Kinetic parameters were derived from the simulated spectra.

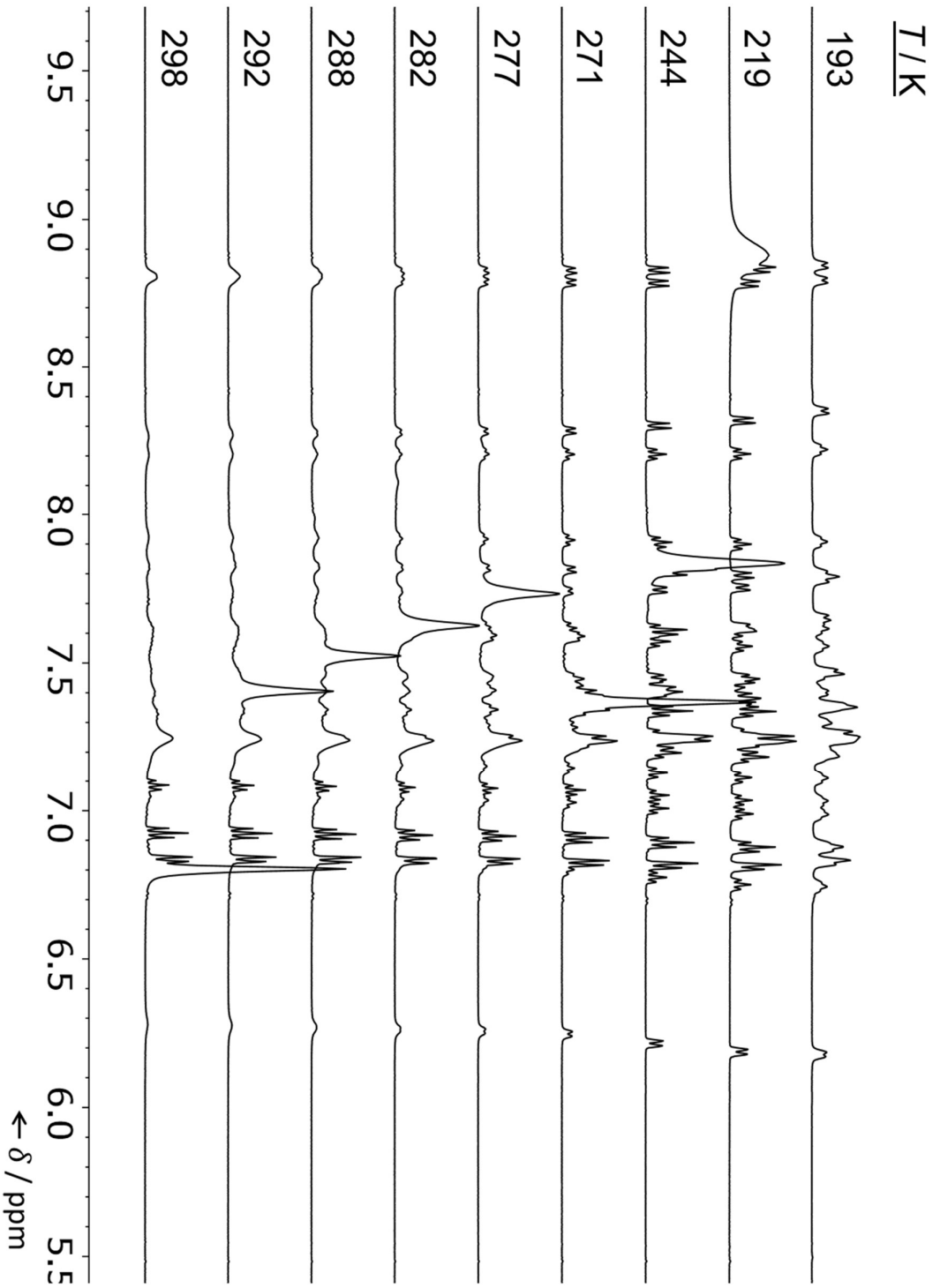

Figure 2.7. Variable-temperature ^{1}H NMR spectra of **4**·$SbCl_6$.

2.4.3. Exchange NMR Spectroscopy

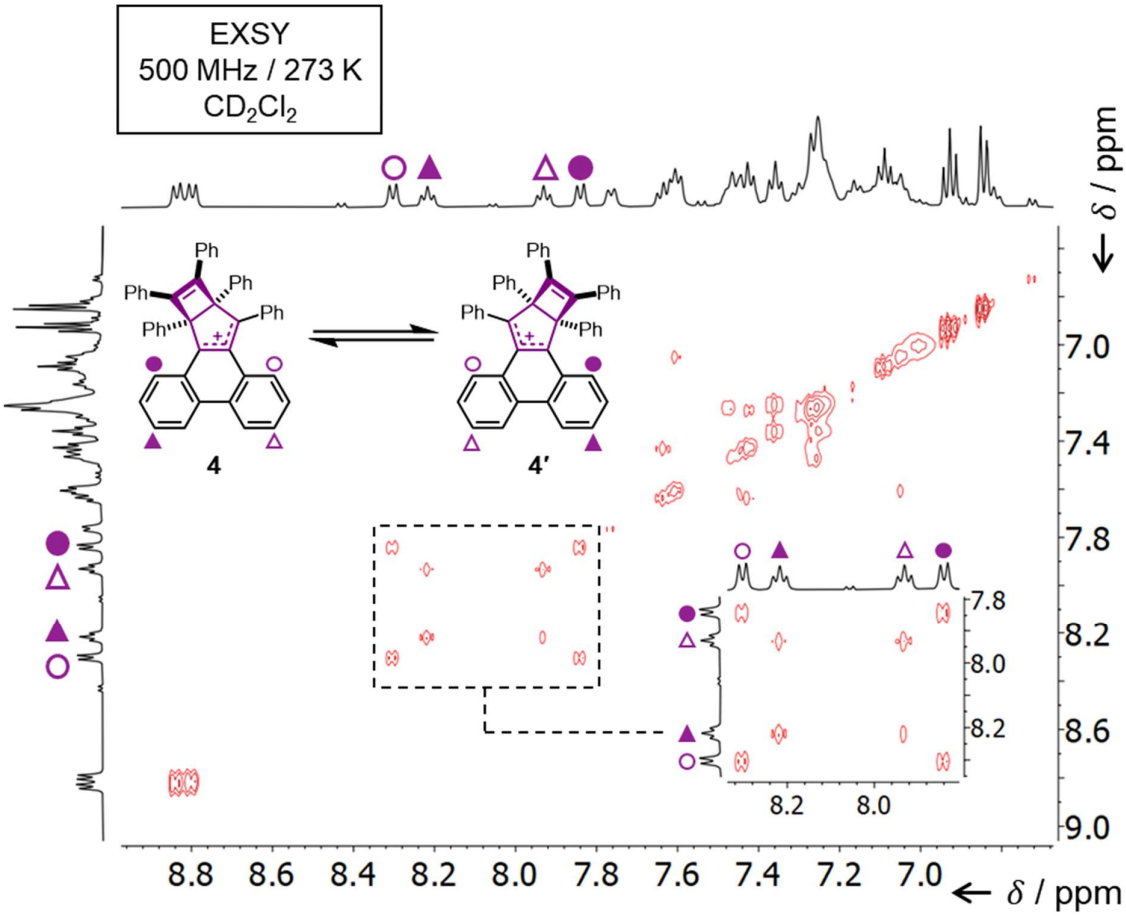

Figure 2.8. Partial EXSY NMR spectrum of **4** and **4′** with a mixing time τ_m = 200 ms at 270 K. The spectrum shows exchange correlations between ^{1}H environments 4-● and 4′-○, as well as 4-▲ and 4′-△ (see inset).

As the chosen proton environments are too far apart to exhibit through-space coupling, the possibility that the observed correlations arise from the nuclear Overhauser effect (NOE) can be ruled out. The correlations arise through dynamic exchange of isomers **4** and **4′**, which is consistent with our lineshape analysis of the ^{1}H NMR spectra at different temperatures.

2.4.4. X-Ray Crystallographic Analysis

2.4.4.1. 1·ICl_2

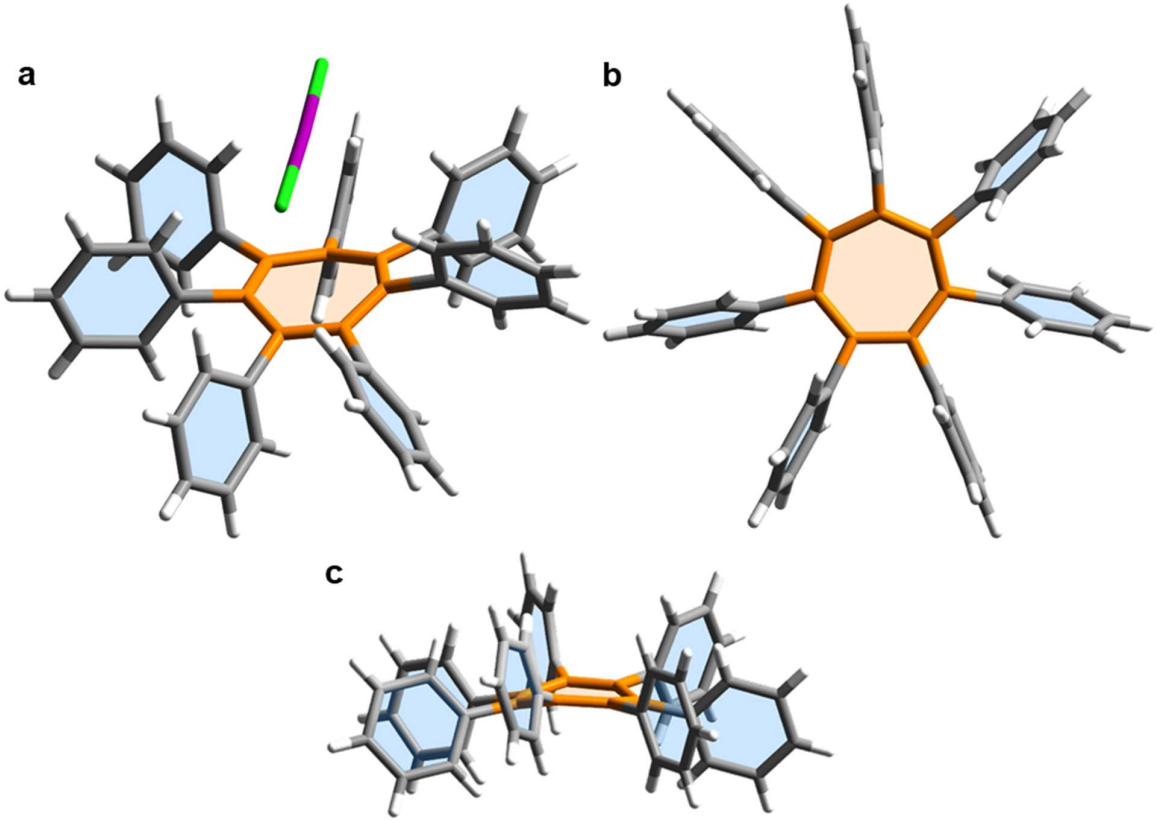

Figure 2.9. Solid-state structure of **1**·ICl_2 viewed (**a**) face-on to the tropylium with ICl_2 counter-ion, (**b**) from above the tropylium and (**c**) side-on to the tropylium. The counter-ion is omitted for clarity from (**b**) and (**c**).

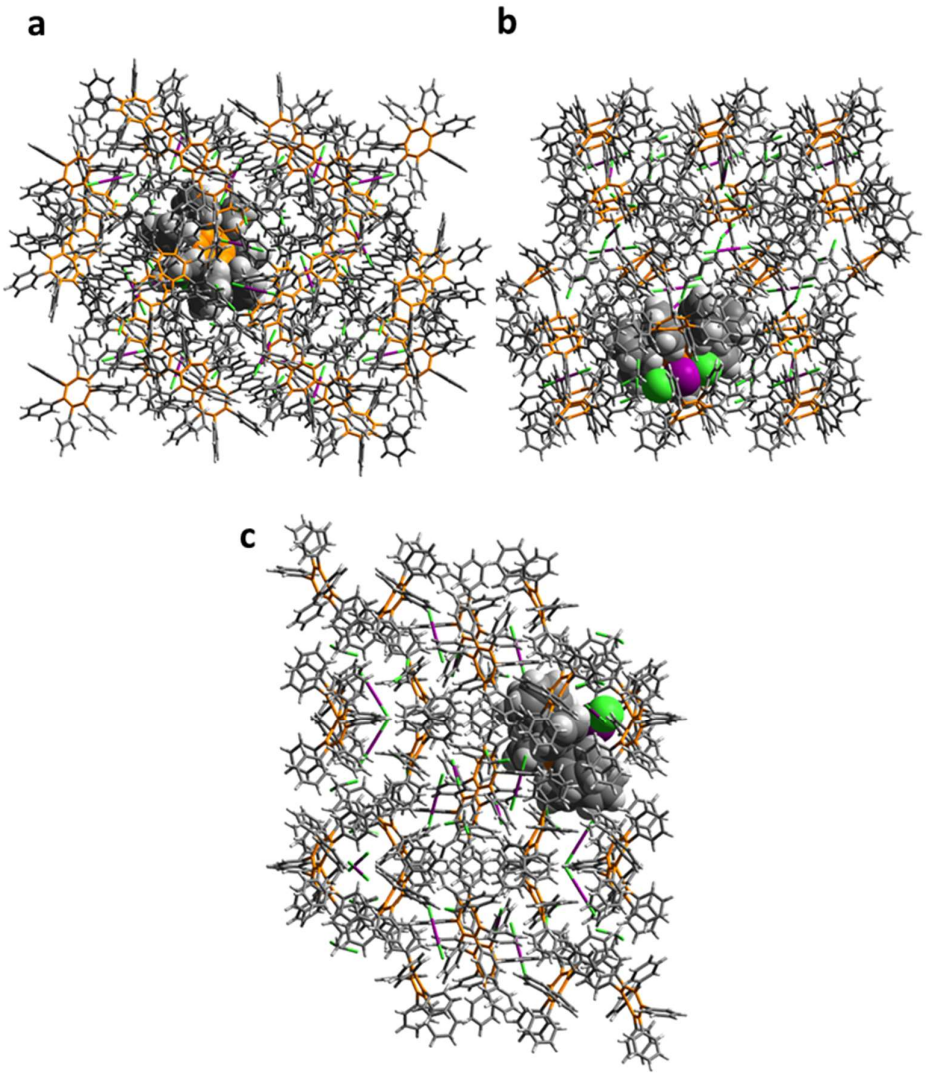

Figure 2.10. Solid-state superstructure of **1**·ICl_2**.** A central molecule (space filling representation) is shown embedded in a section of the lattice made up of 2×2×2 unit cells in order to illustrate the crystal packing. Projections are viewed along the crystallographic (**a**) *a*-, (**b**) *b*-, and (**c**) *c*-axes.

Table 2.2. Crystal data and structure refinement for **1**·ICl_2.

	1·ICl_2
CCDC Number	2141786
Empirical formula	$C_{50}H_{37}Cl_4I$
Formula weight	906.49
Temperature/K	120.0
Crystal system	monoclinic
Space group	$P2_1/c$
a/Å	26.964(2)

b/Å	27.059(2)
c/Å	22.8873(17)
α/°	90
β/°	94.601(3)
γ/°	90
Volume/Å^3	16645(2)
Z	16
ρ_{calc}g/cm^3	1.447
μ/mm^{-1}	1.061
F(000)	7328.0
Crystal size/mm^3	0.3 × 0.21 × 0.11
Radiation	MoKα (λ = 0.71073)
2Θ range for data collection/°	3.874 to 57
Index ranges	-36 ≤ h ≤ 36, -36 ≤ k ≤ 36, -30 ≤ l ≤ 30
Reflections collected	314988
Independent reflections	42199 [R_{int} = 0.0636, R_{sigma} = 0.0452]
Data/restraints/parameters	42199/6/1978
Goodness-of-fit on F^2	1.033
Final R indexes [I>=2σ (I)]	R_1 = 0.0531, wR_2 = 0.1305
Final R indexes [all data]	R_1 = 0.0867, wR_2 = 0.1495
Largest diff. peak/hole / e Å^{-3}	3.07/-1.32

Crystals of **1**·ICl_2 suitable for X-ray diffraction were grown by slow evaporation of a saturated CH_2Cl_2 solution.

2.4.4.2. 8

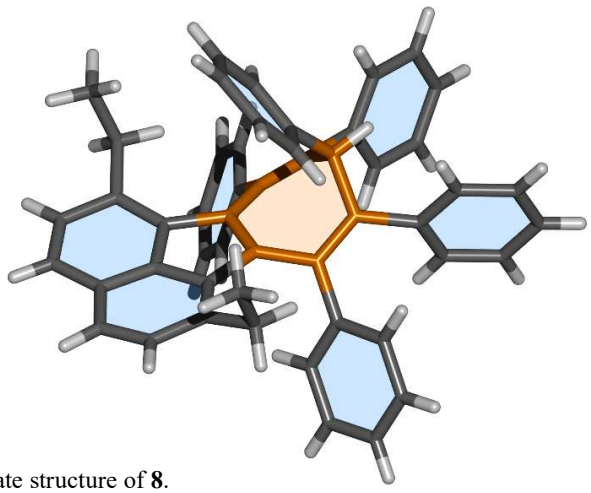

Figure 2.11. Solid-state structure of **8**.

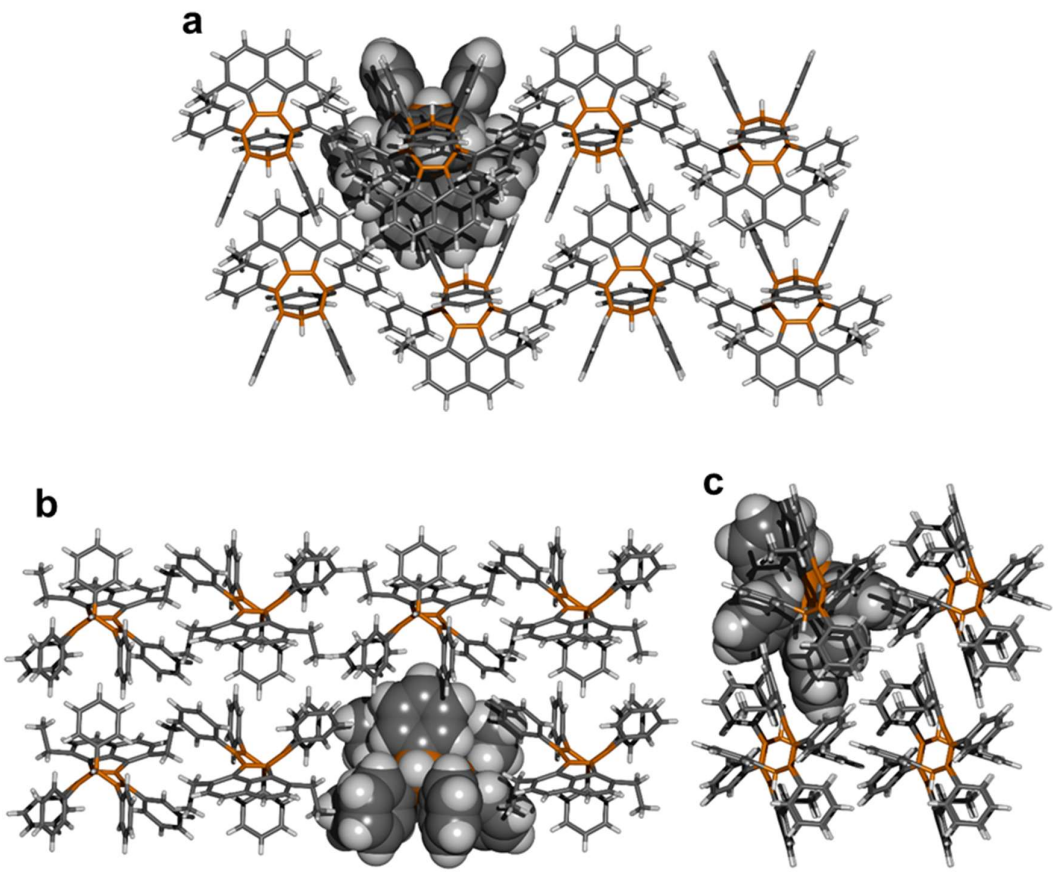

Figure 2.12. Solid-state superstructure of **8.** A central molecule (space filling representation) is shown embedded in a section of the lattice made up of 2×2×2 unit cells in order to illustrate the crystal packing. Projections are viewed along the crystallographic (**a**) *a*-, (**b**) *b*-, and (**c**) *c*-axes.

Table 2.3. Crystal data and structure refinement for **8**.

	8
CCDC Number	2141790
Empirical formula	$C_{51}H_{40}$
Formula weight	652.83
Temperature/K	120.0
Crystal system	triclinic
Space group	P-1
a/Å	9.549(2)
b/Å	9.987(2)
c/Å	19.991(5)
α/°	78.699(7)
β/°	88.107(6)
γ/°	79.154(7)

Volume/Å^3	1836.1(8)
Z	2
ρ_{calc}g/cm^3	1.181
μ/mm^{-1}	0.067
F(000)	692.0
Crystal size/mm^3	0.25 × 0.05 × 0.02
Radiation	MoKα (λ = 0.71073)
2Θ range for data collection/°	4.232 to 51.994
Index ranges	-11 ≤ h ≤ 11, -12 ≤ k ≤ 11, -24 ≤ l ≤ 24
Reflections collected	30569
Independent reflections	7231 [R_{int} = 0.2068, R_{sigma} = 0.2472]
Data/restraints/parameters	7231/0/463
Goodness-of-fit on F^2	0.959
Final R indexes [I>=2σ (I)]	R_1 = 0.0769, wR_2 = 0.1307
Final R indexes [all data]	R_1 = 0.2207, wR_2 = 0.1704
Largest diff. peak/hole / e Å^{-3}	0.26/-0.24

Crystals of **8** suitable for X-ray diffraction were grown by slow evaporation of a saturated CH_2Cl_2 solution.

2.4.4.3. 3·BBr$_4$

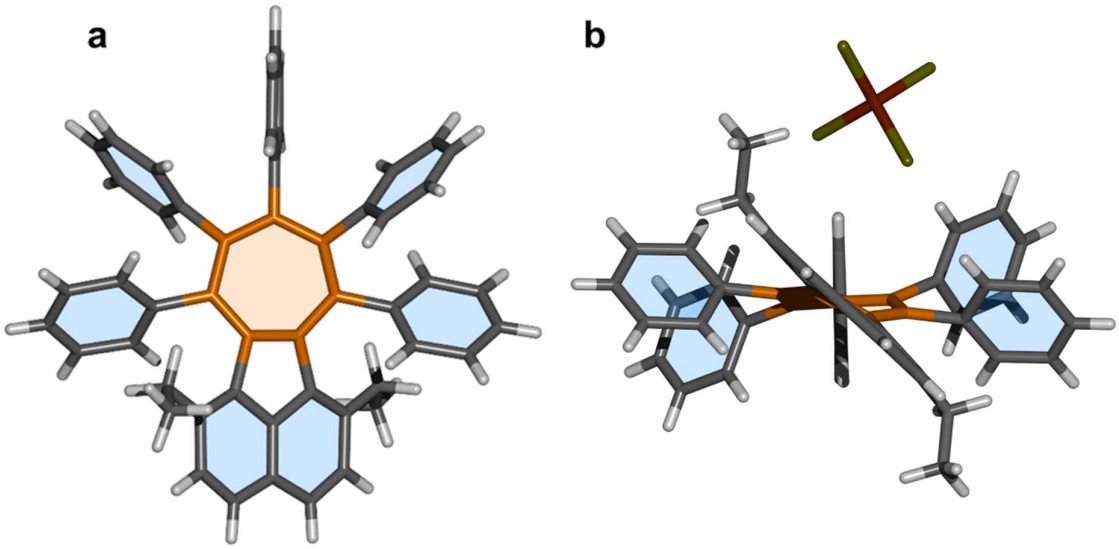

Figure 2.13. Solid-state structure of **3**·BBr_4 viewed (**a**) face-on to the tropylium, omitting the counterion, and (**b**) side-on to the tropylium, including the BBr_4. The CH_2Cl_2 solvent has been omitted for clarity.

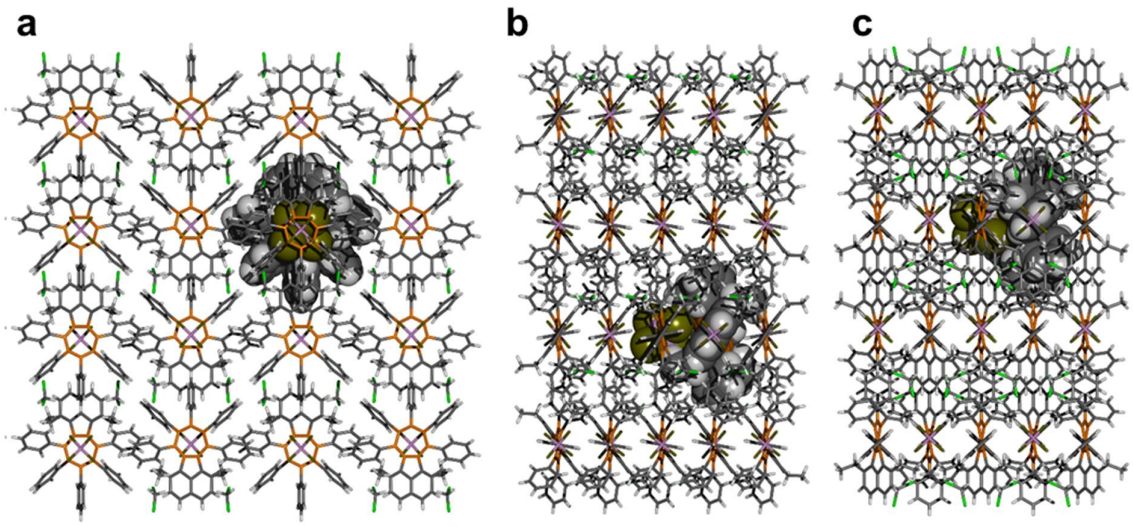

Figure 2.14. Solid-state superstructure of **3**·BBr_4 (as a CH_2Cl_2 solvate). A central molecule (space filling representation) is shown embedded in a section of the lattice made up of 2×2×2 unit cells in order to illustrate the crystal packing. Projections are viewed along the crystallographic (**a**) *a*-, (**b**) *b*-, and (**c**) *c*-axes. Two solvent molecules are present for each molecule of **3**.

Table 2.4. Crystal data and structure refinement for **3**·BBr_4.

	3·BBr_4
CCDC Number	2141788
Empirical formula	$C_{51}H_{39}$×BBr_4×2 CH_2Cl_2
Formula weight	1152.12
Temperature/K	120.0
Crystal system	orthorhombic
Space group	$C222_1$
a/Å	10.1647(10)
b/Å	21.424(2)
c/Å	21.601(2)
α/°	90
β/°	90
γ/°	90
Volume/Å^3	4703.8(8)
Z	4
ρ_{calc}g/cm^3	1.627
μ/mm^{-1}	3.687
F(000)	2296.0
Crystal size/mm^3	0.11 × 0.06 × 0.02
Radiation	MoKα (λ = 0.71073)
2Θ range for data collection/°	1.886 to 49.998

Index ranges	$-12 \leq h \leq 12, -25 \leq k \leq 25, -25 \leq l \leq 25$
Reflections collected	23165
Independent reflections	4141 [R_{int} = 0.0979, R_{sigma} = 0.0801]
Data/restraints/parameters	4141/7/286
Goodness-of-fit on F^2	1.040
Final R indexes [I>=2σ (I)]	R_1 = 0.0876, wR_2 = 0.2249
Final R indexes [all data]	R_1 = 0.1404, wR_2 = 0.2639
Largest diff. peak/hole / e $Å^{-3}$	1.01/-0.94
Flack parameter	-0.008(10)

Crystals of **3**·BBr_4 suitable for X-ray diffraction were grown by slow evaporation of a solution of **3**·BBr_4 generated *in situ* from **11** and BBr_3 in anhydrous CH_2Cl_2, then layering with anhydrous hexanes in a freezer.

2.4.4.4. Diels-Alder Intermediate (S4)

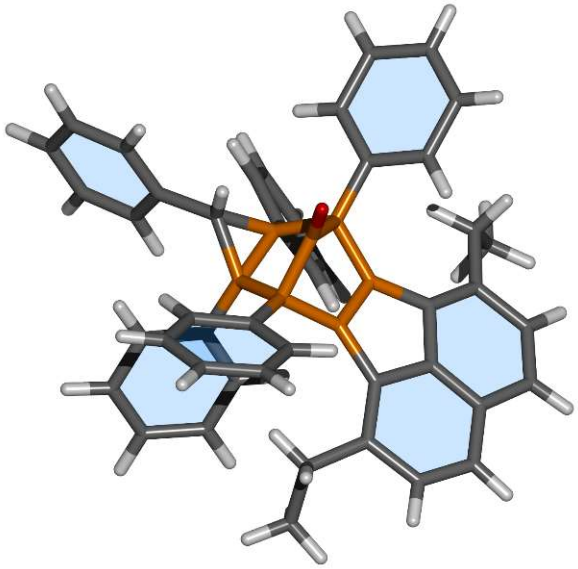

Figure 2.15. Solid-state structure of **S4**.

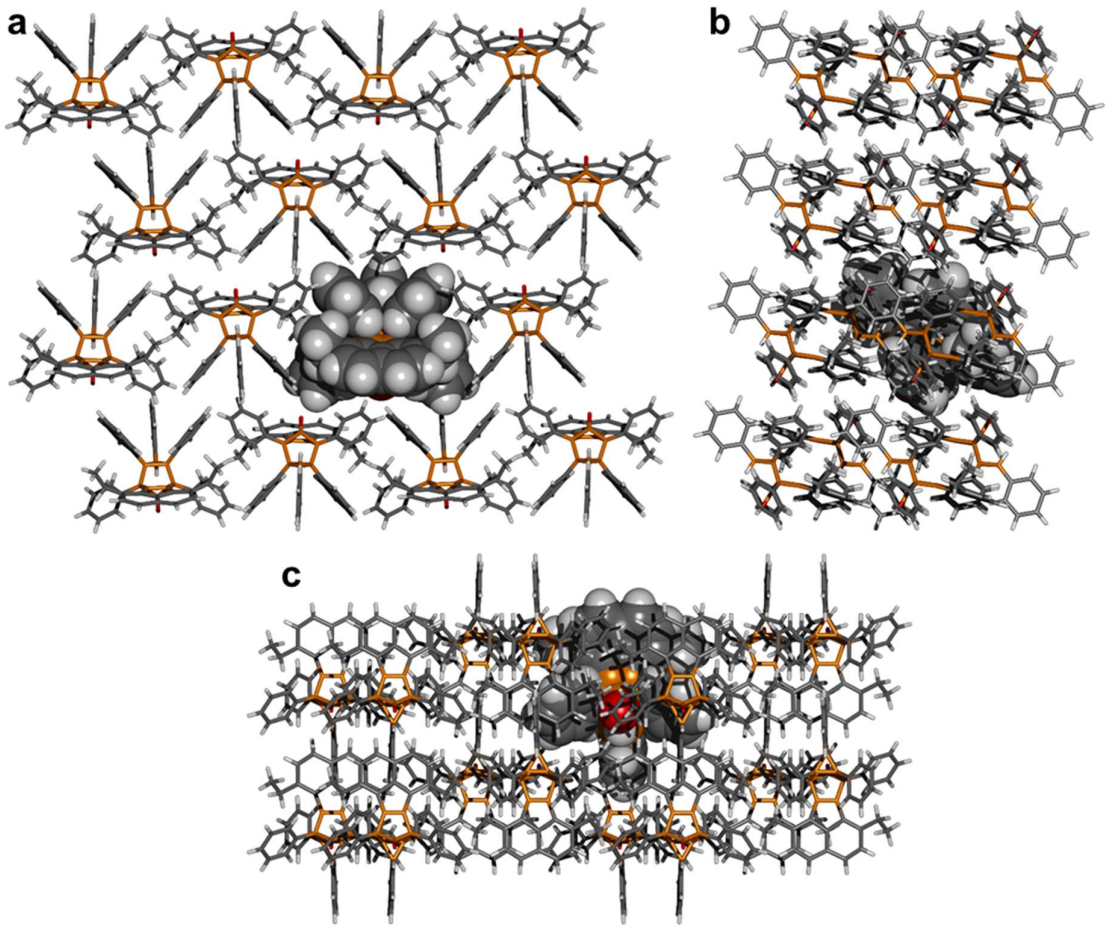

Figure 2.16. Solid-state superstructure of **S4.** A central molecule (space filling representation) is shown embedded in a section of the lattice made up of 2×2×2 unit cells in order to illustrate the crystal packing. Projections are viewed along the crystallographic (**a**) *a*-, (**b**) *b*-, and (**c**) *c*-axes.

Table 2.5. Crystal data and structure refinement for **S4**.

	S4
CCDC Number	2141795
Empirical formula	$C_{52}H_{40}O$
Formula weight	680.84
Temperature/K	120.0
Crystal system	monoclinic
Space group	$P2_1/c$
a/Å	9.6957(2)
b/Å	20.4272(5)
c/Å	18.3325(4)
α/°	90
β/°	96.6351(13)

γ/°	90
Volume/Å^3	3606.54(14)
Z	4
ρ_{calc}g/cm^3	1.254
μ/mm^{-1}	0.555
F(000)	1440.0
Crystal size/mm^3	0.29 × 0.19 × 0.13
Radiation	CuKα (λ = 1.54178)
2Θ range for data collection/°	6.502 to 141.986
Index ranges	-11 ≤ h ≤ 11, -24 ≤ k ≤ 25, -21 ≤ l ≤ 22
Reflections collected	44694
Independent reflections	6951 [R_{int} = 0.0492, R_{sigma} = 0.0292]
Data/restraints/parameters	6951/0/638
Goodness-of-fit on F^2	1.022
Final R indexes [I>=2σ (I)]	R_1 = 0.0424, wR_2 = 0.1080
Final R indexes [all data]	R_1 = 0.0577, wR_2 = 0.1170
Largest diff. peak/hole / e Å^{-3}	0.30/-0.24

Crystals of **S4** suitable for X-ray diffraction were grown by slow evaporation of a saturated CH_2Cl_2 solution of **S4** layered with hexanes.

2.4.4.5. 1,6-Diethyl-7,8,9,10-tetraphenylfluoranthene (S5)

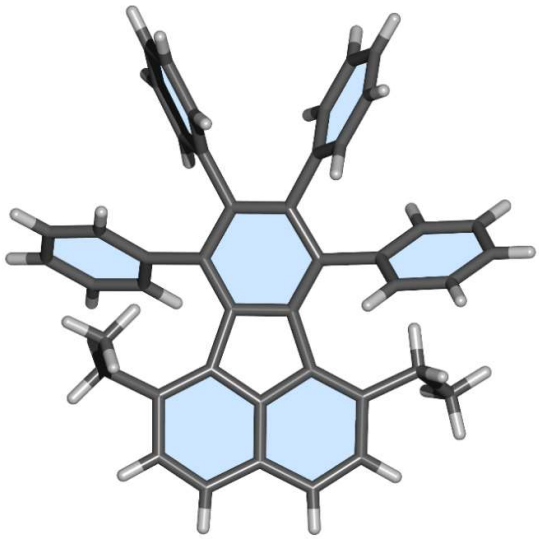

Figure 2.17. Solid-state structure of **S5.**

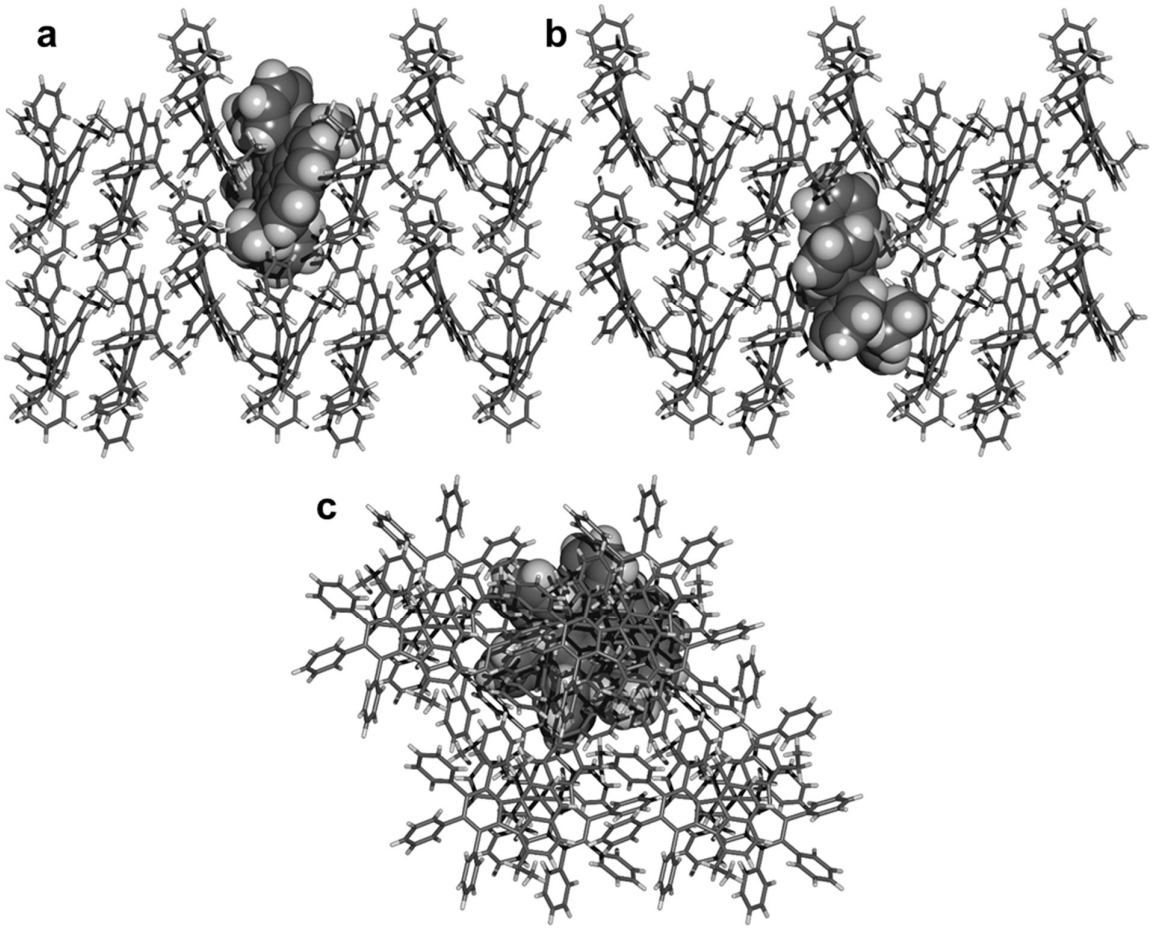

Figure 2.18. Solid-state superstructure of **S5.** A central molecule (space filling representation) is shown embedded in a section of the lattice made up of 2×2×2 unit cells in order to illustrate the crystal packing. Projections are viewed along the crystallographic (**a**) *a*-, (**b**) *b*-, and (**c**) *c*-axes.

Table 2.6. Crystal data and structure refinement for **S5**.

S5	
CCDC Number	2141796
Empirical formula	$C_{44}H_{34}$
Formula weight	562.71
Temperature/K	120.0
Crystal system	trigonal
Space group	$P3_2$
a/Å	13.1637(2)
b/Å	13.1637(2)
c/Å	15.4431(4)
α/°	90
β/°	90
γ/°	120

Volume/Å^3	2317.51(9)
Z	3
ρ_{calc}g/cm^3	1.210
μ/mm^{-1}	0.068
F(000)	894.0
Crystal size/mm^3	0.32 × 0.16 × 0.07
Radiation	Mo Kα (λ = 0.71073)
2Θ range for data collection/°	4.442 to 57.966
Index ranges	-17 ≤ h ≤ 17, -17 ≤ k ≤ 17, -21 ≤ l ≤ 21
Reflections collected	39603
Independent reflections	8165 [R_{int} = 0.0461, R_{sigma} = 0.0402]
Data/restraints/parameters	8165/2/404
Goodness-of-fit on F^2	1.032
Final R indexes [I>=2σ (I)]	R_1 = 0.0542, wR_2 = 0.1169
Final R indexes [all data]	R_1 = 0.0633, wR_2 = 0.1217
Largest diff. peak/hole / e Å^{-3}	0.60/-0.44
Flack parameter	-0.1(10)

Crystals of **S5** suitable for X-ray diffraction were grown by slow evaporation of a saturated solution of **S5** in hexanes–CH_2Cl_2.

2.4.4.6. 9

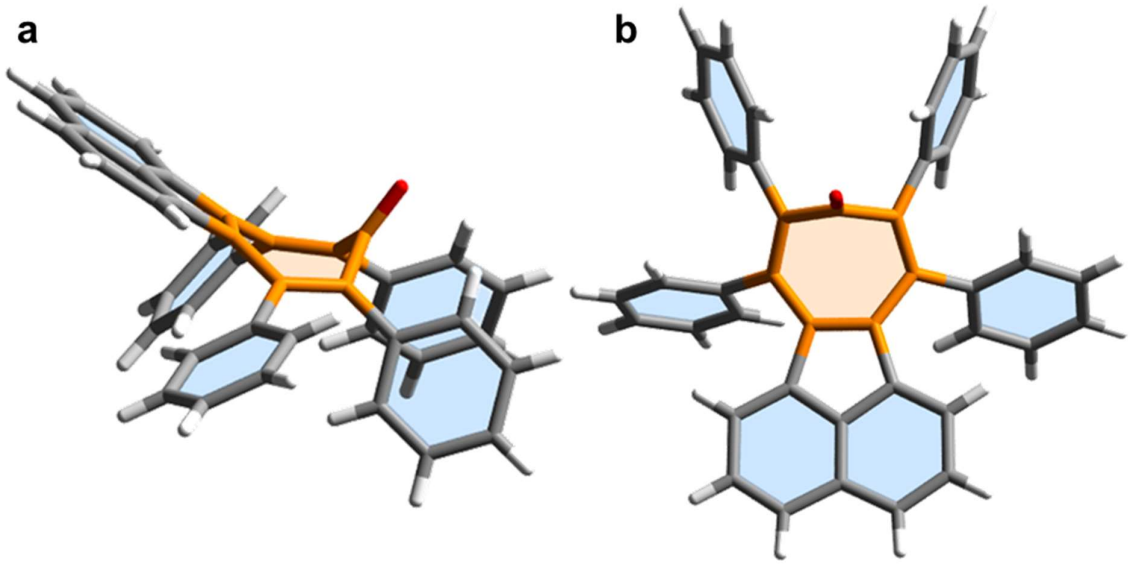

Figure 2.19. Solid-state structure of **9** viewed (**a**) side-on to the tropone and (**b**) face-on to the tropone.

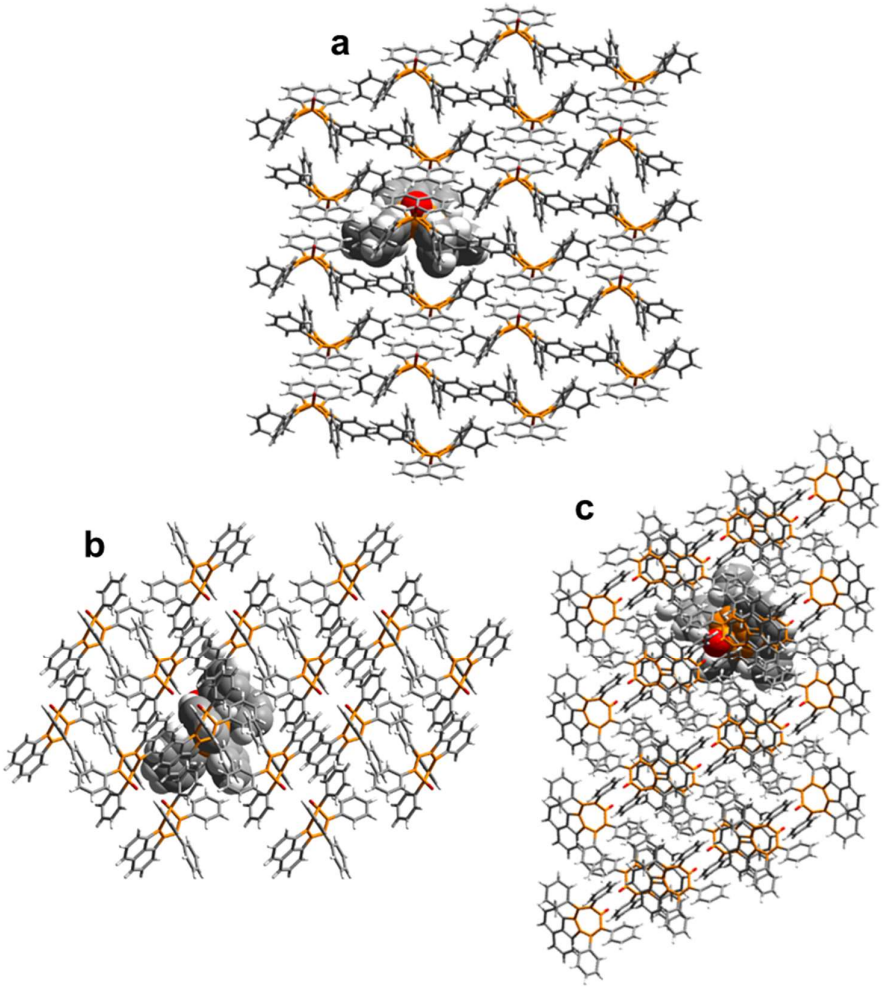

Figure 2.20. Solid-state superstructure of **9.** A central molecule (space filling representation) is shown embedded in a section of the lattice made up of 2×2×2 unit cells in order to illustrate the crystal packing. Projections are viewed along the crystallographic (**a**) *a*-, (**b**) *b*-, and (**c**) *c*-axes.

Table 2.7. Crystal data and structure refinement for **9**.

	9
CCDC Number	2141791
Empirical formula	$C_{41}H_{26}O$
Formula weight	534.62
Temperature/K	120.0
Crystal system	triclinic
Space group	P-1
a/Å	10.3889(6)
b/Å	11.1459(7)

c/Å	14.2952(9)
α/°	103.530(2)
β/°	103.151(2)
γ/°	112.377(2)
Volume/Å^3	1392.85(15)
Z	2
ρ_{calc}g/cm^3	1.275
μ/mm^{-1}	0.075
F(000)	560.0
Crystal size/mm^3	0.31 × 0.13 × 0.08
Radiation	MoKα (λ = 0.71073)
2Θ range for data collection/°	4.23 to 58
Index ranges	-14 ≤ h ≤ 14, -15 ≤ k ≤ 15, -19 ≤ l ≤ 19
Reflections collected	29172
Independent reflections	7415 [R_{int} = 0.0557, R_{sigma} = 0.0678]
Data/restraints/parameters	7415/0/379
Goodness-of-fit on F^2	1.030
Final R indexes [I>=2σ (I)]	R_1 = 0.0523, wR_2 = 0.1043
Final R indexes [all data]	R_1 = 0.1002, wR_2 = 0.1190
Largest diff. peak/hole / e Å^{-3}	0.28/-0.28

Crystals of **9** suitable for X-ray diffraction were grown by slow evaporation of a saturated solution of **9** in CH_2Cl_2–hexanes.

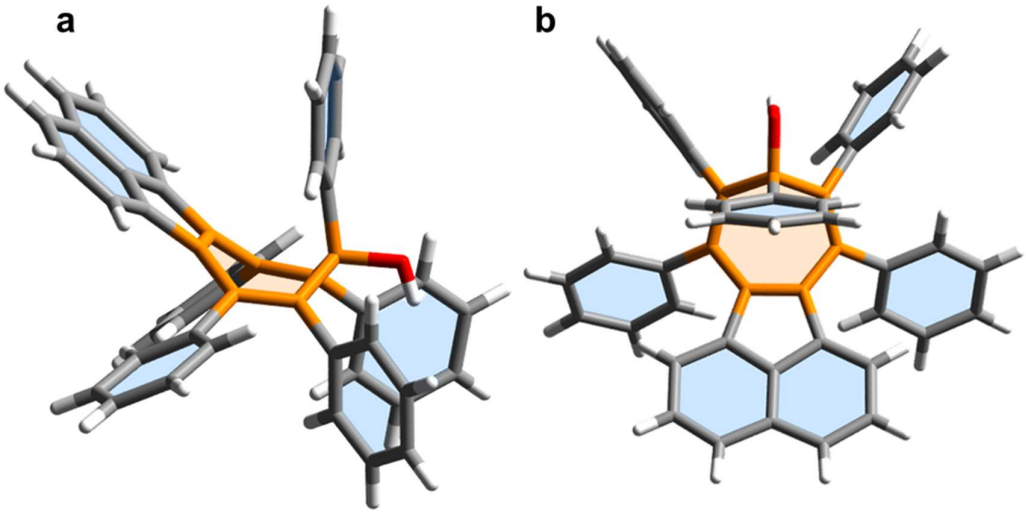

2.4.4.7. S2

Figure 2.21. Solid-state structure of **S2** viewed (**a**) side-on and (**b**) face-on to the seven-membered ring.

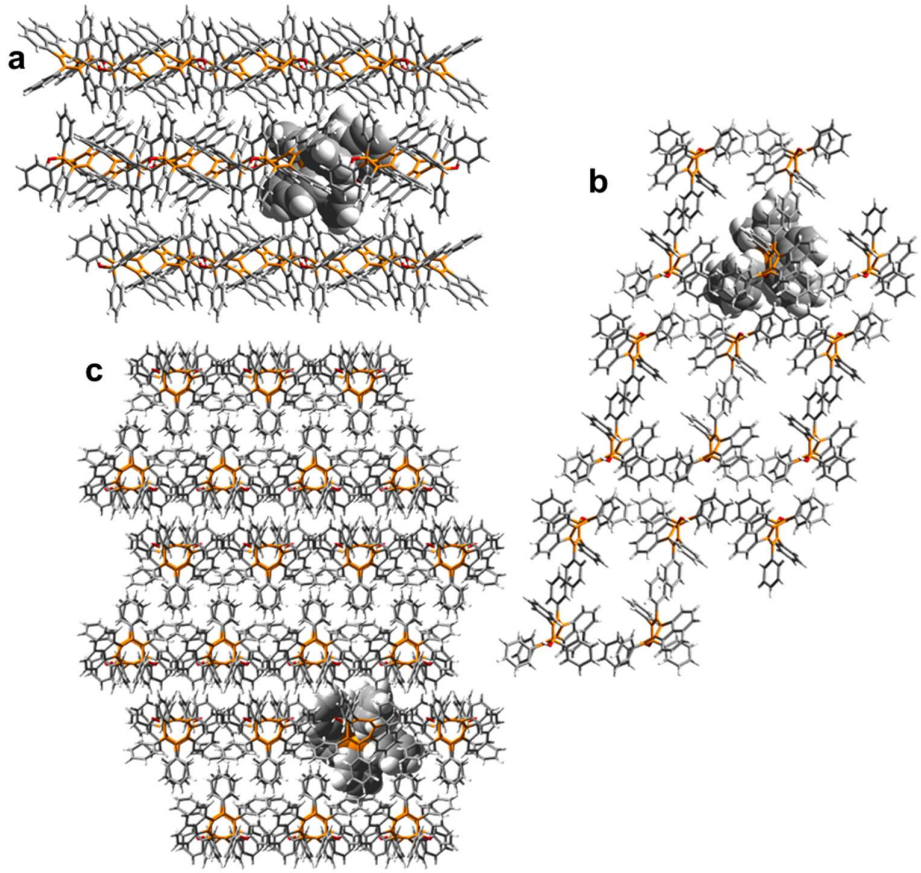

Figure 2.22. Solid-state superstructure of **S2.** A central molecule (space filling representation) is shown embedded in a section of the lattice made up of 2×2×2 unit cells in order to illustrate the crystal packing. Projections are viewed along the crystallographic (**a**) *a*-, (**b**) *b*-, and (**c**) *c*-axes.

Table 2.8. Crystal data and structure refinement for **S2**.

	S2
CCDC Number	2141793
Empirical formula	$C_{51}H_{40}O_2$
Formula weight	684.83
Temperature/K	120.0
Crystal system	monoclinic
Space group	$P2_1/c$
a/Å	19.5114(12)

b/Å	9.7395(6)
c/Å	19.9893(12)
α/°	90
β/°	107.714(4)
γ/°	90
Volume/Å^3	3618.5(4)
Z	4
ρ_{calc}g/cm^3	1.257
μ/mm^{-1}	0.577
F(000)	1448.0
Crystal size/mm^3	0.08 × 0.05 × 0.02
Radiation	CuKα (λ = 1.54178)
2Θ range for data collection/°	4.754 to 134.988
Index ranges	-23 ≤ h ≤ 23, -11 ≤ k ≤ 11, -22 ≤ l ≤ 23
Reflections collected	46456
Independent reflections	6478 [R_{int} = 0.3108, R_{sigma} = 0.2019]
Data/restraints/parameters	6478/13/475
Goodness-of-fit on F^2	0.987
Final R indexes [I>=2σ (I)]	R_1 = 0.1092, wR_2 = 0.2279
Final R indexes [all data]	R_1 = 0.2278, wR_2 = 0.2929
Largest diff. peak/hole / e Å^{-3}	0.39/-0.31

Crystals of **S2** suitable for X-ray diffraction were grown by slow evaporation of a saturated solution of Et_2O layered with hexanes.

2.4.4.8. 2·$SbCl_6$ (120 K)

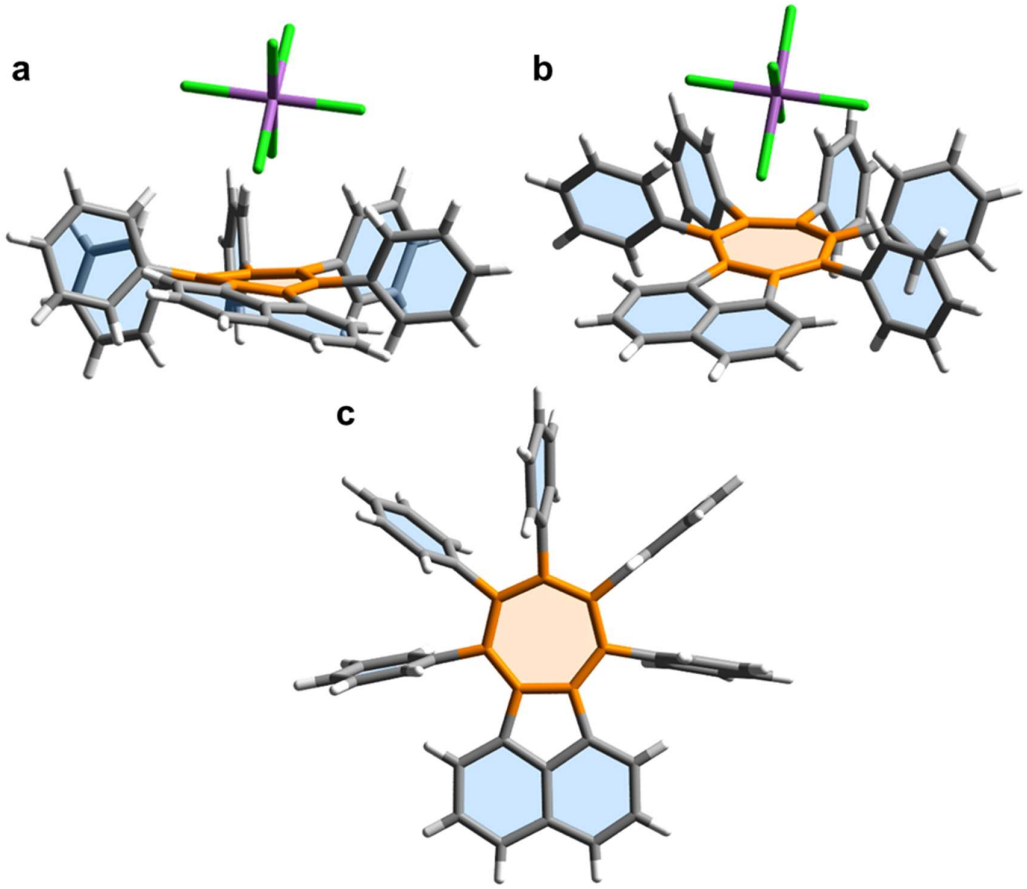

Figure 2.23. Solid-state structure of **2**·$SbCl_6$ (120 K) in its (**a**) twisted and (**b**) shallow boat conformations, and (**c**) viewed face-on. The counter-ion is omitted for clarity from (**c**). $CHCl_3$ present in the unit cell is also omitted for clarity.

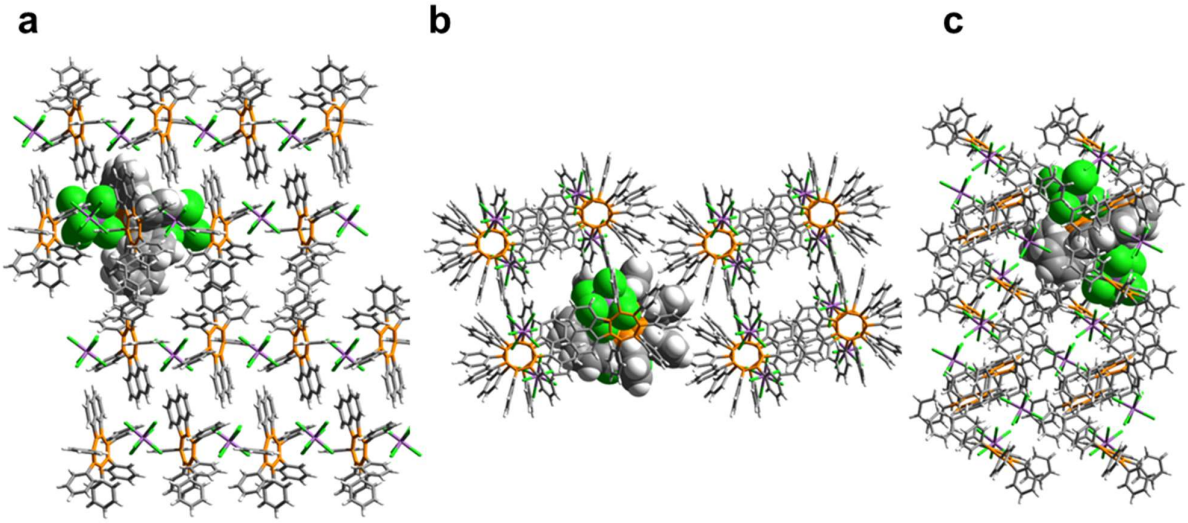

Figure 2.24. Solid-state superstructure of **2**·$SbCl_6$ (120 K)**.** A central molecule (space filling representation) is shown embedded in a section of the lattice made up of 2×2×2 unit cells in order to

illustrate the crystal packing. Projections are viewed along the crystallographic (**a**) *a*-, (**b**) *b*-, and (**c**) *c*-axes.

Table 2.9. Crystal data and structure refinement for **2**·$SbCl_6$ at 120 K.

2·$SbCl_6$	
CCDC Number	2141787
Empirical formula	$C_{47}H_{31} \times SbCl_6 \times 1.5\ CHCl_3$
Formula weight	1109.22
Temperature/K	120.0
Crystal system	triclinic
Space group	P-1
a/Å	11.853(2)
b/Å	17.680(3)
c/Å	23.961(4)
α/°	76.709(5)
β/°	76.366(5)
γ/°	89.443(6)
Volume/$Å^3$	4743.8(14)
Z	4
$\rho_{calc}g/cm^3$	1.553
μ/mm^{-1}	1.207
F(000)	2212.0
Crystal size/mm^3	0.27 × 0.24 × 0.02
Radiation	MoKα (λ = 0.71073)
2Θ range for data collection/°	3.818 to 54
Index ranges	$-15 \leq h \leq 14$, $-22 \leq k \leq 22$, $-30 \leq l \leq 30$
Reflections collected	73608
Independent reflections	20630 [R_{int} = 0.0645, R_{sigma} = 0.0751]
Data/restraints/parameters	20630/6/1082
Goodness-of-fit on F^2	1.060
Final R indexes [I>=2σ (I)]	R_1 = 0.0890, wR_2 = 0.2404
Final R indexes [all data]	R_1 = 0.1134, wR_2 = 0.2664
Largest diff. peak/hole / e $Å^{-3}$	2.21/-2.99

Crystals of **2**·$SbCl_6$ suitable for X-ray diffraction were grown by slow evaporation of a saturated CH_2Cl_2 solution.

2.4.4.9. 2·$SbCl_6$ (270 K)

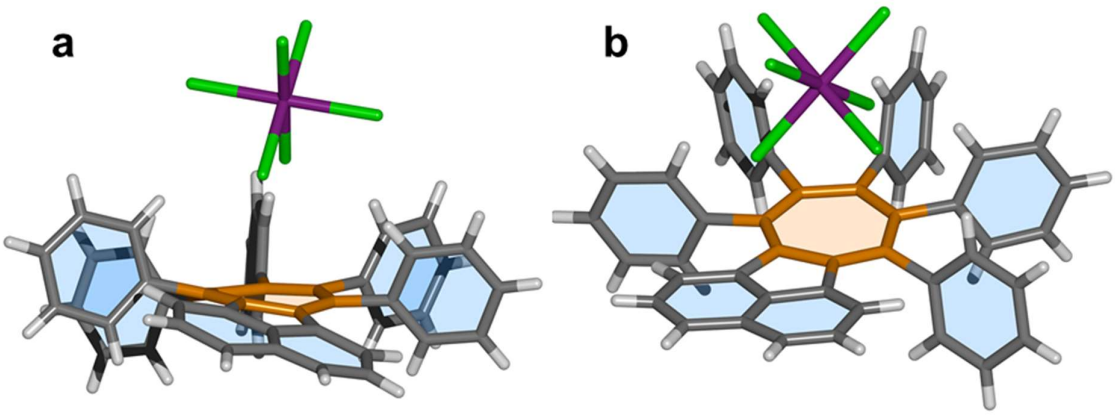

Figure 2.25. Solid-state structure of **2**·$SbCl_6$ (270 K) in its (**a**) twisted and (**b**) shallow boat conformations. $CHCl_3$ present in the unit cell is also omitted for clarity.

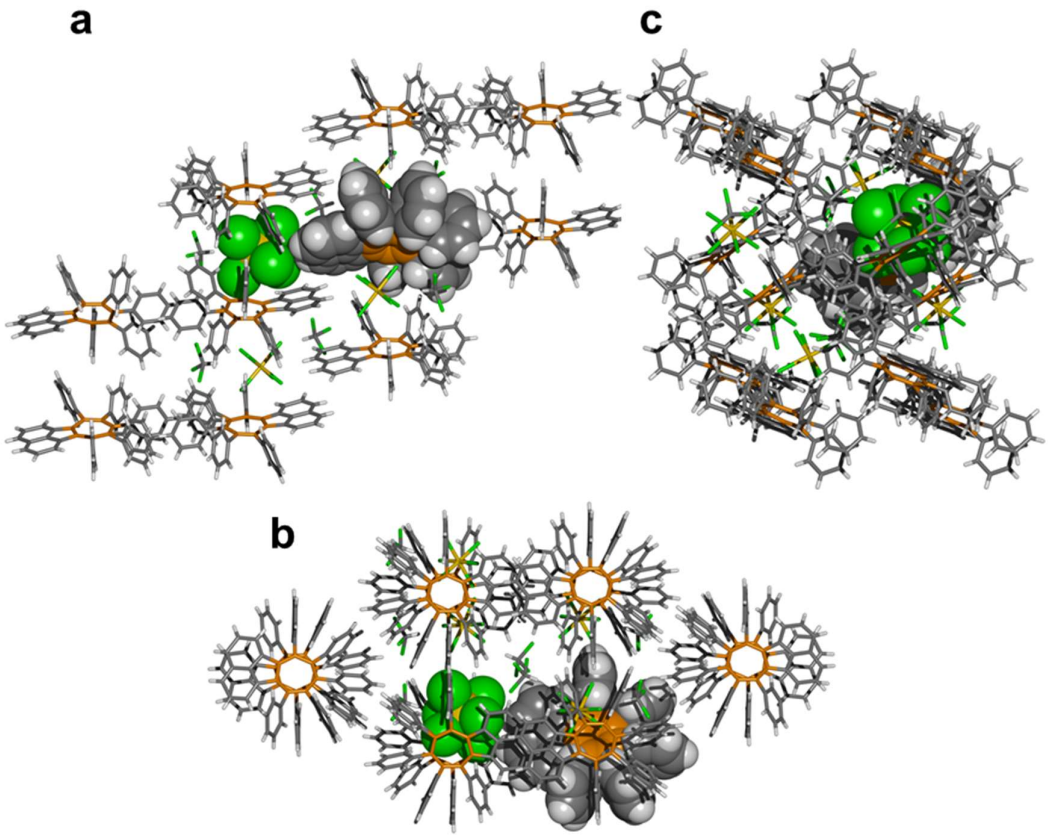

Figure 2.26. Solid-state superstructure of **2**·$SbCl_6$ (270 K)**.** A central molecule (space filling representation) is shown embedded in a section of the lattice made up of 2×2×2 unit cells in order to illustrate the crystal packing. Projections are viewed along the crystallographic (**a**) *a*-, (**b**) *b*-, and (**c**) *c*-axes.

Table 2.10. Crystal data and structure refinement for **2**·$SbCl_6$ (270 K).

2·$SbCl_6$	
CCDC Number	2173731
Empirical formula	$C_{47}H_{31} \times SbCl_6 \times CHCl_3$
Formula weight	1049.53
Temperature/K	270.00
Crystal system	triclinic
Space group	P-1
a/Å	11.953(4)
b/Å	17.868(5)
c/Å	24.504(7)
α/°	104.594(9)
β/°	103.956(9)
γ/°	90.055(10)
Volume/Å3	4905(2)
Z	4
ρcalcg/cm3	1.421
μ/mm 1	1.084
F(000)	2096.0
Crystal size/mm3	0.28 × 0.09 × 0.06
Radiation	Mo Kα (λ = 0.71073)
2Θ range for data collection/°	4.106 to 54.998
Index ranges	-15 ≤ h ≤ 15, -23 ≤ k ≤ 23, -31 ≤ l ≤ 31
Reflections collected	93109
Independent reflections	22495 [Rint = 0.1009, Rsigma = 0.1095]
Data/restraints/parameters	22495/274/1100
Goodness-of-fit on F2	1.064
Final R indexes [I>=2σ (I)]	R1 = 0.0998, wR2 = 0.2292
Final R indexes [all data]	R1 = 0.1612, wR2 = 0.2645
Largest diff. peak/hole / e Å-3	1.94/-0.91

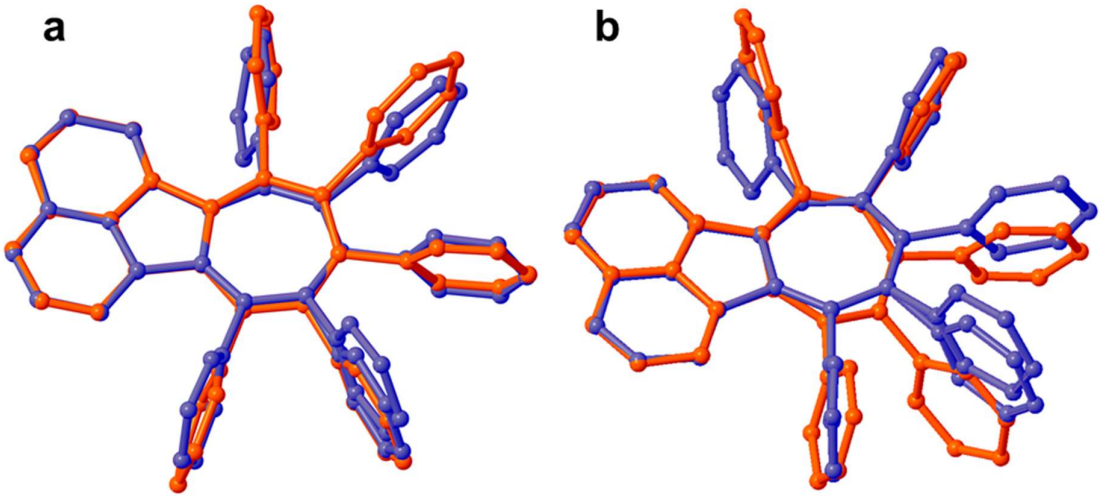

Figure 2.27. Overlays of the solid-state structures of **2**·$SbCl_6$ at 120 K (orange) and 270 K (blue). Panel (**a**) shows the twisted conformer and (**b**) shows the planar conformer.

Table 2.11. Comparison of key structural data for the twisted conformer of **2**·$SbCl_6$ at low temperatures (T = 120 K) and high temperatures (T = 270 K).

T / K	120	270
Φ_{bow} / °	6.7	2.7
Φ_{stern} / °	13.7	14.0
$\varphi(C_4\text{-}C_2\text{-}C_\beta\text{-}C_{\beta'})$ / °	18.4	17.6

2.4.4.10. 10

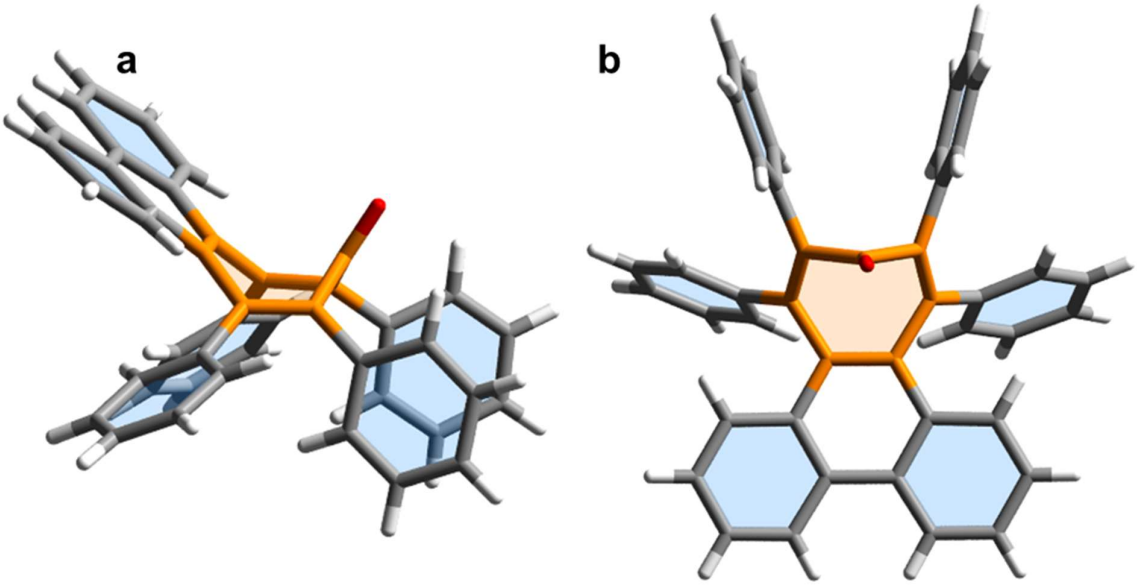

Figure 2.28. Solid-state structure of **10** viewed (**a**) side-on and (**b**) face-on to the tropone.

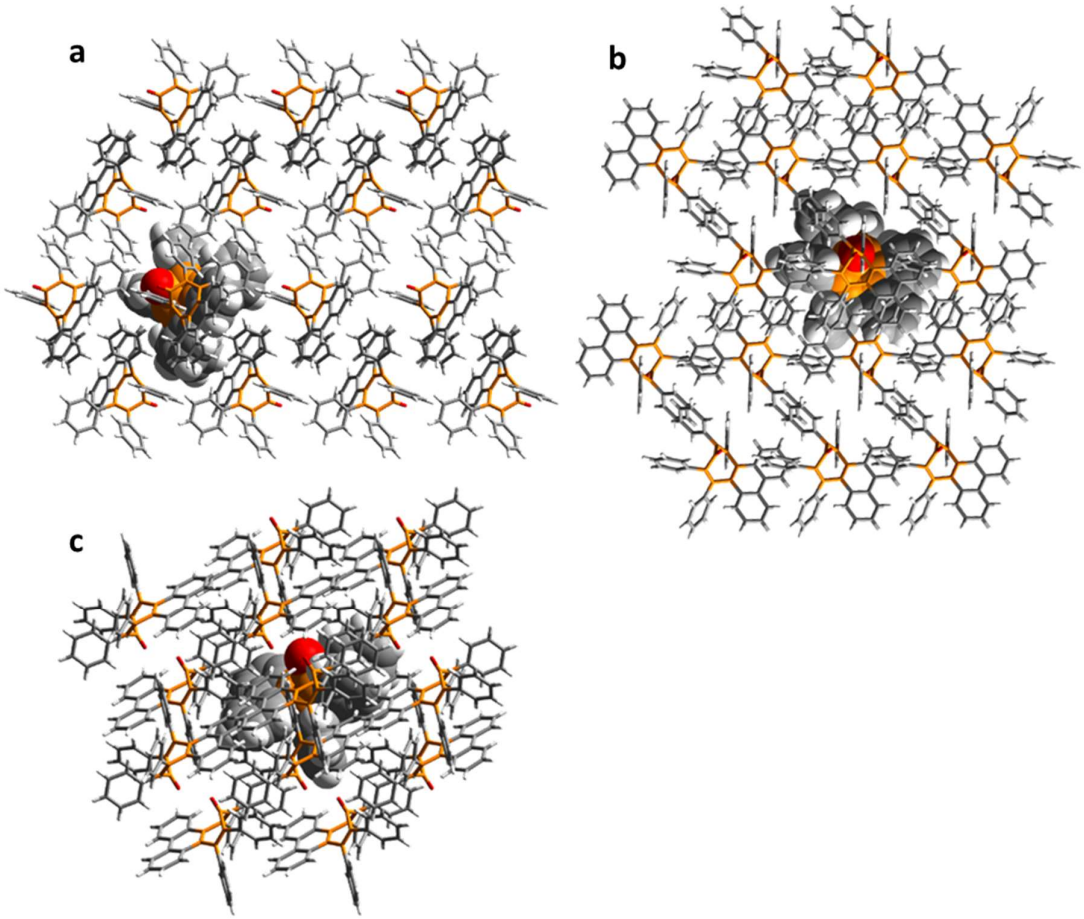

Figure 2.29. Solid-state superstructure of **10.** A central molecule (space filling representation) is shown embedded in a section of the lattice made up of 2×2×2 unit cells in order to illustrate the crystal packing. Projections are viewed along the crystallographic (**a**) *a*-, (**b**) *b*-, and (**c**) *c*-axes.

Table 2.12. Crystal data and structure refinement for **10**.

10	
CCDC Number	2141792
Empirical formula	$C_{43}H_{28}O$
Formula weight	560.65
Temperature/K	120.0
Crystal system	triclinic
Space group	P-1
a/Å	9.3113(6)
b/Å	10.5095(7)

c/Å	16.2093(10)
α/°	84.875(3)
β/°	80.864(3)
γ/°	75.921(3)
Volume/Å^3	1516.90(17)
Z	2
ρ_{calc}g/cm^3	1.227
μ/mm^{-1}	0.072
F(000)	588.0
Crystal size/mm^3	0.19 × 0.14 × 0.06
Radiation	MoKα (λ = 0.71073)
2Θ range for data collection/°	4.556 to 55.998
Index ranges	-12 ≤ h ≤ 12, -13 ≤ k ≤ 13, -21 ≤ l ≤ 21
Reflections collected	29340
Independent reflections	7327 [R_{int} = 0.0530, R_{sigma} = 0.0648]
Data/restraints/parameters	7327/0/397
Goodness-of-fit on F^2	1.034
Final R indexes [I>=2σ (I)]	R_1 = 0.0489, wR_2 = 0.1018
Final R indexes [all data]	R_1 = 0.0960, wR_2 = 0.1168
Largest diff. peak/hole / e Å^{-3}	0.24/-0.26

Crystals of **10** suitable for X-ray diffraction were grown by slow evaporation of a PhMe solution.

2.4.4.11. S3

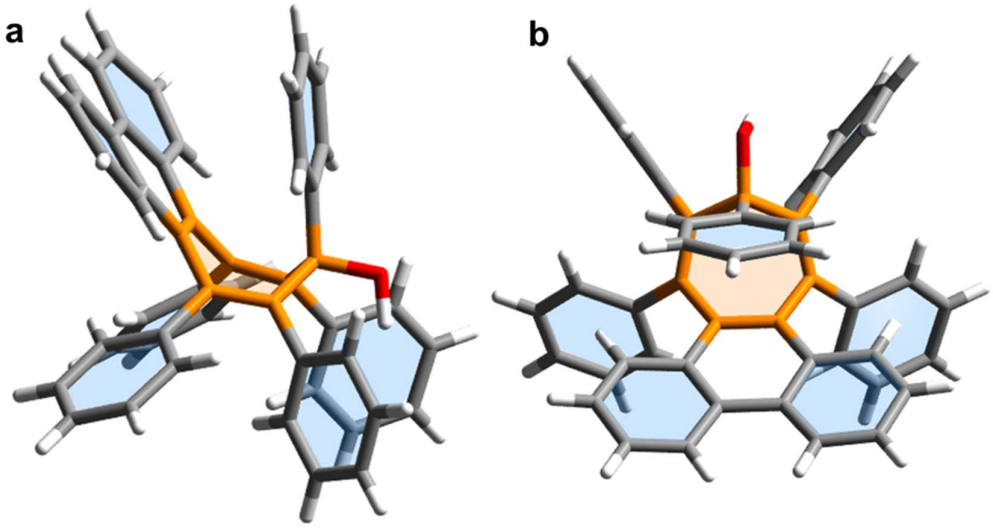

Figure 2.30. Solid-state structure of **S3** viewed (**a**) side-on and (**b**) face-on to the seven-membered ring.

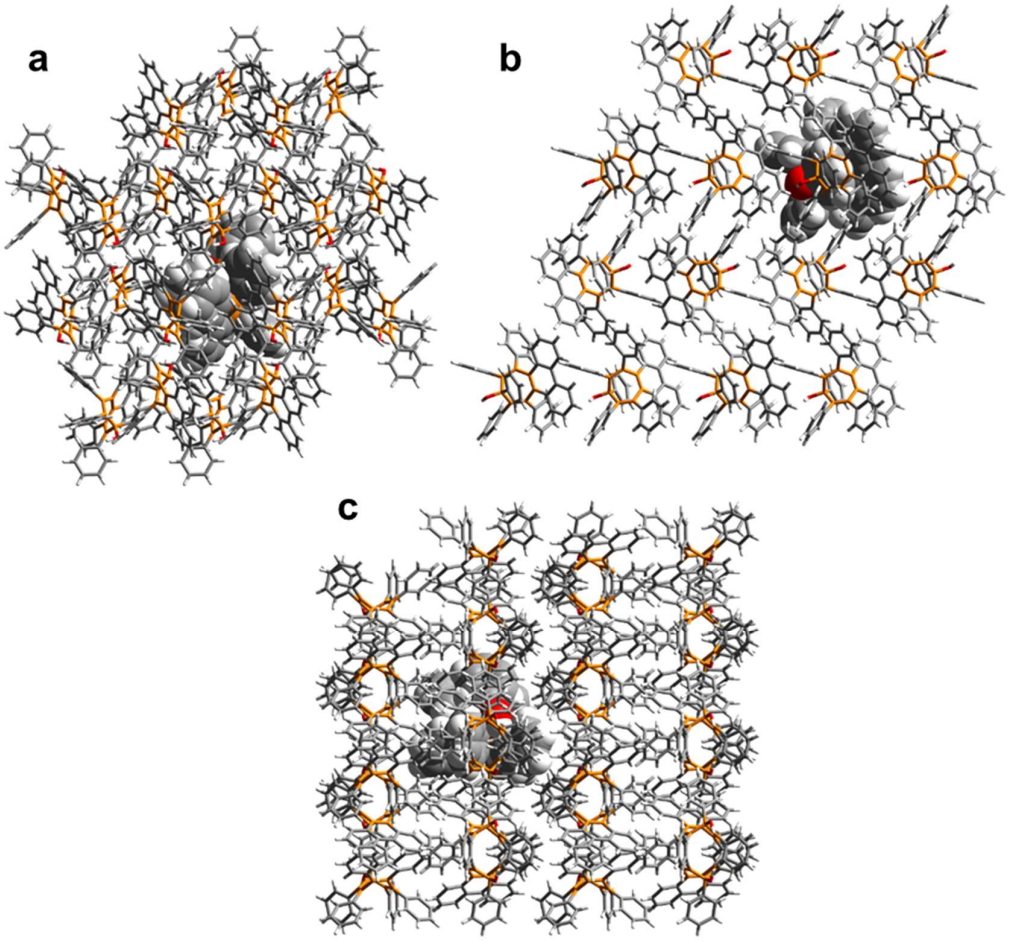

Figure 2.31. Solid-state superstructure of **S3.** A central molecule (space filling representation) is shown embedded in a section of the lattice made up of 2×2×2 unit cells in order to illustrate the crystal packing. Projections are viewed along the crystallographic (**a**) *a*-, (**b**) *b*-, and (**c**) *c*-axes.

Table 2.13. Crystal data and structure refinement for **S3**.

S3	
CCDC Number	2141794
Empirical formula	$C_{49}H_{34}O$
Formula weight	638.76
Temperature/K	120.0
Crystal system	monoclinic
Space group	$P2_1/c$
a/Å	20.8941(13)
b/Å	9.4305(4)
c/Å	18.9622(10)
α/°	90

β/°	115.035(7)
γ/°	90
Volume/Å^3	3385.3(4)
Z	4
ρ_{calc}g/cm^3	1.253
μ/mm^{-1}	0.073
F(000)	1344.0
Crystal size/mm^3	0.54 × 0.23 × 0.22
Radiation	MoKα (λ = 0.71073)
2Θ range for data collection/°	4.872 to 57.994
Index ranges	-28 ≤ h ≤ 25, -9 ≤ k ≤ 12, -25 ≤ l ≤ 25
Reflections collected	34168
Independent reflections	8981 [R_{int} = 0.0717, R_{sigma} = 0.0781]
Data/restraints/parameters	8981/0/455
Goodness-of-fit on F^2	1.056
Final R indexes [I>=2σ (I)]	R_1 = 0.0611, wR_2 = 0.1299
Final R indexes [all data]	R_1 = 0.1037, wR_2 = 0.1519
Largest diff. peak/hole / e Å^{-3}	0.40/-0.27

Crystals of **S3** suitable for X-ray diffraction were grown by slow evaporation of a mixture of CH_2Cl_2–Et_2O.

2.4.4.12. 4·$SbCl_6$

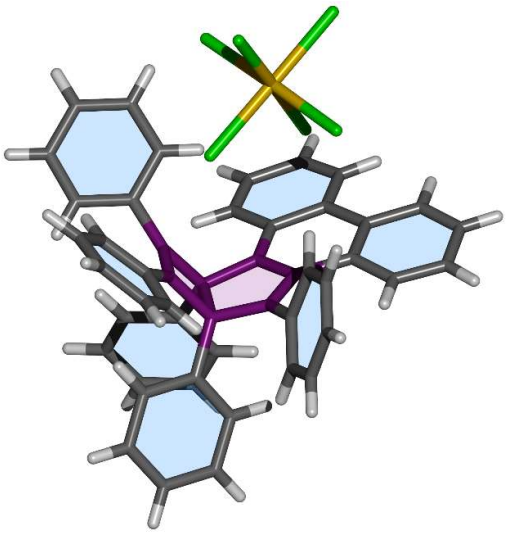

Figure 2.32. Solid-state structure of **4**·$SbCl_6$ viewed side-on to the Dewar tropylium. The $SbCl_6^-$ counterion is included but the CH_2Cl_2 solvent has been omitted for clarity.

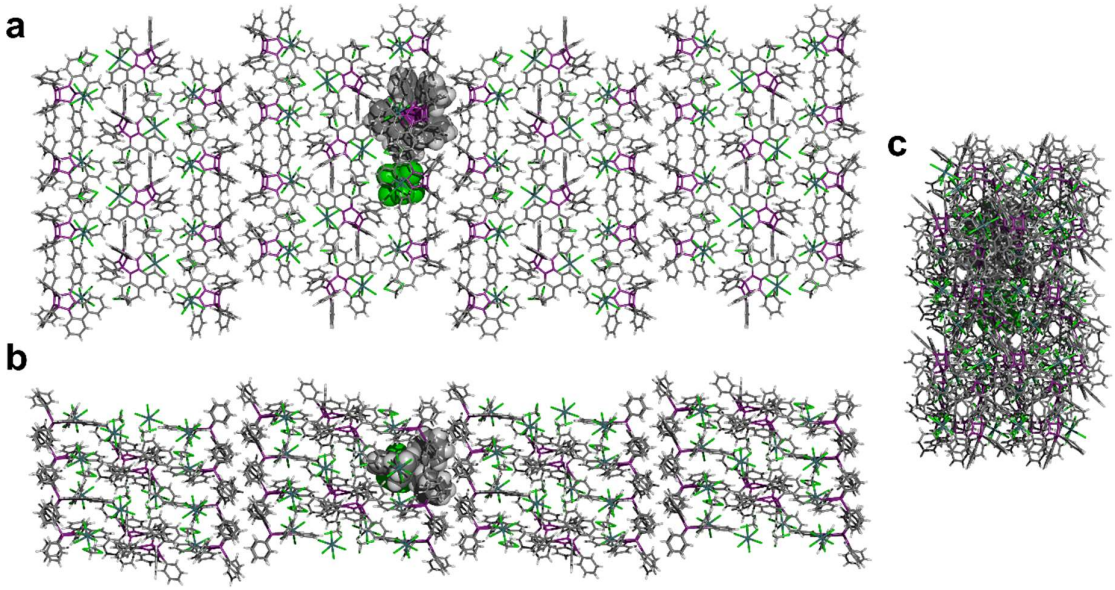

Figure 2.33. Solid-state superstructure of **4**·$SbCl_6$**.** A central molecule (space filling representation) is shown embedded in a section of the lattice made up of 2×2×2 unit cells in order to illustrate the crystal packing. Projections are viewed along the crystallographic (**a**) *a*-, (**b**) *b*-, and (**c**) *c*-axes.

Table 2.14. Crystal data and structure refinement for **4**·$SbCl_6$.

	4·$SbCl_6$
CCDC Number	2141789
Empirical formula	$C_{49}H_{33} \times SbCl_6 \times 0.67\ CH_2Cl_2$
Formula weight	1012.82
Temperature/K	120
Crystal system	monoclinic
Space group	$P2_1/n$
a/Å	11.0794(6)
b/Å	19.5994(11)
c/Å	59.837(3)
α/°	90
β/°	93.9088(15)
γ/°	90
Volume/Å^3	12963.3(12)
Z	12
ρ_{calc}g/cm^3	1.557
μ/mm^{-1}	1.128
F(000)	6096.0

Crystal size/mm^3	0.323 × 0.133 × 0.029
Radiation	MoKα (λ = 0.71073)
2Θ range for data collection/°	4.092 to 50.054
Index ranges	-13 ≤ h ≤ 13, -23 ≤ k ≤ 23, -71 ≤ l ≤ 71
Reflections collected	187925
Independent reflections	22893 [R_{int} = 0.0843, R_{sigma} = 0.0545]
Data/restraints/parameters	22893/1467/1566
Goodness-of-fit on F^2	1.197
Final R indexes [I>=2σ (I)]	R_1 = 0.0724, wR_2 = 0.1408
Final R indexes [all data]	R_1 = 0.0958, wR_2 = 0.1483
Largest diff. peak/hole / e Å^{-3}	1.21/-1.50

Crystals of **4**·$SbCl_6$ suitable for X-ray diffraction were grown by slow evaporation of a mixture of CH_2Cl_2–hexane.

2.4.4.13. *anti*-11

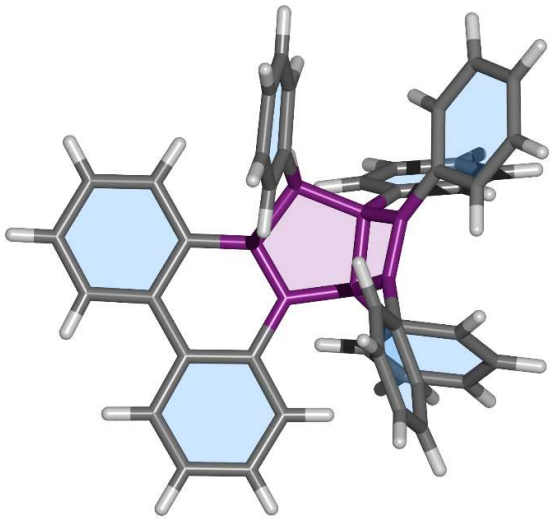

Figure 2.34. Solid-state structure of *anti*-**11** viewed face-on to the bicyclo[3.2.0]heptadiene.

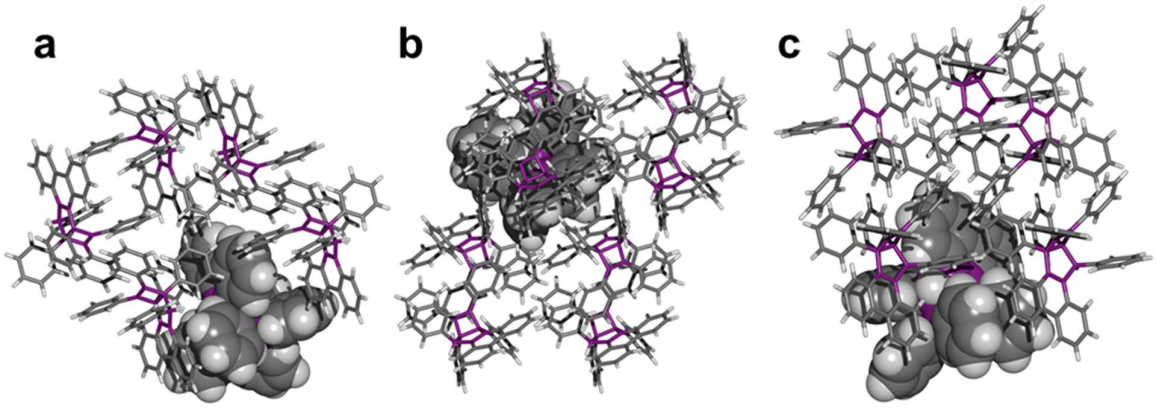

Figure 2.35. Solid-state superstructure of *anti*-**11**. A central molecule (space filling representation) is shown embedded in a section of the lattice made up of 2×2×2 unit cells in order to illustrate the crystal packing. Projections are viewed along the crystallographic (**a**) *a*-, (**b**) *b*-, and (**c**) *c*-axes.

Table 2.15. Crystal data and structure refinement for *anti*-**11**.

anti-**11**	
Identification code	2182241
Empirical formula	$C_{49}H_{34}$
Formula weight	622.76
Temperature/K	120.00
Crystal system	triclinic
Space group	P-1
a/Å	11.4217(3)
b/Å	12.4870(4)
c/Å	13.5958(4)
α/°	104.5864(11)
β/°	105.3593(12)
γ/°	110.6846(10)
Volume/Å^3	1615.99(8)
Z	2
ρ_{calc}g/cm^3	1.280
μ/mm^{-1}	0.072
F(000)	656.0
Crystal size/mm^3	0.11 × 0.07 × 0.01
Radiation	Mo Kα (λ = 0.71073)

2Θ range for data collection/°	3.774 to 55
Index ranges	$-14 \leq h \leq 14$, $-16 \leq k \leq 16$, $-17 \leq l \leq 17$
Reflections collected	41725
Independent reflections	7421 [R_{int} = 0.0745, R_{sigma} = 0.0585]
Data/restraints/parameters	7421/0/578
Goodness-of-fit on F^2	1.058
Final R indexes [I>=2σ (I)]	R_1 = 0.0650, wR_2 = 0.1239
Final R indexes [all data]	R_1 = 0.0950, wR_2 = 0.1354
Largest diff. peak/hole / e $Å^{-3}$	0.29/-0.32

Crystals of *anti*-**11** suitable for X-ray diffraction were grown by slow evaporation of a mixture of CH_2Cl_2–hexane.

2.5. *In Silico* Modelling

2.5.1. General Methods

DFT calculations were carried out in Gaussian 16.[69]The minimum energy ground state (GS) and transition state (TS) geometries of all cations were optimised using the B3LYP functional and the D3 version of Grimme's dispersion correction with Becke–Johnson damping (GD3BJ) was included. Calculations were performed using the 6-31G(d) basis set using the integral equation formalism variant (IEFPCM) to approximate CH_2Cl_2 as the solvent. The tropylium and Dewar tropylium isomers of compound **4** (**4-TP** and **4** respectively) were also studied using a number of other functionals/basis sets (see section 2.5.2), and aromatic stabilisation energies were also calculated using the M06-2X functional and 6-31G(d) basis set with the integral equation formalism variant (IEFPCM) to approximate CH_2Cl_2 as the solvent (see section 2.5.6).

Frequency calculations were carried out to confirm the lack of any negative vibrational frequencies for GS structures and to confirm their presence for TS structures (saddle points). Potential energy scans (PES) were carried out to predict the energetic penalty of twisting in **Naph**, fluoranthene, and **2**. Intrinsic reaction coordinate (IRC)

calculations were performed to confirm that TS geometries identified lie on a potential surface linking the tropylium (**TP**), Möbius tropylium (**MT**), and Dewar tropylium (**DT**) GS structures. Aromatic stabilisation energies (ASEs) were calculated using an isodesmic reaction, following the isomerisation stabilisation energy (ISE) method. The aromatic character of the **TP**-isomers of the cations synthesised in this work was assessed using nucleus-independent chemical shifts (NICS)[63], anisotropy of the induced current density (ACID) plots[60], and the electron density of the delocalised bonds (EDDB) index. DFT-optimised geometries were used for all aromaticity probes.

2.5.2. Basis Set and Functional Screen

We screened basis sets and functionals to find the combination that most accurately reproduces our experimental results, using the ~96:4 ratio of **DT**- and **TP**-derived products obtained in our hydride trapping experiment as the benchmark. The results are summarised below.

Table 2.16. Predicted free energy differences between the tropylium and Dewar tropylium isomers of compound **4** (**4-TP** and **4** respectively), using a range of functionals and basis sets. The IEFPCM was used to approximate CH_2Cl_2 as the solvent.

Functional[a]	Basis Set[b]	Isomer	*G* / Hartrees	ΔG / kJ·mol^{-1}	**4**:**4-TP** [b]
ωB97X-D	6-31G(d)	**4-TP**	-1885.692947	33.0	—
		4	-1885.705513		
	6-311G(d)	**4-TP**	-1886.036435	29.1	—
		4	-1886.047512		
	6-311G(d,p)	**4-TP**	-1886.090614	29.5	—
		4	-1886.101846		
M06-2X	6-31G(d)	**4-TP**	-1885.527902	21.0	99.98:0.02
		4	-1885.5359		
	6-311G(d)	**4-TP**	-1885.925552	14.6	99.7:0.03
		4	-1885.931109		
	6-311G(d,p)	**4-TP**	-1885.970401	15.1	99.8:0.02
		4	-1885.976134		
CAM-B3LYP	6-31G(d)	**4-TP**	-1885.186164	23.3	99.99:0.01
		4	-1885.19504		
	6-311G(d)	**4-TP**	-1885.564101	16.4	99.9:0.01

B3LYP (GD3BJ)	6-311G(d,p)	**4**	-1885.570339	17.2	99.9:0.01
		4-TP	-1885.619595		
		4	-1885.62614		
	6-31G(d)	**4-TP**	-1886.558425	5.31	90:10
		4	-1886.560446		
	6-311G(d)	**4-TP**	-1886.928045	–1.25	38:62
		4	-1886.927568		
	6-311G(d,p)	**4-TP**	-1886.985344	–1.24	38:62
		4	-1886.98487		

[a] Our choice of B3LYP was guided by previous computational studies that assessed the aromaticity and physical behaviour of similar structures (see, for example, references 21, 23, 27, 29, 37, 42, and 51). However, as discussed in section 2.5.6, this functional is known to overestimate ASEs, so we included a dispersion correction (GD3BJ) and compared our results with functionals that take long-range interactions into account. [b] Due to the structural complexity these molecules, we were limited to small Pople basis sets. [c] As predicted by the Boltzmann distribution of isomers. For details, see section 2.5.10.

The B3LYP functional with a GD3BJ empirical dispersion correction and 6-31G(d) basis set using CH_2Cl_2 as the solvent gave the closest isomeric distribution.

2.5.3. Intrinsic Reaction Coordinate (IRC) Calculations

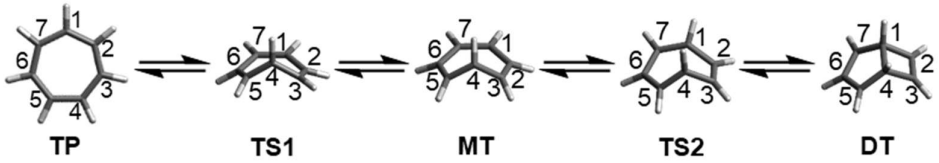

Figure 2.36. Rearrangement of **TP**-$(CH)_7^+$ to the **DT** isomer *via* the **MT** intermediate.

Table 2.17. Relative energies (G_{rel} / kJ·mol^{-1}), d(C_1–C_4) / Å (internuclear distance between C_1 and C_4), and H_4–C_4–C_5–H_5 dihedral angles (Φ / °) of the key structures in the isomerism of **TP**-$(CH)_7^+$.

Structure	d(C_1–C_4) / Å	Φ / °	G_{rel} / kJ·mol^{-1} [a]
TP	3.14	0.00	0
TS1	2.65	113	302
MT	2.55	152	249
TS2	2.07	119	289
DT	1.55	52.8	219

[a] G_{rel} refers to the energy of each species relative to the energy of **TP-$C_7H_7^+$** (the lowest-energy structure).

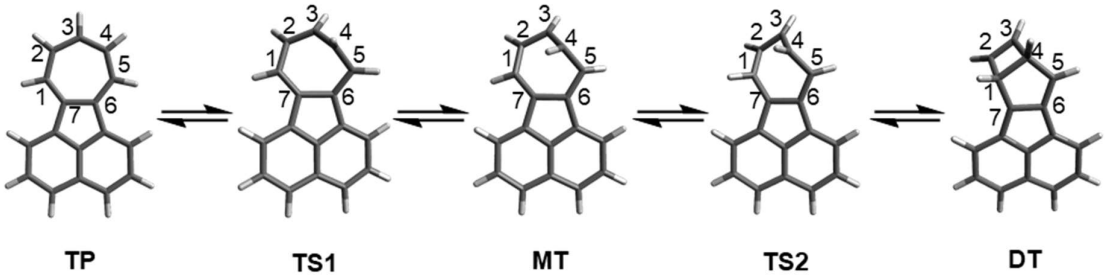

Figure 2.37. Rearrangement of the **TP** isomer of acenaphthyltropylium (**Naph**) to the **DT** isomer *via* the **MT** intermediate.

Table 2.18. Relative energies (G_{rel} / kJ·mol^{-1}), d(C_1–C_4) / Å (internuclear distance between C_1 and C_4), and H_4–C_4–C_5–H_5 dihedral angles (Φ / °) of the key structures in the isomerism of **TP-Naph.**

Structure	d(C_1–C_4) / Å	Φ / °	G_{rel} / kJ·mol^{-1} [a]
TP	3.15	0.00	0
TS1	2.80	64.4	311
MT	2.58	153	259
TS2	2.10	117	316
DT	1.57	53.9	220

[a] G_{rel} refers to the energy of each species relative to the energy of **TP-$C_7H_7^+$** (the lowest-energy structure).

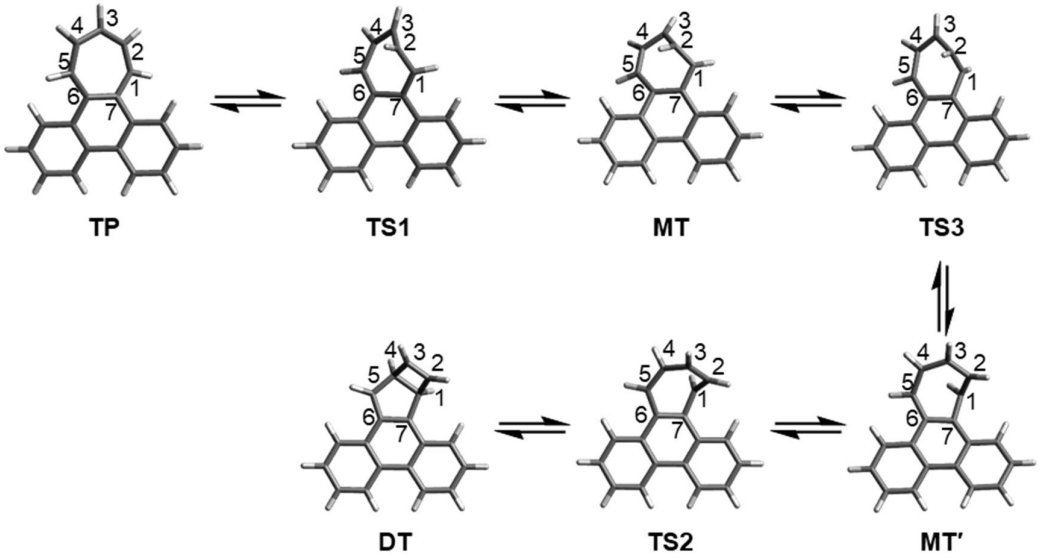

Figure 2.38. Rearrangement of the **TP** isomer of phenanthrenyltropylium (**Phen**) to the **DT** isomer *via* the **MT** intermediate.

Table 2.19. Relative energies (G_{rel} /·kJ mol^{-1}), d(C$_1$–C$_4$) / Å (internuclear distance between C$_1$ and C$_4$), and H$_4$–C$_4$–C$_5$–H$_5$ dihedral angles (Φ / °) of the key structures in the isomerism of **TP-Phen.**

Structure	d(C$_1$–C$_4$) / Å	Φ / °	G_{rel} / kJ·mol^{-1} [a]
TP	3.08	0.827	0
TS1	2.83	116	297
MT	3.03	165	232
TS3	2.77	175	261
MT′	2.54	156	209
TS2	2.11	107	250
DT	1.56	61.4	143

[a] G_{rel} refers to the energy of each species relative to the energy of **TP-Phen** (the lowest-energy structure).

2.5.4. Potential Energy Surface (PES) Scan

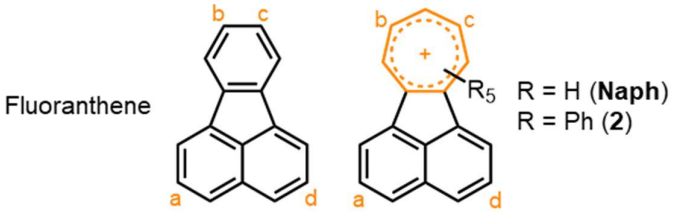

Figure 2.39. Atom numbering for the torsional angle twisting θ(a–b–c–d) in fluoranthene, **Naph** (R=H), and **2** (R = Ph).

Table 2.20. PES scan of deforming naphthalene-annulated aromatic rings. The relative energy (E_{rel}) (compared to the lowest energy, planar conformer) is shown as a function of the torsional angle θ(a–b–c–d), which defines the end-to-end twist of the molecule.

	Fluoranthene	**Naph**	**2**
θ(a–b–c–d)		**E_{rel} / kJ·mol^{-1}**	
-25	38.33	27.99	5.48
-24	34.92	25.50	4.54
-23	31.72	23.16	3.73
-22	28.72	20.94	3.02
-21	25.91	18.85	2.41
-20	23.29	16.91	1.88
-19	20.84	15.10	1.41
-18	18.55	13.41	1.03

-17	16.42	11.84	0.73
-16	14.45	10.39	0.50
-15	12.62	9.05	0.32
-14	10.92	7.81	0.19
-13	9.36	6.69	1.01
-12	7.93	5.65	1.25
-11	6.63	4.71	1.12
-10	5.45	3.87	0.96
-9	4.39	3.11	0.83
-8	3.45	2.45	0.74
-7	2.62	1.87	0.65
-6	1.92	1.38	0.53
-5	1.32	0.96	0.41
-4	0.84	0.62	0.31
-3	0.47	0.35	0.21
-2	0.21	0.15	0.12
-1	0.05	0.04	0.05
0	0.00	0.00	0.00
1	0.05	0.04	0.05
2	0.21	0.15	0.12
3	0.47	0.35	0.21
4	0.84	0.62	0.31
5	1.32	0.96	0.41
6	1.92	1.38	0.53
7	2.62	1.87	0.65
8	3.45	2.45	0.74
9	4.39	3.11	0.83
10	5.45	3.87	0.96
11	6.63	4.71	1.12
12	7.93	5.65	1.25
13	9.36	6.69	1.01
14	10.92	7.81	0.19
15	12.62	9.05	0.32
16	14.45	10.39	0.50
17	16.42	11.84	0.73
18	18.55	13.41	1.03
19	20.84	15.10	1.41
20	23.29	16.91	1.88
21	25.91	18.85	2.41
22	28.72	20.94	3.02

23	31.72	23.16	3.73
24	34.92	25.50	4.54
25	38.33	27.99	5.48

2.5.5. Relative Stabilities of Tropylium Isomers

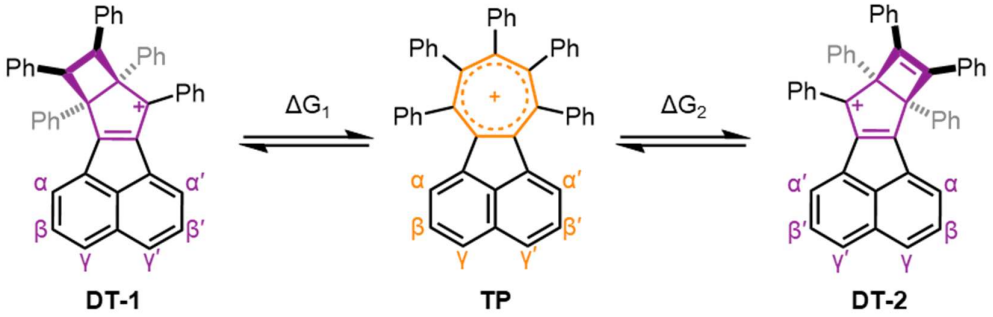

Figure 2.40. Two possible isomers of asymmetrically substituted Dewar tropyliums (**DT-1** and **DT-2**) that form upon the rearrangement of the tropylium (**TP**) isomer.

Table 2.21. Calculated (B3LYP (GD3BJ) / 6-31G(d) – CH_2Cl_2) free energy differences of the **DT** isomers ($\Delta G_{1,2}$) relative to the **TP** isomer in a series of substituted analogues of **2**. The numbering pattern is outlined in **Figure 2.40.** The number in bold denotes the lower energy **DT** isomer.

Compound	ΔG_1 / kJ·mol^{-1}	ΔG_2 / kJ·mol^{-1}	Predicted Isomer
Naph	219.5	—	**TP**
$(CH)_7^+$	218.6	—	**TP**
Phen	142.7	—	**TP**
β-NO_2	**79.9**	80.0	**TP**
β-Cl	78.9	**78.8**	**TP**
2	75.4	—	**TP**
β-Me	77.7	**74.7**	**TP**
β-OMe	**74.0**	75.5	**TP**
β-F	**72.9**	74.7	**TP**
γ-Cl	74.3	**72.5**	**TP**
γ-F	79.0	**70.9**	**TP**
γ-NO_2	**70.3**	81.3	**TP**
γ-OMe	83.9	**65.8**	**TP**
α-F	64.5	**62.3**	**TP**
α-NO_2	**59.2**	64.8	**TP**
α-NMe_2	**56.3**	64.5	**TP**
α-Cl	54.5	**54.4**	**TP**
α-^{t}Bu	**51.0**	53.9	**TP**

α-OMe	61.7	**48.9**	**TP**
α,β′-Me_2	51.6	**46.9**	**TP**
α-Me	51.8	**45.8**	**TP**
α,β-Me_2	52.8	**44.8**	**TP**
α,α′-Me_2	41.9	—	**TP**
α-Et	50.6	**41.8**	**TP**
α-^{i}Pr	53.7	**41.8**	**TP**
β,β′-Me_2	40.7	—	**TP**
α,α′-$(OMe)_2$	30.4	—	**TP**
α,α′-Cl_2	30.0	—	**TP**
1	26.1	—	**TP**
3	15.4	—	**TP**
α,α′-$^i Pr_2$	8.4	—	**TP**
4	–5.3	—	**DT**

2.5.6. Aromatic Stabilisation Energy (ASE) Calculations

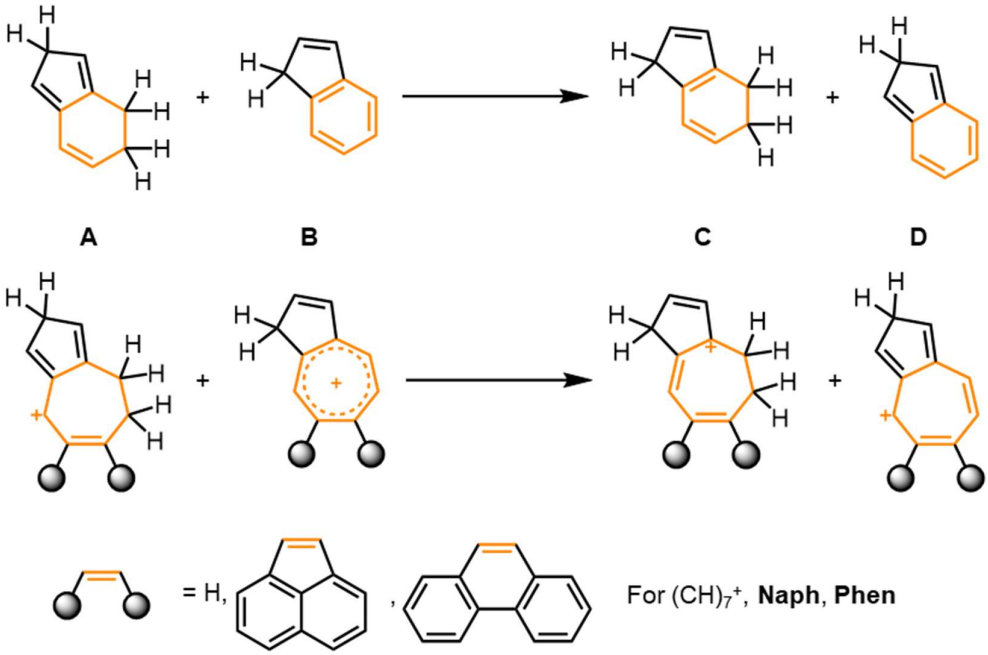

Figure 2.41. Hyperhomodesmotic reactions used to predict the ASEs of $(CH)_6$, $(CH)_7^+$, **Naph**, and **Phen**.

Aromatic stabilisation energies (ASEs) of the parent cations of the compounds studied in this work were calculated using the indene–isoindene isomerisation stabilisation energy following a hyperhomodesmotic reaction,[51] as shown above. DFT-optimised

geometries were used for the calculation, and frequency calculations were performed to obtain the enthalpy change (ΔH) of the reaction, determined as:

$$\Delta H = [H(C) + H(D)] - [H(A) + H(B)]$$

The enthalpies of structures **A**–**D** for $(CH)_7^+$, **Naph**, and **Phen** are given in below.

Table 2.22. Calculated (B3LYP / 6-31G(d) GD3BJ – CH_2Cl_2) enthalpies (*H*) of the reagents and products in the hyperhomodesmotic reaction used to calculated aromatic stabilisation energies (ASEs) of $(CH)_6$, $(CH)_7^+$, **Naph**, and **Phen**.

Structure	*H* / Hartree	Σ(*H*) / kJ·mol^{-1}	ASE / kJ·mol^{-1}
$(CH)_6$-A	-348.802168	-1828533.043	–98.5
$(CH)_6$-B	-347.649191		
$(CH)_6$-C	-348.799555	-1828434.513	
$(CH)_6$-D	-347.614276		
$(CH)_7^+$-A	-387.297591	-2030682.617	–50.3
$(CH)_7^+$-B	-386.148464		
$(CH)_7^+$-C	-387.314453	-2030632.276	
$(CH)_7^+$-D	-386.112428		
Naph-A	-770.751992	-4044185.412	–55.1
Naph-B	-769.59667		
Naph-C	-770.762603	-4044130.266	
Naph-D	-769.565055		
Phen-A	-848.147453	-4450572.86	–50.7
Phen-B	-846.985992		
Phen-C	-848.162064	-4450522.196	
Phen-D	-846.952084		

Table 2.23. Calculated (M06-2X / 6-31G(d) – CH_2Cl_2) enthalpies (*H*) of the reagents and products in the hyperhomodesmotic reaction used to calculated aromatic stabilisation energies (ASEs) of $(CH)_6$, $(CH)_7^+$, **Naph**, and **Phen**.

Structure	*H* / Hartree	Σ(*H*) / kJ·mol^{-1}	ASE / kJ·mol^{-1}
$(CH)_6$-A	-348.60346	-1827510.571	–104
$(CH)_6$-B	-347.45846		
$(CH)_6$-C	-348.601043		
$(CH)_6$-D	-347.421181	-1827406.349	
$(CH)_7^+$-A	-387.06396	-2029473.362	–56.0
$(CH)_7^+$-B	-385.921514		
$(CH)_7^+$-C	-387.080672	-2029417.323	

$(CH)_7^+$-D	-385.883458		
Naph-A	-770.324038	-4041955.467	–61.2
Naph-B	-769.175283		
Naph-C	-770.334106	-4041894.249	
Naph-D	-769.141898		
Phen-A	-847.675849	-4448113.651	–54.4
Phen-B	-846.520933		
Phen-C	-847.690569	-4448059.269	
Phen-D	-846.4855		

2.5.7. Nucleus-Independent Chemical Shift (NICS) Values

NICS values were calculated 1 Å above and below the average plane generated by the seven C atoms forming the tropylium carbocycle using the Multiwfn software package.[70] Only the magnetic field in the *z*-direction (perpendicular to the plane of the studied ring) was considered. This corresponds to the *zz*-component of the magnetic shielding tensor (σ_{zz}).[61,62]

2.5.8. Anisotropy of the Induced Current Density (ACID) Plots

ACID plots were generated using version ACID-3.0.4. The magnetic field in the ACID plots was applied perpendicular to the plane of the tropylium and induced a clockwise, aromatic ring current in the conjugated system. An isovalue of 0.01 was used for all calculations. The molecular orbitals (determined from frequency calculations) used to visualise the plots are given below:

1: 150, 149, 146, 127, 102
2: 155, 154, 152 – 148, 144–142, 135, 131, 130, 123, 109, 98
3: 171 – 168, 166, 164–163, 160–157, 138, 128, 106, 105
4-TP: 162–160, 152–148, 131–129, 125, 124, 103

2.5.9. Electron Density of the Delocalised Bonds (EDDB^k)

EDDB^k calculations were run using the runEDDB program and MRAN 4.0.2. Population analysis was conducted using NBO v. 3.1. EDDB$_P^k$ plots of $(CH)_7^+$, **Naph**,

and **Phen**, **1**–**3** and **4-TP** were used to assess the local aromaticity of the tropylium ring, as well as the global aromaticity of the larger polycyclic aromatic scaffold. The 'limit for uniformly delocalised electrons' output value was used for $EDDB_P^k$ analysis.

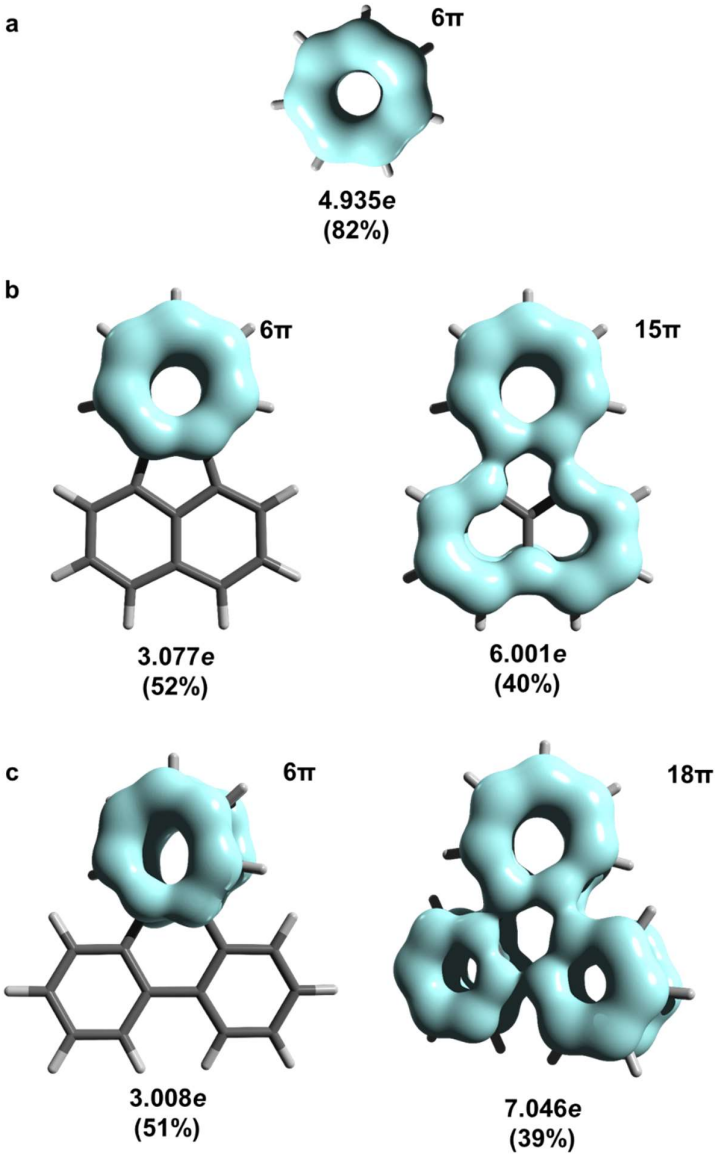

Figure 2.42. π-$EDDB_P^k$ plots and values of (a) $(CH)_7^+$, (b) **Naph**, and (c) **Phen**, showing delocalisation pathways around the tropylium moiety (left) and the peripheral circuit (right). The effectiveness of delocalisation (value in parentheses) was determined assuming the formal number of π-electrons in each structure. Isovalue = 0.008.

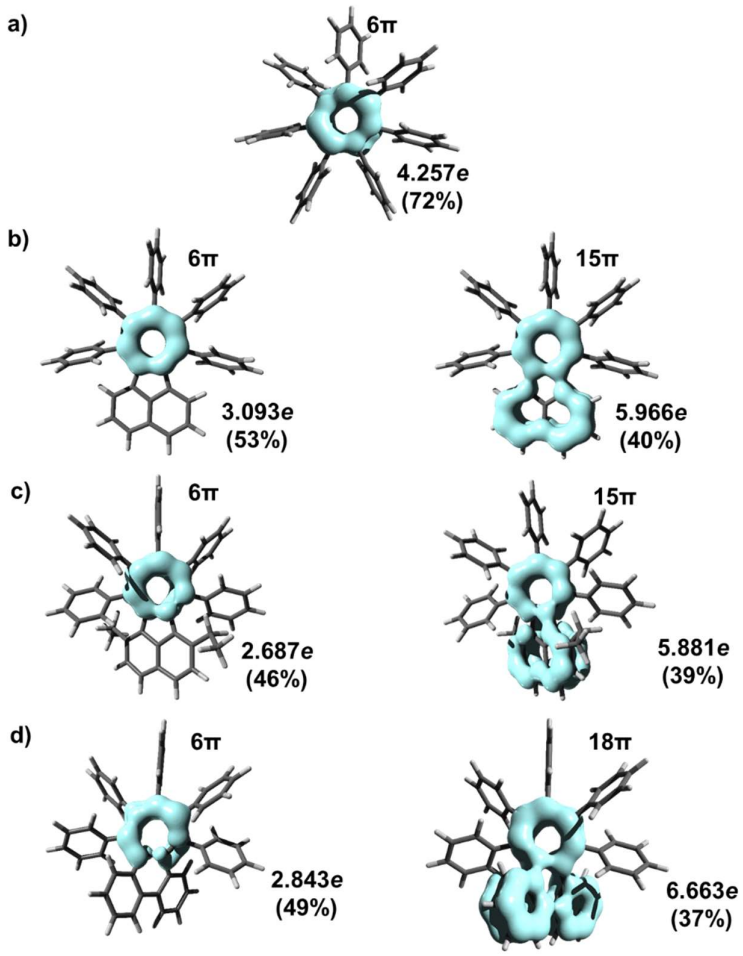

Figure 2.43. ***π*-EDDB$_P^k$** plots and values of (a) **1**, (b) **2**, (c) **3**, and (d) **4-TP**, showing delocalisation pathways around the tropylium moiety (left) and the peripheral circuit (right). The effectiveness of delocalisation (value in parentheses) was determined assuming the formal number of π-electrons in each structure. Isovalue = 0.008.

2.5.10. Boltzmann Distribution of 4/4-TP

Using the ΔG of −5.3 kJ·mol^{-1} calculated for compound **4**, we calculated the probability of the higher energy tropylium state (**4-TP**) being populated. We applied the following equation to determine the Boltzmann distribution:

$$P_i = \frac{g_i e^{-\frac{\varepsilon_i}{kT}}}{\sum_i g_i e^{-\frac{\varepsilon_i}{kT}}}$$

where P_i is the probability of a state i, g_i is the degeneracy of a state i, ε_i is the energy of the state i relative to the lowest energy isomer (**4**), k is the Boltzmann constant (0.695 cm^{-1}·K^{-1}), and T is the temperature.

Two degenerate forms (i.e., $g_i = 2$) of the Dewar tropylium structure (**4** and **4′**) and two degenerate forms (*P* and *M* helical twist enantiomers) of **4-TP** are present at equilibrium.

The full set of parameters and the resulting probabilities are shown in Table 2.24 for **4**/**4-TP**.

Table 2.24. Probabilities of **4** and **4-TP** being occupied at rt.

	i	g_i	ε_i / J·mol^{-1}	ε_i / cm^{-1}	T / K	$g_i e^{-\frac{\varepsilon_i}{kT}}$	P_i
4	0	2	0	0	298	2	0.90
4-TP	1	2	5310	444	298	0.23	0.10

2.6. References

1 H. E. Armstrong, *Proc. Chem. Soc. London*, 1890, **6**, 101–105.

2 E. Hückel, *Zeitschrift für Phys.*, 1931, **70**, 204–286.

3 K. B. Wiberg, *Chem. Rev.*, 2001, **101**, 1317–1331.

4 P. von Ragué Schleyer and H. Jiao, *Pure Appl. Chem.*, 1996, **68**, 209–218.

5 U. Fleischer, V. Mühlenkamp, W. Kutzelnigg and P. Lazzeretti, *J. Am. Chem. Soc.*, 1994, **116**, 5298–5306.

6 R. Gershoni-Poranne and A. Stanger, *Chem. Soc. Rev.*, 2015, **44**, 6597–6615.

7 P. von Ragué Schleyer, H. Jiao, B. Goldfuss and P. K. Freeman, *Angew. Chem. Int. Ed. Engl.*, 1995, **34**, 337–340.

8 U. D. Priyakumar, T. C. Dinadayalane and G. N. Sastry, *New J. Chem.*, 2002, **26**, 347–353.

9 P. J. Harman, J. E. Kent, M. F. O'Dwyer and D. W. T. Griffith, *J. Phys. Chem.*, 1981, **85**, 2731–2733.

10 W. von E. Doering and L. H. Knox, *J. Am. Chem. Soc.*, 1954, **76**, 3203–3206.

11 D. J. M. Lyons, R. D. Crocker, M. Blümel and T. V. Nguyen, *Angew. Chem. Int. Ed.*, 2017, **56**, 1466–1484.

12 D. J. M. Lyons, R. D. Crocker and T. V. Nguyen, *Chem.—Eur. J.*, 2018, **24**, 10959–10965.

13 A. Tamoto, N. Aratani and H. Yamada, *Chem.—Eur. J.*, 2017, **23**, 16388–16392.

14 Y. Sasaki, M. Takase, T. Okujima, S. Mori and H. Uno, *Org. Lett.*, 2019, **21**, 1900–1903.

15 C. Zhu, K. Shoyama and F. Würthner, *Angew. Chem. Int. Ed.*, 2020, **59**, 21505–21509.

16 M. Tamm, B. Dreßel and R. Fröhlich, *J. Org. Chem.*, 2000, **65**, 6795–6797.

17 S. Brydges, J. F. Britten, L. C. F. Chao, H. K. Gupta, M. J. McGlinchey and D. L. Pole, *Chem.—Eur. J.*, 1998, **4**, 1201–1205.

18 Chaolumen, I. A. Stepek, K. E. Yamada, H. Ito and K. Itami, *Angew. Chem. Int. Ed.*, 2021, **60**, 23508–23532.

19 G. Portella, J. Poater, J. M. Bofill, P. Alemany and M. Solà, *J. Org. Chem.*, 2005, **70**, 2509–2521.

20 Y. Xiao, J. T. Mague, R. H. Schmehl, F. M. Haque and R. A. Pascal, *Angew. Chem. Int. Ed.*, 2019, **58**, 2831–2833.

21 J. Ma, Y. Fu, E. Dmitrieva, F. Liu, H. Komber, F. Hennersdorf, A. A. Popov, J. J. Weigand, J. Liu and X. Feng, *Angew. Chem. Int. Ed.*, 2020, **59**, 5637–5642.

22 D. Ajami, O. Oeckler, A. Simon and R. Herges, *Nature*, 2003, **426**, 819–821.

23 G. Naulet, L. Sturm, A. Robert, P. Dechambenoit, F. Röhricht, R. Herges, H. Bock and F. Durola, *Chem. Sci.*, 2018, **9**, 8930–8936.

24 M. Rickhaus, M. Jirasek, L. Tejerina, H. Gotfredsen, M. D. Peeks, R. Haver, H. W. Jiang, T. D. W. Claridge and H. L. Anderson, *Nature Chem. 2020 123*, 2020, **12**, 236–241.

25 E. J. Leonhardt and R. Jasti, *Nature Rev. Chem.*, 2019, **3**, 672–686.

26 M. Jirásek, M. Rickhaus, L. Tejerina and H. L. Anderson, *J. Am. Chem. Soc.*, 2021, **143**, 2403–2412.

27 G. Povie, Y. Segawa, T. Nishihara, Y. Miyauchi and K. Itami, *Science*, 2017, **356**, 172–175.

28 K. Y. Cheung, K. Watanabe, Y. Segawa and K. Itami, *Nature Chem.*, 2021, **13**, 255–259.

29 J. Luo, X. Xu, R. Mao and Q. Miao, *J. Am. Chem. Soc.*, 2012, **134**, 13796–13803.

30 I. R. Márquez, N. Fuentes, C. M. Cruz, V. Puente-Muñoz, L. Sotorrios, M. L. Marcos, D. Choquesillo-Lazarte, B. Biel, L. Crovetto, E. Gómez-Bengoa, M. T. González, R. Martin, J. M. Cuerva and A. G. Campaña, *Chem. Sci.*, 2017, **8**, 1068–1074.

31 K. K. Baldridge and J. S. Siegel, *J. Am. Chem. Soc.*, 1992, **114**, 9583–9587.

32 A. Stanger, *Chem. Commun.*, 2009, 1939–1947.

33 S. Shaik, A. Shurki, D. Danovich and P. C. Hiberty, *Chem. Rev.*, 2001, **101**, 1501–1539.

34 L. W. Jenneskens, F. J. J. De Kanter, P. A. Kraakman, L. A. M. Turkenburg, W. E. Koolhaas, W. H. De Wolf, F. Bickelhaupt, Y. Tobe, K. Kakiuchi and Y. Odaira, *J. Am. Chem. Soc.*, 1985, **107**, 3716–3717.

35 L. W. Jenneskens, R. W. A. Havenith, A. Soncini and P. W. Fowler, *Phys. Chem. Chem. Phys.*, 2011, **13**, 16861–16866.

36 G. B. M. Kostermans, M. Bobeldijk and W. H. De Wolf, *J. Am. Chem. Soc.*, 1987, **109**, 2471–2475.

37 M. Okuyama and T. Tsuji, *Angew. Chem. Int. Ed. Engl.*, 1997, **36**, 1085–1087.

38 M. Okuyama, M. Ohkita and T. Tsuji, *Chem. Commun.*, 1997, 1277–1278.

39 C. J. Kingsbury and M. O. Senge, *Coord. Chem. Rev.*, 2021, **431**, 213760.

40 E. E. van Tamelen, T. M. Cole, R. Greeley and H. Schumacher, *J. Am. Chem. Soc.*, 1968, **90**, 1372–1374.

41 M. W. D. Hanson-Heine, D. M. Rogers, S. Woodward and J. D. Hirst, *J. Phys. Chem. Lett.*, 2020, **11**, 3769–3772.

42 M. Dračínský, O. Castaño, M. Kotora and P. Bouř, *J. Org. Chem.*, 2010, **75**, 576–581.

43 Š. Janková, M. Dračínský, I. Císařová and M. Kotora, *Eur. J. Org. Chem.*, 2008, 47–51.

44 R. P. Johnson and K. J. Daoust, *J. Am. Chem. Soc.*, 1996, **118**, 7381–7385.

45 A. D. Becke, *J. Chem. Phys.*, 1993, **98**, 1372–1377.

46 H. Schröder, A. Creon and T. Schwabe, *J. Chem. Theory Comput.*, 2015, **11**, 3163–3170.

47 R. Krishnan, J. S. Binkley, R. Seeger and J. A. Pople, *J. Chem. Phys.*, 1980, **72**, 650–654.

48 S. Miertuš and J. Tomasi, *Chem. Phys.*, 1982, **65**, 239–245.

49 K. Fukui, *Acc. Chem. Res.*, 1981, **14**, 363–368.

50 S. E. Wheeler, K. N. Houk, P. von Ragué Schleyer and W. D. Allen, *J. Am. Chem. Soc.*, 2009, **131**, 2547–2560.

51 C. S. Wannere, D. Moran, N. L. Allinger, B. A. Hess, L. J. Schaad and P. von Ragué Schleyer, *Org. Lett.*, 2003, **5**, 2983–2986.

52 I. Casademont-Reig, T. Woller, J. Contreras-García, M. Alonso, M. Torrent-Sucarrat and E. Matito, *Phys. Chem. Chem. Phys.*, 2018, **20**, 2787–2796.

53 M. A. Battiste, *J. Am. Chem. Soc.*, 1963, **85**, 2175–2176.

54 K. Y. and I. Murata, *Angew. Chem. Int. Ed. Engl.*, 1976, **15**, 240–241.

55 I. M. Kimiaki Yamamura, Hideyoshi Miyake, Kazuko Azumi, *Chem. Lett.*, 1989, **18**, 1511–1514.

56 J. Sturala, M. K. Etherington, A. N. Bismillah, H. F. Higginbotham, W. Trewby, J. A. Aguilar, E. H. C. Bromley, A.-J. Avestro, A. P. Monkman and P. R. Mcgonigal, *J. Am. Chem. Soc.*, 2017, **139**, 17882–17889.

57 R. A. Pascal, C. M. Wang, G. C. Wang and L. V. Koplitz, *Cryst. Growth Des.*, 2012, **12**, 4367–4376.

58 D. B. Amabilino and R. M. Kellogg, *Isr. J. Chem.*, 2011, **51**, 1034–1040.

59 A. T. Turley, P. K. Saha, A. Danos, A. N. Bismillah, A. P. Monkman, D. S. Yufit, B. F. E. Curchod, M. K. Etherington and P. R. McGonigal, *Angew. Chem. Int. Ed.*, 2022, **61**, e202202193.

60 D. Geuenich, K. Hess, F. Köhler and R. Herges, *Chem. Rev.*, 2005, **105**, 3758–3772.

61 P. von Ragué Schleyer, M. Manoharan, Z. X. Wang, B. Kiran, H. Jiao, R. Puchta and N. J. R. Van Eikema Hommes, *Org. Lett.*, 2001, **3**, 2465–2468.

62 H. Fallah-Bagher-Shaidaei, C. S. Wannere, C. Corminboeuf, R. Puchta and P. von Ragué Schleyer, *Org. Lett.*, 2006, **8**, 863–866.

63 P. von Ragué Schleyer, C. Maerker, A. Dransfeld, H. Jiao and N. J. R. Van Eikema Hommes, *J. Am. Chem. Soc.*, 1996, **118**, 6317–6318.

64 D. W. Szczepanik, M. Andrzejak, K. Dyduch, E. Żak, M. Makowski, G. Mazur and J. Mrozek, *Phys. Chem. Chem. Phys.*, 2014, **16**, 20514–20523.

65 D. W. Szczepanik, M. Andrzejak, J. Dominikowska, B. Pawełek, T. M. Krygowski, H. Szatylowicz and M. Solà, *Phys. Chem. Chem. Phys.*, 2017, **19**, 28970–28981.

66 L. E. Friedrich and R. A. Cormier, *J. Org. Chem.*, 1970, **35**, 450–454.

67 R. Breslow and H. W. Chang, *J. Am. Chem. Soc.*, 1965, **87**, 2200–2203.

68 G. Y. Wooi and J. M. White, *Org. Biomol. Chem.*, 2005, **3**, 872–974.

69 Gaussian 16, Revision C.01, M. J. Frisch, G. W. Trucks, H. B. Schlegel, G. E. Scuseria, M. A. Robb, J. R. Cheeseman, G. Scalmani, V. Barone, G. A. Petersson, H. Nakatsuji, X. Li, M. Caricato, A. V. Marenich, J. Bloino, B. G. Janesko, R. Gomperts, B. Mennucci, H. P. Hratchian, J. V. Ortiz, A. F. Izmaylov, J. L. Sonnenberg, D. Williams-Young, F. Ding, F. Lipparini, F. Egidi, J. Goings, B. Peng, A. Petrone, T. Henderson, D. Ranasinghe, V. G. Zakrzewski, J. Gao, N. Rega, G. Zheng, W. Liang, M. Hada, M. Ehara, K. Toyota, R. Fukuda, J. Hasegawa, M. Ishida, T. Nakajima, Y. Honda, O. Kitao, H. Nakai, T. Vreven, K. Throssell, J. A. Montgomery, Jr., J. E. Peralta, F. Ogliaro, M. J. Bearpark, J. J. Heyd, E. N. Brothers, K. N. Kudin, V. N. Staroverov, T. A. Keith, R. Kobayashi, J. Normand, K. Raghavachari, A. P. Rendell, J. C. Burant, S. S. Iyengar, J. Tomasi, M. Cossi, J. M. Millam, M. Klene, C. Adamo, R. Cammi, J. W. Ochterski, R. L. Martin, K. Morokuma, O. Farkas, J. B. Foresman, and D. J. Fox, Gaussian, Inc., Wallingford CT, 2016.

70 T. Lu and F. Chen, *J. Comput. Chem.* 2012, **33**, 580–592.

CHAPTER 3 |

EXTENDED CONJUGATION ATTENUATES THE QUENCHING OF AGGREGATION-INDUCED EMITTERS BY PHOTOCYCLISATION PATHWAYS

Published as '*Extended Conjugation Attenuates the Quenching of Aggregation-Induced Emitters by Photocyclization Pathways*'. A. T. Turley, P. K. Saha, A. Danos, Aisha N. Bismillah, A. P. Monkman, D. S. Yufit, B. F. E. Curchod, M. K. Etherington, and Paul R. McGonigal*. *Angew. Chem. Int. Ed.*, 2022, **61**, e202202193.

Abstract

Herein, we expose how the antagonistic relationship between solid-state luminescence and photocyclisation of oligoaryl alkenes chromophores is modulated by the conjugation length of their alkenyl backbones. Heptaaryl cycloheptatriene molecular rotors exhibit aggregation-induced emission characteristics, undergoing photoluminescence in the solid state. We show that their emission is turned off upon breaking the conjugation of the cycloheptatriene through epoxide formation. While this modification is deleterious to photoluminescence, it enables formation of extended polycyclic aromatic frameworks by Mallory reactions. We exploit this dichotomy (i) to manipulate emission properties in a controlled manner and (ii) as a synthetic tool to link together pairs of phenyl rings around the periphery of the cycloheptatriene in a specific sequence. This method to alter the tendency of oligoaryl alkenes to undergo photocyclisation can inform the design of solid-state emitters that avoid this quenching mechanism, while also allowing selective linking of rings during the synthesis of polycyclic aromatic hydrocarbons.

Acknowledgements

The following people are gratefully acknowledged for their contribution to this chapter: Dr. A. Turley developed the synthetic routes towards the cycloheptatriene and cycloheptatriene-epoxides, which were subsequently optimised and repeated by the Author. Dr. A. Turley and Dr. M. K. Etherington collected the photophysical data, alongside the Author. Dr. A. Danos measured solid-state PLQYs and assisted in the study of prolonged excitation effects. Dr. B. E. Curchod carried out all DFT calculations. Dr. D. S. Yufit solved the X-ray crystal structures. Dr. A. N. Bismillah performed the variable-temperature NMR measurements. Dr. A. T. Turley wrote an initial draft of the published work, which was refined together with the Author and Dr. P. R. McGonigal, who also conceived of the research..

3.1. Introduction

The quest to maximise photoluminescence efficiencies of organic luminogens has spurred progress from classical planar polycyclic aromatics, which are susceptible to aggregation-caused quenching (ACQ),[1–3] toward non-planar molecular rotor-type frameworks that exhibit aggregation-induced emission (AIE).[4–7] The enhanced luminescence of AIE-active materials in aggregated states is thought to arise from their restricted intramolecular motion (RIM),[8,9] which minimises the nonradiative decay of their excited states, thereby maximising photoluminescent emission. However, this mechanistic description of AIE has been a topic of ongoing debate[9–13] that has progressed in parallel to the development of new AIE luminogens and their applications. Various possible quenching pathways that are 'turned off' by RIM[14,15] have been identified, such as through-space aromatic dimerisation,[16–18] *E*/*Z* isomerisation[19] and, more generally, restricted access to a conical intersection (RACI).[20,21]

Oligoaryl alkenes, such as tetraphenylethylene (TPE), are a recurring structural motif in the pursuit of efficient emitters. These materials are regarded as the simplest, archetypal AIE-active structures, possessing a molecular rotor-type framework with rotatable phenyl rings.[22,23] An added complication for these types of emissive materials is that their 1,2-diphenyl ethylene (DPE) units are also known to undergo the Mallory reaction[24,25]—a photochemical cyclisation–elimination reaction that has been exploited synthetically to access polycyclic aromatic hydrocarbon structures.[26,27] Indeed, the formation of Mallory reaction intermediates has been invoked as one of the quenching pathways for oligoaryl alkene AIE luminogens and has previously been studied through ultra-fast spectroscopy,[28] suggesting that photocyclisation-induced quenching (PIQ) is a dominant nonradiative loss pathway in the RACI mechanism.

Herein, we report synthetic modification of our previously reported[16] AIE-active molecular rotor compound *sym*-hepta-phenylcycloheptatriene (**Ph$_7$C$_7$H**) to study the effects of structural changes on its nonradiative energy loss pathways. Our strategy to modify the structure of **Ph$_7$C$_7$H** alters the extent of electronic conjugation present in the oligoaryl alkene rotor while limiting geometric changes to the system, allowing us to effectively decouple electronic and geometric effects. We demonstrate that by interrupting the conjugation of **Ph$_7$C$_7$H**, its characteristic dual-state emission is

quenched. Instead of luminescing, it undergoes facile photocyclisation. Our investigations also lead to new understanding of the Mallory reaction in highly conjugated, oligoaryl alkene AIE luminogens. DPE units with extended π-electron conjugation exhibit attenuated Mallory-type reactivity, which correlates with suppressed PIQ and enhanced luminescence that is desirable for designing more efficient AIE materials. We exploit the facile photocyclisation of 'isolated' DPE units in a stepwise synthetic process that combines Mallory conditions with intermediate reactions to curtail or extend π-conjugation. In doing so, we access fused polyaromatics that were previously inaccessible by direct Scholl oxidation or Mallory reactions alone.

3.2. Results and Discussion

3.2.1. Synthesis, Structure, and Conformation

We initially synthesised modified derivatives of **Ph_7C_7H** (Figure 3.1) to further investigate its unusual dual-state emission properties.[14] See section 3.4.1 for full synthetic details. Two types of structural modifications were introduced: (i) formal ring fusion of two peripheral phenyl groups to form a phenanthrene unit or (ii) epoxidation of the central seven-membered ring. Together, **Ph_7C_7H** and its symmetrical (***sym*-phenPh_5C_7H**) and asymmetrical (***asym*-phenPh_5C_7H**) 9,10-phenanthryl analogues (Figure 3.1) make up a series of three triene rotors that differ by the introduction of a single C–C bond between two of the peripheral rings.

Subsequent epoxidation of each triene rotor expands the series to six compounds, giving rise (Figure 3.1) to **Ph_7C_7H-O**, ***sym*-phenPh_5C_7H-O**, and ***asym*-phenPh_5C_7H-O**. Epoxidation occurs both stereoselectively and regioselectively in the presence of an excess of *meta*-chloroperbenzoic acid (*m*CPBA). In each case, a singly epoxidised product was isolated. While epoxidation occurs at one end of the ***sym*-phenPh_5C_7H** triene to give a diene system, the reaction occurs at the central double bonds of **Ph_7C_7H** and ***asym*-phenPh_5C_7H**, splitting the trienes to give separated double bonds.

We gained insight into the conformations adopted by the rotor molecules by analysing their X-ray crystal structures (Figure 3.1).[29] In the solid-state, the cycloheptatriene rings exhibit similar, shallow boat-like conformations across the series of six compounds. In

each case, the phenyl group at the sp^3-C position occupies the bow of the boat conformation with a pseudo-axial orientation. We have previously reported that this orientation influences the emissive excited state of **Ph$_7$C$_7$H** by formation of through-space interactions between the phenyl rings at the bow and stern.[16]

In general, the proximity of the peripheral phenyl groups to one another disfavours conformations in which the rings are coplanar with the central double bonds, giving rise instead to perpendicular propeller-like geometries. Nonetheless, enforcing coplanarity of two peripheral rings as part of a biphenylene substituent (forming a phenanthrene ring system) has little impact on the geometry (Table 3.1) of the central cycloheptatriene ring. For example, the interplane angles (Figure 3.1, inset) Φ_{bow} = 54.9° and Φ_{stern} = 35.3° that characterise the boat conformation of **Ph$_7$C$_7$H** vary (Table 3.1) by less than 10° for each of its five derivatives in Figure 3.1.

Comparison of bond length alternation (BLA) parameters[30] gives quantifiable insight into the influence of peripheral ring fusion and epoxidation on the conjugation of the central cycloheptatriene ring (Table 3.1). Higher BLA is indicative of reduced π-electron delocalisation of a conjugated system. Relative to **Ph$_7$C$_7$H**, the BLA of ***sym*-phenPh$_5$C$_7$H** remains essentially unchanged, suggesting that the symmetrically placed phenanthrene ring has little impact on conjugation within the triene system. However, shortening this π-system to a diene by epoxidation, *i.e.*, ***sym*-phenPh$_5$C$_7$H-O**, causes a significant (~20%) increase in BLA, which demonstrates its reduced π-electron delocalisation. The asymmetrically substituted phenanthrene isomer, ***asym*-phenPh$_5$C$_7$H**, is an intermediate case, exhibiting a slight increase (~10%) in BLA relative to **Ph$_7$C$_7$H**. On the other hand, epoxidation of either ***asym*-phenPh$_5$C$_7$H** or **Ph$_7$C$_7$H** cleaves the triene system in two, producing at least one 'isolated' double bond in each case, e.g., the C–C double bond between positions 1 and 2 of the seven-membered ring (Figure 3.1). For both of these epoxides, the double bond length $d_{1–2}$

(Table 3.1) has decreased by ≥1 pm relative to the triene precursor, which is consistent with its reduced conjugation.

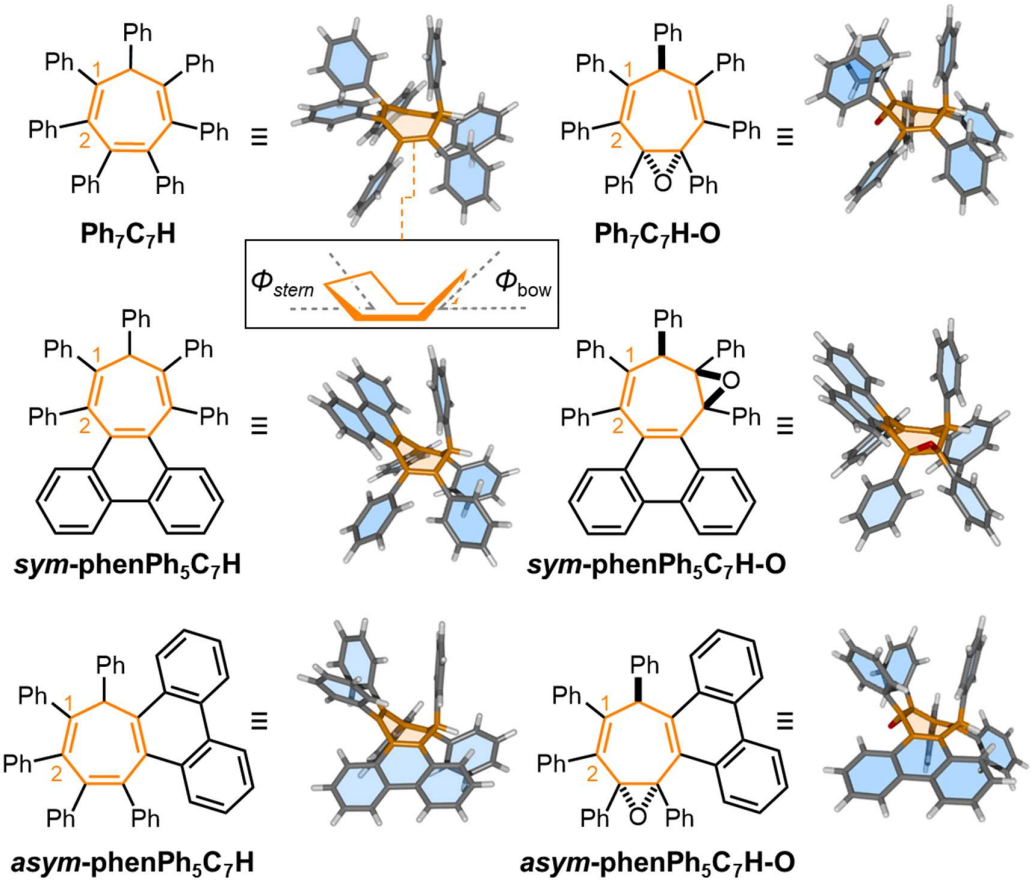

Figure 3.1. Structural formulas and X-ray crystal structures of **Ph$_7$C$_7$H** derivatives. Inset: the boat conformation of a seven-membered ring.

The geometric similarities observed between the cycloheptatrienes in the solid state are reflected in the solution-state dynamics for the 180˚ rotation of their most hindered phenyl rings. Variable-temperature (VT) nuclear magnetic resonance (NMR) spectroscopic analysis (Figures 3.6–3.13) reveals Gibbs energy barriers ($\Delta G^{\ddagger}$) to phenyl ring rotation at 298 K of 44.5 kJ·mol^{-1} and 40.5 kJ·mol^{-1} for ***sym*-phenPh$_5$C$_7$H** and **Ph$_7$C$_7$H-O**, respectively (Table 3.1). These values are similar to the $\Delta G^{\ddagger}$ measured for phenyl ring rotation in **Ph$_7$C$_7$H** of 48.2 kJ·mol^{-1}.[16]

Table 3.1. Geometric parameters of the molecular rotors

Rotor	Φ_{bow} [a] (°)	Φ_{stern} [a] (°)	BLA [b] (pm)	$d_{1\text{-}2}$ [c] (pm)	$\Delta G^{\ddagger}$ [d] (kJ·mol^{-1})
Ph$_7$C$_7$H	54.9	35.3	12.2	135.1(3)	48.2
***sym*-phenPh$_5$C$_7$H**	58.4	41.2	12.1	135.9(2)	44.5
***asym*-phenPh$_5$C$_7$H**	50.9	43.9	13.5	135.5(5)	-
Ph$_7$C$_7$H-O	49.0	33.1	-	134.1(2)	40.5
***sym*-phenPh$_5$C$_7$H-O**	53.2	42.2	14.8	135.4(2)	-
***asym*-phenPh$_5$C$_7$H-O**	46.1	35.2	-	133.8(2)	-

[a] Torsion angles and bond lengths were determined from X-ray crystallographic data. [b] Measured by subtracting the average length of double bonds from the average length of single bonds that are part of the diene or triene system.[27] [c] Estimated standard deviations in parentheses. [d] Measured by ^{1}H VT NMR spectroscopy for rotation of the most hindered phenyl ring (Figures 3.6–3.13).

In summary, neither epoxidation nor ring fusion causes large deviations in the overall geometries and conformational freedom of the seven-membered rings or rotatable phenyl groups. However, epoxidation does cause significant changes to the lengths of the conjugated systems, modifying the electronic properties of the individual diaryl alkene units.

We found that exposing a 1.5 mM toluene solution of ***sym*-phenPh$_5$C$_7$H-O** to UV irradiation causes a colour change from colourless to yellow (Figure 3.2a), which is reversed in ambient light over time. Similar reversible yellowing of TPE films has previously been attributed to formation of a photocyclised species.[28] No such colour change (or reactivity, *vide infra*) was observed for ***sym*-phenPh$_5$C$_7$H**, which suggests that the broken conjugation of ***sym*-phenPh$_5$C$_7$H-O** significantly alters its photophysical behaviour. The proposed intermediate species **IM** formed under irradiation was subsequently oxidised (*vide infra*) to ***asym*-phen$_2$Ph$_3$C$_7$H-O** under Mallory reaction conditions, confirming the photocyclisation reactivity. Similarly, a Mallory reaction of **Ph$_7$C$_7$H-O** gives rise to ***sym*-phen$_2$Ph$_3$C$_7$H-O**, which was confirmed by two-dimensional NMR spectroscopy and X-ray crystallography (Figure 3.2b). To elucidate the origins of this enhanced photocyclisation reactivity in the compounds with truncated conjugation, we conducted deeper photophysical analyses of the series of six rotors shown in Figure 3.1.

3.2.2. Luminescence of the Triene Rotors

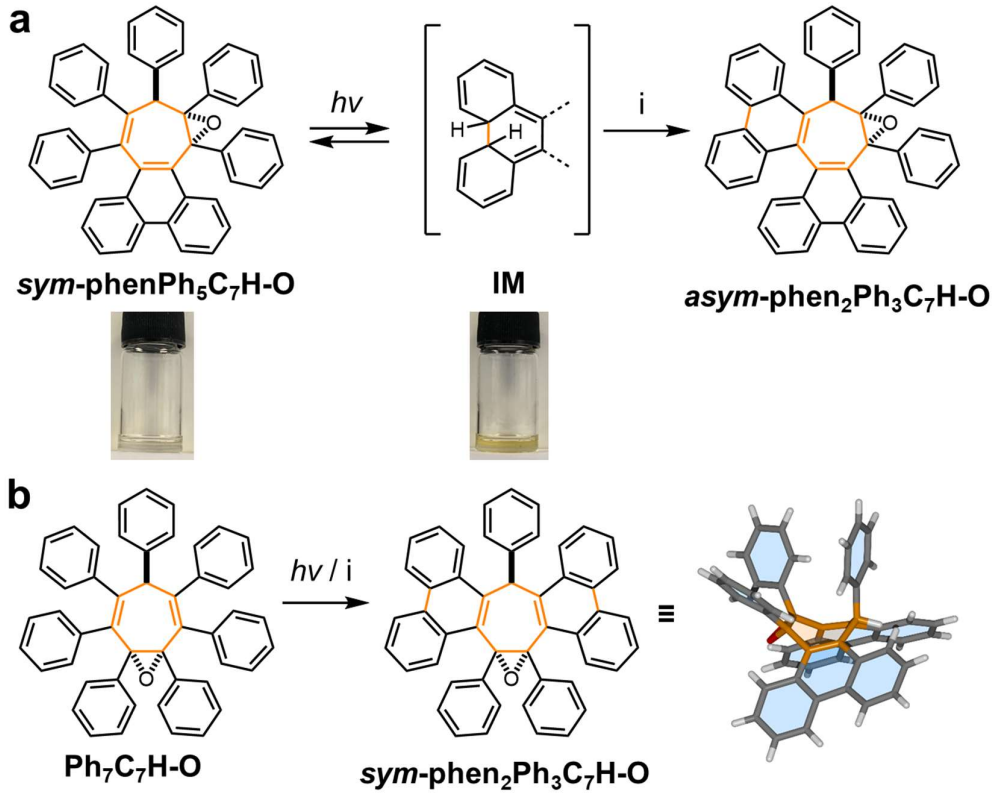

Figure 3.2. Photocyclisations of rotors containing 'isolated' DPE units. Reagents and conditions: (i) I_2, propylene oxide, THF, *hv* (4.88 eV), 3 h. An X-ray structure of ***sym*-phen$_2$Ph$_3$C$_7$H-O** shows the presence of two new phenanthrene units.

We first confirmed that the triene molecular rotors are AIE-active by preparing 1% w/w dispersions in ZEONEX—an optically clear cyclic olefin polymer matrix. Photoluminescene quantum yield (Φ_{film}) measurements carried out on the ZEONEX films show that all three fully conjugated rotors emit in the solid state with similar efficiencies (Table 3.2) of 1.7–6.7%. We gained further insights into the influence of biphenylene substitution on the optical properties relative to **Ph$_7$C$_7$H** by acquiring (Figure 3.3) steady-state emission spectra[31] using dilute (2 μM) 2-methyl tetrahydrofuran (2-MeTHF) solutions of each rotor. The spectra were recorded at a series of temperatures (290 K to 90 K) to alter rates of nonradiative decay (k_{nr}) through RIM and RACI in a controlled manner.

We measured (Table 3.2) the ratios between emission intensities at 290 K and 90 K, $\Delta I_{290–90}$. The emission intensities, I, of the three triene rotors increase at lower

temperatures as k_{nr} is decreased. The phenanthrenyl derivatives both have much smaller ΔI_{290-90} than **Ph$_7$C$_7$H**. This observation is consistent with them having fewer intramolecular vibrational degrees of freedom, which renders them less susceptible to increased nonradiative decay at higher temperatures.

In common with **Ph$_7$C$_7$H** (Figure 3.3a), ***sym*-phenPh$_5$C$_7$H** shows (Figure 3.3b) a gradual hypsochromic shift in the energy of the emission maximum (E_{max}) from 2.84 eV to 3.15 eV as the temperature decreases (Table 3.2). By analogy to our previous investigation,[16] we attribute this shift to two-state emission that emerges from accessing a relaxed dimer state, whereby a face-to-face interaction develops between the phenanthrene moiety and the phenyl group at the bow of the seven-membered ring after photoexcitation. The compound-specific relationships between the E_{max} and temperature are plotted in Figure 3.30.

There is no indication of this dual emission in the analogous spectra (Figure 3.3c) of ***asym*-phenPh$_5$C$_7$H**. However, we do observe (Figure 3.3d) a bathochromic shift from 3.33 eV to 2.70 eV at 130 K using a higher solution concentration of 200 μM, suggesting the formation of intermolecular dimers rather than the intramolecular aromatic interactions. This behaviour mirrors the dimerisation of molecular phenanthrene.[32] Presumably, the phenanthrene moiety of ***asym*-phenPh$_5$C$_7$H** is sufficiently exposed and unhindered that it is available to undergo intermolecular dimerisation in the ground state driven by solvophobic forces. Indeed, the vibronic structure of the emission from ***asym*-PhenPh$_5$C$_7$H** at 200 μM matches closely with the emission from phenanthrene (Figure 3.3e). We note that no concentration-dependent emission changes were observed in the spectra of other rotors in the series (Figure 3.32).

Overall, the photophysical characteristics of both ***sym*-** and ***asym*-phenPh$_5$C$_7$H** broadly resemble **Ph$_7$C$_7$H**. All three are AIE-active rotors that give photoluminescence quantum yields of 1.7–6.7% in the solid state (*i.e.*, dispersed in ZEONEX films). The relative position of the biphenylene unit of the molecular rotor tunes the propensity for face-to-face interactions of their aromatic rings, which can occur intramolecularly in the excited state or intermolecularly in the ground state. Yet, there is no evidence in their optical spectra to suggest that these fully conjugated compounds are prone to photocyclisation.

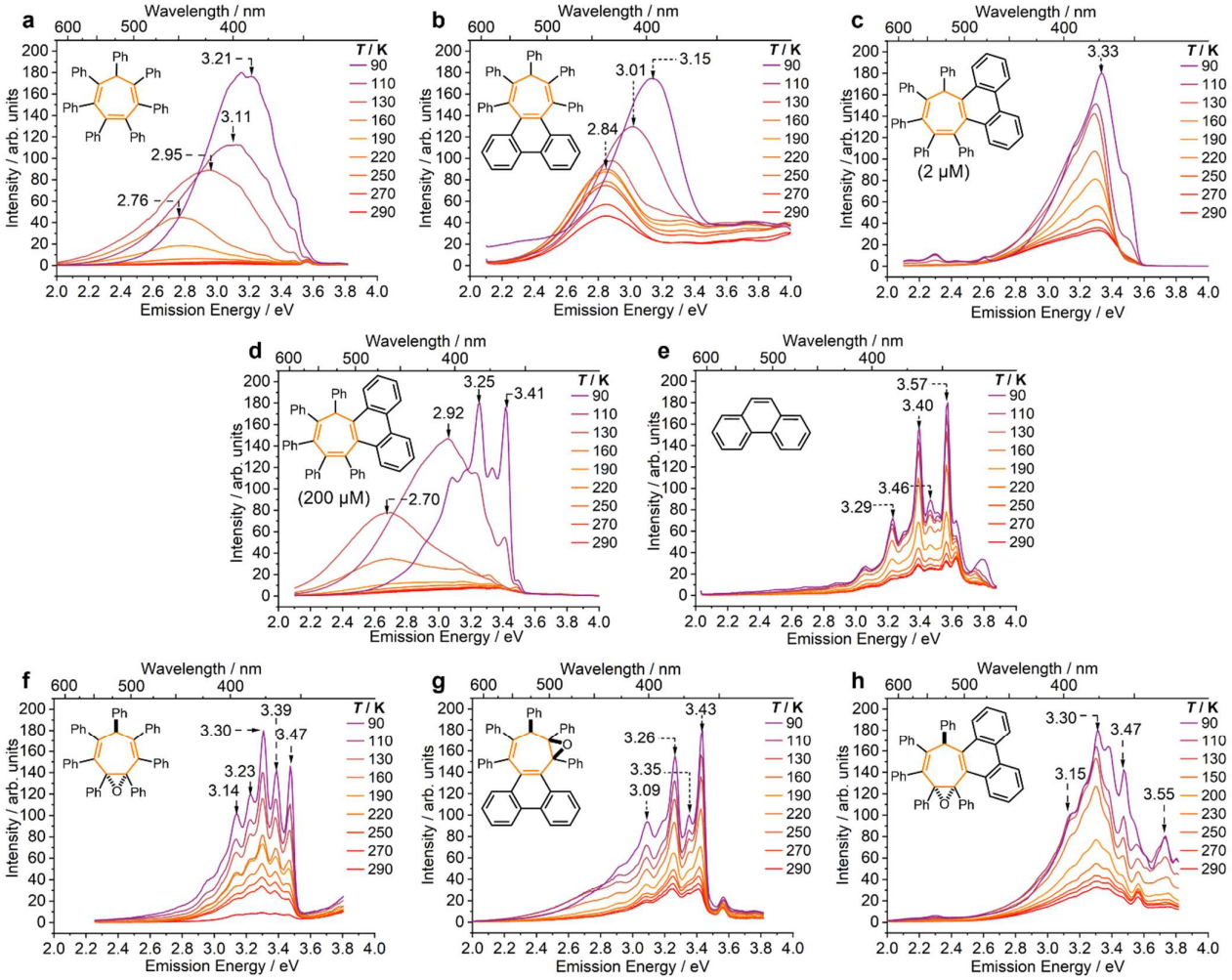

Figure 3.3. VT steady-state photoluminescence spectra of 2-MeTHF solutions of **(a) Ph$_7$C$_7$H**, excitation energy E_{ex} = 3.95 eV, concentration c = 2 μM; **(b) *sym*-phenPh$_5$C$_7$H**, E_{ex} = 4.13 eV, c = 2 μM; **(c) *asym*-phenPh$_5$C$_7$H**, E_{ex} = 3.95 eV, c = 2 μM; **(d) *asym*-phenPh$_5$C$_7$H**, E_{ex} = 3.95 eV, c = 200 μM; **(e)** phenanthrene, E_{ex} = 4.13 eV, c = 2 μM; **(f) Ph$_7$C$_7$H-O**, E_{ex} = 4.35 eV, c = 2 μM; **(g) *sym*-phenPh$_5$C$_7$H-O**, E_{ex} = 3.95 eV, c = 2 μM; and **(h) *asym*-phenPh$_5$C$_7$H-O**, E_{ex} = 3.95 eV, c = 2 μM.

3.2.3. Optical Properties of the Epoxide Rotors

Interrupting the conjugation of the triene systems by epoxidation causes significant changes in their emission properties. The broad fluorescence peaks observed for the trienes are replaced (Figures 3.3f–h) by structured emission at high energy (3.09–3.55 eV). The emission intensities are very weak in both the solution and solid states regardless of temperature (Figure 3.33), giving low Φ_{film} values (Table 3.2). ZEONEX films[i] of **Ph$_7$C$_7$H-O** and ***sym*-phenPh$_5$C$_7$H-O** both give quantum yields below the

[i] ZEONEX is a transparent olefin polymer resin that is commonly used to prepare thin films of organic fluorophores

threshold for reliable measurement (≤0.1%).[33] Therefore, the reduced conjugation of the epoxides is associated with substantially diminished luminescence.

Table 3.2. Photophysical properties of the molecular rotors and phenanthrene.

Rotor	E_{ex} [a] (eV)	E_{max} (eV)			τ (ns) [b,c]	ΔI_{290-90} [b,d]		Φ_{film} [e,f] (%)
		160 K [b]	90 K [b]	Film [g]	290 K	Sol [b]	Film [e]	
Ph_7C_7H	3.95	2.76	3.21	3.02	6.5	52.1	9.91	6.7
***sym*-phenPh_5C_7H**	4.13	2.84	3.15	3.01	20.4	3.75	2.13	1.7
***asym*-phenPh_5C_7H**	4.13	3.33	3.33	3.07	8.2	6.24	2.63	4.0
Ph_7C_7H-O[e]	4.35	3.30	3.30	3.47	12.6[g]	4.82	1.19	≤0.1
***sym*-phenPh_5C_7H-O**[e]	3.94	3.43	3.43	3.34	11.9[g]	5.76	0.69	≤0.1
***asym*-phenPh_5C_7H-O**[e]	3.94	3.30	3.30	3.47	9.0[g]	5.47	2.62	3.3
***sym*-phen$_2Ph_3C_7H$-O**	4.00	3.72	3.76	3.43	-	1.67	1.50	6.4
***asym*-phen$_2Ph_3C_7H$-O**	4.00	3.43	3.43	3.43	-	4.50	2.65	9.8
***sym*-phen$_3PhC_7H$**	3.95	3.40	3.40	3.22	8.4	3.97	-	4.5
phenanthrene	4.13	3.56	3.56	3.06	15.0	5.13	0.56	-

[a] E_{ex} were chosen to match peaks in absorption spectra (Figure 3.27). [b] 2 μM solution in 2-MeTHF. [c] See Table 3.6 for full lifetime data. [d] Difference in intensity between the emission peaks at 290 K and 90 K. [e] 1% w/w film in ZEONEX. [f] Measured by integrating sphere under ambient conditions. [g] The τ values reported for the epoxide series are the apparent lifetimes of the weak emission observed upon excitation of a sample of the pure epoxide starting material, some of which may photocyclise during the measurement.

We ascribe these observations to PIQ occurring in both the solution state and amorphous ZEONEX films. Rather than undergoing photoluminescence, the excited rotors are prone to form a C–C bond to give **IM** structures (Figure 3.2a), which enables the aforementioned Mallory reactivity. This enhanced PIQ pathway is responsible for the absence of the broad emission peak observed for the trienes.

A further experimental indication of this photocyclisation occurring in solution came when sequentially repeated steady-state photoluminescence measurements of a 2-MeTHF solution of **Ph_7C_7H-O** resulted in increases in emission intensity. We compared (Figure 3.4a) the emission spectrum before and after irradiating a sample with 4.0 eV light for 5 min. Irradiation causes a fourfold increase in emission intensity, consistent with a photochemical reaction taking place to build up a higher concentration

of a more emissive compound. An experiment monitoring the emission intensity at 3.30 eV over time as the sample is irradiated (Figure 3.4b) shows the build-up of the new species during continued irradiation. The emission intensity decreases when the irradiation is stopped, consistent with the reversible colour change described above (Figure 3.2).

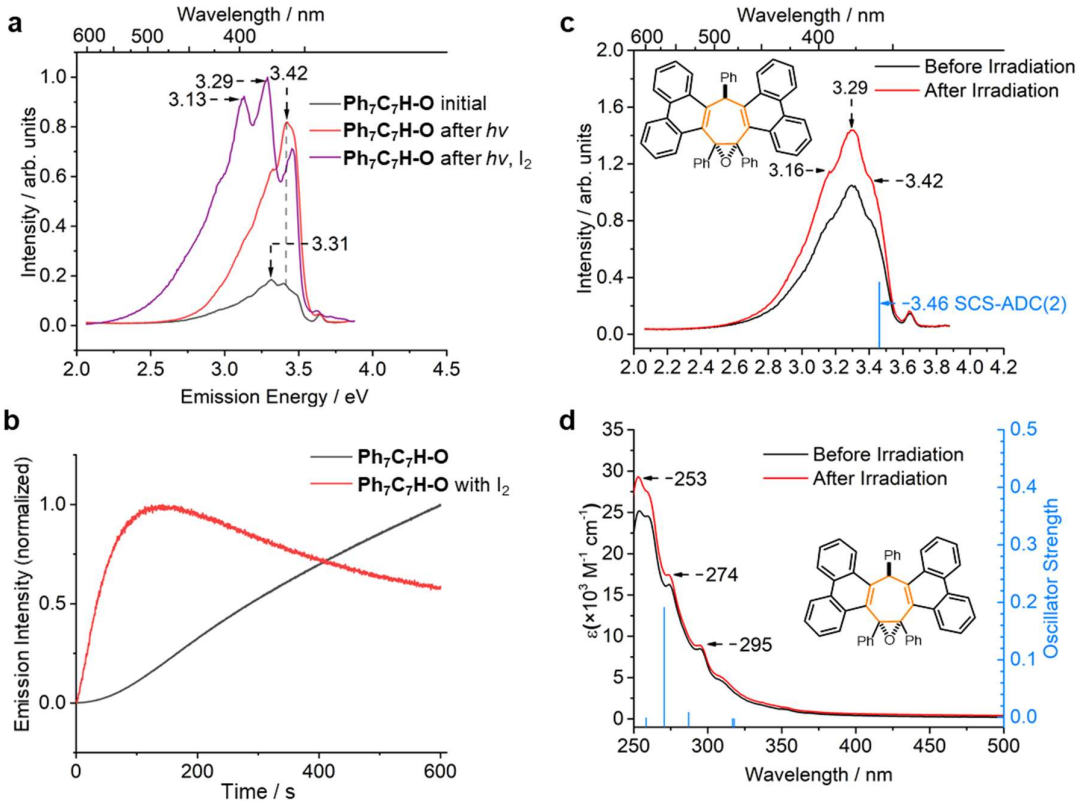

Figure 3.4. Steady-state photoluminescence spectra of 2-MeTHF solutions of **Ph_7C_7H-O**, (E_{ex} = 4.35 eV, c = 2 μM) **(a)** before and after irradiation with 4.0 eV light for 10 min with and without I_2; **(b)** the change in the emission intensity at 3.30 eV over time, with and without I_2; **(c)** emission (2-MeTHF, c = 2 μM) and **(d)** absorption (MeCN, c = 20 μM) spectra of ***sym*-$phen_2Ph_3C_7H$-O** before and after irradiation with 4.0 eV light for 10 min. Theoretical emission (vertical transition from the S_1 geometry) and absorption (five lowest vertical transitions from the S_0 geometry) transitions shown in panels **(c)** and **(d)** were obtained at the SCS-ADC(2)/TZVP//SCS-ADC(2)/SVP and SCS-ADC(2)/TZVP//SCS-MP2 levels of theory, respectively.

Performing a similar series of experiments for the full series of six rotors (Figure 3.36), we found that the three epoxide rotors exhibit the same behaviour, whereas the trienes require prolonged irradiation times of >1 h before changes in their emission profiles are observed.

These observations are all consistent with PIQ. To confidently rule out the possibility of the structured emission stemming from solvatochromic, or intermolecular interactions, we also acquired absorption (Figure 3.27) and emission spectra (Figure 3.34) using (i) solvents of different polarities and (ii) amorphous film samples prepared as 1% w/w dispersions in ZEONEX (Figure 3.33). We observed that, in general, the spectral features are independent of solvent polarity and temperature.

In light of the proposed photocyclisation pathway (Figure 3.2), we tested whether atmospheric O_2 was acting as an oxidant to complete the irreversible formation of ***sym*-phen$_2$Ph$_3$C$_7$H-O** upon irradiating a 2-MeTHF solution of **Ph$_7$C$_7$H-O**. A solution sample of **Ph$_7$C$_7$H-O** was deaerated by performing freeze–pump–thaw cycles and backfilling with N_2, before irradiating with UV light. The same emission profile was observed under these conditions or using an aerated sample (Figure 3.34). It is, therefore, unlikely that significant oxidation of the planarised **IM** compounds is occurring under these conditions. Instead, the weak, structured emission spectra recorded in Figures 3.3f–h should be attributed to emission from the **IM** structures themselves. Trace amounts of **IM** compounds formed during the measurement may become photoexcited and subsequently luminesce.

3.2.4. Epoxide Rotors Undergo Facile Mallory Reaction

We further probed the susceptibility of the epoxides to undergo photocyclisation by purposefully applying Mallory reaction conditions (Figure 3.2). Excesses of the oxidants I_2 and propylene oxide were added to a 15 mM solution of **Ph$_7$C$_7$H-O** in tetrahydrofuran (THF) to trap transient **IM** compounds through the irreversible formation of a new phenanthrene ring system (Figure 3.2b). The double photocyclisation product, ***sym*-phen$_2$Ph$_3$C$_7$H-O**, was isolated in quantitative yield after 3 h of irradiation with 4.88 eV light. Two new phenanthrene moieties form from the two ‘isolated’ (i.e., non-conjugated) DPE units of **Ph$_7$C$_7$H-O**. Adding further equivalents of I_2 and extending the irradiation time does not promote further photocyclisation of the remaining phenyl groups.

The same reaction conditions were also applied to *sym*-phenPh_5C_7H-O, which has a diene system in its central seven-membered ring. Photooxidation of its sole DPE group produced (Figure 3.2a) ***asym*-phen$_2$Ph$_3$C$_7$H-O** in 85% yield. These Mallory reaction conditions were also applied successfully to the third epoxide rotor, ***asym*-phenPh$_5$C$_7$H-O**, which can be considered as a monocyclised intermediate species that forms (Figure 3.5a) during the irreversible transformation of **Ph$_7$C$_7$H-O** to ***sym*-phen$_2$Ph$_3$C$_7$H-O**. As expected, the photocyclisation also gave ***sym*-phen$_2$Ph$_3$C$_7$H-O**, doing so in quantitative yield.

Conversely, none of the triene rotors shown in Figure 3.1 underwent photooxidation under these reaction conditions. Even upon irradiating for extended periods, ^{1}H NMR spectroscopic analyses of the crude reaction mixtures indicated that no observable reactions occur. Therefore, these synthetic results are in agreement with our spectroscopic experiments. Photocyclisation of isolated DPE units occurs rapidly. The diene ***sym*-phenPh$_5$C$_7$H-O** shows similar reactivity and photophysical properties to the isolated DPE compounds. But the extended conjugation of the three triene rotors improves their resistance to photocyclisation, both under Mallory reaction conditions and in the context of a quenching pathway for photoluminescence.

3.2.5. Exhaustive Photocyclisation

Once formed, the doubly photocyclised product ***sym*-phen$_2$Ph$_3$C$_7$H-O** displays an emission spectrum that is distinct from the spectrum of its **IM** precursors (Figure 3.5a). The time-dependent increase in emission intensity at 3.30 eV observed previously during irradiation of **Ph$_7$C$_7$H-O** (Figure 3.4b) is also changed as the **IM** compounds are consumed by onward reaction with I_2 to form ***sym*-phen$_2$Ph$_3$C$_7$H-O**.

We tested the emission (Figure 3.4c) and absorption (Figure 3.4d) spectra of solutions of isolated ***sym*-phen$_2$Ph$_3$C$_7$H-O** before and after irradiation at 4.88 eV to probe whether further photocyclisation can occur. Only small differences in intensity were observed, which likely arise because of minor changes in temperature and concentration following irradiation. In keeping with the outcome of the Mallory reactions, it does not appear that the remaining phenyl groups are prone to undergo further photocyclisation. The first five vertical transitions of ***sym*-phen$_2$Ph$_3$C$_7$H-O** calculated with SCS-ADC(2) (see section 3.5 for computational details) are in good agreement with the experimental

absorption spectrum (Figure 3d). These transitions, which are within the range of the photoexcitation energy used experimentally, involve orbitals on the phenanthrenes or the central seven-membered ring, validating the observation that no further cyclisation from the phenyl rings is to be expected. The vertical emission energy from the optimised S_1 geometry obtained at the SCS-ADC(2)/TZVP//SCS-ADC(2)/SVP is calculated to be 3.46 eV (Figure 3.4c), closely matching the high-energy tail of the experimental spectrum. The orbitals involved in the emission (Figure 5b) are located on the phenanthrene and central rings and do not extend to the remaining phenyl groups. The shape of the emission band of ***sym*-phen$_2$Ph$_3$C$_7$H-O** was further analysed by including non-Condon effects using the nuclear ensemble approach combined with linear-response time-dependent density functional theory (Figure 3.42).

3.2.6. Control of Conjugation Length Enables Synthesis

Based on the differing reactivities of the trienes and the epoxides, we hypothesised that by synthetically manipulating the conjugation lengths in our oligoaryl alkene systems we could enable otherwise inaccessible reactivity. Accordingly, we targeted (Figure 3.5a) the *meso* double helicene ***sym*-phen$_3$PhC$_7$H**. Attempts to prepare this compound directly from Ph_7C_7H using a range of classical intramolecular cyclodehydrogenation reaction conditions[34] have been unsuccessful.[35]

After breaking the triene conjugation of Ph_7C_7H by epoxidation, the Mallory reaction of **Ph$_7$C$_7$H-O** to give ***sym*-phen$_2$Ph$_3$C$_7$H-O** proceeds smoothly on gram scale. The reaction was performed using I_2 in THF solution while irradiating with 4.88 eV UV-light. Having confirmed that no further photocyclisation occurs in ***sym*-phen$_2$Ph$_3$C$_7$H-O**, the epoxide unit was then reverted to an olefin to reestablish a DPE unit in the structure. We treated ***sym*-phen$_2$Ph$_3$C$_7$H-O** with a 1 M solution of $LiAlH_4$ in THF at 70 °C, which yielded ***sym*-phen$_2$Ph$_3$C$_7$H**.

Pleasingly, upon reformation of this DPE unit, further cyclisation to give ***sym*-phen$_3$PhC$_7$H** occurs readily—a $CDCl_3$ solution sample of ***sym*-phen$_2$Ph$_3$C$_7$H** cyclised when left under ambient atmosphere and light for 7 d. The process is accelerated by applying our standard Mallory reaction conditions, which gives rise to the double helicene product in 81% yield after 15 min. By analogy to the increased BLA of ***asym*-PhenPh$_5$C$_7$H** (Table 3.1), we attribute the ease of this final photocyclisation to

reduced electron delocalisation in the π-system of the central seven-membered ring, which is caused by the two phenanthrene units at either end of the conjugated system.[36]

Overall, the efficiency of the central ring epoxidation and subsequent 'deprotection' to return the olefin functionality provides an attractive tactic to manipulate photocyclisations of DPE-containing molecules. The method complements existing approaches for the synthesis of polycyclic aromatic hydrocarbons.[34] Conceptually, the steps involved are: (1) Disrupting conjugation to form an 'isolated' DPE unit, (2) carrying out a Mallory reaction, then (3) re-establishing the conjugated system by reversing step 1.

3.2.7. Minimising PIQ

Comparing the full series of DPE-containing rotor compounds (Table 3.2), we suggest two strategies for molecular design to minimise PIQ and optimise their solid-state emission. The propensity of DPE units to undergo photocyclisation can be reduced by incorporating them as part of an extended conjugated system. **Ph$_7$C$_7$H**, ***sym*-** and ***asym*-PhenPh$_5$C$_7$H** have not shown spectroscopic evidence of rapid PIQ or synthetic evidence of Mallory reaction. They give Φ_{film} values of 1.7–6.7%, which are higher than those measured for their epoxide counterparts with reduced conjugation. Alternatively, rotor compounds that are prone to PIQ can be treated with Mallory reaction conditions to purposefully exhaust the available photocyclisation pathways. Our experiments have shown that ***sym*-phen$_2$Ph$_5$C$_7$H-O**, ***asym*-phen$_2$Ph$_5$C$_7$H-O** and ***sym*-phen$_3$PhC$_7$H** are all resistant to photocyclisation under Mallory conditions. Their three-dimensional structures and remaining rotatable phenyl groups presumably contribute to them retaining their AIE properties. In the solid state, they give Φ_{film} values of 4.5–9.8%, which exceed their precursors.

Depending on the structure of the AIE compound and its intended use, one of these two strategies may be more appropriate than the other. Low molecular weight AIE luminogens may be required for use in some applications, which may place limitations on the length of the oligoalkenyl backbone that can be used.

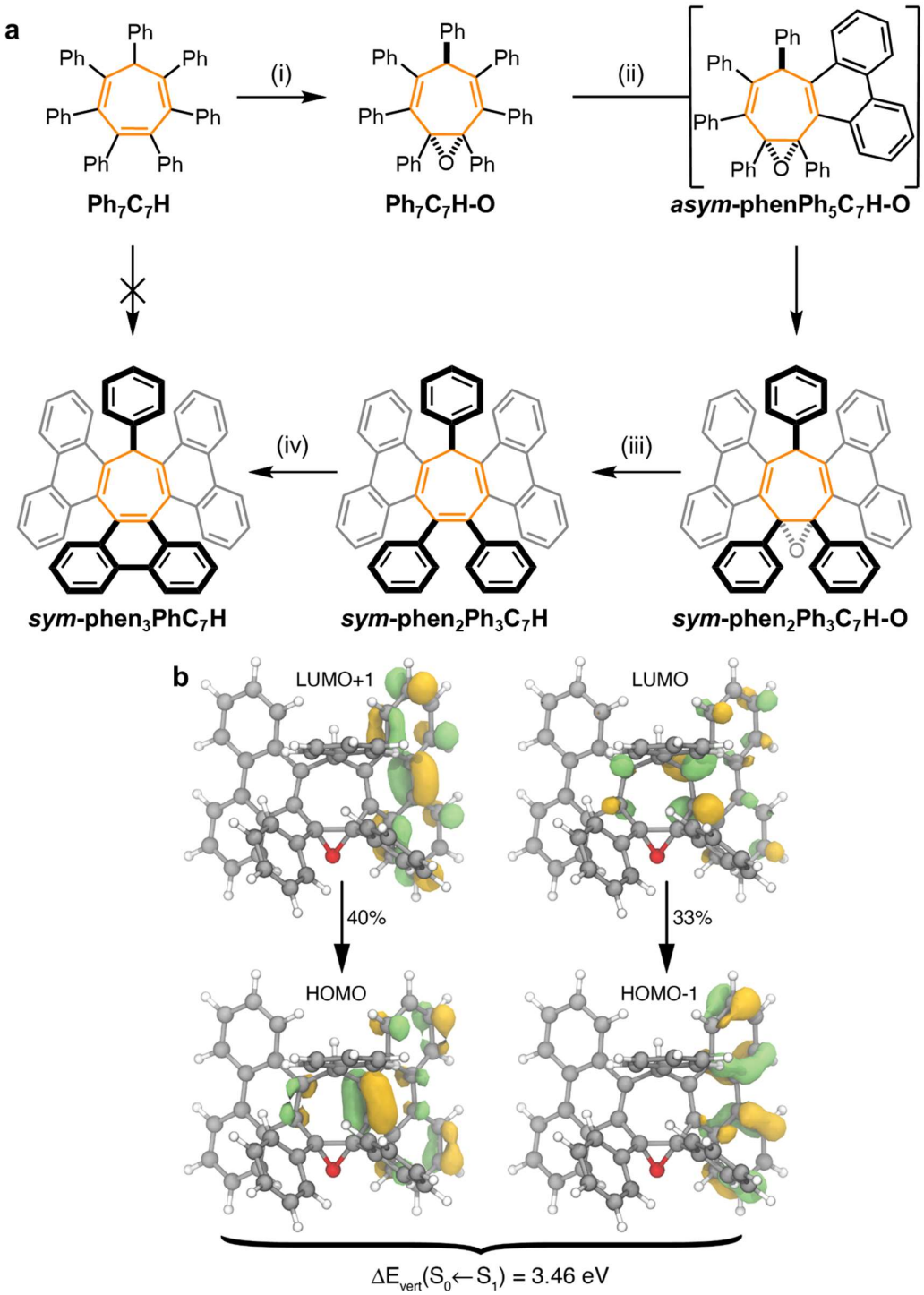

Figure 3.5. (a) Sequential Mallory reactions by isolating and revealing DPE groups. Reagents and conditions: (i) *m*CPBA, $CHCl_3$, 0 °C to 55 °C, 24 h, 70%; (ii) I_2, THF, propylene oxide, *hv* (4.88 eV), 3 h, >99%; (iii) $LiAlH_4$, THF, 70 °C, 72 h, 47%; (iv) I_2, THF, propylene oxide, *hv* (4.88 eV), 15 min, 81%. (b) Calculated MOs of ***sym*-phen$_2$Ph$_3$C$_7$H-O**, SCS-ADC(2)/TZVP.

3.3. Conclusions

In summary, by making minor structural changes to an AIE-active molecular rotor, **Ph$_7$C$_7$H**, we have exerted influence over the prevalence of PIQ and the formation of intramolecular phenyl-ring dimer excited states. PIQ is disfavoured in these rotor compounds when their individual DPE units form part of a larger conjugated system. A parallel can be drawn to the related Mallory photocyclisation reaction; compounds that are prone to PIQ undergo facile reaction to form annulated derivatives under Mallory conditions. We have leveraged this property by reversibly disrupting conjugation through epoxidation, which gives access to fused polyaromatics that were previously inaccessible through conventional aryl–aryl coupling reactions. These methods to manipulate the photophysical properties of oligoaryl alkene units can be exploited in the design of more efficient AIE materials or to improve photochemical syntheses of polycyclic aromatic hydrocarbons.

3.4. Experimental Details

3.4.1. Synthetic Procedures

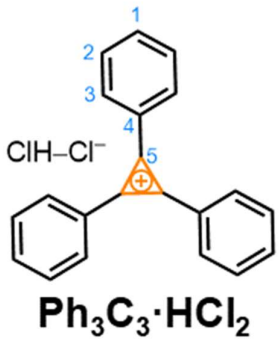

Triphenylcyclopropenylium hydrogen dichloride (**Ph$_3$C$_3$·HCl$_2$**): Anhydrous benzene (200 mL) was added to diphenylacetylene (18.5 g, 104 mmol) and KO^{t}Bu (35.0 g, 312 mmol) in an oven-dried two-necked 500 mL round-bottomed flask fitted with a septum under an inert atmosphere. α,α-Dichlorotoluene (25.0 g, 155 mmol) was added uniformly over a period of 30 min using a syringe pump, and the reaction mixture was then heated to reflux for 3 h. After cooling, H_2O (200 mL) was added to dissolve the inorganic salts. The layers were separated and the aqueous layer was extracted with Et_2O (2 × 200 mL). The combined organic extracts were dried over $MgSO_4$, and the solvents were removed under reduced pressure to yield orange residue. This was dissolved in a mixture of 2:1 Et_2O–CH_2Cl_2 (200 mL) and sparged with gaseous HCl, leading to the formation of a colourless precipitate. Sparging was continued until no more precipitation was observed. The precipitate was collected by filtration, and the solid was washed with Et_2O, then dried under vacuum to yield the

title compound as cream powder (18.6 g, 61.4 mmol, 43%). **M.P.** 186–188 °C. **^{1}H NMR** (600 MHz, CD_3CN) δ 8.83–8.39 (m, 6H, H_3), 8.20–8.00 (m, 3H, H_1), 7.97–7.86 (m, 6H, H_2). **^{13}C NMR** (151 MHz, CD_3CN) δ 154.1 (C_5), 139.1 (C_1), 136.6 (C_2), 131.4 (C_3), 121.6 (C_4). **HRESI-MS** *m/z* = 267.1169 $[M]^+$ (calculated for $C_{21}H_{15}^+$ = 267.1168).

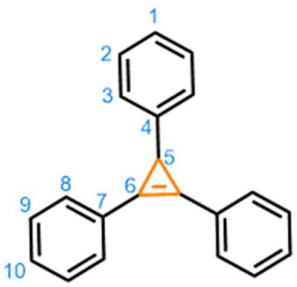

Ph_3C_3H

***sym*-Triphenylcyclopropene**: $NaBH_4$ (9.3 g, 246 mmol) was added to a solution of **$Ph_3C_3 \cdot HCl_2$** (18.6 g, 61.4 mmol) in EtOH (460 mL) at 0°C. The mixture was stirred overnight at rt. The reaction was quenched with H_2O (500 mL) then extracted with Et_2O (3 × 200 mL). The combined organic extracts were washed with H_2O (500 mL), then brine (500 mL), and dried over $MgSO_4$. The solvents were removed under reduced pressure to give **5** as a colourless solid (14.2 g, 53.1 mmol, 97%). **M.P.** 113–115 °C (lit.[3] 114–116 °C). **^{1}H NMR** (400 MHz, $CDCl_3$) δ 7.71–7.66 (m, 4H, H_8), 7.47–7.40 (m, 4H, H_9), 7.38–7.32 (m, 2H, H_{10}), 7.24 (br s, 2H, H_2), 7.23–7.22 (m, 2H, H_3), 7.17–7.10 (m, 1H, H_1), 3.27 (s, 1H, H_5). **^{13}C NMR** (101 MHz, $CDCl_3$) δ 144.6 (C_4), 130.0 (C_8), 128.9 (C_9), 128.8 (C_{10}), 128.7 (C_7), 128.3 (C_3), 126.0 (C_2), 125.6 (C_1), 112.7 (C_6), 24.5 (C_5). **HR-ESI MS** *m/z* = 267.1172 $[M-H]^+$ (calculated for $C_{21}H_{15}^+$ = 267.1168).

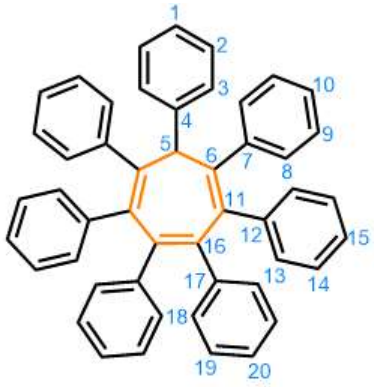

Ph_7C_7H

***sym*-Heptaphenylcycloheptatriene (Ph_7C_7H)**: Anhydrous *p*-xylene (13.5 mL) was added to **5** (1.2 g, 4.47 mmol) and tetraphenylcyclopentadienone (1.79 g, 4.47 mmol) in a sealed, oven-dried microwave vial under an inert atmosphere. The mixture was deoxygenated (3 × freeze–pump–thaw cycles under N_2) then stirred for 36 h at 140 °C in a microwave reactor. Upon cooling to rt, a crystalline solid formed, which was isolated by filtration, and washed with Et_2O (3 × 10 mL). The solid was dried under vacuum to yield **7** as a pale pink solid (2.30 g, 3.68 mmol, 82%) in high purity (no observable impurities by ^{1}H NMR spectroscopy). Samples for analytical measurements were further purified by

recrystallisation. A saturated solution of **7** in $CHCl_3$–EtOH (1:1) was allowed to evaporate slowly, yielding colourless crystals of analytically pure **7**. **M.P.** 291–292 °C (lit.[37] 285–288 °C). **^{1}H NMR** (700 MHz, $(CD_3)_2CO$) δ 8.17–7.99 (m, 2H, H_3), 7.62–7.48 (m, 2H, H_2), 7.44–7.34 (m, 1H, H_1), 7.26–7.18 (m, 4H, H_8), 7.15 (br s, 4H, H_{13}), 7.05–7.02 (m, 4H, H_{14}), 7.02–6.98 (m, 4H, H_9), 6.98–6.96 (m, 2H, H_{15}), 6.96–6.93 (m, 2H, H_{10}), 6.63–6.59 (m, 2H, H_{20}), 6.60–6.55 (m, 4H, H_{19}), 6.36–6.32 (m, 4H, H_{18}), 5.35 (s, 1H, H_5). **^{13}C NMR** (176 MHz, $(CD_3)_2CO$) δ 144.8 (C_{16}), 144.4 (C_7), 144.1 (C_4), 141.9 (C_{12}), 141.6 (C_{17}), 140.2 (C_6), 138.0 (C_{11}), 132.7 (C_{13}), 132.3 (C_{18}), 130.7 (C_8), 129.4 (C_2), 128.5 (C_9), 128.1 (C_{14}), 127.9 (C_3), 127.7 (C_1), 127.3 (C_{10}), 126.93 (C_{15}), 126.87 (C_{19}), 126.0 (C_{20}), 59.0 (C_5). **HR-ESI MS** *m/z* = 625.2892 $[M+H]^+$ (calculated for $C_{47}H_{37}^+$ = 625.2890).

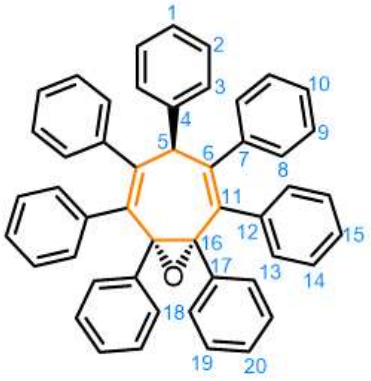

Ph_7C_7H-O

Ph_7C_7H-O: *sym*-Heptaphenylcycloheptatriene (1.0 g, 1.6 mmol) was dissolved in $CHCl_3$ (50 mL) and cooled to 0 °C. The mixture was stirred for 5 min. A cooled solution of *m*CPBA (1.6 g, 6.5 mmol) in $CHCl_3$ (20 mL) was added and stirred for a further 5 min before being allowed to warm to rt. The mixture was slowly heated to 55 °C and left to stir for 16 h. The mixture was allowed to cool to rt and a further equivalent of *m*CPBA (0.28 g, 1.6 mmol) was added. The mixture was heated to 55 °C for 3 h before allowing to cool to rt. A saturated aqueous solution of $NaHCO_3$ (20 mL) was added and the resulting biphasic mixture was stirred for 15 min. The organic layer was separated and then washed with a saturated aqueous solution of $NaHCO_3$ (2 × 20 mL) and brine (30 mL), before being dried over $MgSO_4$, filtered and evaporated to dryness to give a crude orange solid. The crude mixture was recrystallised by slow evaporation of a saturated EtOAc solution to yield the title compound as a crystalline colourless solid (0.72 g, 1.12 mmol, 70%). **M.P.** > 350 °C. **^{1}H NMR** (700 MHz, $CDCl_3$) δ 8.11–8.05 (m, 2H, H_3), 7.60 (t, J = 7.7 Hz, 2H, H_2), 7.49–7.43 (m, 1H, H_1), 7.14–7.12 (m, 4H, H_8), 7.11–7.08 (m, 4H, H_{13}), 7.06–6.98 (m, 12H, H_9, H_{10}, H_{14} and H_{15}), 6.81–6.75 (m, 2H, H_{20}), 6.72–6.66 (m, 4H, H_{19}), 6.63–6.52 (m, 4H, H_{18}), 5.14 (s, 1H, H_5). **^{13}C NMR** (176 MHz, $CDCl_3$) δ 146.7 (C_6), 144.6 (C_4), 144.5 (C_7), 140.4 (C_{12}), 138.8 (C_{11}), 137.4 (C_{17}), 131.0 (C_{13}), 129.0 (C_8), 128.9 (C_2 or C_3), 128.8 (C_2 or C_3), 128.8 (C_{18}), 128.0 (C_9 or C_{14}), 127.4 (C_9 or C_{14}), 127.2 (C_1), 126.6 (C_{10}

or C_{15} or C_{20}), 126.5 (2C, C_{10} and/or C_{15} and/or C_{20}), 126.4 (C_{19}), 74.7 (C_{16}), 58.4 (C_5). **HRASAP-MS** *m/z* = 641.2834 $[M+H]^+$, calculated for $C_{49}H_{37}O^+$: 641.2839.

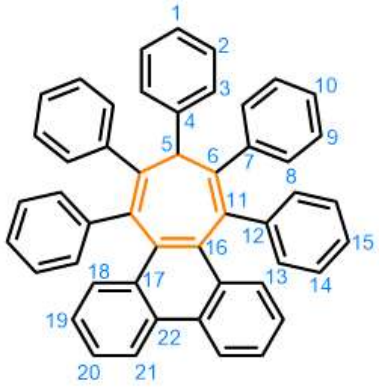

***sym*-phenPh$_5$C$_7$H**

***sym*-phenPh$_5$C$_7$H**: Phencyclone (0.71 g, 1.86 mmol), *sym*-triphenylcyclopropene (0.50 g, 1.86 mmol) and anhydrous *p*-xylene (30 mL) were added to a 100 mL round bottom flask. The mixture was deoxygenated (3 × freeze-pump-thaw cycles under argon) before being heated to reflux at 165 °C for 66 h. The mixture was allowed to cool to rt, producing a white precipitate. Me_2CO (20 mL) was added to induce further precipitation. The solid was isolated by filtration and washed with cold *p*-xylene (3 mL), then dried under vacuum to give ***sym*-phenPh$_5$C$_7$H** as a colourless solid (0.30 g, 0.48 mmol, 26%). Where possible, ^{1}H and ^{13}C NMR resonances have been assigned using bidimensional NMR techniques. However, some resonances could not be assigned because of overlap between peaks and the similarity of some nuclear environments. **M.P.** 318–321 °C. **^{1}H NMR** (700 MHz, 1:7 CD_2Cl_2–CS_2) δ 8.31 (d, *J* = 8.3, 1.2 Hz, 2H, H_{21}), 7.82 (d, *J* = 8.4, 1.2 Hz, 2H, H_{18}), 7.46 (d, *J* = 8.1, 1.2 Hz, 2H, H_3), 7.35–7.29 (m, 2H, H_{20}), 7.15–7.11 (m, 4H, $H_{8–10}$ or $H_{13–15}$), 7.11–7.08 (m, 2H, H_{19}), 7.08–7.04 (m, 11H, $H_{8–10}$ or $H_{13–15}$), 7.04–7.02 (m, 5H, $H_{8–10}$ or $H_{13–15}$), 6.63–6.58 (m, 2H, H_2), 6.56–6.53 (m, 1H, H_1), 5.21 (s, 1H, H_5). **^{13}C NMR** (176 MHz, 1:7 CD_2Cl_2–CS_2) δ 146.4, 143.1, 143.1, 140.0 (C_4), 137.3 (C_{16}), 133.8, 131.2, 130.3 (C_{17}), 130.3 (C_{18}), 129.9, 129.4 (C_{22}), 128.0, 127.8 (C_2), 127.3, 126.7, 126.0, 125.8 (C_{20}), 125.5 (C_1), 125.4 (C_{19}), 124.8 (C_3), 122.0 (C_{21}), 60.5 (C_5). **HRASAP-MS** *m/z* = 622.2685 $[M]^+$, calculated for $C_{49}H_{34}^+$: 622.2655.

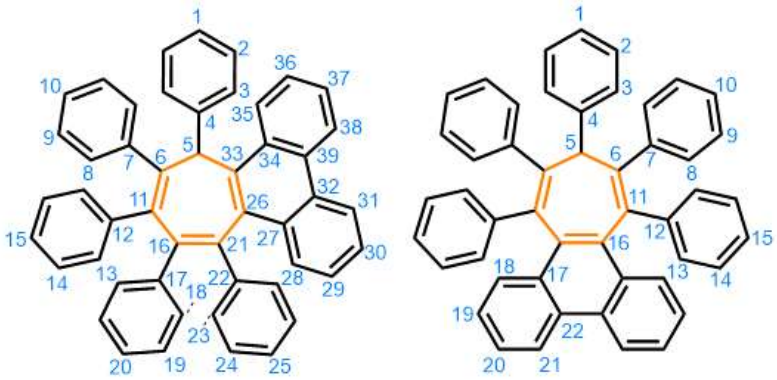

***asym*-phenPh$_5$C$_7$H** **_sym_-phenPh$_5$C$_7$H**

A 2:1 mixture of ***asym*-phenPh$_5$C$_7$H** and ***sym*-phenPh$_5$C$_7$H**: *sym*-Triphenylcyclopropene (297 mg, 1.10 mmol), phencyclone (424 mg, 1.10 mmol) and *p*-xylene (2.20 mL) were added to a microwave vial. The vial was sealed with a septum and the mixture degassed (3 × freeze-pump-thaw cycles under argon), then stirred for 12 h at 200 °C in a microwave reactor. Upon cooling, a precipitate formed, which was isolated by filtration, washing with cold *p*-xylene (3 × 5 mL). This solid was dried under vacuum to yield a light-yellow solid, which was recrystallised by slow evaporation of a 2:1 CH_2Cl_2–EtOH solution to give the first batch of a mixture of ***asym*-phenPh$_5$C$_7$H** and ***sym*-phenPh$_5$C$_7$H** as a colourless solid (262 mg, 0.421 mmol, 38%). Separately, the filtrate was concentrated under reduced pressure and the resulting residue was purified by column chromatography (Teledyne Isco CombiFlash Rf+ system, 40 g SiO_2, petroleum ether−EtOAc, gradient elution). A fraction containing a mixture of ***asym*-phenPh$_5$C$_7$H** and ***sym*-phenPh$_5$C$_7$H** was isolated, which was concentrated under reduced pressure yielding a colourless solid (84 mg, 0.14 mmol, 12%). A second fraction was isolated containing the desired products along with impurities. This fraction was further purified by recrystallisation by slow evaporation of a 5:3 CH_2Cl_2–EtOH solution, yielding a third batch of ***asym*-phenPh$_5$C$_7$H** and ***sym*-phenPh$_5$C$_7$H** as a colourless solid (181 mg, 0.29 mmol, 26%). The three batches were combined, giving ***asym*-phenPh$_5$C$_7$H** and ***sym*-phenPh$_5$C$_7$H** (527 mg, 0.76 mmol, 72% overall yield). **^{1}H NMR** spectroscopic analysis (Figure S11) showed the two isomers were present in a 2:1 ratio of ***asym*-phenPh$_5$C$_7$H** to ***sym*-phenPh$_5$C$_7$H**. This ratio corresponds to a statistical mixture, as ***asym*-phenPh$_5$C$_7$H** is present as a racemic mixture of *R*- and *S*-stereoisomers. **M.P.**: 288–290 °C. **HRASAP-MS** *m/z* = 622.2668 $[M]^+$, calculated for $C_{49}H_{34}^+$: 622.2655.

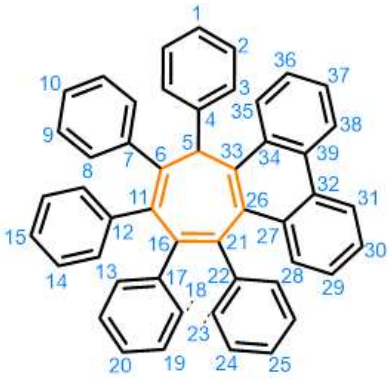

***asym*-phenPh$_5$C$_7$H:** A pure sample of ***sym*-phenPh$_5$C$_7$H** (300 mg, 0.48 mmol) was placed in a sealed 5 mL vial. The solid was heated using a heat gun until a melt formed (~320 °C), before being allowed to cool to rt and solidify. This heat/cool cycle was repeated five times. The resulting black solid was sonicated in Me_2CO (4 mL), and the supernatant was collected. Evaporation to dryness gave a crude yellow solid of a 6:1 mixture of *asym*:*sym* isomers. The crude solid was purified by column chromatography (Teledyne Isco CombiFlash Rf+ system**,** high performance 24 g SiO_2, hexanes). Pure factions were identified by TLC and combined. The title compound was isolated as a colourless crystalline solid of the ***asym*-phenPh$_5$C$_7$H** isomer (5 mg, 8.0 μM, 1.7%). The remaining solid was isolated as a mixture of the *asym:sym* isomers. **M.P.** 302–304 °C. **^{1}H NMR** (700 MHz, $CDCl_3$) δ 8.76 (dd, J = 8.4, 1.2 Hz, 2H, H_{28}), 8.64 (dd, J = 8.4, 1.2 Hz, 1H, H_{38}), 8.16 (d, J = 8.4 Hz, 2H, H_{31}), 7.96–7.92 (m, 1H, H_{35}), 7.66 (ddd, J = 8.2, 6.9, 1.2 Hz, 1H, H_{29}), 7.58 (d, J = 7.6 Hz, 2H, H_{18}), 7.57–7.53 (m, 1H, H_{30}), 7.49–7.45 (m, 1H, H_{37}), 7.28–7.25 (m, 3H, H_{19+36}), 7.24–7.21 (m, 1H, H_{20}), 7.13–7.08 (m, 3H, H_{13+15}), 7.02–6.95 (m, 5H, H_{8-10}), 6.88–6.84 (m, 1H, H_1), 6.79–6.76 (m, 1H, H_{25}), 6.75–6.72 (m, 2H, H_{25}), 6.72–6.69 (m, 2H, H_{23}), 6.69–6.66 (m, 2H, H_2), 6.36 (s, 1H, H_5), 5.70 (d, J = 7.7 Hz, 2H, H_3). **^{13}C NMR** (176 MHz, $CDCl_3$) δ 143.8 (C_6), 143.5 (C_{26}), 143.4 (C_{16}), 143.1 (C_{11}), 142.7 (C_{21}), 142.5 (C_{33}), 142.1 (C_4), 140.7 (C_{22}), 140.2 (C_{17}), 139.5 (C_{12}), 138.4 (C_7), 138.0 (C_{39}), 132.2 (C_{32}), 131.7 (C_{23}), 131.5 (C_{34}), 131.5 (C_{27}), 131.2 (C_3), 129.5 (C_{35}), 129.43 (C_{14}), 129.0 ($C_{8 \text{ or } 9 \text{ or } 10}$), 128.7 ($C_{36}$), 127.7 ($C_{8 \text{ or } 9 \text{ or } 10}$), 127.67 ($C_{15}$), 127.6 ($C_{30}$), 127.1 ($C_{18}$), 126.9 ($C_{29}$), 126.79 ($C_{24}$), 126.7 ($C_{13}$), 126.5 ($C_{20}$), 126.5 ($C_2$), 126.3 ($C_{8 \text{ or } 9 \text{ or } 10}$), 125.9 ($C_{19}$), 125.8 ($C_{37}$), 125.7 ($C_{25}$), 125.7 ($C_1$), 124.4 ($C_{31}$), 123.2 ($C_{28}$), 122.7 ($C_{38}$), 50.3 ($C_5$). **HR-ASAP MS** m/z = 622.2662 $[M]^+$, calculated for $C_{49}H_{34}^+$: 622.2655.

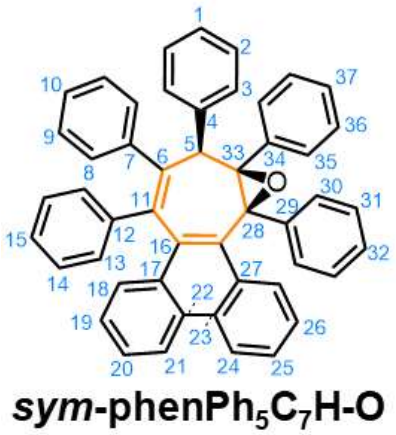

***sym*-phenPh$_5$C$_7$H-O:** An isomerically pure sample of ***sym*-phenPh$_5$C$_7$H** (400 mg, 0.64 mmol) was dissolved in $CHCl_3$ (20 mL) and cooled to 0 °C before adding a saturated aqueous solution of $NaHCO_3$ (0.5 mL). Solid *m*CPBA (800 mg, 4.6 mmol) was added. The biphasic mixture was heated to 70 °C and stirred for 22 h before being cooled to rt. A saturated aqueous solution of $NaHCO_3$ (30 mL) was added and the resulting biphasic mixture was stirred for 15 min. The reaction mixture was diluted with $CHCl_3$ (50 mL) and the organic layer was separated and washed with a saturated aqueous solution of $NaHCO_3$ (2 × 25 mL) and brine (5 mL), before being dried over $MgSO_4$, filtered and evaporated to dryness to give a crude yellow solid. The crude solid was purified by column chromatography (Teledyne Isco CombiFlash Rf+ system, 24 g SiO_2, hexanes–CH_2Cl_2, 0–25% gradient elution). The title compound was isolated as a colourless crystalline solid (30 mg, 0.048 mmol, 8%) **M.P.** > 350 °C. **^{1}H NMR** (700 MHz, $CDCl_3$) δ ^{1}H NMR (700 MHz, $CDCl_3$) δ 8.47–8.43 (m, 2H, H_{18+27}), 8.05 (d, J = 8.4 Hz, 1H, H_{24}), 8.00 (d, J = 8.4 Hz, 1H, H_{25}), 7.49–7.45 (m, 2H, H_{37}), 7.45–7.39 (m, 2H, H_{19+26}), 7.31–7.25 (m, 6H, $H_{3+20+25+32}$), 7.25–7.21 (m, 2H, H_{14}), 7.16–7.13 (m, 2H, H_8), 7.12–7.09 (m, 3H, H_{1+2}), 7.08–7.03 (m, 6H, $H_{9+10+13+15}$), 7.02–6.98 (m, 3H, H_{33+34}), 6.74–6.70 (m, 2H, H_{38}), 6.68–6.65 (m, 1H, H_{39}), 4.90 (s, 1H, H_5). **^{13}C NMR** (176 MHz, $CDCl_3$) δ 143.8 (C_{11}), 143.6 (C_{16}), 142.5 (C_6), 140.9 (C_{12}), 140.1 (C_{31}), 138.8 (C_{36}), 136.4 (C_7), 135.9 (C_4), 131.5 (C_{28}), 131.5 (C_{23}), 131.1 (C_{17}), 130.7(C_{22}), 129.9 (C_{29}), 129.6 (C_8), 129.5 (C_{21}), 129.4 (C_{20}), 128.6 (C_{37}), 128.2 (C_{24}), 127.9 (C_2), 127.9 ($C_{9\text{ or }10}$), 127.8 ($C_{9\text{ or }10}$), 127.6 (C_3), 127.6 (C_{15}), 127.2 (C_{14}), 127.1 (C_{13}), 126.9 (C_{38}), 126.9 (C_{33}), 126.9 (C_{34}), 126.7 (C_1), 126.5 (C_{25}), 126.4 (C_{19}), 126.3 (C_{26}), 125.6 (C_{32}), 125.4 (C_{39}), 122.5 (C_{18}), 122.2 (C_{27}), 78.9 (C_{35}), 66.3 (C_{30}), 58.0 (C_5). **HR-ESI MS** *m/z* = 639.2664 $[M+H]^+$, calculated for $C_{49}H_{35}O^+$: 639.2688.

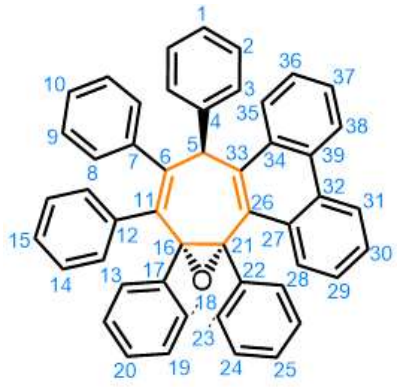

***asym*-phenPh$_5$C$_7$H-O**: The previously obtained 2:1 mixture of ***asym*-phenPh$_5$C$_7$H** and ***sym*-phenPh$_5$C$_7$H** (20 mg, 32 μmol) was dissolved in $CHCl_3$ (0.5 mL). Solid *m*CPBA (40 mg, 230 μmol) was added. The mixture was heated to 70 °C and stirred for 22 h before being cooled to rt. A saturated aqueous solution of $NaHCO_3$ (2 mL) was added and the resulting biphasic mixture was stirred for 15 min. The reaction mixture was diluted with $CHCl_3$ (5 mL) and the organic layer was separated and then washed with a saturated aqueous solution of $NaHCO_3$ (2 × 5 mL) and brine (5 mL), before being dried over $MgSO_4$, filtered and evaporated to dryness to give a crude off-white solid. The crude mixture was purified by column chromatography (Teledyne Isco CombiFlash Rf+ system, 24 g SiO_2, hexanes–CH_2Cl_2, 0–30% gradient elution). The title compound was isolated as a colourless crystalline solid (5 mg, 8 μmol, 25%). **M.P.** > 350 °C. **^{1}H NMR** (700 MHz, $CDCl_3$) δ 8.82 (dd, J = 8.4, 1.2 Hz, 1H, H_{38}), 8.72 (d, J = 8.3 Hz, 1H, H_{31}), 8.22 (dd, J = 8.3, 1.2 Hz, 1H, H_{28}), 8.16 (d, J = 8.4 Hz, 1H, H_{35}), 7.76–7.67 (m, 3H, H_{3+37}), 7.61 (ddd, J = 8.3, 6.9, 1.3 Hz, 1H, H_{36}), 7.57 (ddd, J = 8.3, 6.9, 1.3 Hz, 1H, H_{29}), 7.44–7.34 (m, 3H, H_{1+2}) 7.34–7.28 (m, 1H, H_{10}), 7.10–6.94 (m, 12H, $H_{8+9+13+14+23+24}$), 6.91 (tt, J = 7.4, 1.3 Hz, 1H, H_{15}), 6.84–6.75 (m, 1H, H_{25}), 6.78–6.64 (m, 6H, $H_{18+19+20,30}$), 6.41 (s, 1H, H_5). **^{13}C NMR** (176 MHz, $CDCl_3$) δ 145.8 (C_{11}), 144.4 (C_{33}), 143.2 (C_4), 140.1 (C_{22}), 139.5(C_{17}), 139.1 (C_7), 138.9 (C_6), 137.9 (C_{27}), 135.6 (C_{32}), 132.5 (C_{39}), 132.3 (C_8), 132.3 (C_9), 131.3 (C_{14}), 130.9 (C_{26}), 130.9 (C_{34}), 130.5 (C_{12}), 128.9 (C_{24}), 128.8 (C_3), 128.7 (C_{13}), 128.2 ($C_{18\text{ or }20}$), 128.1 (C_2), 127.8 (C_{28}), 127.4 (C_{36}), 127.1 (C_{23}), 126.9 (C_{37}), 126.83 (C_{15}), 126.8 (C_{10}), 126.6 (C_1), 126.5 ($C_{20\text{ or }18}$), 126.5 (C_{25}), 126.4 (C_{29}), 126.23 (C_{19+37}), 124.7 (C_{30}), 123.3 (C_{35}), 122.6 (C_{38}), 122.5(C_{31}) 74.2 (C_{16}), 71.9 (C_{21}), 50.5 (C_5). **HR-ESI MS** m/z = 639.2671 $[M+H]^+$, calculated for $C_{49}H_{35}O^+$: 639.2688.

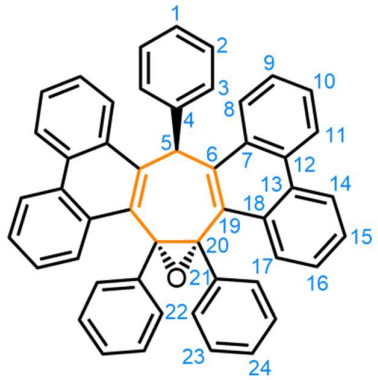

***sym*-phen$_2$Ph$_3$C$_7$H-O**

***sym*-phen$_2$Ph$_3$C$_7$H-O**: **Ph$_7$C$_7$H-O** (55 mg, 90 µmol) and I_2 (51 mg, 20 µmol, 2.1 equiv) were added to a 7 mL quartz tube, which was fitted with a septum and purged with $N_{2(g)}$. Anhydrous THF (6 mL) was deoxygenated (3 × freeze-pump-thaw cycles under argon). The mixture was sparged with $N_{2(g)}$ for 10 min followed by the addition of propylene oxide (0.5 mL) and sparging with $N_{2(g)}$ for a further 5 min. The reaction mixture was then irradiated by 4 × 9W 254 nm bulbs for 3 h, while being sparged with $N_{2(g)}$. A saturated aqueous solution of $Na_2S_2O_3$ (2 mL) was added and the resulting biphasic mixture was stirred for 2 min. The reaction mixture was diluted with $CHCl_3$ (5 mL) and the organic layer was separated and then washed with a saturated aqueous solution of $Na_2S_2O_3$ (2 × 5 mL) and brine (5 mL), before being dried over $MgSO_4$, filtered and evaporated to dryness to give a dark solid. The crude solid was purified by column chromatography (Teledyne Isco CombiFlash Rf+ system, 12 g SiO_2, hexanes–CH_2Cl_2, 0–30% gradient elution). The title compound was isolated as a colourless crystalline solid (54 mg, 90 µmol, >99%). **M.P.** > 350 °C. **^{1}H NMR** (600 MHz, $CDCl_3$) δ 8.81–8.77 (m, 2H, H_8), 8.73–8.69 (m, 2H, H_{14}), 8.62–8.58 (m, 2H, H_{11}), 8.54–8.50 (m, 2H, H_{17}), 7.91 (s, 1H, H_5), 7.75–7.70 (m, 2H, H_{16}), 7.69–7.65 (m, 2H, H_{17}), 7.56–7.51 (m, 6H, H_{2+9+10}), 7.34–7.30 (m, 2H, H_3), 7.30–7.26 (m, 1H, H_1), 7.21–7.17 (m, 4H, H_{22}), 6.87–6.82 (m, 2H, H_{24}), 6.82–6.77 (m, 4H, H_{23}).**^{13}C NMR** (151 MHz, $CDCl_3$) δ 141.8 (C_6), 138.2 (C_4), 137.4 (C_{21}), 133.4 (C_{18}), 133.2 (C_{13}), 131.4 (C_{12}), 130.9 (C_{19}), 130.9 (C_7), 129.9 (C_9), 129.4 (C_{22}), 128.5 (C_3), 127.9 (C_{16}), 127.9 (C_8), 127.9 (C_2), 126.9 (C_{24}), 126.9 (C_{10}), 126.8 (C_{23}), 126.7 (C_{15}), 126.7 (C_1), 124.7 (C_{17}), 123.4 (C_{14}), 122.6 (C_{11}), 71.3 (C_{20}), 44.0 (C_5). **HRMS-ASAP** *m/z* = 637.2505 $[M+H]^+$, calculated for $C_{49}H_{33}O^+$: 637.2531.

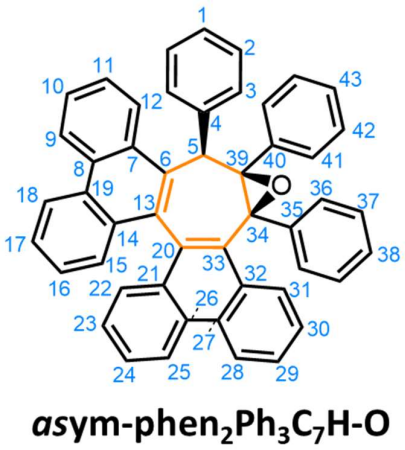

***asym*-phenPh$_5$C$_7$H-O: *sym*-phenPh$_5$C$_7$H-O** (30 mg, 46 µmol) and iodine (13 mg, 51 µmol, 1.1 equiv) were added to a 10 mL quartz tube, which was fitted with a septum and sparged with $N_{2(g)}$. Anhydrous THF (8 mL) was degassed through 3 × freeze-pump-thaw cycles and added. The mixture was sparged with $N_{2(g)}$ for 10 min followed by the addition of propylene oxide (1 mL) and sparging with $N_{2(g)}$ for a further 5 min. The reaction mixture was then irradiated by 4 × 9W 254 nm bulbs for 2 h, while being sparged with $N_{2(g)}$. A saturated aqueous solution of $Na_2S_2O_3$ (5 mL) was added and the resulting biphasic mixture was stirred for 2 min. The reaction mixture was diluted with $CHCl_3$ (5 mL) and the layers were separated. The organic layer was washed with a saturated aqueous solution of $Na_2S_2O_3$ (2 × 10 mL) and brine (10 mL), before being dried over $MgSO_4$, filtered and evaporated to dryness to give a yellow solid. The crude solid was washed with MeOH (5 mL) and Et_2O (5 mL) to afford the title compound as a colourless crystalline solid (29 mg, 45 µmol, 98%). **^{1}H NMR** (600 MHz, $CDCl_3$): δ 8.90 (d, J = 8.4 Hz, 1H, H_{14}), 8.88 (d, J = 8.4 Hz, 1H, H_{11}), 8.56–8.51 (m, 2H, $H_{25,28}$), 8.15–8.11 (m, 1H, H_{31}), 7.77–7.69 (m, 3H, $H_{8,15,17}$), 7.67–7.63 (m, 1H, H_{10}), 7.54–7.48 (m, 2H, $H_{24,29}$), 7.48–7.44 (m, 1H, H_{16}), 7.44–7.40 (m, 1H, H_{30}), 7.40–7.36 (m, 1H, H_9), 7.21–7.17 (m, 1H, H_{23}), 7.12–7.08 (m, 3H, $H_{3,22}$), 7.07–7.03 (m, 2H, H_{36}), 7.03–6.53 (m, 8H, $H_{37,38,41–43}$), 6.52 (t, J = 7.2 Hz, H_1), 6.49–6.44 (m, 2H, H_2), 5.88 (s, 1H, H_5). **^{13}C NMR** (151 MHz, $CDCl_3$): δ 140.3 (C_6), 138.8 (C_{35}), 137.7 (C_7), 136.8 (C_4), 134.3 (C_{19}), 134.2 (C_{20}), 133.0 (C_{18}), 132.5 (C_{13}), 131.3 (C_{33}), 130.6 (C_{26}), 130.3 (C_{27}), 130.1 ($C_{21/40}$), 130.1 ($C_{40/21}$), 129.8 ($C_{12/32}$), 129.8 ($C_{32/12}$), 129.1 (C_{22}), 128.1 (C_{17}), 128.0 (C_3), 127.5 ($C_{41/42/43}$), 127.4 ($C_{42/41/43}$), 127.3 ($C_{43/42/41}$), 127.2 (C_9), 127.0 (C_{31}), 126.8 (C_{10}), 126.8 ($C_{15/16}$), 126.8 ($C_{16/15}$), 126.8 ($C_{30/38}$), 126.8 ($C_{38/30}$), 126.6 (C_{37}), 126.6 (C_{36}), 126.6 ($C_{24/29}$), 126.6 ($C_{29/24}$), 126.5 (C_2), 126.1 (C_{23}), 125.0 (C_1), 124.3 (C_8), 123.3 (C_{14}), 123.2 (C_{11}), 122.6 ($C_{25/28}$), 122.4 ($C_{28/25}$), 79.9 (C_{39}), 66.9 (C_{34}), 49.0 (C_5). **HRMS-ASAP** *m/z* = 637.2538 $[M+H]^+$, calculated for $C_{49}H_{33}O^+$: 637.2531

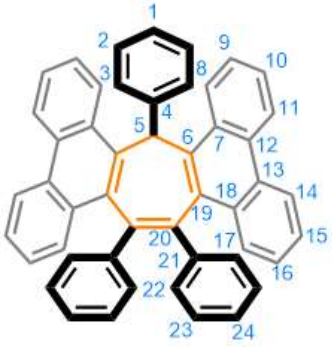

***sym*-phen$_2$Ph$_3$C$_7$H**

***sym*-phen$_2$Ph$_3$C$_7$H**: To a stirred solution of ***sym*-phen$_2$Ph$_3$C$_7$H-O** (50 mg, 0.079 mmol) in anhydrous THF (3 mL) was added a solution of $LiAlH_4$ (1 M in THF, 0.40 mL, 0.40 mmol) under an $N_{2(g)}$ atmosphere, and the mixture was heated to refluxed for 48 h. The mixture was then allowed to cool to rt and another aliquot of $LiAlH_4$ (1 M in THF, 0.40 mL, 0.40 mmol) was added. The mixture was refluxed for an additional 24 h. Upon cooling to rt, the reaction was quenched by the dropwise addition of a saturated aqueous solution of NH_4Cl (10 mL) and extracted with CH_2Cl_2 (5 × 5 mL). The combined organic extracts were dried over $MgSO_4$, filtered and evaporated to dryness to give a pale-yellow solid. The crude material was washed with cold Et_2O (3 × 5 mL) to yield the title compound as a colourless solid (23 mg, 0.037 mmol, 47%). **M.P.** > 350 °C. **^{1}H NMR** (600 MHz, $CDCl_3$) δ 8.67 (d, *J* = 8.2 Hz, 2H, H_{11}), 8.56 (d, *J* = 8.4 Hz, 2H, H_8), 8.54 (d, *J* = 8.3 Hz, 2H, H_{14}), 8.17 (d, *J* = 8.2 Hz, 2H, H_{17}), 7.72–7.66 (m, 2H, H_9), 7.66–7.60 (m, 2H, H_{10}), 7.49–7.43 (m, 3H, $H_{5,15}$), 7.42–7.37 (m, 2H, H_{16}), 7.13 (d, J = 7.7 Hz, 2H, H_3), 7.06–7.00 (m, 1H, H_1), 6.99–6.89 (m, 4H, $H_{2,24}$), 6.86–6.74 (m, 8H, $H_{22,23}$). **^{13}C NMR** (151 MHz, $CDCl_3$): δ 142.3 (C_4), 142.2 (C_6), 140.6 ($C_{20/21}$), 140.4 ($C_{21/20}$), 135.5 (C_{19}), 132.1 (C_{18}), 131.9 (C_7), 131.4 (C_{22}), 130.6 (C_{12}), 130.3 (C_{13}), 129.2 (C_{17}), 128.6 (C_2), 127.7 (C_9), 127.4 (C_{23}), 127.1 (C_3), 126.6 (C_{24}), 126.5 (C_{10}), 126.1 (C_{16}), 126.1 (C_1), 126.0 (C_{15}), 123.6 (C_8), 123.4 (C_{11}), 122.7 (C_{14}), 43.3 (C_5). **HRMS-ASAP** *m/z* = 621.2567 $[M+H]^+$, calculated for $C_{49}H_{33}^+$: 621.2582.

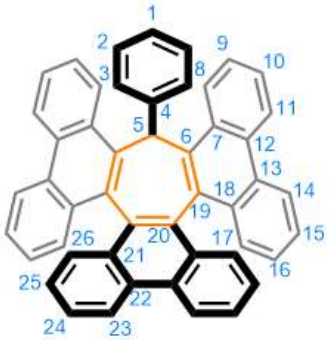

***sym*-phen$_3$PhC$_7$H**

***sym*-phen$_3$PhC$_7$H**: ***sym*-Phen$_2$Ph$_3$C$_7$H** (15 mg, 24 μmol) and I_2 (6.5 mg, 25 μmol) were added to a 4 mL quartz cuvette, which was fitted with a septum and sparged with $N_{2(g)}$. Anhydrous THF (1.2 mL) was deoxygenated (5 × freeze-pump-thaw cycles) and added to the cuvette. The mixture was sparged with $N_{2(g)}$ for 10 min followed by the addition of propylene oxide (0.1 mL, 2.1 mmol) and sparging with $N_{2(g)}$ for a further 5 min. The reaction mixture was then irradiated by 4 × 9W 254 nm bulbs for 15 min, while being sparged with $N_{2(g)}$. A saturated aqueous solution of $Na_2S_2O_3$ (5 mL)

was added and the resulting biphasic mixture was stirred for 2 min. The reaction mixture was diluted with $CHCl_3$ (5 mL) and the organic layer was separated and then washed with a saturated aqueous solution of $Na_2S_2O_3$ (2 × 5 mL) and brine (5 mL), before being dried over $MgSO_4$, filtered and evaporated to dryness to give a colourless solid (12 mg, 20 μmol, 81%). **M.P.** > 350°C. **^{1}H NMR** (500 MHz, $CDCl_3$, 313 K) δ 8.77 (d, *J* = 8.3 Hz, 2H, H_{11}), 8.70 (d, *J* = 8.3 Hz, 2H, H_8), 8.62 (d, *J* = 8.4 Hz, 2H, H_{14}), 8.54 (d, *J* = 8.4 Hz, 2H, H_{23}), 7.77–7.71 (m, 2H, H_9), 7.71–7.66 (m, 2H, H_{10}), 7.66–7.61 (m, 2H, H_{17}), 7.53 (s, 1H, H_5), 7.51–7.44 (m, 4H, $H_{15,24}$), 7.29–7.21 (m, 4H, $H_{16,26}$), 7.21–7.15 (m, 2H, H_{25}), 6.75 (d, *J* = 7.7 Hz, 2H, H_3), 6.36 (t, *J* = 7.4 Hz, 1H, H_1), 6.27–6.20 (m, 2H, H_2). **^{13}C NMR** (126 MHz, $CDCl_3$, 313 K): δ 144.3 (C_6), 140.2 (C_4), 135.1 ($C_{19/20}$), 132.9 (C_{18}), 132.0 ($C_{20/19}$), 131.5 (C_7), 130.8 (C_{12}), 130.6 (C_{21}), 130.0 (C_{22}), 129.5 (C_{26}), 129.4 (C_{13}), 128.9 (C_{17}), 127.5 (C_9), 126.7 (C_{10}), 126.6 (C_2), 126.5 (C_{16}), 126.3 (C_{24}), 126.2 (C_{15}), 125.9 (C_{25}), 125.4 (C_3), 124.7 (C_1) 123.8 (C_8), 123.6 (C_{11}), 122.7 (C_{14}), 122.4 (C_{23}), 43.3 (C_5). **HRMS-ASAP** *m/z* = 619/2435 $[M+H]^+$, calculated for $C_{49}H_{31}^+$: 619.2426.

3.4.2. Variable Temperature NMR Spectroscopy

We performed VT NMR measurements to determine the energy barrier to rotation of phenyl rings in ***sym*-phenPh$_5$C$_7$H**. As we were not able to unambiguously assign all ^{13}C resonances based on 2D NMR spectra, we have assigned (Figure 3.6) the phenyl group that experiences the highest energy barrier to rotation as ring c by analogy to our investigation of **Ph$_7$C$_7$H** reported previously.[37] VT ^{13}C NMR spectra were acquired to facilitate analysis using a two-spin system model in the WinDNMR[4] software package. In order to obtain a solution of ***sym*-phenPh$_5$C$_7$H** with a low freezing point and of sufficiently high concentration (20 mg in 0.8 mL) for ^{13}C NMR analysis, a mixture of CS_2 (0.7 mL) with CD_2Cl_2 (0.1 mL) was used as solvent. A series of spectra ranging from 24 to –98 °C was recorded.

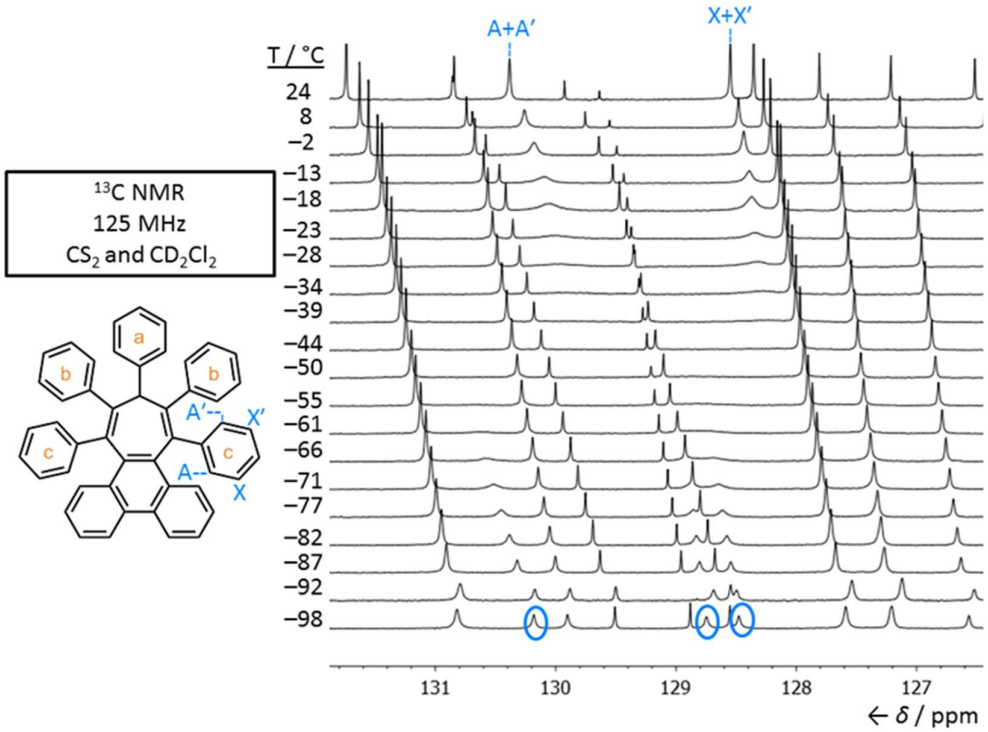

Figure 3.6. Partial ^{13}C VT NMR spectra of ***sym*-phenPh$_5$C$_7$H**. Peaks corresponding to the carbon pairs A/A′ and X/X′ are observed as individual, averaged signals in the fast exchange regime, but appear as distinct signals at low temperature in the slow exchange regime. Only three of the four signals can be distinguished at low temperature on account of overlapping signals; however, only one pair is needed to perform lineshape analysis.

Analysis of the ^{13}C spectra reveals that within the temperature range studied, signals corresponding to ring c carbons broaden, merge into the baseline, and then re-emerge as four separate peaks as the temperature is decreased. There are two pairs of resonances in slow exchange below –60 °C. Only three resonances can be observed as distinct peaks as the fourth overlaps with other signals. In order to determine which of the three re-emerged peaks correspond to a pair of exchanging sites, a HSQC experiment was performed at –98 °C (Figure 3.7). Both ^{1}H NMR and ^{13}C NMR spectra had been recorded from 24 to −98 °C.

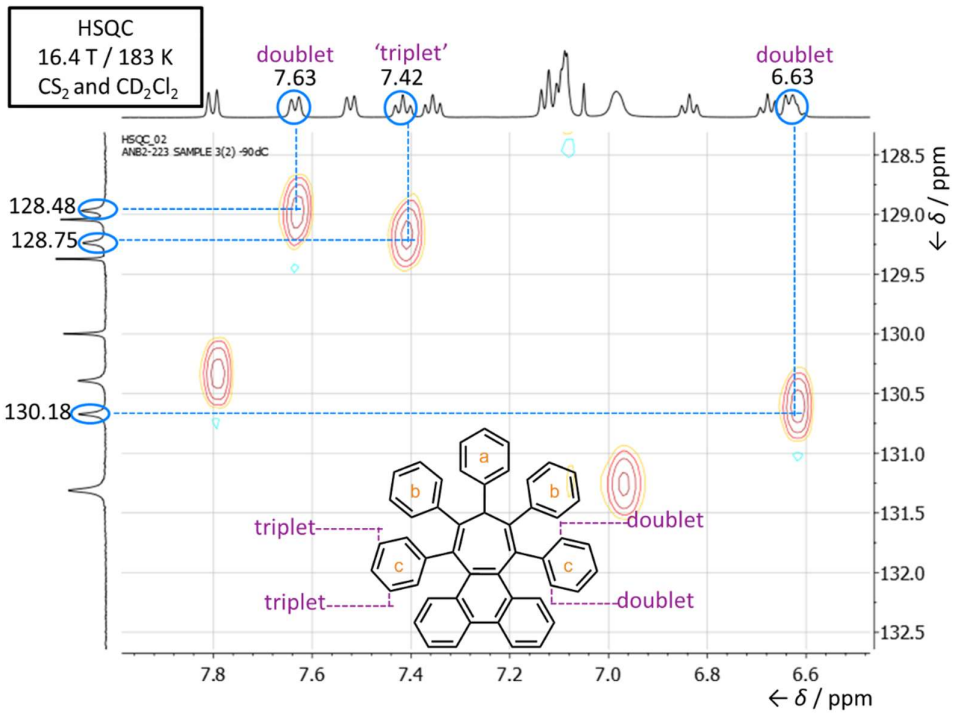

Figure 3.7. Partial HSQC NMR spectrum of ***sym*-phenPh$_5$C$_7$H** recorded at –98 °C. Correlations are highlighted between the ^{13}C signals observed to be in slow exchange by VT NMR and the corresponding ^{1}H signals. Inset: based on the *J* coupling patterns, the different positions of ring c can be distinguished.

Analysis of the HSQC spectrum reveals that the three ^{13}C signals that have re-emerged from the baseline correlate with two doublets and a signal that appears as an apparent triplet in the ^{1}H NMR. The signals correlating to the two doublets must be the pair of exchanging nuclear environments. The doublet at 6.63 ppm looks broad, but this is due to peaks under the doublet and this has been confirmed by integration. Thus, we can assign (Figure 3.8) the labels A+A′ to these resonances.

We selected eight spectra for further analysis, choosing temperatures close to the transition of ring c resonances from fast to the slow exchange regimes. Lineshape analysis[ii] was performed to derive rate constants by comparison to model spectra produced using WinDNMR (see section 2.4.2 for further details).[38]

[ii] Non-linear behaviour of data points collected can be attributed to (i) uncertainty/error in the temperature at which spectra were recorded; (ii) insufficient data points; and (iii) human error associated with comparing simulated rates to experimental rates.

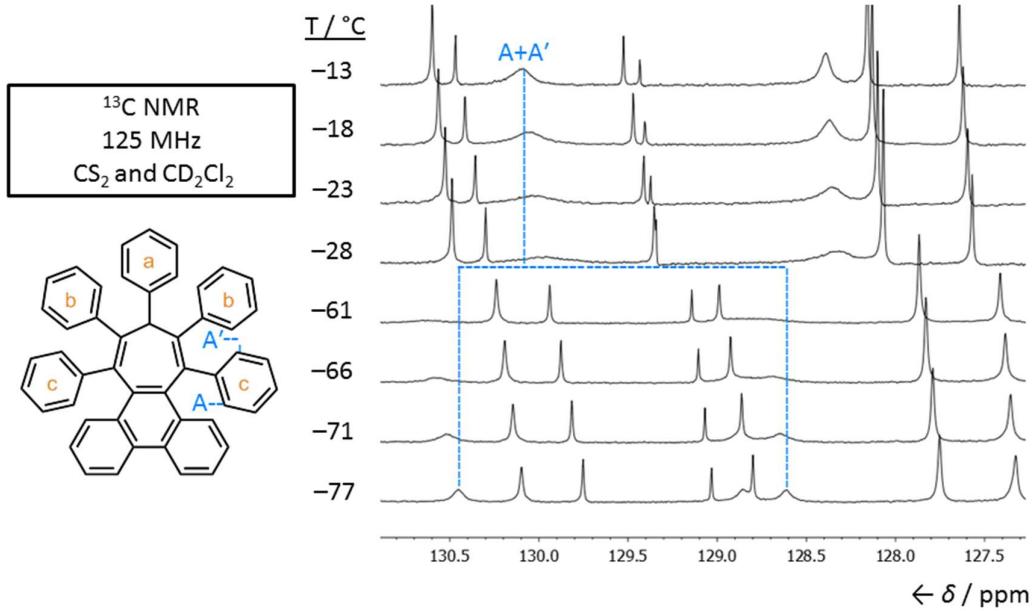

Figure 3.8. ^{13}C VT NMR spectra of ***sym*-phenPh$_5$C$_7$H** used for lineshape analysis. The dashed blue lines illustrate the resolution of a single peaks into a pair of peaks as temperature decreases.

Activation energy barriers for the rotation of ring c were calculated for each of the eight temperatures using equation 3.1:

$$\Delta G^{\ddagger} = -RT \ln \frac{k_r h}{k_B T}$$

Equation 3.1. A variation of the Eyring equation, where k_r is the measured rate constant, k_B is the Boltzmann constant, T is temperature, h is Planck's constant, and R is the ideal gas constant.

Table 3.3. Calculated activation energies ($\Delta G^{\ddagger}$) for the rotation of ring c of ***sym*-phenPh$_5$C$_7$H**.

Entry	Temperature / K (± 0.64)	$\Delta G^{\ddagger}$ / kJ mol^{-1}
1	260.4	43.3
2	255.1	43.4
3	249.7	43.2
4	244.4	43.0
5	212.5	41.8
6	207.2	42.0
7	201.9	41.8
8	196.6	41.8

A line was fitted (Figure 3.9) to a plot of $\Delta G^{\ddagger}$ vs T. The slope of the line corresponds to $-\Delta S^{\ddagger}$ and the y-axis intercept to $\Delta H^{\ddagger}$. The entropy of activation $\Delta S^{\ddagger}$ was calculated to be –27.9 J·mol^{-1}·K^{-1} and enthalpy of activation $\Delta H^{\ddagger}$ was calculated to be 36.2 kJ·mol^{-1}.

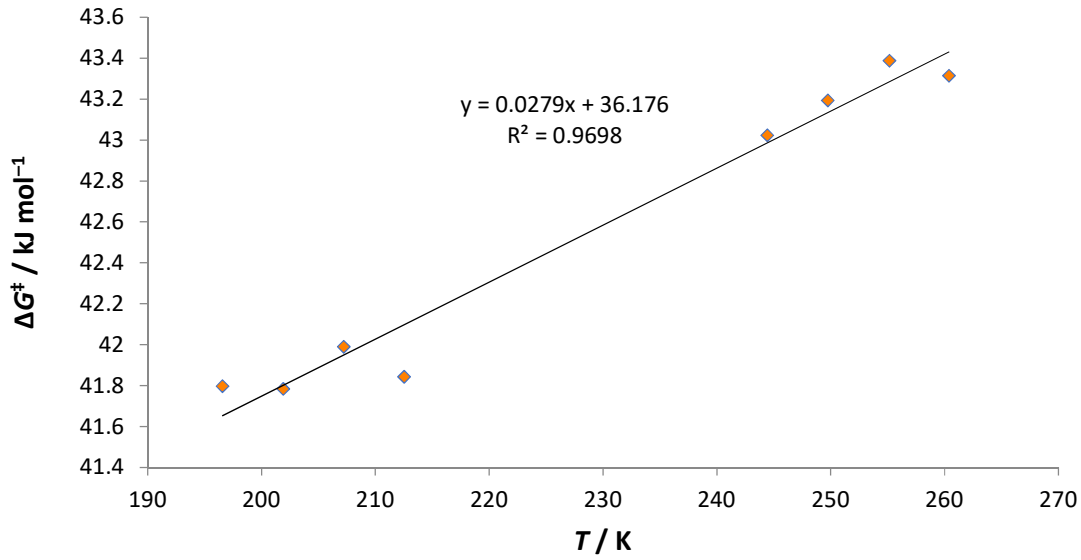

Figure 3.9. A plot of the experimentally measured free energy of activation $\Delta G^{\ddagger}$ for rotation of ring c of ***sym*-phenPh$_5$C$_7$H** as a function of temperature.

We also performed VT NMR measurements to determine the energy barrier to rotation of phenyl rings in **Ph$_7$C$_7$H-O**, using the same approach. Based on 2D NMR, we were able to assign ring d (Figure 3.10) as the phenyl group that experiences the highest energy barrier to rotation. A 20 mg sample of **Ph$_7$C$_7$H-O** was dissolved in a mixture of CS_2 (0.7 mL) with CD_2Cl_2 (0.1 mL) as the NMR solvent and a series of ^{13}C NMR spectra ranging from 24 to −87 °C was recorded.

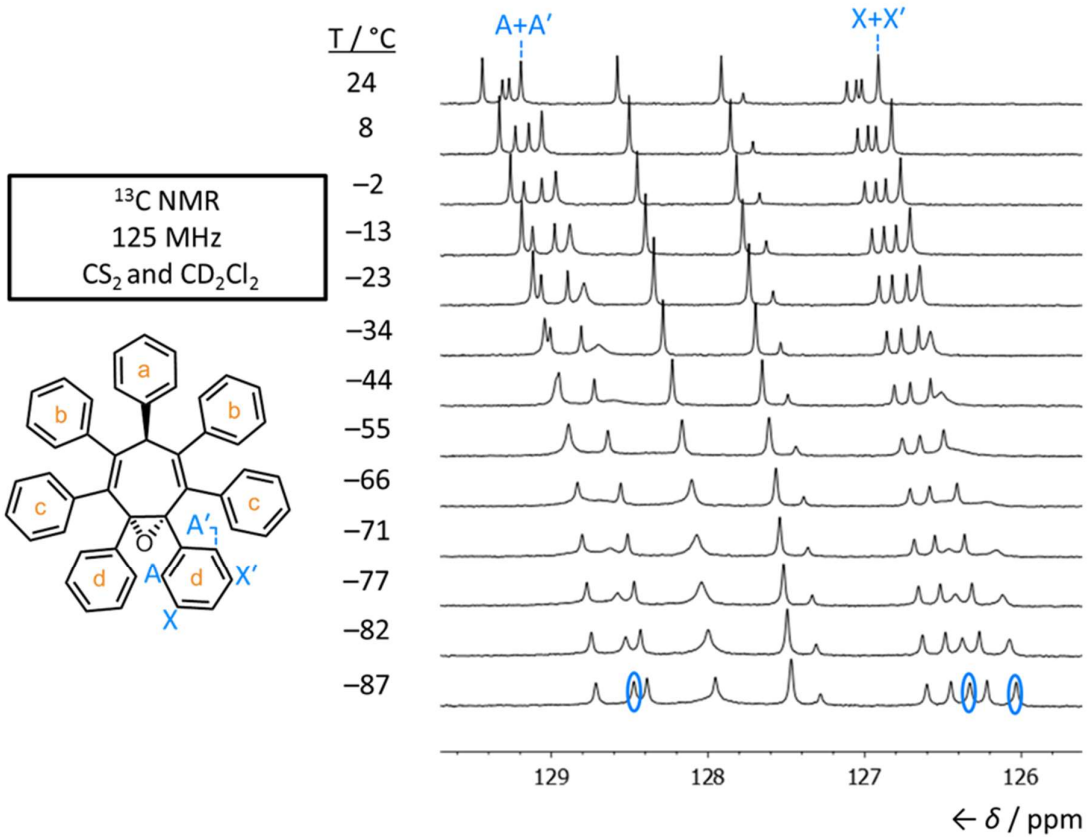

Figure 3.10. Partial ^{13}C VT NMR spectra of **Ph$_7$C$_7$H-O**. Peaks corresponding to the carbon pairs A/A′ and X/X′ are observed as individual, averaged signals in the fast exchange regime, but appear as distinct signals at low temperature in the slow exchange regime. Only three of the four signals can be distinguished at low temperature on account of overlapping signals; however, only one pair is needed to perform lineshape analysis.

Analysis of the ^{13}C NMR spectra reveals that, within the temperature range studied, signals corresponding to ring d carbons broaden, merge into the baseline, and then re-emerge as four separate peaks as the temperature is decreased made up of two pairs of resonances in slow exchange. Only three resonances are observed as distinct peaks because the fourth overlaps with other signals. In order to determine which of the three re-emerged peaks are a pair a HSQC spectrum was acquired (Figure 3.10) at –87 °C. Both ^{1}H NMR and ^{13}C NMR spectra had been recorded from 24 °C to –87 °C.

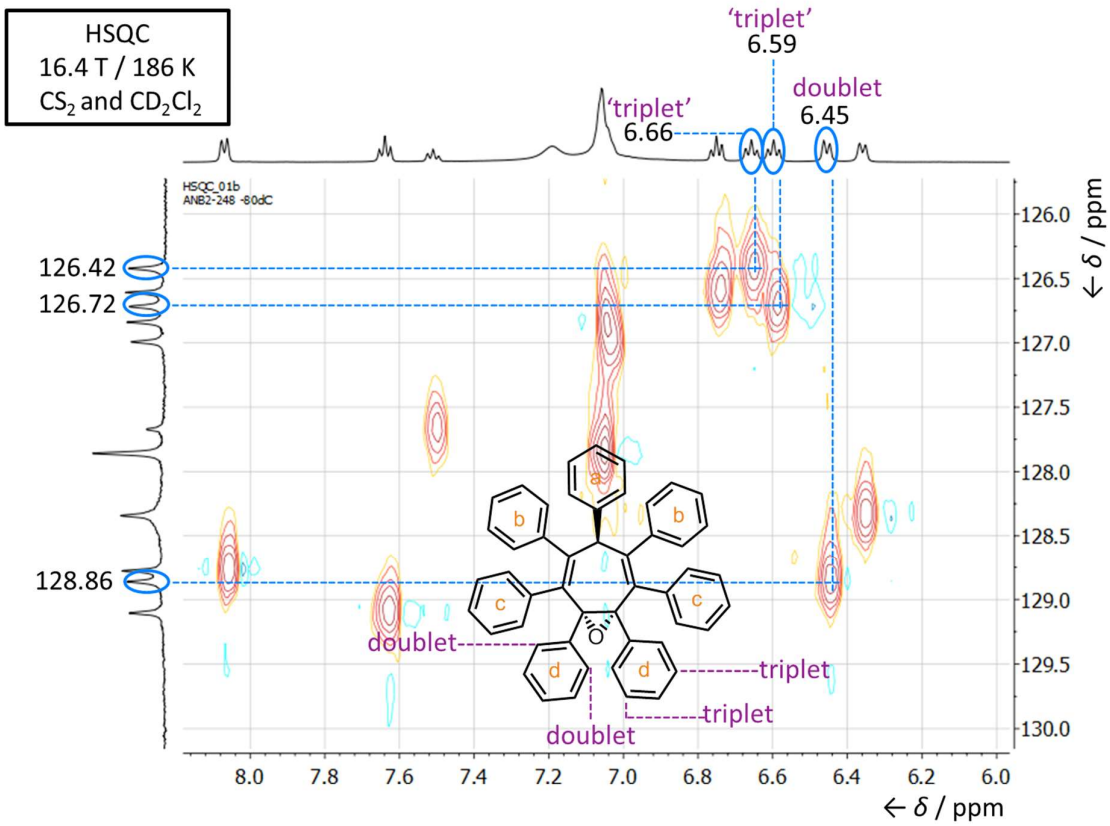

Figure 3.11. Partial HSQC NMR spectrum of **Ph$_7$C$_7$H-O** recorded at –87 °C. Correlations are highlighted between the ^{13}C signals observed to be in slow exchange by VT NMR (Figure 3.10) and the corresponding ^{1}H signals. Inset: based on the *J* coupling patterns, the different positions of ring d can be distinguished.

By matching the *J* coupling patterns of the ^{1}H signals following the approach described above for ***sym*-phenPh$_5$C$_7$H**, we can assign (Figure 3.12) the ^{13}C signals of **Ph$_7$C$_7$H-O** corresponding to X and X′. We selected five ^{13}C NMR spectra for further analysis, choosing temperatures close to the transition of ring d resonances from fast to the slow exchange regimes. As above, line shape analysis was performed to derive rate constants by comparison to model spectra produced using WinDNMR and activation energy barriers were calculated using equation 1.

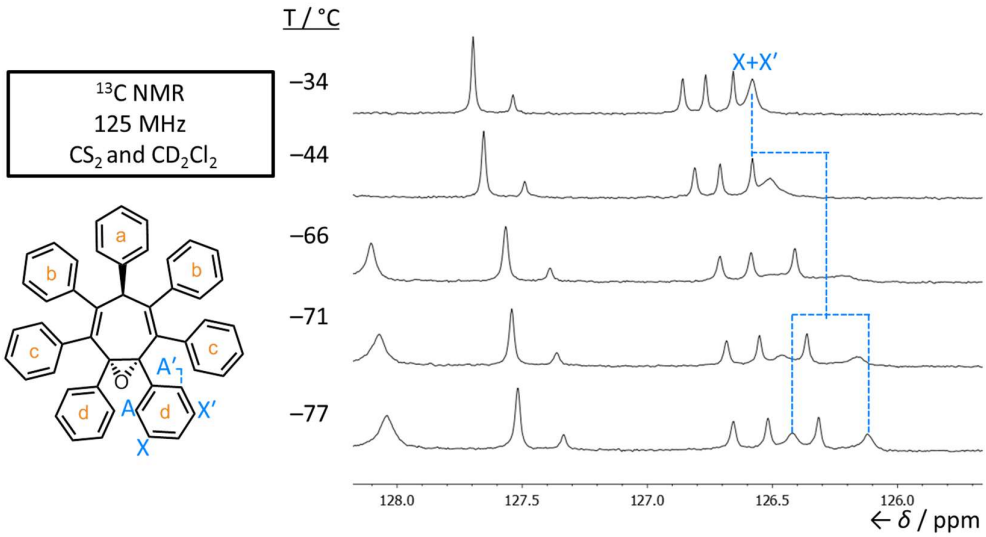

Figure 3.12. ^{13}C VT NMR spectra of **Ph$_7$C$_7$H-O** used for lineshape analysis. The dashed blue lines illustrate the resolution of a single peak into a pair of peaks as temperature decreases.

Table 3.4. Calculated activation energies ($\Delta G^{\ddagger}$) for the rotation of ring d of **Ph$_7$C$_7$H-O**.

Entry	Temperature / K (± 0.64)	$\Delta G^{\ddagger}$ / kJ mol^{-1}
1	239.2	42.2
2	228.5	42.3
3	207.2	42.7
4	201.9	42.9
5	196.2	43.6

A line was fitted (Figure 3.9) to a plot of $\Delta G^{\ddagger}$ vs T. The entropy of activation $\Delta S^{\ddagger}$ was measured to be +27.0 J mol^{-1} K^{-1} and enthalpy of activation $\Delta H^{\ddagger}$ was measured as 48.5 kJ·mol^{-1}.

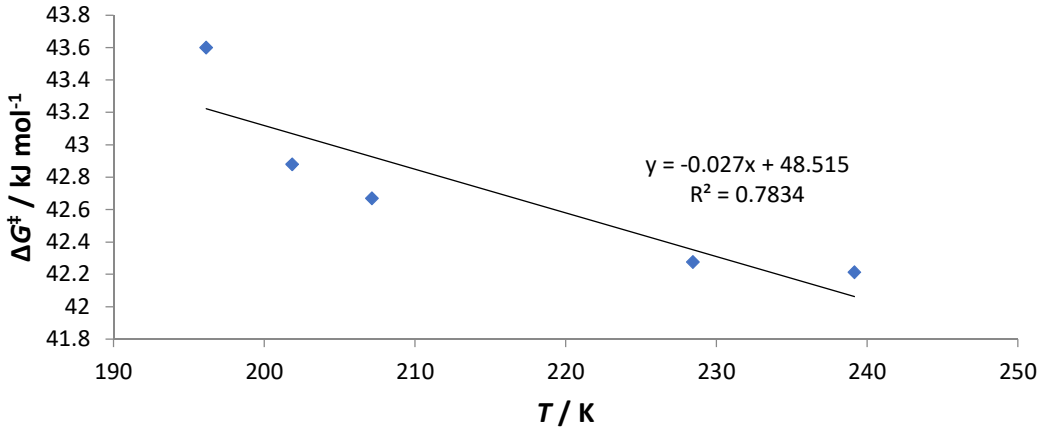

Figure 3.13. A plot of the experimentally measured free energy of activation $\Delta G^{\ddagger}$ for rotation of ring d of **Ph$_7$C$_7$H-O** as a function of temperature.

3.4.3. X-Ray Crystallographic Analysis

Analysis of all crystal structures and their packing are shown (Figure 3.14–3.26) with the crystal system, space group, unit cell parameters, bond lengths, bond angles and dihedral angles reported below. Direct comparisons of important bond lengths and centroid-centroid distance between the phenyl ring bound to the tertiary sp^3-centre and the opposite phenyl ring are outlined in Table 3.5 below. Notably, the C_5–C_6 distance is 1.47–1.49 Å for the triene compounds but 1.50–1.51 Å for the epoxides. This increase of 2–4 pm is characteristic of the increased single–bond character in the nonconjugated epoxides.

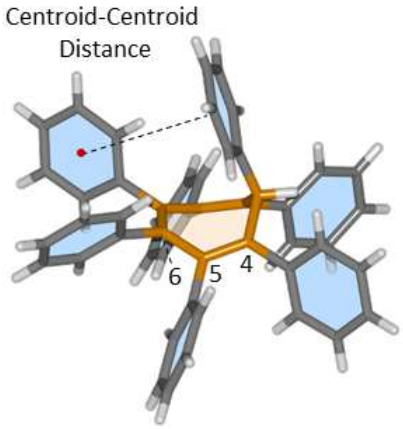

Figure 3.14. Solid-state structure of **Ph_7C_7H** viewed side-on to the seven-membered ring showing the centroid-centroid distance on the two rings associated with through-space dimers.

Table 3.5. Summarised bond lengths and centroid distances for the molecular rotors.

Rotor	Centroid-Centroid distance (Å)	C_4-C_5 distance (Å)	C_5-C_6 distance (Å)
C_7Ph_7H-O	5.21	1.34	1.50
sym-phenPh_5C_7H-O	4.99	1.36	1.51
asym-phenPh_5C_7H-O	5.07	1.34	1.50
C_7Ph_7H	5.15	1.35	1.47
sym-phenPh_5C_7H	4.57	1.35	1.49
asym-phenPh_5C_7H	5.02	1.35	1.49
sym-$phen_2Ph_3C_7H$-O	5.23	1.36	1.51

Analysis of the single-crystal X-ray structure of **Ph_7C_7H** has been reported previously.[37]

3.4.3.1. Ph_7C_7H-O

Crystals of **Ph_7C_7H-O** suitable for X-ray diffraction were grown by slow cooling of a saturated MeCN solution.

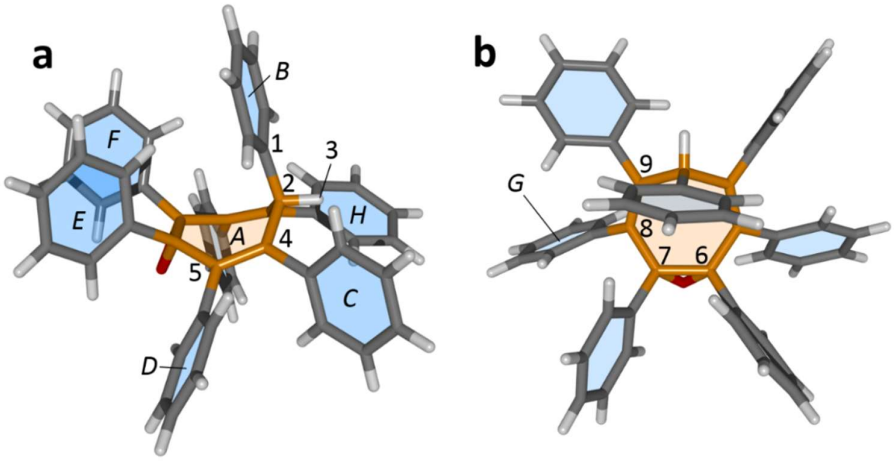

Figure 3.15. Solid-state structure of **Ph_7C_7H-O** viewed (a) side-on to the cycloheptatriene and (b) from above the cycloheptatriene. Selected atoms are labelled numerically, the planes of the carbocyclic rings are labelled by italicised uppercase letters. As central ring *A* is puckered, individual planes α^n are defined by a carbon vertex *n* and its two nearest neighbours within the ring, e.g., A^5 is the plane defined by atoms 4, 5, and 6.

Crystal System: Monoclinic

Space group: P21/c

Unit Cell Parameters: a = 15.9229(7) Å, b = 12.6701(5) Å, c = 17.9495(7) Å, β = 108.8982(16)°, V = 3426.02(24) Å3, Z = 4

Bond lengths (Å): C2–C4, 1.53; C4–C5, 1.34; C5–C6, 1.50; C6–C7, 1.49; C7–C8, 1.50; C8–C9, 1.34; C2–C9, 1.54.

Bond angles (°): C1–C2–H3, 104.4; C1–C2–C4, 117.6; C1–C2–C9, 113.9; C4–C2–C9, 110.6; C2–C4–C5, 123.5; C4–C5–C6, 123.7; C5–C6–C7, 123.4; C6–C7–C8, 122.6; C7–C8–C9, 124.5; C2–C9–C8, 123.4; C6–O–C7, 61.6.

Dihedral angles (°): A2–B, 36.1; A4–C, 60.2; A5–D, 55.9; A6–E, 76.6; A7–F, 73.0; A8–G, 78.6; A9–H, 52.5; B–C, 60.9; C–D, 53.9; D–E, 62.2; E–F, 58.9; F–G, 58.7; G–H, 64.8; B–H, 53.2

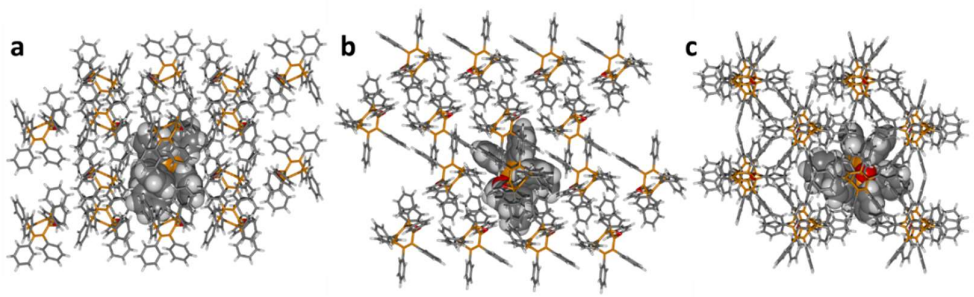

Figure 3.16. Solid-state superstructure of **Ph_7C_7H-O**. A central molecule (space filling representation) is shown embedded in a section of the lattice made up of 2×2×2 unit cells in order to illustrate the crystal packing. Projections are viewed along the crystallographic (a) *a*-, (b) *b*-, and (c) *c*-axes

3.4.3.2. *sym*-phenPh_5C_7H

Crystals of ***sym*-phenPh_5C_7H** suitable for X-ray diffraction were grown by slow cooling of a saturated MeCN solution of pure ***sym*-phenPh_5C_7H**.

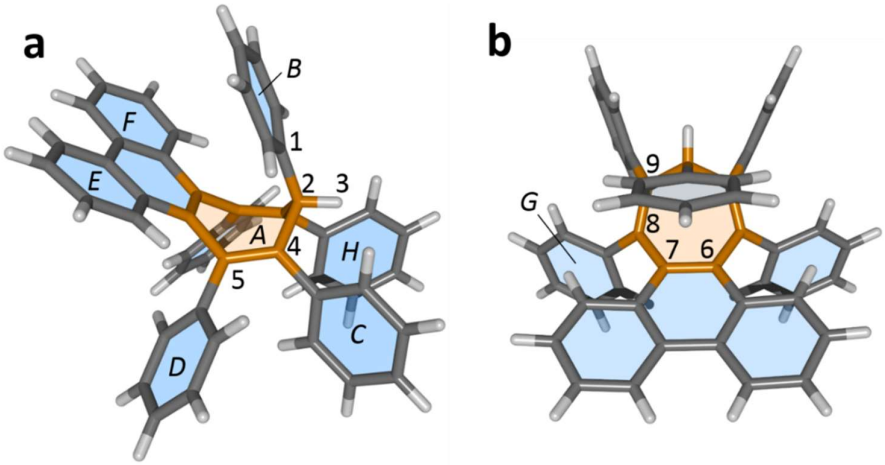

Figure 3.17. Solid-state structure of ***sym*-phenPh_5C_7H** viewed (a) side-on to the cycloheptatriene and (b) from above the cycloheptatriene. Selected atoms are labelled numerically, the planes of the carbocyclic rings are labelled by italicised uppercase letters. As central ring *A* is puckered, individual planes α^n are defined by a carbon vertex *n* and its two nearest neighbours within the ring, e.g., A^5 is the plane defined by atoms 4, 5, and 6.

Crystal System: Triclinic

Space group: P-1

Unit Cell Parameters: a = 9.4506(6) Å, b = 9.4870(6) Å, c = 19.2332(12) Å, α = 91.297(2)°, β = 103.684(2)°, γ = 91.779(2)°, V = 1673.85(18) Å3, Z = 2

Bond lengths (Å): C2–C4, 1.53; C4–C5, 1.35; C5–C6, 1.49; C6–C7, 1.38; C7–C8, 1.48; C8–C9, 1.36; C2–C9, 1.53.

Bond angles (°): C1–C2–H3, 107.3; C1–C2–C4, 116.6; C1–C2–C9, 116.5; C4–C2–C9, 99.9; C2–C4–C5, 119.8; C4–C5–C6, 120.9; C5–C6–C7, 121.5; C6–C7–C8, 121.3; C7–C8–C9, 120.9; C2–C9–C8, 119.6.

Dihedral angles (°): A2–B, 48.4; A4–C, 59.2; A5–D, 51.5; A6–E, 6.6; A7–F, 6.3; A8–G, 46.2;

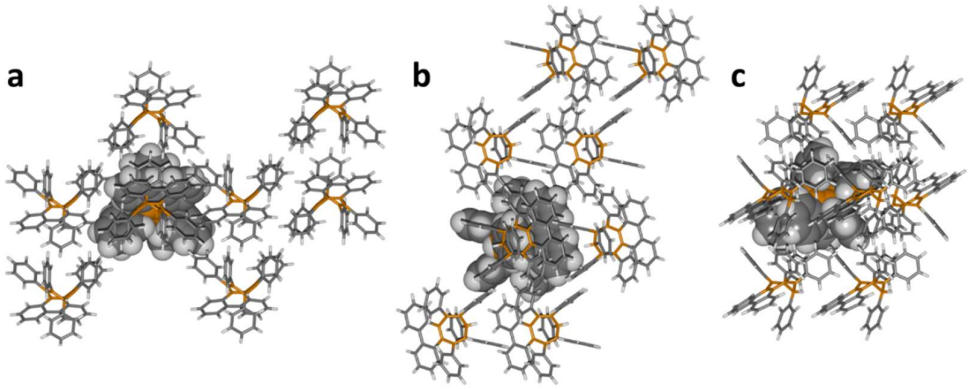

A9–H, 50.6; B–C, 65.0; C–D, 54.7; D–E, 83.2; E–F, 11.3; F–G, 82.6; G–H, 47.3; B–H, 73.6.

Figure 3.18. Solid-state superstructure of ***sym*-phenPh$_5$C$_7$H**. A central molecule (space filling representation) is shown embedded in a section of the lattice made up of 2×2×2 unit cells in order to illustrate the crystal packing. Projections are viewed along the crystallographic (a) *a*-, (b) *b*-, and (c) *c*-axes.

3.4.3.3. *asym*-phenPh$_5$C$_7$H

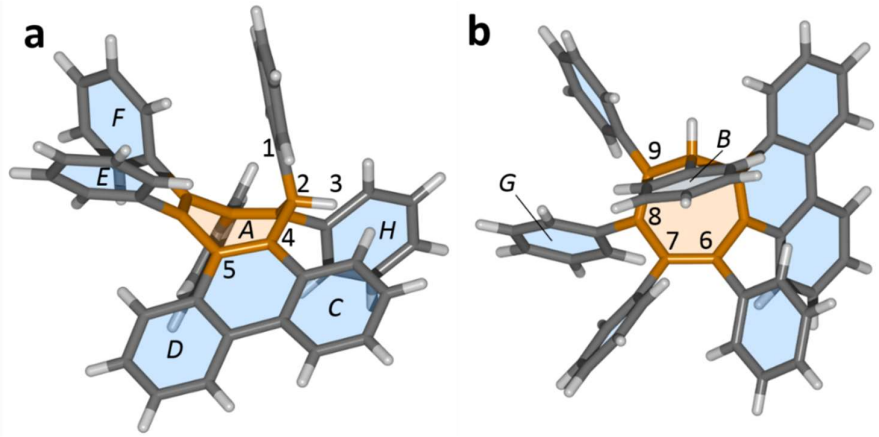

Figure 3.19. Solid-state structure of ***asym*-phenPh$_5$C$_7$H** viewed (a) side-on to the cycloheptatriene and (b) from above the cycloheptatriene. Selected atoms are labelled numerically, the planes of the carbocyclic rings are labelled by italicised uppercase letters. As central ring *A* is puckered, individual planes α^n are defined by a carbon vertex *n* and its two nearest neighbours within the ring, e.g., A^5 is the plane defined by atoms 4, 5, and 6.

A single crystal of ***asym*-phenPh$_5$C$_7$H** suitable for X-ray diffraction were grown by slow cooling of a saturated MeCN solution of a 2:1 mixture of ***asym*-phenPh$_5$C$_7$H** and ***sym*-phenPh$_5$C$_7$H**.

Crystal System: Triclinic

Space group: P-1

Unit Cell Parameters: a = 9.6538(4) Å, b = 18.4913(7) Å, c = 20.4317(7) Å, α = 74.979(2)°, β = 77.015(2)°, γ = 74.871(2)°, V = 3351.98(22) Å^3, Z = 4

Bond lengths (Å): C2–C4, 1.53; C4–C5, 1.36; C5–C6, 1.49; C6–C7, 1.36; C7–C8, 1.49; C8–C9, 1.35; C2–C9, 1.53.

Bond angles (°): C1–C2–H3, 105.8; C1–C2–C4, 115.6; C1–C2–C9, 115.6; C4–C2–C9, 107.4; C2–C4–C5, 119.9; C4–C5–C6, 120.9; C5–C6–C7, 122.4; C6–C7–C8, 122.6; C7–C8–C9, 120.8; C2–C9–C8, 122.3.

Dihedral angles (°): A^2–*B*, 42.0; A^4–*C*, 11.4; A^5–*D*, 10.4; A^6–*E*, 47.5; A^7–*F*, 62.5; A^8–*G*, 69.5; A^9–*H*, 49.1; *B*–*C*, 76.6; *C*–*D*, 7.3; *D*–*E*, 87.2; *E*–*F*, 50.3; *F*–*G*, 63.4; *G*–*H*, 48.5; *B*–*H*, 74.6.

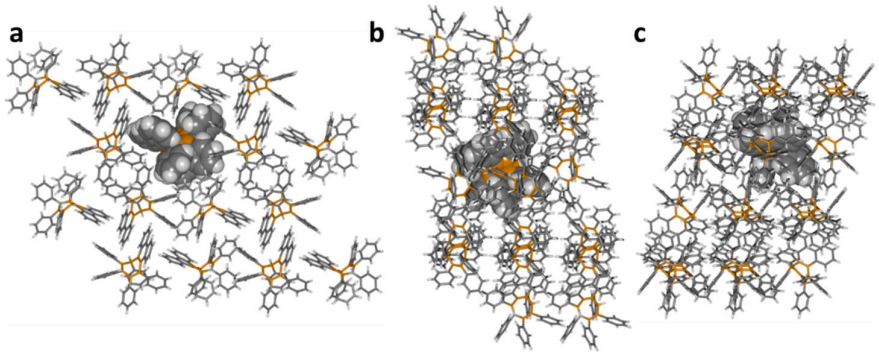

Figure 3.20. Solid-state superstructure of ***asym*-phenPh$_5$C$_7$H**. A central molecule (space filling representation) is shown embedded in a section of the lattice made up of 2×2×2 unit cells in order to illustrate the crystal packing. Projections are viewed along the crystallographic (a) *a*-, (b) *b*-, and (c) *c*-axes.

3.4.3.4. *sym*-phenPh$_5$C$_7$H-O

A single crystal of ***sym*-phenPh$_5$C$_7$H-O** suitable for X-ray diffraction were grown by slow cooling of a saturated MeCN solution.

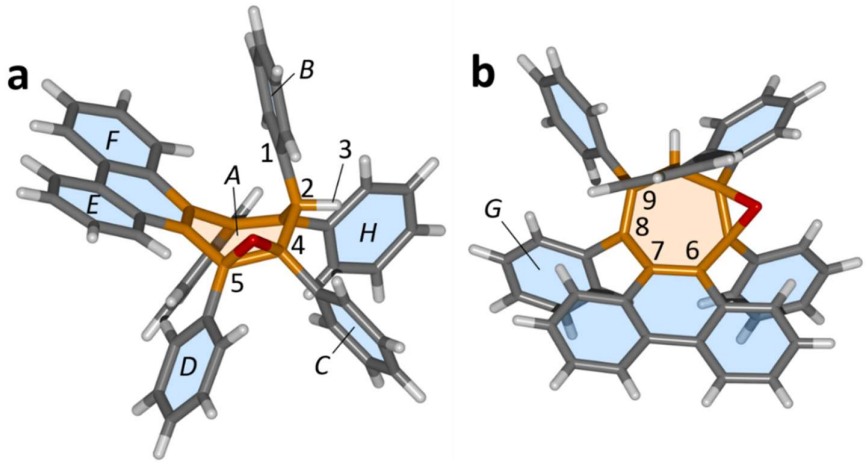

Figure 3.21. Solid-state structure of ***sym*-phenPh$_5$C$_7$H-O** viewed (a) side-on to the cycloheptatriene and (b) from above the cycloheptatriene. Selected atoms are labelled numerically, the planes of the carbocyclic rings are labelled by italicised uppercase letters. As central ring *A* is puckered, individual planes α^n are defined by a carbon vertex *n* and its two nearest neighbours within the ring, e.g., A^5 is the plane defined by atoms 4, 5, and 6.

Crystal System: Monoclinic

Space group: $P2_1/c$

Unit Cell Parameters: a = 9.6891(6) Å, b = 31.178(2) Å, c = 11.5786(8) Å, α = β = 109.132(3)° V = 3304.55(38) Å^3, Z = 4

Bond lengths (Å): C2–C4, 1.55; C4–C5, 1.48; C5–C6, 1.50; C6–C7, 1.37; C7–C8, 1.51; C8–C9, 1.35; C2–C9, 1.53.

Bond angles (°): C1–C2–H3, 105.3; C1–C2–C4, 118.8; C1–C2–C9, 114.5; C4–C2–C9, 106.5; C2–C4–C5, 120.1; C4–C5–C6, 119.3; C5–C6–C7, 122.6; C6–C7–C8, 123.5; C7–C8–C9, 121.7; C2–C9–C8, 120.3; C4–O–C5, 61.2.

Dihedral angles (°): A^2–*B*, 37.7; A^4–*C*, 81.6; A^5–*D*, 51.5; A^6–*E*, 5.9; A^7–*F*, 10.4; A^8–*G*, 55.2; A^9–*H*, 47.1; *B*–*C*, 30.4; *C*–*D*, 63.3; *D*–*E*, 82.4; *E*–*F*, 10.1; *F*–*G*, 83.4; *G*–*H*, 41.8; *B*–*H*, 72.0.

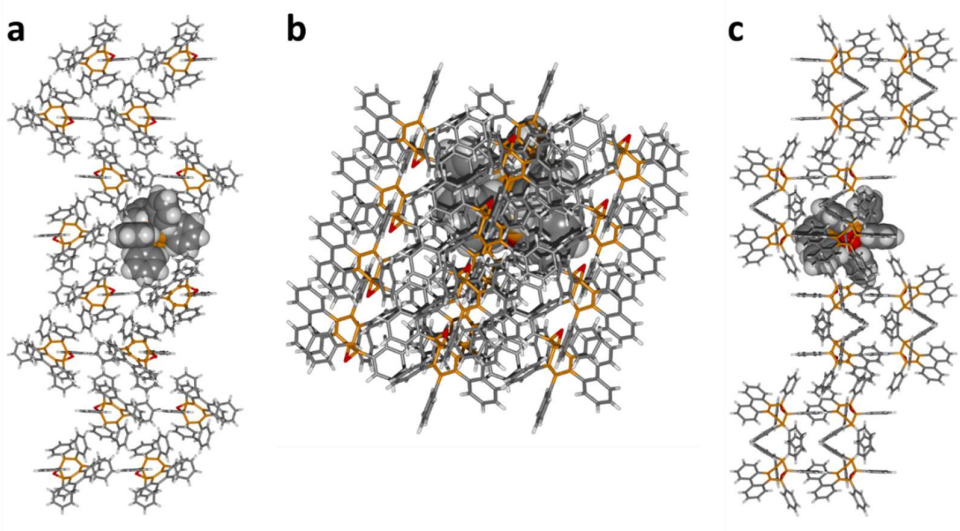

Figure 3.22. Solid-state superstructure of ***sym*-phenPh$_5$C$_7$H-O**. A central molecule (space filling representation) is shown embedded in a section of the lattice made up of 2×2×2 unit cells in order to illustrate the crystal packing. Projections are viewed along the crystallographic (a) *a*-, (b) *b*-, and (c) *c*-axes.

3.4.3.5. *asym*-phenPh$_5$C$_7$H-O

Single crystal of ***asym*-phenPh$_5$C$_7$H-O** suitable for X-ray diffraction were grown by slow cooling of a saturated MeCN solution.

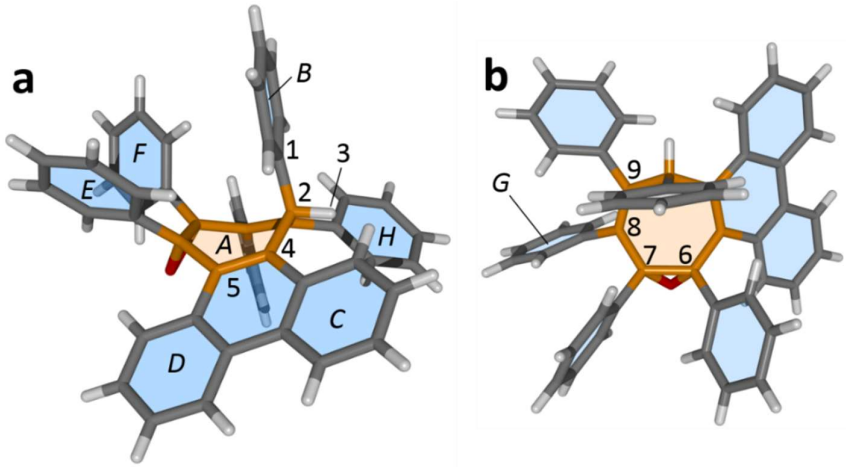

Figure 3.23. Solid-state structure of ***asym*-phenPh$_5$C$_7$H-O** viewed (a) side-on to the cycloheptatriene and (b) from above the cycloheptatriene. Selected atoms are labelled numerically, the planes of the carbocyclic rings are labelled by italicised uppercase letters. As central ring *A* is puckered, individual planes α^n are defined by a carbon vertex *n* and its two nearest neighbours within the ring, e.g., A^5 is the plane defined by atoms 4, 5, and 6.

Crystal System: Orthorhombic

Space group: $P2_12_12_1$

Unit Cell Parameters: a = 10.1203(6) Å, b = 16.5120(9) Å, c = 20.0664(11) Å, V = 3353.22(33) Å^3, Z = 4

Bond lengths (Å): C2–C4, 1.53; C4–C5, 1.36; C5–C6, 1.51; C6–C7, 1.49; C7–C8, 1.50; C8–C9, 1.34; C2–C9, 1.53.

Bond angles (°): C1–C2–H3, 103.8; C1–C2–C4, 114.8; C1–C2–C9, 115.8; C4–C2–C9, 113.0; C2–C4–C5, 121.8; C4–C5–C6, 123.4; C5–C6–C7, 123.4; C6–C7–C8, 122.7; C7–C8–C9, 123.2; C2–C9–C8, 125.5; C6–O–C7, 61.6.

Dihedral angles (°): A^2–*B*, 34.4; A^4–*C*, 9.4; A^5–*D*, 2.9; A^6–*E*, 47.7; A^7–*F*, 88.4; A^8–*G*, 76.3; A^9–*H*, 56.9; *B*–*C*, 76.0; *C*–*D*, 6.3; *D*–*E*, 88.3; *E*–*F*, 53.1; *F*–*G*, 40.5; *G*–*H*, 59.3; *B*–*H*, 56.2.

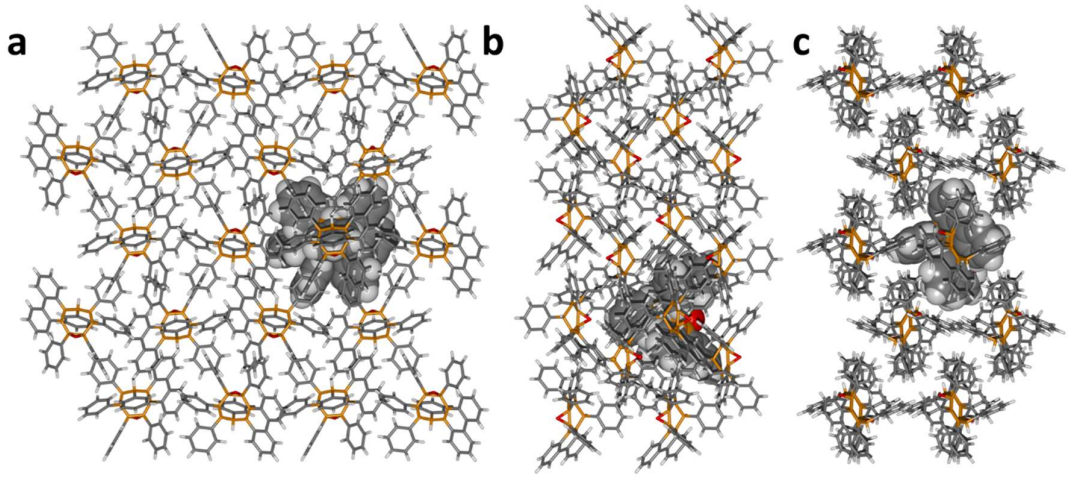

Figure 3.24. Solid-state superstructure of ***asym*-phenPh$_5$C$_7$H-O**. A central molecule (space filling representation) is shown embedded in a section of the lattice made up of 2×2×2 unit cells in order to illustrate the crystal packing. Projections are viewed along the crystallographic (a) *a*-, (b) *b*-, and (c) *c*-axes.

3.4.3.5. *sym*-phen$_2$Ph$_3$C$_7$H-O

A single crystal of ***sym*-phenPh$_5$C$_7$H-O** suitable for X-ray diffraction were grown by slow cooling of a saturated MeCN solution.

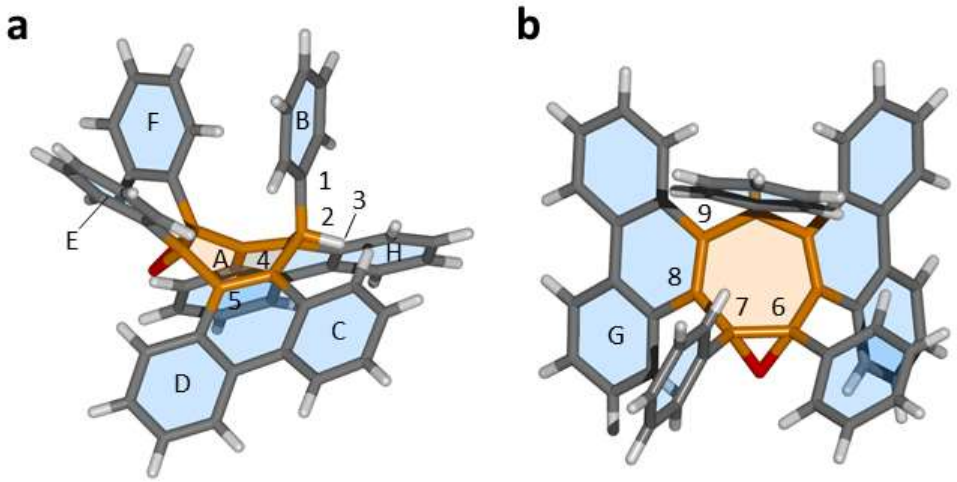

Figure 3.25. Solid-state structure of ***sym*-phen$_2$Ph$_3$C$_7$H-O** viewed (a) side-on to the seven-membered ring and (b) from above the seven-membered ring. Selected atoms are labelled numerically, the planes of the carbocyclic rings are labelled by italicised uppercase letters. As central ring *A* is puckered, individual planes α^n are defined by a carbon vertex *n* and its two nearest neighbours within the ring, e.g., A^5 is the plane defined by atoms 4, 5, and 6.

Crystal System: Monoclinic

Space group: $P2_1/n$

Unit Cell Parameters: a = 10.4829(6) Å, b = 13.2982(7) Å, c = 22.9502(13) Å, V = 3197.6(3) Å^3, Z = 4

Bond lengths (Å): C2–C4, 1.54; C4–C5, 1.36; C5–C6, 1.51; C6–C7, 1.50; C7–C8, 1.50; C8–C9, 1.37; C2–C9, 1.54.

Bond angles (°): C1–C2–H3, 102.9; C1–C2–C4, 115.4; C1–C2–C9, 117.6; C4–C2–C9, 112.4; C2–C4–C5, 122.9; C4–C5–C6, 121.4; C5–C6–C7, 120.7; C6–C7–C8, 119.41; C7–C8–C9, 121.3; C2–C9–C8, 124.0; C6–O–C7, 59.21.

Dihedral angles (°): A^2–*B*, 34.1; A^4–*C*, 12.9; A^5–*D*, 4.4; A^6–*E*, 67.6; A^7–*F*, 104.2; A^8–*G*, 10.9; A^9–*H*, 44.8; *B*–*C*, 97.4; *C*–*D*, 11.4; *D*–*E*, 76.7; *E*–*F*, 4.3; *F*–*G*, 73.9; *G*–*H*, 14.4; *B*–*H*, 77.2.

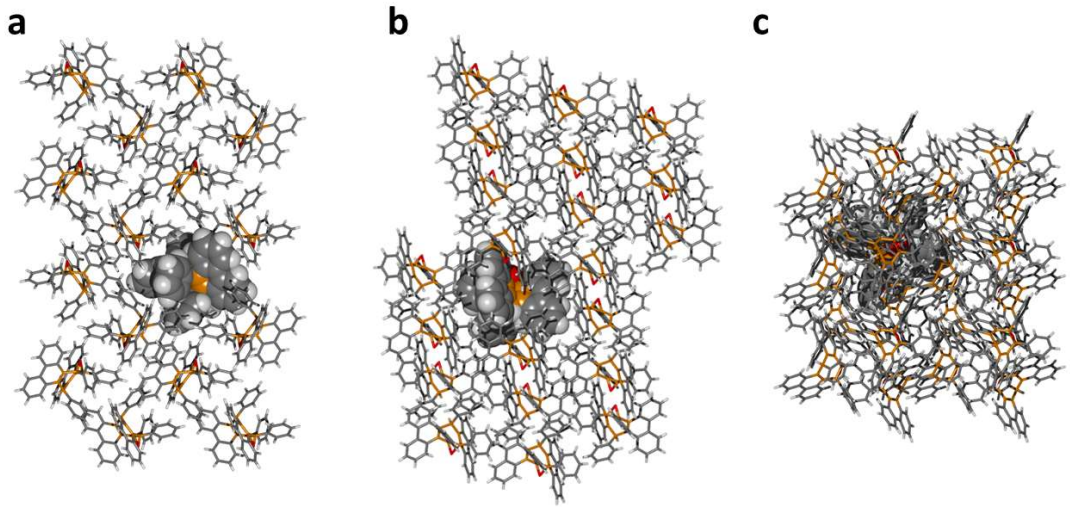

Figure 3.26. Solid-state superstructure of ***sym*-phen$_2$Ph$_3$C$_7$H-O**. A central molecule (space filling representation) is shown embedded in a section of the lattice made up of 2×2×2 unit cells in order to illustrate the crystal packing. Projections are viewed along the crystallographic (a) *a*-, (b) *b*-, and (c) *c*-axes.

3.4.4. UV-Vis Absorption Spectra

All spectra show (Figure 3.27) that the UV-vis absorption characteristics of the carbocycles are independent of the choice of solvent. UV-vis measurements were performed using anhydrous solvents: CH_2Cl_2, methylcyclohexane (MCH), MeCN, MeOH, tetrahydrofuran (THF) or 2-methyltetrahydrofuran (2-MeTHF). Spectra were measured in 10 mm path-length cuvette at room temperature. A 10 μM Sample concentration of carbocycles **Ph$_7$C$_7$H** and 20 μM sample concentrations of carbocycles (**Ph$_7$C$_7$H-O**, ***sym*-phenPh$_5$C$_7$H**, ***asym*-phenPh$_5$C$_7$H**, ***sym*-phenPh$_5$C$_7$H-O** and ***asym*-phenPh$_5$C$_7$H-O**) were used for all measurements in Figure 3.27. The intensities were plotted as molar absorptivity ε defined by the formula:

$$\varepsilon = \frac{I}{c \cdot l}$$

Equation 3.2. The Beer–Lambert law, where I is the measured intensity, c is the concentration of sample, and l is path length of the cuvette.

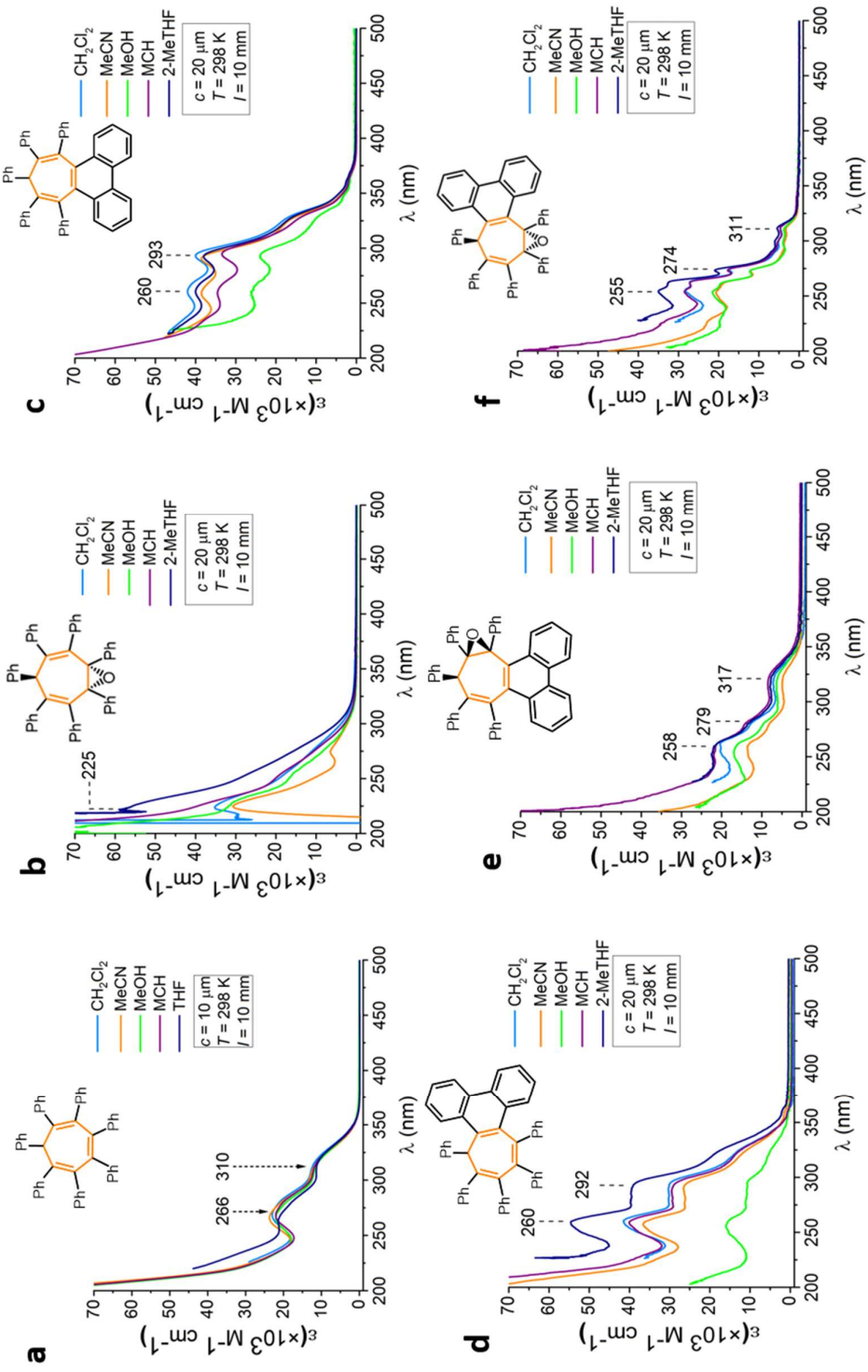

Figure 3.27. UV-vis absorption spectra of solutions of **(a) Ph7C7H, (b) Ph7C7H-O, (c) *sym*-phenPh5C7H, (d) *asym*-phenPh5C7H, (e) *sym*-phenPh5C7H-O, (f) *asym*-phenPh5C7H-O** in a series of non-polar and polar media

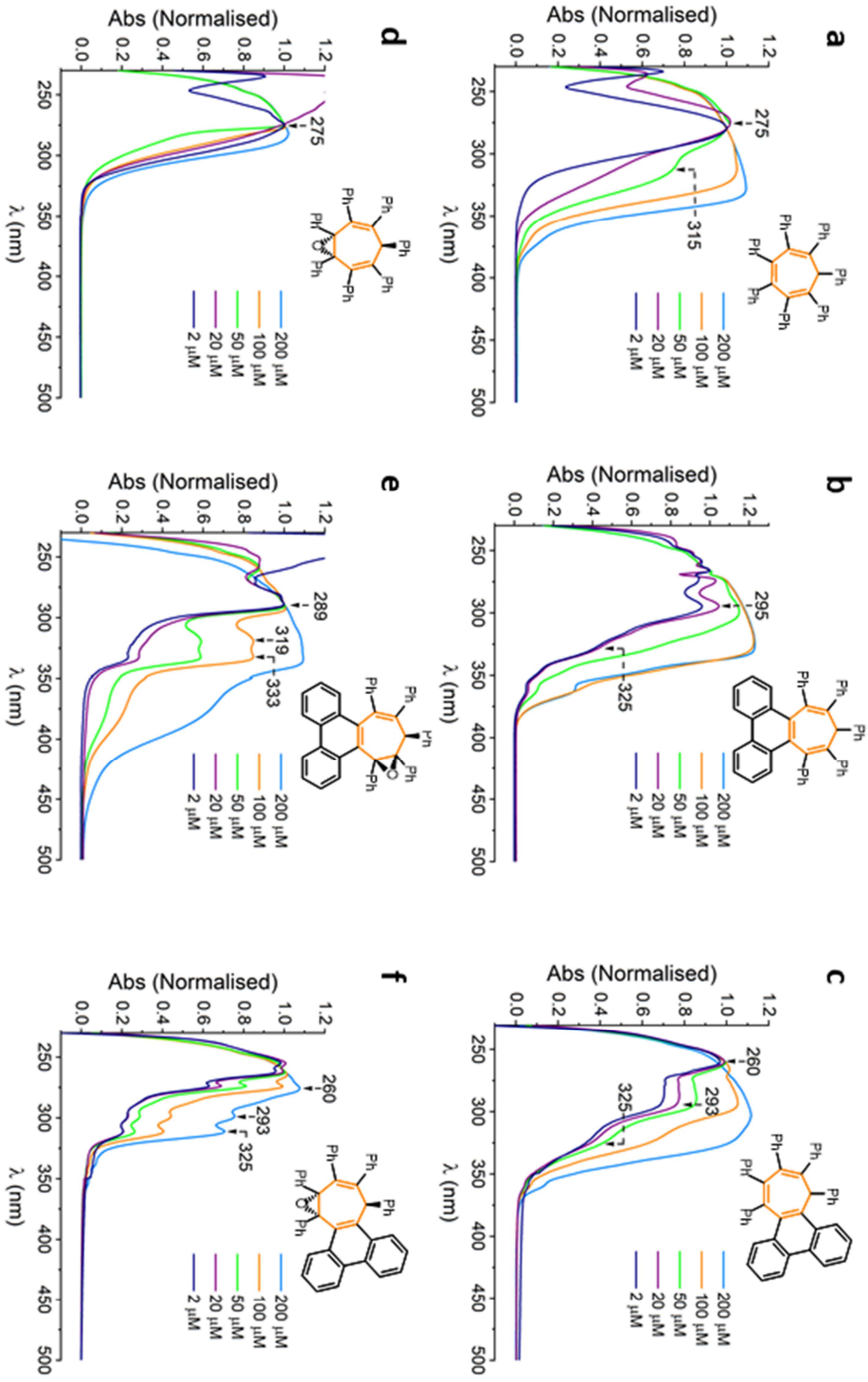

Figure 3.28. UV-vis absorption spectra of solutions of **(a) Ph$_7$C$_7$H**, **(b) Ph$_7$C$_7$H-O**, **(c) *syn*-phenPh$_5$C$_7$H**, **(d) *asym*-phenPh$_5$C$_7$H**, **(e) *syn*-phenPh$_5$C$_7$H-O**, **(f) *asym*-phenPh$_5$C$_7$H-O** at a series of concentrations in 2-MeTHF.

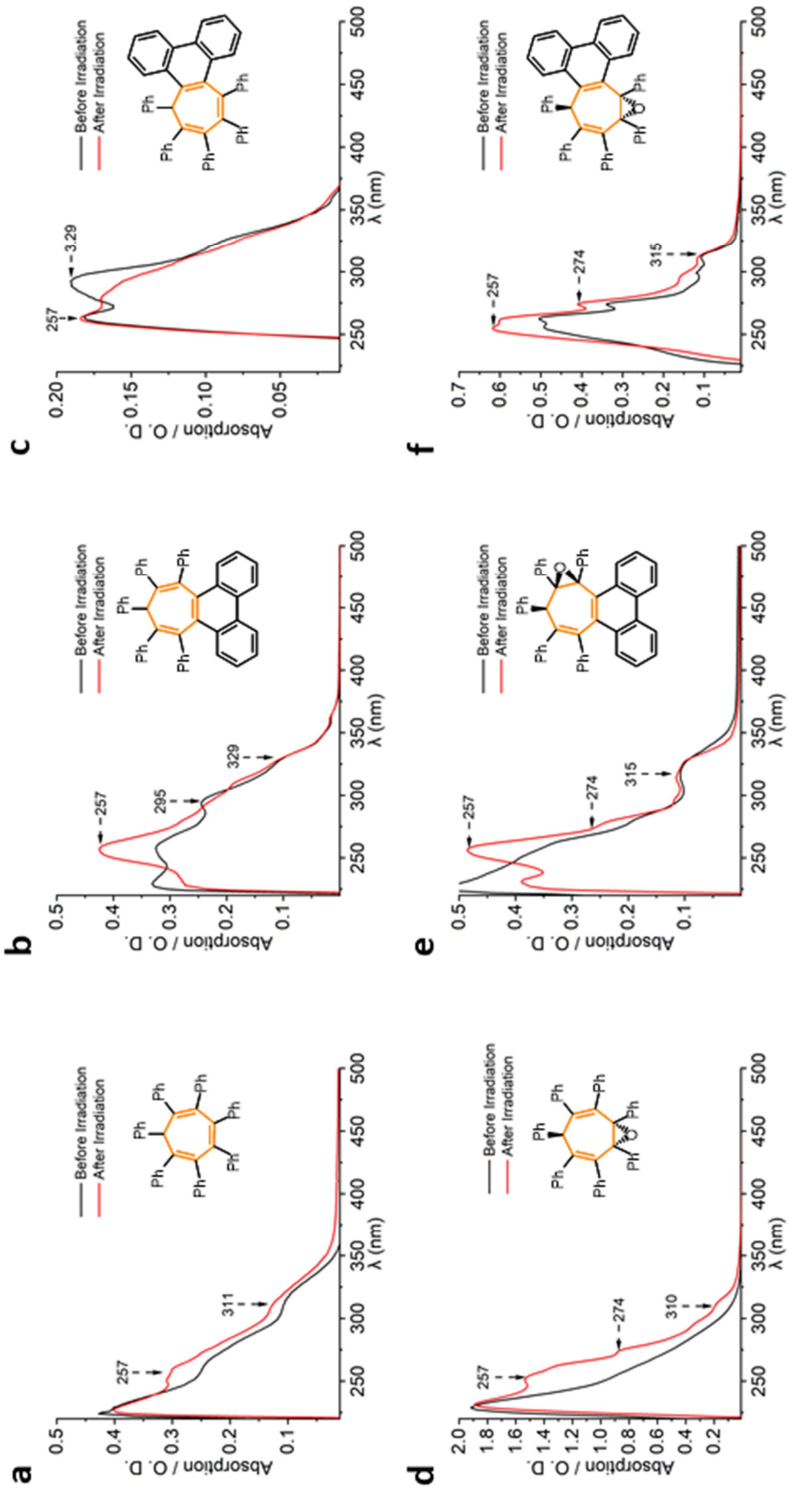

Figure 3.29. UV-vis absorption spectra of solutions of **(a) Ph-C_7H**, **(b) *sym*-phenPh_5C_7H**, **(c) *asym*-phenPh_5C_7H**, **(d) Ph-C_7H-O**, **(e) *sym*-phenPh_5C_7H-O**, **(f) *asym*-phenPh_5C_7H-O** in MeCN before and after irradiation under 4.0 eV light for 10 min for d-f and 1h for **a–c**.

3.4.5. Variable-Temperature Fluorescence

Samples for VT fluorescence were prepared using 200 μM THF stock solutions. The desired quantity was measured into a vial, evaporated to dryness, then the solid residue diluted to 20 μM and 2 μM concentration in the solvent used for the measurements. Anhydrous 2-MeTHF were used as the solvent system because it forms a stable organic glass which is UV-vis transparent at low temperatures. The samples were always kept at each temperature for at least 10 min to equilibrate prior to recording the spectra. The results of VT fluorescence are summarised in Figures 3.30–3.33.

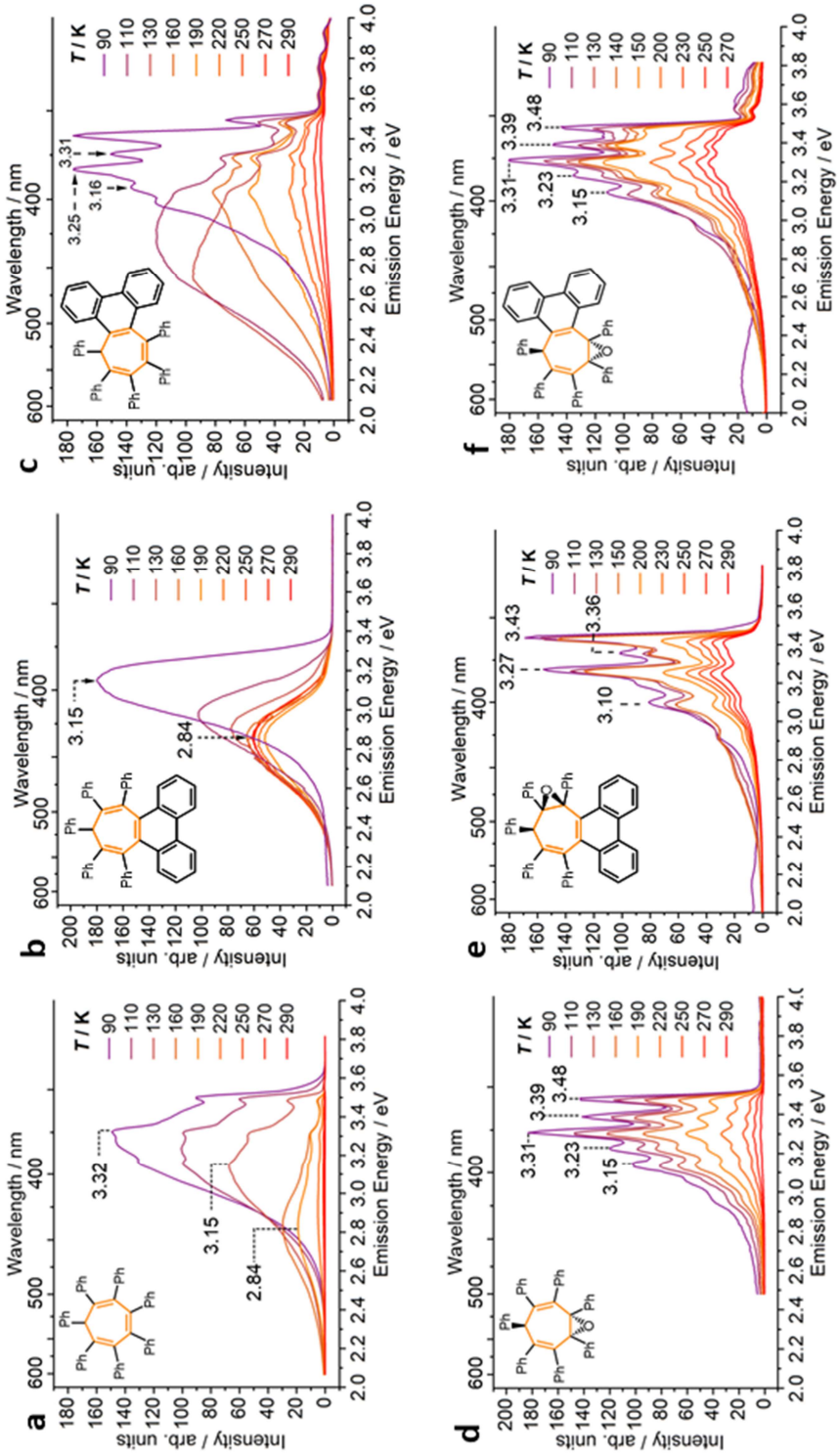

Figure 3.30. VT fluorescence spectra of 2-MeTHF solutions (l = 10 mm, T = 90–290 K) of **(a) Ph$_7$C$_7$H** λ_{ex} = 315 nm, c = 10 μM; **(b) Ph$_7$C$_7$H-O** λ_{ex} = 280 nm, c = 20 μM; **(c)** ***sym*-phenPh$_5$C$_7$H** λ_{ex} = 300 nm, c = 20 μM; **(d)** ***asym*-phenPh$_5$C$_7$H** λ_{ex} = 315 nm, c = 20 μM; **(e)** ***sym*-phenPh$_5$C$_7$H-O** λ_{ex} = 315 nm, c = 20 μM; **(f)** ***asym*-phenPh$_5$C$_7$H-O** λ_{ex} = 315 nm, c = 20 μM. Inset in panel **(a)**: legend for temperatures in all panels.

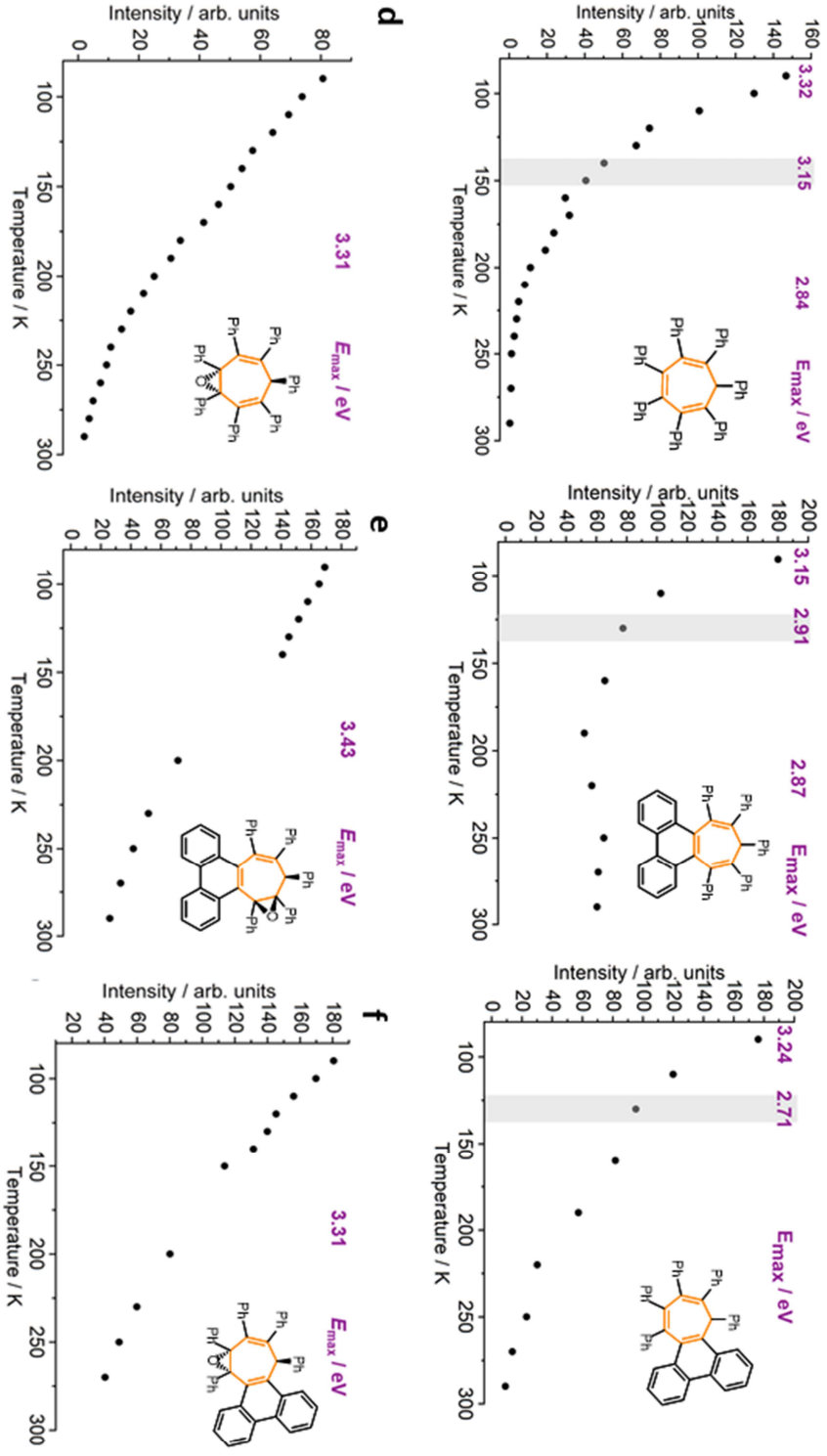

Figure 3.31. Peak emission intensities from VT fluorescence spectra of 2-MeTHF solutions (l = 10 mm, T = 90–290 K) of **(a) Ph$_7$C$_7$H** λ_{ex} = 315 nm, c = 10 μM; **(b) Ph$_7$C$_7$H-O** λ_{ex} = 280 nm, c = 20 μM; **(c)** ***sym*-phenPh$_5$C$_7$H** λ_{ex} = 300 nm, c = 20 μM; **(d)** ***asym*-phenPh$_5$C$_7$H** λ_{ex} = 315 nm, c = 20 μM; **(e)** ***sym*-phenPh$_5$C$_7$H-O** λ_{ex} = 315 nm, c = 20 μM; **(f)** ***asym*-phenPh$_5$C$_7$H-O** λ_{ex} = 315 nm, c = 20 μM. The emission energy of the most intense peak at each temperature was chosen. These energies are given on each panel. The most intense emission peaks of **Ph$_7$C$_7$H** and ***sym*-phenPh$_5$C$_7$H** vary with temperature, so the plots are divided into sections corresponding to different peak energies.

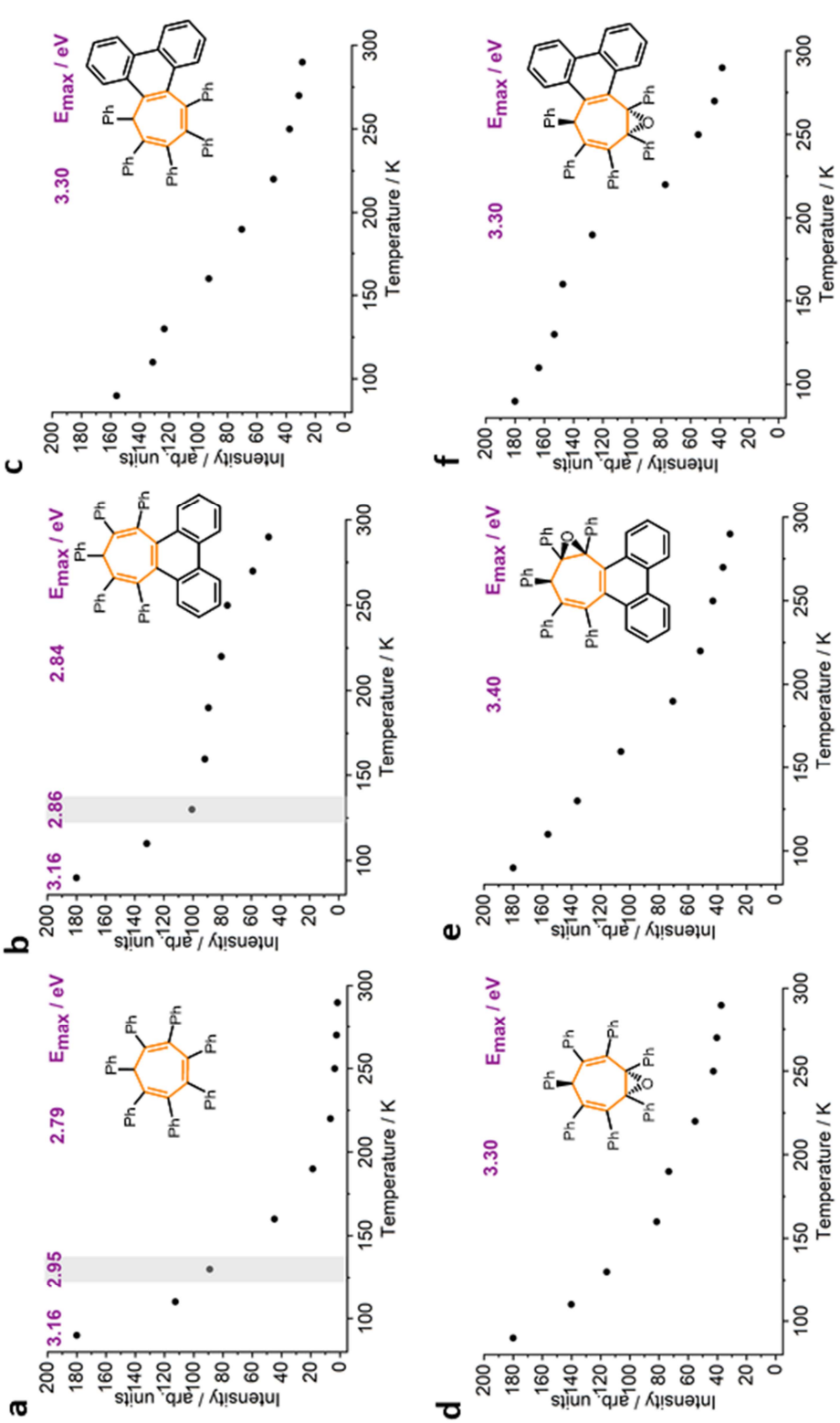

Figure 3.32. Peak emission intensities from VT fluorescence spectra of 2-MeTHF solutions (l = 10 mm, T = 90–290 K) of **(a) Ph$_7$C$_7$H** λ_{ex} = 315 nm, c = 2 μM; **(b) Ph$_7$C$_7$H-O** λ_{ex} = 280 nm, c = 2 μM; **(c)** ***sym*-phenPh$_5$C$_7$H** λ_{ex} = 300 nm, c = 2 μM; **(d)** ***asym*-phenPh$_5$C$_7$H** λ_{ex} = 315 nm, c = 2 μM; **(e)** ***sym*-phenPh$_5$C$_7$H-O** λ_{ex} = 315 nm, c = 2 μM; **(f)** ***asym*-phenPh$_5$C$_7$H-O** λ_{ex} = 315 nm, c = 2 μM. The emission energy of the most intense peak at each temperature was chosen. These energies are given on each panel. The most intense emission peaks of **Ph$_7$C$_7$H** and ***sym*-phenPh$_5$C$_7$H** vary with temperature, so the plots are divided into sections corresponding to different peak energies.

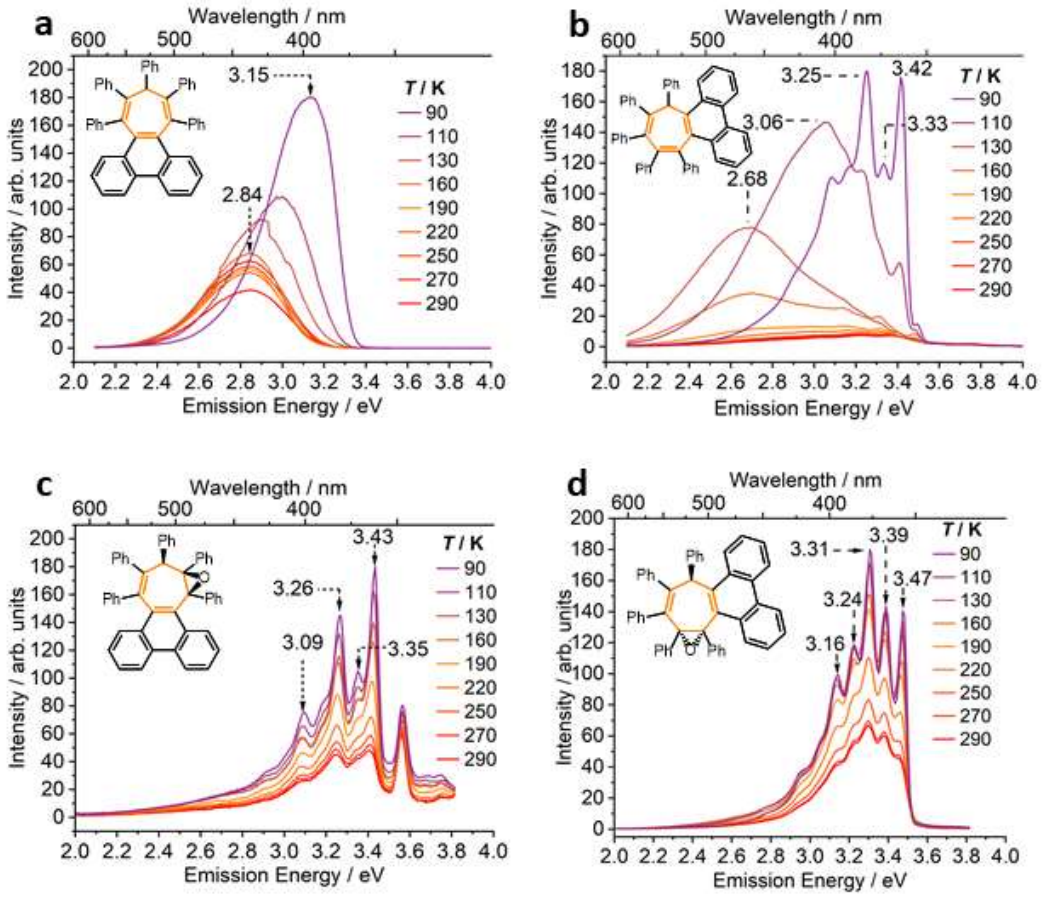

Figure 3.33. VT fluorescence spectra of 2-MeTHF solutions (l = 10 mm, T = 90–290 K) of **(a)** ***sym*-phenPh$_5$C$_7$H** λ_{ex} = 300 nm, c = 200 μM; **(b)** ***asym*-phenPh$_5$C$_7$H** λ_{ex} = 300 nm, c = 200 μM; **(c)** ***sym*-phenPh$_5$C$_7$H-O** λ_{ex} = 315 nm, c = 200 nM; **(d)** ***asym*-phenPh$_5$C$_7$H-O** λ_{ex} = 315 nm, c = 200 μM. Inset in panel **(a)**: legend for temperatures in all panels.

3.4.5.1. Temperature-dependent Solid-state Photoluminescence

The solid-state photoluminescence of carbocycles **Ph$_7$C$_7$H, Ph$_7$C$_7$H-O**, ***sym*-phenPh$_5$C$_7$H**, ***asym*-phenPh$_5$C$_7$H**, ***sym*-phenPh$_5$C$_7$H-O** and ***asym*-phenPh$_5$C$_7$H-O** were measured at a temperature range (290–90 K). The molecules were dispersed as a 1% optically clear ZEONEX cyclic olefin polymer matrix (Figure 3.34).

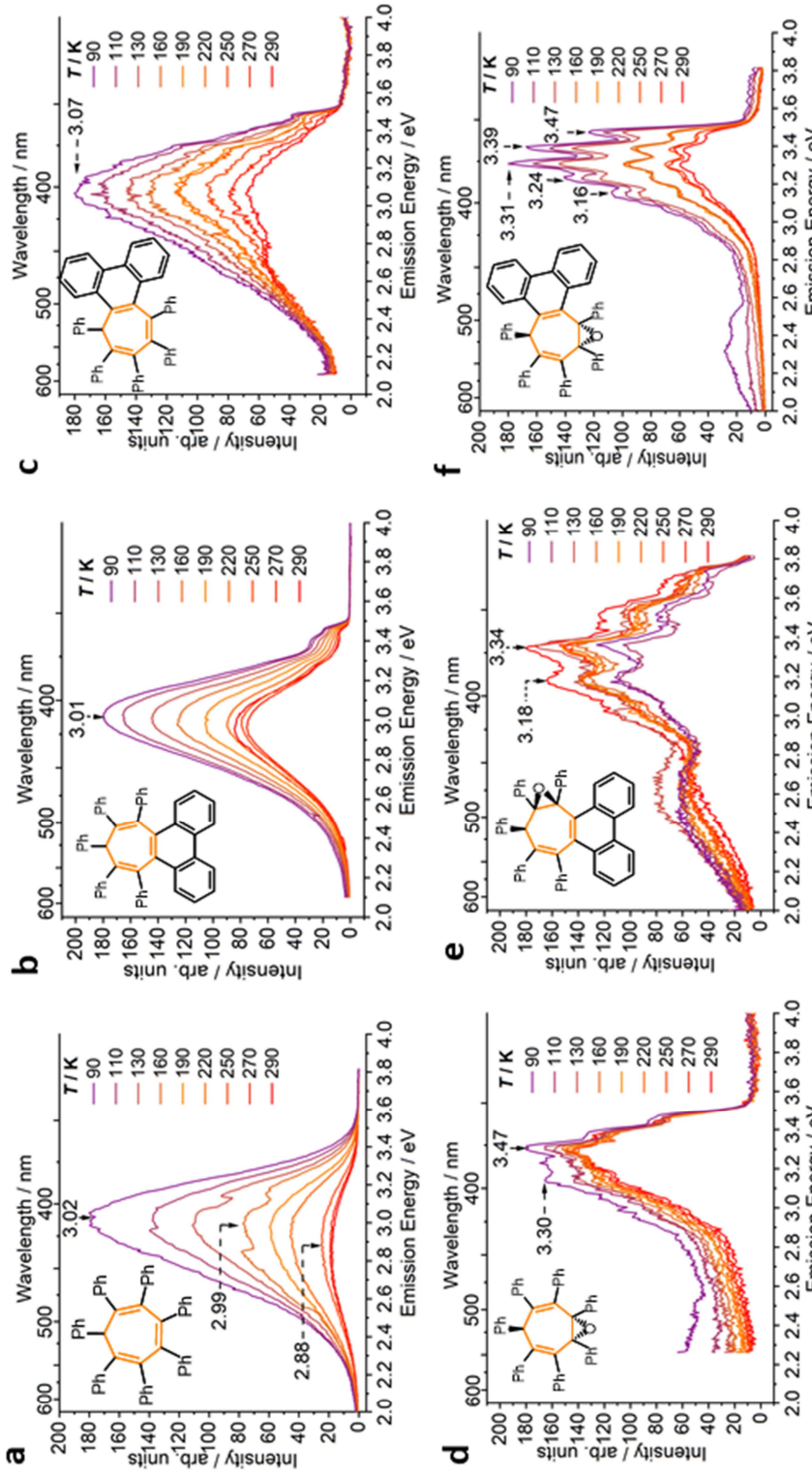

Figure 3.34. VT fluorescence spectra of ZEONEX matrices containing **(a) Ph7C7H** λ_{ex} = 315 nm; **(b) Ph7C7H-O** λ_{ex} = 280 nm; **(c) *sym*-phenPh5C7H** λ_{ex} = 300 nm; **(d) *asym*-phenPh5C7H** λ_{ex} = 315 nm; **(e) *sym*-phenPh5C7H-O** λ_{ex} = 315 nm; **(f) *asym*-phenPh5C7H-O** λ_{ex} = 315 nm. Inset in panel **(a)**: legend for temperatures in all panels.

3.4.6. Fluorescence Solvatochromism

Fluorescence spectra were acquired (Figure 3.35) for solutions of different polarities. The samples for fluorescence were prepared using 200 μM CH_2Cl_2 stock solutions. The desired quantity was measured into a vial, evaporated to dryness, then the solid residue was diluted to 20 μM concentration in the solvent used for the measurements. Although the solvents used cover a large range of polarities, the changes in emission wavelengths were below 0.1 eV, with the exception of ***asym*-phenPh$_5$C$_7$H** in methylcyclohexane (MCH) where the fluorescence was slightly more red-shifted (presumably as a result of phenanthrene dimer formation in the apolar solvent system). The small magnitude of these differences indicates that the observed emission does not arise from charge transfer states. Such states would be much more influenced by solvent polarity and emission wavelength would vary by larger amounts.

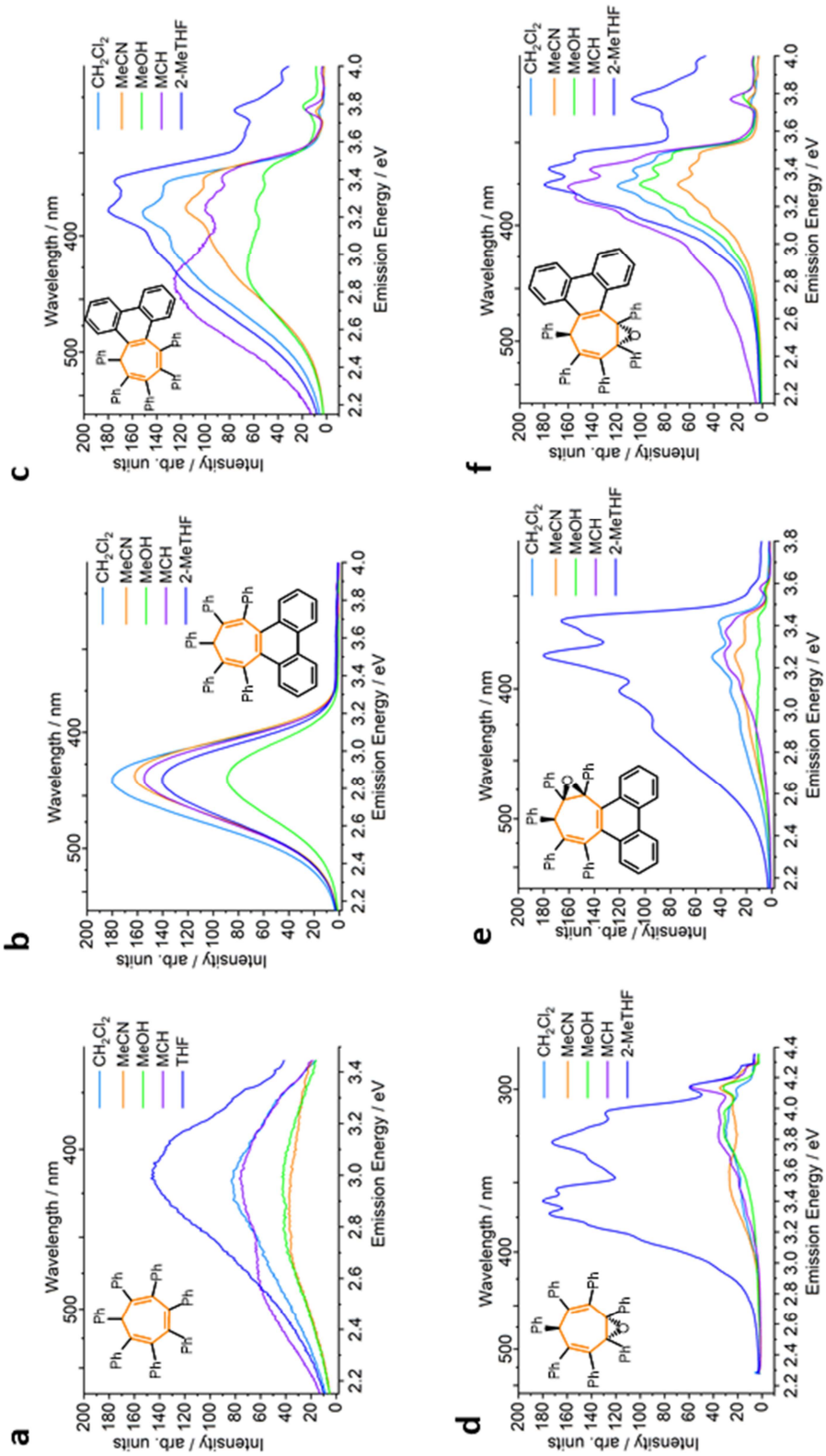

Figure 3.35. Fluorescence solvatochromism of **(a) Ph$_7$C$_7$H**; **(b) sym-phenPh$_5$C$_7$H**; **(c) asym-phenPh5C7H**; **(d) Ph$_7$C$_7$H-O**; **(e) sym-phenPh$_5$C$_7$H-O**; **(f) asym-phenPh$_5$C$_7$H-O** in MCH, CH_2Cl_2, MeOH, MeCN, and 2-MeTHF or THF.

3.4.7. Phenanthrene

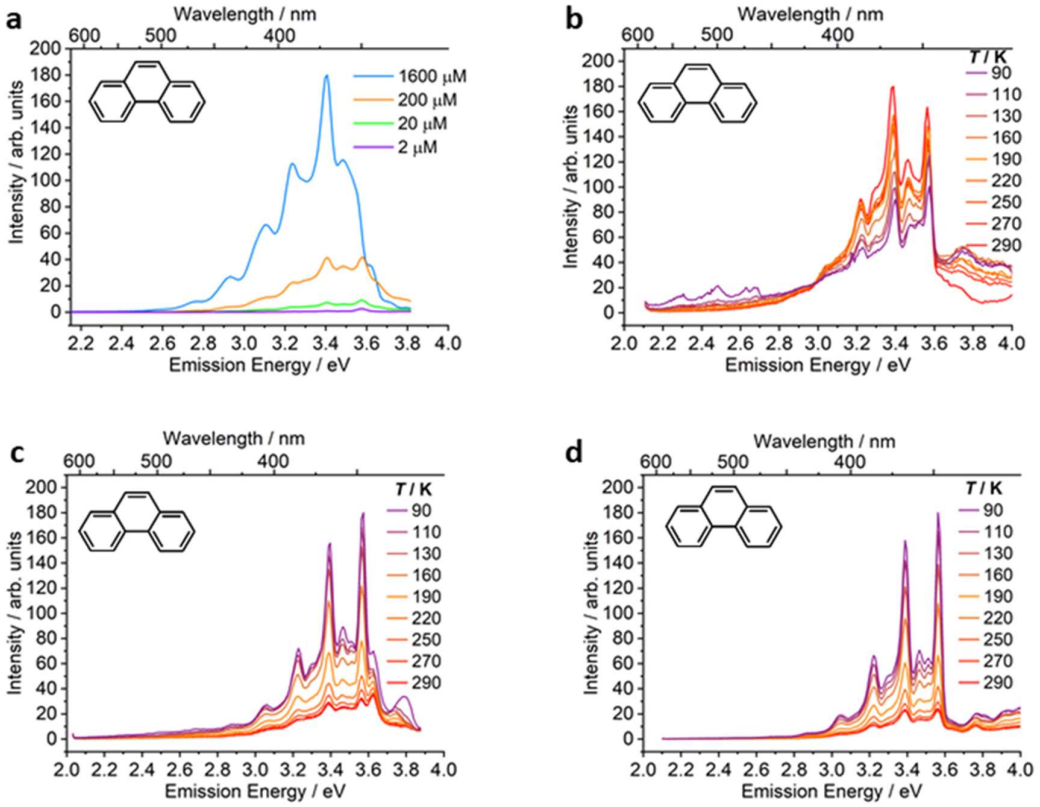

Figure 3.36. (a) Fluorescence spectra of **phenanthrene** (l = 10 mm, T = 290 K); Insert in panel **(a)**: Legend for concentration. VT fluorescence spectra of phenanthrene in a ZEONEX film; **(b) phenanthrene** λ_{ex} = 300 nm. VT fluorescence spectra of phenanthrene in a 2-MeTHF solutions (l = 10 mm, T = 90–290 K) of **(c) phenanthrene** λ_{ex} = 310 nm, c = 20 μM; **(d) phenanthrene** λ_{ex} = 300 nm, c = 20 μM; Inset in panel (b-d): legend for temperatures.

Fluorescence spectra were acquired for molecular phenanthrene. A concentration study (Figure 3.36a) demonstrated the formation of phenanthrene dimers at concentrations >20 μM showing vibronic emission similar to high concentration samples of ***asym*-phenPh$_5$C$_7$H**. Variable temperature fluorescent spectroscopy of a 1% ZEONEX film (Figure 3.36b) shows similar vibronic structure and E_{max} to both 2 μM and 20 μM 2-MeTHF samples (Figure 3.36c,d) with no observed bathochromic shift as the temperature decreases. This suggests that forming phenanthrene-like units in our molecular rotors via photocyclisation, may give rise to vibronic emission from

exciting the reversible intermediate form **IM** or oxidised phenanthrene containing products. Also, this indicates that the formation of vibronic emission in epoxides is a result of the more favourable formation of phenanthrene moieties

3.4.8. Photooxidation

The room temperature photoluminescence spectra of solutions of the rotors in this study are included below.

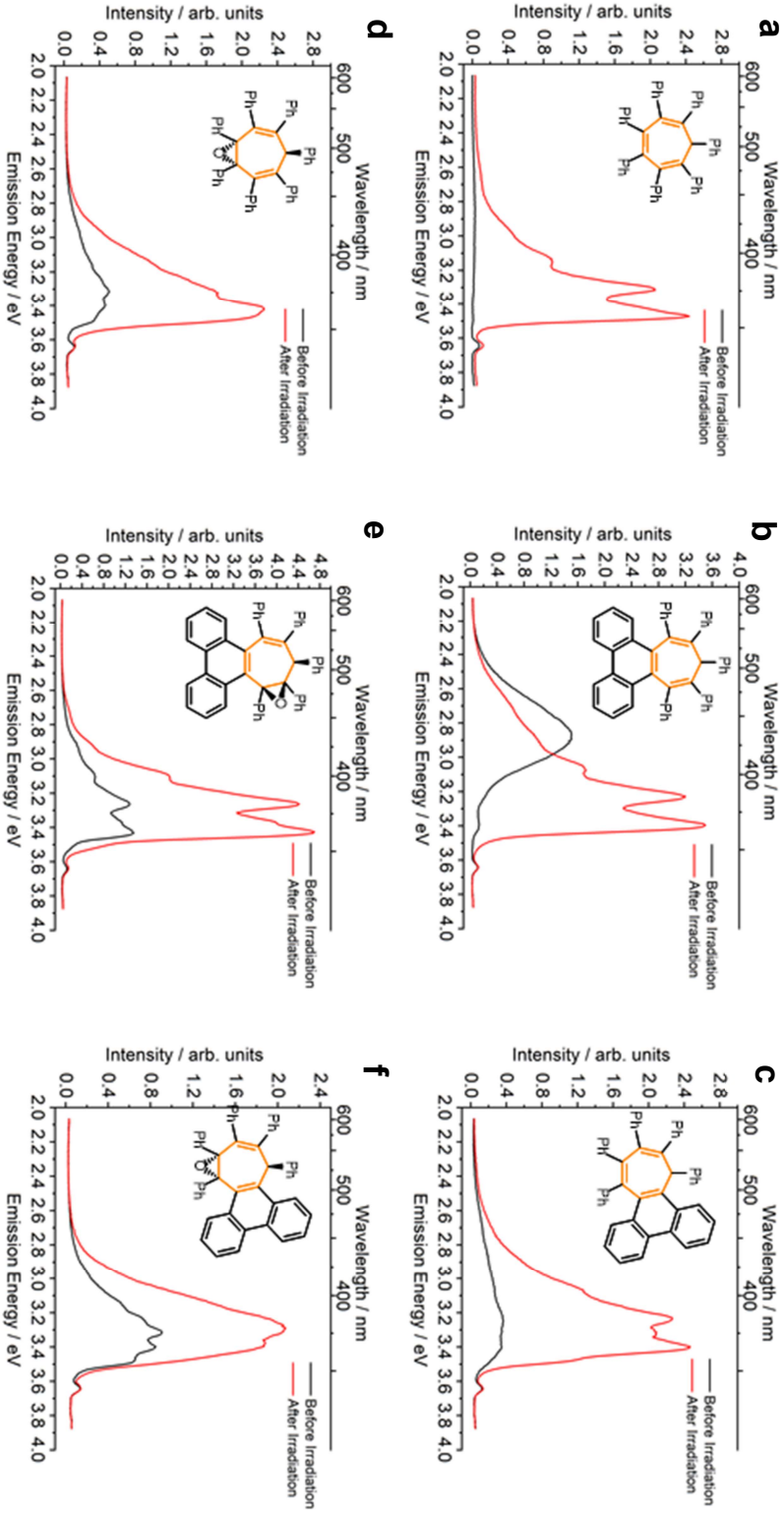

Figure 3.37. Room temperature emission spectra of 2 μM 2-MeTHF solutions of **(a) Ph$_7$C$_7$H**; **(b) *sym*-phenPh$_5$C$_7$H**; **(c) *asym*-phenPh$_5$C$_7$H**; (d) Ph$_7$C$_7$H-O**; **(e) *sym*-phenPh$_5$C$_7$H-O**; **(f) *asym*-phenPh$_5$C$_7$H-O,** showing changes in the emission profile before (black) and after (red) prolonged exposure to 4.0 eV light. **a**–**c** shows the result of >1 h irradiation whereas **d**–**f** show the result of <5 min irradiation.

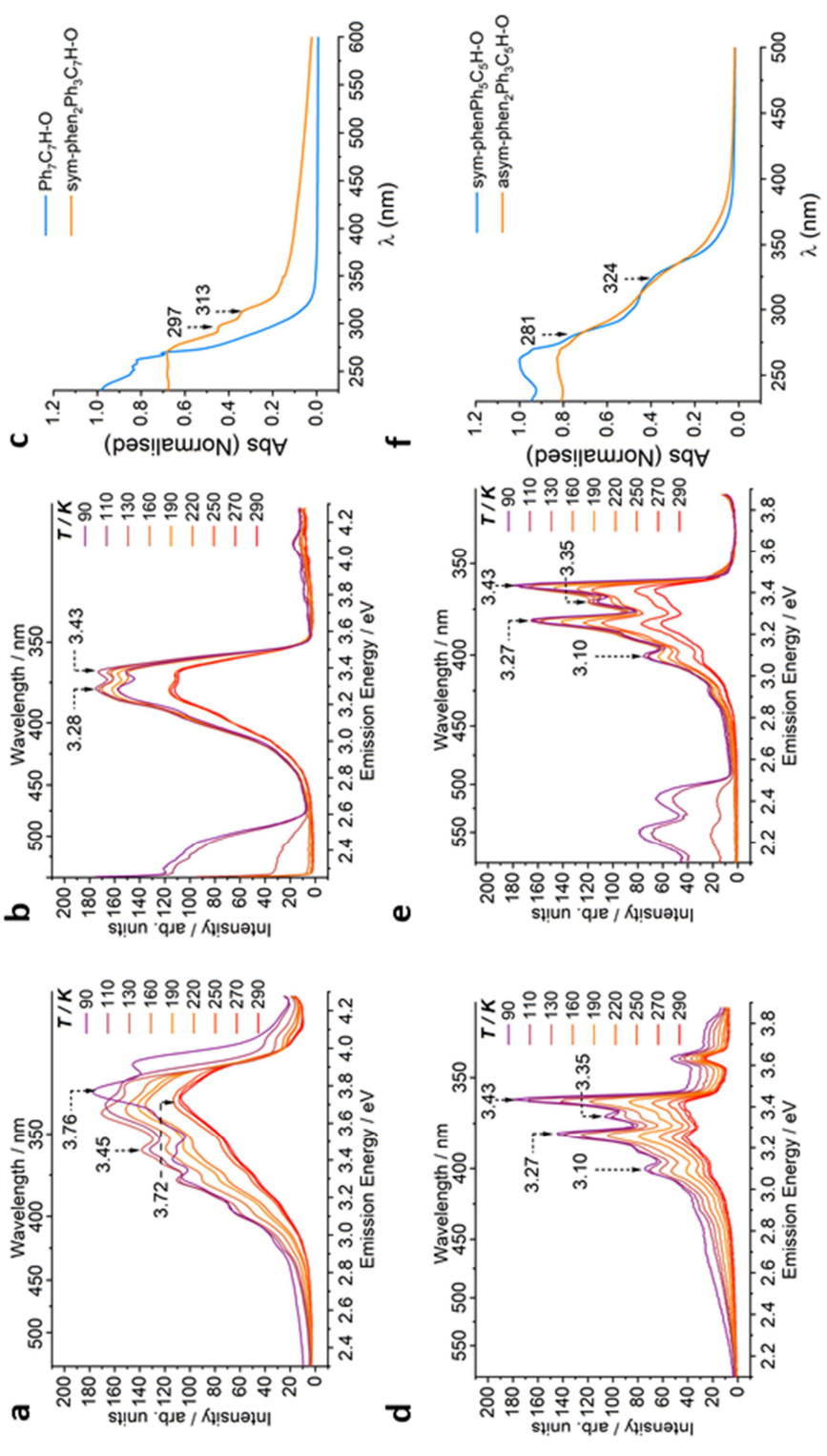

Figure 3.38. VT fluorescence spectra of photooxidised molecular rotors in 2-MeTHF solutions (l = 10 mm, T = 90–290 K) of **(a)** ***sym*-phen$_2$Ph$_3$C$_7$H-O** λ_{ex} = 310 nm, c = 20 μM; **(d)** ***asym*-phen$_2$Ph$_3$C$_7$H-O** λ_{ex} = 310 nm, c = 20 μM; VT fluorescence spectra of photooxidised molecular rotors 1% ZEONEX film of **(b)** ***sym*-phen$_2$Ph$_3$C$_7$H-O** λ_{ex} = 310 nm, **(e)** ***asym*-phen$_2$Ph$_3$C$_7$H-O** λ_{ex} = 310 nm; Inset in panel (**a**,**b**,**d**, and **e**): legend for temperatures. UV-absorption spectra in 1% ZEONEX film of **(c)** ***sym*-phen$_2$Ph$_3$C$_7$H-O** and **(f)** ***asym*-phen$_2$Ph$_3$C$_7$H-O**.

3.4.9. Time-Correlated Single Photon Counting (TCSPC)

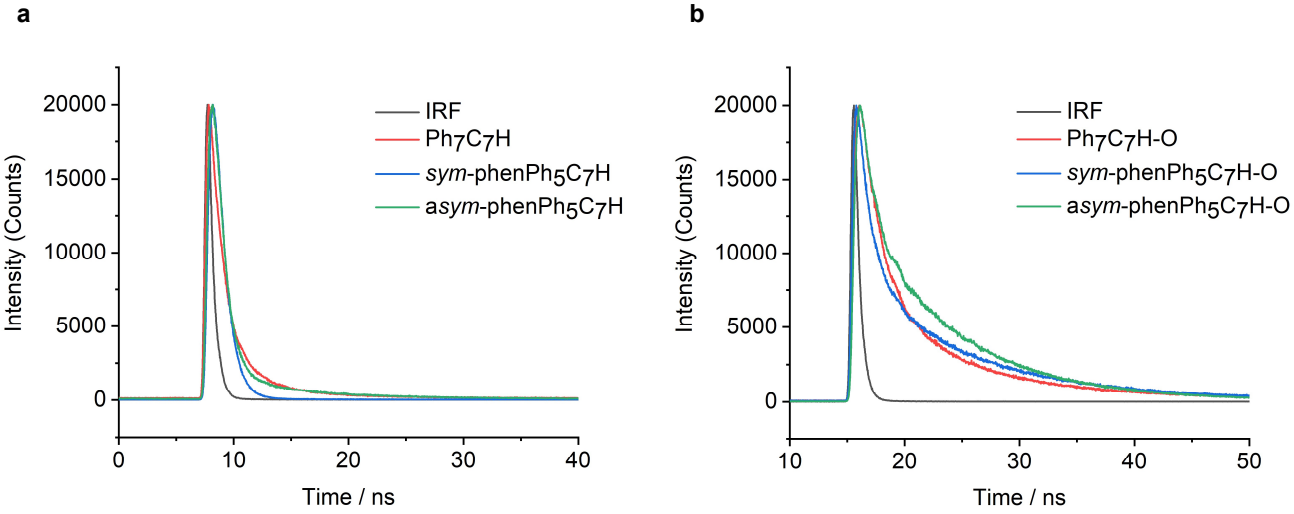

Figure 3.39. TCSPC decays of molecular rotors in a 2-MeTHF solutions (l = 10 mm, T = 290 K, c = 2 μM) of (left): **Ph$_7$C$_7$H** λ_{em} = 450 nm, ***sym*-phenPh$_5$C$_7$H,** λ_{em} = 440 nm and ***asym*-phenPh$_5$C$_7$H** λ_{em} = 370 nm b) **Ph$_7$C$_7$H-O** λ_{em} = 370 nm, ***sym*-phenPh$_5$C$_7$H-O** λ_{em} = 370 nm and ***asym*-phenPh$_5$C$_7$H-O** λ_{em} = 370 nm.

Table 3.6. Lifetimes from the exponential fits for the days of molecular rotors in 2-MeTHF solutions. Associated IRF set labelled, after rotor name in each case. IRF data outlined in Table 3.7. [a]Single exponential fit y = y0 + A1*exp(-(x-x0)/t1) used.

Rotor	IRF	R^2	y = y0 + A1*exp(-(x-x0)/t1) + A2*exp(-(x-x0)/t2)			
			a1	τ1 /ns	a2	τ2 /ns
C$_7$Ph$_7$H-O	A	0.997	0.48233	2.68932	0.20257	12.6032
sym-phenPh$_5$C$_7$H-O	A	0.997	0.45193	1.98772	0.32792	11.90997
asym-phenPh$_5$C$_7$H-O	A	0.999	0.22227	1.5013	0.5146	8.96569
C$_7$Ph$_7$H	B	0.997	0.65983	1.2868	0.09034	6.53826
sym-phenPh$_5$C$_7$H	B	0.996	0.85205	0.91697	0.00233	20.43031
asym-phenPh$_5$C$_7$H	B	0.997	2.96577	0.95146	0.08254	8.16175
sym-phen$_3$PhC$_7$H[a]	C	0.998	1	8.41089	-	-

Table 3.7. Lifetimes from the exponential fits for the days of molecular rotors in 2-MeTHF solutions.

IRF	R^2	double z = (x-xc)/w - w/t0; y = y0 + A/t0 * exp(0.5*(w/t0)^2-(x-xc)/t0)*(erf(z/sqrt(2))+1)/2;)				
		y0	A	xC	w	t0
A	0.997	0±0	0.88151	15.36179	0.17497	0.48048
B	0.997	0±0	0.88217	7.52282	0.16955	0.49436
C	0.998	0±0	0.87172	23.23267	0.16619	0.49784

3.4.10. New Photocyclised Rotors

Optical data for the new photocyclised rotors are included below.

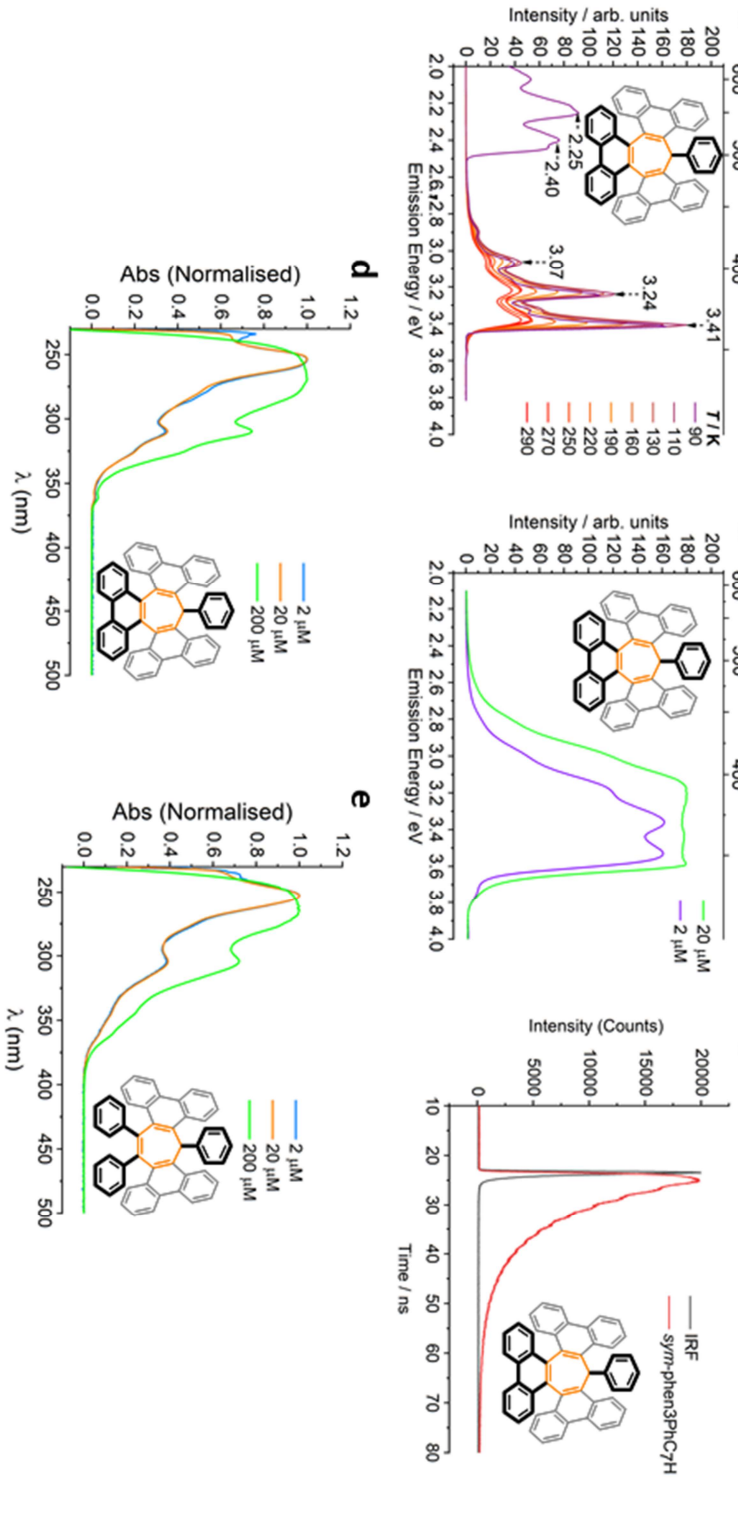

Figure 3.40. (a) VT fluorescence spectra of photooxidised molecular rotors in a 2-MeTHF solutions (l = 10 mm, T = 90–290 K) of ***syn*-phen3PhC7H** λ_{ex} = 315 nm, c = 2 μM; **(b)** Fluorescence spectra of ***syn*-phen3PhC7H** (l = 10 mm, T = 290 K); Insert in panel **(b)**: Legend for concentration; **(c)** TCSPC decays of molecular rotors in a 2-MeTHF solutions (l = 10 mm, T = 290 K, c = 2 μM) of **(a) *syn*-phen3PhC7H** λ_{em} = 365 nm; UV-Vis absorption spectra of solutions of **(d) *syn*-phen3PhC7H**, **(e) *syn*-phen2Ph3C7H** at a series of concentrations in 2-MeTHF.

3.4.11. Hyperchromism

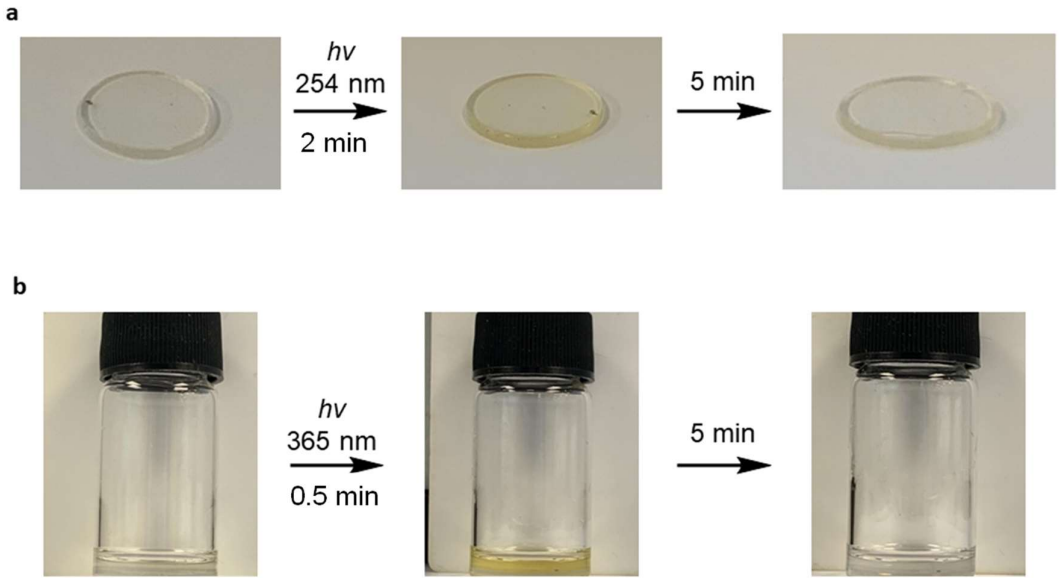

Figure 3.41. Photographs demonstrating the hyperchromic effect in ***sym*-phenPh$_5$C$_7$H-O** through reversible yellowing upon short irradiation with 365 nm light in: **(a)** 1% ZEONEX film; **(b)** 1.5 mmol solution in PhMe.

3.5. Computational Details

Ground state geometry optimisation of ***sym*-phen$_2$Ph$_3$C$_7$H-O** was conducted *in vacuo* employing the SCS-MP2 method (spin-component-scaled Møller–Plesset perturbation theory of second order)[39] along with an SVP basis set. The S_1 excited-state geometry optimisation was performed with SCS-ADC(2) method (spin-component-scaled adiabatic diagrammatic construction up to second order)[40] with an SVP basis set. All electronic transitions were calculated with SCS-ADC(2) using a TZVP basis set, on the S_0 or S_1 geometries obtained with SCS-MP2/SVP or SCS-ADC(2)/SVP. All calculations were performed with the Turbomole 7.4.1 program package.[41]

To further investigate the shape of the S_1 emission band, we included non-Condon effects in our calculations by using the nuclear ensemble approach.[42] We optimised the S_1 geometry of ***sym*-phen$_2$Ph$_3$C$_7$H-O** using linear-response time-dependent density functional theory (LR-TDDFT) within the Tamm-Dancoff approximation, the ωB97X-D functional, and a 6-31G*

basis set. The minimum-energy geometry obtained on S_1 shows a similar electronic character to the one calculated with SCS-ADC(2). At the LR-TDDFT/TDA S_1 geometry, LR-TDDFT/TDA/ωB97X-D/6-31G* gives a vertical S_1/S_0 energy of 3.98 eV, while SCS-ADC(2)/TZVP (on the same geometry) indicates a transition energy of 3.64 eV. Frequencies were obtained at the same level of theory and used to calculate an approximated Wigner distribution for the lowest vibrational states of the S_1 electronic state. A total of 100 geometries were sampled from this Wigner distribution. For each of these geometries, S_1/S_0 emission energy and oscillator strength were calculated at the LR-TDDFT/TDA/ωB97X-D/6-31G* level of theory. An emission spectrum accounting for non-Condon effects is then obtained by grouping all the transitions, each broadened by a Gaussian with a width of 0.1 eV. The obtained emission spectrum (Figure 3.42) reproduces the width of the experimental one. The NEA spectrum was obtained with Newton-X 2.0[43] interfaced with Gaussian 09 revision D.01 for the electronic structure.[44]

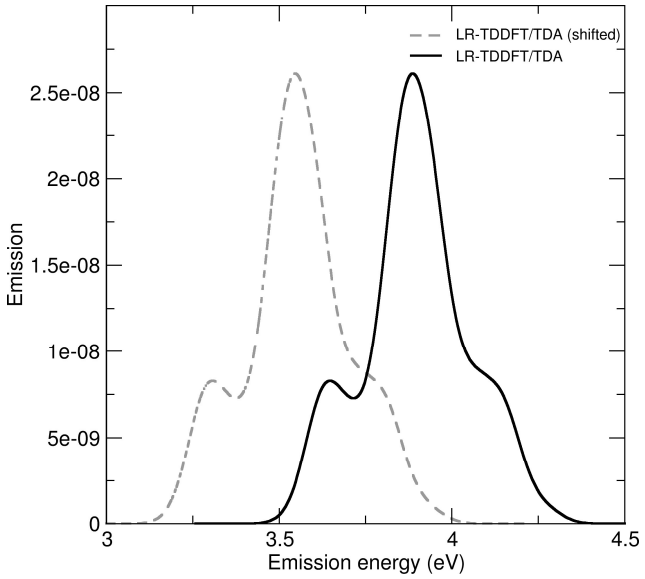

Figure 3.42. Emission spectrum calculated with the NEA using LR-TDDFT/TDA/ωB97X-D/6-31G* (see text for details). The shifted spectrum corresponds to the original LR-TDDFT/TDA spectrum shifted by the energy difference (0.34 eV) between the transition calculated with SCS-ADC(2)/TZVP and LR-TDDFT/TDA/ωB97X-D/6-31G* at the S_1 optimised geometry (obtained with LR-TDDFT/TDA/ωB97X-D/6-31G*).

3.6. References

1 K. Zhang, J. Liu, Y. Zhang, J. Fan, C. K. Wang, and L. Lin, *J. Phys. Chem. C*, 2019, **123**, 24705–24713.

2 Y. Huang, J. Xing, Q. Gong, L. C. Chen, G. Liu, C. Yao, Z. Wang, H. L. Zhang, Z. Chen, and Q. Zhang, *Nat. Commun.*, 2019, **10**, 169.

3 Y. Hong, J. W. Y. Lam, and B. Z. Tang, *Chem. Commun.*, 2009, 4332–4353.

4 H. Zhang, Z. Zhao, A. T. Turley, L. Wang, P. R. McGonigal, Y. Tu, Y. Li, Z. Wang, R. T. K. Kwok, J. W. Y. Lam, and B. Z. Tang, *Adv. Mater.* 2020, **32**, 2001457.

5 S. Ma, S. Du, G. Pan, S. Dai, B. Xu, and W. Tian, *Aggregate*, 2021, **2**, e96.

6 A. Qin and B. Z. Tang, *Aggregation-Induced Emission: Fundamentals and Applications,* Vol. 1–2, John Wiley & Sons, Hoboken, 2013.

7 Q. Peng and Z. Shuai, *Aggregate*, 2021, **2**, e91.

8 Y. Tu, Z. Zhao, J. W. Y. Lam, and B. Z. Tang, *Natl. Sci. Rev.*, 2021, **8**, nwaa260.

9 J. Zhang, H. Zhang, J. W. Y. Lam, and B. Z. Tang, *Chem. Res. Chin. Univ.*, 2021, **37**, 1–15.

10 P. Zhou, P. Li, Y. Zhao, and K. Han, *J. Phys. Chem. Lett.*, 2019, **10**, 6929–6935.

11 Y. Tu, J. Liu, H. Zhang, Q. Peng, J. W. Y. Lam, and B. Z. Tang, *Angew. Chem. Int. Ed.*, 2019, **58**, 14911–14914; *Angew. Chem.* 2019, **131**, 15053–15056.

12 W. Ota, K. Takahashi, K. Higashiguchi, K. Matsuda, and T. Sato, *J. Mater. Chem. C*, 2020, **8**, 8036–8046.

13 F. Würthner, *Angew. Chem. Int. Ed.*, 2020, **59**, 14192; *Angew. Chem.*, 2020, **132**, 14296–14301.

14 N. L. C. Leung, N. Xie, W. Yuan, Y. Liu, Q. Wu, Q. Peng, Q. Miao, J. W. Y. Lam, and B. Z. Tang, *Chem.—Eur. J.*, 2014, **20**, 15349–15353.

15 S. Suzuki, S. Sasaki, A. S. Sairi, R. Iwai, B. Z. Tang, and G. Konishi, *Angew. Chem. Int. Ed.*, 2020, **59**, 9856–9867; *Angew. Chem.*, 2020, **132**, 9940–9951.

16 J. Sturala, M. K. Etherington, A. N. Bismillah, H. F. Higginbotham, W. Trewby, J. A. Aguilar, E. H. C. Bromley, A.-J. Avestro, A. P. Monkman, and P. R. McGonigal, *J. Am. Chem. Soc.*, 2017, **139**, 17882–17889.

17 H. Zhang, Z. Zhao, P. R. McGonigal, R. Ye, S. Liu, J. W. Y. Lam, R. T. K. Kwok, W. Z. Yuan, J. Xie, A. L. Rogach, and B. Z. Tang, *Mater. Today*, 2020, **32**, 275–292.

18 H. Zhang and B. Z. Tang, *JACS Au*, 2021, **1**, 1805–1814.

19 (a) L. le Bras, C. Adamo, and A. Perrier, *J. Phys. Chem. C*, 2017, **121**, 25603–25616. (b) K. Kokada and K. Sada, *Angew. Chem. Int. Ed.*, 2019, **58**, 8632–8639; *Angew. Chem.*, 2019, **131**, 8724–8731.

20 X. L. Peng, S. Ruiz-Barragan, Z. S. Li, Q. S. Li, and L. Blancafort, *J. Mater. Chem. C*, 2016, **4**, 2802–2814.

21 Q. Li and L. Blancafort, *Chem. Commun.*, 2013, **49**, 5966–5968.

22 H. T. Feng, C. Liu, Q. Li, H. Zhang, J. W. Y. Lam, and B. Z. Tang, *ACS Mater. Lett.*, 2019, **1**, 192–202.

23 H. Tong, Y. Hong, Y. Dong, M. Häußler, J. W. Y. Lam, Z. Li, Z. Guo, Z. Guo, and B. Z. Tang, *Chem. Commun.* 2006, 3705–3707.

24 "Photocyclisation of Stilbenes and Related Molecules": F. B. Mallory, C. W. Mallory in *Organic Reactions*, Vol. 30 (Ed.: W. G. Dauben), Wiley, New York, 1984, pp. 1–456.

25 N. Hoffmann, *Chem. Rev.*, 2008, **108**, 1052–1103.

26 A. G. Lvov, *J. Org. Chem.*, 2020, **85**, 8749–8759.

27 A. Ghosh, D. Csókás, M. Budanović, R. D. Webster, I. Pápai, and M. C. Stuparu, *Chem. Sci.*, 2021, **12**, 3977–3983.

28 Y. Cai, L. Du, K. Samedov, X. Gu, F. Qi, H. H. Y. Sung, B. O. Patrick, Z. Yan, X. Jiang, H. Zhang, J. W. Y. Lam, I. D. Williams, D. Phillips, A. Qin, and B. Z. Tang, *Chem. Sci.*, 2018, **9**, 4662–4670.

29 Cambridge Crystallographic Data Centre (CCDC) depository numbers: 2144322 (***asym*-phenPh$_5$C$_7$H**), 2144323 (***sym*-phenPh$_5$C$_7$H**), 2144324 (**Ph$_7$C$_7$H-O**), 2144325 (***asym*-phenPh$_5$C$_7$H-O**), 2144326 (***sym*-phen$_2$Ph$_3$C$_7$H-O**), 2144327 (***sym*-phenPh$_5$C$_7$H-O**), 2144328 (**Ph$_3$C$_3$·HCl$_2$**).

30 N. A. Murugan, J. Kongsted, Z. Rinkevicius, and H. Ågren, *Proc. Natl. Acad. Sci. USA*, 2010, **107**, 16453–16458.

31 Emission spectra are reported in eV and are Jacobian corrected to allow meaningful comparisons of Stokes shifts between compounds, see: J. Mooney and P. Kambhampati. *J. Phys. Chem. Lett.*, 2013, **4**, 3316–3318.

32 E. A. Chandross and H. T. Thomas, *J. Am. Chem. Soc.*, 1972, **94**, 2421–2424.

33 Unlike in similar reports of vibronic emission from TPE, decreasing the excitation energy to match a lower energy absorption band does not curb this phenomenon, see: M. P. Aldred, C. Li, and M.-Q. Zhu, *Chem.—Eur. J.*, 2012, **18**, 16037–16045.

34 M. Grzybowski, B. Sadowski, H. Butenschön, and D. T. Gryko, *Angew. Chem. Int. Ed.*, 2020, **59**, 2998–3027; *Angew. Chem.*, 2020, **132**, 3020–3050.

35 A. T. Turley, PhD thesis, University of Durham (UK), 2020.

36 R. Vaughan Williams, W. D. Edwards, P. Zhang, D. J. Berg, and R. H. Mitchell, *J. Am. Chem. Soc.*, 2012, **134**, 16742–16752.

37 J. Sturala, M. K. Etherington, A. N. Bismillah, H. F. Higginbotham, W. Trewby, J. A. Aguilar, E. H. C. Bromley, A.-J. Avestro, A. P. Monkman and P. R. McGonigal, *J. Am. Chem. Soc.*, 2017, **139**, 17882–17889.

38 H. J. Reich, *J. Chem. Educ.*, 1995, **72**, 1086.

39 S. Grimme, L. Goerigk and R. F. Fink. *Wiley Interdiscip. Rev. Comput. Mol. Sci.*, 2012, **2**, 886–906.

40 A. Dreuw and M. Wormit. *Wiley Interdiscip. Rev. Comput. Mol. Sci*. **2015**, 5, 82–95.

41 F. Furche, R. Ahlrichs, C. Hättig, W. Klopper, M. Sierka and F. Weigend. *Wiley Interdiscip. Rev. Comput. Mol. Sci*, 2013, **4**, 91–100.

42 Crespo-Otero, R.; Barbatti, M. *Theor. Chem. Acc*. 2012, **131**, 1237.

43 Barbatti, M.; Ruckenbauer, M.; Plasser, F.; Pittner, J.; Granucci, G.; Persico, M.; Lischka, H. *Wiley Interdiscip. Rev. Comput. Mol. Sci*. 2014, **4**, 26−33.

44 Gaussian 16, Revision C.01, M. J. Frisch, G. W. Trucks, H. B. Schlegel, G. E. Scuseria, M. A. Robb, J. R. Cheeseman, G. Scalmani, V. Barone, G. A. Petersson, H. Nakatsuji, X. Li, M. Caricato, A. V. Marenich, J. Bloino, B. G. Janesko, R. Gomperts, B. Mennucci, H. P. Hratchian, J. V. Ortiz, A. F. Izmaylov, J. L. Sonnenberg, D. Williams-Young, F. Ding, F. Lipparini, F. Egidi, J. Goings,

B. Peng, A. Petrone, T. Henderson, D. Ranasinghe, V. G. Zakrzewski, J. Gao, N. Rega, G. Zheng, W. Liang, M. Hada, M. Ehara, K. Toyota, R. Fukuda, J. Hasegawa, M. Ishida, T. Nakajima, Y. Honda, O. Kitao, H. Nakai, T. Vreven, K. Throssell, J. A. Montgomery, Jr., J. E. Peralta, F. Ogliaro, M. J. Bearpark, J. J. Heyd, E. N. Brothers, K. N. Kudin, V. N. Staroverov, T. A. Keith, R. Kobayashi, J. Normand, K. Raghavachari, A. P. Rendell, J. C. Burant, S. S. Iyengar, J. Tomasi, M. Cossi, J. M. Millam, M. Klene, C. Adamo, R. Cammi, J. W. Ochterski, R. L. Martin, K. Morokuma, O. Farkas, J. B. Foresman, and D. J. Fox, Gaussian, Inc., Wallingford CT, 2016.

CHAPTER 4 |

TOWARDS A REDOX-ACTIVE WARPED NANOGRAPHENE

Abstract

The molecular structure of polycyclic aromatic hydrocarbons has an enormous impact on their chemical, photophysical, and optoelectronic properties. Over the past decades, synthetic chemists have succeeded in preparing a diverse range of PAHs with non-hexagonal rings, however in most cases, these are nonaromatic. This chapter presents our on-going attempts to synthesise a tropylium-embedded warped nanographene, as well as its partially-fused helical analogue. Or findings indicate that traditional oxidative cyclodehydrogenation reactions, such as the Scholl oxidation do not afford the target nanographene. Instead, they form complex mixtures of inseparable materials. A more modular approach involving Pd-catalysed C–H couplings has proven to be more successful, although the efficacy of this methodology is limited by the intrinsic instability of the precursors required for the C–H activation step.

Acknowledgements

The following people are gratefully acknowledged for their contribution to this chapter: Dr. A. Turley, Dr. A. Mallick, and Dr. S. K. Kabali attempted Scholl oxidations on cycloheptatriene- and tropone-based precursors. S. Dadwal contributed to the synthesis of tropone precursor **42**. Dr. D. S. Yufit solved the X-ray crystal structures. Dr. P. R. McGonigal carried out all DFT-calculations and conceived of the research.

4.1. Introduction

Polycyclic aromatic hydrocarbons have garnered extensive interest in recent decades, due to their desirable optoelectronic and redox properties.[1] It is well-established that twisting or bending planar PAHs through molecular strain (exo-skeletal methods) or intrinsic defects (endo-skeletal methods) can alter their properties immensely.[2] Indeed, nonplanar PAHs and larger warped nanographenes have been noted for their improved solubility, enhanced fluorescence, and higher charge-carrier mobilities compared to their planar analogues.[3] Strain can also endow molecules with helical chirality, forming helicenes, which have been exploited in spintronics[4], as circularly polarised luminogens[5], as well as ligands in enantioselective catalysis.[6]

Though a diverse library of PAHs with non-hexagonal rings incorporated within the polycyclic framework has been reported to produce highly warped structures, these rings are usually nonaromatic.[7] Reports of non-benzenoid aromatic rings within a strained framework—especially tropyliums—remain sparse. Such molecules are of general interest, because: i) the inclusion of seven- or eight-membered rings grants molecules with a saddle-shaped geometry[8], and ii) they exhibit interesting redox-behaviour due to the charge associated with the tropylium.[9]

Here, we report synthetic attempts toward hepta-*peri*-heptabenzo-[7]-circulene (**1**), as well as its partially-fused, helical derivative **2**. These can be considered heptagonal homologues of *peri*-hexabenzocoronene (HBC) and hexabenzotriphenylene respectively. DFT calculations indicate that **1** is expected to have a highly distorted saddle-shaped geometry.

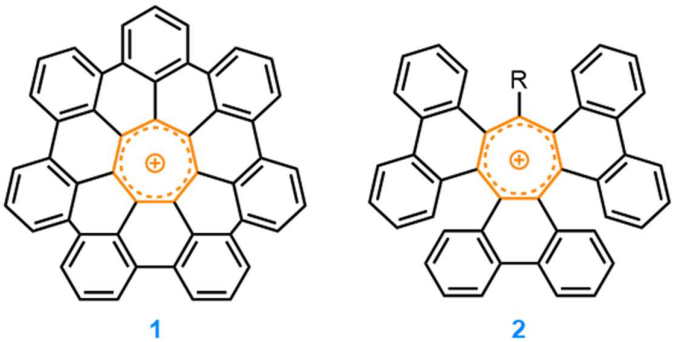

Figure 4.1. Target molecules for this chapter.

4.2. Results and Discussion

Part A: Syntheses towards warped nanographene 1

4.2.1. The Scholl Oxidation

As discussed in Chapter 1, the traditional route to synthesizing polycyclic aromatics involves IOCD reactions such as the Scholl oxidation.[10] A suitable precursor to prepare **1** is heptaphenylcycloheptatriene (**3**). Unfortunately, **3** was found to be inert to $FeCl_3$, while harsher conditions (DDQ/TfOH) preferentially oxidised the cycloheptatrienyl core to a tropylium, forming heptaphenyltropylium (**4**). This cationic species is deactivated toward Scholl conditions, which is known to proceed *via* an arenium or radical cation mechanism. Similarly, the phenanthrene-annulated cycloheptatriene **5** formed a complex mixture of products when subjected to Scholl conditions. Notably, treatment with $FeCl_3$ led to chlorination of the phenanthrene moiety. These findings are summarised below in Figure 4.2.

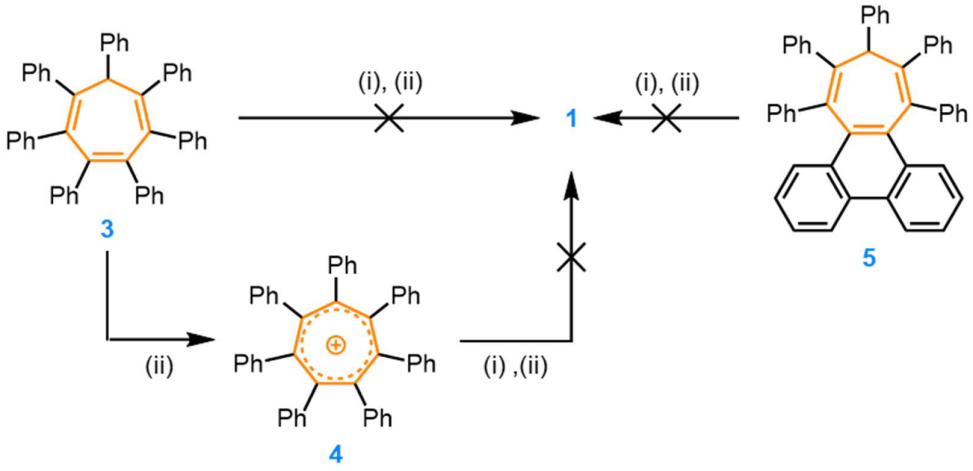

Figure 4.2. Attempted synthesis of **1** using Scholl conditions. Reagents and conditions: (i) $FeCl_3$, CH_2Cl_2, 0 °C → rt, 3 h; (ii) DDQ, TfOH, CH_2Cl_2, 0 °C → rt, 1 h.

King's computational report from 2007 predicts that the addition of methoxy groups can activate *ortho*- and *para*-positions of aryl rings to the Scholl oxidation by increasing their relative proton affinities (Figure 4.3a).[11] Inspired by this, we prepared a series of cycloheptatrienes with 4-methoxy- and 3,5-dimethoxyphenyl groups from suitable triarylcyclopropenes and tetraarylcyclopentadienones (Figure 4.3b). Further

details regarding the synthesis of these precursors is summarised in Dr. Andrew Turley's thesis.[12]

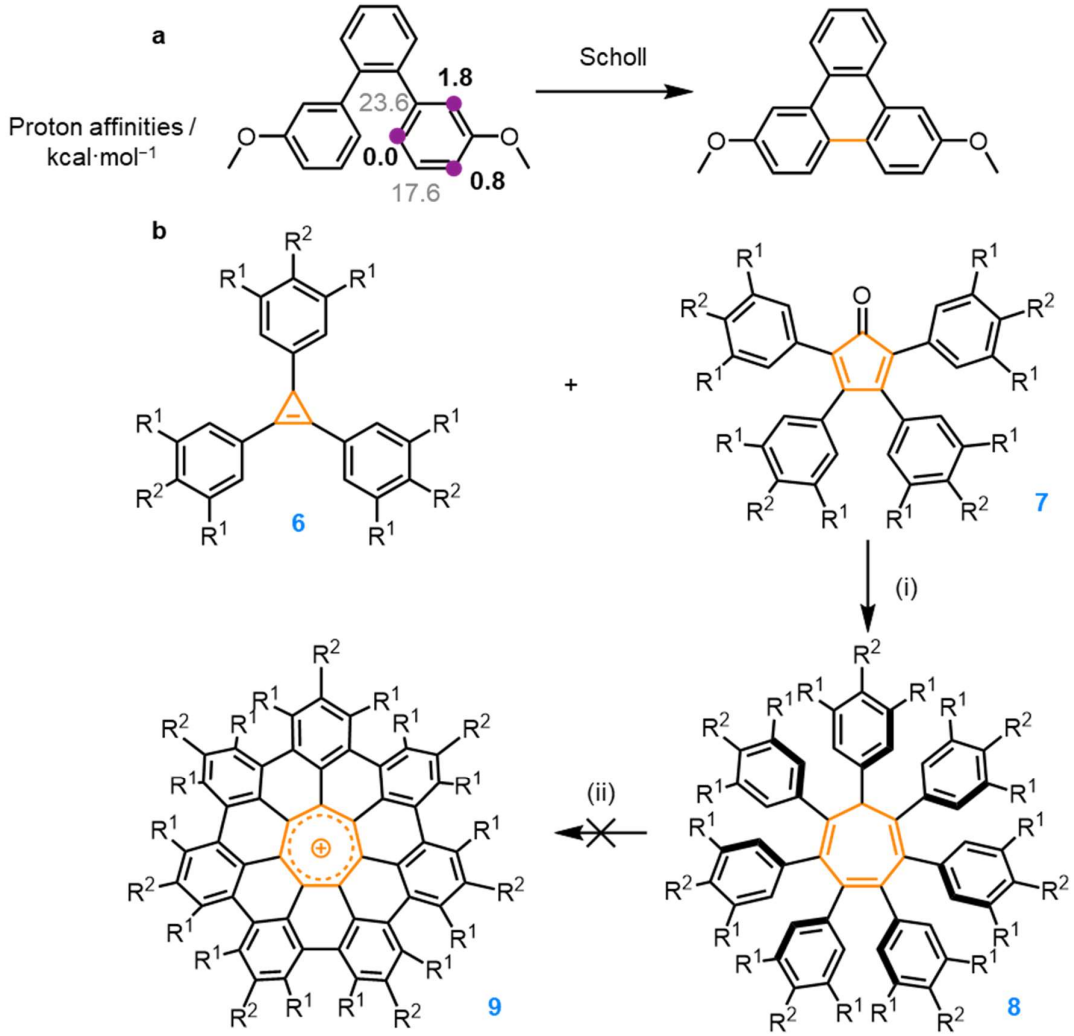

Figure 4.3. a) Proton affinities of OMe-substituted aryl rings. The Scholl-activated positions are highlighted in purple; **b)** Attempted OMe-directed IOCD to form the target nanographene. Reagents and conditions: i) *p*-xylene, 160 °C, 66 h (**a**=75%, **b**=30%); ii) DDQ, TfOH, 0 °C → rt, 1 h. **a)** R^1=H, R^2=OMe; **b)** R^1=OMe, R^2=H.

Miao had moderate success using cyclodehydrogenation conditions on tropone **13** (Figure 4.4), with two activated 3,5-dimethoxybenzene units. Tropone **13** was prepared *via* a Diels–Alder reaction between phencyclone **12** and diphenylcyclopropenone.[13] This tropone was found to undergo IOCD to afford **14** cleanly. Alternatively, a Grignard reaction of **13** with 4-isopropoxyphenylmagnesium bromide formed **15**, which could subsequently be oxidised to **16** with $AlCl_3$. When subjected to Scholl conditions, this substrate only underwent partial ring closure to

form **17**, which in turn gave a complex mixture of products when subjected to harsher oxidizing or acidic conditions. The authors attributed this to the large increase in strain upon fusion of the final ring.

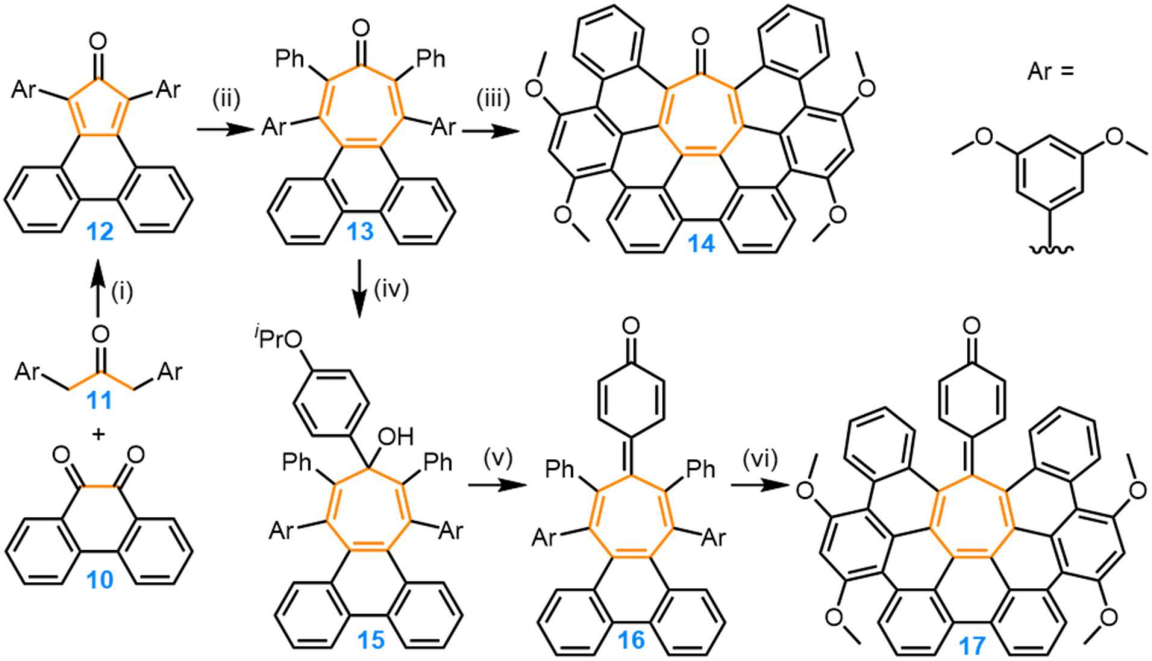

Figure 4.4. Miao's attempted synthesis of the target nanographene. Reagents and conditions: i) KOH, MeOH, reflux, 10 min (80%); ii) diphenylcyclopropenone, PhMe, reflux, 96 h (64%); iii) $FeCl_3$, $MeNO_2$, CH_2Cl_2, 0 °C, 15 min (75%); iv) 1. Mg, I_2, 1-bromo-4-isopropoxybenzene, THF, reflux, 18 h, 2. H_2O (90%); iv) $AlCl_3$, CH_2Cl_2, 0 °C → rt, 15 min (53%); v) $FeCl_3$, $MeNO_2$, CH_2Cl_2, 0 °C → rt, 30 min (60%).

4.2.2. Pd-Catalysed C-H Activation

In light of the Scholl oxidation's failure to produce the target nanographene, we turned to Pd-catalysed ring fusions as an alternate strategy. We postulated that—unlike the Scholl oxidation, where ring fusion was hampered by a large surge in strain—the bridging Pd atom would alleviate the strain associated with ring closure. Two key cycloheptatrienes (**18** and **19**) that would enable the synthesis of nanographene **1** as well as their retrosynthetic analyses are shown below in Figure 4.5. Both **18** and **19** contain heavily functionalised aryl rings. Their syntheses require pre-functionalised starting materials, which themselves are only accessible through multi-step syntheses. In addition, side-reactions may compete with the desired cyclodehydrohalogenation, giving rise to complex mixtures of compounds that are difficult to analyse.

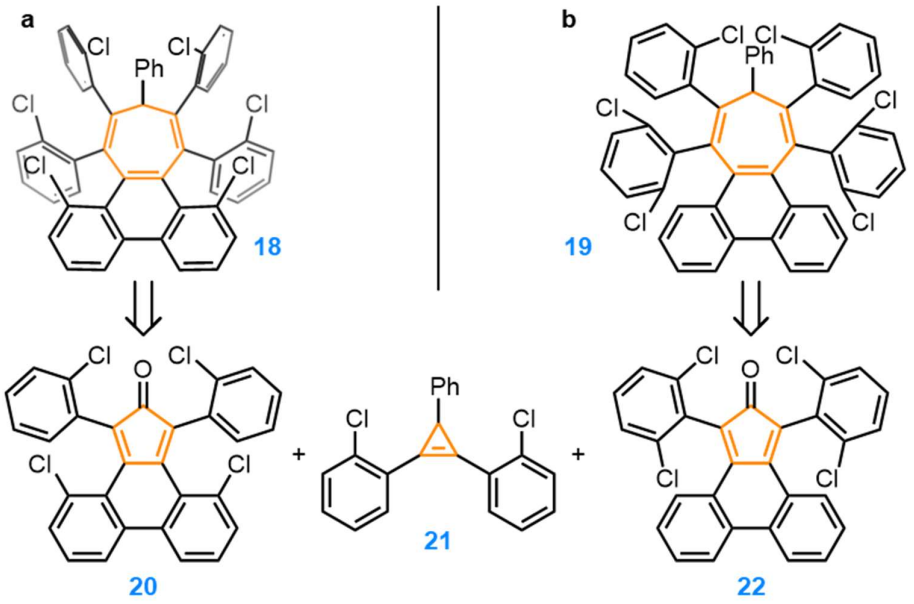

Figure 4.5. Intermediates **18** and **19** and the building blocks required to access them.

CHT **25** is a simpler, more easily accessible substrate that allows for reaction condition optimisation and better understanding of the regiochemical outcome of the C–H activation. The synthesis of **25** (shown in Figure 4.6) begins with a DCC coupling of 2-chlorophenylacetic acid to form di(2-chlorophenyl)acetone **23**. A Knoevenagel condensation of **23** with 9,10-phenanthrenequinone afforded phencyclone **24**, which underwent a Diels–Alder cycloaddition to form the target CHT in a 12% yield.

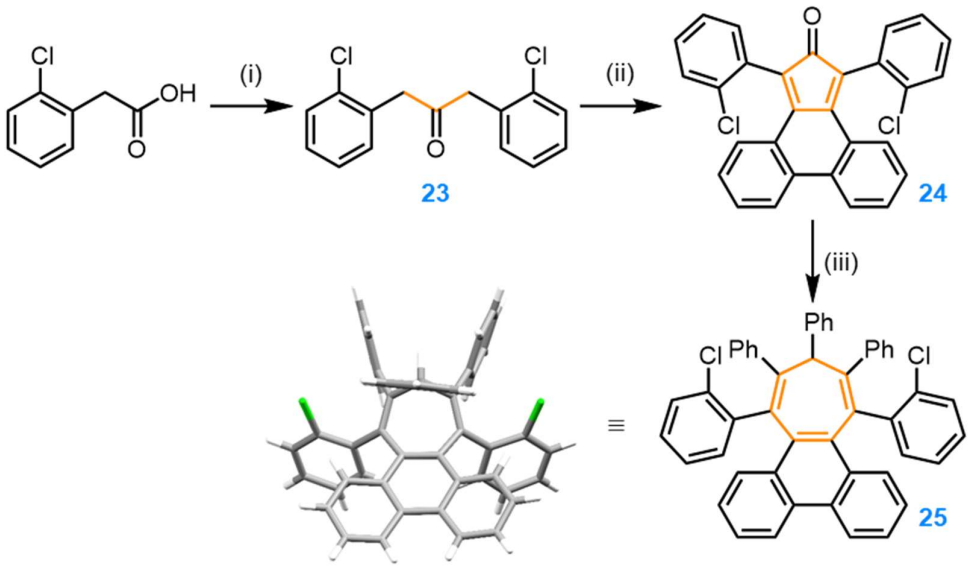

Figure 4.6. Synthesis of CHT **25** (single crystal X-ray structure shown on the right). Reagents and conditions: i) DCC, DMAP, CH_2Cl_2, rt, 16 h (81%); ii) 9,10-phenanthrenequinone, NaOH, EtOH, reflux, 30 min (33%); iii) *sym*-triphenylcyclopropene, *p*-xylene, reflux, 72 h (12%).

CHT **25** can undergo ring closures with multiple fusion patterns (Figure 4.7), or even polymerise. A number of conditions was screened to investigate the regioselectivity of the reaction. As shown in Table 1, **25** was inert toward $Pd(PPh_3)_4/Cs_2CO_3$, even at high catalyst loadings. However, high loadings of $Pd(PCy_3)_2Cl_2$ (80%) proved more successful, selectively yielding the double helicene **26a**. None of the other fused, asymmetric cycloheptatrienes, nor any polymerisation were observed.

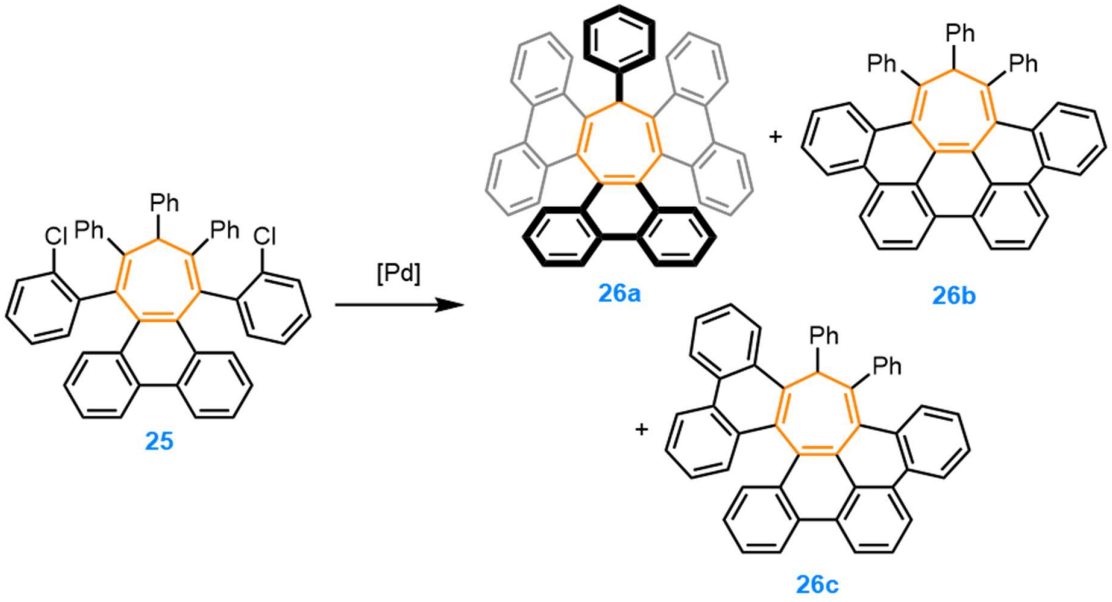

Figure 4.7. Possible fusion patterns of **25**.

Table 4.1. Conditions screened for the Pd-catalysed cyclodehydrohalogenation of **25** and the yield for each fused CHT formed.

Conditions	Pd Loading / mol%	T / °C	*t* / h	Yield[a]	Comment
$Pd(PPh_3)_4$, Cs_2CO_3, PhMe	20	110	48	–	
$Pd(PPh_3)_4$, Cs_2CO_3, PhMe	80	110	48	–	Only SM in crude
$Pd(PCy_3)_2Cl_2$, DBU, DMF	20	160	48	–	
$Pd(PCy_3)_2Cl_2$, DBU, DMF	50	160	48	35	–
$Pd(PCy_3)_2Cl_2$, DBU, DMF	80	160	48	47	–

[a] Yield given for **26a**

Scholl oxidation of the double helicene **26a** (using conditions (ii) described in Figure 4.3) produced a complex mixture of products, rather than the target nanographene (**1**). Interestingly, the ^{1}H NMR spectrum of **26a** indicates that it adopts a C_2-symmetric *meso*-isomer, where the [5]-helicene moiety on the left has (*M*)-chirality, and the

helicene on the right has (*P*)-chirality. The phenyl and distal phenanthrenyl moieties point upwards in the CHT boat, forming a π–π interaction, while the other two phenanthrene groups are oriented downwards. DFT calculations (Figure 4.8) predict that this folded isomer is massively favored over the twisted isomers. Despite multiple attempts, no single crystals could be grown of this compound.

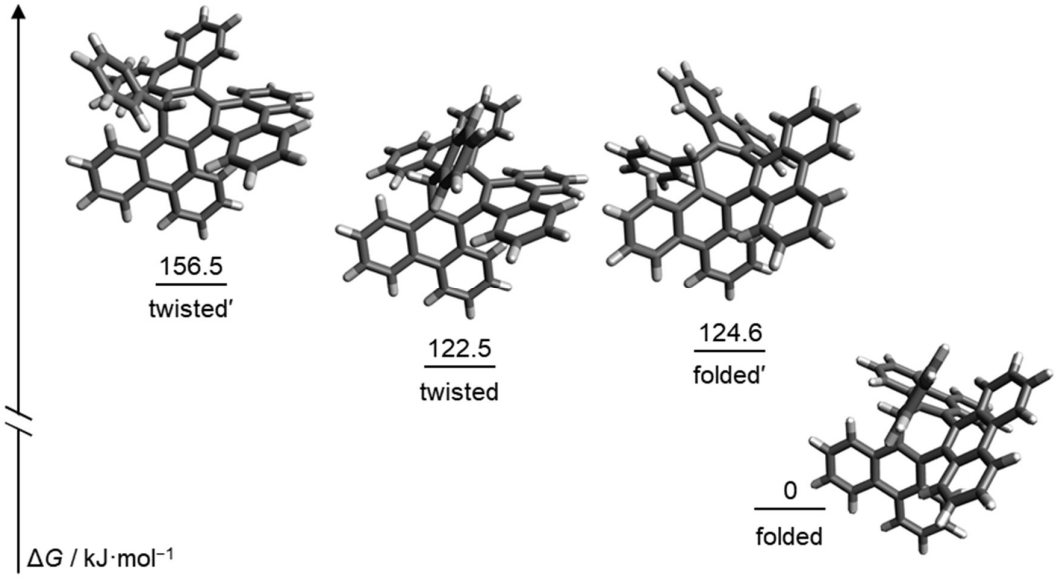

Figure 4.8. DFT-calculated relative Gibbs energies (Δ*G*) of the twisted and folded isomers of **26a**. The isomers marked with ′ have protons (rather than a phenyl ring) pointing up from the cycloheptatriene boat. (ωB97XD / 3-21G – $CHCl_3$).

4.2.3. Precursor Synthesis

Armed with this knowledge, we began the synthesis of CHTs **18** and **19**, both of which share a common dienophile: cyclopropene **21**. To begin, a Sonogashira homocoupling of 2-chloro-1-iodobenzene quantitatively afforded di(2-chlorophenyl)acetylene (**27**) (Figure 4.9). Typically, triarylcyclopropenes are prepared *via* a [2+1] cycloaddition of diarylacetylenes with a carbene precursor, such as α,α′-dichlorotoluene in the presence of a base. An acidic work-up forms a cyclopropenium (**28**), which can subsequently be reduced to a cyclopropene using $NaBH_4$. These conditions failed to produce the cyclopropenium intermediate. Instead, a masked carbene strategy (first reported by Bi) proved more successful.[14] This reaction employs *N*-nosylhydrazone **31** (prepared from *o*-nitro-*p*-toluenesulfonyl chloride in two steps) as a diazo-surrogate, rapidly decomposing to a carbene upon addition of a base. Following this, a silver-mediated

[2+1] cycloaddition directly forms the target cyclopropene in one (low-yielding) step, effectively bypassing the need to form a cyclopropenium, which may form a mixture of regioisomers upon reduction.

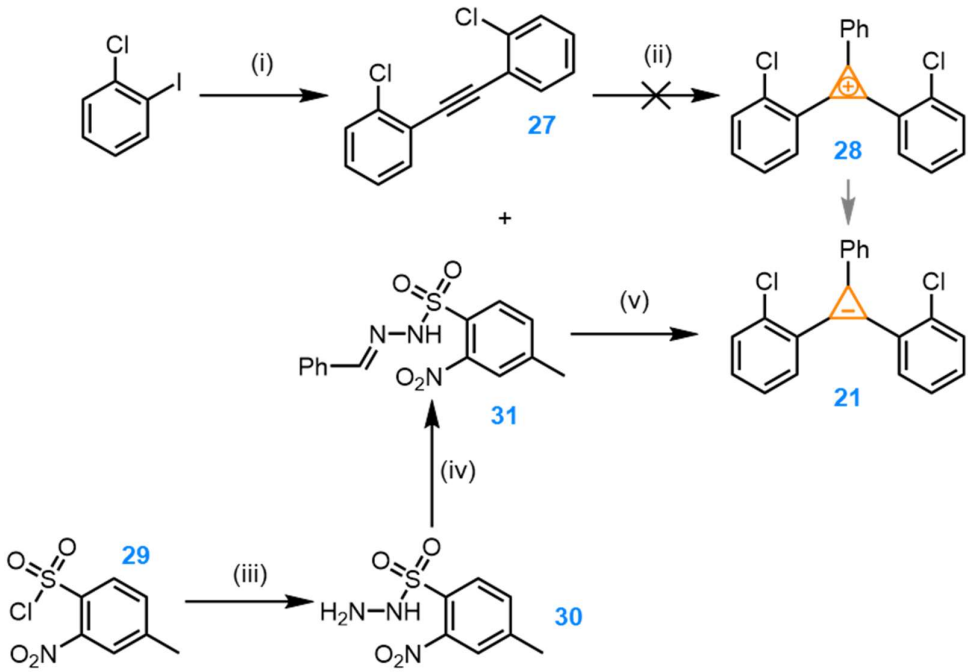

Figure 4.9. Synthesis of dienophile **21**. Reagents and conditions: i) 2-methyl-but-3-yn-2-ol, $Pd(PPh_3)_2Cl_2$, CuI, KOH, $^iPr_2NH$, 50 °C → 110 °C, 16 h (quant.); ii) 1. α,α′-dichlorotoluene, KO^{t}Bu, C_6H_6, rt → 80 °C, 3 h, 2. HBr (33% wt. in AcOH), Et_2O; iii) $H_2NNH_2 \cdot H_2O$, THF, −30 °C, 1.5 h (95%); iv) benzaldehyde, EtOH, rt, 18 h (74%); v) NaH, AgOTf, CH_2Cl_2, reflux, 16 h (16%).

The synthetic route to the diene **20** the other component in the Diels–Alder reaction to form **18** is outlined below in Figure 4.10. A Wittig reaction between 2-chlorobenzaldehyde and 2-chlorobenzyl-triphenylphosphonium bromide yielded a mixture of *cis*- and *trans*-di(2-chlorophenyl)ethene. Photocyclisation of this alkene under Mallory conditions produced 1,8-dichlorophenanthrene, which was oxidised to 1,8-dichlorophenanthrene-9,10-quinone (**35**). Surprisingly, the Knoevenagel condensation between **35** and di(2-chlorophenyl)acetone (**23**) did not proceed under base catalysis. As summarised in Table 4.2, all conditions tried only afforded the starting materials in nearly quantitative yields. It is unclear whether this lack of

reactivity is due to poor solubility of **35** or inherent instability of the highly electron-deficient cyclopentadienone **20**.

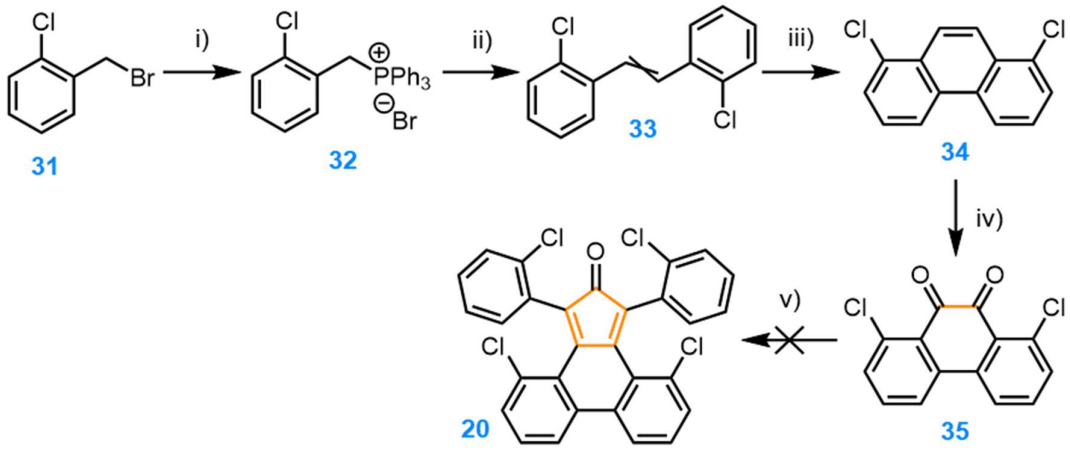

Figure 4.10. Attempted synthesis of **20**. Reagents and conditions: i) PPh_3, PhMe, 80 °C, 20 h (96%); ii) 2-chlorobenzaldehyde, KO^{t}Bu, THF, 0 °C → rt, 20 h; iii) I_2, PO, THF, *hv* (254 nm), rt, 7 d (46%); iv) CrO_3, H_5IO_6, MeCN, CH_2Cl_2 (5:3), 40 °C, 24 h (63%); iv) *see Table 4.2.*

As mentioned in Figure 4.5, route b) entails the synthesis of **19**, which can be obtained from cyclopentadienone **22**. The synthetic approach to this diene is shown below in Figure 4.11. Due to poor solubility, a DCC-homocoupling of 2,6-dichlorophenylacetic acid to form bis(2,6-dichlorophenyl)acetone (**37**) was unsuccessful. Instead, **37** was obtained from 2,6-dichlorobenzyl bromide (**36**) in two steps *via* a TosMIC coupling in moderate yields. As with **20**, the Knoevenagel condensation of **22** was challenging. All conditions attempted (see Table 4.2) only yielded the starting materials. As the solubility of phenanthrenequinone is high in the solvent systems below, it is likely the inherent instability of the cyclopentadienone that is responsible for the failure of this reaction.

Table 4.2. Conditions screened for the synthesis of **20** and **22**.

Base	Solvent	*t* / h	*T* / °C	Outcome
NaOH	MeOH (anhydrous)	0.5	reflux	SM only
KOH	MeOH	1.5	reflux	SM only
KOH	EtOH (anhydrous)	1.5	reflux	SM only
DBU	MeCN (anhydrous)	1.5	reflux	Complex mixture

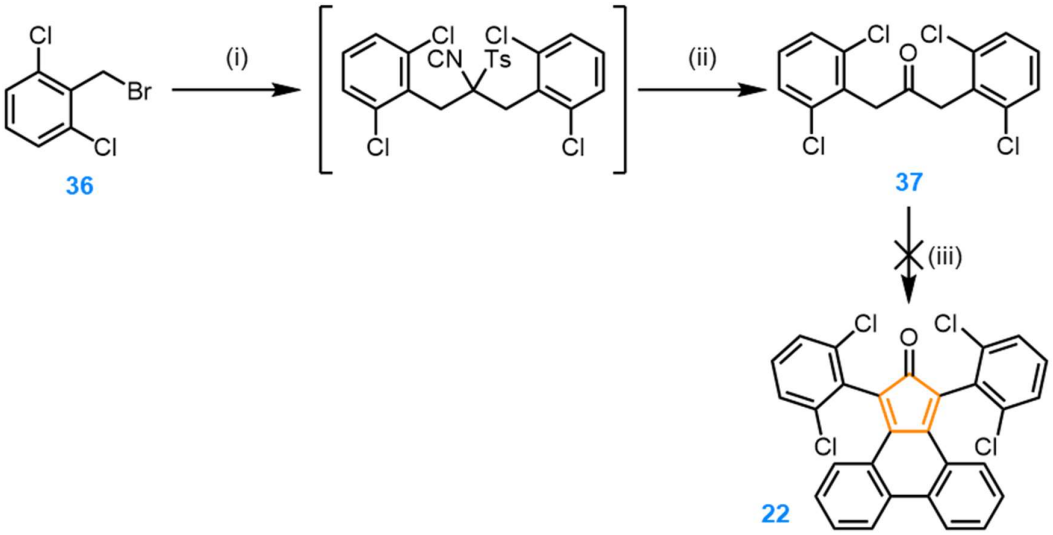

Figure 4.11. Attempted synthesis of **22**. Reagents and conditions: i) TosMIC, NaH, DMSO, rt, 16 h; ii) HCl, Et_2O, 0 °C → rt, 18 h (58% over two steps); iii) phenanthrenequinone, *see Table 4.2.*

In lieu of suitable, synthetically accessible dienes **20** and **22**, A Diels–Alder reaction was attempted between **21** and **24**. Despite prolonged heating and long reaction times, no cycloheptatriene could be isolated for further cyclodehydrohalogenation reactions. This sluggish reactivity toward cycloadditions can most likely be attributed to the steric hindrance from the *ortho*-chlorophenyl groups, which inhibit effective orbital overlap between the diene and dienophile.

Part B: Syntheses towards double helicene 2

4.2.4. Tetraaryltropones

The tropylium moiety in **2** can be generated in two steps from tropone **38** (Figure 4.12). The synthesis of this tropone should mirror that of its cycloheptatriene analogue **26a**. As such, tropones **39** (Route **a**) and **40** (Route **b**) are two possible substrates to access **38** *via* Pd-catalysed C–H activation as discussed above. A Diels–Alder reaction between **24** and diphenylcyclopropenone, or phencyclone and diarylcyclopropenone **41** affords **39** and **40** respectively. A series of conditions (Table 4.3) was screened for the cycloaddition to form **39**, but it was concluded that the high temperatures and prolonged reaction times required to affect the cycloaddition consistently led to a

complex mixture of products (which included decomposition products from both starting materials). No product could be isolated from any attempts.

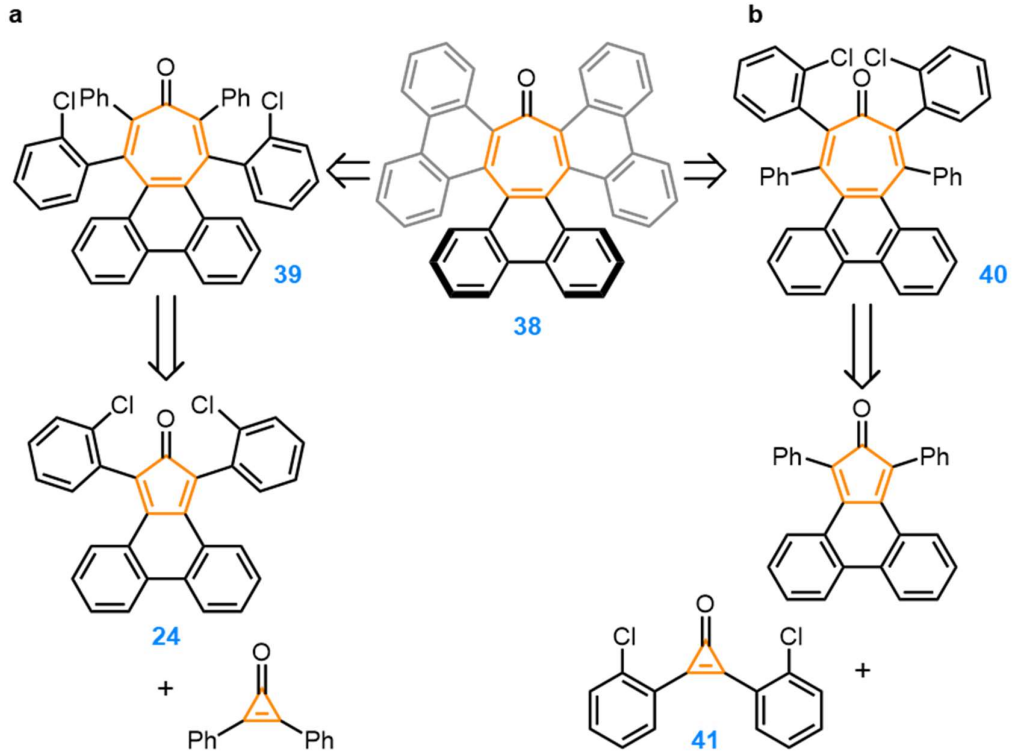

Figure 4.12. Retrosynthetic analysis of tropone **38**.

Table 4.3. Conditions screened for the Diels–Alder cycloaddition between diphenylcyclopropenone and **24**.

Solvent	*T* / °C	*t* / h	Outcome
PhMe	130	24	SMs only
PhMe	130	48	No product formation observed
PhMe	120	96	No product formation observed
PhMe–$CHCl_3$ (3:2)	120 [a]	48	No product formation observed
PhMe–$CHCl_3$ (3:2)	130 [a]	48	No product formation observed

[a] Microwave heating was used

Route **b** required the synthesis of diarylcyclopropenone **41**, which was obtained from di(2-chlorophenyl)acetone **23** over two steps in moderate yields, as shown in Figure 4.13. Unfortunately, as with route **a**, the Diels–Alder step was unsuccessful, due to decomposition of the dienophile **41** to di(2-chlorophenyl)acetylene.

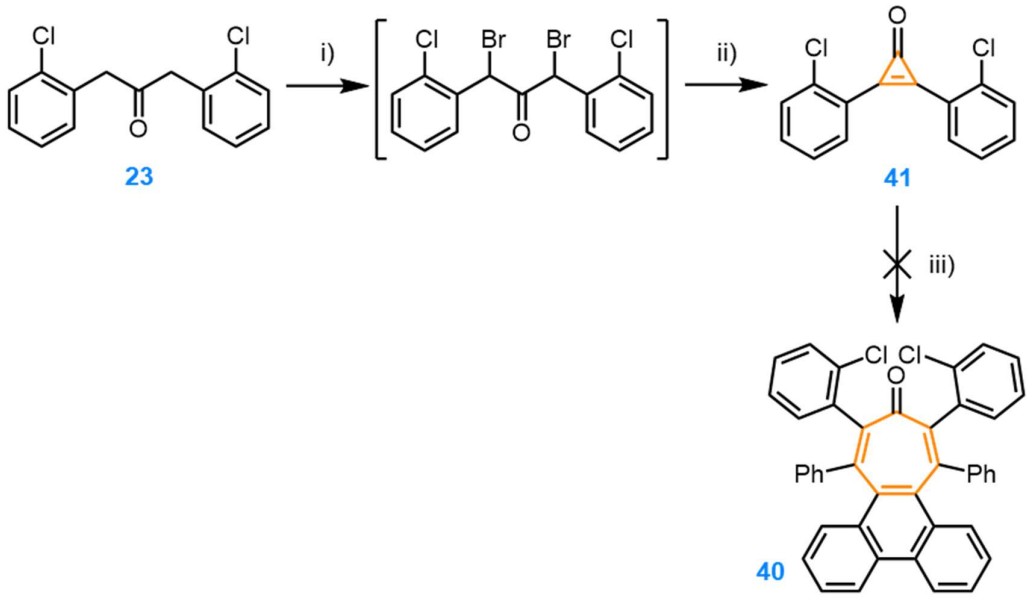

Figure 4.13. Attempted synthesis of tropone **40**. Reagents and conditions: i) Br_2, AcOH, rt, 6 h; ii) Et_3N, CH_2Cl_2, rt, 1 h (54% over two steps); iii) phencyclone, *see Table 4.4.*

Table 4.4. Conditions screened for the Diels–Alder cycloaddition between phencyclone and **41**.

Solvent	*T* / °C	*t* / h	Outcome
PhMe	110	48	SMs only
PhMe	120	48	Complete decomposition of SM [a]
PhMe	130	48	Complete decomposition of SM [a]
PhMe–$CHCl_3$ (3:2)	120	48	Complete decomposition of SM [a]

[a] The main decomposition product observed was di(2-chlorophenyl)acetylene, which forms upon loss of $CO_{(g)}$ from **41**.

4.2.5. The Condensation Approach

The inability to form **39** or **40** led us to explore different routes toward tropone-helicene **38**. A recent report by Tobisu discussed the synthesis of 2,6-dubstituted tropones, through condensation–elimination reactions (Figure 4.14a).[15] We hypothesised that Tobisu's method could be adapted to form tropone **42**. A two-fold Suzuki coupling on this substrate would afford **43**, with two *ortho*-chlorobiphenyl groups, which could subsequently be fused to the tropone core by Pd-catalysed cyclodehydrohalogenation.

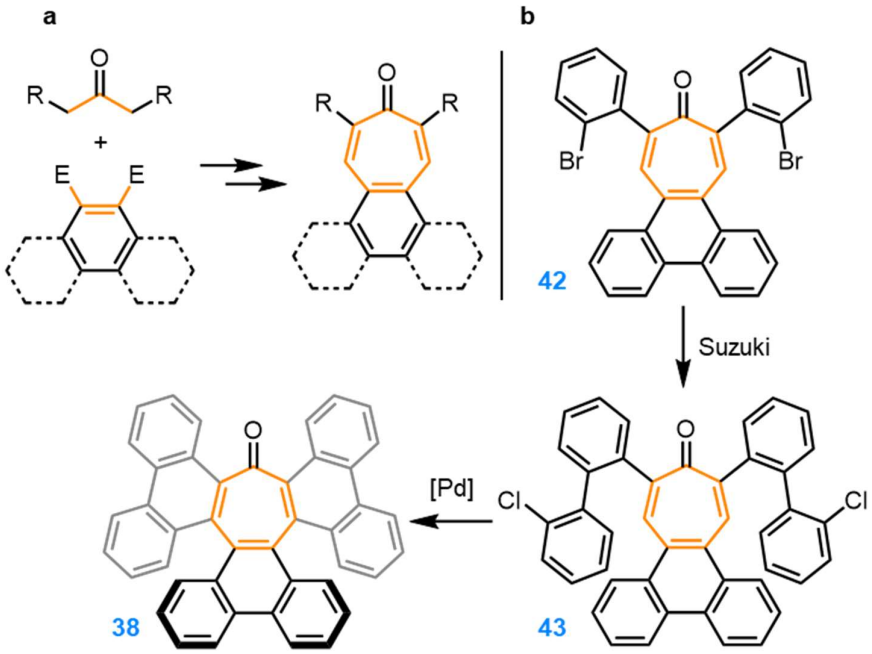

Figure 4.14. a) Tobisu's synthesis of 2,6-substituted 4,5-benzo- and phenanthrenyltropones. **E** = CHO or CH_2Br; **b)** Target molecule **42**, which can be converted to **38** *via* a Suzuki coupling, followed by cyclodehydrohalogenation.

As shown in Figure 4.15, the key step in the synthesis of **42** involves an aldol condensation of 9,10-dibromomethylphenanthrene (**46**) and di(2-bromophenyl)acetone (**48**) under basic conditions to form the cycloheptenone **49**. Compound **46** was obtained in three steps from commercially available 9,10-phenanthrenequinone (**10**), while **48** was synthesised from **47** *via* a DCC-coupling. Molecule **49** was isolated as a mixture of *syn*- and *anti*-diasteromers, which was treated with bromine in acetic acid to form the α,α′-dibromoketone **50**. Due to the small amount of material obtained, as well as the inherent instability of this compound, no high-resolution or two-dimensional spectroscopic characterisation could be obtained. However, the formation of **50** was confirmed by ^{1}H NMR spectroscopy and high-resolution mass spectrometry. Tobisu reported that treatment of α,α′-dibromoketones in the presence of LiBr and a base (Li_2CO_3) cleanly formed the tropone (albeit on a different substrate), however, this reaction was unsuccessful in our hands, instead forming a mixture of unidentified side-products. The conditions screened to convert **50** to **42** are summarised in Table 4.5. Extended reaction times led to over-reaction, while shorter, milder conditions only formed the partially-eliminated product. Optimisation of this step is currently underway in our laboratory.

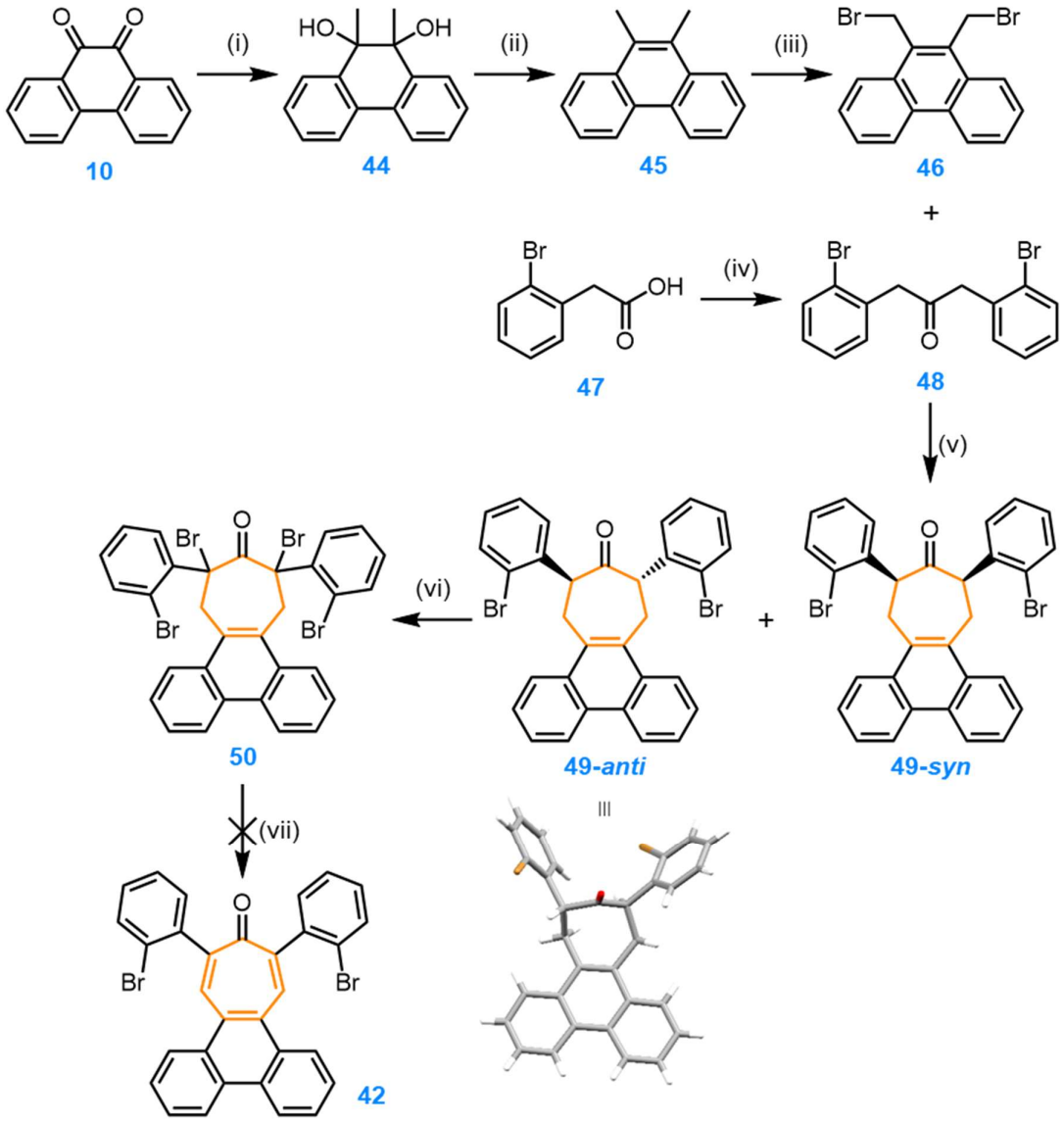

Figure 4.15. Synthetic route to **42**. Reagents and conditions: i) 1. MeMgBr, THF, rt, 2h, 2. $HCl_{(aq)}$ (0.25 M), rt, 10 min (95%); ii) HI, AcOH, reflux, 16 h (quant.); iii) NBS, BPO, CCl_4, 80 °C, 24 h (44%); iv) DCC, DMAP, CH_2Cl_2, rt, 18 h (61%); v) KOH, EtOH, THF (3:1), 0 °C → 70 °C, 5 h (90%); vi) Br_2, AcOH, $CHCl_3$ (2:1), rt, 3.5 h (32%); vii) LiBr, Li_2CO_3, DMF, s*ee Table 4.5.* The single crystal X-ray structure for **49-*anti*** is included above.

Table 4.5. Conditions screened for the elimination of **50** to yield **42**.

T **/ °C**	***t*** **/ h**	**Outcome**
100	1	Possibly partially eliminated product
120	16	Complex mixture

4.3. Conclusions and Future Work

The syntheses of nanographene **1** remains a formidable challenge. Traditional Scholl oxidations have failed to yield this target, leading instead to the formation of multiple, inseparable compounds. Meanwhile, the inherent instability of early building blocks impedes the formation of key substrates that could undergo cyclodehydrohalogenations reactions to yield the target molecule. A successful strategy to obtain **1** requires careful design of precursors that i) are synthetically accessible, and ii) can accommodate the large increases in strain associated with ring fusion.

Similarly, the formation of **2**—the helical, partially fused derivative of the target nanographene—has been challenging due to the inactivity of a number of dienes (phencyclone and **24**) and dienophiles (diphenylcyclopropenone and **41**) in crucial Diels–Alder cycloadditions. This has required a different approach based on Knoevenagel condensations to synthesise suitable substrates for cyclisations. While this approach is promising, it involves long, multi-step syntheses, which are often low-yielding. We are currently studying the use of the Mallory reaction to access tropone **38**. Such photocyclisations benefit from the fact that they do not require highly functionalised starting materials to proceed. Indeed, as demonstrated in Chapter 3, minor structural variations can switch-on a molecule's reactivity to photocyclisations.

4.4. Experimental Details

4.4.1. Synthetic Procedures

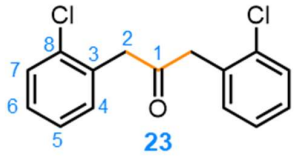

1,3-Di(2-chlorophenyl)acetone (23): A solution of 2-chlorophenylacetic acid (6.8 g, 40 mmol) in anhydrous CH_2Cl_2 (40 mL) was added dropwise over 1 h to a solution of DCC (5.9 g, 28 mmol) and DMAP (1.5 g, 12 mmol) in anhydrous CH_2Cl_2 (40 mL) in an oven-dried three-necked round-bottomed flask under an inert atmosphere. The mixture was stirred at rt for 16 h. The resulting precipitate was removed by filtration, and the solvent was removed *in vacuo*, leaving an orange residue, which was purified by column chromatography (SiO_2,

hexanes–EtOAc, 9:1) to yield the title compound as a colourless solid (4.5 g, 16 mmol, 81%). **^{1}H NMR** (400 MHz, $CDCl_3$): δ 7.41–7.36 (m, 2H), 7.24–7.20 (m, 6H), 3.92 (s, 4H). Spectroscopic data are consistent with literature reports.[16]

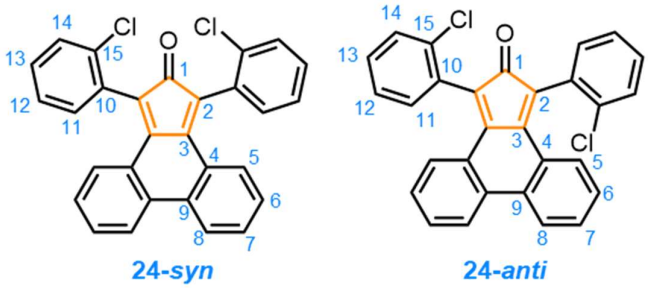

24: A solution of NaOH (0.26 g, 6.5 mmol) in EtOH (20 mL) was added dropwise to a suspension of 9,10-phenanthrenequinone (0.71 g, 3.4 mmol) and **23** (1.0 g, 3.6 mmol) in refluxing EtOH (20 mL), and the mixture was refluxed for a further 30 min, then allowed to cool to rt slowly, and finally placed in a fridge for 24 h. The resulting precipitate was collected by filtration and washed with cold EtOH (2 × 5 mL) to afford the title compound (a mixture of the *syn*- and *anti*-isomers) as a dark green solid. The filtrate was placed in the fridge for another 24 h, and the resulting precipitate was collected by filtration to afford a second batch of the product (0.50 g, 1.1mol, 34%).**^{1}H NMR** (600 MHz, $CDCl_3$) δ 7.84 (d, J = 8.1 Hz, 4H, $H_{8,8'}$), 7.54–7.48 (m, 4H, $H_{14,14'}$), 7.38–7.27 (m, 16H, $H_{7,7',11–13,11'–13'}$), 7.17–7.13 (m, 4H, $H_{5,5'}$), 7.00–6.94 (m, 4H, $H_{6,6'}$). **^{13}C NMR** (151 MHz, $CDCl_3$) δ 198.8 ($C_{1/1'}$), 198.6 ($C_{1'/1}$), 149.2 ($C_{3/3'}$), 149.0 ($C_{3'/3}$), 134.9 ($C_{15/15'}$), 134.6 ($C_{15'/15}$), 133.4 ($C_{9,9'}$), 132.3 ($C_{10/10'/11/11'/12/12'/13/13'}$), 132.2 ($C_{10/10'/11/11'/12/12'/13/13'}$), 132.1 ($C_{10/10'/11/11'/12/12'/13/13'}$), 131.8 ($C_{7/7'10/10'/11/11'/12/12'/13/13'}$), 131.8 ($C_{7/7'10/10'/11/11'/12/12'/13/13'}$), 131.7 ($C_{7/7'10/10'/11/11'/12/12'/13/13'}$), 130.2 ($C_{14/14'}$), 130.0 ($C_{14'/14}$), 129.7 ($C_{11/11'/12/12'/13/13'}$), 129.7 ($C_{11/11'/12/12'/13/13'}$), 129.4 ($C_{5/5}$ $C_{5'/5}$), 129.4 ($C_{5'/5}$), 128.8 ($C_{6,6'}$), 128.7 ($C_{4/4'}$), 128.6 ($C_{4'/4}$), 127.2 ($C_{11/11'/12/12'/13/13'}$), 127.2 ($C_{11/11'/12/12'/13/13'}$), 124.4 ($C_{8/8'}$), 124.4 ($C_{8'/8}$), 121.4 ($C_{2/2'}$), 120.9 ($C_{2'/2}$). **HR-ASAP-MS** *m/z* = 451.0655 $[M+H]^+$ (calculated for $C_{29}H_{17}Cl_2O^+$ = 451.0656).

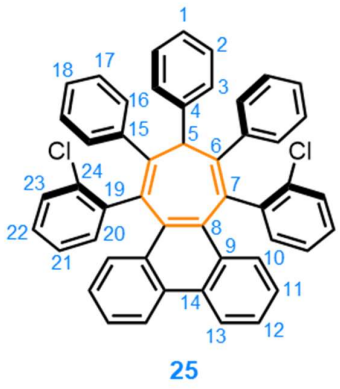

25

25: **24** (50 mg, 0.11 mmol) and *sym*-triphenylcyclopropene (30 mg, 0.11 mmol) were added to an oven-dried microwave vial under an inert atmosphere, followed by anhydrous *p*-xylene (2.5 mL). The mixture was degassed *via* 3 × freeze-pump-thaw cycles and heated to reflux for 72 h. Upon cooling to rt, the solvent was removed in *vacuo*, leaving a green residue, which was purified by column chromatography (Teledyne Isco CombiFlash Rf+ system, 12 g SiO_2, hexanes–CH_2Cl_2 gradient elution, 0–30%) to yield the title compound as a white solid (8.9 mg, 0.013 mmol, 12%). **^{1}H NMR** (600 MHz, $CDCl_3$) δ 8.33 (d, J = 8.2 Hz, 2H, H_{13}), 7.93 (d, J = 8.3 Hz, 2H, H_{10}), 7.65 (d, J = 7.8 Hz, 2H, H_3), 7.34–7.30 (m, 2H, H_{12}), 7.20–7.14 (m, 4H, $H_{11,20/23}$), 7.12–6.83 (br, m, 16H, $H_{16–18,20–23}$), 6.76–6.72 (m, 2H, H_2), 6.62–6.58 (m, 1H, H_1), 5.59 (s, 1H, H_5). **^{13}C NMR** (151 MHz, $CDCl_3$) δ 146.1 (C_6), 142.6 (C_7), 142.2 (C_{19}), 140.5 (C_4), 138.0 (C_8), 134.2 (C_{24}), 132.7 ($C_{20/23}$), 130.3 ($C_{10/11/14/16/17/18}$), 130.1 ($C_{10/11/14/16/17/18}$), 130.0 ($C_{10/11/14/16/17/18}$), 130.0 ($C_{10/11/14/16/17/18}$), 130.0 ($C_{10/11/14/16/17/18}$), 129.8 (C_9), 129.3 (C_{15}), 127.9 ($C_{21/22}$), 127.5 (C_2), 126.8 ($C_{10/11/14/16/17/18}$), 126.6 ($C_{22/21}$), 126.3 (C_{12}), 125.7 (C_1), 125.6 (C_3), 125.5 ($C_{23/20}$), 121.9 (C_{13}), 60.4 (C_5). **HR-ASAP-MS** *m/z* = 691.1987 $[M+H]^+$ (calculated for $C_{49}H_{33}Cl_2^+$ = 691.1959).

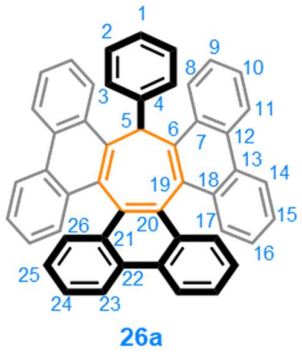

26a

26a: Anhydrous DMF (2 mL), degassed through 5 × freeze-pump-thaw cycles was added to **25** (20 mg, 29 µmol, 1.0 equiv.), $Pd(PCy_3)_2Cl_2$ (17 mg, 23 µmol, 0.80 equiv.), and DBU (26 mg, 170 µmol, 6.0 equiv.) in a sealed microwave vial. The reaction mixture was heated to 160 °C for 48 h. Upon cooling to rt, brine (10 mL) was added. The layers were separated, and the organic layer was extracted with CH_2Cl_2 (5 × 5 mL). The combined organic extracts were dried over $MgSO_4$, and the solvents were removed *in vacuo*, leaving a brown residue, which was purified by column chromatography (Teledyne Isco CombiFlash Rf+ system, 4 g SiO_2, hexanes: CH_2Cl_2, 0–30%), to give a pale-yellow solid, which was washed with Et_2O (2 × 5 mL) to yield the title

compound as a colourless solid (8.5 mg, 14 µmol, 47%). **^{1}H NMR** (500 MHz, $CDCl_3$, 313 K) δ 8.77 (d, *J* = 8.3 Hz, 2H, H_{11}), 8.70 (d, *J* = 8.3 Hz, 2H, H_8), 8.62 (d, *J* = 8.4 Hz, 2H, H_{14}), 8.54 (d, *J* = 8.4 Hz, 2H, H_{23}), 7.77–7.71 (m, 2H, H_9), 7.71–7.66 (m, 2H, H_{10}), 7.66–7.61 (m, 2H, H_{17}), 7.53 (s, 1H, H_5), 7.51–7.44 (m, 4H, $H_{15,24}$), 7.29–7.21 (m, 4H, $H_{16,26}$), 7.21–7.15 (m, 2H, H_{25}), 6.75 (d, *J* = 7.7 Hz, 2H, H_3), 6.36 (t, *J* = 7.4 Hz, 1H, H_1), 6.27–6.20 (m, 2H, H_2). **^{13}C NMR** (126 MHz, $CDCl_3$, 313 K): δ 144.3 (C_6), 140.2 (C_4), 135.1 ($C_{19/20}$), 132.9 (C_{18}), 132.0 ($C_{20/19}$), 131.5 (C_7), 130.8 (C_{12}), 130.6 (C_{21}), 130.0 (C_{22}), 129.5 (C_{26}), 129.4 (C_{13}), 128.9 (C_{17}), 127.5 (C_9), 126.7 (C_{10}), 126.6 (C_2), 126.5 (C_{16}), 126.3 (C_{24}), 126.2 (C_{15}), 125.9 (C_{25}), 125.4 (C_3), 124.7 (C_1) 123.8 (C_8), 123.6 (C_{11}), 122.7 (C_{14}), 122.4 (C_{23}), 43.3 (C_5). **HRMS-ASAP** *m/z* = 619/2435 $[M+H]^+$, calculated for $C_{49}H_{31}^+$: 619.2426.

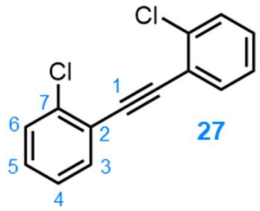

Di(2-chlorophenylacetylene) (27): $^{i}Pr_2NH$ (20 mL), degassed *via* 3 × freeze-pump-thaw cycles was added to CuI (0.0952 g, 0.500 mmol) and $Pd(PPh_3)_2Cl_2$ (0.351 g, 0.500 mmol) in an oven-dried two-necked round-bottomed flask fitted with a reflux condenser and a septum under an inert atmosphere. 2-chloro-1-iodobenzene (2.38 g, 10.0 mmol) and 2-methyl-3-butyn-ol (1.09 g, 13.0 mmol) were added, and the mixture was heated to 50 °C for 90 min and another aliquot of 2-chloro-1-iodobenzene (2.38 g, 10.0 mmol), CuI (0.0952 g, 0.500 mmol), and $Pd(PPh_3)_2Cl_2$(0.351 g, 0.500 mmol) was added, and the mixture was heated to 110 °C for 16 h. Upon cooling to rt, an aqueous solution of hydrochloric acid (1 M, 100 mL) and CH_2Cl_2 (75 mL) were added. The layers were separated and the aqueous layer was extracted with CH_2Cl_2 (4 × 75 mL). The combined organic extracts were washed with brine (200 mL) and dried over $MgSO_4$. The solvent was removed *in vacuo*, leaving a brown residue, which was purified by chromatography (SiO_2, eluting in hexanes) to yield the title compound as a pale-yellow solid (2.50 g, 10.0 mmol, quant.). **^{1}H NMR** (400 MHz, $CDCl_3$) δ 7.66–7.54 (m, 2H), 7.50–7.39 (m, 2H), 7.36–7.20 (m, 4H). Spectroscopic data are consistent with literature reports.[17]

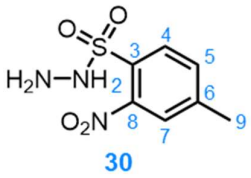

30

2-Nitro-4-methylbenzenesulfonyl hydrazide (30): $H_2NNH_2 \cdot H_2O$ (2.82 g, 56.4 mmol) was added dropwise to a solution of 2-nitrobenzenesulfonyl chloride (5.00 g, 22.6 mmol) in THF (25 mL) at −30 °C. The reaction mixture was stirred at this temperature for 90 min. The resultant white precipitate was removed, and the filtrate was diluted with EtOAc (25 mL). The organic layer was washed with an ice-cold aqueous solution of NaCl (10% wt., 5 × 25 mL), then dried over $MgSO_4$ at 0 °C. The filtrate was slowly poured into hexanes (250 mL), and the mixture was placed in the freezer for 1 h. The off-white precipitate was collected by vacuum filtration and washed with ice-cold hexanes (2 × 10 mL) to yield the title compound as an off-white solid (4.65 g, 21.4 mmol, 95%). **^{1}H NMR** (400 MHz, $CDCl_3$): δ 8.28–8.19 (m, 1H), 7.96–7.87 (m, 1H), 7.87–7.77 (m, 2H), 6.54 (s, 1H), 3.84 (s, 2H). Spectroscopic data are consistent with literature reports.[18]

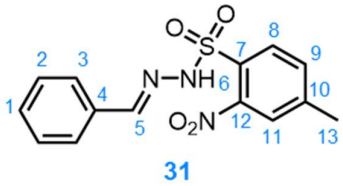

31

***N*-Phenylnosylhydrazone (31)**: Benzaldehyde (1.07 g, 10.1 mmol) was added dropwise to a solution of 2-nitrobenzenesulfonyl hydrazine (2.00 g, 9.21 mmol) in EtOH (30 mL). The mixture was stirred at rt for 18 h. The resultant pale-yellow precipitate was collected by vacuum filtration and washed with cold EtOH (2 × 15 mL) to yield the title compound as a pale-yellow solid (2.07 g, 6.78 mmol, 74%). **^{1}H NMR** (400 MHz, $CDCl_3$): δ 8.42 (s, 1H), 8.39–8.30 (m, 1H), 7.96 (s, 1H), 7.91–7.80 (m, 2H), 7.80–7.73 (m, 2H), 7.66–7.58 (m, 3H), 7.46–7.34 (m, 4H). Spectroscopic data are consistent with literature reports.[14]

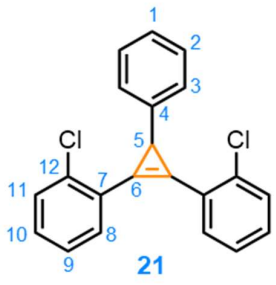

21

21: *N*-phenylnosylhydrazone (217 mg, 0.710 mmol) and NaH (60 % suspension in mineral oil, 42.6 mg, 1.07 mmol) were added to an oven-dried Schlenk under an inert atmosphere. Anhydrous CH_2Cl_2 (5 mL) was added, and the reaction mixture was stirred at rt for 1 h. A solution of AgOTf (36.5 mg, 0.142 mmol) and **27** (350 mg, 1.42 mmol) in anhydrous CH_2Cl_2 (3 mL) was added dropwise, and the reaction mixture was heated

to 40 °C for 24 h. Upon cooling to rt, the reaction mixture was passed through a short pad of silica, eluting in EtOAc. The solvents were removed *in vacuo*, leaving a dark green residue, which was purified by column chromatography (SiO_2, hexanes–CH_2Cl_2, gradient elution, 0–5%) to yield the title compound as a colourless solid (39.2 mg, 0.116 mmol, 16%). **^{1}H NMR** (600 MHz, $CDCl_3$) δ 7.70–7.64 (m, 2H, H_8), 7.45–7.38 (m, 2H, H_{11}), 7.30–7.17 (m, 8H, $H_{2,3,9,10}$), 7.17–7.10 (m, 1H, H_1), 3.45 (s, 1H, H_5). **^{13}C NMR** (151 MHz, $CDCl_3$) δ 145.2 (C_4), 135.2 (C_{12}), 132.9 (C_8), 130.2 (C_{11}), 130.0 (C_{10}), 128.3 (C_2), 128.1 (C_7), 126.7 (C_9), 126.1 (C_3), 125.8 (C_1), 112.6 (C_6), 28.4 (C_5). **HR-APCI-MS** *m/z* = 337.0535 $[M+H]^+$ (calculated for $C_{21}H_{15}Cl_2^+$ = 337.0545).

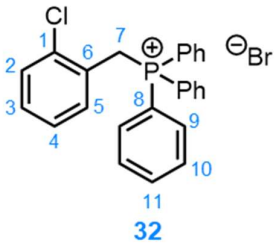

32

2-Chlorobenzyl-triphenylposphine bromide (32): PPh_3 (5.11 g, 4.87 mmol) was added to an oven-dried Schlenk flask. Anhydrous PhMe (60 mL) was added, followed by 2-chlorobenzyl bromide (4.00 g, 19.5 mmol), and the reaction mixture was heated to 80 °C for 20 h. The reaction mixture was cooled to 0 °C, and the resultant white precipitate was collected by vacuum filtration to yield the title compound as a colourless solid (8.74 g, 18.7 mmol, 96%). **^{1}H NMR** (400 MHz, CD_3CN): δ 7.94–7.84 (m, 2H), 7.73–7.62 (m, 6H), 7.62–7.51 (m, 6H), 7.40–7.28 (m, 2H), 7.24–7.10 (m, 2H), 4.82 (dd, *J* = 14.3, 1.6 Hz, 2H). Spectroscopic data are consistent with literature reports.[19]

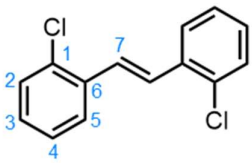

(*E*)-33

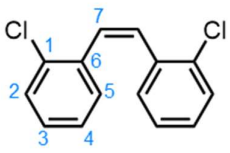

(*Z*)-33

33: KO^{t}Bu (0.280 g, 2.50 mmol) was added to a suspension of **32** (1.00 g, 2.14 mmol) in anhydrous THF (20 mL) at 0 °C. The mixture was allowed to stir at this temperature for 30 min, before a solution of 2-chlorobenzaldehyde (0.251 g, 1.78 mmol) in anhydrous THF (20 mL) was added dropwise over 10 min, and the reaction mixture was stirred at rt for 20 h. EtOAc (20 mL) and H_2O (20 mL) were added. The layers were separated, and the aqueous layer was extracted with EtOAc (2 × 20 mL). The combined organic extracts were washed with brine (20 mL), then dried over $MgSO_4$. The solvent was removed *in*

vacuo, leaving an off-white solid. The crude residue was passed through a silica plug, eluting in hexanes, to yield the title compound as a colourless oil (7:93 ratio of E:Z isomers) (0.443 g, 1.78 mmol, quant.). **(*Z*)-33: ^{1}H NMR** (400 MHz, $CDCl_3$): δ 7.39 (dd, J = 8.1, 1.2 Hz, 2H), 7.14 (ddd, J = 8.0, 7.1, 2.0 Hz, 2H), 7.05–6.95 (m, 4H), 6.87 (s, 2H). Spectroscopic data are consistent with literature reports.[20]

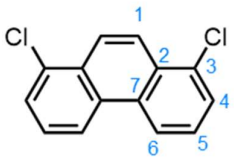

34

1,8-Dichlorophenanthrene (34): Anhydrous THF (90 mL), degassed *via* 3 × freeze-pump-thaw cycles was added to I_2 (1.12 g, 4.42 mmol) and **33** (1.00 g, 4.01 mmol) in an oven-dried quartz tube under an inert atmosphere. Propylene oxide (10 mL) was added, and the reaction mixture was sparged with $N_{2\,(g)}$ for 10 min. The reaction mixture was irradiated for 288 h with 4 × 254 nm 9 W UV light bulbs. The reaction mixture was diluted with EtOAc (50 mL) and CH_2Cl_2 (10 mL), and washed with a saturated aqueous solution of $Na_2S_2O_3$ (2 × 50 mL), followed by brine (100 mL). The organic layer was dried over $MgSO_4$, and the solvent was removed *in vacuo*, leaving a tan residue, which was washed with hexanes (10 mL) and MeOH (10 mL) to yield the title compound as a colourless solid (0.451 g, 1.82 mmol, 46%). **^{1}H NMR** (600 MHz, $CDCl_3$) δ 8.62 (d, J = 8.4 Hz, 2H, H_6), 8.36 (s, 2H, H_1), 7.73 (d, J = 7.5 Hz, 2H, H_4), 7.62–7.58 (m, 2H, H_5). **^{13}C NMR** (151 MHz, $CDCl_3$) δ 133.1 ($C_{2/3/7}$), 131.7 ($C_{2/3/7}$), 129.5 ($C_{2/3/7}$), 127.8 (C_4), 127.1 (C_5), 124.0 (C_1), 122.1 (C_6). **HR-APCI-MS** *m/z* = 247.0078 $[M+H]^+$ (calculated for $C_{14}H_9Cl_2^+$ = 247.0076).

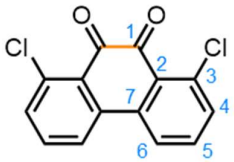

35

1,8-Dichlorophenanthrene-9,10-dione (35): A solution of **34** (50 mg, 0.20 mmol) in anhydrous CH_2Cl_2 (1.5 mL) was added dropwise to a solution of CrO_3 (40 mg, 0.40 mmol) and H_5IO_6 (383 mg, 2.0 mmol) in anhydrous MeCN (2.5 mL) under an inert atmosphere, and the reaction mixture was heated to 40 °C for 24 h. Upon cooling to rt, CH_2Cl_2 (10 mL) and water (30 mL) were added. The layers were separated, and the aqueous layer was extracted with CH_2Cl_2 (2 × 10 mL). The combined organic extracts were washed with brine (20 mL) and dried over $MgSO_4$. The solvent was removed *in vacuo*, leaving an orange residue, which was

washed with cold hexanes–CH_2Cl_2 (3:1, 2 mL), then hexanes (2 × 1 mL), to yield the title compound as an orange solid (35 mg, 0.13 mmol 63%). **^{1}H NMR** (600 MHz, CD_2Cl_2) δ 7.94 (d, J = 8.0 Hz, 2H, H_6), 7.66–7.63 (m, 2H, H_5), 7.55–7.52 (m, 2H, H_4). **^{13}C NMR** (151 MHz, CD_2Cl_2) δ 183.3 (C_1), 138.8 (C_7), 136.8 (C_3), 135.8 (C_5), 133.3 (C_4), 127.8 (C_2), 124.8 (C_6). **HR-APCI-MS** *m/z* = 276.9821 $[M+H]^+$ (calculated for $C_{14}H_7Cl_2O_2^+$ = 276.9818).

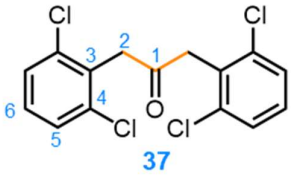

37

1,3-Bis(2,6-dichlorophenyl)acetone (37): A solution of 2,6-dichlorobenzyl bromide (5.00 g, 20.8 mmol) and *p*-toluenesulfonylmethylisocyanide (TOSMic) (2.03 g, 10.4 mmol) in anhydrous DMSO (20 mL) was added dropwise to a suspension of NaH (60% in mineral oil, 1.00 g, 25.0 mmol) in anhydrous DMSO (20 mL) under an inert atmosphere, and the resulting mixture was stirred at rt for 16 h. The reaction was quenched by careful addition of water and extracted with CH_2Cl_2 (3 × 100 mL). The combined organic extracts were washed with an aqueous solution of HCl (1 M, 100 mL) and brine (100 mL), then dried over $MgSO_4$. The CH_2Cl_2 was removed *in vacuo*, leaving a tan residue. Concentrated aqueous HCl (37%, 10 mL) was added to a suspension of this residue in Et_2O–CH_2Cl_2 (2:1, 300 mL) at 0 °C, and the suspension was stirred at rt for 18 h. The reaction was quenched by careful addition of a saturated solution of $NaHCO_{3\,(aq)}$ (250 mL), and the mixture was extracted with CH_2Cl_2 (3 × 50 mL). The combined organic extracts were dried over $MgSO_4$, and the solvents were removed *in vacuo*, to yield a tan residue, which was purified by column chromatography (SiO_2, hexanes–CH_2Cl_2, 7:3) to afford a pale-orange residue, which was washed with cold hexanes (10 mL) to give the title compound as an off-white solid (2.09 g, 6.00 mmol, 58%). **^{1}H NMR** (600 MHz, $CDCl_3$) δ 7.35–7.31 (m, 4H, H_6), 7.19–7.14 (m, 2H, H_5), 4.19 (s, 4H, H_2). **^{13}C NMR** (151 MHz, $CDCl_3$) δ 200.1 (C_1), 136.3 (C_4), 131.6 (C_3), 129.1 (C_6), 128.2 (C_5), 45.0 (C_2). **HR-APCI-MS** *m/z* = 346.9568 $[M+H]^+$ (calculated for $C_{15}H_{11}Cl_4O^+$ = 346.9564).

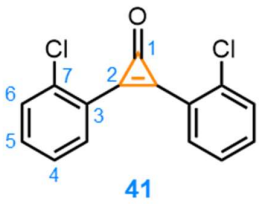

41

2,3-Di(2-chlorophenyl)-2-cyclopropen-1-one (41): A solution of Br_2 (0.83 g, 5.2 mmol) in AcOH (4 mL) was added dropwise to a solution of **23** (0.70 g, 2.5 mmol) in AcOH (4 mL), and the resultant mixture was allowed to stir for 4 h. The mixture was poured onto water (100 mL) and extracted with CH_2Cl_2 (5 × 25 mL). The combined organic extracts were dried over $MgSO_4$, and the solvent was removed *in vacuo* to yield a pale orange oil. Et_3N (1.5 mL, 11 mmol) was added dropwise to a solution of this residue in anhydrous CH_2Cl_2 (15 mL), and the mixture was stirred at rt for 1 h. The reaction was quenched by addition of an aqueous solution of HCl (1 M, 20 mL). The organic layer was washed with brine (20 mL) and dried over $MgSO_4$. The solvent was removed *in vacuo* to yield a brown residue, which was purified by column chromatography (Teledyne Isco CombiFlash Rf+ system, 40 g SiO_2, hexanes–CH_2Cl_2 gradient elution) to yield the title compound as a colourless solid (0.37 g, 1.4 mmol, 54%). **^{1}H NMR** (600 MHz, $CDCl_3$) δ 7.82 (d, J = 7.7 Hz, 2H, H_7), 7.53–7.50 (m, 2H, H_4), 7.50–7.45 (m, 2H, H_6), 7.43–7.38 (m, 2H, H_5). **^{13}C NMR** (151 MHz, $CDCl_3$) δ 153.9 (C_1), 149.0 (C_3), 136.7 (C_8), 133.6 (C_6), 132.1 (C_7), 130.4 (C_4), 127.2 (C_5), 124.2 (C_2). **HR-ASAP-MS** *m/z* = 275.0042 $[M+H]^+$ (calculated for $C_{15}H_9Cl_2O^+$ = 275.0030).

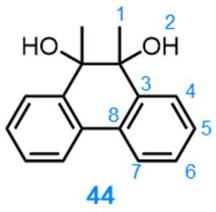

44

9,10-Dimethyl-9,10-dihydrophenanthrene-9,10-diol (44): MeMgBr (42 mL, 120 mmol, 3 M in Et_2O) was added slowly over 15 min to a solution of 9,10-phenanthrenequinone (10.0 g, 48.0 mmol) in anhydrous THF (120 mL). The reaction mixture was stirred at rt for 3 h, then quenched by careful addition of an aqueous solution of HCl (0.25 M, 40 mL). The layers were separated, and the organic layer was extracted with EtOAc (3 × 100 mL). The combined organic extracts were dried over $MgSO_4$, and the solvents were removed *in vacuo* to yield an orange residue, which was purified by column chromatography (Teledyne Isco CombiFlash Rf+ system, 40 g SiO_2, hexanes: EtOAc, 0–25%), giving the title compound as a pale-yellow solid (10.95 g, 45.6 mmol, 95%). **^{1}H NMR** (400 MHz, $CDCl_3$) δ 7.76–7.64 (m, 4H), 7.42–7.30 (m, 4H), 2.20 (s, br, 2H), 1.31 (s, 6H). The spectroscopic data are consistent with literature reports.[21]

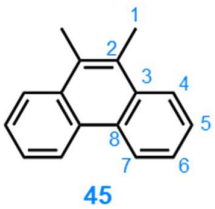

45

9,10-Dimethylphenanthrene (45): HI (57% wt. in water, 30 mL, 210 mmol) was added dropwise to a solution of **44** (10 g, 42 mmol) in AcOH (350 mL), and the mixture was heated to reflux for 16 h. Upon cooling to rt, a saturated aqueous solution of $Na_2S_2O_3$ (200 mL) was added, and the mixture was stirred for 15 min. The layers were separated, and the aqueous layer was extracted with CH_2Cl_2 (3 × 75 mL). The combined organic extracts were washed with a saturated aqueous solution of $NaHCO_3$ (150 mL) and brine (150 mL), and dried over $MgSO_4$. The solvent was removed *in vacuo*, to yield the title compound as an orange solid, which was used in the next step without further purification (8.58 g, 41.6 mmol, quant.). **^{1}H NMR** (400 MHz, $CDCl_3$) δ 8.76–8.67 (m, 2H), 8.18–8.07 (m, 2H), 7.67–7.56 (m, 4H), 2.74 (s, 6H). The spectroscopic data are consistent with literature reports.[21]

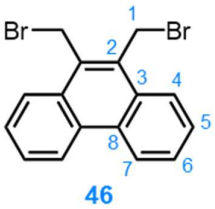

46

9,10-Dibromomethylphenanthrene (46): A solution of **45** (1.00 g, 4.84 mmol), NBS (1.90 g, 10.7 mmol), and BPO (75% with water, 1.41 g, 4.37 mmol) in CCl_4 was heated to 80 °C in a microwave vial for 24 h. Upon cooling to rt, brine (25 mL) was added, and the layers were separated. The aqueous layer was extracted with CH_2Cl_2 (2 × 20 mL). The combined organic extracts were washed with $MgSO_4$, and the solvent was removed *in vacuo*, leaving a brown residue, which was purified by column chromatography (SiO_2, hexanes–CH_2Cl_2, 95:5) to afford the title compound as a colourless solid (0.778 g, 2.14 mmol, 44%). **^{1}H NMR** (400 MHz, $CDCl_3$) δ 8.78–8.69 (m, 2H), 8.27–8.15 (m, 2H), 7.78–7.62 (m, 4H), 5.13 (s, 4H). The spectroscopic data are consistent with literature reports.[21]

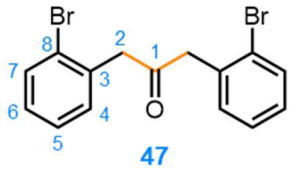

47

1,3-Di(2-bromophenyl)acetone (47): A solution of 2-bromophenylacetic acid (8.00 g, 37.2 mmol) in anhydrous CH_2Cl_2 (40 mL) was added dropwise over 1 h to a solution of DCC (5.37 g, 26.0 mmol) and DMAP (1.36 g, 11.2 mmol) in anhydrous CH_2Cl_2 (40 mL) in an oven-dried three-necked round-bottomed flask under an inert atmosphere. The mixture was stirred at rt for 24 h. The resulting precipitate was removed by filtration, and the solvent was removed *in vacuo*,

leaving an orange residue, which was purified by column chromatography (SiO_2, hexanes–EtOAc, 9:1) to yield the title compound as a colourless solid (4.08 g, 11.1 mmol, 60%). **^{1}H NMR** ($CDCl_3$, 400 MHz): δ 7.57 (d, *J* = 8.0 Hz, 2H), 7.32–7.20 (m, 4H), 7.15 (ddd, *J* = 8.0, 7.2, 2.0 Hz, 2H), 3.96 (s, 2H). Spectroscopic data are consistent with literature reports.[22]

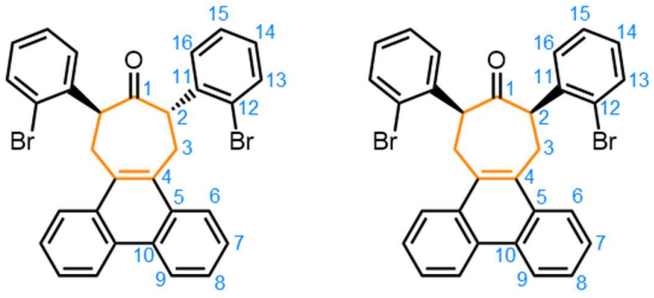

49: A solution of KOH (333 mg, 5.93 mmol) in anhydrous EtOH (6 mL) was added dropwise over 30 min to a solution of **46** (800 mg, 2.19 mmol) and **47** (809 mg, 2.19 mmol) in anhydrous THF (80 mL) in a two-necked round-bottomed flask fitted with a reflux condenser and a septum under an inert atmosphere at 0 °C. The reaction mixture was heated to 70 °C for 5 h. Upon cooling to rt, the solvent was removed *in vacuo*, leaving a red residue, which was washed with cold MeOH (3 × 5 mL) to yield the title compound as a mixture of *anti*- and *syn*-isomers in a 45:55 ratio (1.26 g, 2.19 mmol, quant.). The diasteroisomers were separated by column chromatography (Teledyne Isco CombiFlash Rf+ system, 40 g SiO_2, hexanes–EtOAc gradient elution, 0–10%). The *anti*-isomer could be isolated selectively as a colourless solid. **^{1}H NMR** (600 MHz, $CDCl_3$) δ 8.84 (d, *J* = 8.3 Hz, 2H, H_9), 8.09 (d, *J* = 8.5 Hz, 2H, H_6), 7.73–7.68 (m, 2H, H_8), 7.66–7.62 (m, 2H, H_7), 7.62–7.58 (m, 2H, H_{15}), 7.51–7.46 (m, 2H, H_{12}), 7.43–7.37 (m, 2H, H_{13}), 7.21–7.16 (m, 2H, H_{14}), 4.50 (d, *J* = 11.0 Hz, 2H, H_2), 4.08 (dd, *J* = 15.0, 2.1 Hz, 2H H_3), 3.83–3.73 (m, 2H, $H_{3'}$). **^{13}C NMR** (151 MHz, $CDCl_3$) δ 206.3 (C_1), 139.9 (C_{11}), 134.3 (C_4), 132.9 (C_{15}), 130.4 (C_{10}), 130.2 (C_{12}), 128.7 (C_{14}), 127.6 (C_{13}), 127.3 (C_7), 126.6 (C_8), 125.0 (C_{16}), 123.9 (C_6), 123.5 (C_9), 58.3 (C_2), 31.8 (C_3). **HR-ASAP-MS** *m/z* = 569.0110 $[M+H]^+$ (calculated for $C_{31}H_{23}OBr_2^+$ = 569.0116).

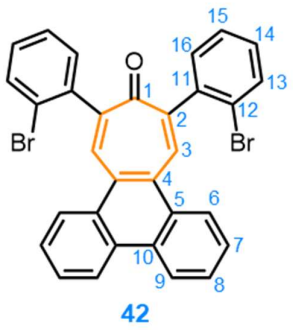

42

Attempted synthesis of **42**: A solution of Br_2 (364 mg, 2.28 mmol) in AcOH (2 mL) was added to a solution of **49** (100 mg, 0.175 mmol) in a mixture of AcOH and $CHCl_3$ (1:1, 4 mL), and the mixture was stirred at rt for 3.5 h. The reaction mixture was poured into water (10 mL), and the aqueous layer was extracted with CH_2Cl_2 (3 × 5 mL). The combined organic extracts were washed with a saturated aqueous solution of $NaHCO_3$ (10 mL) and brine (10 mL), then dried over $MgSO_4$. The solvent was removed *in vauo*, leaving a yellow residue, which was washed with a mixture of hexanes and Et_2O (1:1, 1 mL) and hexanes (1 mL) to yield **50** as an off-white solid (42.5 mg, 0.0584 mmol, 32%). This was used for the next step without further purification.

A suspension of **50** (51 mg, 70 µmol) in anhydrous DMF (1.2 mL) was added to a solution of LiBr (38 mg, 44 µmol) and Li_2CO_3 (33 mg, 44 µmol) in anhydrous DMF (1.3 mL) in an oven-dried Schlenk flask under an inert atmosphere. *See Table 4.5 for the temperatures and reaction times used.* Upon cooling to rt, water (10 mL) and CH_2Cl_2(10 mL) were added. The layers were separated, and the organic layer was washed with water (2 × 10 mL), followed by brine (10 mL), then dried over $MgSO_4$. The solvent was removed *in vacuo*, leaving a brown residue, which was purified by column chromatography (SiO_2, hexanes–EtOAc, 9:1).

The outcome of this reaction is described on page 215.

4.4.2. X-ray Crystallographic Analysis

4.4.2.1. 24-*anti*

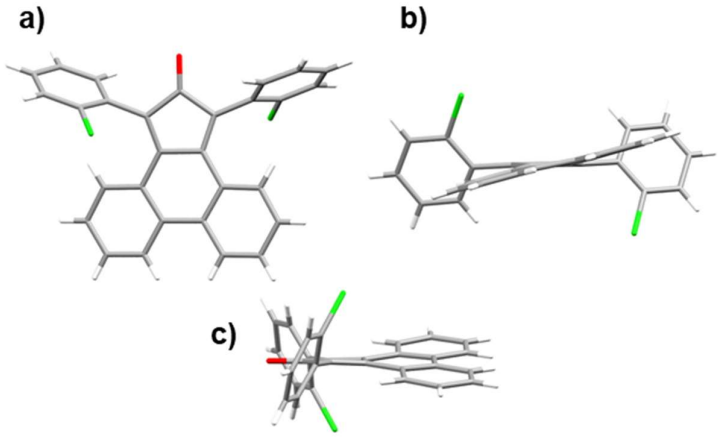

Figure 4.16. Solid state structure of **24-*anti*** viewed **a)** face-on; **b)** side-on from the phenanthrenyl moiety; and **c)** side-on from the 2-chlorophenyl rings.

Table 4.6. Crystal data and structure refinement for **24-*anti***.

24-*anti*	
Identification code	22srv024
Empirical formula	$C_{29}H_{16}Cl_2O$
Formula weight	451.32
Temperature/K	120.00
Crystal system	monoclinic
Space group	C2/c
a/Å	19.1197(7)
b/Å	10.3930(4)
c/Å	10.6898(4)
α/°	90
β/°	101.5960(15)
γ/°	90
Volume/Å^3	2080.83(14)
Z	4
ρ_{calc}g/cm^3	1.441
μ/mm^{-1}	0.333
F(000)	928.0
Crystal size/mm^3	0.23 × 0.19 × 0.02

Radiation	Mo Kα (λ = 0.71073)
2Θ range for data collection/°	4.35 to 54.982
Index ranges	-24 ≤ h ≤ 24, -13 ≤ k ≤ 13, -13 ≤ l ≤ 13
Reflections collected	18169
Independent reflections	2386 [R_{int} = 0.0442, R_{sigma} = 0.0273]
Data/restraints/parameters	2386/0/146
Goodness-of-fit on F^2	1.110
Final R indexes [I>=2σ (I)]	R_1 = 0.0590, wR_2 = 0.1410
Final R indexes [all data]	R_1 = 0.0674, wR_2 = 0.1454
Largest diff. peak/hole / e $Å^{-3}$	0.79/-0.49

4.4.2.2. 25

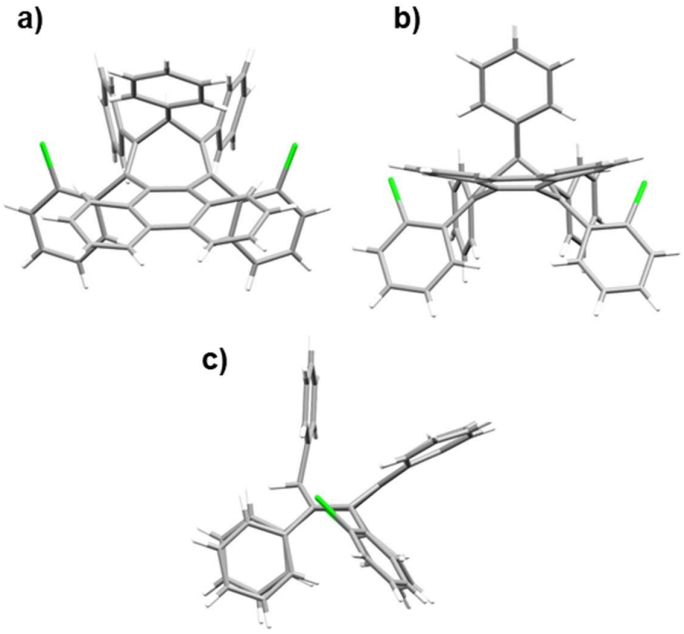

Figure 4.17. Solid state structure of **25** viewed **a)** face-on; **b)** side-on from the phenanthrenyl moiety; and **c)** side-on from the 2-chlorophenyl rings

Table 4.7. Crystal data and structure refinement for **25**.

25	
Identification code	21srv323
Empirical formula	$C_{49}H_{32}Cl_2$
Formula weight	691.64
Temperature/K	120.0
Crystal system	orthorhombic
Space group	Pbca
a/Å	18.4612(8)

b/Å	18.9206(8)
c/Å	20.4458(8)
α/°	90
β/°	90
γ/°	90
Volume/Å^3	7141.7(5)
Z	8
ρ_{calc}g/cm^3	1.287
μ/mm^{-1}	0.217
F(000)	2880.0
Crystal size/mm^3	0.16 × 0.12 × 0.07
Radiation	MoKα (λ = 0.71073)
2Θ range for data collection/°	3.67 to 59.992
Index ranges	-25 ≤ h ≤ 25, -26 ≤ k ≤ 26, -28 ≤ l ≤ 28
Reflections collected	125510
Independent reflections	10400 [R_{int} = 0.0896, R_{sigma} = 0.0417]
Data/restraints/parameters	10400/0/460
Goodness-of-fit on F^2	1.062
Final R indexes [I>=2σ (I)]	R_1 = 0.0577, wR_2 = 0.1261
Final R indexes [all data]	R_1 = 0.0791, wR_2 = 0.1364
Largest diff. peak/hole / e Å^{-3}	0.53/-0.47

4.4.2.3. 49-*anti*

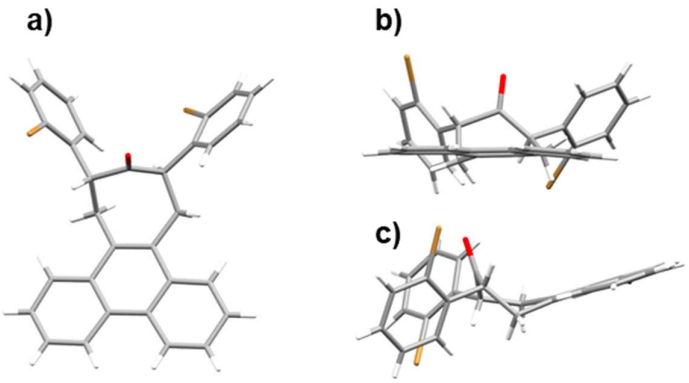

Figure 4.18. Solid state structure of **49-*anti*** viewed **a)** face-on; **b)** side-on from the phenanthrenyl moiety; and **c)** side-on from the 2-bromophenyl rings.

Due to the poor quality and disorder of the crystal, diffraction was quite weak (R1 value = 13%), so no structural parameters could be collected.

4.5. References

1 V. G. Jiménez, R. Tapia, M. A. Medel, I. F. A. Mariz, T. Ribeiro, V. Blanco, J. M. Cuerva, E. Maçôas and A. G. Campaña, *Chem. Commun.*, 2018, **54**, 3359–3362.

2 T. Fujikawa, Y. Segawa and K. Itami, *J. Am. Chem. Soc.*, 2016, **138**, 3587–3595.

3 K. Kawasumi, Q. Zhang, Y. Segawa, L. T. Scott and K. Itami, *Nature Chem*, 2013, **5**, 739–744.

4 K. Gü, N. Grabicki, B. Battistella, L. Grubert and O. Dumele, *J. Am. Chem. Soc*, 2022, **144**, 8707–8716.

5 C. M. Cruz, S. Castro-Fernández, E. Maçôas, J. M. Cuerva and A. G. Campaña, *Angew. Chem. Int. Ed.*, 2018, **57**, 14782–14786.

6 P. Aillard, A. Voituriez and A. Marinetti, *Dalton Trans.*, 2014, **43**, 15263–15278.

7 K. Y. Cheung, X. Xu and Q. Miao, *J. Am. Chem. Soc.*, 2015, **137**, 3910–3914.

8 Y. Zhang, Y. Zhu, D. Lan, S. H. Pun, Z. Zhou, Z. Wei, Y. Wang, H. K. Lee, C. Lin, J. Wang, M. A. Petrukhina, Q. Li and Q. Miao, *J. Am. Chem. Soc.*, 2021, **143**, 5231–5238.

9 C. Zhu, K. Shoyama and F. Würthner, *Angew. Chem. Int. Ed.*, 2020, **59**, 21505–21509.

10 Y. Zhang, S. H. Pun and Q. Miao, *Chem. Rev*, 2022, **122**, 14554–14593.

11 B. T. King, J. Kroulík, C. R. Robertson, P. Rempala, C. L. Hilton, J. D. Korinek and L. M. Gortari, *J. Org. Chem.*, 2007, **72**, 2279–2288.

12 A. T. Turley, PhD thesis, University of Durham (UK), 2020.

13 X. Yang and Q. Miao, *Synlett*, 2016, **27**, 2091–2094.

14 Z. Liu, Q. Li, P. Liao and X. Bi, *Chem.—Eur. J.*, 2017, **23**, 4756–4760.

15 T. Kodama, Y. Kawashima, K. Uchida, Z. Deng and M. Tobisu, *J. Org. Chem.*, 2021, **86**, 13800–13807.

16 A. Velasco-Rubio, J. A. Varela and C. Saá, *Org. Lett*, 2020, **22**, 3591–3595.

17 W. Li, J. Tang, S. Li, X. Zheng, M. Yuan, B. Xu, W. Jiang, H. Fu, R. Li and H. Chen, *Org. Lett.*, 2020, **22**, 7814–7819.

18 K. J. Winstanley and D. K. Smith, *J. Org. Chem.*, 2007, **72**, 2803–2815.

19 P. A. Byrne and D. G. Gilheany, *J. Am. Chem. Soc.*, 2012, **134**, 9225–9239.

20 D. C. Fabry, M. A. Ronge and M. Rueping, *Chem.—Eur. J.*, 2015, **21**, 5350–5354.

21 D. Mi, J. B. Park, F. Xu, H. U. Kim, J. H. Kim and D. H. Hwang, *Bull. Korean Chem. Soc.*, 2014, **35**, 1647–1653.

22 D. Sälinger and R. Brückner, *Chem.—Eur. J.*, 2009, **15**, 6688–6703.

CHAPTER 5 |

TUNING PHOTOLUMINESCENCE BY MODULATION OF EXCITED-STATE DYNAMICS

Abstract

Molecules that exhibit aromaticity in their ground-state become antiaromatic in the excited state. If given a route to escape this excited-state antiaromaticity, such molecules undergo rapid rearrangement or proton transfer to more long-lived excited-state species. Here we report a series of hydroxybenzotropyliums, and we study their potential to undergo excited-state intramolecular proton transfer (ESIPT) emission. In general, these cations are accessible *via* a concise synthesis to form benzotropones, which are then protonated by strong acids. Computational studies indicate that substituent effects have a large impact on not only molecular conformation in both the ground- and excited-states, but also the feasibility of ESIPT. Preliminary spectroscopic measurements are in agreement with our computational studies, and they indicate that hydroxybenzotropyliums demonstrate dual emission behaviour characteristic of ESIPT emitters. Though further investigation is required to fully understand the electronic character of these molecules, our initial studies shed light on the fundamental nature of ESIPT in nonbenzenoid systems and identify hydroxybenzotropyliums as promising candidates for pH-responsive sensors and ESIPT-fluorophores.

Acknowledgements

The following people are gratefully acknowledged for their contribution to this chapter: Dr. R. Ayub carried out all calculations. The author developed the synthetic routes to all compounds included in this chapter and conducted their spectroscopic characterisation. Dr. D. S. Yufit solved the X-ray crystal structures. Dr. A. N. Bismillah performed the high-temperature NMR measurements of compound **6b**. Dr. P. R. McGonigal and the author conceived of the research.

5.1. Introduction

In 1972, Baird postulated on the basis of semi-empirical calculations that the rules for aromaticity in the ground state were reversed in the lowest $\pi\pi^*$ (triplet) excited state.[1] Ground-state aromatic molecules (with $4n+2$ π-electrons) become antiaromatic, while annulenes with $4n$ π-electrons become aromatic in the T_1 excited state. Aihara later extended Baird's conclusions to the singlet excited state (S_1) as well.[2] Since these contributions, the concept of excited-state antiaromaticity has been explored extensively.[3] Experimentally, Itoh and Aida have found that a gain in excited-state aromaticity in the S_1 and T_1 states lowers the energy barrier to the tub-to-tub inversion of a substituted cyclooctatetraene by 21–22 kcal·mol^{-1} compared to the S_0 state.[4]

Conversely, the relief of excited-state antiaromaticity (ESAA) is a powerful driving force to effect unusual structural rearrangements; benzene (C_6H_6) is known to isomerise to nonaromatic benzvalene, fulvene, and Dewar benzene upon irradiation with different wavelengths of UV light.[5] Smaller structural rearrangements, such as proton transfers are also known to occur rapidly (with rates of 10^{12} s^{-1}) in an attempt to escape ESAA.[6] To illustrate, the pK_a of phenol drops from 9.82 to ~4 upon irradiation, concomitant with excited-state intramolecular proton transfer (ESIPT) to form the *keto*-tautomer transiently (Figure 5.1a).[7]

The effects of ESIPT on the optical properties of a molecule are marked. Weller first discovered[8] that *o*-salicylic acid (Figure 5.1b) shows a large Stokes shift (~150 nm) and dual fluorescence emission, which Nagaoka attributed to emission from both the phenolic and carboxylic tautomers of the analyte, as a result of ESIPT.[9] Since Weller's discovery, a myriad of ESIPT-emitters has been studied as colour-tunable fluorophores[10–17], fluorescent sensors[18–28], and white-light emitters.[21,29–36] A general mechanism outlining the source of dual emission in ESIPT emitters is outlined in Figure 5.1c

Yet, there is a paucity of structural diversity in the design of ESIPT emitters; most feature a benzoxazole or a benzothiazole proton acceptor and a phenol (or, less commonly, an aniline)-based proton donor (Figure 5.1d). A small number of reports (most recently by Yang[37] and Zysman-Colman[38]) have noted that molecules with a β-diketone core (which exist in an enol-form in the ground-state, stabilised by hydrogen-bonding) can also undergo ESIPT upon photoirradiation (Figure 5.1e).[39–41] By

incorporating an ESIPT-active acceptor moiety in a molecule with a donor–π–acceptor– π–donor type structure, the authors were able to achieve thermally activated delayed fluorescence (TADF)-emitters with high Stokes shifts and external quantum efficiencies in OLED devices.

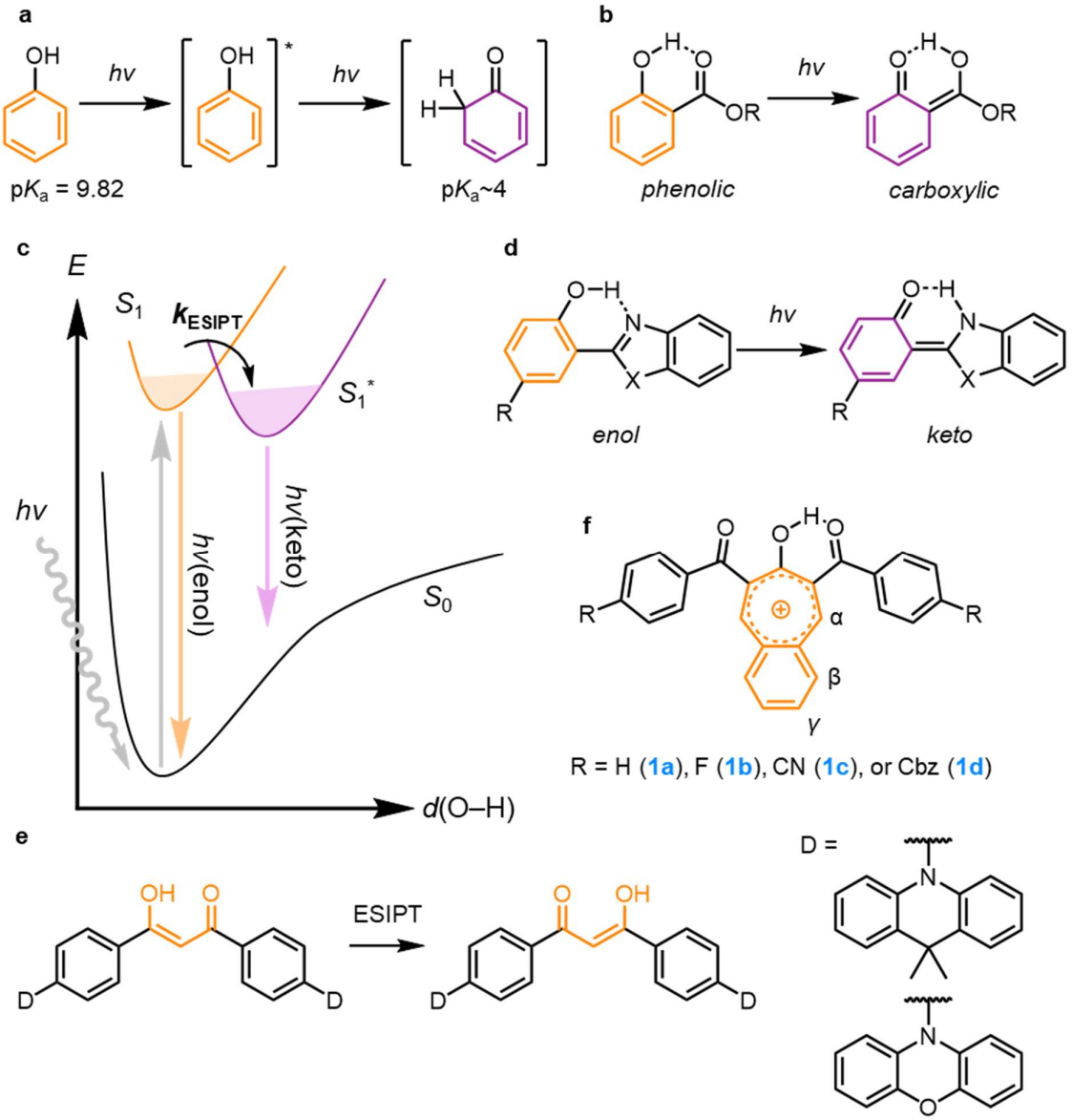

Figure 5.1. (a) Large difference in the pK_a of phenol in its ground- and excited states; **(b)** The phenolic- and carboxylic-tautomers of *o*-salicylic acid (**R** = H) and methyl *o*-salicylate (**R** = Me), responsible for its dual fluorescence; **c)** Energy profile of dual emission in ESIPT emitters, plotted as a function of O–H bond distance. k_{ESIPT} refers to the rate of proton transfer. The triplet states are omitted for clarity; **(d)** A typical ESIPT emitter (**X** = O,S); **(e)** ESIPT-TADF emitters reported by Yang; **(f)** Target molecules in this chapter. Cbz = 9*H*-carbazole.

It is unknown whether non-benzenoid aromatic systems (which benefit from lower aromatic stabilisation) undergo similar excited-state processes. Here, we investigate the ESIPT behaviour of a series of hydroxybenzotropyliums (HBTs) (**1a**–**d** in Figure 5.1f) with acetyophenyl groups that can act as hydrogen bond acceptors with tunable electronic properties. Computational studies show that the rate of ESIPT in these structures can be modulated by varying the substituent on the *para*-position of the phenyl rings. Electron-donating groups disfavour the ESIPT process, while the addition of electron-withdrawing groups "switch-on" proton transfer.

5.2. Results and Discussion

5.2.1. Barriers to ESIPT

We began by modelling the geometries and Gibbs energies (G) of a series of HBTs (**1a**–**d**), hydroxytropyliums (HTs) (**2a**–**d** in Figure 5.2b), as well as *o*-salicylaldehyde (**3**) as a control compound in the lowest T_1 state. The T_1 states were chosen over the S_1 states for preliminary studies, as their modelling is less computationally demanding. The difference in Gibbs energies (ΔG^*) between the phenolic/tropylium tautomers and the keto-tautomers are shown below in Figure 5.2a. In general, the keto-forms of the HTs and HBTs are less favoured than the keto-form of **3**. Using von Ragué Schleyer's indene–isoindene isomerisation stabilisation (ISE-II) method[42], Zhu evaluated the antiaromatic destabilisation energies of both benzene and tropylium in the T_1 state as 64.9 and 75.5 kJ·mol^{-1} respectively, which suggests that both species experience similar degrees of destabilisation.[43] Although no such analysis has been conducted for HTs or HBTs, it is likely that these species experience lower ESAA, which in turn provides a weaker driving force for ESIPT, and hence, a less favourable keto-tautomer. However, ESIPT remains an exergonic process as long as **R** is an electron-withdrawing group. Preliminary internal reaction coordinate (IRC) calculations indicate that ESIPT is a nearly barrierless transformation, with activation energy barriers ($\Delta G^{\ddagger}$) close to 0 in **1a**–**c**, **2**, and **2a**–**c**. Curiously, an electron-donating group in the *para*-position massively reduces the stability of the keto-isomer, effectively switching off the ESIPT process in **1d** and **2d**.

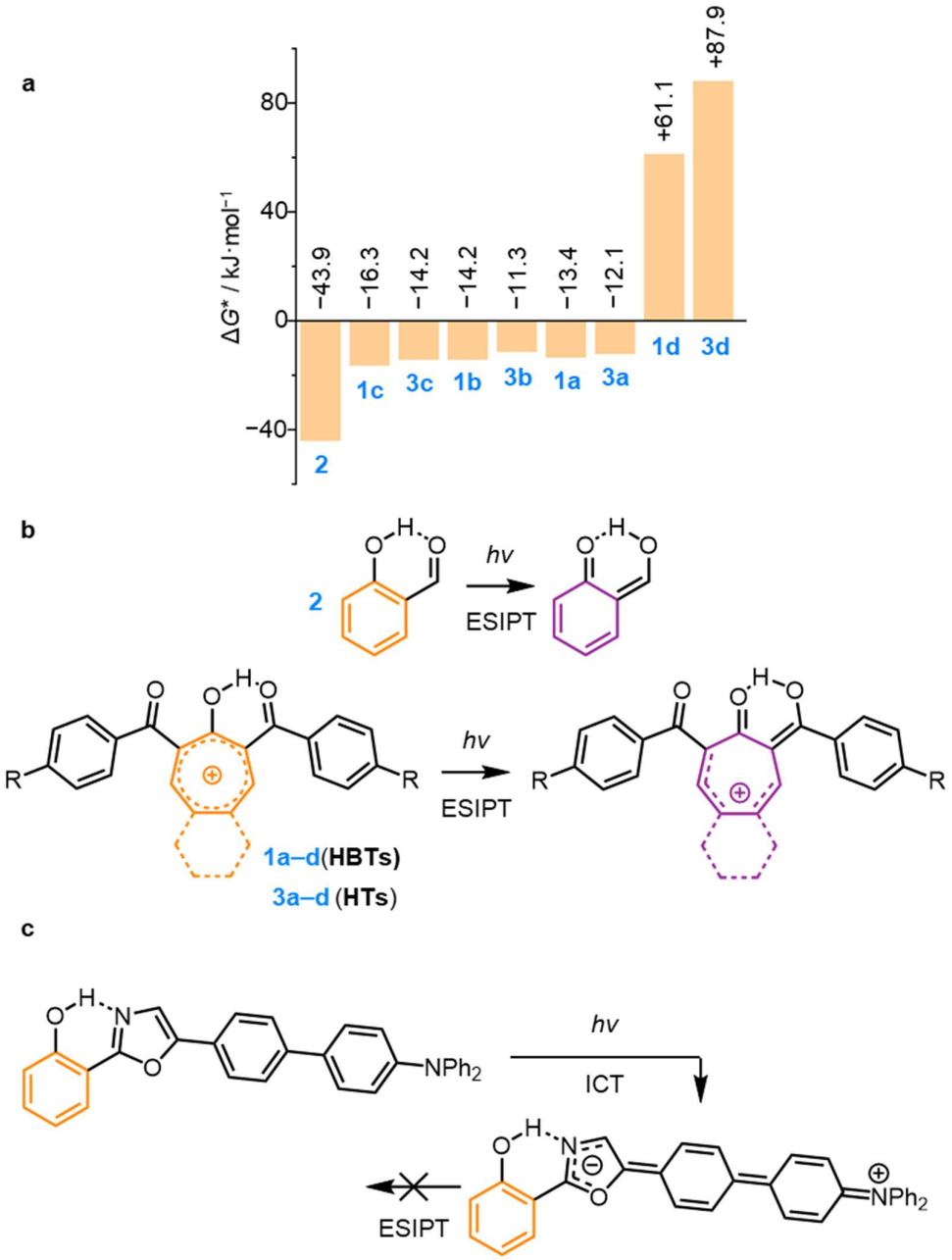

Figure 5.2. (a) Calculated Gibbs energy differences (ΔG^* / kJ·mol^{-1}) between the phenolic/tropylium tautomer (orange) and the keto-tautomer (purple) in a series of compounds in the T_1 excited-state; **(b)** Chemical structures of the compounds in their ground state and after ESIPT. **R** = H (**1a**), F (**1b**), CN (**1c**), 9H-carbazole (Cbz) (**1d**). ωB97XD / 6-311+G(d,p); **(c)** Unfavourable ESIPT in You's oxazole molecule substituted with an electron-donating diphenylamine group.

You and co-workers made a similar observation when exploring the effect of an electron-donating diphenylamine group on a series of 2-(2′-hydroxyphenyl)-5-phenyloxazoles (Figure 5.2c).[44] The authors noted that ultrafast intramolecular charge transfer (ICT) occurs upon photoexcitation in the push-pull structure shown above (Figure 5.2c) featuring an electron donor and acceptor. The authors claim that subsequent ESIPT is disfavoured, as it disrupts electron delocalisation in this charge transfer state, leading to fluorescence emission from the phenolic tautomer only.

Moreover, Chou and co-workers demonstrated that substituent effects in a series of 2-(2′-aminophenyl)-benzothiazole-based systems had a direct effect on the activation barrier to ESIPT.[45] The authors were able to correlate the energy differences between the 'normal' and tautomerised forms of their molecules directly to the NH···N hydrogen-bond length (in both the ground- and excited-states), and found that shorter H-bond lengths provided a lower energy barrier, as well as a greater thermodynamic driving force for ESIPT. Upon inspection of the OH···O hydrogen-bond distances in the HBTs studied in this work, no clear trend (Table 5.1) could be observed between bond distances and the Gibbs energy differences between the keto- and enol-tautomers. Further, it is unclear why the calculated hydrogen-bond distances are significantly smaller than the expected values in similar molecules (~1.7 Å).[45]

Table 5.1. OH···O hydrogen bond lengths (d / Å) in the S_0 and T_1 states in compounds **1a**–**d** (ωB97XD / 6-311+G(d,p)).

Compound	**ΔG / kJ·mol^{-1}**	***d*(OH···O) / Å (S_0)**	***d*(OH···O) / Å (T_1)**
1a	−13.4	1.564	1.409
1b	−14.2	1.567	1.435
1c	−16.3	1.572	1.442
1d	+61.1	1.602	1.499

Analysis of the geometry-optimised structures of compounds **1a**–**d** revealed three predominant conformers (Figure 5.3a): coplanar and twisted 'T-shaped' (Pl and Tw respectively), as well as 'L-shaped' (L). In the S_0 state, compounds **1a**–**c** and **3a**–**c** display a strong preference for the Tw or L conformer, which are close in energy. The keto-tautomers of these HBTs adopt an L-shaped conformation. Upon excitation to the T_1 state, the tropylium tautomers adopt either a Tw or Pl T-shaped conformation, whereas the tautomerised keto-form remains L-shaped.

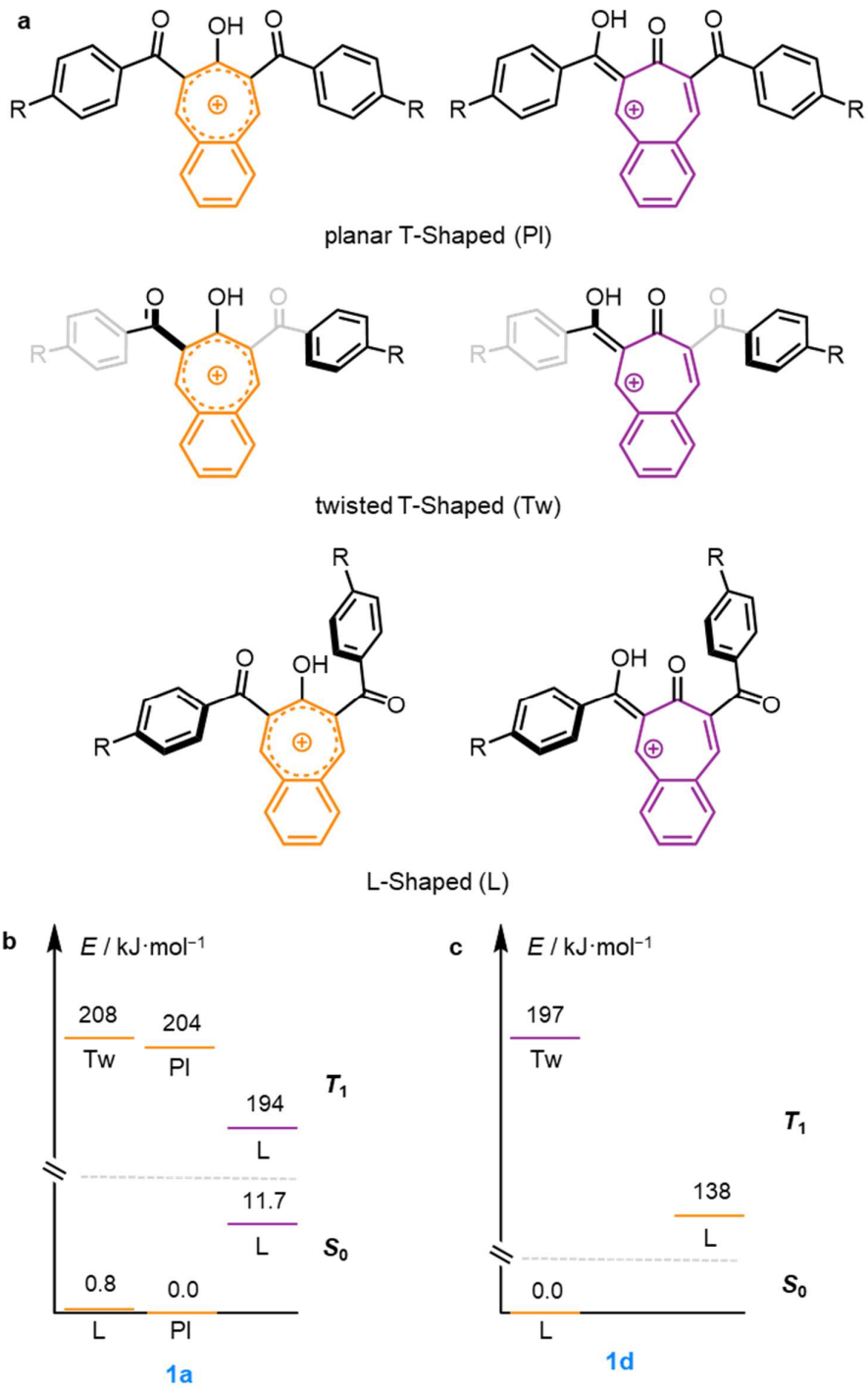

Figure 5.3. a) Possible conformations adopted by HBTs **1a**–**d**; Relative Gibbs energies (G_{rel} / kJ·mol^{-1}) between the various conformations for the tropylium (orange) and keto-tautomers (purple) in the ground- (S_0) and excited-state (T_1) (ωB97XD / 6-31G(d)) for **b**) compound **1a** and **c**) compound **1d**.

Conversely, we did not observe the Tw conformation of **1d** and **3d** in the S_0 ground state. Instead, these electron donor-bearing HBTs only exist in the L-conformation. In

the T_1 state, the tropylium tautomer (largely disfavoured, as discussed above) only forms the Tw geometry, whereas the tautomerised keto-analogue exists as the more stable L-shape. The cause for this conformational preference is likely to be steric, owing to the bulky nature of the amine groups involved. Energy diagrams representative of compounds **1a**–**c** and **3a** included below in Figure 5.3b–c.

5.2.2. Synthesis of Benzotropones

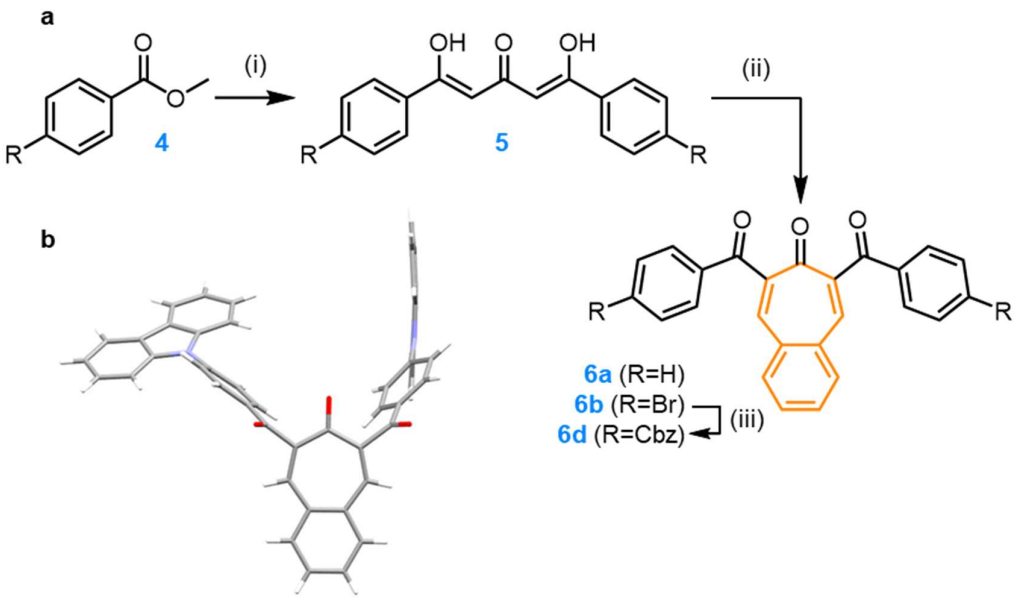

Figure 5.4. **(a)** Benzotropone synthesis. Reagents and conditions: (i) Me_2CO, NaH, rt → reflux, 24 h, 84% (**5a**), 54% (**5b**+**9**, see section 5.4.1); (ii) *o*-phthalaldehyde, piperidine, EtOH, reflux, 15 min, 81% (**6a**), 40% (**6b**); (iii) **6b**, $Pd_2(dba)_3$, XPhos, Cs_2CO_3, PhMe, reflux, 24 h, 74% (**6d**). **a**: **R** = H, **b**: **R** = Br; (**b**) the single crystal X-ray structure of **6d**.

Guided by our DFT calculations, we aimed to synthesise compounds **1a** and **d** to explore excited-state proton transfer dynamics. We focused on synthesizing hydroxybenzotropyliums rather than their hydroxytropyliums, as the latter are known to undergo 4π-photocyclisation to form bicyclo[3.2.0]heptadienyl (Dewar tropylium) cations upon irradiation.[46] A recent report by Tobisu shows that hydroxybenzotropyliums are accessible by protonation of the corresponding 4.5-benzotropones with a strong acid.[45] The authors also note that HBTs exhibit the hallmarks of aromaticity (according to magnetic criteria). We justify the use of the aromatic amine carbazole as a donor group (as in **1d**), rather than an aliphatic amine

(with higher basicity), as the carbazole moiety will not be prone to protonation under the strongly acidic conditions required to stabilise the HBT. The synthesis of suitable benzotropones is shown above in Figure 5.4.

First, a double Claisen condensation of methyl benzoate or methyl 4-bromobenzoate with acetone afforded **5a** and **5b** respectively. Subsequently, Knoevenagel condensations of these substrates with *o*-phthalaldehyde form benzotropones **6a** and **6b**. Finally, a Buchwald–Hartwig coupling between **6b** and 9H-carbazole (synthesised in two steps from 2-aminobiphenyl to avoid the presence of any isomeric impurities in commercially-available samples[47]) provided benzotropone **6d**. The structure of **6d** was confirmed by NMR spectroscopy, as well as single-crystal XRD (Figure 5.4b). In the solid state, **6d** crystallises as the *syn*-conformer, where both ketones and the appended carbazole groups point in the same direction. The dihedral angle between the phenyl ring and the carbazole moiety is 50.2°.

5.2.3. Hydroxytropyliums

Treatment of **6a** with an excess of strong acid (MsOH) led to quantitative conversion to HBT **1a**·OMs *in situ*, as confirmed by ^{1}H NMR spectroscopic analysis (Figure 5.5). Key spectral changes upon protonation include a downfield chemical shift ($\Delta\delta$) by ~1.1 ppm of the α-protons of the HBT core compared to benzotropone **6a** (Figure 5.5a). A similar, but less pronounced downfield shift of the β- and γ-protons was also observed. Analogously, protonation of **6d** with an excess of MsOH also quantitatively afforded hydroxybenzotropylium **1d**·OMs. The ^{1}H NMR spectrum of this cation (Figure 5.5b) reveals the α-protons experience an even larger $\Delta\delta$~1.4 ppm compared to its parent benzotropone (Figure 5.6a).

Compound **1d** was also accessible from **6d** using $HBF_4{\cdot}Et_2O$ and TfOH, but TFA was found to be too weak an acid to achieve full protonation. Due to the inherent hygroscopicity and instability of **1a**·OMs and **1d**·OMs, they could not be isolated as solid materials. Although no single crystals of the protonated tropyliums could be obtained for XRD analysis, we were able to confirm the complete protonation by NMR titrations.

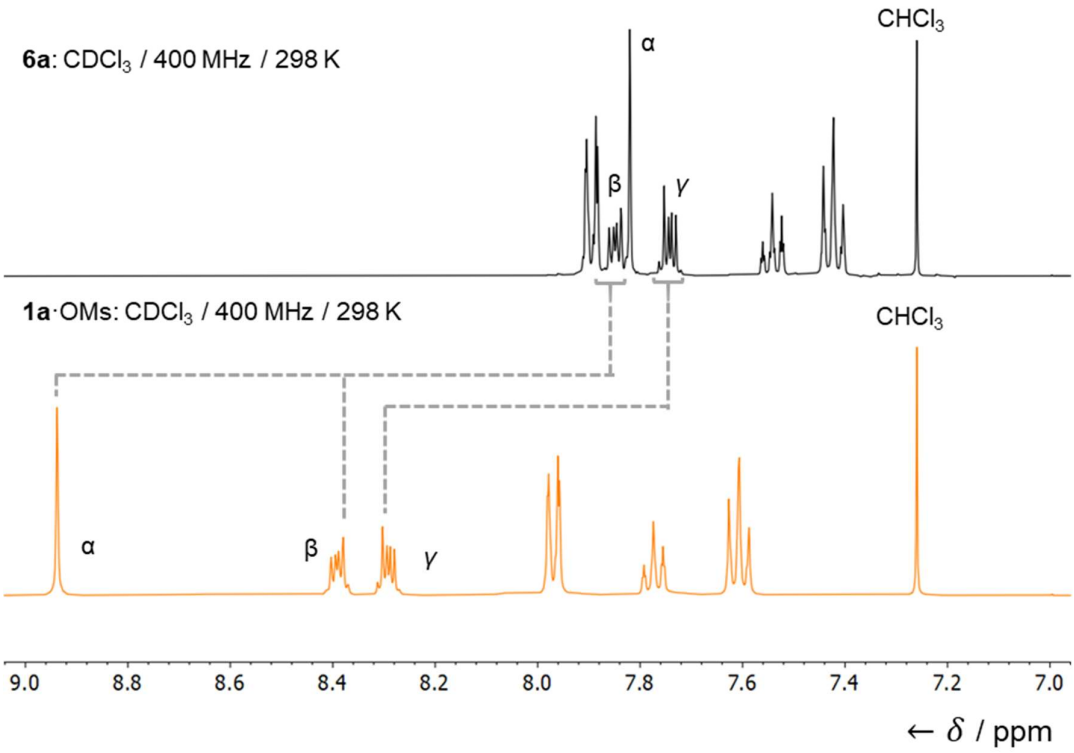

Figure 5.5. Comparison of partial ^{1}H NMR spectra of benzotropone **6a** (top) and HBT **1a**·OMs (bottom). ^{1}H environments on the HBT core are labelled according to Figure 5.1e.

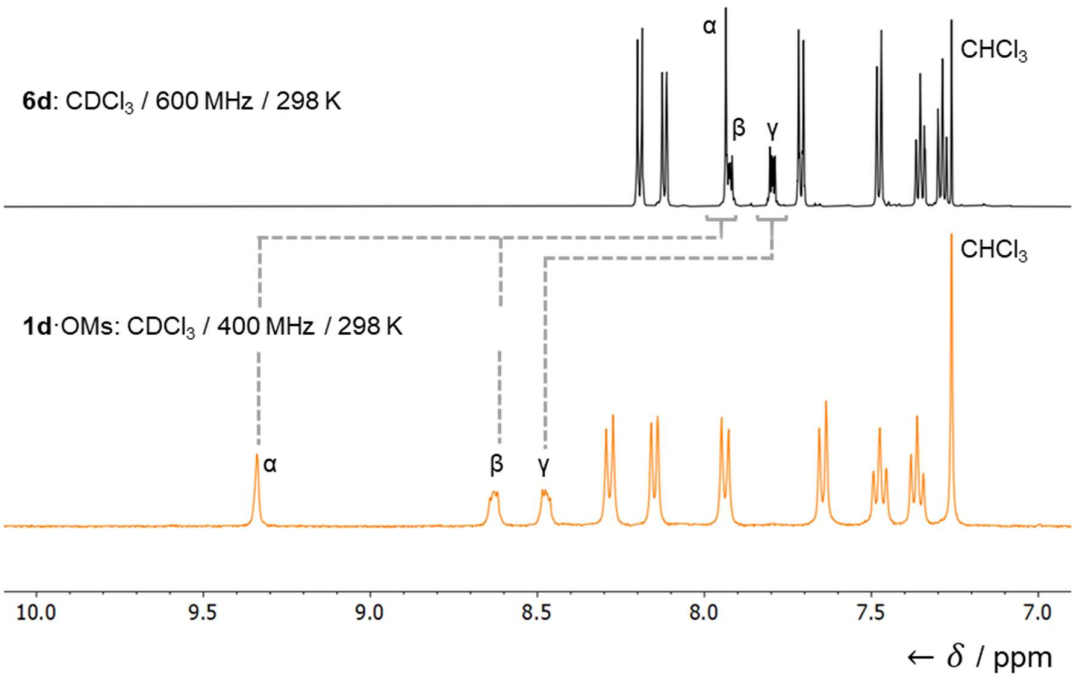

Figure 5.6. Comparison of partial ^{1}H NMR spectra of benzotropone **6d** (top) and HBT **1d**·OMs (bottom). ^{1}H environments on the HBT core are labelled according to Figure 5.1e.

The pK_a of **1d** was measured by conducting a ^{1}H NMR titration, with $HBF_4{\cdot}Et_2O$ in $CDCl_3$ (Figures 5.10–11 in Section 5.4.3). The experiment revealed a pK_a = 1.21±0.22 for **1d**, which is slightly lower than the pK_a values (~1.5) reported for similar dicarbonyl-substituted HBTs.[45] These data indicate that HBT **1d** is fully protonated under the conditions we used for optical spectroscopy (see section 5.2.5), and only partially protonated at higher pH.

5.2.4. Optical Spectroscopy

UV-vis absorption and emission spectra were collected for compounds **6a**, **6d**, **1a**·OMs, and **1d**·OMs. HBTs **1a** and **1d** were generated *in situ* by dissolution of the parent benzotropones in a strongly acidic medium (1.0 M MsOH in CH_2Cl_2). Unfortunately, due to a lack of solvents compatible with the strongly acidic media required to protonate the parent benzotropones, we could not conduct a solvent screen to probe the behaviour of the HBTs in polar and nonpolar media.

Comparison of the UV-vis absorption spectra of benzotropone **6a** (Figure 5.7a) and HBT **1a**·OMs (Figure 5.8a), reveals red-shifted absorption peaks and the emergence of a new peak with λ_{max} = 370 nm upon protonation, which is consistent with the increased conjugation present in **1a**·OMs. Interestingly, upon protonation of **6d** to form **1d**·OMs, a new, broad absorption peak appears around 564 nm (Figure 5.8b). As this peak is not present in the UV-vis spectrum of **1a**·OMs, it most likely arises to a strong charge transfer interaction from the carbazole (donor) moiety to the acetophenyl (acceptor) moiety, which forms a strong hydrogen bond with the cationic hydroxytropylium moiety.

The fluorescence intensity of **6a** (Figure 5.7c) decreases with concentration, indicating it undergoes aggregation-caused quenching (ACQ). Nonetheless, its fluorescence intensity at low concentrations (0.1–2 μM) is significantly higher than that of **6d** (Figure 5.7d), which can be considered essentially non-fluorescent. However, photoluminescent quantum yield (PLQY) measurements are required for a quantitative comparison of the fluorescence intensities of these molecules. Both **6a** and **1a**·OMs are yellow light emitters, but the emission spectrum of **1a**·OMs (Figure 5.8c) is much broader than that of **6a**, and it exhibits two distinct peaks (λ_{max} = 421,

521 nm). The lower energy emission band exhibits a large Stokes shift of 151 nm. These spectral features are characteristic of an ESIPT emitter, such as methyl salicylate. Compound **1d**·OMs (Figure 5.7d) exhibits weak fluorescence and broad dual emission peaks that cover most of the visible spectrum. As a consequence, at low concentrations, **1d**·OMs appears to emit white light (Figure 5.8d, inset). However, the Stokes shift for the lower energy emission is notably smaller ($\Delta\lambda_{max}$ = 122 nm). It is unclear (based solely on the emission data at hand) whether this apparent dual emission behaviour is caused by ESIPT or large conformational changes in a highly flexible molecule.

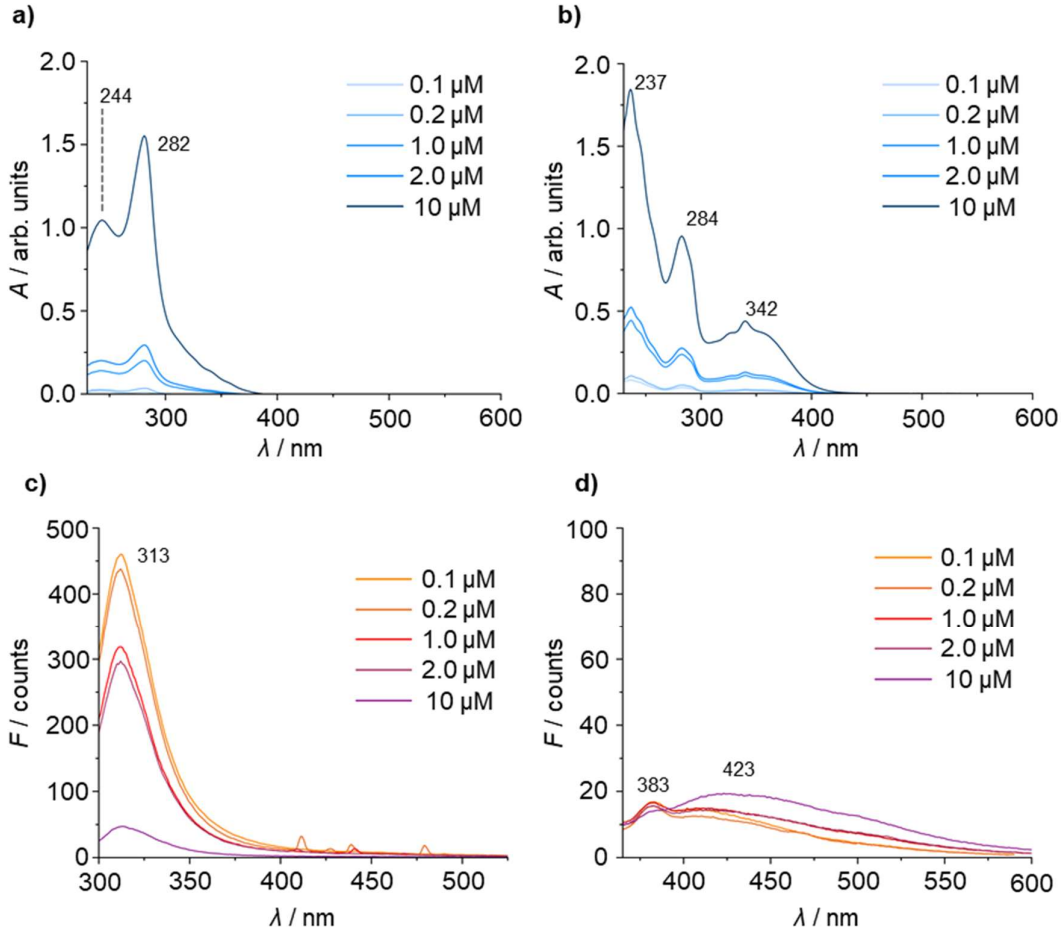

Figure 5.7. Optical properties of benzotropones. **(a,b)** UV-vis absorption spectra of **6a** and **6d** respectively at a range of concentrations; **(c,d)** Emission spectra (λ_{ex} = 280 nm, 340 nm respectively) of **6a** and **6d** respectively at a range of concentrations. All spectra were recorded in a CH_2Cl_2.

It is also noteworthy that—while the emission intensity of **1a**·OMs increases with concentration—**1d**·OMs is prone to aggregation-caused quenching. This indicates the presence of a possible intermolecular charge-transfer interaction between electron-rich carbazole moiety and the electron-deficient hydroxybenzotropylium core.

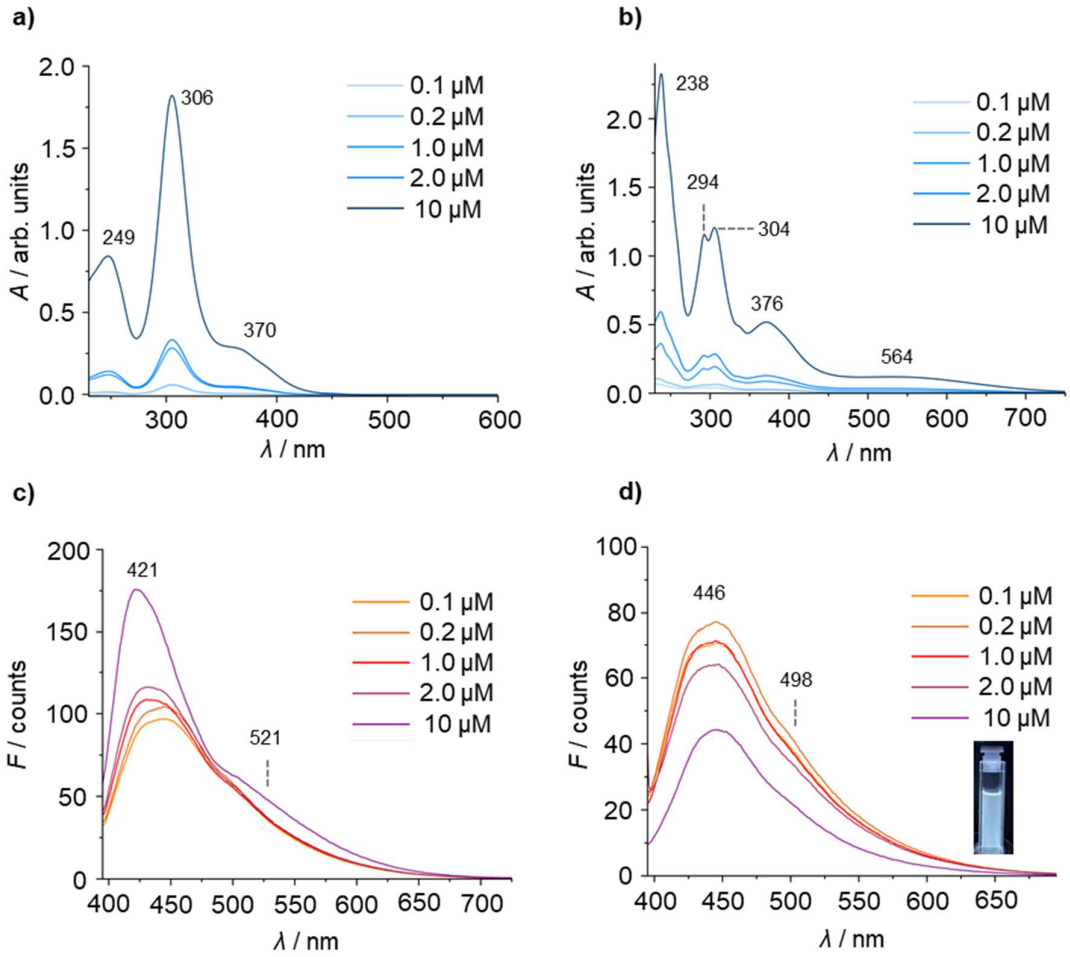

Figure 5.8. Optical spectroscopy of hydroxybenzotropyliums; **(a,b)** UV-vis absorption spectra of **1a**·OMs and **1d**·OMs at a range of concentrations; **(c,d)** Emission spectra (λ_{ex} = 375 nm) of **1a**·OMs and **1d**·OMs at a range of concentrations. All spectra were recorded in a solution of MsOH in CH_2Cl_2 (1.0 M). **Inset:** cuvette containing a solution of **1d**·OMs (0.2 μM) under irradiation (λ_{ex} = 365 nm).

5.3. Conclusions and Future Work

In summary, we report preliminary studies to explore the ESIPT behaviour of a series of HBTs (**1a**–**d**) bearing both phenyl rings whose electronic character could be tuned by addition of an electron-donating or withdrawing group. Initial DFT calculations indicated that—while these compounds are in principle capable of undergoing

ESIPT—this process can be switched off by inclusion of an electron-donating group. Further computational studies are required to understand the origin of the large differences in electronic state stabilities upon inclusion of an electron-donating group. Aromaticity indices (in both the ground- and excited states) must be employed to probe the aromatic character of the hydroxybenzotropylium motif. The key question to be answered is: can the rate and driving force of ESIPT be correlated with a set of parameters that change upon altering the electronic characters of the HBTs? Finally, TD-DFT calculations must be extended to compare and contrast molecular geometries and energies in the ground- and excited states. These data must be correlated with experimental results from spectroscopic studies to identify a suitable basis set and functional for more in-depth analysis.

Benzotropone precursors (**6a**, **6b**, and **6d**) were prepared *via* a concise three-step synthetic protocol. HBTs **1a** and **1d** could be generated for spectroscopic studies *in situ*, by protonation with a strong acid, and the pK_a of **1d** was measured to be 1.21±0.22. Preliminary fluorescence studies on **1a** reveals the hallmarks of ESIPT-emission, while the emission behaviour of **1d** remains unclear. In order to confirm whether ESIPT is truly taking place in these systems, time-resolved spectroscopic studies are required.[18] Specifically, transient fluorescence spectroscopy would indicate whether the two emission bands observed for **1a** (and possibly **1d**) originate from an initial excited-state antiaromatic tropylium species, which subsequently undergoes ESIPT to a more stable keto-tautomer, which emits a red-shifted wavelength of light over a longer timescale. While these experiments would provide information about the singlet excited state (S_1), time-gated emission spectroscopy would be required to observe whether **1a** or **1d** produce any phosphorescence emission, to calculate the energy of the T_1 state.

5.4. Experimental Details

5.4.1. Synthetic Procedures

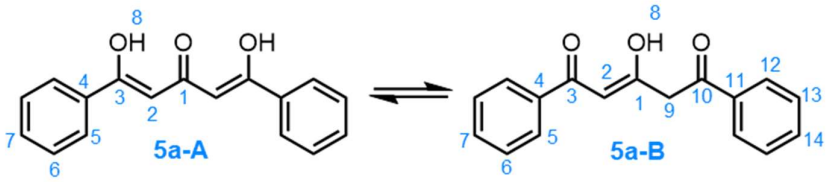

5a: Anhydrous acetone (1.4 mL, 18 mmol, 1 eq.) was added dropwise to a suspension of NaH (60% in mineral oil, 4.4 g, 110 mmol, 6 eq.) in anhydrous THF (125 mL) in a flame-dried three-necked round bottomed flask fitted with a reflux condenser under an inert atmosphere at rt, followed by methyl benzoate (5.0 g, 37 mmol, 2 eq.). The mixture was heated to reflux for 24 h. Upon cooling to rt, the reaction mixture was poured onto a mixture of ice and water (300 mL) and neutralised by careful addition of a solution of concentrated HCl (37% by wt.). The aqueous layer was extracted with $CHCl_3$ (3 × 75 mL). The combined organic extracts were washed with brine (150 mL) and dried over $MgSO_4$. The solvents were removed under reduced pressure, leaving a dark yellow residue, which was washed with MeOH (3 × 10 mL) to yield the title compound as a pale-yellow solid (4.12 g, 15 mmol, 84%). **^{1}H NMR** (400 MHz, $CDCl_3$): δ 14.77 (s, 2H, H_8, **A**), 8.07–7.41 (m, 20 H, $H_{5–7}$ in **A**, $H_{5–7,12–14}$ in **B**), 6.32 (s, 2H, H_2, **B**), 6.03 (s, 2H, H_2, **A**), 4.12 (s, 2H, H_9, **B**). Spectroscopic data are consistent with literature reports.[48]

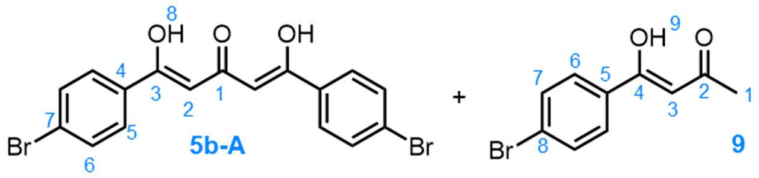

5b: Anhydrous acetone (0.52 mL, 8.95 mmol, 1 eq.) was added dropwise to a suspension of NaH (60% in mineral oil, 2.15 g, 53.7 mmol, 6 eq.) in anhydrous THF (100 mL) in a flame-dried three-necked round bottomed flask fitted with a reflux condenser under an inert atmosphere at rt, followed by methyl 4-bromobenzoate (3.85 g, 17.9 mmol, 2 eq.). The mixture was heated to reflux for 24 h. Upon cooling to rt, the reaction mixture was poured onto a mixture of ice and water (200 mL) and neutralised by careful addition of a solution of concentrated HCl (37% by wt.). The

aqueous layer was extracted with $CHCl_3$ (3 × 75 mL). The combined organic extracts were washed with brine (100 mL) and dried over $MgSO_4$. The solvent was removed under reduced pressure, leaving an orange residue, which was washed with MeOH (3 × 10 mL) to yield the title compound and **9** (partially-reacted side-product) as an inseparable mixture (**5b**:**9** = 53:47, 2.04 g, 4.81 mmol, 54%).

5b: **^{1}H NMR** (600 MHz, $CDCl_3$): δ 14.70 (s, 2H, H_8), 7.72–7.69 (m, 4H, H_5), 7.60–7.58 (m, 4H, H_6), 5.99 (s, 2H, H_2). **^{13}C NMR** (151 MHz, $CDCl_3$): 194.1 (C_1), 172.9 (C_3), 132.7 (C_4), 131.8 (C_6), 128.1 (C_5), 126.6 (C_7), 96.9 (C_2). **HR-ASAP-MS**: *m/z* = 422.9236 $[M+H]^+$ (calculated for $C_{17}H_{13}O_3Br_2^+$ = 422.9231).

9: **^{1}H NMR** (600 MHz, $CDCl_3$): δ 16.08 (s, 1H), 7.75–7.73 (m, 2H), 7.60–7.57 (m, 2H) 6.14 (s, 1H), 2.20 (s, 3H). Spectroscopic data are consistent with literature reports.[49]

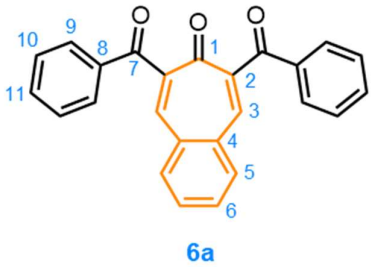

6a

6a: Piperidine (0.12 g, 1.4 mmol, 0.5 eq.) was added dropwise to a refluxing solution of **5a** (1.0 g, 3.8 mmol, 1.4 equiv.) and phthalaldehyde (0.37 g, 2.74 mmol, 1 eq.) in refluxing anhydrous EtOH (12 mL). The solution was refluxed at this temperature for a further 15 min. Upon cooling to rt, a precipitate formed, which was collected by filtration and washed with cold EtOH (2 × 5 mL) to afford the title compound as a colourless solid (0.81 g, 2.2 mmol, 81%). **M.P.** = 244–245 °C. **^{1}H NMR** (400 MHz, $CDCl_3$) δ 7.93–7.86 (m, 4H, H_9), 7.86–7.80 (m, 4H, $H_{3,5}$), 7.77–7.71 (m, 2H, H_6), 7.57–7.51 (m, 2H, H_{11}), 7.46–7.38 (m, 4H, H_{10}). **^{13}C NMR** (100 MHz, $CDCl_3$) δ 196.0 (C_7), 184.6 (C_1), 145.4 (C_2), 141.1 (C_3), 136.3 (C_8), 135.4 (C_5), 135.1 (C_4), 133.6 (C_{11}), 132.1 (C_6), 129.5 (C_9), 128.7 (C_{10}). **HR-APCI-MS** *m/z* = 365.1200 $[M+H^+]$ (calculated for $C_{25}H_{17}O_3^+$ = 365.1135).

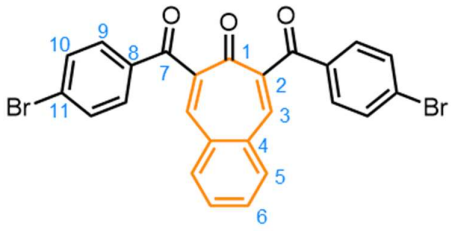

6b

6b: Piperidine (0.10 g, 1.2 mmol, 0.5 eq.) was added dropwise to a refluxing solution of **5b** and **9** (1.0 g, 2.4 mmol, 1 eq.) and phthalaldehyde (0.32 g, 2.4 mmol, 1 eq.) in refluxing anhydrous EtOH (12 mL). The solution was refluxed at this temperature for a further 15 min. Upon cooling to rt, a precipitate formed, which was collected by filtration and washed with cold EtOH (2 × 5 mL) to afford the title compound as a colourless solid (0.49 g, 0.94 mmol, 40%). **M.P.** >350 °C. **^{1}H NMR** (500 MHz, $(CD_3)_2SO$, 353 K) δ 8.17–8.12 (m, 2H, H_5), 8.10 (s, 2H, H_3), 7.89–7.84 (m, 2H, H_6), 7.83–7.78 (m, 4H, H_9), 7.73–7.68 (m, 4H, H_{10}). **^{13}C NMR** (126 MHz, $(CD_3)_2SO$, 353 K), 194.0 (C_7), 184.0 (C_1), 143.5 (C_2), 141.2 (C_3), 135.1 (C_5), 134.9 (C_8), 134.5 (C_4), 131.9 (C_6), 131.4 (C_{10}), 130.4 (C_9), 127.2 (C_{11}). **HR-ASAP-MS** *m/z* = 520.9374 $[M+H]^+$ (calculated for $C_{25}H_{15}O_3Br_2^+$ = 520.9388).

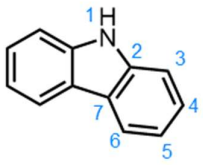

9*H*-Carbazole: An aqueous solution of HCl (2.0 M, 13.5 mL, 27 mmol) was added 2-aminobiphenyl (2.0 g, 12 mmol), and the mixture was stirred for 10 min. An aqueous solution of $NaNO_2$ (3.0 M, 4.3 mL, 13 mmol) was added dropwise, and the mixture was stirred for 10 min. An aqueous solution of NaN_3 (6.0 M, 2.1 mL, 13 mmol) was added dropwise, and the mixture was stirred for 20 min. CH_2Cl_2 (20 mL) was added, and the layer was separated. The aqueous layer was extracted with CH_2Cl_2 (2 × 20 mL), and the combined organic extracts were washed with brine, then dried over $MgSO_4$. The solvent was removed *in vacuo*, leaving a brown residue. A solution of this residue in *o*-DCB (60 mL) was heated to 180 °C for 1 h. Upon cooling to rt, a precipitate formed, which was collected by vacuum filtration and washed with hexanes (3 × 10 mL) to afford the title compound as an off-white solid (1.4 g, 8.1 mmol, 69%). **^{1}H NMR** (400 MHz, $CDCl_3$): 8.14–7.97 (m, 3H), 7.47–38 (m, 4H), 7.29–7.19 (m, 2H). Spectroscopic data are consistent with literature reports.[50]

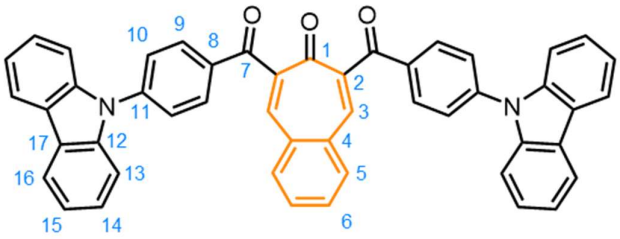

7

7: Anhydrous PhMe (5 mL), degassed through 3 × freeze-pump-thaw cycles was added to a flame-dried Schlenk flask containing **6b** (50 mg, 96 µmol, 1 eq.), carbazole (32 mg, 192 µmol, 2 eq.), $Pd_2(dba)_3$ (8.8 mg, 9.6 µmol, 0.1 eq.), XPhos (18 mg, 38 µmol, 0.4 eq.), and Cs_2CO_3 (69 mg, 210 µmol, 2.2 eq.) under an inert atmosphere. The solution was sparged with Ar for 15 min, and the reaction was heated to reflux for 24 h. Upon cooling to rt, the reaction mixture was passed through a pad of SiO_2, eluting in CH_2Cl_2. The solvent was removed under reduced pressure, leaving a brown residue, which was dissolved in CH_2Cl_2 (1 mL) and triturated with Et_2O (4 mL) to yield the title compound as an off-white solid (50 mg, 72 µmol, 75%). **M.P.** = 203–204 °C. **^{1}H NMR** (600 MHz, $CDCl_3$) δ 8.22–8.17 (m, 4H, H_9), 8.14–8.10 (m, 4H, H_{16}), 7.96–7.90 (m, 4H, $H_{3,5}$), 7.82–7.78 (m, 2H, H_6), 7.73–7.69 (m, 4H, H_{10}), 7.50–7.45 (m, 4H, H_{13}), 7.38–7.32 (m, 4H, H_{14}), 7.32–7.27 (m, 4H, H_{15}). **^{13}C NMR** (151 MHz, $CDCl_3$) δ 194.8 (C_7), 184.8 (C_1), 145.4 (C_2), 142.8 (C_{11}), 141.8 (C_3), 140.2 (C_{12}), 135.6 (C_5), 135.2 (C_4), 134.6 (C_8), 132.3 (C_6), 131.5 (C_9), 126.6 (C_{10}), 126.4 (C_{14}), 124.0 (C_{17}), 120.8 (C_{15}), 120.5 (C_{16}), 110.0 (C_{13}). **HR-ASAP-MS** *m/z* = 695.2356 [M+H$^+$] (calculated for $C_{49}H_{31}N_2O_3^+$ = 695.2335).

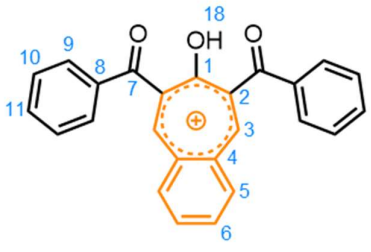

1a·OMs

1a·OMs: MsOH (32 µL) was added to a solution of **6a** (3.5 mg, 9.6 µmol) in anhydrous $CDCl_3$ (0.5 mL) in an oven-dried NMR tube under an inert atmosphere at rt. NMR spectroscopic analysis indicated quantitative conversion of the starting material to **1a**·OMs. **^{1}H NMR** (400 MHz, $CDCl_3$) δ 8.98–8.95 (m, 2H, H_3), 8.42–8.36 (m, 2H, H_5), 8.31–8.25 (m, 2H, H_6), 7.98–7.91 (m, 4H, H_9), 7.80–7.72 (m, 2H, H_{11}), 7.65–7.55 (m, 4H, H_{10}). **^{13}C NMR** (100 MHz, $CDCl_3$) δ198.5 (C_7), 186.2 (C_1), 155.9 (C_3), 138.9 (C_5), 137.4 (C_6), 136.9 ($C_{2/4}$), 135.9 ($C_{4/2}$), 135.8 (C_{11}), 134.6 (C_8), 130.9 (C_9), 129.6 (C_{10}).

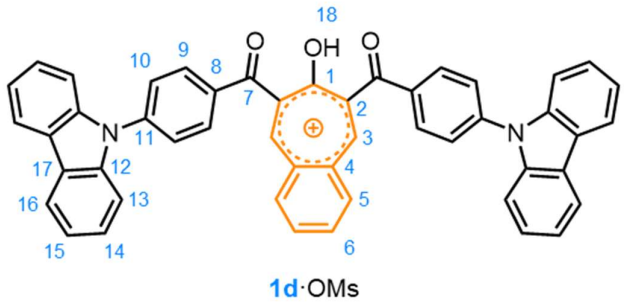

1a·OMs: MsOH (32 µL) was added to a solution of **6a** (5.0 mg, 9.6 µmol) in anhydrous $CDCl_3$ (0.5 mL) in an oven-dried NMR tube under an inert atmosphere at rt. NMR spectroscopic analysis indicated quantitative conversion of the starting material to **1d**·OMs. **^{1}H NMR** (400 MHz, $CDCl_3$) δ 9.34 (s, 2H, H_3), 8.68–8.54 (m, 2H, H_5), 8.52–8.41 (m, 2H, H_6), 8.28 (d, *J* = 8.4 Hz, 4H, H_9), 8.15 (d, *J* = 7.7 Hz, 4H, H_{16}), 7.94 (d, *J* = 8.3 Hz, 4H, H_{10}), 7.65 (d, *J* = 8.2 Ha, 4H, H_{13}), 7.53–7.41 (m, 4H, H_{14}), 7.39–7.30 (m, 4H, H_{15}). **^{13}C NMR** (100 MHz, $CDCl_3$) δ 197.5 (C_7), 186.6 (C_1), 157.0 (C_3), 145.2 (C_2), 139.8 (C_{12}), 139.4 (C_{11}), 138.0 (C_5), 137.2 (C_6), 133.4 (C_9), 132.2 (C_8), 126.8 (C_{10}), 126.7 (C_{14}), 124.4 (C_{17}), 121.5 (C_{15}), 120.8 (C_{16}), 110.2 (C_{13}).

5.4.2. X-ray Crystallographic Analysis

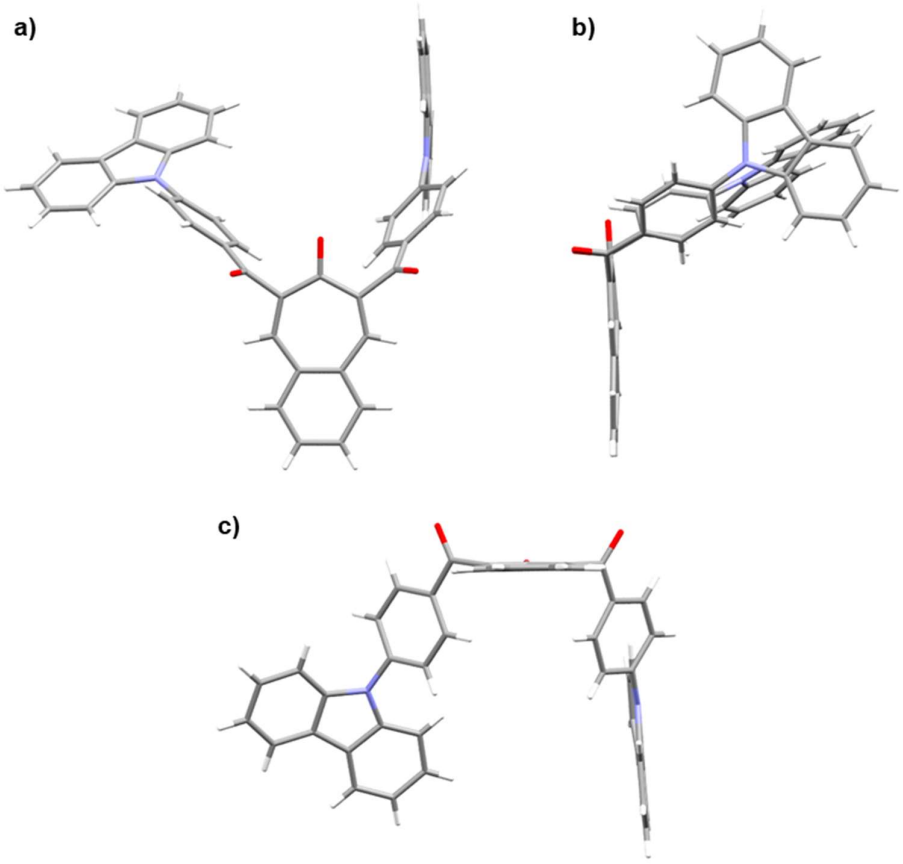

Figure 5.9. Single-crystal XRD structure of **6d** viewed **a)** face-on, **b)** side-on, and **c)** from the bottom of the benzotropone moiety.

Table 5.2. Crystal data and structure refinement for **6d**.

6d	
Empirical formula	$C_{49}H_{30}N_2O_3$
Formula weight	694.75
Temperature/K	120.00
Crystal system	monoclinic
Space group	$P2_1/n$
a/Å	16.2592(14)
b/Å	9.2374(8)
c/Å	25.157(2)
α/°	90
β/°	92.693(3)
γ/°	90
Volume/Å^3	3774.3(6)
Z	4

ρ_{calc}g/cm^3	1.223
μ/mm^{-1}	0.076
F(000)	1448.0
Crystal size/mm^3	0.31 × 0.06 × 0.01
Radiation	Mo Kα (λ = 0.71073)
2Θ range for data collection/°	4.698 to 51.996
Index ranges	-20 ≤ h ≤ 20, -11 ≤ k ≤ 11, -31 ≤ l ≤ 31
Reflections collected	88594
Independent reflections	7416 [R_{int} = 0.1350, R_{sigma} = 0.0736]
Data/restraints/parameters	7416/0/488
Goodness-of-fit on F^2	1.066
Final R indexes [I>=2σ (I)]	R_1 = 0.0754, wR_2 = 0.1458
Final R indexes [all data]	R_1 = 0.1086, wR_2 = 0.1587
Largest diff. peak/hole / e Å^{-3}	0.26/-0.27

5.4.3. pK_a Determination

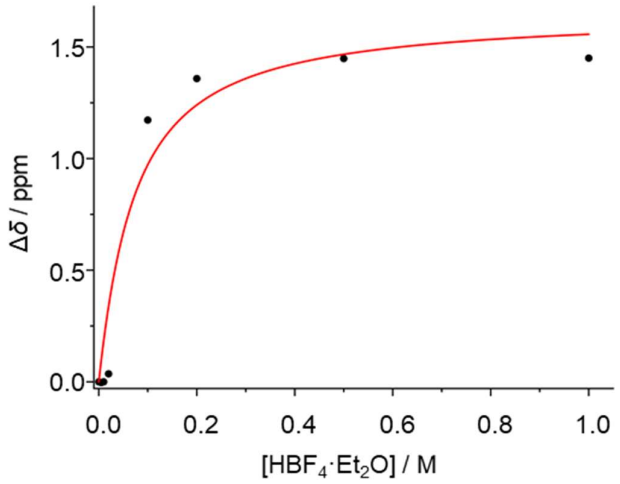

[HBF_4·Et_2O] / M	δ / ppm
0.0	7.938
0.0050	7.934
0.010	7.938
0.020	7.974
0.10	9.111
0.20	9.296
0.50	9.386
1.00	9.388

Figure 5.10 (left) and **Table 5.3** (right)**.** Chemical shifts (δ / ppm) of the α-proton of **1d** (as shown in Figure 5.1e) at different concentrations of HBF_4·Et_2O / M. The difference in chemical shifts ($\Delta\delta$ / ppm) was taken as $\Delta\delta = \delta - \delta_0$, where δ_0 is the chemical shift of the α-proton in unprotonated **7**. The data points were fitted to **Equation 1** (see below).

The pK_a of **1d** was determined by a ^{1}H NMR titration (anhydrous $CDCl_3$, 298 K), where the change in chemical shifts of the α-proton of **1d** (as shown in Figure 5.1e) were measured at different concentrations of [HBF_4·Et_2O]. The data points were fitted to **Equation 1** (below):[45]

$$\Delta\delta = \frac{\Delta\delta_{\text{sat}}}{2K_{\text{b}}[\mathbf{1d}]}\left(1 + K_{\text{b}}[\mathbf{1d}] + K_{\text{b}}[\text{HBF}_4] - \sqrt{\{1 + K_{\text{b}}[\mathbf{1d}] + K_{\text{b}}[\text{HBF}_4]\}^2 - 4{K_{\text{b}}}^2[\mathbf{1d}][\text{HBF}_4]}\right)$$

Equation 1. Where $\Delta\delta_{\text{sat}}$ / ppm is the saturated difference in chemical shift when a large excess of acid has been added, K_{b} is the base dissociation constant of the conjugate benzotropone of **1d** (*i.e.*, **6d**). $\Delta\delta_{\text{sat}}$ and K_{b} were determined by non-linear least-squares of the plot obtained by plotting $\Delta\delta$ *vs.* [HBF_4]. [**1d**] was kept constant at 20 mM for this experiment. From this, the pK_{a} of **1d** was calculated as:

$$\text{p}K_{\text{a}} = -\log\left(\frac{1}{K_b}\right)$$

Equation 2

Using this binding fit afforded $\Delta\delta_{\text{sat}}$ = 1.66 ± 0.18 and K_{b} = 16.2 ± 8.2 (R^2 = 0.94). A ^{1}H NMR stack of the titration experiment is included below in Figure 5.11.

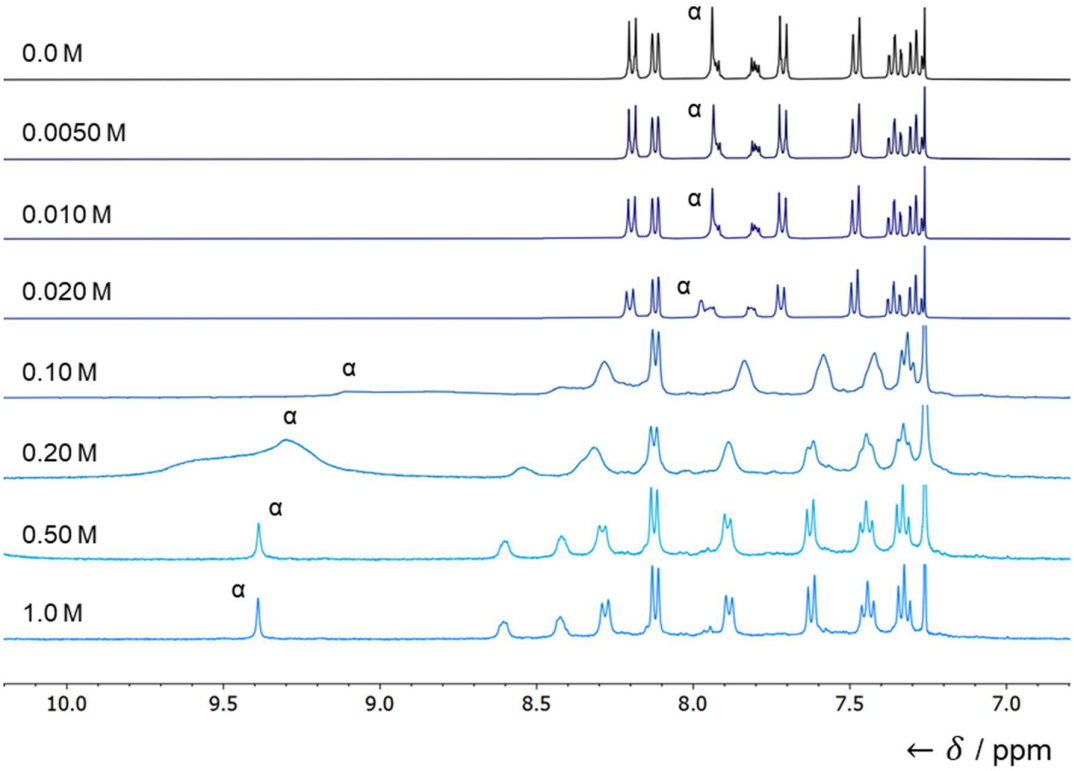

Figure 5.11. Partial ^{1}H NMR spectrum stack (400 MHz, $CDCl_3$) following the chemical shifts of **1d** (α-proton environment labelled) in increasingly higher concentrations of [HBF_4·Et_2O].

5.4.4. Optical Spectroscopy

Samples for UV-vis absorption and fluorescence spectroscopy were prepared by placing a suitable aliquot of a stock solution in a solution of anhydrous CH_2Cl_2 in an oven-dried cuvette under an inert atmosphere. The solvent was removed under a flow of Ar before the required solvent system (1.0 M MsOH in anhydrous CH_2Cl_2) was added.

5.5. References

1 N. C. Baird, *J. Am. Chem. Soc.*, 1972, **94**, 4941–4948.

2 J. Aihara, *Bull. Chem. Soc. Jpn.*, 1978, **51**, 1788–1792.

3 M. Rosenberg, C. Dahlstrand, K. Kilså and H. Ottosson, *Chem. Rev.*, 2014, **114**, 5379–5425.

4 M. Ueda, K. Jorner, Y. M. Sung, T. Mori, Q. Xiao, D. Kim, H. Ottosson, T. Aida and Y. Itoh, *Nature Commun.*, 2017, **8**, 1–9.

5 T. T. Slanina, R. Ayub, J. Toldo, J. Sundell, W. Rabten, M. Nicaso, I. Alabugin, I. F. Galvángalván, A. K. Gupta, R. Lindh, A. Orthaber, R. J. Lewis, G. Grö, J. Bergman and H. Ottosson, *J. Am. Chem. Soc*, 2020, **142**, 10942–10954.

6 C. H. Wu, L. J. Karas, H. Ottosson and J. I. C. Wu, *Proc. Natl. Acad. Sci. U. S. A.*, 2019, **116**, 20303–20308.

7 G. Granucci, J. T. Hynes, P. Millié and T. H. Tran-Thi, *J. Am. Chem. Soc.*, 2000, **122**, 12243–12253.

8 A. Weller, *Zeitschrift Elektrochem. Ber. Bunsenges. Phys. Chem.*, 1956, **60**, 1144–1147.

9 S. Nagaoka and U. Nagashima, *Chem. Phys.*, 1989, **136**, 153–163.

10 J. J. M. Hurley and L. Zhu, *J. Phys. Chem. A*, 2022, **126**, 5711–5720.

11 J. Piechowska and G. Angulo, *Dyes Pigm.*, 2019, **165**, 346–353.

12 D. Göbel, P. Rusch, D. Duvinage, N. C. Bigall and B. J. Nachtsheim, *Chem. Commun.*, 2020, **56**, 15430–15433.

13 P. T. Chou, M. Chao, J. H. Clements, M. L. Martinez and C. P. Chang, *Chem. Phys. Lett.*, 1994, **220**, 229–234.

14 Y. Hao and Y. Chen, *Dyes Pigm.*, 2016, **129**, 186–190.

15 K. Das, N. Sarkar, A. K. Ghosh, D. Majumdar, D. N. Nath and K. Bhattacharyya, *J. Phys. Chem.*, 1994, **98**, 9126–9132.

16 J. Ma, J. Zhao, P. Yang, D. Huang, C. Zhang and Q. Li, *Chem. Commun.*, 2012, **48**, 9720–9722.

17 S. Kim, D. W. Chang, S. Y. Park, K. Kim and J.-I. Jin, *Bull. Korean Chem. Soc*, 2001, **22**, 1407–1409.

18 J. Zhao, S. Ji, Y. Chen, H. Guo and P. Yang, *Phys. Chem. Chem. Phys.*, 2012, **14**, 8803–8817.

19 Z. Hu, H. Zhang, Y. Chen, Q. Wang, M. R. J. Elsegood, S. J. Teat, X. Feng, M. M. Islam, F. Wu and B. Z. Tang, *Dyes Pigm.*, 2020, **175**, 108175.

20 L. Chen, H. Zhang, M. Pan, Z. W. Wei, H. P. Wang, Y. N. Fan and C. Y. Su, *Chem. Asian J.*, 2016, **11**, 1765–1769.

21 L. Chen, C. Yan, M. Pan, H. P. Wang, Y. N. Fan and C. Y. Su, *Eur. J. Inorg. Chem.*, 2016, 2676–2680.

22 L. Chen, S. Y. Yin, M. Pan, K. Wu, H. P. Wang, Y. N. Fan and C. Y. Su, *J. Mater. Chem. C*, 2016, **4**, 6962–6966.

23 M. Porel, V. Ramalingam, M. E. Domaradzki, V. G. Young, V. Ramamurthy and R. S. Muthyala, *Chem. Commun.*, 2013, **49**, 1633–1635.

24 S. Kim, S. Somasundaram and S. Park, *Bull. Korean Chem. Soc.*, 2019, **40**, 937–938.

25 H. Wang, Y. Xiao, Z. Xie, H. Sun, X. Zhang, J. Wang and R. Huang, *Front. Chem.*, 2021, **9**, 766179.

26 D. Maity, V. Kumar and T. Govindaraju, *Org. Lett.*, 2012, **14**, 6008–6011.

27 L. Wang, Q. Zang, W. Chen, Y. Hao, Y.-N. Liu and J. Li, *RSC Adv.*, 2013, **3**, 8674–8676.

28 D. P. Murale, H. Kim, W. S. Choi and D. G. Churchill, *Org. Let.t*, 2013, **15**, 3946–3949.

29 I. E. Serdiuk, *J. Phys. Chem. C*, 2017, **121**, 5277–5286.

30 S. Samanta, U. Manna and G. Das, *New J. Chem.*, 2017, **41**, 1064–1072.

31 S. Kim, J. Seo, H. K. Jung, J. J. Kim and S. Y. Park, *Adv. Mater.*, 2005, **17**, 2077–2082.

32 H. Liu, X. Cheng, H. Zhang, Y. Wang, H. Zhang and S. Yamaguchi, *Chem. Commun.*, 2017, **53**, 7832–7835.

33 F. Panahi, A. Mahmoodi, S. Ghodrati, A. A. Abdi and F. Eshghi, *Sci. Rep.*, 2022, **12**, 2385.

34 H. Shono, T. Ohkawa, H. Tomoda, T. Mutai and K. Araki, *ACS Appl. Mater. Interfaces*, 2011, **3**, 654–657.

35 K. C. Tang, M. J. Chang, T. Y. Lin, H. A. Pan, T. C. Fang, K. Y. Chen, W. Y. Hung, Y. H. Hsu and P. T. Chou, *J. Am. Chem. Soc.*, 2011, **133**, 17738–17745.

36 A. Nano, M. P. Gullo, B. Ventura, N. Armaroli, A. Barbieri and R. Ziessel, *Chem. Commun.*, 2015, **51**, 3351–3354.

37 K. Wu, T. Zhang, Z. Wang, L. Wang, L. Zhan, S. Gong, C. Zhong, Z. H. Lu, S. Zhang and C. Yang, *J. Am. Chem. So.c*, 2018, **140**, 8877–8886.

38 A. K. Gupta, W. Li, A. Ruseckas, C. Lian, C. L. Carpenter-Warren, D. B. Cordes, A. M. Z. Slawin, D. Jacquemin, I. D. W. Samuel and E. Zysman-Colman, *ACS Appl. Mater. Interfaces*, 2021, **13**, 15459–15474.

39 B. Tang, H. Zhang, X. Cheng, K. Ye and H. Zhang, *Chempluschem*, 2016, **81**, 1320–1325.

40 P. K. Verma, A. Steinbacher, A. Schmiedel, P. Nuernberger and T. Brixner, *Struct. Dyn.*, 2016, **3**, 023606.

41 V. Leen, M. Laine, J. M. Ngongo, P. Lipkowski, B. Verbelen, A. Kochel, W. Dehaen, M. Van Der Auweraer, V. Nadtochenko and A. Filarowski, *J. Phy. Chem. A*, 2018, **122**, 5955–5961.

42 C. S. Wannere, D. Moran, N. L. Allinger, B. A. Hess, L. J. Schaad and P. von Ragué. Schleyer, *Org. Lett.*, 2003, **5**, 2983–2986.

43 K. An and J. Zhu, *Eur. J. Org. Chem.*, 2014, 2764–2769.

44 H. W. Tseng, J. Q. Liu, Y. A. Chen, C. M. Chao, K. M. Liu, C. L. Chen, T. C. Lin, C. H. Hung, Y. L. Chou, T. C. Lin, T. L. Wang and P. T. Chou, *J. of Phys. Chem. Lett.*, 2015, **6**, 1477–1486.

45 T. Kodama, Y. Kawashima, K. Uchida, Z. Deng and M. Tobisu, *J. Org. Chem.*, 2021, **86**, 13800–13807.

46 J. P. Lowe, N. R. Halcovitch and S. C. Coote, *J. Org. Chem.*, 2023, **88**, 9514–9517.

47 C. Chen, Z. Chi, K. C. Chong, A. S. Batsanov, Z. Yang, Z. Mao, Z. Yang and B. Liu, *Nature Mater.*, 2020, **20**, 175–180.

48 Y. Liu, J. Oble and G. Poli, *Beilstein J. Org. Chem.*, 2019, **15**, 1107–1115.

49 Z. An, Y. Liu, P. Zhao and R. Yan, *Adv. Synth. Catal.*, 2021, **363**, 3240–3244.

50 S. Da Wang, B. Yang, H. Zhang, J. P. Qu and Y. B. Kang, *Org. Lett.*, 2023, **25**, 816–820.

PUBLISHED PAPERS |

nature chemistry

Article

https://doi.org/10.1038/s41557-023-01149-6

Rupturing aromaticity by periphery overcrowding

Received: 10 February 2022

Accepted: 26 January 2023

Published online: 6 March 2023

Check for updates

Promeet K. Saha[1], Abhijit Mallick[1], Andrew T. Turley[1], Aisha N. Bismillah[1], Andrew Danos[2], Andrew P. Monkman[2], Alyssa-Jennifer Avestro[3], Dmitry S. Yufit[1] & Paul R. McGonigal[1,3]

The balance between strain relief and aromatic stabilization dictates the form and function of non-planar π-aromatics. Overcrowded systems are known to undergo geometric deformations, but the energetically favourable π-electron delocalization of their aromatic ring(s) is typically preserved. In this study we incremented the strain energy of an aromatic system beyond its aromatic stabilization energy, causing it to rearrange and its aromaticity to be ruptured. We noted that increasing the steric bulk around the periphery of π-extended tropylium rings leads them to deviate from planarity to form contorted conformations in which aromatic stabilization and strain are close in energy. Under increasing strain, the aromatic π-electron delocalization of the system is broken, leading to the formation of a non-aromatic, bicyclic analogue referred to as 'Dewar tropylium'. The aromatic and non-aromatic isomers have been found to exist in rapid equilibrium with one another. This investigation demarcates the extent of steric deformation tolerated by an aromatic carbocycle and thus provides direct experimental insights into the fundamental nature of aromaticity.

Aromaticity has been one of the fundamental tenets of chemical structure for over a century[1–3]. One school of thought defines it as the ability of a molecule to maintain a diatropic ring current when placed in a magnetic field[4–6]. The cyclic electron delocalization in aromatic systems gives rise to extraordinary stability, equal bond lengths, modified chemical reactivity and unique electronic properties[4,7]. For example, benzene, the archetypal aromatic compound, exhibits exceptionally high stability relative to other $(CH)_6$ isomers, such as prismane, benzvalene, Möbius benzene and Dewar benzene (Fig. 1a)[8,9].

The extraordinary electronic stabilization brought about by aromatic electron delocalization is also evident in the properties of tropylium—an aromatic homologue of benzene that exists as a stable C_7-symmetric carbocation (Fig. 1a). Since Doering and Knox's seminal work[10] on its isolation and structural elucidation, its electronic properties have been exploited in organocatalysis[11], stimuli-responsive dyes[12] and redox-active polycyclic aromatic hydrocarbons (PAHs)[13–15]. Relative to benzene, its larger ring size, increased conformational flexibility and the smaller angles subtended by its substituents (51.4° versus 60.0° for benzene) allow tropylium to undergo more facile strain-induced deformations[16,17]. Consequently, it has the potential to form highly twisted structures and to serve as a versatile subunit to probe aromaticity in geometrically deformed systems[18].

In recent years, there has been increasing interest in non-planar aromatic structures, including helicenes[19], twistacenes[20,21], Möbius aromatics[22,23], nanohoops[24–26], nanobelts[27,28] and warped nanographenes[29,30]. Relatively large deviations from planarity induced by strain are accommodated in these structures while maintaining substantial π-electron delocalization. However, it is challenging to probe the limits of such deformations experimentally. At what point is the aromatic stabilization energy[26] (ASE) of a ring system outweighed by its strain?

Certain annulated aromatic rings, such as Siegel's trisbicyclo[2.1.1]hexabenzene[31], experience large amounts of bond angle strain, which causes them to undergo substantial geometric distortion[32,33]. Yet, despite the distorted bond lengths present in these π-systems, effective delocalization still occurs and the system remains aromatic[32].

[1]Department of Chemistry, Durham University, Durham, UK. [2]Department of Physics, Durham University, Durham, UK. [3]Department of Chemistry, University of York, York, UK. e-mail: paul.mcgonigal@york.ac.uk

https://doi.org/10.1038/s41557-023-01149-6

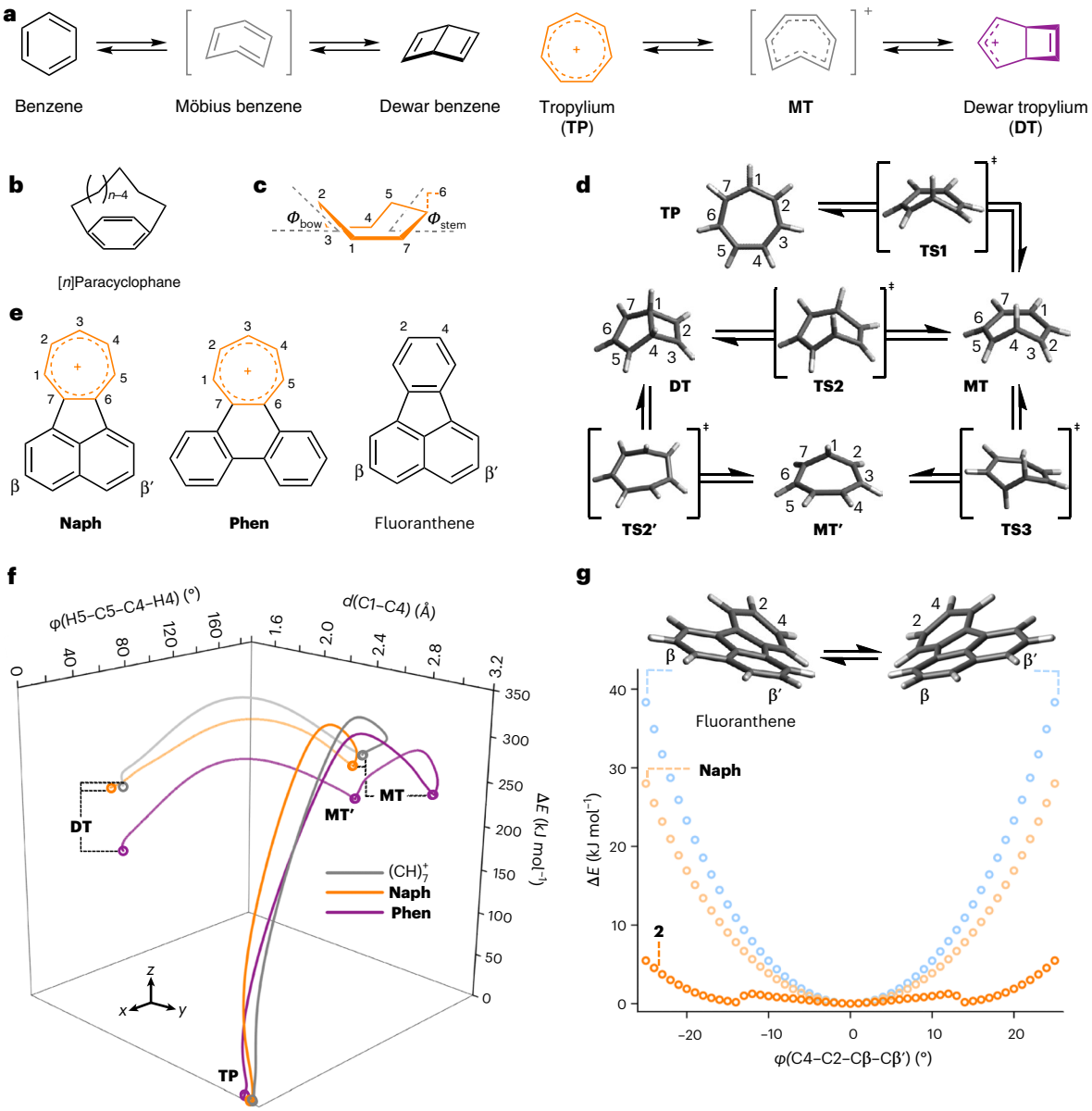

Fig. 1 | Aromatic ring systems undergo geometric and valence isomerism. **a**, The aromatic, planar isomers of $(CH)_6$ and $(CH)_7^+$ are linked to non-aromatic, bicyclic (Dewar) isomers by geometric deformation. **b**, This has been investigated in the distorted benzene rings of [*n*]paracyclophanes. **c**,**d**, Seven-membered ring boat conformations **(c)** are accessed via DFT-optimized energy minima and transition states in the isomerization pathway between tropylium and Dewar tropylium (**d**). **e**, Structural formulae of 1,2-acenaphthylene-annulated tropylium (**Naph**), 9,10-phenanthene-annulated tropylium (**Phen**) and fluoranthene. **f**, The IRCs for the rearrangement of $(CH)_7^+$, **Naph** and **Phen** plotted against C1–C4 internuclear distance, *d*, and H5–C5–C4–H4 dihedral angle, *φ*, show that the tropylium rings must become twisted to access the high-energy **MT** and **DT** isomers, which is facilitated by steric overcrowding. **g**, Plots of the energy of the twisted aromatic systems of fluoranthene, **Naph** and pentaphenyl-substituted **Naph** (**2**) relative to their planar geometries, Δ*E*, obtained by performing a relaxed potential energy scan as the C4–C2–Cβ–Cβ′ torsion angle is varied in 1° increments. See Fig. 2a for the structural formula of **2**. Two-dimensional plots of the data in **f** are shown in Supplementary Fig. 79. All DFT calculations were performed at the B3LYP(GD3BJ)/6-31G(d)/CH_2Cl_2 level of theory.

Similarly, bending of a benzene ring into a boat conformation with an out-of-plane angle of 23.2°, enforced by the pentamethylene 'strap' in [5]paracyclophanes (Fig. 1b), diminishes the magnitude of its π-ring current by only 17% (refs. [34,35]). Altering the length of the strap gives some crude control of the strain energy. But a decrease of just one methylene group causes a large jump in strain. For example, [4]paracyclophanes are enormously strained structures that have tentatively been assigned[36–38] to undergo thermally irreversible isomerization to the corresponding Dewar benzenes. However, the inherent instability and reactivity of these short-lived systems have limited their analysis to spectroscopic studies at low temperatures. So far, it has not been possible to fine-tune the level of strain present in an aromatic system, titrating it to the point at which the ASE is overcome. The consequences of precisely offsetting the ASE through strain have not been investigated.

Here we report the use of periphery overcrowding[20,39], that is, the introduction of sterically demanding substituents around the exterior of a molecule, to tune the geometric deformations experienced by π-extended tropylium ring systems beyond the point at which strain exceeds ASE. On one side of this energetic balance point, we identify structures that exhibit twisted geometries while retaining aromaticity. In the most extreme case, single-crystal X-ray diffraction (XRD) analysis

https://doi.org/10.1038/s41557-023-01149-6

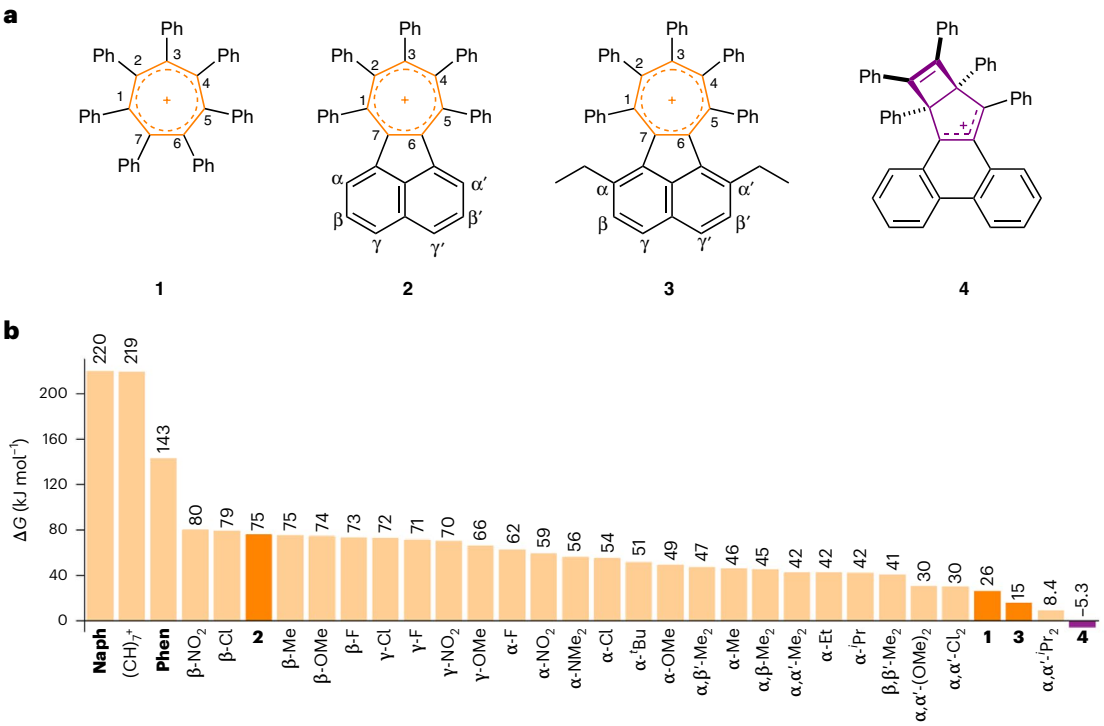

Fig. 2 | Periphery overcrowding tunes the balance of steric strain and aromatic stabilization. a,**b**, Cations **1**–**4** synthesized in this work (**a**) were selected on the basis of the calculated Gibbs energy differences, Δ*G*, between tropylium and the Dewar tropylium forms of $(CH)_7^+$, **Naph**, **Phen**, **1**–**4** and a series of derivatives of **2** (B3LYP(GD3BJ)/6-31G(d)/CH_2Cl_2) (**b**). The most overcrowded derivative, **4**, is predicted to lose aromaticity in favour of relieving strain by rearranging to its Dewar tropylium form. In **b**, the indicated positions of the different substituents of the derivatives of **2** correspond to the labelling shown in the structure of **2** in **a**. Positive Δ*G* values (orange bars) indicate an energetically favourable tropylium isomer, while negative Δ*G* values (purple bar) denote a bias towards Dewar tropylium. For asymmetric substitution patterns that break the C_2 symmetry, the lower energy of the two possible Dewar tropylium isomers has been used to estimate Δ*G*.

shows (1) an end-to-end twist angle along the π-extended ring system of 45.2° and (2) that the tropylium is in a distorted boat conformation (Φ_{bow} = 13.0° and Φ_{stern} = 29.0°; Fig. 1c), while computational modelling of its electronic properties indicates that these large geometric distortions reduce its aromatic character by only ~13%. On the other side of the energetic balance point, the π-extended ring systems sacrifice aromaticity in favour of relieving strain, that is, by collapse of their tropylium rings into bicyclic Dewar tropylium structures[40]. Dynamic nuclear magnetic resonance (NMR) spectroscopic analysis shows that an overcrowded Dewar tropylium undergoes reversible exchange between degenerate structures, passing through a twisted tropylium intermediate. This exchange is indicative of a dynamic intramolecular aromatic-to-non-aromatic equilibrium process that arises by counterbalancing aromaticity against substantial ring strain. Understanding these competing energetics in sterically strained systems is integral to designing and exploiting non-planar PAHs that exist at the limits of aromaticity[41].

Results and discussion

Previous computational studies[42] in conjunction with kinetic measurements[43] have shown that Dewar benzene-to-benzene isomerization proceeds (Fig. 1a) through a conrotatory electrocyclic ring opening. Initially, a highly strained *cis*,*cis*,*trans*-cyclohexatriene (Möbius benzene) intermediate is formed, before a π-bond rotation produces benzene. Relative to benzene, Dewar benzene is destabilized by 326 kJ mol^{-1}, while the largest activation energy barrier along the isomerization pathway lies at 443 kJ mol^{-1} (ref. [44]). With this benchmark in mind, we used density functional theory (DFT) to establish the energetic characteristics of deforming and isomerizing $(CH)_7^+$ through its tropylium (**TP**), Möbius-like tropylium (**MT**) and Dewar tropylium (**DT**) isomers (Fig. 1), as well as isomerizing our subsequent synthetic targets **1**–**4** (Fig. 2). Note that **MT** is named by analogy to Möbius benzene, but lacks the C_2 symmetry of a genuine Möbius topology.

Aromatic-to-non-aromatic $(CH)_7^+$ isomerization

A screen of functionals and basis sets (Supplementary Table 15) indicated that the B3LYP functional[45] with the D3 version of Grimme's dispersion correction and Becke–Johnson damping[46], the 6-31G(d) basis set[47] and a CH_2Cl_2 polarizable continuum solvent model (using the integral equation formalism variant)[48] is suitable for modelling the energetics of these systems. Using this level of theory, we identified (Fig. 1d) a series of possible transition states and Möbius-like tropylium intermediates that could link tropylium and Dewar tropylium. We also modelled (Fig. 1e) the same processes for two π-extended tropylium derivatives containing *ortho*-fused 1,2-acenaphthylene (**Naph**) or 9,10-phenanthrene (**Phen**) ring systems—the parent compounds of our subsequent targets **2**–**4** (Fig. 2a).

We visualized the isomerization pathways (Fig. 1f) through intrinsic reaction coordinate (IRC) calculations[49] using the optimized transition-state geometries. Transition state **TS1** connects the high-energy **MT** intermediate to the aromatic **TP** isomer. During this transformation, the most important geometric change occurs in the torsion angle φ(H5–C5–C4–H4) as it varies (Fig. 1f) from 0° (**TP**) to approximately 180° (**MT**). Starting from transition state **TS2** (the conrotatory ring-opening transition state), the IRC paths for $(CH)_7^+$ and **Naph** provide the aforementioned Möbius-like intermediates in one direction and the Dewar tropylium isomers in the other, completing the tropylium-to-Dewar tropylium isomerization pathway. This structural evolution is best visualized by following (Fig. 1f) the change in the internuclear distance *d*(C1–C4), which is shortest (~1.6 Å) when

https://doi.org/10.1038/s41557-023-01149-6

Table 1 | Torsion angles and tropylium aromaticity

	$(CH)_7^+$	Naph	Phen	1	2	3	4-TP
φ(C4–C2–Cβ–Cβ′) calc.[a] (°)	–	0	31.6	–	14.3, 0.4[e]	45.4	61.7
φ(C4–C2–Cβ–Cβ′) exp.[b] (°)	–	0	–	–	18.4, 0.4[e]	45.2	–
Φ_{bow} calc.[a] (°)	0	0	5.3	16.3	2.8[f]	15.0	16.3
Φ_{bow} exp.[b] (°)	0	–	–	13.6	6.7[f]	13.0	–
Φ_{stern} calc.[a] (°)	0	0	14.8	18.4	7.3[f]	28.8	31.8
Φ_{stern} exp.[b] (°)	0	–	–	12.2	13.7[f]	29.0	-
ASE (kJ mol^{-1})	−50.3	−55.1	−50.7	–	–	–	–
$NICS_{zz}(1)$[a,c]	−29.11	−18.38	−19.22	−18.91	−15.59[f]	−14.01	−16.90
$NICS_{zz}(-1)$[a,c]	−29.11	−18.38	−19.22	−18.90	−15.57[f]	−14.07	−16.90
EDDB[k,d]	4.94	3.08, 6.00	3.01, 7.05	4.26	3.09, 5.97[f]	2.69, 5.89	2.84, 6.66

[a]Calculated (calc.) using DFT-optimized geometries (B3LYP(GD3BJ)/6-31G(d)/CH_2Cl_2). [b]Experimentally measured (exp.) by single-crystal XRD analysis. [c]$NICS_{zz}(\pm)$ values were calculated 1 Å above and below the averaged plane of the tropylium rings. [d]Where two values are given, they correspond to the number of delocalized electrons in the tropylium ring circuit and the number delocalized over the entire annulated framework, respectively. [e]Energy minima with two different torsion angles are predicted to be similar in energy by DFT (5.6 kJ mol^{-1}), matching closely the conformers of **2** observed in the crystal lattice. [f]Values are given for the twisted conformer of **2**.

C1 and C4 share a single bond in a Dewar tropylium structure and longest (~3.1 Å) when they are separated across an aromatic tropylium ring. Our calculations suggest that a slightly modified isomerization pathway is preferred for **Phen**. The **MT** state evolves first to another Möbius-like intermediate (**MT′**), in which C1 rather than C4 is in the out-of-plane position, before shortening of d(C1–C4) leads to the **DT** structure. **TS1** corresponds to the highest energy point along the IRCs of $(CH)_7^+$ and **Phen**, presenting rate-limiting activation energy barriers, $\Delta G^‡$, of 302 and 297 kJ mol^{-1}, respectively (Supplementary Tables 16–21). **TS2** is the highest energy point along the IRC of **Naph**, with $\Delta G^‡$ = 316 kJ mol^{-1}. Further details, including the full structures of all energy minima and transition states, are included in Supplementary Figs. 71–73.

Overall, the aromatic-to-non-aromatic isomerization of tropylium generally mirrors that of benzene (Fig. 1). Similar distortions of the aromatic ring geometry occur, albeit with the increased flexibility and reduced ASE[26] of the seven-membered ring contributing to a lower overall activation energy barrier, $\Delta G^‡$ (302 kJ mol^{-1} for tropylium versus 443 kJ mol^{-1} for benzene). We quantified the magnitude of this reduced ASE by calculating the energetics of hyperhomodesmotic[50] reactions (Supplementary Fig. 76) according to von Ragué Schleyer and co-workers' isomerization stabilization energy method[51]. Using the same level of theory outlined above, we found $(CH)_7^+$, **Naph** and **Phen** to have ASEs of approximately −50 kJ mol^{-1} (Table 1), which are approximately half the ASE of benzene (−98.5 kJ mol^{-1}). As the B3LYP functional is known to overestimate aromatic stabilization in larger aromatic circuits[52], we also estimated ASEs using the M06-2X functional and found them to be comparable to our B3LYP predictions (Supplementary Tables 24 and 25).

Thermodynamic tuning by periphery overcrowding

We postulated that the introduction of sterically bulky groups around the periphery of $(CH)_7^+$ and its π-extended derivatives would decrease the aromatic-to-non-aromatic ΔG by favouring twisted geometries that more closely resemble the non-planar Möbius-like and Dewar structures. To test this hypothesis, we performed a series of geometry optimizations for fluoranthene, **Naph** and **2** (Fig. 1g). The torsion angle φ(C4–C2–Cβ–Cβ′) was scanned in increments of 1° to determine the energetic cost of twisting deformations. This end-to-end twisting in **Naph** carries a lower energy penalty than its six-membered ring counterpart, fluoranthene, as would be expected given the greater degrees of freedom of its seven-membered ring. The additional peripheral overcrowding caused by the phenyl groups of **2** destabilizes the fully coplanar tropylium structure, dramatically flattening (Fig. 1g) the energy well for twisting deformation. Indeed, through subsequent unrestrained geometry optimizations, we identified two local energy minima for structures with φ(C4–C2–Cβ–Cβ′) of 14.3° and 0.4° (Table 1). These two conformations strike different balances between the optimal π-electron delocalization of the planar structure and the reduced steric strain of the non-planar structure. In keeping with this phenomenon, our calculations also show that this peripheral overcrowding makes the Möbius-like isomers much more energetically accessible. The ΔG between tropylium **2** and its Möbius-like form, **2-MT**, was calculated to be only 96 kJ mol^{-1} (compared with a gap of 259 kJ mol^{-1} for the model compound **Naph**, which lacks Ph groups). Similarly for compound **4**, the two Möbius-like isomers **4-MT** and **4-MT′** are only 67 and 28 kJ mol^{-1} higher in energy than the tropylium form **4-TP** (again showing a substantial decrease relative to the analogous structures **Phen-MT** and **Phen-MT′** with ΔG = 232 and 209 kJ mol^{-1}, respectively).

We further investigated the impacts of steric and electronic factors on the aromatic-to-non-aromatic Gibbs energy gap by modelling an extended series of compounds. Starting from the previously reported heptaphenyltropylium cation **1** (ref. [17]), which exhibits a 26 kJ mol^{-1} preference for the aromatic tropylium isomer, we sought to increase the steric bulk in the plane of the tropylium core. Cation **2** provides an ideal scaffold for this purpose[53]. Despite its overcrowding, this species has an increased preference for the tropylium isomer (ΔG = 75 kJ mol^{-1}) on account of the extensive π-electron delocalization between the tropylium and the annulated naphthyl rings[54]. By contrast, the phenyl groups of **1** and **2** lie almost orthogonal to the central rings to minimize steric strain, so they have minimal π-overlap with the tropylium rings.

Our calculations suggest (Fig. 2) that while electron-donating or -withdrawing substituents at the β- and γ-positions of the acenaphthyl ring system tune the energetic balance of isomers by a few kilojoules per mole, increasing the steric bulk at the α- and α′-positions (which abut the phenyl rings) tunes the relative isomer energies over a larger range. For example, α,α′-dimethyl substitution reduces the energy gap to 42 kJ mol^{-1}. The gap is reduced to 15 kJ mol^{-1} by the α,α′-diethyl substitution of compound **3** and further still to 8.4 kJ mol^{-1} by α,α′-diisopropyl substitution. The low thermodynamic bias in favour of the aromatic isomer for these overcrowded systems approaches the critical point where the ASE and strain energy are evenly balanced. Consequently, the tropylium ring geometries would be expected to be among the most distorted possible. Indeed, increasing the size of the appended moiety to a phenanthrene-annulated system pushes the thermodynamic preference towards the Dewar tropylium isomer. The tropylium form of the parent **Phen** is already destabilized[55] (Fig. 2b) relative to $(CH)_7^+$ and **Naph** on account of a more sterically congested tropylium-to-PAH

https://doi.org/10.1038/s41557-023-01149-6

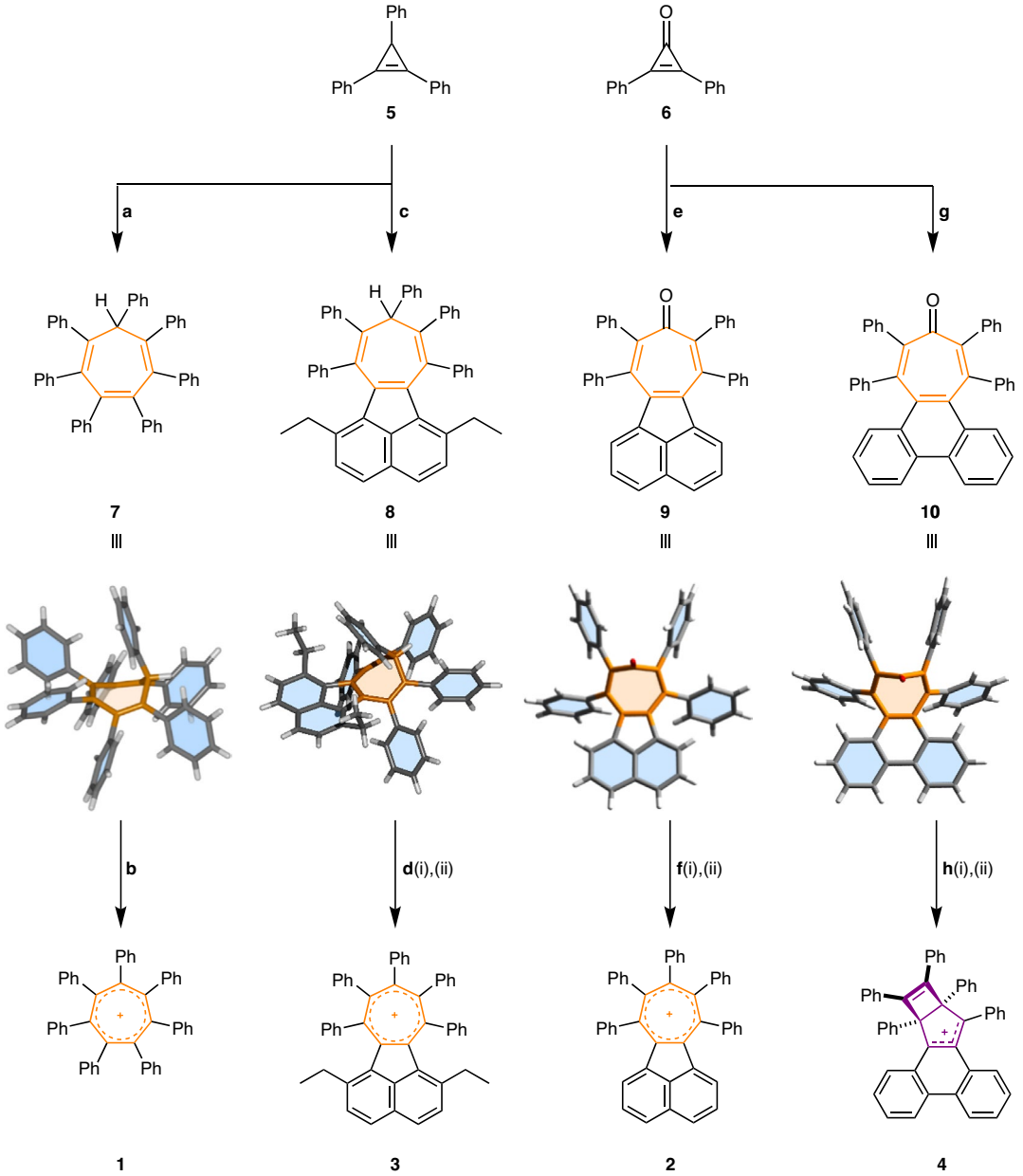

Fig. 3 | Synthesis of sterically overcrowded tropyliums 1–4. a–h, Reagents and conditions: **a**, **5**, tetracyclone, *p*-xylene, 140 °C, 36 h, 82%; **b**, ICl (1.0 M in CH_2Cl_2), rt, 24 h, 60%; **c**, **5**, diethylacecyclone, *p*-xylene, 190 °C, 84 h, 22%; **d**(i) *m*CPBA, $CHCl_3$, saturated aqueous $NaHCO_3$, reflux, 20 h, 12%; (ii) BBr_3, CH_2Cl_2, rt, 10 min; **e**, **6**, acecyclone, PhMe–$CHCl_3$ (5:3), 130 °C, 24 h, 34%; **f**(i) PhMgBr, THF, 0 °C → rt, 3 h, 68%; (ii) $Et_3O{\cdot}SbCl_6$, $CDCl_3$, rt, 6 h, quantitative; **g**, **6**, phencyclone, PhMe, 130 °C, 24 h, 40%; **h**(i) PhMgBr, THF, 0 °C → rt, 3 h, 60%; (ii) $Et_3O{\cdot}SbCl_6$, $CDCl_3$, rt, 6 h, quantitative. rt, room temperature; *m*CPBA = *m*-chloroperbenzoic acid. Solid-state structures determined by XRD analysis are shown for the four key intermediates **7**–**10**.

bay region. The added strain caused by the five proximal phenyl rings of **4** is sufficient to tune the energetic balance in favour of the Dewar tropylium by 5.3 kJ mol^{-1}.

Synthesis of twisted and Dewar tropyliums

Cations **1**–**4** were selected as synthetic targets that span a wide range of calculated Δ*G* values: **1** and **2** favour an aromatic tropylium, **4** is biased towards a Dewar tropylium isomer and **3** is close to the border between the two. Their syntheses are outlined in Fig. 3.

Firstly, dienophiles **5** and **6** were both prepared from diphenylacetylene (Supplementary Fig. 1). As a precursor to **1**, *sym*-heptaphenylcycloheptatriene, **7**, was formed (Fig. 3) by the Diels–Alder cycloaddition of **5** with tetraphenylcyclopentadienone (tetracyclone) and subsequent cheletropic elimination of CO (ref. [56]). Oxidation of **7** using an excess of ICl then yielded **1** as its iodine dichloride salt (**1**·ICl_2). The analogous phenanthrene- and acenaphthene-annulated cycloheptatrienes, as well as an α,α′-diethyl derivative, **8**, were also accessed through the same approach by treating **5** with an appropriate cyclopentadienone reagent (phencyclone, acecyclone and diethylacecyclone, respectively). However, attempts to oxidize these compounds with ICl or Br_2 led to unwanted halogenation of the electron-rich annulated ring systems in preference to oxidation of the cycloheptatrienes. Hydride abstraction reactions were also unsuccessful.

Instead, the target cations **2** and **4** were prepared successfully (Fig. 3) by first treating acecyclone and phencyclone with **6** to afford tropones **9** and **10**, respectively. Subsequent nucleophilic attack by PhMgBr at the carbonyl introduced a final phenyl ring as well as a tertiary alcohol group, which was readily eliminated by treatment

with triethyloxonium hexachloroantimonate to give **2**·$SbCl_6$ and **4**·$SbCl_6$, respectively.

We attempted a similar strategy to prepare **3**. However, cycloaddition between **6** and diethylacecyclone did not yield the desired tropone. We observed that the high temperature (190 °C) required for the reaction of this sterically crowded diene caused the rapid decomposition of **6**. Instead, we employed a stepwise oxidation protocol to convert cycloheptatriene **8** into tropylium **3**. Oxidation of **8** using *m*CPBA in refluxing $CHCl_3$ led to a mixture of products, from which we isolated an epoxide intermediate (**S1**). By treating the epoxide with a stoichiometric amount of BBr_3 under the inert conditions of a glove box, we were able to form **3** in trace amounts and isolate single crystals of its tetrabromoborate salt **3**·BBr_4 by slow evaporation of the reaction mixture. The apparently high reactivity of the contorted cation **3** and associated low yield prevented us from obtaining solution-state spectroscopic data. However, XRD analysis of the crystals confirmed its identity and allowed us to measure its geometric parameters (vide infra).

Geometric distortions of tropylium rings

We determined the solid-state structures of **1**–**4** (Fig. 4a) by single-crystal XRD analysis. While the geometries of the cations are influenced by crystal packing effects and the enforced proximity to their anions, we found that the crystal structures of **1**–**4** are in good agreement with our calculated solution-state cation geometries[57]. The geometry of **1** in crystals of **1**·ICl_2 is similar to that found previously for its trifluoroacetate salt[17]. Its tropylium ring adopts a shallow boat conformation to minimize steric interactions between adjacent phenyl rings, giving interplanar angles (Table 1) at the bow and stern (Fig. 1c) of $\Phi_{bow} = 13.6°$ and $\Phi_{stern} = 12.2°$.

Orange crystals of **2**·$SbCl_6$ were grown by slow evaporation of a $CDCl_3$ solution. Pleasingly, the facile twisting of **2** predicted by DFT (Fig. 1g) is evident in the solid-state structure determined by XRD analysis (Fig. 4a). We found two non-degenerate conformers present in the unit cell—a near-planar structure with φ(C4–C2–Cβ–Cβ′) = 0.4° and a twisted conformer with φ(C4–C2–Cβ–Cβ′) = 18.4°, which match the two minima predicted by DFT calculations.

Taking the twisting deformation to its extreme, the solid-state structure of **3**·BBr_4 (Fig. 4a) shows that its cation adopts an extremely distorted geometry on account of the severe peripheral overcrowding, while remaining as the aromatic tropylium isomer (rather than a Dewar tropylium). It has a large end-to-end twist with φ(C4–C2–Cβ–Cβ′) = 45.2°, which matches closely the predicted twist of φ(C4–C2–Cβ–Cβ′) = 45.4° (Table 1). Examination of the crystal packing showed that the twisted acenaphthyltropylium units all have the same helical screw sense as one another, that is, the crystal has formed as a conglomerate[58]. The seven-membered ring of **3** is distorted from planarity to a much greater extent than that of **1** or **2** (Table 1). It has a boat conformation characterized by interplanar angles of $\Phi_{bow} = 13.0°$ and $\Phi_{stern} = 29.0°$. An informative comparison can also be made with the neutral, benzenoid homologue of this tropylium, 1,6-diethyl-7,8,9,10-tetraphenylfluoranthene (**S5**), which was isolated as a side-product during the synthesis of **3**. The benzene-centred molecule is significantly less distorted than **3** (Supplementary Fig. 51). Its torsion angle of φ(C4–C2–Cβ–Cβ′) = 22.7° and interplanar angles of $\Phi_{bow} = 4.4°$ and $\Phi_{stern} = 13.2°$ are smaller than those measured for **3**, reflecting the greater inherent flexibility and increased propensity for peripheral overcrowding of tropylium compared with benzene.

Non-aromatic-to-aromatic dynamics of a Dewar tropylium

The ^{1}H NMR spectrum of **2**·$SbCl_6$ (Fig. 4b) shows that, as expected for the tropylium structure, the cation retains the C_2 symmetry of its cycloheptatriene precursor. The ^{1}H NMR spectrum of **4**·$SbCl_6$, however, exhibits a larger number of resonances, indicating that **4** lacks C_2 symmetry. Its lower symmetry is consistent with the formation of a Dewar tropylium structure in solution. As an illustrative example, the NMR signal arising from the two *peri* positions of **2** (γ and γ′), which appears as a sharp doublet (that is, a single resonance), can be contrasted with the two distinct doublets arising from the phenanthrene bay region of **4** (open and filled star symbols, Fig. 4b) that appear in the ^{1}H NMR spectrum recorded at 179 K. These solution-state NMR data are complemented by the XRD analysis of dark-purple single crystals grown by the slow evaporation of **4**·$SbCl_6$ in CH_2Cl_2 (Fig. 4a), which confirmed the presence of the Dewar tropylium ring system in the solid state. To our knowledge, this is the first non-aromatic valence isomer of a tropylium derivative that has been isolated.

Close to room temperature, several of the ^{1}H NMR peaks of **4** broaden and merge (Supplementary Fig. 41), which we attribute to dynamic exchange between its two degenerate valence isomers (Fig. 4c). Taking the phenanthrene bay protons as an example, these nuclei trade magnetic environments as **4** rearranges to **4′**. A ^{1}H–^{1}H exchange NMR spectroscopy experiment (Supplementary Fig. 42) confirmed that these proton environments are in exchange. We performed NMR lineshape analysis (Fig. 4d) to derive exchange rates for this process at a series of temperatures close to the signal coalescence point. An Eyring plot based on these data (Fig. 4e) gives an enthalpy of activation, $\Delta H^‡$, of 50.0 kJ mol^{-1} and an entropy of activation, $\Delta S^‡$, of −41.5 J K^{-1} mol^{-1}, corresponding to a $\Delta G^‡$ of 62.4 kJ mol^{-1} at 298 K.

By analogy to the isomerization pathways identified (Fig. 1f) for $(CH)_7^+$, **Naph** and **Phen**, the exchange between **4** and **4′** presumably involves cleavage of the C1–C4 bond to form an aromatic intermediate, **4-TP** (Fig. 4c). Indeed, DFT modelling of **4-TP** indicates that, despite it having a large end-to-end twist angle of φ(C4–C2–Cβ–Cβ′) = 61.7°, it is an energetically viable intermediate. It lies only 5.3 kJ mol^{-1} higher in energy than **4**. Consequently, it should exist as a minor, but detectable, species at equilibrium. With the thermal energy available at 298 K, the Boltzmann distribution of isomers (Supplementary Table 26) for this Gibbs energy gap gives an ~10% probability of any given cation occupying the **4-TP** state, that is, the dynamic rearrangement of **4** to **4-TP** has an equilibrium constant $K = 0.12$. To test this prediction, we performed a hydride 'trapping' experiment by treating a solution of **4** with $NaBH_4$ (Fig. 4c). ^{1}H NMR spectroscopic analysis of the crude mixture obtained after aqueous work-up showed that two bicyclo[3.2.0]heptadiene diastereoisomers, *anti*-**11** and *syn*-**11**, were produced along with a cycloheptatriene product[59], **12**, in a 38:58:4 ratio (Fig. 4c and Supplementary Figs. 38 and 39). The structure of *anti*-**11** was confirmed by XRD analysis (Supplementary Fig. 68). The observation of **12** is consistent with its tropylium precursor, **4-TP**, being present at equilibrium in solution.

Overall, therefore, the peripheral overcrowding dictates the energy gap between the non-aromatic isomer **4** and its aromatic form **4-TP**, and tunes the kinetics of their interconversion. It does so by selectively destabilizing the aromatic tropylium isomer relative to its Dewar and Möbius-like tropylium isomers, as well as the transition-state structure(s) that bridge(s) them. The **4** and **4-TP** isomers have been brought to within a few kilojoules per mole of one another, establishing a non-aromatic-to-aromatic equilibrium that is weighted in a ratio of ~90:10 towards the non-aromatic form. The experimentally measured $\Delta G^‡$ of 62.4 kJ mol^{-1} for this rearrangement is significantly lower than the $\Delta G^‡$ of the parent compound (**Phen**) lacking the bulky phenyl groups, which is predicted (Fig. 1f) to be 297 kJ mol^{-1}. Consequently, the equilibrium is established rapidly with the thermal energy available at room temperature, which is reflected experimentally in the broadening of the NMR peaks and the formation of a cycloheptatriene product following reaction with $NaBH_4$.

Aromaticity probes

Our experimental results led us to the following question: are the large geometric distortions of **3** and the ruptured aromaticity observed

https://doi.org/10.1038/s41557-023-01149-6

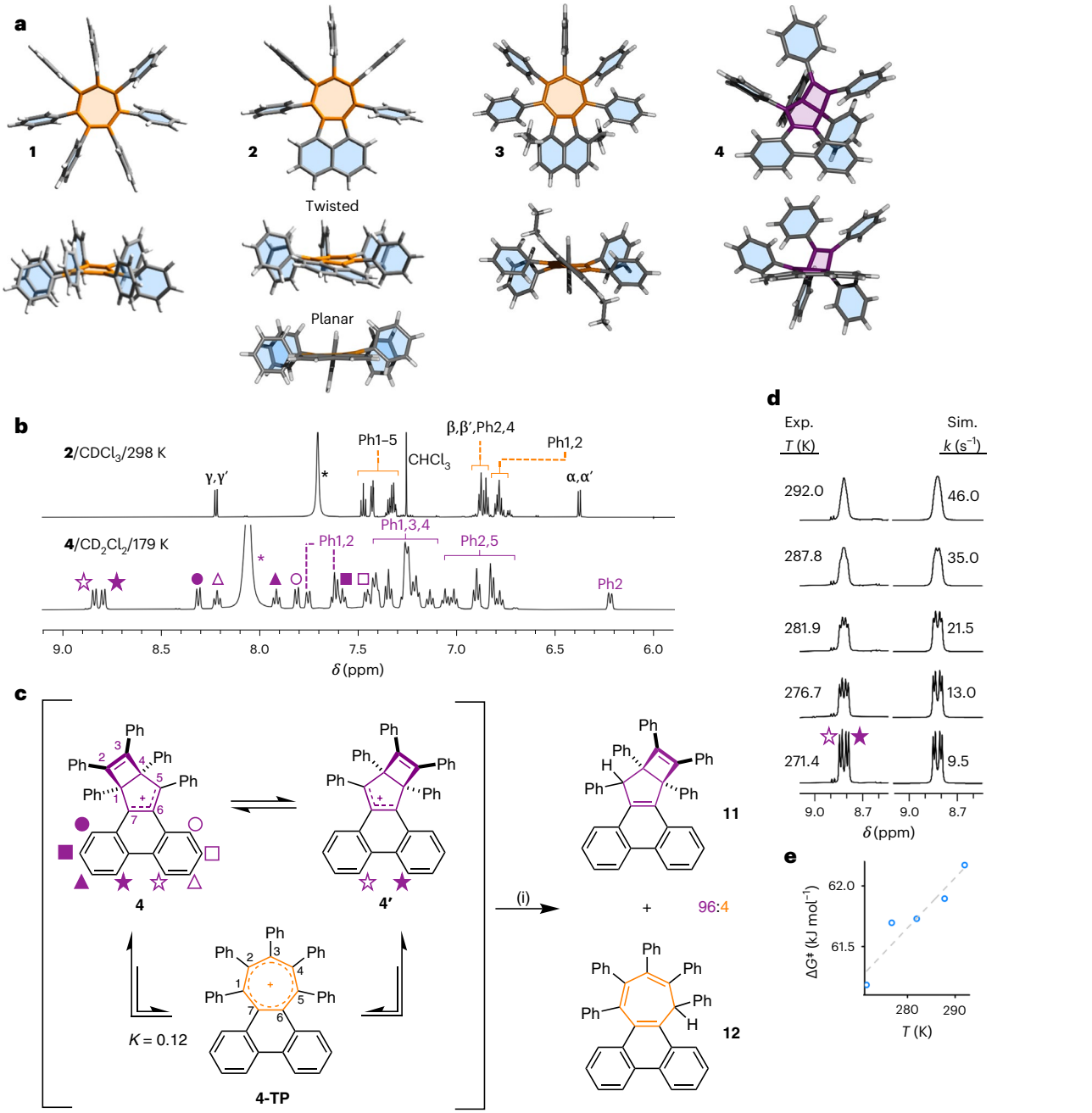

Fig. 4 | Highly twisted tropyliums are found to undergo a non-aromatic-to-aromatic equilibrium. a–**e**, Single-crystal XRD analysis and NMR spectroscopy show the increasingly twisted geometries of **1**–**3** and the preferred Dewar tropylium structure of **4**, which is in equilibrium with **4-TP**. **a**, Plan and side views of single-crystal X-ray structures of cations **1**–**4**. Counterions and solvent molecules have been omitted for clarity. Both of the conformers present in the unit cell of **2** are shown in side view. **b**, Partial ^{1}H NMR spectra of **2**·$SbCl_6$ (top, 700 MHz) and **4**·$SbCl_6$ (bottom, 500 MHz). Full spectra are shown in Supplementary Figs. 26 and 32, respectively. The peaks of **2** are labelled according to the numbering scheme shown in Fig. 2. Asterisks denote signals corresponding to R_2OH^+ (R = H or Et), formed as a byproduct from the reaction of the Et_3O^+ reagent. Filled and hollow shape symbols represent pairs of inequivalent resonances that arise by breaking the tropylium C_2 symmetry upon forming the Dewar tropylium. **c**, The dynamic exchange between two degenerate Dewar tropylium isomers of **4** and its tropylium form was intercepted by reduction to give **11** and **12** in a ratio of 96:4. Reagents and conditions: (i) $NaBH_4$, THF, rt, 30 min. **d**, This dynamic rearrangement causes broadening of NMR resonance lineshapes as the temperature is raised from 271.4 to 292.0 K. Full NMR spectra are shown in Supplementary Fig. 41. The rate data were obtained by comparing the experimental (Exp.) and simulated (Sim.) lineshapes. **e**, Fitting the rate data to the Eyring equation gives an Eyring plot of $\Delta G^‡$ versus T for the exchange. The linear fit (dashed grey line) indicates $\Delta H^‡ = 50.0$ kJ mol^{-1} and $\Delta S^‡ = -41.5$ J K^{-1} mol^{-1}.

for **4** best attributed to them having increased strain relative to the other derivatives (that is, **1** and **2**), or to them having reduced aromatic character? To investigate the aromaticity of cations **1**–**3** and **4-TP**, we characterized their tropylium units using both magnetic and electronic criteria. Anisotropy of the induced current density (ACID) plots (Fig. 5) show the presence of a clockwise ring current in all four species, which is indicative of aromaticity[60]. The aromatic ring current in **2** extends to the appended naphthalene moiety, corroborating its stabilizing effect through extensive charge delocalization. The extent of this π-electron delocalization is reduced in **3** and **4-TP**, as the annulated acenaphthyl

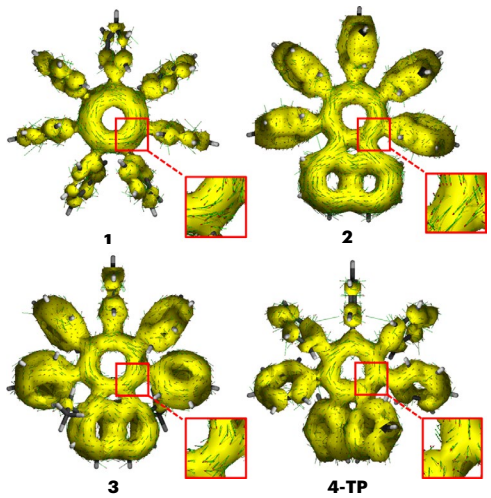

Fig. 5 | ACID plots. The DFT-optimized geometries (B3LYP(GD3BJ)/6-31G(d)/CH_2Cl_2) of **1**–**3** and **4-TP** overlaid with the ACID isosurfaces (isovalue = 0.01) for their respective π-orbitals (see Supplementary Section 6.8 for orbital numbers). The red-headed arrows demonstrate clockwise current density vectors for the seven-membered rings (see the magnified areas), which are indicative of aromatic electron delocalization.

and phenanthrenyl groups are twisted further from the plane of the tropylium.

We calculated the *zz* components of the nucleus-independent chemical shifts ($NICS_{zz}(\pm1)$; refs. [61,62]), to gain insights into the local aromaticity of the tropylium rings (Table 1). Negative and positive NICS values are characteristic of aromaticity and antiaromaticity, respectively, whereas a NICS value of around zero suggests non-aromatic character[63]. The $NICS_{zz}(\pm1)$ values of −14.01 to −18.91 calculated for **1**–**3** and **4-TP** (Table 1) are consistent with the aromatic character predicted by their ACID plots.

To complement this magnetic assessment, we also determined electron density of delocalized bond ($EDDB^k$) values (Table 1) for the cyclic delocalization of π-electrons through pathways that can be represented by Kekulean resonance forms. $EDDB^k$ is a quantitative electronic index that estimates the number of electrons delocalized in an aromatic circuit[64]. We assessed electron delocalization involving the tropylium ring alone (local aromaticity) and, for the π-extended systems **2**, **3**, **4-TP**, **Naph** and **Phen**, we also assessed electron delocalization involving the entire polycyclic framework of the molecule (global aromaticity, shown in Supplementary Figs. 77 and 78)[65]. A direct comparison is most easily drawn between **Naph**, **2** and **3**, which share the same cyclic framework. The $EDDB^k$ values of **2** are almost identical to those of **Naph**, suggesting perphenylation has little impact on the effectiveness of electron delocalization along both pathways. Even with the severe deviation from planarity imposed by the additional ethyl groups of **3**, the $EDDB^k$ value for the local aromaticity of the tropylium drops by just 13% compared with **Naph** (from 3.08 to 2.69), suggesting a modest decrease in aromatic character. Similarly, the tropylium moiety in **1** suffers a 13% drop in aromatic character compared with $(CH)_7^+$, while **4-TP** experiences a very small 6% reduction compared with **Phen**.

Together, these analyses demonstrate that cyclic π-electron delocalization persists despite the steric deformation of these tropyliums. The aromaticity of the tropylium isomer **4-TP** is comparable to that of **1**–**3**. Therefore, its rearrangement to the Dewar tropylium isomer and associated rupture of aromaticity occur primarily as a consequence of its greatly increased strain (relative to **Phen**) exceeding the ASE, rather than the geometric changes causing any substantial decrease in the aromatic character of the tropylium.

Conclusions

Peripheral overcrowding causes considerable structural deformations in a series of π-extended aromatic cations. These deformations manifest as boat-type conformations of their tropylium cores and helical twists along the length of their π-extended polycyclic frameworks, giving experimentally measured torsion angles of up to 45.2° in **3**. The Gibbs energy gap between the aromatic and non-aromatic isomers of **3** is only 15 kJ mol^{-1}, placing it among the most overcrowded and twisted tropylium structures that can feasibly be synthesized. By imposing even greater peripheral overcrowding, the balance between strain and aromatic stabilization tips in favour of a bicyclic Dewar tropylium structure, as observed in **4**. Spectroscopic and DFT evidence show that **4** exists as a dynamic mixture in solution. At room temperature, it passes back and forth rapidly between non-aromatic (**4** and **4′**) and aromatic (**4-TP**) isomers in an ~90:10 ratio, establishing a non-aromatic-to-aromatic equilibrium. Our calculations suggest that even the most deformed aromatic tropylium isomers **3** and **4-TP** retain the electronic and magnetic hallmarks of aromaticity. Yet, when bulky groups are introduced in a manner that raises steric overcrowding for the aromatic isomer preferentially, the ASE can be outweighed by the strain energy, and the equilibrium shifts towards a non-aromatic species.

Online content

Any methods, additional references, Nature Portfolio reporting summaries, source data, extended data, supplementary information, acknowledgements, peer review information; details of author contributions and competing interests; and statements of data and code availability are available at https://doi.org/10.1038/s41557-023-01149-6.

References

1. Armstrong, H. E. The structure of cycloid hydrocarbons. *Proc. Chem. Soc. Lond.* **6**, 101–105 (1890).
2. Hückel, E. Quantentheoretische Beiträge zum Benzolproblem. I. Die Elektronenkonfiguration des Benzols und verwandter Verbindungen. *Z. Phys.* **70**, 204–286 (1931).
3. Wiberg, K. B. Antiaromaticity in monocyclic conjugated carbon rings. *Chem. Rev.* **101**, 1317–1331 (2001).
4. von Ragué Schleyer, P. & Jiao, H. What is aromaticity? *Pure Appl. Chem.* **68**, 209–218 (1996).
5. Fleischer, U., Mühlenkamp, V., Kutzelnigg, W. & Lazzeretti, P. IGLO study of benzene and some of its isomers and related molecules. Search for evidence of the ring current model. *J. Am. Chem. Soc.* **116**, 5298–5306 (1994).
6. Gershoni-Poranne, R. & Stanger, A. Magnetic criteria of aromaticity. *Chem. Soc. Rev.* **44**, 6597–6615 (2015).
7. von Ragué Schleyer, P., Jiao, H., Goldfuss, B. & Freeman, P. K. Aromaticity and antiaromaticity in five-membered C_4H_4X ring systems: 'classical' and 'magnetic' concepts may not be 'orthogonal'. *Angew. Chem. Int. Ed. Engl.* **34**, 337–340 (1995).
8. Priyakumar, U. D., Dinadayalane, T. C. & Sastry, G. N. A computational study of the valence isomers of benzene and their group V hetero analogs. *New J. Chem.* **26**, 347–353 (2002).
9. Harman, P. J., Kent, J. E., O'Dwyer, M. F. & Griffith, D. W. T. Photochemistry of benzene isomers. 2. Benzvalene and Dewar benzene. *J. Phys. Chem.* **85**, 2731–2733 (1981).
10. von Eggers Doering, W. & Knox, L. H. The cycloheptatrienylium (tropylium) ion. *J. Am. Chem. Soc.* **76**, 3203–3206 (1954).
11. Lyons, D. J. M., Crocker, R. D., Blümel, M. & Nguyen, T. V. Promotion of organic reactions by non-benzenoid carbocyclic aromatic ions. *Angew. Chem. Int. Ed.* **56**, 1466–1484 (2017).
12. Lyons, D. J. M., Crocker, R. D. & Nguyen, T. V. Stimuli-responsive organic dyes with tropylium chromophore. *Chem. Eur. J.* **24**, 10959–10965 (2018).

13. Tamoto, A., Aratani, N. & Yamada, H. Contraction of π-conjugated rings upon oxidation from cyclooctatetraene to benzene via the tropylium cation. *Chem. Eur. J.* **23**, 16388–16392 (2017).
14. Sasaki, Y., Takase, M., Okujima, T., Mori, S. & Uno, H. Synthesis and redox properties of pyrrole- and azulene-fused azacoronene. *Org. Lett.* **21**, 1900–1903 (2019).
15. Zhu, C., Shoyama, K. & Würthner, F. Conformation and aromaticity switching in a curved non-alternant sp^2 carbon scaffold. *Angew. Chem. Int. Ed.* **59**, 21505–21509 (2020).
16. Tamm, M., Dreßel, B. & Fröhlich, R. Molecular structure of a heptadentate cogwheel: $C_7Me_7^+$ is not planar. *J. Org. Chem.* **65**, 6795–6797 (2000).
17. Brydges, S. et al. The structure of a seven-bladed propeller: $C_7Ph_7^+$ is not planar. *Chem. Eur. J.* **4**, 1201–1205 (1998).
18. Chaolumen, I. A. S., Yamada, K. E., Ito, H. & Itami, K. Construction of heptagon-containing molecular nanocarbons. *Angew. Chem. Int. Ed.* **60**, 23508–23532 (2021).
19. Portella, G., Poater, J., Bofill, J. M., Alemany, P. & Solà, M. Local aromaticity of [*n*]acenes, [*n*]phenacenes, and [*n*]helicenes (*n* = 1–9). *J. Org. Chem.* **70**, 2509–2521 (2005).
20. Xiao, Y., Mague, J. T., Schmehl, R. H., Haque, F. M. & Pascal, R. A. Dodecaphenyltetracene. *Angew. Chem. Int. Ed.* **58**, 2831–2833 (2019).
21. Ma, J. et al. Helical nanographenes containing an azulene unit: synthesis, crystal structures, and properties. *Angew. Chem. Int. Ed.* **59**, 5637–5642 (2020).
22. Ajami, D., Oeckler, O., Simon, A. & Herges, R. Synthesis of a Möbius aromatic hydrocarbon. *Nature* **426**, 819–821 (2003).
23. Naulet, G. et al. Cyclic tris-[5]helicenes with single and triple twisted Möbius topologies and Möbius aromaticity. *Chem. Sci.* **9**, 8930–8936 (2018).
24. Rickhaus, M. et al. Global aromaticity at the nanoscale. *Nat. Chem.* **12**, 236–241 (2020).
25. Leonhardt, E. J. & Jasti, R. Emerging applications of carbon nanohoops. *Nat. Rev. Chem.* **3**, 672–686 (2019).
26. Jirásek, M., Rickhaus, M., Tejerina, L. & Anderson, H. L. Experimental and theoretical evidence for aromatic stabilization energy in large macrocycles. *J. Am. Chem. Soc.* **143**, 2403–2412 (2021).
27. Povie, G., Segawa, Y., Nishihara, T., Miyauchi, Y. & Itami, K. Synthesis of a carbon nanobelt. *Science* **356**, 172–175 (2017).
28. Cheung, K. Y., Watanabe, K., Segawa, Y. & Itami, K. Synthesis of a zigzag carbon nanobelt. *Nat. Chem.* **13**, 255–259 (2021).
29. Luo, J., Xu, X., Mao, R. & Miao, Q. Curved polycyclic aromatic molecules that are π-isoelectronic to hexabenzocoronene. *J. Am. Chem. Soc.* **134**, 13796–13803 (2012).
30. Márquez, I. R. et al. Versatile synthesis and enlargement of functionalized distorted heptagon-containing nanographenes. *Chem. Sci.* **8**, 1068–1074 (2017).
31. Baldridge, K. K. & Siegel, J. S. Bond alternation in triannelated benzenes: dissection of cyclic π from 'Mills–Nixon' effects. *J. Am. Chem. Soc.* **114**, 9583–9587 (1992).
32. Stanger, A. What is aromaticity: a critique of the concept of aromaticity-can it really be defined?. *Chem. Commun.* **101**, 1939–1947 (2009).
33. Shaik, S., Shurki, A., Danovich, D. & Hiberty, P. C. A different story of π-delocalization—the distortivity of π-electrons and its chemical manifestations. *Chem. Rev.* **101**, 1501–1539 (2001).
34. Jenneskens, L. W. et al. [5]Paracyclophane. *J. Am. Chem. Soc.* **107**, 3716–3717 (1985).
35. Jenneskens, L. W., Havenith, R. W. A., Soncini, A. & Fowler, P. W. Aromaticity of strongly bent benzene rings: persistence of a diatropic ring current and its shielding cone in [5] paracyclophane. *Phys. Chem. Chem. Phys.* **13**, 16861–16866 (2011).
36. Kostermans, G. B. M., Bobeldijk, M. & De Wolf, W. H. [4] Paracyclophane intercepted. *J. Am. Chem. Soc.* **109**, 2471–2475 (1987).
37. Okuyama, M. & Tsuji, T. Kinetically stabilized [4]paracyclophane—the 1,4-bis(dicyanomethylene)-2-ene derivative: ^{1}H NMR measurement and assessment of its diatropicity. *Angew. Chem. Int. Ed. Engl.* **36**, 1085–1087 (1997).
38. Okuyama, M., Ohkita, M. & Tsuji, T. The first observation of thermal transformation of strained paracyclophane into the Dewar isomer. *Chem. Commun.* 1277–1278 (1997).
39. Kingsbury, C. J. & Senge, M. O. The shape of porphyrins. *Coord. Chem. Rev.* **431**, 213760 (2021).
40. van Tamelen, E. E., Cole, T. M., Greeley, R. & Schumacher, H. Photolysis of triphenylcarbonium, tropylium, and triphenylcyclopropenium ions. *J. Am. Chem. Soc.* **90**, 1372–1374 (1968).
41. Hanson-Heine, M. W. D., Rogers, D. M., Woodward, S. & Hirst, J. D. Dewar benzenoids discovered in carbon nanobelts. *J. Phys. Chem. Lett.* **11**, 3769–3772 (2020).
42. Dračínský, M., Castaño, O., Kotora, M. & Bouř, P. Rearrangement of Dewar benzene derivatives studied by DFT. *J. Org. Chem.* **75**, 576–581 (2010).
43. Janková, Š., Dračínský, M., Císařová, I. & Kotora, M. Synthesis and rearrangement of Dewar benzenes into biaryls: experimental evidence for conrotatory ring opening. *Eur. J. Org. Chem.* 47–51 (2008).
44. Johnson, R. P. & Daoust, K. J. Electrocyclic ring opening modes of Dewar benzenes: ab initio predictions for Möbius benzene and *trans*-Dewar benzene as new C_6H_6 isomers. *J. Am. Chem. Soc.* **118**, 7381–7385 (1996).
45. Becke, A. D. A new mixing of Hartree–Fock and local density functional theories. *J. Chem. Phys.* **98**, 1372–1377 (1993).
46. Schröder, H., Creon, A. & Schwabe, T. Reformulation of the D3(Becke–Johnson) dispersion correction without resorting to higher than C_6 dispersion coefficients. *J. Chem. Theory Comput.* **11**, 3163–3170 (2015).
47. Krishnan, R., Binkley, J. S., Seeger, R. & Pople, J. A. Self-consistent molecular orbital methods. XX. A basis set for correlated wave functions. *J. Chem. Phys.* **72**, 650–654 (1980).
48. Miertuš, S. & Tomasi, J. Approximate evaluations of the electrostatic free energy and internal energy changes in solution processes. *Chem. Phys.* **65**, 239–245 (1982).
49. Fukui, K. The path of chemical reactions—the IRC approach. *Acc. Chem. Res.* **14**, 363–368 (1981).
50. Wheeler, S. E., Houk, K. N., v. R. Schleyer, P. & Allen, W. D. A hierarchy of homodesmotic reactions for thermochemistry. *J. Am. Chem. Soc.* **131**, 2547–2560 (2009).
51. Wannere, C. S. et al. On the stability of large [4*n*]annulenes. *Org. Lett.* **5**, 2983–2986 (2003).
52. Casademont-Reig, I. et al. New electron delocalization tools to describe the aromaticity in porphyrinoids. *Phys. Chem. Chem. Phys.* **20**, 2787–2796 (2018).
53. Battiste, M. A. The cyclohept[*a*]acenaphthylene cation: synthesis of a pentaphenyl derivative. *J. Am. Chem. Soc.* **85**, 2175–2176 (1963).
54. Yamamura, K. & Murata, I. The cyclohept[*a*]acenaphthylenylium ion. *Angew. Chem. Int. Ed. Engl.* **15**, 240–241 (1976).
55. Yamamura, K., Miyake, H., Azumi, K. & Murata, I. Cyclohepta[*l*] phenanthrenylium ions. Intramolecular cyclization of 2-biphenylylcycloheptatrienes. *Chem. Lett.* **18**, 1511–1514 (1989).
56. Sturala, J. et al. Excited-state aromatic interactions in the aggregation-induced emission of molecular rotors. *J. Am. Chem. Soc.* **139**, 17882–17889 (2017).
57. Pascal, R. A., Wang, C. M., Wang, G. C. & Koplitz, L. V. Ideal molecular conformation versus crystal site symmetry. *Cryst. Growth Des.* **12**, 4367–4376 (2012).

58. Amabilino, D. B. & Kellogg, R. M. Spontaneous deracemization. *Isr. J. Chem.* **51**, 1034–1040 (2011).
59. Turley, A. T. et al. Extended conjugation attenuates the quenching of aggregation-induced emitters by photocyclization pathways. *Angew. Chem. Int. Ed.* **61**, e202202193 (2022).
60. Geuenich, D., Hess, K., Köhler, F. & Herges, R. Anisotropy of the induced current density (ACID), a general method to quantify and visualize electronic delocalization. *Chem. Rev.* **105**, 3758–3772 (2005).
61. von Ragué Schleyer, P. et al. Dissected nucleus-independent chemical shift analysis of π-aromaticity and antiaromaticity. *Org. Lett.* **3**, 2465–2468 (2001).
62. Fallah-Bagher-Shaidaei, H., Wannere, C. S., Corminboeuf, C., Puchta, R. & von Ragué Schleyer, P. Which NICS aromaticity index for planar π rings is best? *Org. Lett.* **8**, 863–866 (2006).
63. von Ragué Schleyer, P. et al. Nucleus-independent chemical shifts: a simple and efficient aromaticity probe. *J. Am. Chem. Soc.* **118**, 6317–6318 (1996).
64. Szczepanik, D. W. et al. A uniform approach to the description of multicenter bonding. *Phys. Chem. Chem. Phys.* **16**, 20514–20523 (2014).
65. Szczepanik, D. W. et al. The electron density of delocalized bonds (EDDB) applied for quantifying aromaticity. *Phys. Chem. Chem. Phys.* **19**, 28970–28981 (2017).

Publisher's note Springer Nature remains neutral with regard to jurisdictional claims in published maps and institutional affiliations.

Open Access This article is licensed under a Creative Commons Attribution 4.0 International License, which permits use, sharing, adaptation, distribution and reproduction in any medium or format, as long as you give appropriate credit to the original author(s) and the source, provide a link to the Creative Commons license, and indicate if changes were made. The images or other third party material in this article are included in the article's Creative Commons license, unless indicated otherwise in a credit line to the material. If material is not included in the article's Creative Commons license and your intended use is not permitted by statutory regulation or exceeds the permitted use, you will need to obtain permission directly from the copyright holder. To view a copy of this license, visit http://creativecommons.org/licenses/by/4.0/.

© The Author(s) 2023

Data availability

The crystallographic data for the structures reported in this Article have been deposited at the Cambridge Crystallographic Data Centre, under deposition numbers CCDC 2141786 (**1**·ICl_2), 2141787 (**2**·$SbCl_6$ (120 K)), 2173731 (**2**·$SbCl_6$ (270 K)), 2141788 (**3**·BBr_4), 2141789 (**4**·$SbCl_6$), 2141790 (**8**), 2141791 (**9**), 2141792 (**10**), 2182241 (*anti*-**11**), 2141793 (**S2**), 2141794 (**S3**), 2141795 (**S4**) and 2141796 (**S5**). Copies of the data can be obtained free of charge via https://www.ccdc.cam.ac.uk/structures/. All other data supporting the findings of this study are available within the paper and its Supplementary Information. Source data are provided with this paper.

Acknowledgements

P.K.S. and A.T.T. acknowledge the Engineering and Physical Sciences Research Council (EPSRC) for doctoral training grants. A.M., A.P.M., A.-J.A. and P.R.M. thank Universities UK International and the Department for Business, Energy and Industrial Strategy for a Rutherford Strategic Partnership Grant. A.N.B. and P.R.M. acknowledge the support of a Leverhulme Trust Research Project Grant (RPG-2020-218). P.R.M. and A.M. thank the Faraday Institution for funding (FIRG046). A.-J.A. thanks the Royal Society and Global Challenges Research Fund for the award of a Dorothy Hodgkin Fellowship (DHF\R1\180106) and an Enhancement Award (RGF\EA\181065). The funders had no role in study design, data collection and analysis, decision to publish or preparation of the manuscript. We thank D. Szczepanik for advice about EDDB calculations.

Author contributions

P.K.S., A.M. and A.T.T. carried out the syntheses and compound characterization. P.K.S. and P.R.M performed the calculations. A.N.B. and P.R.M. carried out dynamic NMR analysis. D.S.Y. solved the X-ray crystal structures. P.K.S. and A.M. prepared the Supplementary Information. P.K.S. and P.R.M. wrote the manuscript. All authors analysed the data and commented on manuscript drafts. P.R.M. conceived and directed the research.

Competing interests

The authors declare no competing interests.

Additional information

Supplementary information The online version contains supplementary material available at https://doi.org/10.1038/s41557-023-01149-6.

Correspondence and requests for materials should be addressed to Paul R. McGonigal.

Peer review information *Nature Chemistry* thanks Kjell Jorner and the other, anonymous, reviewer(s) for their contribution to the peer review of this work.

Reprints and permissions information is available at www.nature.com/reprints.

How to cite: *Angew. Chem. Int. Ed.* **2022,** *61,* e202202193
International Edition: doi.org/10.1002/anie.202202193
German Edition: doi.org/10.1002/ange.202202193

Aggregation-Induced Emission

Extended Conjugation Attenuates the Quenching of Aggregation-Induced Emitters by Photocyclization Pathways

*Andrew T. Turley, Promeet K. Saha, Andrew Danos, Aisha N. Bismillah, Andrew P. Monkman, Dmitry S. Yufit, Basile F. E. Curchod, Marc K. Etherington, and Paul R. McGonigal**

Abstract: Herein, we expose how the antagonistic relationship between solid-state luminescence and photocyclization of oligoaryl alkene chromophores is modulated by the conjugation length of their alkenyl backbones. Heptaaryl cycloheptatriene molecular rotors exhibit aggregation-induced emission characteristics. We show that their emission is turned off upon breaking the conjugation of the cycloheptatriene by epoxide formation. While this modification is deleterious to photoluminescence, it enables formation of extended polycyclic frameworks by Mallory reactions. We exploit this dichotomy (i) to manipulate emission properties in a controlled manner and (ii) as a synthetic tool to link together pairs of phenyl rings in a specific sequence. This method to alter the tendency of oligoaryl alkenes to undergo photocyclization can inform the design of solid-state emitters that avoid this quenching mechanism, while also allowing selective cyclization in syntheses of polycyclic aromatic hydrocarbons.

Introduction

The quest to maximize photoluminescence efficiencies of organic luminogens has spurred progress from classical planar polycyclic aromatics, which are susceptible to aggregation-caused quenching (ACQ),[1–3] toward non-planar molecular rotor-type frameworks that exhibit aggregation-induced emission (AIE).[4–7] The enhanced luminescence of AIE-active materials in aggregated states is thought to arise from their restricted intramolecular motion (RIM),[8,9] which minimizes the nonradiative decay of their excited states, thereby maximizing photoluminescent emission. However, this mechanistic description of AIE has been a topic of ongoing debate[9–13] that has progressed in parallel to the development of new AIE luminogens and their applications. Various possible quenching pathways that are "turned off" by RIM[14,15] have been identified, such as through-space aromatic dimerization,[16–18] *E*/*Z* isomerization[19] and, more generally, restricted access to a conical intersection (RACI).[20,21]

Oligoaryl alkenes, such as tetraphenylethylene (TPE), are a recurring structural motif in the pursuit of efficient emitters. These materials are regarded as the simplest, archetypal AIE-active structures, possessing a molecular rotor-type framework with rotatable phenyl rings.[22,23] An added complication for these types of emissive materials is that their 1,2-diphenyl ethylene (DPE) units are also known to undergo the Mallory reaction[24,25] (a photochemical cyclization–elimination reaction that has been exploited synthetically to access polycyclic aromatic hydrocarbon structures).[26,27] Indeed, the formation of Mallory reaction intermediates has been invoked as one of the quenching pathways for oligoaryl alkene AIE luminogens and has previously been studied through ultra-fast spectroscopy,[28] suggesting that photocyclization-induced quenching (PIQ) is a dominant nonradiative loss pathway in the RACI mechanism.

Herein, we report synthetic modification of our previously reported[16] AIE-active molecular rotor compound *sym*-heptaphenylcycloheptatriene (**Ph_7C_7H**) to study the effects of structural changes on its nonradiative energy loss pathways. Our strategy to modify the structure of **Ph_7C_7H** alters the extent of electronic conjugation present in the oligoaryl alkene rotor while limiting geometric changes to the system, allowing us to effectively decouple electronic and geometric effects. We demonstrate that by interrupting the conjugation of **Ph_7C_7H**, its characteristic dual-state emission is quenched. Instead of luminescing, it undergoes facile photocyclization. Our investigations also lead to new understanding of the Mallory reaction in highly conjugated, oligoaryl alkene AIE luminogens. DPE units with extended π-electron conjugation exhibit attenuated Mallory-type re-

[*] Dr. A. T. Turley, P. K. Saha, Dr. A. N. Bismillah, Dr. D. S. Yufit, Dr. B. F. E. Curchod, Dr. P. R. McGonigal
Department of Chemistry, Durham University
Lower Mountjoy, Stockton Road, Durham, DH1 3LE (UK)
E-mail: paul.mcgonigal@durham.ac.uk
Dr. A. Danos, Prof. A. P. Monkman, Dr. M. K. Etherington
Department of Physics, Durham University
Lower Mountjoy, Stockton Road, Durham, DH1 3LE (UK)
Dr. M. K. Etherington
Department of Mathematics, Physics and Electrical Engineering, Northumbria University
Ellison Place, Newcastle upon Tyne, NE1 8ST (UK)

© 2022 The Authors. Angewandte Chemie International Edition published by Wiley-VCH GmbH. This is an open access article under the terms of the Creative Commons Attribution License, which permits use, distribution and reproduction in any medium, provided the original work is properly cited.

© 2022 The Authors. Angewandte Chemie International Edition published by Wiley-VCH GmbH

activity, which correlates with suppressed PIQ and enhanced luminescence that is desirable for designing more efficient AIE materials. We exploit the facile photocyclization of "isolated" DPE units in a stepwise synthetic process that combines Mallory conditions with intermediate reactions to curtail or extend π-conjugation. In doing so, we access fused polyaromatics that were previously inaccessible by direct Scholl oxidation or Mallory reactions alone.

Results and Discussion

Synthesis, Structure and Conformation

We initially synthesized modified derivatives of **Ph_7C_7H** (Figure 1) to further investigate its unusual dual-state emission properties.[16] See Scheme S1 of the Supporting Information for full synthetic details. Two types of structural modifications were introduced: (i) Formal ring fusion of two peripheral phenyl groups to form a phenanthrene unit or (ii) epoxidation of the central seven-membered ring. Together, **Ph_7C_7H** and its symmetrical (***sym*-phenPh_5C_7H**) and asymmetrical (***asym*-phenPh_5C_7H**) 9,10-phenanthryl analogs (Figure 1) make up a series of three triene rotors that differ by the introduction of a single C–C bond between two of the peripheral rings.

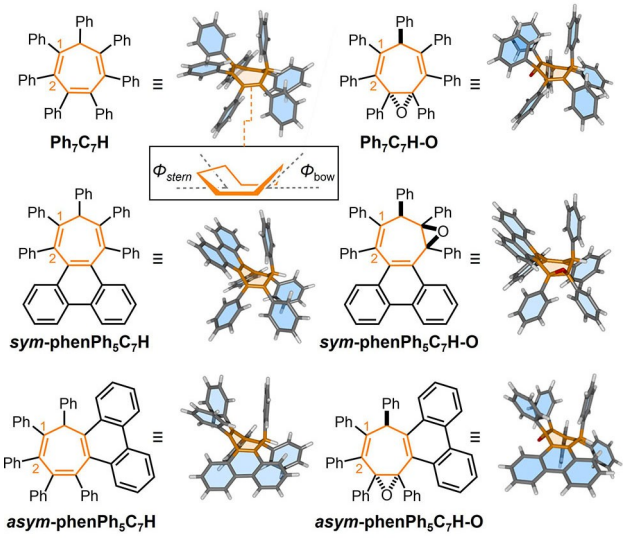

Figure 1. Structural formulas and X-ray crystal structures of **Ph_7C_7H** derivatives. Inset: the boat conformation of a seven-membered ring.

Subsequent epoxidation of each triene rotor expands the series to six compounds, giving rise (Figure 1) to **Ph_7C_7H-O**, ***sym*-phenPh_5C_7H-O**, and ***asym*-phenPh_5C_7H-O**. Epoxidation occurs both stereoselectively and regioselectively in the presence of an excess of *meta*-chloroperbenzoic acid (*m*CPBA). In each case, a singly epoxidized product was isolated. While epoxidation occurs at one end of the ***sym*-phenPh_5C_7H** triene to give a diene system, the reaction occurs at the central double bonds of **Ph_7C_7H** and ***asym*-phenPh_5C_7H**, splitting the trienes to give separated double bonds.

We gained insight into the conformations adopted by the rotor molecules by analyzing their X-ray crystal structures (Figure 1).[29] In the solid state, the cycloheptatriene rings exhibit similar, shallow boat-like conformations across the series of six compounds. In each case, the phenyl group at the sp^3-C position occupies the bow of the boat conformation with a pseudo-axial orientation. We have previously reported that this orientation influences the emissive excited state of **Ph_7C_7H** by formation of through-space interactions between the phenyl rings at the bow and stern.[16]

In general, the proximity of the peripheral phenyl groups to one another disfavors conformations in which the rings are coplanar with the central double bonds, giving rise instead to perpendicular propeller-like geometries. Nonetheless, enforcing coplanarity of two peripheral rings as part of a biphenylene substituent (forming a phenanthrene ring system) has little impact on the geometry (Table 1) of the central cycloheptatriene ring. For example, the interplane angles (Figure 1, inset) $\Phi_{bow} = 54.9°$ and $\Phi_{stern} = 35.3°$ that characterize the boat conformation of **Ph_7C_7H** vary (Table 1) by less than 10° for each of its five derivatives in Figure 1.

Comparison of bond length alternation (BLA) parameters[30] gives quantifiable insight into the influence of peripheral ring fusion and epoxidation on the conjugation of the central cycloheptatriene ring (Table 1). Higher BLA is indicative of reduced π-electron delocalization of a conjugated system. Relative to **Ph_7C_7H**, the BLA of ***sym*-phenPh_5C_7H** remains essentially unchanged, suggesting that the symmetrically placed phenanthrene ring has little impact

Table 1: Geometric parameters of the molecular rotors.

Rotor	Φ_{bow}[a] [°]	Φ_{stern}[a] [°]	BLA[b] [pm]	d_{1-2}[c] [pm]	$\Delta G^{\ddagger}$[d] (kJ mol^{-1})
Ph_7C_7H	54.9	35.3	12.2	135.1(3)	48.2
***sym*-phenPh_5C_7H**	58.4	41.2	12.1	135.9(2)	44.5
***asym*-phenPh_5C_7H**	50.9	43.9	13.5	135.5(5)	–
Ph_7C_7H-O	49.0	33.1	–	134.1(2)	40.5
***sym*-phenPh_5C_7H-O**	53.2	42.2	14.8	135.4(2)	–
***asym*-phenPh_5C_7H-O**	46.1	35.2	–	133.8(2)	–

[a] Torsion angles and bond lengths were determined from X-ray crystallographic data. [b] Measured by subtracting the average length of double bonds from the average length of single bonds that are part of the diene or triene system.[30] [c] Estimated standard deviations in parentheses. [d] Measured by ^{1}H VT NMR spectroscopy for rotation of the most hindered phenyl ring (Figures S25–S32).

© 2022 The Authors. Angewandte Chemie International Edition published by Wiley-VCH GmbH

15213773, 2022, 24, Downloaded from https://onlinelibrary.wiley.com/doi/10.1002/anie.202202193 by University Library, Wiley Online Library on [28/09/2023]. See the Terms and Conditions (https://onlinelibrary.wiley.com/terms-and-conditions) on Wiley Online Library for rules of use; OA articles are governed by the applicable Creative Commons License

on conjugation within the triene system. However, shortening this π-system to a diene by epoxidation, i.e., ***sym*-phenPh$_5$C$_7$H-O**, causes a significant (≈20 %) increase in BLA, which demonstrates its reduced π-electron delocalization. The asymmetrically substituted phenanthrene isomer, ***asym*-phenPh$_5$C$_7$H**, is an intermediate case, exhibiting a slight increase (≈10 %) in BLA relative to **Ph$_7$C$_7$H**. On the other hand, epoxidation of either ***asym*-phenPh$_5$C$_7$H** or **Ph$_7$C$_7$H** cleaves the triene system in two, producing at least one "isolated" double bond in each case, e.g., the C–C double bond between positions 1 and 2 of the seven-membered ring (Figure 1). For both of these epoxides, the double bond length d_{1-2} (Table 1) has decreased by ≥1 pm relative to the triene precursor, which is consistent with its reduced conjugation.

The geometric similarities observed between the cycloheptatrienes in the solid state are reflected in the solution-state dynamics for the 180° rotation of their most hindered phenyl rings. Variable-temperature (VT) nuclear magnetic resonance (NMR) spectroscopic analysis (Figures S25–S32) reveals Gibbs energy barriers ($\Delta G^{\ddagger}$) to phenyl ring rotation at 298 K of 44.5 kJ mol^{-1} and 40.5 kJ mol^{-1} for ***sym*-phenPh$_5$C$_7$H** and **Ph$_7$C$_7$H-O**, respectively (Table 1). These values are similar to the $\Delta G^{\ddagger}$ measured for phenyl ring rotation in **Ph$_7$C$_7$H** of 48.2 kJ mol^{-1}.[16]

In summary, neither epoxidation nor ring fusion causes large deviations in the overall geometries and conformational freedom of the seven-membered rings or rotatable phenyl groups. However, epoxidation does cause significant changes to the lengths of the conjugated systems, modifying the electronic properties of the individual diaryl alkene units.

We found that exposing a 1.5 mM toluene solution of ***sym*-phenPh$_5$C$_7$H-O** to UV irradiation causes a color change from colorless to yellow (Scheme 1a), which is reversed in ambient light over time. Similar reversible yellowing of TPE films has previously been attributed to formation of a photocyclized species.[28] No such color change (or reactivity, vide infra) was observed for ***sym*-phenPh$_5$C$_7$H**, which suggests that the broken conjugation of ***sym*-phenPh$_5$C$_7$H-O** significantly alters its photophysical behavior. The proposed intermediate species **IM** formed under irradiation was subsequently oxidized (vide infra) to ***asym*-phen$_2$Ph$_3$C$_7$H-O** under Mallory reaction conditions, confirming the photocyclization reactivity. Similarly, a Mallory reaction of **Ph$_7$C$_7$H-O** gives rise to ***sym*-phen$_2$Ph$_3$C$_7$H-O**, which was confirmed by two-dimensional NMR spectroscopy and X-ray crystallography (Scheme 1b). To elucidate the origins of this enhanced photocyclization reactivity in the compounds with truncated conjugation, we conducted deeper photophysical analyses of the series of six rotors shown in Figure 1.

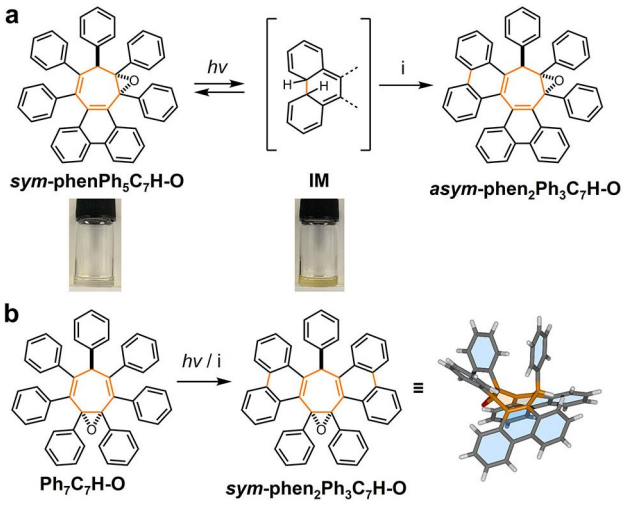

Scheme 1. Photocyclizations of rotors containing "isolated" DPE units. Reagents and conditions: i) I_2, propylene oxide, THF, *hv* (4.88 eV), 3 h. An X-ray structure of ***sym*-phen$_2$Ph$_3$C$_7$H-O** shows the presence of two new phenanthrene units.

Luminescence of the Triene Rotors

We first confirmed that the triene molecular rotors are AIE-active by preparing 1 % w/w dispersions in ZEONEX—an optically clear cyclic olefin polymer matrix. Photoluminescence quantum yield (Φ_{film}) measurements carried out on the ZEONEX films show that all three fully conjugated rotors emit in the solid state with similar efficiencies (Table 2) of 1.7–6.7 %. We gained further insights into the influence of biphenylene substitution on the optical properties relative to **Ph$_7$C$_7$H** by acquiring (Figure 2) steady-state emission spectra[31] using dilute (2 μM) 2-methyl tetrahydrofuran (2-MeTHF) solutions of each rotor. The spectra were recorded at a series of temperatures (290 K to 90 K) to alter rates of nonradiative decay (k_{nr}) through RIM and RACI in a controlled manner.

We measured (Table 2) the ratios between emission intensities at 290 K and 90 K, ΔI_{290-90}. The emission intensities, I, of the three triene rotors increase at lower temperatures as k_{nr} is decreased. Both phenanthrenyl derivatives have much smaller ΔI_{290-90} than **Ph$_7$C$_7$H**. This observation is consistent with them having fewer intramolecular vibrational degrees of freedom, which renders them less susceptible to increased nonradiative decay at higher temperatures.

In common with **Ph$_7$C$_7$H** (Figure 2a), ***sym*-phenPh$_5$C$_7$H** shows (Figure 2b) a gradual hypsochromic shift in the energy of the emission maximum (E_{max}) from 2.84 eV to 3.15 eV as the temperature decreases (Table 2). By analogy to our previous investigation,[16] we attribute this shift to two-state emission that emerges from accessing a relaxed dimer state, whereby a face-to-face interaction develops between the phenanthrene moiety and the phenyl group at the bow of the seven-membered ring after photoexcitation. The compound-specific relationships between the E_{max} and temperature are plotted in Figure S52.

There is no indication of this dual emission in the analogous spectra (Figure 2c) of ***asym*-PhenPh$_5$C$_7$H**. However, we do observe (Figure 2d) a bathochromic shift from 3.33 eV to 2.70 eV at 130 K using a higher solution concentration of 200 μM, suggesting the formation of

© 2022 The Authors. Angewandte Chemie International Edition published by Wiley-VCH GmbH

15213773, 2022, 24, Downloaded from https://onlinelibrary.wiley.com/doi/10.1002/anie.202202193 by University Library, Wiley Online Library on [28/09/2023]. See the Terms and Conditions (https://onlinelibrary.wiley.com/terms-and-conditions) on Wiley Online Library for rules of use; OA articles are governed by the applicable Creative Commons License

Table 2: Photophysical properties of the molecular rotors and phenanthrene.

Rotor	E_{ex}[a] [eV]	E_{max} [eV] 160 K[b]	90 K[b]	Film[e]	τ [ns][b,c] 290 K	ΔI_{290-90}[b,d] Sol[b]	Film[e]	Φ_{film}[e,f] [%]
Ph_7C_7H	3.95	2.76	3.21	3.02	6.5	52.1	9.91	6.7
***sym*-$phenPh_5C_7H$**	4.13	2.84	3.15	3.01	20.4	3.75	2.13	1.7
***asym*-$phenPh_5C_7H$**	3.94	3.33	3.33	3.07	8.2	6.24	2.63	4.0
Ph_7C_7H-O[e]	4.35	3.30	3.30	3.47	12.6[g]	4.82	1.19	≤0.1
***sym*-$phenPh_5C_7H$-O**[e]	3.94	3.43	3.43	3.34	11.9[g]	5.76	0.69	≤0.1
***asym*-$phenPh_5C_7H$-O**[e]	3.94	3.30	3.30	3.47	9.0[g]	5.47	2.62	3.3
***sym*-$phen_2Ph_3C_7H$-O**	4.00	3.72	3.76	3.43	–	1.67	1.50	6.4
***asym*-$phen_2Ph_3C_7H$-O**	4.00	3.43	3.43	3.43	–	4.50	2.65	9.8
***sym*-$phen_3PhC_7H$**	3.95	3.40	3.40	3.22	8.4	3.97	–	4.5
phenanthrene	4.13	3.56	3.56	3.06	15.0	5.13	0.56	–

[a] E_{ex} were chosen to match peaks in absorption spectra (Figure S48). [b] 2 μM solution in 2-MeTHF. [c] See Table S4 for full lifetime data. [d] Difference in intensity between the emission peaks at 290 K and 90 K. [e] 1% w/w film in ZEONEX. [f] Measured by integrating sphere under ambient conditions. [g] The τ values reported for the epoxide series are the apparent lifetimes of the weak emission observed upon excitation of a sample of the pure epoxide starting material, some of which may photocyclize during the measurement.

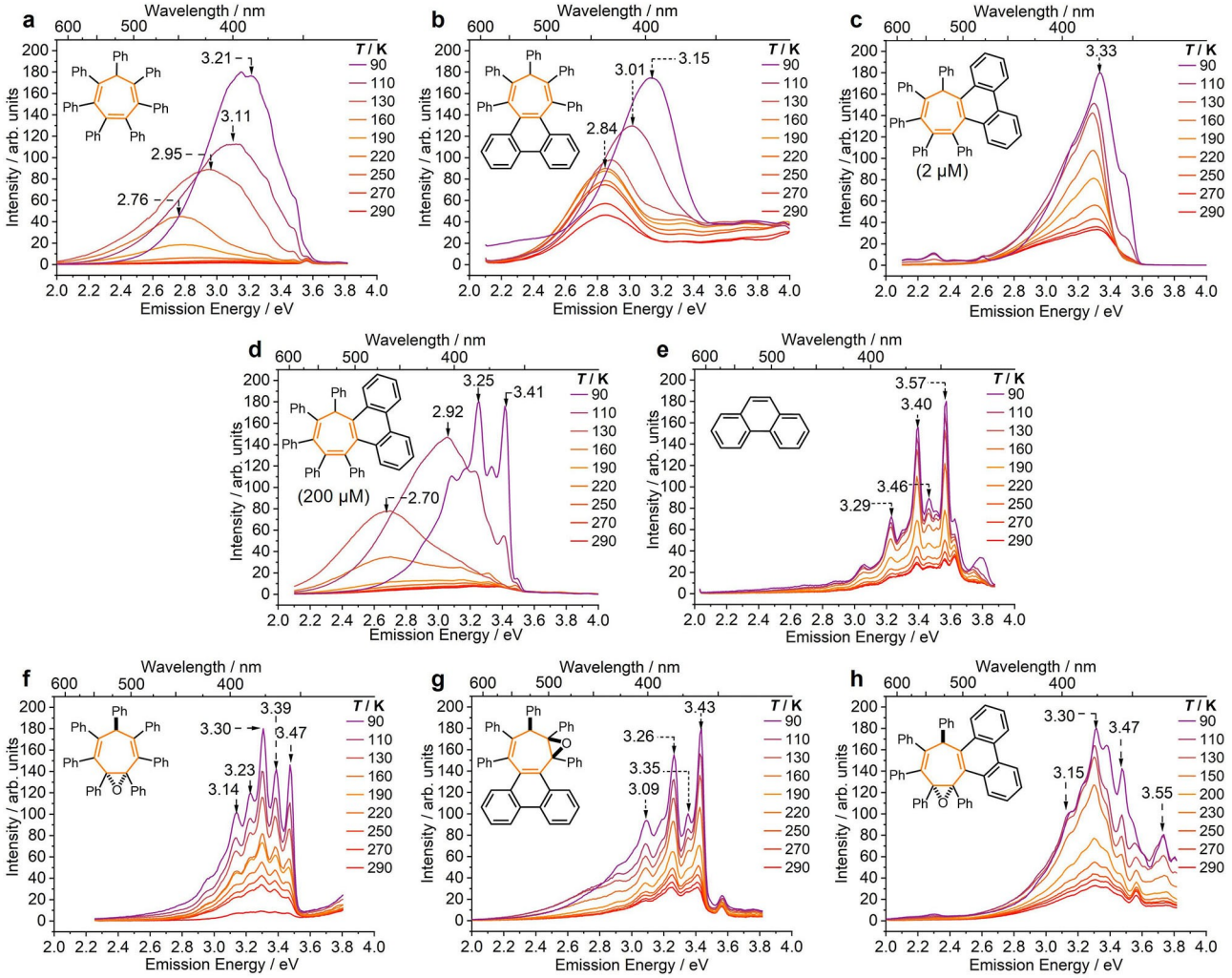

Figure 2. VT steady-state photoluminescence spectra of 2-MeTHF solutions of a) **Ph_7C_7H**, excitation energy E_{ex} = 3.94 eV, concentration c = 2 μM, b) ***sym*-$phenPh_5C_7H$**, E_{ex} = 4.13 eV, c = 2 μM, c) ***asym*-$phenPh_5C_7H$**, E_{ex} = 3.94 eV, c = 2 μM, d) ***asym*-$phenPh_5C_7H$**, E_{ex} = 3.94 eV, c = 200 μM, e) phenanthrene, E_{ex} = 4.13 eV, c = 2 μM, f) **Ph_7C_7H-O**, E_{ex} = 4.35 eV, c = 2 μM, g) ***sym*-$phenPh_5C_7H$-O**, E_{ex} = 3.94 eV, c = 2 μM, and h) ***asym*-$phenPh_5C_7H$-O**, E_{ex} = 3.95 eV, c = 2 μM.

© 2022 The Authors. Angewandte Chemie International Edition published by Wiley-VCH GmbH

15213773, 2022, 24, Downloaded from https://onlinelibrary.wiley.com/doi/10.1002/anie.202202193 by University Library, Wiley Online Library on [28/09/2023]. See the Terms and Conditions (https://onlinelibrary.wiley.com/terms-and-conditions) on Wiley Online Library for rules of use; OA articles are governed by the applicable Creative Commons License

intermolecular dimers rather than the intramolecular aromatic interactions. This behavior mirrors the dimerization of molecular phenanthrene.[32] Presumably, the phenanthrene moiety of ***asym*-phenPh$_5$C$_7$H** is sufficiently exposed and unhindered that it is available to undergo intermolecular dimerization in the ground state driven by solvophobic forces. Indeed, the vibronic structure of the emission from ***asym*-PhenPh$_5$C$_7$H** at 200 μM matches closely with the emission from phenanthrene (Figure 2e). We note that no concentration-dependent emission changes were observed in the spectra of other rotors in the series (Figure S54).

Overall, the photophysical characteristics of both ***sym***- and ***asym*-phenPh$_5$C$_7$H** broadly resemble **Ph$_7$C$_7$H**. All three are AIE-active rotors that give photoluminescence quantum yields of 1.7–6.7 % in the solid state (i.e., dispersed in ZEONEX films). The relative position of the biphenylene unit of the molecular rotor tunes the propensity for face-to-face interactions of their aromatic rings, which can occur intramolecularly in the excited state or intermolecularly in the ground state. Yet, there is no evidence in their optical spectra to suggest that these fully conjugated compounds are prone to photocyclization.

Optical Properties of the Epoxide Rotors

Interrupting the conjugation of the triene systems by epoxidation causes significant changes in their emission properties. The broad fluorescence peaks observed for the trienes are replaced (Figures 2f–h) by structured emission at high energies (3.09–3.55 eV). The emission intensities are very weak in both the solution and solid states regardless of temperature (Figure S55), giving low Φ_{film} values (Table 2). ZEONEX films of **Ph$_7$C$_7$H-O** and ***sym*-phenPh$_5$C$_7$H-O** both give quantum yields below the threshold for reliable measurement ($\leq$0.1 %).[33] Therefore, the reduced conjugation of the epoxides is associated with substantially diminished luminescence.

We ascribe these observations to PIQ occurring in both the solution state and amorphous ZEONEX films. Rather than undergoing photoluminescence, the excited rotors are prone to form a C–C bond to give **IM** structures (Scheme 1a), which enables the aforementioned Mallory reactivity. This enhanced PIQ pathway is responsible for the absence of the broad emission peak observed for the trienes.

A further experimental indication of this photocyclization occurring in solution came when sequentially repeated steady-state photoluminescence measurements of a 2-MeTHF solution of **Ph$_7$C$_7$H-O** resulted in increased emission intensity. We compared (Figure 3a) the emission spectrum before and after irradiating a sample with 4.0 eV light for 5 min. Irradiation causes a fourfold increase in emission intensity, consistent with a photochemical reaction taking place to build up a higher concentration of a more emissive compound. An experiment monitoring the emission intensity at 3.30 eV over time as the sample is irradiated (Figure 3b) shows the buildup of the new species during continued irradiation. The emission intensity decreases

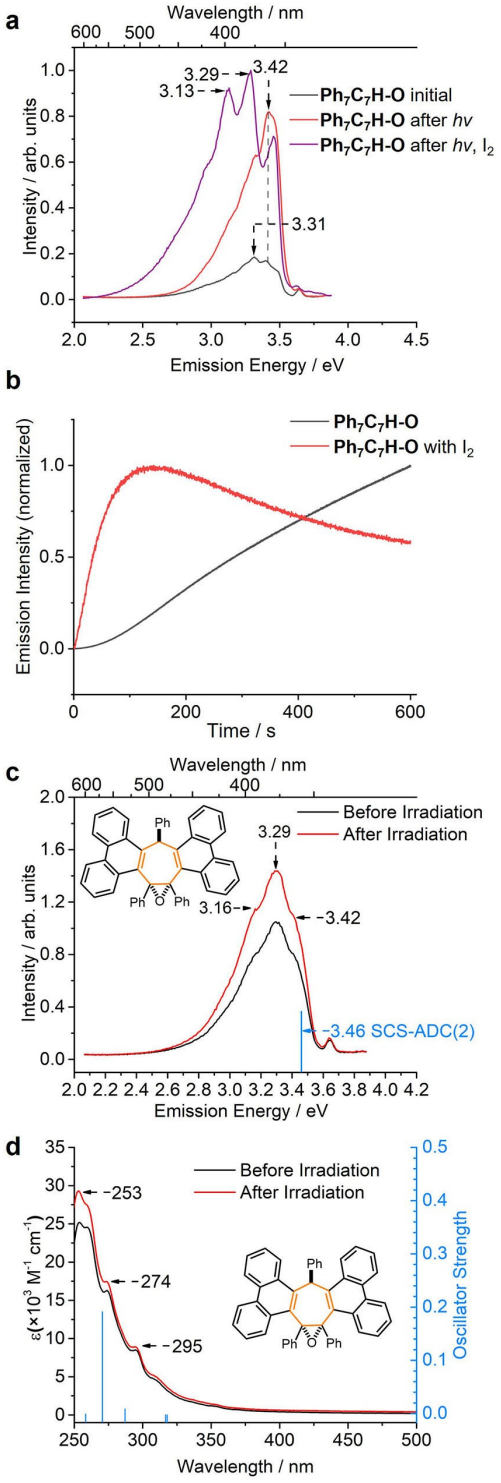

Figure 3. Steady-state photoluminescence spectra of 2-MeTHF solutions of **Ph$_7$C$_7$H-O**, (E_{ex} = 4.35 eV, c = 2 μM) a) before and after irradiation with 4.0 eV light for 10 min with and without I_2; b) the change in the emission intensity at 3.30 eV over time, with and without I_2; c) emission (2-MeTHF, c = 2 μM) and d) absorption (MeCN, c = 20 μM) spectra of ***sym*-phen$_2$Ph$_3$C$_7$H-O** before and after irradiation with 4.0 eV light for 10 min. Theoretical emission (vertical transition from the S_1 geometry) and absorption (five lowest vertical transitions from the S_0 geometry) transitions shown in panels c and d were obtained at the SCS-ADC(2)/TZVP//SCS-ADC(2)/SVP and SCS-ADC-(2)/TZVP//SCS-MP2/SVP levels of theory, respectively.

© 2022 The Authors. Angewandte Chemie International Edition published by Wiley-VCH GmbH

15213773, 2022, 24, Downloaded from https://onlinelibrary.wiley.com/doi/10.1002/anie.202202193 by University Library, Wiley Online Library on [28/09/2023]. See the Terms and Conditions (https://onlinelibrary.wiley.com/terms-and-conditions) on Wiley Online Library for rules of use; OA articles are governed by the applicable Creative Commons License

when the irradiation is stopped, consistent with the reversible color change described above (Scheme 1).

Performing a similar series of experiments for the full series of six rotors (Figure S58), we found that the three epoxide rotors exhibit the same behavior, whereas the trienes require prolonged irradiation times of >1 h before changes in their emission profiles are observed.

These observations are all consistent with PIQ. To confidently rule out the possibility of the structured emission stemming from solvatochromic, or intermolecular interactions, we also acquired absorption (Figure S48) and emission spectra (Figure S56) using (i) solvents of different polarities and (ii) amorphous film samples prepared as 1% w/w dispersions in ZEONEX (Figure S55). We observed that, in general, the spectral features are independent of solvent polarity and temperature.

In light of the proposed photocyclization pathway (Scheme 1), we tested whether atmospheric O_2 was acting as an oxidant to complete the irreversible formation of ***sym*-phen$_2$Ph$_3$C$_7$H-O** upon irradiating a 2-MeTHF solution of **Ph$_7$C$_7$H-O**. A solution sample of **Ph$_7$C$_7$H-O** was deaerated by performing freeze-pump-thaw cycles and backfilling with N_2, before irradiating with UV light. The same emission profile was observed under these conditions or using an aerated sample (Figure S56). It is, therefore, unlikely that significant oxidation of the planarized **IM** compounds is occurring under these conditions. Instead, the weak, structured emission spectra recorded in Figures 2f–h should be attributed to emission from the **IM** structures themselves. Trace amounts of **IM** compounds formed during the measurement may become photoexcited and subsequently luminesce.

Epoxide Rotors Undergo Facile Mallory Reaction

We further probed the susceptibility of the epoxides to undergo photocyclization by purposefully applying Mallory reaction conditions (Scheme 1). An excess of the oxidants I_2 and propylene oxide were added to a 15 mM solution of **Ph$_7$C$_7$H-O** in tetrahydrofuran (THF) to trap transient **IM** compounds through the irreversible formation of a new phenanthrene ring system (Scheme 1b). The double photocyclization product, ***sym*-phen$_2$Ph$_3$C$_7$H-O**, was isolated in quantitative yield after 3 h of irradiation with 4.88 eV light. Two new phenanthrene moieties form from the two "isolated" (i.e., non-conjugated) DPE units of **Ph$_7$C$_7$H-O**. Adding further equivalents of I_2 and extending the irradiation time does not promote further photocyclization of the remaining phenyl groups.

The same reaction conditions were also applied to ***sym*-phenPh$_5$C$_7$H-O**, which has a diene system in its central seven-membered ring. Photooxidation of its sole DPE group produced (Scheme 1a) ***asym*-phen$_2$Ph$_3$C$_7$H-O** in 98% yield.

These Mallory reaction conditions were also applied successfully to the third epoxide rotor, ***asym*-phenPh$_5$C$_7$H-O**, which can be considered as a monocyclized intermediate species that forms (Scheme 2a) during the irreversible transformation of **Ph$_7$C$_7$H-O** to ***sym*-phen$_2$Ph$_3$C$_7$H-O**. As expected, the photocyclization also gave ***sym*-phen$_2$Ph$_3$C$_7$H-O**, doing so in quantitative yield.

Conversely, none of the triene rotors shown in Figure 1 underwent photooxidation under these reaction conditions. Even upon irradiating for extended periods, ^{1}H NMR spectroscopic analyses of the crude reaction mixtures indicated that no observable reactions occur.

Therefore, these synthetic results are in agreement with our spectroscopic experiments. Photocyclization of isolated DPE units occurs rapidly. The diene ***sym*-phenPh$_5$C$_7$H-O**

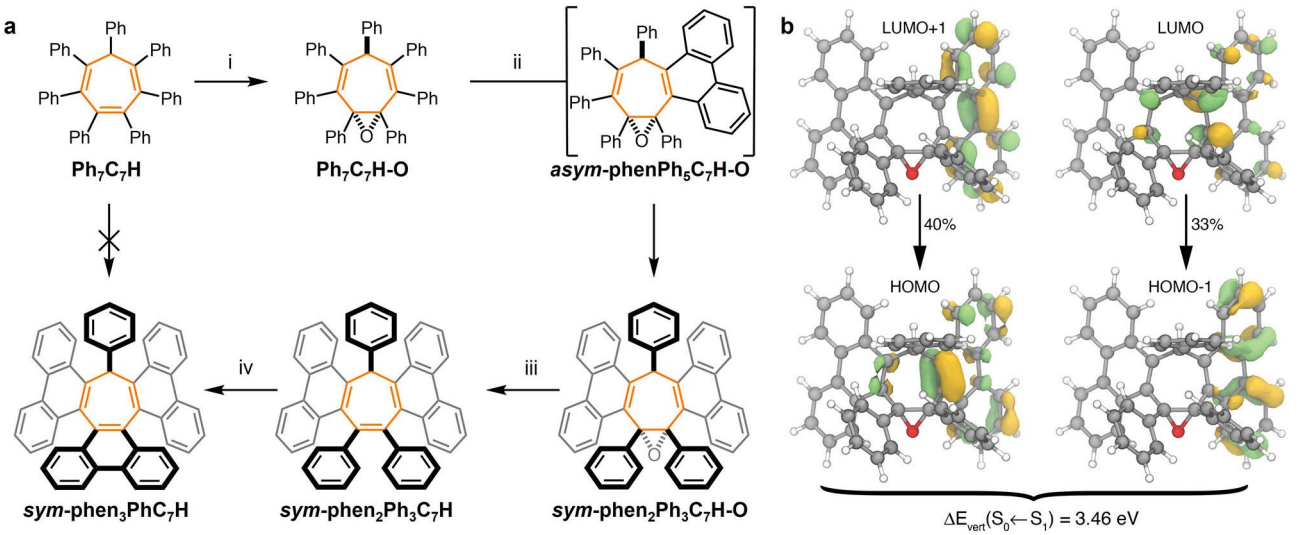

Scheme 2. a) Sequential Mallory reactions by isolating and revealing DPE groups. Reagents and conditions: i) *m*CPBA, $CHCl_3$, 0 °C to 55 °C, 24 h, 70%; ii) I_2, THF, propylene oxide, *hν* (4.88 eV), 3 h, >99%; iii) $LiAlH_4$, THF, 70 °C, 72 h, 47%; iv) I_2, THF, propylene oxide, *hν* (4.88 eV), 15 min, 81%. b) Calculated MOs of ***sym*-phen$_2$Ph$_3$C$_7$H-O**, SCS-ADC(2)/TZVP.

© 2022 The Authors. Angewandte Chemie International Edition published by Wiley-VCH GmbH

15213773, 2022, 24, Downloaded from https://onlinelibrary.wiley.com/doi/10.1002/anie.202202193 by University Library, Wiley Online Library on [28/09/2023]. See the Terms and Conditions (https://onlinelibrary.wiley.com/terms-and-conditions) on Wiley Online Library for rules of use; OA articles are governed by the applicable Creative Commons License

shows similar reactivity and photophysical properties to the isolated DPE compounds. But the extended conjugation of the three triene rotors improves their resistance to photocyclization, both under Mallory reaction conditions and in the context of a quenching pathway for photoluminescence.

Exhaustive Photocyclization

Once formed, the doubly photocyclized product ***sym*-phen$_2$Ph$_3$C$_7$H-O** displays (Figure 3a) an emission spectrum that is distinct from the spectrum of its **IM** precursors. The time-dependent increase in emission intensity at 3.30 eV observed previously during irradiation of **Ph$_7$C$_7$H-O** (Figure 3b) is also changed as the **IM** compounds are consumed by onward reaction with I_2 to form ***sym*-phen$_2$Ph$_3$C$_7$H-O**.

We tested the emission (Figure 3c) and absorption (Figure 3d) spectra of solutions of isolated ***sym*-phen$_2$Ph$_3$C$_7$H-O** before and after irradiation at 4.88 eV to probe whether further photocyclization can occur. Only small differences in intensity were observed, which likely arise because of minor changes in temperature and concentration following irradiation. In keeping with the outcome of the Mallory reactions, it does not appear that the remaining phenyl groups are prone to undergo further photocyclization. The first five vertical transitions of ***sym*-phen$_2$Ph$_3$C$_7$H-O** calculated with SCS-ADC(2) (see the Supporting Information for computational details) are in good agreement with the experimental absorption spectrum (Figure 3d). These transitions, which are within the range of the photoexcitation energy used experimentally, involve orbitals on the phenanthrenes or the central seven-membered ring, validating the observation that no further cyclization from the phenyl rings is to be expected. The vertical emission energy from the optimized S_1 geometry obtained at the SCS-ADC(2)/TZVP//SCS-ADC(2)/SVP is calculated at 3.46 eV (Figure 3c), closely matching the high-energy tail of the experimental spectrum. The orbitals involved in the emission (Scheme 2b) are located on the phenanthrene and central rings and do not extend to the remaining phenyl groups. The shape of the emission band of ***sym*-phen$_2$Ph$_3$C$_7$H-O** was further analyzed by including non-Condon effects using the nuclear ensemble approach combined with linear-response time-dependent density functional theory (Figure S63).

Control of Conjugation Length Enables Synthesis

Based on the differing reactivities of the trienes and the epoxides, we hypothesized that by synthetically manipulating the conjugation lengths in our oligoaryl alkene systems we could enable otherwise inaccessible reactivity. Accordingly, we targeted (Scheme 2a) the *meso* double helicene ***sym*-phen$_3$PhC$_7$H**. Attempts to prepare this compound directly from **Ph$_7$C$_7$H** using a range of classical intramolecular cyclodehydrogenation reaction conditions[34] have been unsuccessful.[35]

After breaking the triene conjugation of **Ph$_7$C$_7$H** by epoxidation, the Mallory reaction of **Ph$_7$C$_7$H-O** to give ***sym*-phen$_2$Ph$_3$C$_7$H-O** proceeds smoothly on gram scale. The reaction was performed using I_2 in THF solution while irradiating with 4.88 eV UV light. Having confirmed that no further photocyclization occurs in ***sym*-phen$_2$Ph$_3$C$_7$H-O**, the epoxide unit was then reverted to an olefin to reestablish a DPE unit in the structure. We treated ***sym*-phen$_2$Ph$_3$C$_7$H-O** with a 1 M solution of $LiAlH_4$ in THF at 70 °C, which yielded ***sym*-phen$_2$Ph$_3$C$_7$H**.

Pleasingly, upon reformation of this DPE unit, further cyclization to give ***sym*-phen$_3$PhC$_7$H** occurs readily—a $CDCl_3$ solution sample of ***sym*-phen$_2$Ph$_3$C$_7$H** cyclized when left under ambient atmosphere and light for 7 d. The process is accelerated by applying our standard Mallory reaction conditions, which gives rise to the double helicene product in 81 % yield after 15 min. By analogy to the increased BLA of ***asym*-PhenPh$_5$C$_7$H** (Table 1), we attribute the ease of this final photocyclization to reduced electron delocalization in the π-system of the central seven-membered ring, which is caused by the two phenanthrene units at either end of the conjugated system.[36]

Overall, the efficiency of the central ring epoxidation and subsequent "deprotection" to return the olefin functionality provides an attractive tactic to manipulate photocyclizations of DPE-containing molecules. The method complements existing approaches for the synthesis of polycyclic aromatic hydrocarbons.[34] Conceptually, the steps involved are: (1) Disrupting conjugation to form an "isolated" DPE unit, (2) carrying out a Mallory reaction, then (3) reestablishing the conjugated system by reversing step 1.

Minimizing PIQ

Comparing the full series of DPE-containing rotor compounds (Table 2), we suggest two strategies for molecular design to minimize PIQ and optimize their solid-state emission. The propensity of DPE units to undergo photocyclization can be reduced by incorporating them as part of an extended conjugated system. **Ph$_7$C$_7$H**, ***sym*-** and ***asym*-PhenPh$_5$C$_7$H** have not shown spectroscopic evidence of rapid PIQ or synthetic evidence of Mallory reaction. They give Φ_{film} values of 1.7–6.7 %, which are higher than those measured for their epoxide counterparts with reduced conjugation. Alternatively, rotor compounds that are prone to PIQ can be treated with Mallory reaction conditions to purposefully exhaust the available photocyclization pathways. Our experiments have shown that ***sym*-phen$_2$Ph$_5$C$_7$H-O**, ***asym*-phen$_2$Ph$_5$C$_7$H-O** and ***sym*-phen$_3$PhC$_7$H** are all resistant to photocyclization under Mallory conditions. Their three-dimensional structures and remaining rotatable phenyl groups presumably contribute to them retaining their AIE properties. In the solid state, they give Φ_{film} values of 4.5–9.8 %, which exceed their precursors. Depending on the structure of the AIE compound and its intended use, one of these two strategies may be more appropriate than the other. Low molecular weight AIE luminogens may be required for use in some applications, which may place limitations on the length of the oligoalkenyl backbone that can be used.

© 2022 The Authors. Angewandte Chemie International Edition published by Wiley-VCH GmbH

15213773, 2022, 24, Downloaded from https://onlinelibrary.wiley.com/doi/10.1002/anie.202202193 by University Library, Wiley Online Library on [28/09/2023]. See the Terms and Conditions (https://onlinelibrary.wiley.com/terms-and-conditions) on Wiley Online Library for rules of use; OA articles are governed by the applicable Creative Commons License

Conclusion

In summary, by making minor structural changes to an AIE-active molecular rotor, **Ph_7C_7H**, we have exerted influence over the prevalence of PIQ and the formation of intramolecular phenyl-ring dimer excited states. PIQ is disfavored in these rotor compounds when their individual DPE units form part of a larger conjugated system. A parallel can be drawn to the related Mallory photocyclization reaction; compounds that are prone to PIQ undergo facile reaction to form annulated derivatives under Mallory conditions. We have leveraged this property by reversibly disrupting conjugation through epoxidation, which gives access to fused polyaromatics that were previously inaccessible through conventional aryl-aryl coupling reactions. These methods to manipulate the photophysical properties of oligoaryl alkene units can be exploited in the design of more efficient AIE materials or to improve photochemical syntheses of polycyclic aromatic hydrocarbons.

Acknowledgements

A.T.T., P.K.S. and A.N.B. gratefully acknowledge the Engineering and Physical Sciences Research Council (EPSRC) for Doctoral Training Grants (EP/N509462/1, EP/R513039/1, and EP/M507854/1, respectively). B.F.E.C. thanks the facilities of the Hamilton HPC Service of Durham University. P.R.M. acknowledges funding from the Northeast Centre for Energy Materials (NECEM). We thank Prof Ian Baxendale for useful discussions and access to a photoreactor.

Conflict of Interest

The authors declare no conflict of interest.

Data Availability Statement

The data that support the findings of this study are available in the Supporting Information of this article.

Keywords: Aggregation-Induced Emission · Carbocycles · Fluorescence · Molecular Rotors · Photochemistry

[1] K. Zhang, J. Liu, Y. Zhang, J. Fan, C. K. Wang, L. Lin, *J. Phys. Chem. C* **2019**, *123*, 24705.
[2] Y. Huang, J. Xing, Q. Gong, L. C. Chen, G. Liu, C. Yao, Z. Wang, H. L. Zhang, Z. Chen, Q. Zhang, *Nat. Commun.* **2019**, *10*, 169.
[3] Y. Hong, J. W. Y. Lam, B. Z. Tang, *Chem. Commun.* **2009**, 4332.
[4] H. Zhang, Z. Zhao, A. T. Turley, L. Wang, P. R. McGonigal, Y. Tu, Y. Li, Z. Wang, R. T. K. Kwok, J. W. Y. Lam, B. Z. Tang, *Adv. Mater.* **2020**, *32*, 2001457.
[5] S. Ma, S. Du, G. Pan, S. Dai, B. Xu, W. Tian, *Aggregate* **2021**, *2*, e96.
[6] A. Qin, B. Z. Tang, *Aggregation-Induced Emission: Fundamentals and Applications, Vol. 1–2*, Wiley, Hoboken, **2013**.
[7] Q. Peng, Z. Shuai, *Aggregate* **2021**, *2*, e91.
[8] Y. Tu, Z. Zhao, J. W. Y. Lam, B. Z. Tang, *Natl. Sci. Rev.* **2021**, *8*, nwaa260.
[9] J. Zhang, H. Zhang, J. W. Y. Lam, B. Z. Tang, *Chem. Res. Chin. Univ.* **2021**, *37*, 1.
[10] P. Zhou, P. Li, Y. Zhao, K. Han, *J. Phys. Chem. Lett.* **2019**, *10*, 6929.
[11] Y. Tu, J. Liu, H. Zhang, Q. Peng, J. W. Y. Lam, B. Z. Tang, *Angew. Chem. Int. Ed.* **2019**, *58*, 14911; *Angew. Chem.* **2019**, *131*, 15053.
[12] W. Ota, K. Takahashi, K. Higashiguchi, K. Matsuda, T. Sato, *J. Mater. Chem. C* **2020**, *8*, 8036.
[13] F. Würthner, *Angew. Chem. Int. Ed.* **2020**, *59*, 14192; *Angew. Chem.* **2020**, *132*, 14296.
[14] N. L. C. Leung, N. Xie, W. Yuan, Y. Liu, Q. Wu, Q. Peng, Q. Miao, J. W. Y. Lam, B. Z. Tang, *Chem. Eur. J.* **2014**, *20*, 15349.
[15] S. Suzuki, S. Sasaki, A. S. Sairi, R. Iwai, B. Z. Tang, G. Konishi, *Angew. Chem. Int. Ed.* **2020**, *59*, 9856; *Angew. Chem.* **2020**, *132*, 9940.
[16] J. Sturala, M. K. Etherington, A. N. Bismillah, H. F. Higginbotham, W. Trewby, J. A. Aguilar, E. H. C. Bromley, A.-J. Avestro, A. P. Monkman, P. R. McGonigal, *J. Am. Chem. Soc.* **2017**, *139*, 17882.
[17] H. Zhang, Z. Zhao, P. R. McGonigal, R. Ye, S. Liu, J. W. Y. Lam, R. T. K. Kwok, W. Z. Yuan, J. Xie, A. L. Rogach, B. Z. Tang, *Mater. Today* **2020**, *32*, 275.
[18] H. Zhang, B. Z. Tang, *JACS Au* **2021**, *1*, 1805.
[19] a) L. le Bras, C. Adamo, A. Perrier, *J. Phys. Chem. C* **2017**, *121*, 25603; b) K. Kokado, K. Sada, *Angew. Chem. Int. Ed.* **2019**, *58*, 8632; *Angew. Chem.* **2019**, *131*, 8724.
[20] X. L. Peng, S. Ruiz-Barragan, Z. S. Li, Q. S. Li, L. Blancafort, *J. Mater. Chem. C* **2016**, *4*, 2802.
[21] Q. Li, L. Blancafort, *Chem. Commun.* **2013**, *49*, 5966.
[22] H. T. Feng, C. Liu, Q. Li, H. Zhang, J. W. Y. Lam, B. Z. Tang, *ACS Mater. Lett.* **2019**, *1*, 192.
[23] H. Tong, Y. Hong, Y. Dong, M. Häußler, J. W. Y. Lam, Z. Li, Z. Guo, Z. Guo, B. Z. Tang, *Chem. Commun.* **2006**, 3705.
[24] "Photocyclization of Stilbenes and Related Molecules": F. B. Mallory, C. W. Mallory in *Organic Reactions*, *Vol. 30* (Ed.: W. G. Dauben), Wiley, New York, **1984**, pp. 1–456.
[25] N. Hoffmann, *Chem. Rev.* **2008**, *108*, 1052.
[26] A. G. Lvov, *J. Org. Chem.* **2020**, *85*, 8749.
[27] A. Ghosh, D. Csókás, M. Budanović, R. D. Webster, I. Pápai, M. C. Stuparu, *Chem. Sci.* **2021**, *12*, 3977.
[28] Y. Cai, L. Du, K. Samedov, X. Gu, F. Qi, H. H. Y. Sung, B. O. Patrick, Z. Yan, X. Jiang, H. Zhang, J. W. Y. Lam, I. D. Williams, D. Phillips, A. Qin, B. Z. Tang, *Chem. Sci.* **2018**, *9*, 4662.
[29] Deposition Numbers 2144322 (for ***asym*-phenPh_5C_7H**), 2144323 (for ***sym*-phenPh_5C_7H**), 2144324 (for **Ph_7C_7H-O**), 2144325 (for ***asym*-phenPh_5C_7H-O**), 2144326 (for ***sym*-phen$_2Ph_3C_7H$-O**), 2144327 (for ***sym*-phenPh_5C_7H-O**), 2144328 (for **Ph_3C_3·HCl_2**, see Supporting Information) contain the supplementary crystallographic data for this paper. These data are provided free of charge by the joint Cambridge Crystallographic Data Centre and Fachinformationszentrum Karlsruhe Access Structures service.
[30] N. A. Murugan, J. Kongsted, Z. Rinkevicius, H. Ågren, *Proc. Natl. Acad. Sci. USA* **2010**, *107*, 16453.
[31] Emission spectra are reported in eV and are Jacobian corrected to allow meaningful comparisons of Stokes shifts between compounds, see: J. Mooney, P. Kambhampati, *J. Phys. Chem. Lett.* **2013**, *4*, 3316.
[32] E. A. Chandross, H. T. Thomas, *J. Am. Chem. Soc.* **1972**, *94*, 2421.

© 2022 The Authors. Angewandte Chemie International Edition published by Wiley-VCH GmbH

15213773, 2022, 24, Downloaded from https://onlinelibrary.wiley.com/doi/10.1002/anie.202202193 by University Library, Wiley Online Library on [28/09/2023]. See the Terms and Conditions (https://onlinelibrary.wiley.com/terms-and-conditions) on Wiley Online Library for rules of use; OA articles are governed by the applicable Creative Commons License

[33] Unlike in similar reports of vibronic emission from TPE, decreasing the excitation energy to match a lower energy absorption band does not curb this phenomenon, see: M. P. Aldred, C. Li, M.-Q. Zhu, *Chem. Eur. J.* **2012**, *18*, 16037.
[34] M. Grzybowski, B. Sadowski, H. Butenschön, D. T. Gryko, *Angew. Chem. Int. Ed.* **2020**, *59*, 2998; *Angew. Chem.* **2020**, *132*, 3020.
[35] A. T. Turley, PhD thesis, University of Durham (UK), **2020**.
[36] R. Vaughan Williams, W. D. Edwards, P. Zhang, D. J. Berg, R. H. Mitchell, *J. Am. Chem. Soc.* **2012**, *134*, 16742.

Manuscript received: February 9, 2022
Accepted manuscript online: March 28, 2022
Version of record online: April 13, 2022

© 2022 The Authors. Angewandte Chemie International Edition published by Wiley-VCH GmbH

15213773, 2022, 24, Downloaded from https://onlinelibrary.wiley.com/doi/10.1002/anie.202202193 by University Library, Wiley Online Library on [28/09/2023]. See the Terms and Conditions (https://onlinelibrary.wiley.com/terms-and-conditions) on Wiley Online Library for rules of use; OA articles are governed by the applicable Creative Commons License

nature chemistry

Article

https://doi.org/10.1038/s41557-023-01156-7

Control of dynamic sp^3-C stereochemistry

Received: 11 March 2021

Accepted: 9 February 2023

Published online: 13 March 2023

Check for updates

Aisha N. Bismillah[1], Toby G. Johnson[1], Burhan A. Hussein[1], Andrew T. Turley[1], Promeet K. Saha[1], Ho Chi Wong[1], Juan A. Aguilar[1], Dmitry S. Yufit[1] & Paul R. McGonigal[1,2]

Stereogenic sp^3-hybridized carbon centres are fundamental building blocks of chiral molecules. Unlike dynamic stereogenic motifs, such as sp^3-nitrogen centres or atropisomeric biaryls, sp^3-carbon centres are usually fixed, requiring intermolecular reactions to undergo configurational changes. Here we report the internal enantiomerization of fluxional carbon cages and the consequences of their adaptive configurations for the transmission of stereochemical information. The sp^3-carbon stereochemistry of the rigid tricyclic cages is inverted through strain-assisted Cope rearrangements, emulating the low-barrier configurational dynamics typical for sp^3-nitrogen inversion or conformational isomerism. This dynamic enantiomerization can be stopped, restarted or slowed by external reagents, while the configuration of the cage is controlled by neighbouring, fixed stereogenic centres. As part of a phosphoramidite–olefin ligand, the fluxional cage acts as a conduit to transmit stereochemical information from the ligand while also transferring its dynamic properties to chiral-at-metal coordination environments, influencing catalysis, ion pairing and ligand exchange energetics.

The hugely varied three-dimensional (3D) structures—and therefore the hugely varied properties—of many organic molecules emerge from combining just a few types of atomic building blocks. For example, 19 of the 22 proteinogenic amino acids are formed solely from sp^2- or sp^3-hybridized carbon, nitrogen and oxygen atoms, capped by hydrogen substituents. Of this small array of elemental building blocks, it is tetrahedral sp^3-carbon[1–4] and sp^3-nitrogen[5–10] atoms that have the potential to form stereogenic centres, creating chiral structures.

Chirality also arises in organic molecules by virtue of motifs other than stereogenic atoms. However, although stereochemical inversion of some planar chiral motifs[11–13], helices[14–16] and stereogenic sp^3-nitrogen centres[7–10] can occur rapidly and reversibly through low-barrier conformational isomerism, sp^3-carbon centres cannot generally undergo spontaneous stereochemical changes. For example, the energy barrier to pyramidal inversion of methane is greater than its C–H bond dissociation energy[17–19]. Accordingly, unlike other stereogenic motifs[11–16], sp^3-carbon centres cannot generally adapt to surrounding chiral moieties and cannot be controllably switched by the application of external stimuli.

Instead, intermolecular reactions are usually necessary[20,21] to invert individual stereogenic carbon centres, proceeding through mechanisms involving high-energy bond-breaking and bond-making steps[22] with pentavalent transition states[20] (for example, S_N2 reactions) or trigonal intermediates[21], such as carbocations, carbanions or radicals. Of course, it is this stability of sp^3-carbon's tetrahedral geometry that makes it essential to the chiral skeletal diversity of organic compounds. It allows for predictable synthesis of configurationally stable molecules. Yet, the stability also limits the extent to which the complex 3D connectivity of aliphatic structures can exhibit dynamic, adaptive stereochemistry[23].

There have been impressive, but rare, examples of small covalent systems[24–28] capable of sp^3-carbon enantiomerization by low-barrier intramolecular processes. However, they do so without external control of their rate or direction to a single stereoisomer. Only multicomponent interlocked molecules, in which a ring shuttles along a prochiral axle[29,30], have been amenable to external control. There have been no compact and controllable dynamic sp^3-carbon building blocks. Therefore, it has not been possible to investigate the transmission of stereochemical information through such systems[7,9,10].

In this Article we report a series of chiral fluxional carbon cages[26–29] that exhibit responsive sp^3-carbon-centred stereochemistry, adapting to and transmitting surrounding stereochemical information.

[1]Department of Chemistry, Durham University, Durham, UK. [2]Department of Chemistry, University of York, York, UK. e-mail: paul.mcgonigal@york.ac.uk

https://doi.org/10.1038/s41557-023-01156-7

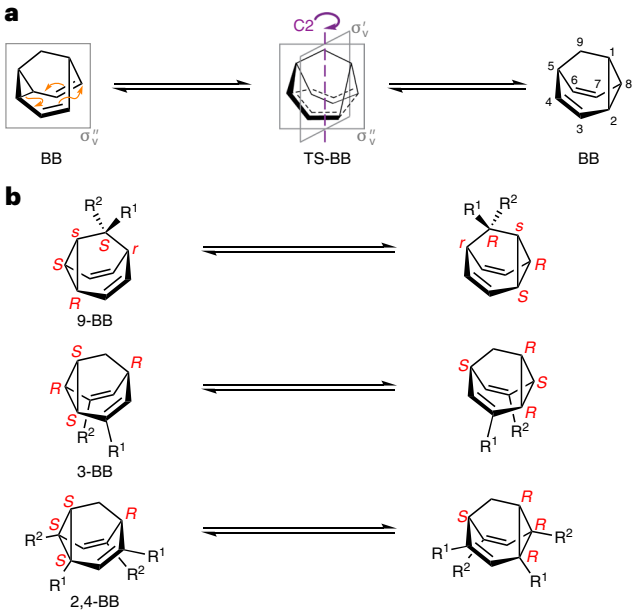

Fig. 1 | Multiple dynamic sp^3-carbon centres. a,**b**, Fluxional sp^3-carbon stereochemistry arises in BBs when the structures interchanged by their Cope rearrangements (**a**) are desymmetrized with any of the three substitution patterns shown in **b**. Cahn–Ingold–Prelog priorities are chosen to be $R^1 > C > R^2$ for the assignment of absolute configuration. When assigning a descriptor to position 9 of 9-BB, the cyclopropyl bridgehead C1 has precedence over the divinyl bridgehead C5 (Supplementary Fig. 1). 3-BB and 2,4-BB each have four chirotopic (*R*/*S*) centres, whereas the 9-BB pattern gives rise to five stereogenic centres, of which three are chirotopic and two are achirotopic (*r*/*s*).

By applying density functional theory (DFT) calculations and solution- and solid-state NMR spectroscopy, in combination with X-ray crystallography, we establish the extent to which their dynamic Cope rearrangements[31,32] are controlled by neighbouring, fixed stereogenic centres. We have found that a substantial energetic bias of more than 10 kJ mol^{-1} can be exercised over the stereochemical equilibria by a single fixed stereocentre. The rearrangements proceed rapidly at rates more commonly associated with low-barrier conformational changes of aliphatic systems (for example, a cyclohexane ring-flip energy barrier of ~43 kJ mol^{-1}) rather than a configurational change. We show that these rapid constitutional dynamics can be halted by covalent modification of the cage through a [2 + 2 + 2] cycloaddition reaction, then subsequently restarted after a cycloreversion. The rearrangement rate is also attenuated upon coordination of the fluxional cage to Pd(II) or Ru(II) as part of a phosphoramidite–olefin ligand. By its inclusion in the simple ligand design, the fluxional cage transmits stereochemical information to the metal ion—either through the covalent ligand backbone or by ion pairing with a chiral counterion. This property is exploited in enantioselective catalysis of an allylic substitution reaction, as well as in creating chiral-at-metal stereogenic centres that adopt the configurational dynamics of the cage.

Results

The Cope rearrangement of barbaralane (BB) is an example (Fig. 1a) of a narcissistic[25,33] automerization—it gives rise to a degenerate structure through a transition state (TS-BB) bearing an internal mirror plane (σ'_v) that is not present in the minimum energy structure. We noted that by desymmetrizing BB (Fig. 1b) using either a 9-BB, 3-BB or 2,4-BB substitution pattern, the mirror plane present at the energy minimum (σ''_v) is lost, while the mirror plane formed in the transition state (σ'_v) is retained. As a result, the Cope rearrangement inverts simultaneously some, or all, of the four or five stereogenic centres present in the structure. Given that the rearrangement of BB is known to proceed with a remarkably low free energy of activation, $\Delta G^{\ddagger}$, of 32.3 kJ mol^{-1} (Supplementary Table 7)[34–38], chiral 9-BB, 3-BB or 2,4-BB derivatives should undergo rapid enantiomerization.

Diastereomeric adaptation

We targeted 9-BB **1** (Fig. 2) as a convenient example of the 9-BB substitution pattern that bears a hydroxyl group for synthetic elaboration. The Cope rearrangement involving positions 2–8 of **1** (Fig. 2a) causes enantiomerization of the whole cage and formally inverts the stereochemistry of position 9 by effectively 'swapping' the cyclopropyl and alkene substituents connected to the stereocentre. Compound **1** was synthesized (Supplementary Scheme 1) by a three-step route from ethynyl magnesium bromide and tropylium tetrafluoroborate, using a gold-catalysed enyne cycloisomerization[39,40] to form the BB backbone. When labelling **1** and subsequent compounds, a single stereochemical descriptor is included to indicate the configuration at position 9 of the BB (Fig. 2a), for example, (*R*)-**1** and (*S*)-**1**, omitting the additional stereochemical labels of positions 1, 2, 5 and 8 for simplicity (Fig. 1). Treatment of **1** with Mosher's acid chloride (Fig. 2a) produces a set of Mosher's esters **2** in which the configurationally fixed stereocentre is introduced at a distance of three covalent bonds from the dynamic BB unit. An additional descriptor for the configuration of the Mosher's ester group is included in the labels for **2**. Derivatization with (*S*)-Mosher's acid gives a dynamic mixture of two diastereomers, (*R*,*S*)-**2** and (*S*,*S*)-**2**, whereas (*R*)-Mosher's acid gives (Fig. 2a) the antipodal mixture, (*S*,*R*)-**2** and (*R*,*R*)-**2**. Solutions of the two antipodal dynamic mixtures give opposite circular dichroism spectra (Fig. 3a), as would be expected.

DFT modelling using the ωB97X-D functional[41], 6-311++G(d,p) basis set[42,43] and a CS_2 polarizable continuum solvent model using the integral equation formalism variant[44] was employed to compare (Supplementary Table 7) the stereoisomerization energetics of BB, **1** and **2**. Using these parameters, the automerization of BB is predicted to proceed with a calculated activation free energy, $\Delta G^{\ddagger}_{calc}$, of 38.5 kJ mol^{-1}, which is ~6 kJ mol^{-1} higher than the experimentally measured[35] activation free energy, $\Delta G^{\ddagger}_{exp}$, of 32.3 kJ mol^{-1}, in keeping with previous DFT investigations[36,37]. DFT methods systematically overestimate the energy barrier to Cope rearrangement of BBs, but nevertheless allow useful comparisons of trends in activation energies and are known to predict accurately the relative energy minima of isomers[36,37]. The computationally predicted $\Delta G^{\ddagger}_{calc}$ values for **1** (38.0 kJ mol^{-1}) and **2** (35.5 kJ mol^{-1}) are very similar to BB, indicating that the hydroxyl or ester group substitutions at position 9 do not appreciably change the rapid kinetics.

The absence of the σ''_v mirror plane in **1** is evident (Fig. 3b) in its solution-state ^{1}H NMR spectrum—H3 and H7 are magnetically inequivalent, for example. However, the rapid enantiomerization induces a σ'_v mirror plane to the time-averaged structure of **1**, so only six distinct methine resonances are observed overall. The additional, fixed stereocentre of **2** breaks this σ'_v symmetry. Consequently, nine distinct signals corresponding to the BB methine groups are observed (Fig. 3b).

An energy difference, ΔG_{calc}, of 4.5 kJ mol^{-1} is computed (Supplementary Table 7) for the rearrangement of **2**. The influence of the (*S*)-Mosher's ester group moulds the configuration of the cage unit, which preferentially adopts its *S* form, biasing the equilibrium towards (*S*,*S*)-**2**. Consistent with this prediction, a single crystal (Fig. 2a) obtained from the dynamic (*S*)-Mosher's ester mixture was found to contain (*S*,*S*)-**2** as a frozen[34], single stereoisomer. An equal and opposite outcome is observed from the (*R*)-Mosher's ester mixture, giving the enantiomeric (*R*,*R*)-**2** solid-state structure.

To establish the nature of the dynamic solution-state mixtures, we compared (Fig. 3c) the solid-state $^{13}C\{^1H\}$ NMR spectrum of enantiopure (*R*,*R*)-**2** crystals to a spectrum obtained using a sample of the (*S*,*S*)-**2** crystals dissolved in 5:1 CS_2–CD_2Cl_2, generating a dynamic mixture of (*R*,*S*)-**2** and (*S*,*S*)-**2**. Cooling the solution to 159 K causes the BB $^{13}C\{^1H\}$ NMR resonances to enter the slow exchange regime.

https://doi.org/10.1038/s41557-023-01156-7

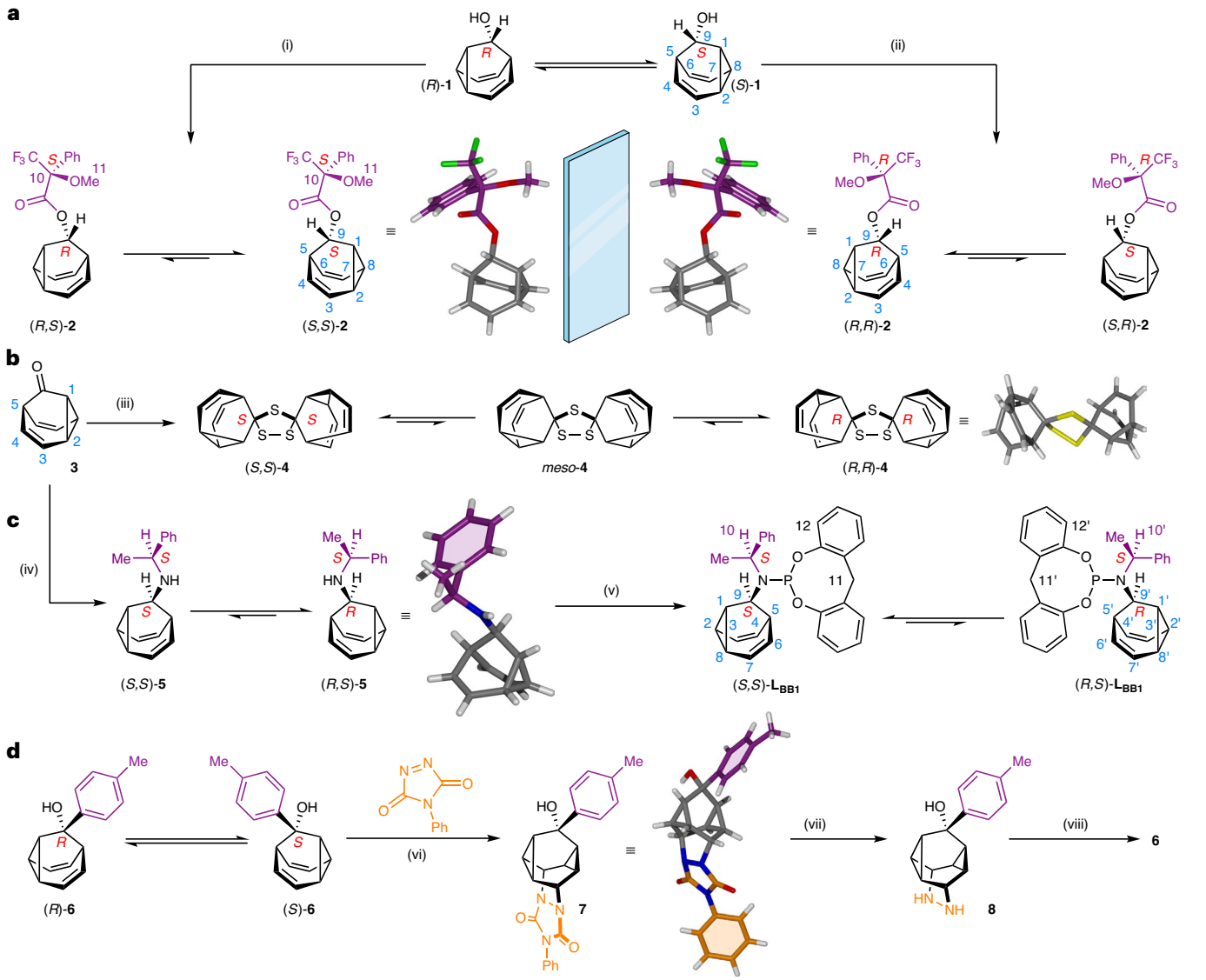

Fig. 2 | Diastereomeric adaptation and manipulation of chiral BBs. a,**b**, The dynamic sp^3-C stereochemical equilibrium of the BB cage is degenerate in **1** but becomes biased towards one stereoisomer upon attaching a chiral auxiliary (**a**) or by dimerization through a spirocyclic bridge (**b**). **c**, The position of the stereochemical equilibrium changes (and inverts) upon modifying the structure of a chiral auxiliary, remote from the BB unit. **d**, Further control of the sp^3-C stereochemistry is exerted by a cycloaddition reaction, which freezes and symmetrizes the structure, before subsequent cycloreversion re-establishes the dynamic stereochemical equilibrium. Reagents and conditions: (i) 1. (*S*)-MTPA, $(COCl)_2$, hexanes, DMF, room temperature (r.t.) to −20 °C, 16 h. 2. **1**, DMAP, Et_3N, $CHCl_3$, r.t., 5 d, 58%. (ii) 1. (*R*)-MTPA, $(COCl)_2$, hexanes, DMF, r.t. to −20 °C, 16 h. 2. **1**, DMAP, Et_3N, $CHCl_3$, r.t., 3 d, 79%. (iii) **3**, Lawesson's reagent, PhMe, 110 °C, 18 h, 13%. (iv) 1. **3**, (*S*)-1-phenylethylamine, AcOH, MeOH, r.t., 30 min. 2. $NaBH_3CN$, 100 °C, 16 h, 89%. (v) **5**, PCl_3, Et_3N, CH_2Cl_2, 0 °C, 3 h. 2. 2,2′-methylenediphenol, CH_2Cl_2, 0 °C to r.t., 16 h, 44%. (vi) **6**, PTAD, CH_2Cl_2, 50 °C, 24 h, 85%. (vii) **7**, NaOH, ^{i}PrOH, 85 °C, 24 h, taken on crude. (viii) $CuCl_2$, $HCl_{(aq)}$, 0 °C, 4 h, 48% from **7**. X-ray structures are shown in stick representation. Compound **4** crystallizes in a centrosymmetric space group, that is, (*S*,*S*)-**4** and (*R*,*R*)-**4** are both present, but only (*R*,*R*)-**4** is shown for clarity. Diffraction data for crystals of (*R*,*S*)-**5** allow only assignment of relative stereochemistry. MTPA, α-methoxy-α-trifluoromethylphenylacetic acid; DMF, *N*,*N*-dimethylformamide; DMAP, 4-(dimethylamino)pyridine; PTAD, phenyl-1,2,4-triazoline-3,5-dione.

As 159 K is only ~20 K below the observed coalescence temperature (Supplementary Fig. 66) for this low-barrier process, some resonances exhibit exchange broadening. At this low temperature, the decrease of available thermal energy causes the Boltzmann distribution to shift (Fig. 3d) further towards the lowest-energy isomer[34]. The solid-state chemical shifts of the BB sp^3-carbons 1, 2, 5, 8 and 9 are assigned (Fig. 3b) by comparison to the calculated chemical shifts of (*R*,*R*)-**2**. The resonances of the solution sample match up well with those of (*R*,*R*)-**2** in the solid state, allowing us to assign the resolved solution-state diastereomer as (*S*,*S*)-**2**. The solution-state analysis is thus consistent with the diastereomeric preference predicted by DFT and observed in the solid state. The 9-BB cage undergoes dynamic diastereomeric adaptation under the influence of the configurationally fixed Mosher's ester group.

The dynamic stereochemical equilibrium can also be biased in the absence of a fixed stereogenic element. Dimerization of two 9-BB-type cages through a spirocylic linkage breaks the degeneracy of the equilibrium. By treating (Fig. 2b) barbaralone **3** with Lawesson's reagent, we isolated trithiolane **4**, which undergoes dynamic rearrangements between an achiral isomer, *meso*-**4**, and a pair of enantiomers, (*S*,*S*)-**4** and (*R*,*R*)-**4**. A small ΔG_{calc} of 0.7 kJ mol^{-1} is predicted (Supplementary Table 7) to favour the pair of enantiomers over the *meso* form in the solution state. Single crystals grown from a solution of **4** contain a racemic mixture of the two chiral stereoisomers.

https://doi.org/10.1038/s41557-023-01156-7

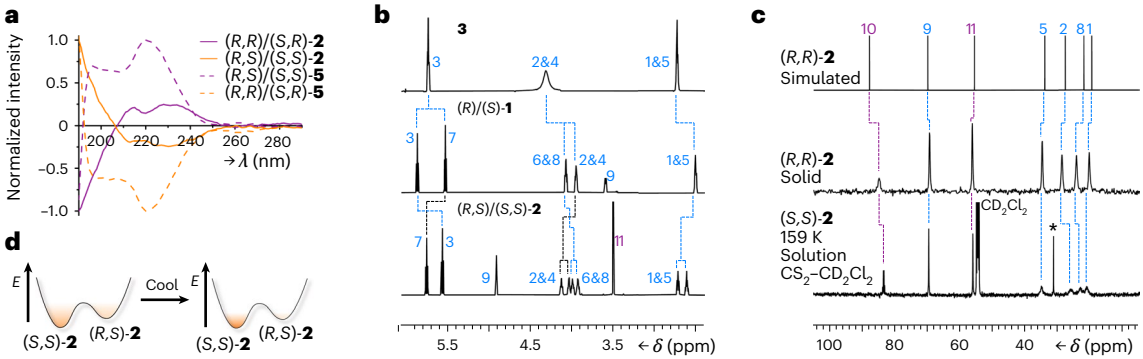

Fig. 3 | Spectroscopic evidence of sp^3-carbon adaptation to covalently tethered chiral auxiliaries. a, Normalized circular dichroism spectra of **2** (115 µM in MeCN) and **5** (210 µM in MeCN) confirm that antipodal equilibrium mixtures give equal and opposite absorbances. **b**, A comparison of partial solution ^{1}H NMR spectra ($CDCl_3$, 298 K) shows the reduced symmetry of the chiral 9-BB motif: top, **3** (700 MHz); middle, (*R*)/(*S*)-**1** (600 MHz); bottom, (*R*,*S*)/(*S*,*S*)-**2** (600 MHz). Resonances are labelled according to the numbering in Fig. 2. **c**, Comparison of partial $^{13}C\{^1H\}$ NMR spectra: top, solid-state chemical shifts calculated from the X-ray crystal structure of (*R*,*R*)-**2** in CASTEP v17.2[65] using the Perdew–Burke–Ernzerhof functional[66] and on-the-fly generated pseudopotentials; middle, (*R*,*R*)-**2** as a powder at ambient temperature (105 MHz); bottom, (*S*,*S*)-**2** as a solution in 5:1 CS_2–CD_2Cl_2 at low temperature (125 MHz, 159 K). The asterisk indicates the resonance of residual acetone. **d**, The Boltzmann distribution of isomers shifts towards a single stereoisomer at low temperatures; for example, a free energy difference of ~5 kJ mol^{-1} would give an ~90:10 equilibrium mixture at room temperature, but >98:2 at 159 K, so NMR data would be expected to show a single, major species, as is apparent when comparing the three spectra in **c**.

Further chemical modification to the substituent at position 9 can substantially influence, and even invert, the cage's equilibrium distribution. The chiral phosphoramidite–olefin[45–47] ligand $\mathbf{L_{BB1}}$ was synthesized (Fig. 2c) by first subjecting **3** to reductive amination with (*S*)-1-phenylethylamine to afford a mixture of (*S*,*S*)-**5** and (*R*,*S*)-**5**. Sequential treatment of the amine with PCl_3 then 2,2′-methylenediphenol affords $\mathbf{L_{BB1}}$. The 2,2′-methylenediphenol functionality was selected as it lacks fixed stereochemistry but has been shown to adopt dynamically chiral conformations as part of phosphoramidite ligands[45]. Comparing $\mathbf{L_{BB1}}$ to **5** reveals that the differing size and shape of the substituent at position 9 drives the dynamic stereochemical equilibria of the fluxional cage towards opposite configurations. The solution-phase equilibrium of the secondary amine is weighted (Supplementary Table 7) towards the (*R*,*S*)-**5** diastereomer by a ΔG_{calc} of 3.8 kJ mol^{-1}, matching the structure observed by X-ray analysis (Fig. 2c) of a single crystal. By contrast, the (*S*,*S*)-$\mathbf{L_{BB1}}$ diastereomer of the phosphoramidite is favoured with a ΔG_{calc} of 20.2 kJ mol^{-1}. The large magnitude of ΔG_{calc} for $\mathbf{L_{BB1}}$ highlights that the configurational dynamics of the 9-BB motif (Fig. 1) correlate with notable changes in its 3D shape[34] and, therefore, its energy. At the same time, the opposing stereochemistry of cages **5** and $\mathbf{L_{BB1}}$ demonstrates that the malleable sp^3-carbon configuration adapts to changes in the nearby steric environment.

Manipulating rates and transfer of stereochemistry

To exert further control over the fluxional enantiomerization, we sought to exploit the reactivity of the BBs' skipped diene units. The fluxional rearrangements can be stopped entirely by engaging the alkene units in covalent bonding, whereas coordination of the π electrons to a transition-metal ion[38] modulates the rearrangement rate instead.

An enantiomerizing mixture of 9-(*p*-tolyl)barbaralol **6** engages (Fig. 2d) in a [2 + 2 + 2] cycloaddition reaction with phenyl-1,2,4-triazoline-3,5-dione[48], giving rise to **7**. This reaction halts the rearrangement while also symmetrizing the structure by forming a second cyclopropyl group. Subsequently, the fluxional cage can be regenerated (Fig. 2d) in a two-step transformation through diazinane **8** (Supplementary Fig. 62), which undergoes cycloreversion with loss of N_2 upon oxidation with $CuCl_2$. Alternatively, coordination of Pd(II) (Fig. 4) or Ru(II) (Fig. 5) to $\mathbf{L_{BB1}}$ causes a reduction in the rate of the Cope rearrangement, as discussed below.

$\mathbf{L_{BB1}}$ and $PdCl_2$ form (Fig. 4a) a chiral-at-metal[49,50] complex, $\mathbf{L_{BB1}}PdCl_2$, linking the sp^3-carbon configurational inversion to the *A*/*C* isomerism[51] of the distorted trigonal bipyramidal (*TBPY*-5-12) coordination environment (Supplementary Fig. 2). Both possible stereoisomers, arising from coordination of (*S*,*S*)-$\mathbf{L_{BB1}}$ or (*R*,*S*)-$\mathbf{L_{BB1}}$ through their phosphorus centre and an alkene, are observed (Fig. 4a) in the X-ray crystal structure of the $\mathbf{L_{BB1}}PdCl_2$ complex. The alkene coordination is also evident (Fig. 4b) in the solution state by ^{1}H NMR spectroscopy. For comparison, a monodentate $\mathbf{L_{BB1}}AuCl$ complex (Fig. 4a) was prepared, which shows only small changes in the ^{1}H NMR chemical shifts of its alkene signals H3 and H7 relative to the free ligand (Fig. 4b). The room-temperature spectrum of $\mathbf{L_{BB1}}PdCl_2$, on the other hand, reveals a large change in the chemical shift of H7, consistent with coordination of Pd(II) to the alkene on the same face as the phosphoramidite group.

At 240 K, the ^{1}H NMR spectrum reveals (Fig. 4b) the two $\mathbf{L_{BB1}}PdCl_2$ isomers in slow exchange. Two sets of signals are observed in a 3:4 ratio, corresponding to a small free energy difference, ΔG_{exp}, of 0.5 kJ mol^{-1} between the two isomers. Consistent with this observation, DFT calculations predict (Supplementary Table 7) a small ΔG_{calc} of 1.8 kJ mol^{-1} in favour of (*C*,*R*,*S*)-$\mathbf{L_{BB1}}PdCl_2$.

Further NMR and DFT analyses elucidate the mechanism by which the $\mathbf{L_{BB1}}PdCl_2$ complex isomerizes. Depending on the placement and nature of substituents around the Cope substrate, metal coordination can either stabilize a charged, intermediate species as part of a stepwise associative rearrangement mechanism, or it can increase the rate of a concerted rearrangement pathway by stabilizing the transition state[52]. Consequently, Pd(II) salts and other cationic metal ions are known to accelerate Cope rearrangements[53,54]. Remarkably, coordination of the Pd(II) to one face of the fluxional cage in $\mathbf{L_{BB1}}PdCl_2$ has the opposite effect, slowing down the Cope rearrangement. Unlike **2**, for example, whose ^{1}H NMR resonances (499 MHz) enter the slow exchange regime below 160 K (Supplementary Fig. 64), the slower rearrangement of $\mathbf{L_{BB1}}PdCl_2$ is resolved by ^{1}H NMR spectroscopy at the higher temperature of 240 K. Using 2D ^{1}H–^{1}H exchange spectroscopy (EXSY) at 240 K (Fig. 4c), we measured a rate of exchange, *k*, of 6.48 s^{-1}, indicating a $\Delta G^{\ddagger}_{exp}$ of 54.6 kJ mol^{-1} for $\mathbf{L_{BB1}}PdCl_2$ (Fig. 4d). The DFT-calculated transition-state structure (Fig. 4e) shows pairs of equidistant C–C bonds, as would be expected for a coordination-coupled Cope (cc-Cope) rearrangement (Fig. 4a) in which the Pd(II) remains bound to the cage through a concerted rearrangement step. The DFT-predicted

https://doi.org/10.1038/s41557-023-01156-7

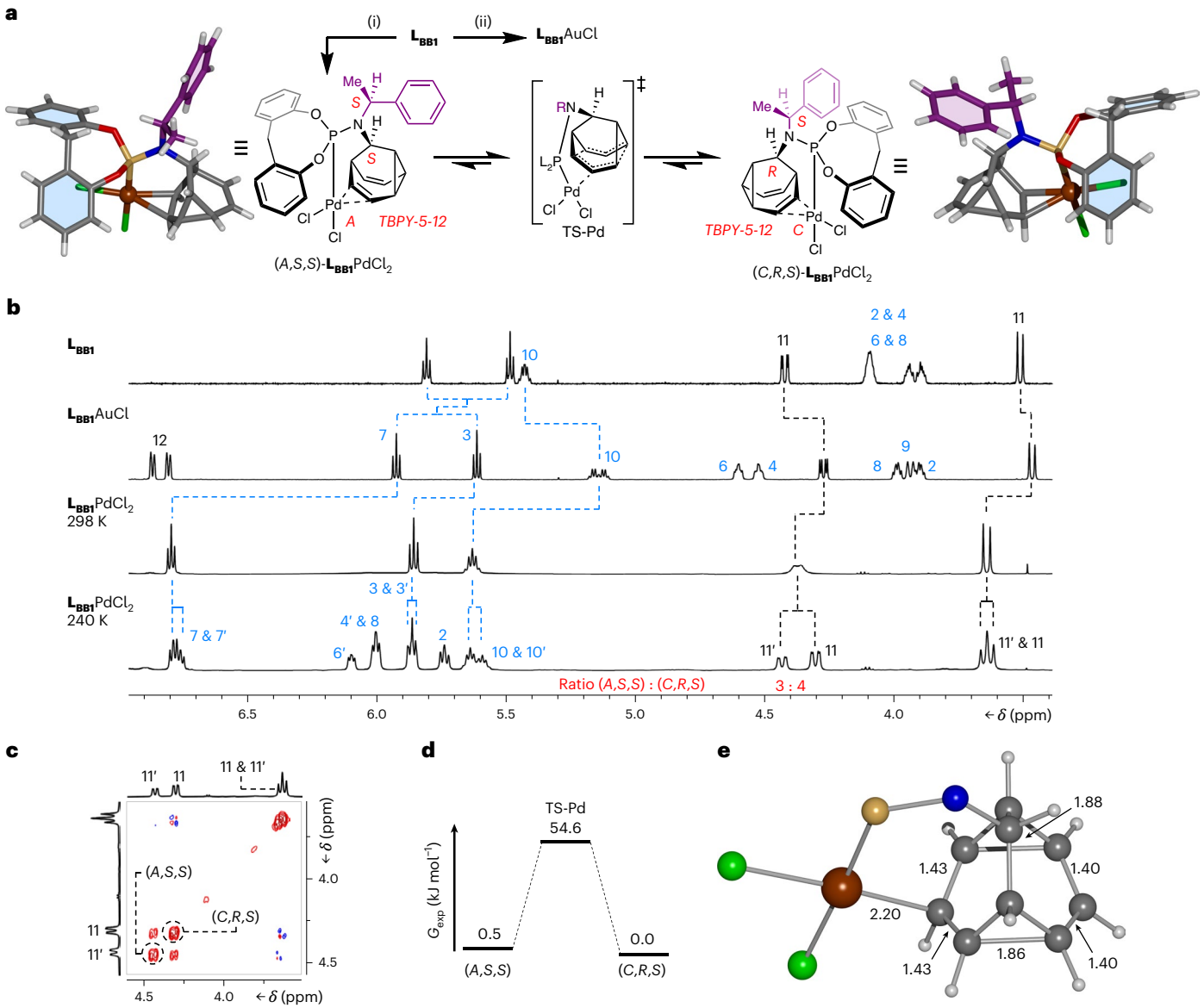

Fig. 4 | Transfer of dynamic sp^3-carbon stereochemistry in Au(I) and Pd(II) complexes. a, Bidentate coordination of $\mathbf{L}_{BB1}$ to $PdCl_2$ leads to cc-Cope rearrangement in which the Pd 'walks' along the side of the BB cage, modulating the rearrangement rate. For comparison, monodentate ligand coordination is observed with AuCl. Reagents and conditions: (i) $\mathbf{L}_{BB1}$, $PdCl_2(NCMe)_2$, $CDCl_3$, r.t., 15 min, 98%. (ii) $\mathbf{L}_{BB1}$, Me_2S·AuCl, $CDCl_3$, r.t., 10 min, 93%. X-ray crystal structures are shown in stick representation, with a ball for metal ions. Solvent molecules are omitted for clarity. Two structurally similar conformers of each $\mathbf{L}_{BB1}PdCl_2$ stereoisomer are present in the unit cell, but only one of each is shown for clarity. **b**, Partial ^{1}H NMR ($CDCl_3$) spectra: top, $\mathbf{L}_{BB1}$ (599 MHz, 298 K); second row, $\mathbf{L}_{BB1}$AuCl (599 MHz, 298 K); third row, $\mathbf{L}_{BB1}PdCl_2$ (499 MHz, 298 K); bottom, $\mathbf{L}_{BB1}PdCl_2$ (499 MHz, 240 K). Resonances are labelled according to the numbering for $\mathbf{L}_{BB1}$ in Fig. 2. The spectrum at 240 K shows the two $\mathbf{L}_{BB1}PdCl_2$ complexes in slow exchange in a ratio of 3:4. **c**, A partial ^{1}H-^{1}H EXSY NMR spectrum (499 MHz, $CDCl_3$, 240 K, mixing time τ_m = 200 ms) showing exchange peaks (red) between resonances of the minor ($H_{11'}$) and major (H_{11}) diastereomers as well as COSY peaks (blue) of geminal proton pairs. **d**, Free energy diagram for the cc-Cope rearrangement. **e**, Ball-and-stick representation of the DFT-calculated (ωB97X-D/6-311++G(d,p)/SDD/CS_2)[67] geometry of $\mathbf{L}_{BB1}PdCl_2$, showing the BB cage at the transition state, TS-Pd. A truncated structure omitting phosphorus and nitrogen substituents is shown for clarity with selected bond lengths given in ångstroms.

$\Delta G^{\ddagger}_{calc}$ of 60.6 kJ mol^{-1} for this cc-Cope mechanism matches well with the $\Delta G^{\ddagger}_{exp}$ of 54.6 kJ mol^{-1}.

These data indicate that the metal ion 'walks' along one side of the BB cage as the Cope rearrangement proceeds, moving back and forth in sync with the pericyclic reaction[52]. Consequently, the BB not only transmits the stereochemical information from the fixed sp^3-carbon stereocentre through its dynamic sp^3-carbon framework, biasing the chiral-at-metal configuration, but it also imparts a novel mechanism of intramolecular configurational change at a pentavalent stereocentre, which differs from the established pseudorotation and turnstile mechanisms[55].

The dynamic sp^3-carbon stereochemistry of $\mathbf{L}_{BB1}$ can also be linked to an intermolecular ligand exchange process. The cyclopentadienyl (Cp) half-sandwich Ru(II) complex[56] $\mathbf{L}_{BB1}$RuCp(NCMe)·PF_6 (Fig. 5) has a stereogenic, distorted square pyramidal Ru(II) centre (Supplementary Fig. 91) coordinated to a labile MeCN ligand. While cc-Cope rearrangements interconvert the *SPY*-5-21 and *SPY*-5-23 configurational isomers[51] (Fig. 5a), MeCN dissociation forms the distorted tetrahedral (*T*-4) chiral-at-metal species $\mathbf{L}_{BB1}$RuCp·PF_6, which mediates *A*/*C* stereochemical inversion.

Ru(II) coordination slows the Cope rearrangement sufficiently for a single stereoisomer to be resolved as a metastable species

https://doi.org/10.1038/s41557-023-01156-7

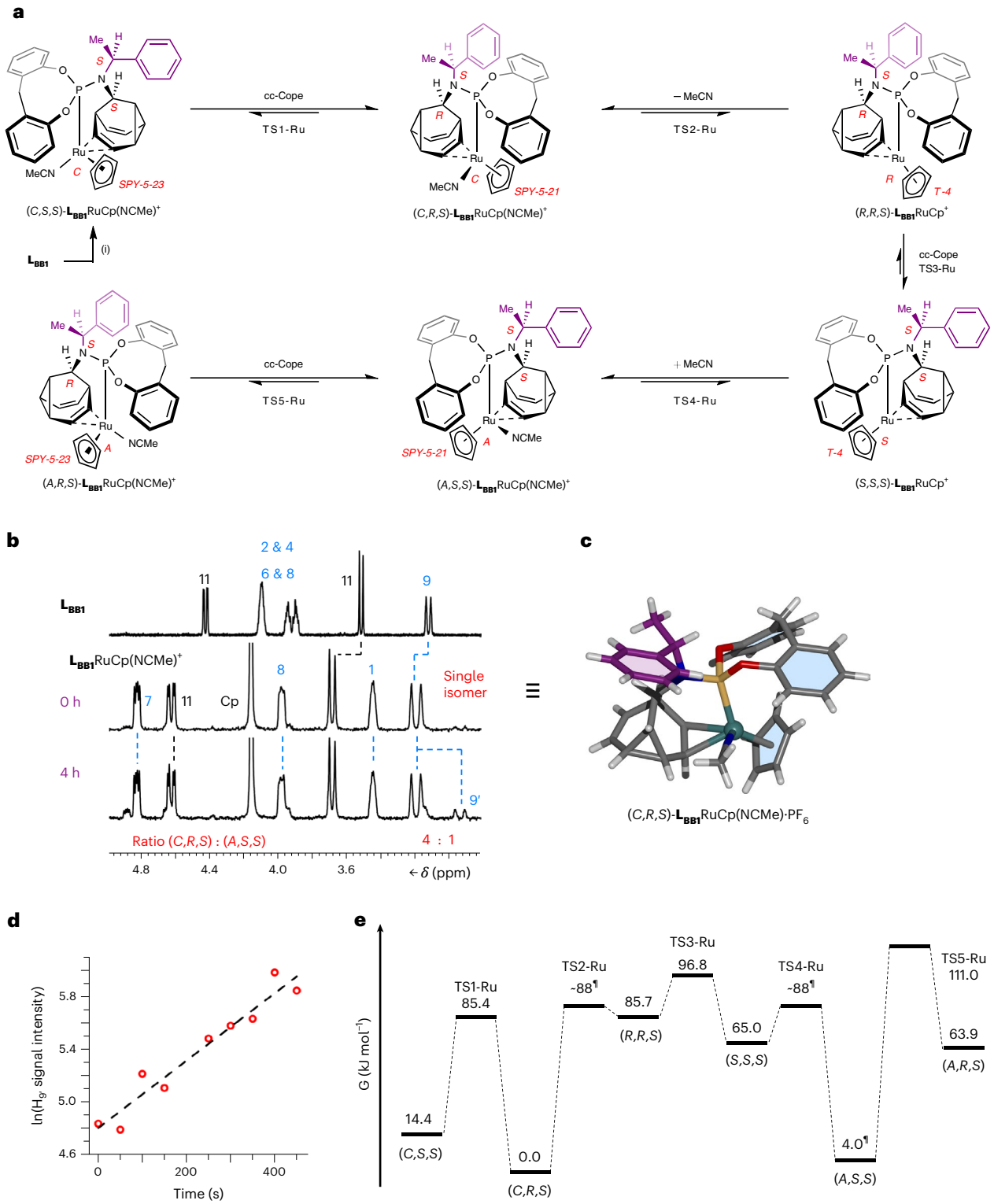

Fig. 5 | Transfer of dynamic sp^3-carbon stereochemistry in chiral-at-Ru(II) complexes. a, Four diastereomeric square pyramidal complexes are linked by cc-Cope rearrangements and exchange of an MeCN ligand, which proceeds through two intermediate tetrahedral complexes. A non-coordinated PF_6^- counterion is omitted from the structural formula of each complex for clarity. Reagents and conditions: (i) $\mathbf{L_{BB1}}$, $CpRu(NCMe)_3{\cdot}PF_6$, $CDCl_3$, r.t., 5 min, 69%. **b**, Comparison of the partial ^{1}H NMR ($CDCl_3$, 298 K) spectra: top, $\mathbf{L_{BB1}}$ (599 MHz); middle, a sample of $\mathbf{L_{BB1}}RuCp(NCMe){\cdot}PF_6$ analysed immediately after dissolving a crystalline sample (400 MHz); bottom, the same sample after allowing it to equilibrate for 4 h (400 MHz), revealing that an initially observed single isomer reaches a 4:1 equilibrium mixture. Resonances are labelled according to the numbering for $\mathbf{L_{BB1}}$ in Fig. 2. **c**, (C,R,S)-$\mathbf{L_{BB1}}RuCp(NCMe){\cdot}PF_6$ is identified in the solid-state X-ray crystal structure, which is shown in stick representation with a ball for the Ru(II) ion. Solvent molecules and the PF_6^- counterion are omitted for clarity. **d**, Integration of the ^{1}H NMR (400 MHz, $CDCl_3$, 298 K) resonance corresponding to H9′ of (A,S,S)-$\mathbf{L_{BB1}}RuCp(NCMe){\cdot}PF_6$ upon dissolving a crystalline sample of (C,R,S)-$\mathbf{L_{BB1}}RuCp(NCMe){\cdot}PF_6$ reveals a first-order increase in concentration with $k_{obs} = 2.56 \times 10^{-3}\ s^{-1}$. **e**, A potential energy surface for isomerization for the cc-Cope processes. Values of ΔG_{calc} and $\Delta G^{\ddagger}_{calc}$ (ωB97X-D/6-311++G(d,p)/SDD/CS_2)[67] are given except where ¶ indicates experimentally measured (**b**,**d**) equilibrium (ΔG_{exp}) and ligand exchange ($\Delta G^{\ddagger}_{exp}$) energies (in units of kJ mol^{-1}).

https://doi.org/10.1038/s41557-023-01156-7

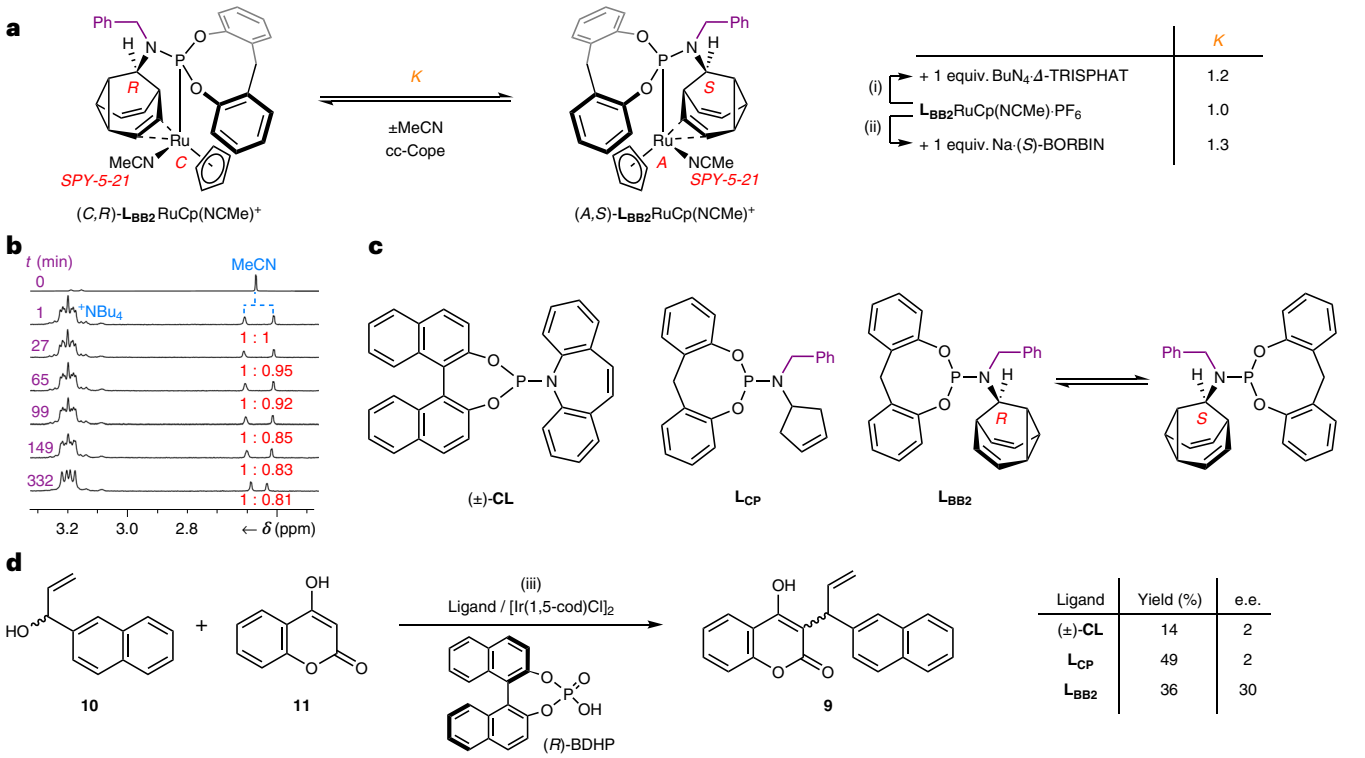

Fig. 6 | Chiral counterion-directed sp^3-carbon and chiral-at-metal stereochemistry applied to enantioselective catalysis. a, The enantiomerization of $\mathbf{L_{BB2}}$RuCp(NCMe)$^+$ is degenerate in the presence of an achiral counterion. In the presence of chiral anions, the ion-pair interactions break the degeneracy and bias the equilibrium towards one stereoisomer of the BB–metal complex, that is, $K \neq 1$. Note: only the two lowest-energy stereoisomers are shown for clarity. Reagents and conditions: (i) $\mathbf{L_{BB2}}$RuCp(NCMe)·PF_6, BuN_4·Δ-TRISPHAT, $CDCl_3$, r.t. (ii) $\mathbf{L_{BB2}}$RuCp(NCMe)·PF_6, Na·(*S*)-BORBIN, $CDCl_3$, r.t. **b**, Comparison of the partial ^{1}H NMR spectra (400 MHz, $CDCl_3$, 298 K) of $\mathbf{L_{BB2}}$RuCp(NCMe)·PF_6 before (top row) and after (other rows) the addition of 1 equiv. of BuN_4·Δ-TRISPHAT. Integration of the MeCN resonances shows that the initially racemic $\mathbf{L_{BB2}}$RuCp(NCMe)$^+$ ion gradually becomes enriched in one stereoisomer ($K = 1.2$). **c**,**d**, The stereoinduction (**c**) arising from three phosphoramidite ligands was compared in an iridium-catalysed allylic substitution (**d**). We hypothesize that the chiral anion formed in situ biases the stereochemical equilibrium of the cationic $\mathbf{L_{BB2}}$Ir π-allyl intermediate, leading to its improved performance relative to the control ligands lacking dynamic sp^3-C stereochemistry. Reagents and conditions: (iii) 1. [Ir(1,5-cod)Cl_2] (4 mol%), ligand (16 mol%), THF, 30 min, r.t. 2. (*R*)-BDHP (10 mol%), r.t., 24 h. Δ-TRISPHAT, Δ-tris(tetrachloro-1,2-benzenediolato)phosphate(V); (*S*)-BORBIN, bis[(*S*)-1,1′-bis-2-naphtholato]borate; 1,5-cod, 1,5-cyclooctadiene; (*R*)-BDHP, (*R*)-1,1′-binaphthyl-2,2′-diyl hydrogen phosphate.

under ambient conditions (Fig. 5b). Upon dissolving single crystals of $\mathbf{L_{BB1}}$RuCp(NCMe)·PF_6, obtained by slow evaporation, the ^{1}H NMR spectrum shows the presence of a single complex (Fig. 5b) with resonances distinct from non-coordinated $\mathbf{L_{BB1}}$. After allowing the sample to fully equilibrate at room temperature for four hours, a new set of peaks is observed (Fig. 5b) at a ratio of 4:1 in favour of the initially observed isomer, equivalent to a ΔG_{exp} of 4.0 kJ mol^{-1}. X-ray analysis (Fig. 5c) of the crystalline sample reveals the identity of the energetically favoured isomer to be (*C*,*R*,*S*)-$\mathbf{L_{BB1}}$RuCp(NCMe)·PF_6.

We measured the isomerization rate of (*C*,*R*,*S*)-$\mathbf{L_{BB1}}$RuCp(NCMe)·PF_6 by monitoring (Fig. 5d) the first-order growth in intensity of the resonance at 3.1 ppm corresponding to the H9′ signal of (*A*,*S*,*S*)-$\mathbf{L_{BB1}}$RuCp(NCMe)·PF_6—the isomer calculated (Fig. 5e) to be the next most stable stereoisomer. The k_{obs} of 2.56×10^{-3} s^{-1} at 298 K allows us to determine a $\Delta G^{\ddagger}_{exp}$ of 87.8 kJ mol^{-1}. Comparison of this value to (1) maxima of the computed potential energy surface (Fig. 5e), (2) a CD_3CN exchange experiment (Supplementary Fig. 70) and (3) literature measurements of MeCN dissociation from Cp half-sandwich Ru(II) complexes[55] suggests that the cc-Cope and MeCN exchange processes occur at similar rates. To achieve the (*C*,*R*,*S*)-to-(*A*,*S*,*S*) isomerization observed by NMR, the complex must undergo both ligand exchange and cc-Cope steps (Fig. 5e). Overall, the energetic bias towards (*C*,*R*,*S*)-$\mathbf{L_{BB1}}$RuCp(NCMe)·PF_6 and observation of its stepwise stereomutation to (*A*,*S*,*S*)-$\mathbf{L_{BB1}}$RuCp(NCMe)·PF_6 illustrate that the fluxional sp^3-carbon cage mediates the transfer of stereochemical information with high fidelity from the single, fixed benzylamino stereocentre through its rigid, tricyclic structure.

Dynamic stereocontrol by ion pairing

Having observed transmission of stereochemical information within the covalent frameworks of the $\mathbf{L_{BB1}}$ complexes, we investigated the influence of chiral counterions[57] on the degenerate enantiomerization (Fig. 6a) of the cationic $\mathbf{L_{BB2}}$RuCp(NCMe)$^+$ complex, which lacks a fixed stereocentre in its ligand structure. The complex was synthesized (Supplementary Scheme 3) as its hexafluorophosphate salt, $\mathbf{L_{BB2}}$RuCp(NCMe)·PF_6, in a manner analogous to its permanently chiral homologue $\mathbf{L_{BB1}}$RuCp(NCMe)·PF_6 (Fig. 5). X-ray analysis of single crystals confirmed (Supplementary Fig. 94) the expected structure of $\mathbf{L_{BB2}}$RuCp(NCMe)·PF_6 and revealed the presence (Supplementary Fig. 95) of both the (*C*,*R*)- and (*A*,*S*)-isomers in the crystal unit cell.

In the absence of chiral anions, a single ^{1}H NMR signal is observed for the coordinated MeCN ligand of $\mathbf{L_{BB2}}$RuCp(NCMe)·PF_6 in $CDCl_3$ solution (Fig. 6b). However, the addition of one molar equivalent of a chiral shift reagent, Bu_4N·Δ-TRISPHAT[58] (Fig. 6b) or Na·(*S*)-BORBIN[59] (Supplementary Fig. 71), splits the signal in two. Rapid and reversible counterion exchange in the presence of Bu_4N·Δ-TRISPHAT establishes an equilibrium mixture that includes diastereomeric ion pairs, for example, (*C*,*R*)-$\mathbf{L_{BB2}}$RuCp(NCMe)·Δ-TRISPHAT and (*A*,*S*)-$\mathbf{L_{BB2}}$RuCp(NCMe)·Δ-TRISPHAT, which give distinct NMR resonances. Therefore, by tracking the relative intensities of these resonances over time (Fig. 6b and Supplementary Fig. 72) we can monitor changes in sample composition as the chiral anion biases the $\mathbf{L_{BB2}}$RuCp(NCMe)$^+$ complex towards one stereoisomer. Under these conditions, the Δ-TRISPHAT sample evolves from a 1:1 mixture of stereoisomers to a

1:0.81 mixture over several hours, corresponding to an equilibrium constant, K, of 1.2, and $\Delta G_{exp} \approx 0.5$ kJ mol^{-1}. The timeframe of the sample's evolution is consistent with the slow kinetics of isomerization measured (Fig. 5) for $\mathbf{L_{BB1}}$RuCp(NCMe)·PF_6, suggesting that the stereomutation is again proceeding by cc-Cope and MeCN ligand exchange. The (*S*)-BORBIN sample reaches (Supplementary Fig. 72) a K of 1.3 over a similar time period. Overall, these experiments establish a means of noncovalent control of the BB stereochemistry. In principle, K could be further increased by removal or omission of any competing achiral anions (such as PF_6^-) from the reaction mixture and optimization of solvent and concentration.

Based on these results, we hypothesized that this counterion-directed stereochemistry of cationic $\mathbf{L_{BB2}}$ complexes could be exploited in enantioselective ion-pair catalysis[60]. Unusually, the fixed stereochemistry of the chiral anion would be passed to the catalytically active, fluxional metal complex to transiently generate an enantioenriched ligand framework in situ. To probe this concept, we screened $\mathbf{L_{BB2}}$ and two control ligands (Fig. 6c) in the enantioselective synthesis of **9** (Fig. 6d) through iridium-catalysed allylic substitution of alcohol **10** by hydroxycoumarin **11**[61]. We used chiral phosphoric acid (*R*)-BDHP, which we expected to protonate **10** and induce formation of the iridium-stabilized allylic cation intermediate while simultaneously generating an equivalent of a chiral phosphate anion. The optimized literature conditions[61] for this allylic substitution employ an achiral Lewis acid ($Yb(OTf)_3$) rather than a Brønsted acid to generate the allylic cation, in conjunction with enantiopure Carreira's[46] phosphoramidite–olefin ligand, **CL**, to impart enantioselectivity. Pleasingly, replacing these reagents with (*R*)-BDHP and racemic (±)-**CL** leads to the formation of **9**, albeit in just 14% isolated yield. Importantly, however, there is essentially no enantioinduction under the influence of (±)-**CL**. The product is obtained with a negligible enantiomeric excess (e.e.) of just 2%. It appears that the chiral phosphoric acid alone does little to override the stereochemical preference (or overall lack of it) arising from the racemic ligand. Using achiral phosphoramidite–olefin ligand $\mathbf{L_{CP}}$ leads to a similar outcome. $\mathbf{L_{CP}}$ bears many of the same structural features of $\mathbf{L_{BB2}}$, but with an achiral cyclopentene unit in place of the dynamically chiral 9-BB substructure. Compound **9** is produced in 49% yield and just 2% e.e. using $\mathbf{L_{CP}}$. Conversely, our fluxionally chiral ligand, $\mathbf{L_{BB2}}$, delivers an improved e.e. Using $\mathbf{L_{BB2}}$, we isolated **9** in 36% yield and 30% e.e. Contrasting this result with the outcome of the reactions using $\mathbf{L_{CP}}$ and (±)-**CL** supports the idea that the chiral phosphate counterion biases the covalent $\mathbf{L_{BB2}}$ ligand stereochemistry of the cationic intermediate complex (Supplementary Scheme 5), which in turn improves the enantioinduction in the key bond-forming step. Although the resulting e.e. is moderate for this particular set of reaction conditions, it suggests that the use of fluxional sp^3-carbon units may enhance the design of ligand frameworks for ion-pair catalysis[60] and other forms of enantioselective synthesis.

Conclusions

Cope rearrangements of chiral 9-BB cages simultaneously invert every stereogenic sp^3-carbon centre of their structures. These configurational rearrangements occur rapidly and reversibly, achieving the uncommon property of dynamic sp^3-carbon stereochemistry—one that has remained surprisingly rare since Le Bel[1] and van't Hoff[2] first identified tetrahedral carbon as a source of molecular chirality in 1874. Both the rate of sp^3-carbon inversion and the equilibrium distribution of isomers are sensitive to changes in the 9-BB structure. On the one hand, the dynamics of the rearrangement processes are controlled through manipulation of covalent bonding or metal coordination of the 9-BB olefin groups, providing convenient functional handles. On the other hand, the cage adapts its configuration to minimize steric interactions with nearby fixed stereogenic elements and, in so doing, is able to transmit the stereochemical information across its rigid, tricyclic backbone. When interfaced with transition-metal complexes, the dynamic cage conveys a stereochemical preference to the chiral-at-metal[49,50] centre. Controllable and adaptable sp^3-carbon stereochemistry of this kind can be exploited in enantioselective synthesis[7,9,10,30,45,62,63] and chiral functional materials[64].

Online content

Any methods, additional references, Nature Portfolio reporting summaries, source data, extended data, supplementary information, acknowledgements, peer review information; details of author contributions and competing interests; and statements of data and code availability are available at https://doi.org/10.1038/s41557-023-01156-7.

References

1. Le Bel, J. A. Sur les relations qui existent entre les formules atomiques des corps organiques, et le pouvoir rotatoire de leurs dissolutions. *Bull. Soc. Chim. Fr.* **22**, 337–347 (1874).
2. van't Hoff, J. H. Sur les formules de structure dans l'espace. *Arch. Néerl.* **9**, 445–454 (1874).
3. Eliel, E. L. & Wilen, S. H. *Stereochemistry of Organic Compounds* (Wiley, 1994).
4. Quasdorf, K. W. & Overman, L. E. Catalytic enantioselective synthesis of quaternary carbon stereocentres. *Nature* **516**, 181–191 (2014).
5. Brois, S. J. Aziridines. XII. Isolation of a stable nitrogen pyramid. *J. Am. Chem. Soc.* **90**, 508–509 (1968).
6. Kizirian, J. C. Chiral tertiary diamines in asymmetric synthesis. *Chem. Rev.* **108**, 140–205 (2008).
7. Sibi, M. P., Zhang, R. & Manyem, S. A new class of modular chiral ligands with fluxional groups. *J. Am. Chem. Soc.* **125**, 9306–9307 (2003).
8. Rowley, J. H., Yau, S. C., Kariuki, B. M., Kennedy, A. R. & Tomkinson, N. C. O. Readily accessible chiral at nitrogen cage structures. *Org. Biomol. Chem.* **11**, 2198–2205 (2013).
9. Adachi, S., Takeda, N. & Sibi, M. P. Evaluation of achiral templates with fluxional Brønsted basic substituents in enantioselective conjugate additions. *Org. Lett.* **16**, 6440–6443 (2014).
10. Dean, C. et al. Readily accessible sp^3-rich cyclic hydrazine frameworks exploiting nitrogen fluxionality. *Chem. Sci.* **11**, 1636–1642 (2020).
11. Fa, S., Egami, K., Adachi, K., Kato, K. & Ogoshi, T. Sequential chiral induction and regulator-assisted chiral memory of pillar[5]arenes. *Angew. Chem. Int. Ed.* **59**, 20353–20356 (2020).
12. Liang, H. et al. Acid/base-tunable unimolecular chirality switching of a pillar[5]azacrown *pseudo*[1]catenane. *J. Am. Chem. Soc.* **142**, 19772–19778 (2020).
13. Xiao, C. et al. Redox-triggered chirality switching and guest-capture/release with a pillar[6]arene-based molecular universal joint. *Angew. Chem. Int. Ed.* **59**, 8094–8098 (2020).
14. Akine, S., Sairenji, S., Taniguchi, T. & Nabeshima, T. Stepwise helicity inversions by multisequential metal exchange. *J. Am. Chem. Soc.* **135**, 12948–12951 (2013).
15. Chen, X. et al. A helicate-based three-state molecular switch. *Angew. Chem. Int. Ed.* **57**, 11817–11820 (2018).
16. Katoono, R., Sakamoto, K. & Suzuki, T. Dual dynamic chirality generated in the assembly of three achiral rods through the three-fold twisting of a macrocycle. *Chem. Commun.* **55**, 5503–5506 (2019).
17. Hoffmann, R., Alder, R. W. & Wilcox, C. F. Planar tetracoordinate carbon. *J. Am. Chem. Soc.* **92**, 4992–4993 (1970).
18. Gordon, M. S. & Schmidt, M. W. Does methane invert through square planar? *J. Am. Chem. Soc.* **115**, 7486–7492 (1993).
19. Rasmussen, D. R. & Radom, L. Planar-tetracoordinate carbon in a neutral saturated hydrocarbon: theoretical design and characterization. *Angew. Chem. Int. Ed.* **38**, 2876–2878 (1999).
20. Walden, P. Ueber die gegenseitige Umwandlung optischer Antipoden. *Ber. Dtsch. Chem. Ges.* **29**, 133–138 (1896).

21. Kancharla, P. K., Kato, T. & Crich, D. Probing the influence of protecting groups on the anomeric equilibrium in sialic acid glycosides with the persistent radical effect. *J. Am. Chem. Soc.* **136**, 5472–5480 (2014).
22. Sugiyama, S. et al. A novel dynamic kinetic resolution accompanied by intramolecular transesterification: asymmetric synthesis of a 4-hydroxymethyl-2-oxazolidinone from serinol derivatives. *Tetrahedron* **59**, 3417–3425 (2003).
23. Wolf, C. *Dynamic Stereochemistry of Chiral Compounds* (RSC, 2007).
24. Kim, B. et al. Stereodynamic quinone-hydroquinone molecules that enantiomerize at sp^3-carbon via redox-interconversion. *J. Am. Chem. Soc.* **139**, 15239–15244 (2017).
25. Gillick-Healy, M. W. et al. Two independent orthogonal stereomutations at a single asymmetric center: a narcissistic couple. *Chem. A Eur. J.* **23**, 2332–2339 (2017).
26. He, M. & Bode, J. W. Racemization as a stereochemical measure of dynamics and robustness in shape-shifting organic molecules. *Proc. Natl. Acad. Sci. USA* **108**, 14752–14756 (2011).
27. Yahiaoui, O., Patel, H. D., Chinner, K. S., Pašteka, L. F. & Fallon, T. Stereomutation of substituted bullvalenes. *Org. Lett.* **23**, 1157–1162 (2021).
28. Sanchez, A. & Maimone, T. J. Taming shapeshifting anions: total synthesis of ocellatusone C. *J. Am. Chem. Soc.* **144**, 7594–7599 (2022).
29. Alvarez-Pérez, M., Goldup, S. M., Leigh, D. A. & Slawin, A. M. Z. A chemically-driven molecular information ratchet. *J. Am. Chem. Soc.* **130**, 1836–1838 (2008).
30. Dommaschk, M., Echavarren, J., Leigh, D. A., Marcos, V. & Singleton, T. A. Dynamic control of chiral space through local symmetry breaking in a rotaxane organocatalyst. *Angew. Chem. Int. Ed.* **58**, 14955–14958 (2019).
31. Cope, A. C. & Hardy, E. M. The introduction of substituted vinyl groups. V. A rearrangement involving the migration of an allyl group in a three-carbon system. *J. Am. Chem. Soc.* **62**, 441–444 (1940).
32. Bismillah, A. N., Chapin, B. M., Hussein, B. A. & McGonigal, P. R. Shapeshifting molecules: the story so far and the shape of things to come. *Chem. Sci.* **11**, 324–332 (2020).
33. Salem, L. et al. Narcissistic reactions. *J. Am. Chem. Soc.* **92**, 4472–4474 (1970).
34. Bismillah, A. N. et al. Shape-selective crystallisation of fluxional carbon cages. *Chem. Sci.* **9**, 8631–8636 (2018).
35. Günther, H., Runsink, J., Schmickler, H. & Schmitt, P. Applications of ^{13}C NMR spectroscopy. 26. Activation parameters for the degenerate Cope rearrangement of barbaralane and 3,7-disubstituted barbaralanes. *J. Org. Chem.* **50**, 289–293 (1985).
36. Ma, Y. Y. et al. Probing the fluxional bonding nature of rapid Cope rearrangements in bullvalene $C_{10}H_{10}$ and its analogs C_8H_8, C_9H_{10} and C_8BH_9. *Sci. Rep.* **9**, 17074 (2019).
37. Karton, A. Can density functional theory 'Cope' with highly fluxional shapeshifting molecules? *Chem. Phys.* **540**, 111013 (2021).
38. Aumann, R. & Runge, M. Organische Synthesen mit übergangsmetall-Komplexen, 57. 4,5-Homotropilidene durch intramolekulare Cyclopropanierung von (cycloheptatrienylmethyl)carbenchrom-oder-Wolfram-Komplexen. *Chem. Ber.* **125**, 259–264 (1992).
39. McGonigal, P. R. et al. Gold for the generation and control of fluxional barbaralyl cations. *Angew. Chem. Int. Ed.* **51**, 13093–13096 (2012).
40. Ferrer, S. & Echavarren, A. M. Synthesis of barbaralones and bullvalenes made easy by gold catalysis. *Angew. Chem. Int. Ed.* **55**, 11178–11182 (2016).
41. Chai, J.-D. & Head-Gordon, M. Long-range corrected hybrid density functionals with damped atom-atom dispersion corrections. *Phys. Chem. Chem. Phys.* **10**, 6615–6620 (2008).
42. Krishnan, R., Binkley, J. S., Seeger, R. & Pople, J. A. Self-consistent molecular orbital methods. XX. A basis set for correlated wave functions. *J. Chem. Phys.* **72**, 650–654 (1980).
43. Clark, T., Chandrasekhar, J., Spitznagel, G. W. & Schleyer, P. V. R. Efficient diffuse function-augmented basis sets for anion calculations. III. The 3-21+G basis set for first-row elements, Li–F. *J. Comput. Chem.* **4**, 294–301 (1983).
44. Miertuš, S. & Tomasi, J. Approximate evaluations of the electrostatic free energy and internal energy changes in solution processes. *Chem. Phys.* **65**, 239–245 (1982).
45. Wakabayashi, K., Aikawa, K., Kawauchi, S. & Mikami, K. Catalyst self-adaptation in conjugate addition to nitroalkenes and nitroacrylates: instant chirality control in diphenylmethane-based phosphoramidite ligands. *J. Am. Chem. Soc.* **130**, 5012–5013 (2008).
46. Rössler, S. L., Petrone, D. A. & Carreira, E. M. Iridium-catalyzed asymmetric synthesis of functionally rich molecules enabled by (phosphoramidite, olefin) ligands. *Acc. Chem. Res.* **52**, 2657–2672 (2019).
47. Teichert, J. F. & Feringa, B. L. Phosphoramidites: privileged ligands in asymmetric catalysis. *Angew. Chem. Int. Ed.* **49**, 2486–2528 (2010).
48. De Bruycker, K. et al. Triazolinediones as highly enabling synthetic tools. *Chem. Rev.* **116**, 3919–3974 (2016).
49. Bauer, E. B. Chiral-at-metal complexes and their catalytic applications in organic synthesis. *Chem. Soc. Rev.* **41**, 3153–3167 (2012).
50. Zhou, Z. et al. Non-C_2-symmetric chiral-at-ruthenium catalyst for highly efficient enantioselective intramolecular C(sp^3)-H amidation. *J. Am. Chem. Soc.* **141**, 19048–19057 (2019).
51. Connelly, N. G. et al. (eds) *Nomenclature of Inorganic Chemistry: IUPAC Recommendations 2005* (RSC, 2005).
52. Siebert, M. R. & Tantillo, D. J. Transition-state complexation in palladium-promoted [3,3] sigmatropic shifts. *J. Am. Chem. Soc.* **129**, 8686–8687 (2007).
53. Jiao, H. & von Ragué Schleyer, P. Elimination of the barrier to Cope rearrangement in semibullvalene by Li^+ complexation. *Angew. Chem. Int. Ed. Engl.* **32**, 1760–1763 (1993).
54. Tantillo, D. J. Speeding up sigmatropic shifts—to halve or to hold. *Acc. Chem. Res.* **49**, 741–749 (2016).
55. Couzijn, E. P. A., Slootweg, J. C., Ehlers, A. W. & Lammertsma, K. Stereomutation of pentavalent compounds: validating the Berry pseudorotation, redressing Ugi's turnstile rotation, and revealing the two- and three-arm turnstiles. *J. Am. Chem. Soc.* **132**, 18127–18140 (2010).
56. Luginbühl, W. et al. Structure and reactivity of ruthenium half-sandwich compounds: crystal and molecular structure and acetonitrile exchange kinetics and mechanism of Ru(η^6-C_6H_6)$(CH_3CN)_3^{2+}$ and Ru(η^5-C_5H_5)$(CH_3CN)^{3+}$. *Inorg. Chem.* **30**, 2350–2355 (1991).
57. Corra, S. et al. Chemical on/off switching of mechanically planar chirality and chiral anion recognition in a [2]rotaxane molecular shuttle. *J. Am. Chem. Soc.* **141**, 9129–9133 (2019).
58. Lacour, J., Ginglinger, C., Favarger, F. & Torche-Haldimann, S. Application of TRISPHAT anion as NMR chiral shift reagent. *Chem. Commun.* **1997**, 2285–2286 (1997).
59. Raskatov, J. A., Brown, J. M. & Thompson, A. L. Chiral selection in the formation of borates from racemic binaphthols and related diols. *CrystEngComm* **13**, 2923–2929 (2011).
60. Fanourakis, A., Williams, B. D., Paterson, K. J. & Phipps, R. J. Enantioselective intermolecular C–H amination directed by a chiral cation. *J. Am. Chem. Soc.* **143**, 10070–10076 (2021).
61. Xu, R. et al. Direct enantioselective allylic substitution of 4-hydroxycoumarin derivatives with branched allylic alcohols via iridium catalysis. *Chem. Commun.* **56**, 8404–8407 (2020).
62. Wang, J. & Feringa, B. L. Dynamic control of chiral space. *Science* **331**, 1429–1432 (2011).

63. Heard, A. W. & Goldup, S. M. Synthesis of a mechanically planar chiral rotaxane ligand for enantioselective catalysis. *Chem* **6**, 994–1006 (2020).
64. Morrow, S. M., Bissette, A. J. & Fletcher, S. P. Transmission of chirality through space and across length scales. *Nat. Nanotechnol.* **12**, 410–419 (2017).
65. Clark, S. J. et al. First principles methods using CASTEP. *Z. Kristallogr.* **220**, 567–570 (2005).
66. Perdew, J. P., Burke, K. & Ernzerhof, M. Generalized gradient approximation made simple. *Phys. Rev. Lett.* **77**, 3865–3868 (1996).
67. Andrae, D., Häußermann, U., Dolg, M., Stoll, H. & Preuß, H. Energy-adjusted ab initio pseudopotentials for the second and third row transition elements. *Theor. Chim. Acta* **77**, 123–141 (1990).

Publisher's note Springer Nature remains neutral with regard to jurisdictional claims in published maps and institutional affiliations.

Open Access This article is licensed under a Creative Commons Attribution 4.0 International License, which permits use, sharing, adaptation, distribution and reproduction in any medium or format, as long as you give appropriate credit to the original author(s) and the source, provide a link to the Creative Commons license, and indicate if changes were made. The images or other third party material in this article are included in the article's Creative Commons license, unless indicated otherwise in a credit line to the material. If material is not included in the article's Creative Commons license and your intended use is not permitted by statutory regulation or exceeds the permitted use, you will need to obtain permission directly from the copyright holder. To view a copy of this license, visit http://creativecommons.org/licenses/by/4.0/.

© The Author(s) 2023

Data availability

Crystallographic data for the structures reported in this Article have been deposited at the Cambridge Crystallographic Data Centre, under deposition numbers CCDC 2068012 (**1**), 2068013 (**4**), 2068014 ((*R*,*S*)-**5**), 2068015 ((*S*,*S*)-**2**), 2068016 ((*R*,*R*)-**2**), 2068017 (**7**), 2068018 ($\mathbf{L_{BB1}}PdCl_2$), 2068019 (**S2**), 2068020 ((*C*,*R*,*S*)-$\mathbf{L_{BB1}}$RuCp(NCMe)·PF_6) and 2173984 ($\mathbf{L_{BB2}}$RuCp(NCMe)·PF_6). Copies of the data can be obtained free of charge via https://www.ccdc.cam.ac.uk/structures/. All other data supporting the findings of this study are available within the paper and its Supplementary Information.

Acknowledgements

A.N.B., A.T.T. and P.K.S. acknowledge Engineering and Physical Sciences Research Council (EPSRC) doctoral training grants. A.N.B. acknowledges grant support from Funds for Women Graduates. B.A.H. and H.C.W. thank the EPSRC Centres for Doctoral Training in Soft Matter and Functional Interfaces (SOFI) and Renewable Energy Northeast Universities (ReNU), respectively, for PhD studentships. B.A.H. acknowledges scholarships from the Society of Chemical Industry (SCI) and the Natural Sciences and Engineering Research Council of Canada (NSERC). A.N.B. and P.R.M. acknowledge a Leverhulme Trust Research Project Grant (RPG-2020-218). P.R.M. thanks the EPSRC for an Early Career Fellowship (EP/V040049/1). We thank D. Apperley for assistance with solid-state NMR measurements and L. Lauchlan and A. Congreve for chiral HPLC.

Author contributions

A.N.B. synthesized **3** and **6**, carried out variable-temperature NMR spectroscopy, performed chiral anion experiments and enantioselective catalysis, and prepared the Supplementary Information. T.G.J. synthesized **2**, **4** and **5** and performed CD spectroscopy. B.A.H. and A.T.T. optimized the trapping and release of **6** by cycloaddition. A.N.B., P.K.S., A.T.T. and H.C.W. performed the preliminary experiments. J.A.A. assisted with NMR measurements. D.S.Y. solved X-ray crystal structures. A.N.B. and P.R.M. synthesized the ligands and metal complexes. P.R.M. conceived and directed the research, carried out DFT calculations and wrote the manuscript. All authors analysed the data and revised the manuscript.

Competing interests

The authors declare no competing interests.

Additional information

Supplementary information The online version contains supplementary material available at https://doi.org/10.1038/s41557-023-01156-7.

Correspondence and requests for materials should be addressed to Paul R. McGonigal.

Peer review information *Nature Chemistry* thanks the anonymous reviewer(s) for their contribution to the peer review of this work.

Reprints and permissions information is available at www.nature.com/reprints.